NanoScience and Technology

Gregor Hlawacek
Armin Gölzhäuser *Editors*

Helium Ion Microscopy

NanoScience and Technology

Series editors

Phaedon Avouris, Yorktown Heights, USA
Bharat Bhushan, Columbus, USA
Dieter Bimberg, Berlin, Germany
Cun-Zheng Ning, Tempe, USA
Klaus von Klitzing, Stuttgart, Germany
Roland Wiesendanger, Hamburg, Germany

The series NanoScience and Technology is focused on the fascinating nano-world, mesoscopic physics, analysis with atomic resolution, nano and quantum-effect devices, nanomechanics and atomic-scale processes. All the basic aspects and technology-oriented developments in this emerging discipline are covered by comprehensive and timely books. The series constitutes a survey of the relevant special topics, which are presented by leading experts in the field. These books will appeal to researchers, engineers, and advanced students.

More information about this series at http://www.springer.com/series/3705

Gregor Hlawacek · Armin Gölzhäuser
Editors

Helium Ion Microscopy

Editors
Gregor Hlawacek
Institute of Ion Beam Physics
and Materials Research
Helmholtz-Zentrum Dresden-Rossendorf
Dresden
Germany

Armin Gölzhäuser
Physics of Supramolecular Systems
and Surfaces
Bielefeld University
Bielefeld
Germany

ISSN 1434-4904 ISSN 2197-7127 (electronic)
NanoScience and Technology
ISBN 978-3-319-41988-6 ISBN 978-3-319-41990-9 (eBook)
DOI 10.1007/978-3-319-41990-9

Library of Congress Control Number: 2016946009

© Springer International Publishing Switzerland 2016
This work is subject to copyright. All rights are reserved by the Publisher, whether the whole or part of the material is concerned, specifically the rights of translation, reprinting, reuse of illustrations, recitation, broadcasting, reproduction on microfilms or in any other physical way, and transmission or information storage and retrieval, electronic adaptation, computer software, or by similar or dissimilar methodology now known or hereafter developed.
The use of general descriptive names, registered names, trademarks, service marks, etc. in this publication does not imply, even in the absence of a specific statement, that such names are exempt from the relevant protective laws and regulations and therefore free for general use.
The publisher, the authors and the editors are safe to assume that the advice and information in this book are believed to be true and accurate at the date of publication. Neither the publisher nor the authors or the editors give a warranty, express or implied, with respect to the material contained herein or for any errors or omissions that may have been made.

Printed on acid-free paper

This Springer imprint is published by Springer Nature
The registered company is Springer International Publishing AG Switzerland

Preface

Scientific research is often characterized by a combination of open questions and specific research tools that are designed to solve them. This interplay happens in both directions, and new scientific instruments can also bring attention to novel scientific questions, or can even define entire scientific periods. Nanotechnology brought us the invention of many instruments that can be used as microscopes to image small things and as fabrication tools to modify them. Prominent examples are charged particle beams: scanning electron microscopy (SEM) and electron beam lithography (EBL) are done with exactly the same instrument; and for transmission electron microscopy (TEM) samples are sliced with focused ion beams (FIB). Since the 1960s the four above-mentioned charged particle methods synergetically evolve, thereby pushing the frontiers of high-resolution microscopy as well as of micro- and nanofabrication technology. In this environment, in 2006 a novel charge particle instrument, the helium ion microscope (HIM), entered the field. With a unique combination of imaging and nanofabrication capabilities it placed itself right at the forefront of current research.

The key technological advantage of the HIM is the fact that it is an integrated multipurpose instrument that does not only excel in a single discipline but by a unique combination of several skills. Its resolution as a microscope is higher than that of the best available SEMs. In nanofabrication it outperforms the FIB with respect to small feature sizes. Without further modification, a HIM is capable to image untreated biological—or other insulating—samples with unprecedented resolution, depth of field, materials contrast and image quality. The HIM thus covers a wide range of tasks that otherwise would require multiple devices or special sample treatments. Since its introduction, the HIM has become a popular instrument that is frequently seen in nanotechnology centers throughout the globe.

Interestingly, the basic technology of the HIM is built on the combination of two long-established techniques, field ion microscopy and scanning electron microscopy. These were combined in one instrument by persistent engineering efforts that led to the development of a stable gas field ion source (GFIS), stable enough to be continuously operated in a scanning ion beam microscope. Currently, about 100

GFIS instruments are in operation worldwide. Many of them go beyond the use of helium ions and can also operate with neon and nitrogen and are often combined with a classical liquid metal FIB.

This book aims at providing an in-depth overview on the current status of HIM for imaging, analysis, and nanofabrication. It is written for the novice to the technique as it explains the basic operation principles and fundamental interaction mechanisms between medium energy light ions and matter. For the more experienced reader the book covers a range of specialized topics dealing with currently ongoing research efforts to further develop the technique in an extensive manner. Here, the chapters of this book range from basic scientific questions to innovative solutions in an industrial environment. All chapters have been written by specialists in their respective fields, their affiliations range from universities and research institutes to industrial laboratories.

Part I *Fundamentals* covers the instrumental and theoretical aspects on two levels. Chapter 1 *The Helium Ion Microscope* provides a detailed description of the components of the ion microscope and its operational principles. Although written for the novice, the chapter also contains valuable technical information for the experienced user that is not available elsewhere in this form. Chapter 2 *Single Atom Gas Field Ion Sources for Scanning Ion Microscopy* is an in-depth description of the gas field ion source (GFIS) its fabrication, modification and operation. The next two Chaps. 3 *Structural Changes in 2D Materials Due to Scattering of Light Ions* and 4 *Monte Carlo Simulations of Focused Ion Beam Induced Processing* contain theoretical descriptions of fundamental ion solid interactions which are important for understanding the processes during imaging as well as during nanolithography with ions. While Chap. 3 deals with the interaction of light ions with 2D materials such as graphene. Chapter 4 covers the processes important for material removal by sputtering and material addition via ion beam induced deposition. To complete this part Chap. 5 *Secondary Electron Generation in the Helium Ion Microscope: Basics and Imaging* describes the details of secondary electron generation which is crucial for the image formation.

Part II *Microscopy* covers the best known application of the HIM, i.e., the imaging of small objects. Chapter 6 *Introduction to Imaging Techniques in the HIM* is the natural starting point for each new HIM user as it provides a flavor of what is possible in terms of high-quality imaging. The following Chap. 7 *HIM of Biological Samples* compiles recent bioimaging studies with the HIM, a special emphasis is laid on a comparison with SEM and optical techniques. It can be read as a motivation for scientists working in biology and medicine to make use of the unprecedented imaging capabilities provided by the Helium Ion Microscope. Chapter 8 *HIM Applications in Combustion Science: Imaging of Catalyst Surfaces and Nascent Soot* touches an environmentally important imaging task that requires the highest resolution and chemical contrasts. In *The Channeling and Backscatter Imaging* (Chap. 9) subsurface imaging and the utilization of channeling for obtaining crystallographic information is presented. Chapters 10 *Helium Ion*

Microscopy of Carbon Nanomembranes and 11 *Helium–Ion Microscopy for Two–Dimensional Materials* deal with a currently very important class of materials. While Chap. 10 focuses on the imaging of a specific example of membranes made from molecules, Chap. 11 also covers various two-dimensional materials and discusses issues such as beam induced damage. In general, Part II contains a manifold of quite aesthetic HIM pictures that will act as a source of inspiration for the novice as well as the experienced reader.

Part III *Analysis* discusses current efforts to implement methodical additions and to overcome existing technical challenges. In Chap. 12 *Backscattering Spectrometry in the Helium Ion Microscope: Imaging Elemental Compositions on the nm Scale* a technique that usually requires large accelerators is adapted to the HIM, where it outperforms the analytic resolution limit of Backscatter Spectroscopy by orders of magnitude. This chapter is complimented by the following Chap. 13 *SIMS on the Helium Ion Microscope: A Powerful Tool for High-resolution High-sensitivity Nanoanalytics* which set the current standard in the achievable lateral resolution limit in analytic applications. Chapter 14 on *Ionoluminescence* describes the possibilities and limitations of using photons to obtain information on the specimen beyond high quality images. Part III is more aimed at experienced users, and it demonstrates potential future development of the HIM technology platform.

Part IV *Modification* deals with the most frequent application of the Helium Ion Microscope, the controlled materials modification by focused ions. Chapter 15 *Direct–write Milling and Deposition with Noble Gases* serves as an introduction. It is full of practical hints on the operation of the HIM for the creation of nanostructures. Chapter 16 *Resist Assisted Patterning* summarizes a number of successful research efforts to use the HIM for resist patterning. It also discusses the resolution limits as well as the modeling of fundamental processes. The next two chapters, Chaps. 17 *Focused Helium and Neon Ion Beam Modification of High–T_C Superconductors and Magnetic Materials* and 18 *Helium Ion Microscope Fabrication of Solid-State Nanopore Devices for Biomolecule Analysis*, discuss three specialized applications of HIM. While Chap. 17 treats the modification of materials properties by partly extremely low ion fluences, Chap. 18 discusses the drilling of fine nanopores for DNA sequencing and other biotechnology applications. The final chapter, Chap. 19 *GFIS Applications in Semiconductors*, provides an in-depth view of the current use of HIM in the semiconductor industry and describes how semiconductor prototyping benefits from HIM-based circuit editing. This chapter is full of information about the industrial application of HIM and is recommended for novices as well as experts.

The book ends with *The ALIS Story*, a personal view on the history of the HIM written by Bill Ward, the inventor of the HIM ion source used today and the founder of the first helium ion microscope company “ALIS Corporation”.

Finally, we would like to thank the University of Bielefeld, the University of Twente and the Helmholtz–Zentrum Dresden–Rossendorf for the privilege to be

among the first users of HIM. We also acknowledge Carl Zeiss and in particular the Ion Microscopy Innovation Center for their continuous technical support. We further thank the American Vacuum Society (AVS) for providing our small group of early HIM adaptors a regular discussion forum that eventually created an active HIM community and ignited the spark for this book.

Dresden, Germany — Gregor Hlawacek
Bielefeld, Germany — Armin Gölzhäuser
May 2016

Contents

Part I Fundamentals

1 The Helium Ion Microscope 3
John Notte and Jason Huang
1.1 Introduction 3
1.2 The GFIS Gun 4
1.3 Cryogenic Cooling 6
1.4 Vacuum System 8
1.5 Gas Delivery System 10
1.6 The Ion Optical Column. 11
1.7 Beam Induced Damage. 21
1.8 Detectors and Signal Chain. 24
1.9 Vibrational Considerations 28
1.10 Conclusion 29
References. 29

2 Single Atom Gas Field Ion Sources for Scanning Ion Microscopy 31
Radovan Urban, Robert A. Wolkow and Jason L. Pitters
2.1 Introduction 31
2.2 FIM Details 37
2.2.1 Anatomy of Gas-Assisted Etching. 38
2.2.2 Precursor Tip. 43
2.2.3 SAT Shaping. 44
2.2.4 SAT Reproducibility 45
2.2.5 Air Exposure, Thermal Stability, and Faceting 47
2.2.6 Iridium and Other Nanotip Materials. 51
2.3 Performance of SATs 53
2.3.1 Best Imaging Voltage 53
2.3.2 Temperature Dependence. 54
2.3.3 Shape Dependence. 56
2.3.4 Current Stability 57

2.4 Conclusions 59
References. 59

3 Structural Changes in 2D Materials Due to Scattering of Light Ions 63
Ossi Lehtinen and Jani Kotakoski
3.1 Introduction 63
3.2 The Scattering Process 64
3.2.1 Elastic Scattering 64
3.2.2 A Note on Inelastic Scattering 66
3.3 Target Evolution Under Ion Impacts 66
3.3.1 After the Binary Collision 66
3.3.2 Molecular Dynamics Simulations of Ion Impacts on 2D Materials 70
3.3.3 Influence of Multiple Impacts 76
3.3.4 A Brief Note on the Substrate 77
3.4 Results 77
3.4.1 Graphene 77
3.4.2 Experimental Results 82
3.4.3 Other 2D Materials 83
3.5 Summary 85
References. 86

4 Monte Carlo Simulations of Focused Ion Beam Induced Processing 89
Rajendra Timilsina and Philip D. Rack
4.1 Introduction 89
4.2 An Example of Monte Carlo Simulation: EnvizION Simulator 91
4.2.1 Material Database 93
4.2.2 Ion Beam Profile 93
4.2.3 Nuclear Energy Loss 93
4.2.4 Electronic Energy Loss and Stopping Cross-Section 95
4.2.5 Ion and Recoil Trajectories 96
4.2.6 Secondary Electrons 97
4.2.7 Precursor Gas Handling 98
4.2.8 Deposition and Etching 99
4.2.9 Sputtering Algorithms 100
4.3 Monte Carlo Simulations of Physical Sputtering 102
4.3.1 Sputtering of Aluminum and Tungsten 105
4.3.2 Sputtering of Copper 109
4.4 EUV Mask Repair 113
4.5 Resolution Limiting and Sputtering Limiting Effects 115
4.6 Summary 117
References. 117

5 Secondary Electron Generation in the Helium Ion Microscope: Basics and Imaging . . . 119
Yuri V. Petrov and Oleg F. Vyvenko
5.1 Introduction . . . 119
5.2 The Processes of Secondary Electron Generation in the Helium Ion Microscope . . . 120
5.3 SE Energy Distribution in HIM . . . 123
5.4 Imaging with SE. . . . 128
5.4.1 Topographic Yield. . . . 128
5.4.2 SE2/SE1 Ratio. . . . 129
5.4.3 SE3 . . . 130
5.4.4 Material Characterization by SE Contrast Measurements with Energy Filtering . . . 133
5.5 Imaging Utilizing a High SE Yield in HIM: Ion-to-SE Conversion . . . 137
5.5.1 Scanning Transmission Ion Microscopy (STIM) with SE Detector . . . 137
5.5.2 Reflection Ion Microscopy. . . . 138
5.6 Summary . . . 143
References. . . . 144

Part II Microscopy

6 Introduction to Imaging Techniques in the HIM . . . 149
Stuart A. Boden
6.1 Introduction . . . 149
6.2 Imaging Signals and Contrast Mechanisms. . . . 150
6.2.1 Secondary Electrons . . . 150
6.2.2 Backscattered Ions. . . . 157
6.2.3 Transmitted and Reflected Ions . . . 159
6.2.4 Photons . . . 161
6.3 HIM Imaging Techniques. . . . 162
6.3.1 High Resolution Imaging. . . . 162
6.3.2 Charge Neutralization . . . 165
6.3.3 Imaging with a Large Depth of Field . . . 166
6.4 Conclusions . . . 170
References. . . . 170

7 HIM of Biological Samples. . . . 173
Armin Gölzhäuser and Gregor Hlawacek
7.1 Introduction . . . 173
7.2 Large Depth of Field Bioimaging. . . . 174
7.3 Summary . . . 184
References. . . . 185

8 HIM Applications in Combustion Science: Imaging of Catalyst Surfaces and Nascent Soot 187
Henning Vieker and André Beyer
8.1 Introduction 188
8.2 Organic Nanoparticles: Nascent Soot Analysis 188
8.2.1 Introduction: Soot 188
8.2.2 Soot Sampling 190
8.2.3 Imaging of Soot 190
8.2.4 Analysis of Soot from Ethylene Flames 191
8.2.5 Imaging of Soot from Different C_4 Fuels 194
8.2.6 Summary: Imaging of Nascent Soot 195
8.3 CVD-Grown Films of Transition Metal Oxides 195
8.3.1 Introduction 195
8.3.2 Binary Mixtures of TMOs 198
8.3.3 Summary: Imaging PSE-CVD Grown Films 199
8.4 Summary and Conclusions 202
References 202

9 Channeling and Backscatter Imaging 205
Gregor Hlawacek, Vasilisa Veligura, Raoul van Gastel and Bene Poelsema
9.1 Introduction 205
9.2 Directional Effects in Ion Solid Interaction 206
9.2.1 Ion Channeling 206
9.2.2 Directional Effects in Secondary Electron Emission 207
9.3 Mapping of Crystal Orientation in the Ion Microscope 210
9.4 Imaging with Ions 215
9.4.1 Backscattered Helium Versus Electrons for Image Generation 215
9.4.2 Subsurface Imaging 216
9.5 Dechanneling Contrast 217
9.5.1 Dechanneling by Thin Films 217
9.5.2 Dechanneling by Lattice Distortions 218
9.6 Summary 222
References 222

10 Helium Ion Microscopy of Carbon Nanomembranes 225
Armin Gölzhäuser
10.1 Introduction 225
10.2 A Comparison Between HIM and SEM 227
10.3 CNMs on Solid Supports 229
10.4 HIM Imaging of Free-Standing CNMs (Porous Supports and TEM Grids) 230
10.5 Visualization of Large Area CNMs 236

10.6 Imaging of Hybrid and Composite Systems 237
10.7 Imaging of Perforated CNMs 238
10.8 Lithography with Nanomembranes 242
10.9 Summary 243
References. 243

11 Helium Ion Microscopy for Two-Dimensional Materials 245
Yangbo Zhou, Daniel S. Fox and Hongzhou Zhang
11.1 Graphene Characterization 246
11.1.1 Lateral Dimension 247
11.1.2 Thickness and Work Function 249
11.1.3 Surface Contamination. 251
11.1.4 Charge Compensation Effect on Graphene Imaging 253
11.1.5 Influence of Beam-Induced Contamination 255
11.2 HIM Modification of Two-Dimensional Materials 256
11.2.1 Controllable Defect Creation in 2D Materials 256
11.2.2 Nano-Patterning of 2D Materials Using HIM 258
References. 261

Part III Analysis

12 Backscattering Spectrometry in the Helium Ion Microscope: Imaging Elemental Compositions on the nm Scale 265
Rene Heller, Nico Klingner and Gregor Hlawacek
12.1 Introduction 265
12.2 Principles of Rutherford Backscattering Spectrometry 267
12.3 Challenges in Performing Rutherford Backscattering Spectrometry in the Helium Ion Microscope. 270
12.3.1 Screening Effects and Cross Sections 271
12.3.2 Dual, Plural and Multiple Scattering 272
12.3.3 Charge Fraction 275
12.3.4 Sputtering 276
12.4 Experimental Approaches 279
12.4.1 Solid State Detectors 280
12.4.2 Electrostatic Analyzers 281
12.4.3 Time of Flight Spectrometry 283
12.5 Pulsed Primary Beam ToF-BS 285
12.5.1 Experimental Setup 285
12.5.2 Backscattering Spectra and Simulation 287
12.5.3 Imaging in ToF-BS Mode 290
12.5.4 Time of Flight Secondary Ion Mass Spectrometry. . . . 292
12.6 Summary 292
References. 293

13 SIMS on the Helium Ion Microscope: A Powerful Tool for High-Resolution High-Sensitivity Nano-Analytics 297
Tom Wirtz, David Dowsett and Patrick Philipp
13.1 Secondary Ion Mass Spectrometry 297
13.1.1 Introduction 297
13.1.2 Underlying Fundamentals 298
13.1.3 Instrumentation 304
13.1.4 SIMS Applications 305
13.2 Fundamental Aspects of SIMS Performed Under He^+ and Ne^+ Bombardment 307
13.2.1 Dimensions of Collision Cascades 307
13.2.2 Sensitivity 308
13.2.3 Detection Limit Versus Pixel/Voxel Size 311
13.3 Instrumentation for SIMS Performed on the HIM 313
13.3.1 Instrumental Constraints 313
13.3.2 Prototype Instrument for SIMS Performed on the HIM 314
13.4 SIMS Applications on the HIM 317
13.4.1 Mass Spectra 317
13.4.2 Depth Profiling 318
13.4.3 Imaging 319
13.4.4 Correlative Microscopy 320
13.5 Conclusions 322
References 323

14 Ionoluminescence 325
Vasilisa Veligura and Gregor Hlawacek
14.1 Introduction 325
14.2 Ionoluminescence in HIM 327
14.2.1 Semiconductors 327
14.2.2 Alkali Halides 332
14.2.3 Other Minerals 336
14.2.4 Immunofluorescence 339
14.3 IL Patterning 342
14.4 Interaction Volume Measurements Using IL 344
14.5 Summary 346
References 347

Part IV Modification

15 Direct–Write Milling and Deposition with Noble Gases 355
Ivan Shorubalko, Lex Pillatsch and Ivo Utke
15.1 Nanostructuring with Focused Noble Gas Ion Beams 355
15.2 FIB Milling with Noble Gas Ions 356
15.2.1 Bulk Material 356
15.2.2 Membranes 368

15.3 Gas Assisted Deposition with Noble Gas Ions 372
15.3.1 Deposition Regimes: Reaction Limited Versus Mass-Transport Limited. 374
15.3.2 Adsorbate Dissociation: ESA, SE, and Thermal Spikes 378
15.3.3 Lateral Resolution 382
15.3.4 Deposit Composition and Internal Structure 387
15.4 Gas Enhanced Etching with Noble Gas Ions 387
15.5 Summary 388
References. 388

16 Resist Assisted Patterning. 395
Nima Kalhor and Paul F.A. Alkemade
16.1 Introduction to Lithography 395
16.2 Helium Ion Beam-Resist Interaction 397
16.2.1 Primary Beam Scattering (Forward Scattering) 400
16.2.2 Secondary Electron (SE) Generation 401
16.2.3 Backscattering of the Primary Beam 403
16.3 HIL Experimental Results on EBL Resists 403
16.3.1 Contrast and Sensitivity. 404
16.3.2 Resolution 405
16.3.3 Point-Spread Function (PSF) 406
16.4 HIL Applications 407
16.4.1 Pre-screening of EUV Resists 407
16.4.2 Fabrication of Nanoimprint Templates. 408
16.5 HIL Dose Optimization Modelling 409
16.6 HIL Versus Milling 410
16.7 Conclusions and Outlook 411
References. 412

17 Focused Helium and Neon Ion Beam Modification of High-T_C Superconductors and Magnetic Materials 415
Shane A. Cybart, Rantej Bali, Gregor Hlawacek, Falk Röder and Jürgen Fassbender
17.1 Introduction 416
17.2 Introduction to Ion Beam Modification of Superconductors 417
17.2.1 Josephson Junctions. 417
17.2.2 Ion Irradiation in High-T_C Superconductors. 419
17.3 Ion Irradiated Josephson Junctions 423
17.3.1 Masked Ion Irradiated Josephson Junctions 423
17.3.2 GFIS Direct-Write Josephson Junctions. 424
17.3.3 GFIS Direct Write Superconducting Quantum Interference Devices 429
17.3.4 Nanowire Josephson Junctions. 430
17.3.5 Concluding Remarks on GFIS Fabricated High-T_C Josephson Junctions. 432

17.4 Nanoscale Manipulation of Magnetization Using GFIS 432
17.4.1 The Effect of Ion-Irradiation on Certain B2 Alloy Thin Film. 434
17.4.2 Application of Nanofocussed Ne^+ Beam to B2 Alloy Thin Films 438
17.4.3 Future Scope of GFIS-Assisted Magnetic Writing 441
17.5 Conclusions 441
References. 442

18 Helium Ion Microscope Fabrication of Solid-State Nanopore Devices for Biomolecule Analysis 447
Osama K. Zahid and Adam R. Hall
18.1 Introduction 447
18.2 HIM Milling of SS-Nanopores 449
18.2.1 Nanopore Formation 450
18.2.2 DNA Translocation 452
18.2.3 Nanopore Arrays 453
18.2.4 Applications of HIM Drilled Nanopores 454
18.3 Manipulation of Device Thickness 456
18.3.1 Membrane Thinning 456
18.3.2 HIM Control of SS-Nanopore Device Dimensions . . . 458
18.3.3 Applications of HIM-Thinned SS-Nanopores 460
18.4 Manipulating Intrinsic Membrane Fluorescence 461
18.4.1 HIM Photoluminescence Reduction. 462
18.4.2 Application of HIM Photoluminescence Reduction 463
18.5 Conclusions and Outlook 464
References. 466

19 Applications of GFIS in Semiconductors 471
Shida Tan and Rick Livengood
19.1 Introduction 471
19.2 GFIS Nanomachining Characteristics 472
19.2.1 Charged Particle Interaction with Materials 472
19.2.2 Charged Particle Interaction in Bulk Versus Membrane Substrates. 474
19.2.3 Ion Beam Probe Current Distribution 477
19.3 Applications of GFIS in Semiconductors 479
19.3.1 Helium Applications 480
19.3.2 Neon Applications. 486
19.4 GFIS Damage Mitigation 491
19.5 Future of GFIS Applications in Semiconductors. 495
References. 496

Appendix A: The ALIS Story 499
Bill Ward

Index 519

Contributors

Paul F.A. Alkemade Kavli Institute of Nanoscience, Delft University of Technology, Delft, The Netherlands

Rantej Bali Helmholtz-Zentrum Dresden-Rossendorf, Institute of Ion Beam Physics and Materials Research, Dresden, Germany

André Beyer Physics of Supramolecular Systems and Surfaces, Bielefeld University, Bielefeld, Germany

Stuart A. Boden Electronics and Computer Science, University of Southampton, Highfield, Southampton, UK

Shane A. Cybart Oxide Nano Electronics Laboratory, University of California Riverside, Riverside, CA, USA

David Dowsett Advanced Instrumentation for Ion Nano-Analytics, Luxembourg Institute of Science and Technology, Belvaux, Luxembourg

Jürgen Fassbender Helmholtz-Zentrum Dresden-Rossendorf, Institute of Ion Beam Physics and Materials Research, Dresden, Germany; Technische Universität Dresden, Dresden, Germany

Daniel S. Fox School of Physics and CRANN, Trinity College Dublin, Dublin, Ireland

Armin Gölzhäuser Physics of Supramolecular Systems and Surfaces, Bielefeld University, Bielefeld, Germany

Adam R. Hall Virginia Tech-Wake Forest School of Biomedical Engineering and Sciences, Wake Forest University School of Medicine, Winston Salem, NC, USA

Rene Heller Helmholtz-Zentrum Dresden-Rossendorf, Dresden, Germany

Gregor Hlawacek Institute for Ion Beam Physics and Materials Research, Helmholtz–Zentrum Dresden-Rossendorf, Dresden, Germany; Physics of Interfaces and Nanomaterials, University of Twente, Enschede, The Netherlands

Jason Huang Ion Microscopy Innovation Center, Carl Zeiss Microscopy, Peabody, MA, USA

Nima Kalhor Kavli Institute of Nanoscience, Delft University of Technology, Delft, The Netherlands

Nico Klingner Helmholtz-Zentrum Dresden-Rossendorf, Dresden, Germany

Jani Kotakoski Faculty of Physics, University of Vienna, Vienna, Austria

Ossi Lehtinen Ulm University, Ulm, Germany

Rick Livengood Intel Corporation, Santa Clara, CA, USA

John Notte Ion Microscopy Innovation Center, Carl Zeiss Microscopy, Peabody, MA, USA

Yuri V. Petrov St. Petersburg State University, Faculty of Physics, Saint-Petersburg, Petrodvoretz, Russia

Patrick Philipp Advanced Instrumentation for Ion Nano-Analytics, Luxembourg Institute of Science and Technology, Belvaux, Luxembourg

Lex Pillatsch Empa, Swiss Federal Laboratories for Materials Science and Technology, Laboratory for Mechanics of Materials and Nanostructures, Thun, Switzerland

Jason L. Pitters National Institute for Nanotechnology, Edmonton, AB, Canada

Bene Poelsema Physics of Interfaces and Nanomaterials, Univerity of Twente, Enschede, The Netherlands

Philip D. Rack Department of Materials Science and Engineering, The University of Tennessee Knoxville, Knoxville, USA; Oak Ridge National Laboratory, Center for Nanophase Materials Sciences, Oak Ridge, USA

Falk Röder Helmholtz-Zentrum Dresden-Rossendorf, Institute of Ion Beam Physics and Materials Research, Dresden, Germany; Technische Universität Dresden, Dresden, Germany

Ivan Shorubalko Empa, Swiss Federal Laboratories for Materials Science and Technology, Laboratory for Reliability Science and Technology, Dübendorf, Switzerland

Shida Tan Intel Corporation, Santa Clara, CA, USA

Rajendra Timilsina Department of Mechanical, Aerospace and Biomedical Engineering, The University of Tennessee Knoxville, Knoxville, USA

Radovan Urban Department of Physics, University of Alberta, Edmonton, AB, Canada; National Institute for Nanotechnology, Edmonton, AB, Canada

Ivo Utke Empa, Swiss Federal Laboratories for Materials Science and Technology, Laboratory for Mechanics of Materials and Nanostructures, Thun, Switzerland

Raoul van Gastel Physics of Interfaces and Nanomaterials, Univerity of Twente, Enschede, The Netherlands

Vasilisa Veligura Physics of Interfaces and Nanomaterials, University of Twente, Enschede, The Netherlands

Henning Vieker Physics of Supramolecular Systems and Surfaces, Bielefeld University, Bielefeld, Germany; CNM Technologies GmbH, Bielefeld, Germany

Oleg F. Vyvenko St. Petersburg State University, Faculty of Physics, Saint-Petersburg, Petrodvoretz, Russia

Bill Ward Inventor and Entrepeneur, Boston, Massachusetts, USA

Tom Wirtz Advanced Instrumentation for Ion Nano-Analytics, Luxembourg Institute of Science and Technology, Belvaux, Luxembourg

Robert A. Wolkow Department of Physics, University of Alberta, Edmonton, AB, Canada; National Institute for Nanotechnology, Edmonton, AB, Canada

Osama K. Zahid Virginia Tech-Wake Forest School of Biomedical Engineering and Sciences, Wake Forest University School of Medicine, Winston Salem, NC, USA

Hongzhou Zhang School of Physics and CRANN, Trinity College Dublin, Dublin, Ireland

Yangbo Zhou School of Physics and CRANN, Trinity College Dublin, Dublin, Ireland

Acronyms

2D	Two-dimensional
3D	Three-dimensional
AFP	Atomic force probing
ALIS	Atomic Level Ion Source
BOA	Born–Oppenheimer approximation
BS	Backscattering spectrometry
BSHe	Backscattered helium
BSY	Backward sputter yield
CD	Critical dimension
CE	Circuit edit
CL	Cathodoluminesence
CFE	Cold field emitter
CM	Center of mass
CNM	Carbon nanomembrane
DFT	Density functional theory
EASA	Electrochemically assisted surfactant assembly
EB	Electron beam
EBL	Electron beam lithography
EBSD	Electron backscattered diffraction
ERD	Elastic recoil detection
ESA	Electrostatic analyzer
ET	Everhart–Thornley
EUV	Extreme ultraviolet
EUVL	Extreme-UV lithography
FA	Failure analysis
FESEM	Field emission scanning electron microscope
FI	Fault isolation
FIB	Focused ion beam
FIBL	Focused ion beam lithography
FIM	Field ion microscope

FOV	Field of view
FSY	Forward sputter yield
FWHM	Full width at half maximum
GAE	Gas-assisted etch
GFIS	Gas field ion source
h-BN	Hexagonal boron nitride
HIL	Helium ion lithography
HIM	Helium ion microscope or helium ion microscopy
HCI	Highly charged ion
HOPG	Highly ordered pyrolytic graphite
IBID	Ion beam induced deposition
IL	Ionoluminesence
iSE	Ion-induced secondary electron
LCE	Laser chemical etching
LED	Light emitting diode
LEIS	Low-energy ion scattering
LMIS	Liquid metal ion source
LoTIS	Low-temperature ion source
LVFESEM	Low voltage field emission scanning electron microscope
MC	Monte carlo
MCA	Multichannel analyzer
MCP	Microchannel plate
MD	Molecular dynamics
MOTIS	Magneto-optical ionization sources
MS	Multiple scattering
NIL	Nano imprint lithography
NW	Nanowire
PMMA	Poly methyl methacrylate
PS	Plural scattering
PSF	Point spread function
PVC	Passive voltage contrast
RBS	Rutherford backscattering spectrometry
RIM	Reflection ion microscopy
RT	Room temperature
SAED	Selected area electron diffractograms
SAT	Single atom tip
SCC	Static capacitive contrast
SE	Secondary electron
SE2	Type-two secondary electron
SEED	Secondary electron energy distribution
SEM	Scanning electron microscope
SEY	Secondary electron yield
SIM	Scanning ion microscope
SIMS	Secondary ion mass spectrometry
SNR	Signal-to-noise ratio

SRIM	Stopping and range of ions in matter
SS	Solid state
SSD	Solid-state detector
STE	Self trapped exciton
STEM	Scanning transmission electron microscope
STIM	Scanning transmission ion microscopy
TDC	Time-to-digital converter
TEM	Transmission Electron Microscope
TIM	Transmission ion microscope
TMD	Transition metal dichalcogenide
ToF	Time of flight
TRIM	Transport of ions in matter
UHV	Ultrahigh vacuum
VC	Voltage contrast
ZBL	Universal repulsive potential by Ziegler, Biersack and Littmark
VPSEM	Variable pressure scanning electron microscope

Part I
Fundamentals

Chapter 1
The Helium Ion Microscope

John Notte and Jason Huang

Abstract The key technologies that comprise the helium ion microscope are described in detail. Specific attention is given the cryogenic cooling system, the vacuum system, the gas delivery system, the ion-optical column, the detector and imaging system, and vibrational considerations.

1.1 Introduction

The family of charged particle microscopes (CPM) includes all instruments that rely upon a charged particle beam for precision imaging, or patterning of a sample. The family originated in the 1930s with the efforts led by Helmut Ruska, and independent work by Manfred von Ardenne, and now includes the SEM, TEM, STEM, FIB, and all of their variants. The CPM family has a long, rich history, and has played a distinguished role in enabling mankind to see matter at the smallest scale. One of the most recent entries into the family is the class of microscope that relies upon the gas field ion source (GFIS). The GFIS itself is an old concept, conceived some 50 years before its eventual commercialization [1] in 2007 in the form of the helium ion microscope (HIM). More broadly, this class of instrument is termed the gas field ion microscope (GFIM), which includes instruments with gas species other than helium (e.g. hydrogen, neon, nitrogen, or argon). The HIM instrument offers distinct imaging advantages such as high resolution [2], long depth of focus, surface sensitivity, high secondary electron yield [3], and several novel contrast mechanisms [4, 5]. The HIM has also been employed for non-imaging applications where it can be used to expose resist [6], directly pattern a substrate [7], drill nanopores [8], induce patterned chemical processes, implant stress [9], or perform material

J. Notte (✉) · J. Huang
Ion Microscopy Innovation Center, Carl Zeiss Microscopy,
1 Corporation Way, Peabody, MA 01960, USA
e-mail: John.Notte@Zeiss.com

J. Huang
e-mail: Jason.Huang@Zeiss.com

© Springer International Publishing Switzerland 2016

G. Hlawacek and A. Gölzhäuser (eds.), *Helium Ion Microscopy*,
NanoScience and Technology, DOI 10.1007/978-3-319-41990-9_1

analysis [10]. Variants of the HIM include the use of the GFIS with other gas species such as neon [11], which enables further nanofabrication [12] and analysis capabilities [13].

This chapter provides an overview of some of the specific technology sub-systems that are contained within the helium ion microscope (HIM). Special attention is given to the technologies that are of unique importance to this class of instrument. At the time of this writing, there is only one commercial provider of the GFIS microscope, but when possible, the technologies described herein are presented in a generic and even hypothetical way, as it might pertain to any such microscope. The topics which are addressed are the GFIS gun (Sect. 1.2), the cryogenic cooling system (Sect. 1.3) the vacuum system (Sect. 1.4), the gas delivery system (Sect. 1.5), the ion optical column (Sect. 1.6), an analysis of sample damage, (Sect. 1.7), the detectors and signal chain (Sect. 1.8), and vibrational considerations (Sect. 1.9).

1.2 The GFIS Gun

The term, gas field ion source gun or "GFIS gun" encompasses the hardware immediately surrounding the gas field ion source, and which enables its basic performance. The term "GFIS emitter", or "GFIS source" is more specific and refers to just the emitter itself, and is addressed in detail in the subsequent chapter. The GFIS gun is distinctly different from other established technologies like the liquid metal ion source (LMIS) for gallium, the thermal field emitter (Schottky source) for electrons, or the cold field emitter (CFE) for electrons. Therefore, we begin this chapter with a review of the requirements for the GFIS gun, and a summary of its performance. The number of requirements, and the engineering challenges in simultaneously addressing them are the main reasons that the GFIS microscope did not become commercialized earlier. Indeed, it is quite likely that Mueller and his group at Penn State envisioned that their field ion microscope (FIM) might one day be the source which powers a powerful new ion beam microscope [14]. But the pathway from FIM to GFIS microscope was littered with a collection of dead ends, distractions, and failures lasting for 50 years. Even after the technology was demonstrated in the laboratory, there are additional hurdles to overcome before it could become a commercial product. A commercialized product has requirements of affordability, serviceability and easy operation in the hands of an operator whose interest lies in their sample—not in the microscope.

GFIS Gun Performance

While a detailed description of the GFIS emitter is addressed in Chap. 2, it is necessary here to give an overview of the overall gun performance before we discuss the technology sub-systems which enable it. Table 1.1 summarizes the key GFIS emitter and gun characteristics under typical operating conditions.

Table 1.1 Typical performance metrics for a GFIS gun

Quantity	Units	Value	Notes
Operating extraction voltage	kV	25–35	This is typical for helium operation, but depends on the shape of the emitter
Operating temperature	Kelvins	60–90	Colder is better, but with limits (see Sect. 1.3)
Base pressure	Torr	$<4 \times 10^{-10}$	(See Sect. 1.4)
Operating gas pressure	Torr	1×10^{-7}–5×10^{-6}	This is the partial pressure of helium or neon indicated on the gun gauge, not the actual pressure at the emitter. (See Sect. 1.5)
Brightness	A cm^{-2} sr^{-1}	5×10^{9}	This is under optimized conditions
Reduced brightness	A m^{-2} sr^{-1} V^{-1}	1×10^{9}	This is under optimal conditions, with an extraction voltage near 30 keV
Pressure normalized brightness	A cm^{-2} sr^{-1} $Torr^{-1}$	2.5×10^{12}	The reference pressure is the species-corrected pressure in the inner gun
Energy spread	eV	~1	This is measured as a FWHM
deBroglie wavelength	pm	~0.080	This is for helium at 30 keV
Virtual source size (diameter)	nm	<0.25	This is inferred from the atomic spacing of emitter atoms (expressed as a FWHM) and represents an upper bound
Total emitted current	pA	~150	This is the total emission from three atoms of a trimer under typical conditions, (gun gauge pressure indicates = 2×10^{-6} Torr)
Angular current density	A/sr	1×10^{-6}	This is the peak angular current density after extraction under typical conditions (gun gauge pressure indicates 2×10^{-6} Torr)
Angular emission	Degrees	0.5°	This is typical for each atomic emission site after extraction, expressed as FWHM measurement
Emission current stability	%/h	<1	This value is typical for helium. The value for neon is considerably greater
Trimer lifetime	μTorr × h	~80	This value is typical for helium. The value is considerably less for neon

GFIS Gun Requirements
The GFIS gun has several prerequisites that must be met before it can be operated—just as the LMIS, Schottky field emitter, or the CFE have their own requirements. For the GFIS, the requirements are relatively simply stated: (1) An emitter in the shape of a sharpened wire should be biased with a positive voltage respect to an adjacent electrode. The details of the emitter, and its composition, and shaping will be discussed in detail in the subsequent chapter. (2) Cryogenic cooling should be provided to cool the GFIS gun to a working temperature of no more than 90 Ks. The reasons for the cryogenic cooling and the practical issues of providing such cooling are the focus of Sect. 1.3. (3) The GFIS gun must be housed in a UHV vacuum vessel to provide a base pressure in the range of 10^{-9} Torr. An analysis of the vacuum requirements and some practical examples are discussed in Sect. 1.4. (4) The GFIS gun must allow the introduction of helium (or other chosen gas) at a sufficient purity and flow rate. The details of the gas delivery system are provided in more detail in Sect. 1.5.

1.3 Cryogenic Cooling

Unlike conventional sources of ions or electrons, the GFIS ion source must be cooled to a steady temperature between 60 and 90 K. Experiments have indicated that emitted current increases markedly with decreased temperature (about 5% per Kelvin). The cold temperatures are thought to improve the collection and surface accommodation [15] of the provided imaging gas. Continued benefits, however, are not realized with further reduced temperature as the emission tends to become erratic. It is suspected that the imaging gas becomes less mobile at the lowest temperatures and cannot be surface transported from the shank and periphery of the emitter to the ionization sites. The low temperature also helps to assure the mechanical integrity of the emitter in the presence of the large electric fields. Thermal motions of the emitter, which could impact virtual source size or energy spread, are also reduced at the cryogenic temperatures. And lastly, the low temperature provides some level of cryo-pumping and cryo-trapping to reduce many of the otherwise corrosive impurities from reaching and damaging the emitter. To achieve these requirements there are entire families of refrigeration technologies capable of achieving these temperatures (e.g. Joule-Thompson, Gifford-McMahon, Pulse Tube, etc.). However, many of these technologies cannot be scaled to provide the cooling power (>2 W) that is required for a practical GFIS gun with the unavoidable heat loads it must contend with. It should be recognized that most of the refrigeration techniques introduce vibrations which can adversely impact the utility of the produced beam. A pulse tube cooler operated with "active" and "quiet" modes has been demonstrated successfully on several of the first commercial HIM systems. However, a standard cryogen in the liquid or solid phase is the most preferred solution because of the incredible cooling power, simplicity, and the lack of any moving parts near to the GFIS gun. When operating over a phase change

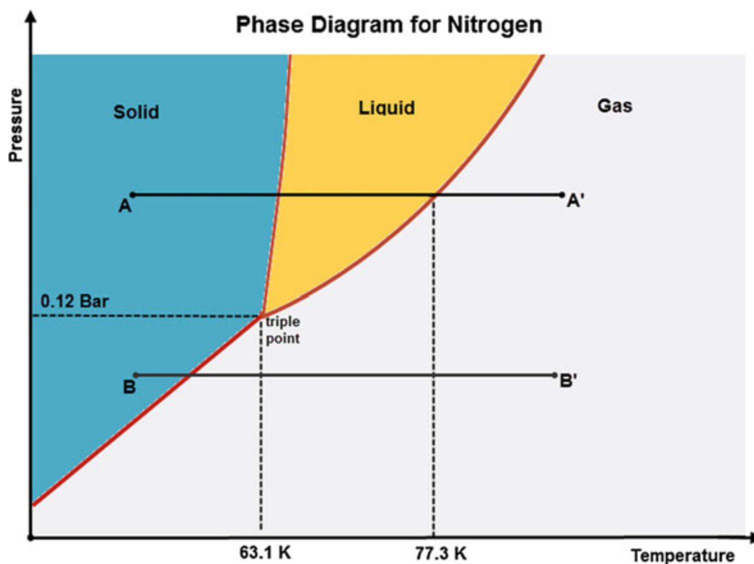

Fig. 1.1 Phase diagram for nitrogen and two paths that take nitrogen from a solid to a gas. The transition from A to A′ involves both melting and vigorous boiling. By comparison, transition from B to B′ involves a more tranquil sublimation process

(Fig. 1.1) the cryogens maintain a fixed temperature as they absorb heat from the system, eliminating thermal drift effects. Both liquid neon and nitrogen have been considered, with liquid nitrogen being more readily available.

The current commercial product, the ORION NanoFab, provides the necessary cryogenic cooling through an integrated dewar (Fig. 1.2) that is thermally connected to the internal GFIS gun through a cold finger. The cryogen is surrounded by an evacuated "jacket" region to provide the necessary thermal insulation. According to a prescribed schedule, the contents of the integrated dewar is filled with liquid nitrogen via a supply valve until it reaches its capacity. As soon as the fill process is completed, the supply valve is closed, and the vacuum valve is opened to draw a vacuum over the contents of the dewar. This causes the liquid nitrogen to change phase to solid nitrogen (removing about 25% of the product in the process) and be further cooled to about 60 K. This temperature is maintained, given the total heat load, for several hours. Thereafter, as per the software scheduled fill time, the supply valve opens again to fill the integrated dewar, now almost empty, with liquid nitrogen from the facility provided LN2 tank. The low temperature achieved with solid nitrogen compared to liquid nitrogen helps to make up for the unavoidable temperature drop along the thermal connections from the integrated dewar to the GFIS gun. The temperature as measured at the GFIS gun is typically 75–80 K. One of the advantages of the solid nitrogen cryogen is the elimination of the boiling, and the vibrations it invariably introduces into the GFIS emitter. As shown in Fig. 1.1, as the heat load is delivered to the dewar, the cryogen will change phases. If

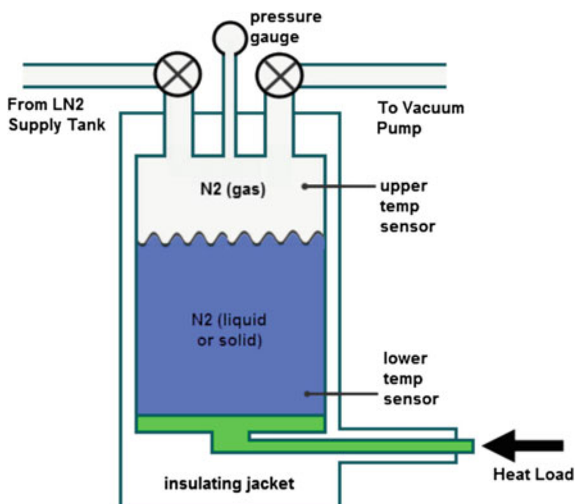

Fig. 1.2 The integrated dewar which provides a temperature of 75–80 K at the GFIS gun

operated at atmospheric pressure, the heat load drives the nitrogen from point A to A′, thereby involving significant boiling and achieving a temperature of only 78 K at the bottom of the dewar. When operated at a vacuum level sustained at about 3 Torr, the same heat load drives the nitrogen from point B to B′, which involves only sublimation, a process which transfers no vibration to the GFIS gun.

1.4 Vacuum System

Adopting the terminology from the FIM literature, the term "base vacuum" refers to the pressure in the absence of the imaging gases (helium, neon, or argon for example). The various constituents of the base vacuum present a risk of adsorption near the emission sites as adatoms, which would destabilize the emission process [16]. The base vacuum levels required for the successful GFIS emitter cannot be underestimated, given that the selected emission site corresponds to a single atom which must be free from adsorbates for about one week at a time! A simple calculation of the monolayer formation time and the condition of less than 10% coverage, suggests a vacuum requirement on the order of 10^{-13} Torr is required in the region of the emitter. There are technologies and techniques that make this otherwise impossible task more tractable. Most importantly, the modern turbo-molecular pump provides extremely high pumping speeds for almost all gas species. All of the commercial GFIS microscopes incorporate a combination of turbo pumps with a total pumping speed of nearly 1000 liter per second! Multiple pumps are required for the multiple chambers separated by differential pumping apertures, since the emitter must be kept under extreme high vacuum (XHV) conditions while the sample chamber must accept the frequent loading and unloading

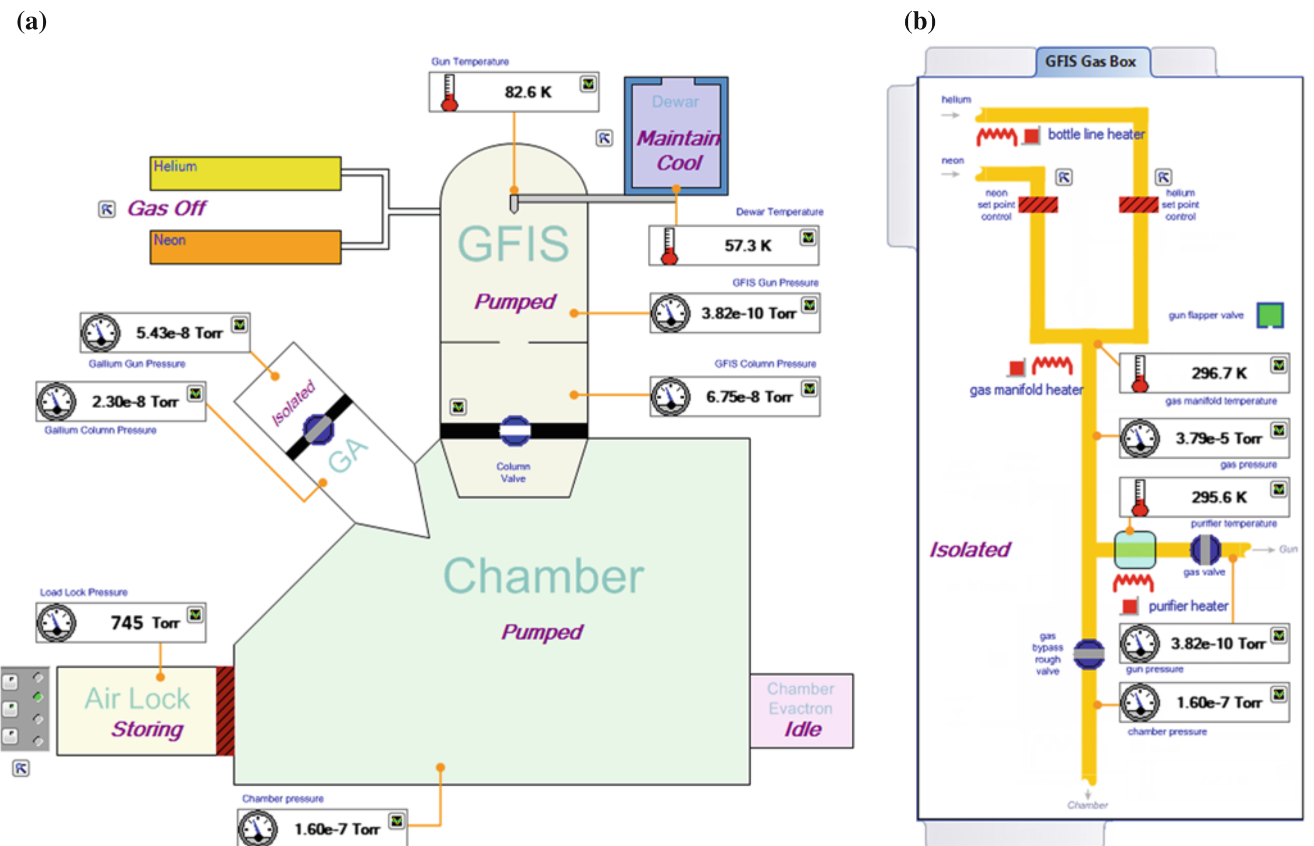

Fig. 1.3 Schematic of **a** the main system and **b** the gas delivery system of the HIM as presented in the vacuum user interface

of samples (Fig. 1.3). Additionally, the previously mentioned cryogenic surfaces surrounding the gun can provide an important additional degree of cryo-pumping and cryo-trapping, but this is only for select species. And lastly, there is a unique property of the high electric field surrounding the emitter which impacts its local vacuum. The high field will tend to polarize any neutral gas atoms in the area, and when subjected to the strong gradient they are drawn in towards the emitter with a force that is proportional to the electric field squared [17]. The undesired gas atoms are ionized as they approach close to the emitter where they experience an electric field surpassing their field ionization limit which is about 2 V/Å. Thereafter, the positive ions are accelerated away from the emitter, leaving a small "bubble" of extreme high vacuum bounded by the contour of critical electric field magnitude. Operating the emitter with a larger extraction field increases the volume of the bubble. In contrast, the helium or neon atoms are typically not ionized until they reaches the surface of the emitter.

1.5 Gas Delivery System

When the imaging gas (neon for example) is turned on, the imaging gas atoms need to be delivered to the emitter with a minimum of contaminants to preserve the trimer and its immediate neighborhood. As described earlier a single adatom adsorbed near the selected atom can result in erratic emission or even cause the selected atom to be lost. Typically, the flux of delivered imaging gas is roughly, $Q = 4 \times 10^{-4}$ Torr liter/s, or 10^{16} atoms/s, or 0.03 sccm. A high quality, "research grade" neon might have contaminants at the 5 ppm level, implying that there may be as many as 5×10^{10} impurity atoms/s delivered to the gun. It is for this reason that HIM instruments incorporate an active chemical purifier integrated into the gas delivery system. The purifier is initially activated as a part of the gas box baking routine, and reaches a peak temperature of about 400 °C. Thereafter, when operating at room temperature, the purifier helps to diminish the abundance of a select subset of the impurities. The purity of the delivered gas is also improved upon its passage through a cryogenically cooled delivery tube to the gun—allowing select gases to be cryo-pumped or cryo-trapped. The rate of gas delivery is controlled by a high precision UHV leak valve which relies upon the adjustable separation between a sapphire surface and an opposing copper surface. The resulting leak rate can be adjusted manually, but more commonly a motorized actuator and regulation software work together to keep the delivered gas pressure constant to within a few percent. Needless to say, the stringent requirements for gas purity require that the entire manifold from gas cylinders to the GFIS gun be constructed of the highest quality vacuum materials, and be thoroughly baked to maintain surface cleanliness.

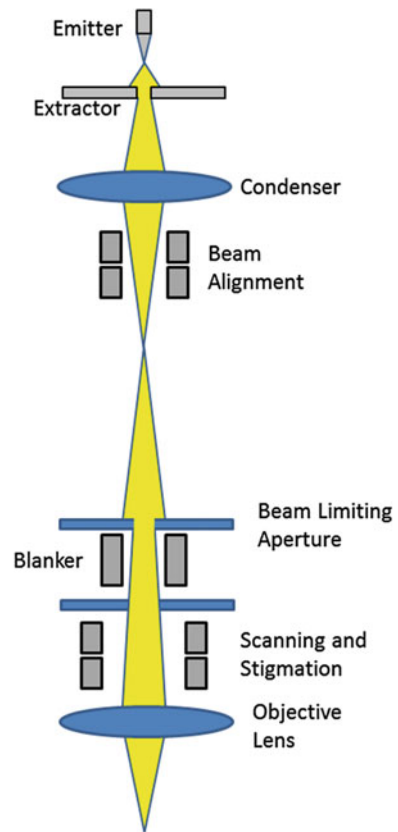

Fig. 1.4 Basic structure of an ion optical column from the ion source to the sample with some of the optical components

1.6 The Ion Optical Column

The primary functions of the optical column in the HIM are: (1) To image the gas field ion source onto the specimen to form a finely focused probe, with a specified probe current; and (2) to scan the probe on the specimen plane to perform various applications, such as imaging or patterning. The first function is often called the DC property of the column, while the second function called the AC property. To accomplish these functions, a typical HIM column can be implemented with a design depicted in Fig. 1.4.

In the column shown in Fig. 1.4, there are two lenses after the extraction optics. The extraction optics extracts the ion beam out of the tip. The first lens (typically called the condenser lens) images the source to a cross-over inside the column. The second lens (typically called the objective lens or final lens) images the cross-over onto the specimen plane. A two-lens system, combined with a variable beam limiting aperture, allows independent control of the column magnification and probe current.

One can estimate the diameter of the probe formed with certain column setting, using the widely known method developed by Barth and Kruit [18]. This method calculates the diameter of the probe containing 50% of the probe current. The calculated diameter using this method is often cited as the d_{50} of the probe. Following this approach, the overall probe size d_p consists of four components:

d_I: the size of the source image
d_A: the contribution due to diffraction
d_S: the contribution due to spherical aberration
d_c: the contribution due to chromatic aberration

For Helium ions, these components can be calculated using the following formulae:

$$d_I = \sqrt{\frac{4I_p}{B_r V_p \pi^2 \alpha_i^2}} \tag{1.1}$$

where I_p is the specified probe current, B_r is the reduced brightness of the source, V_p is the accelerating voltage of the beam and α_i is the half angle of the beam on the image side.

$$d_A = \frac{7.78 \times 10^{-12}}{\sqrt{V_p}\alpha_i} \tag{1.2}$$

$$d_S = 0.18 C_s \alpha_i^3 \tag{1.3}$$

where C_s is the spherical aberration coefficient of the column at a given column magnification.

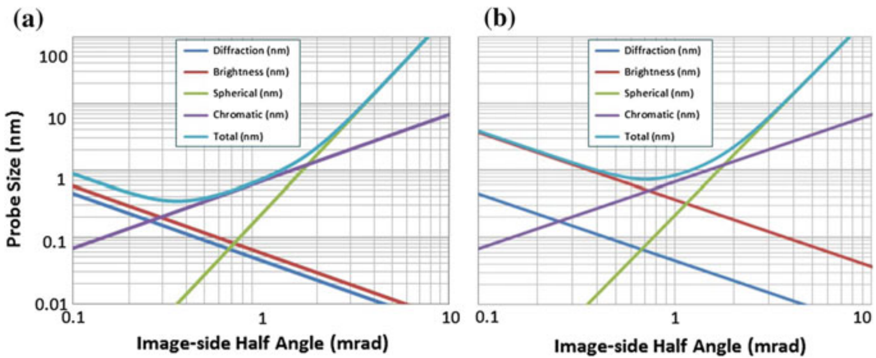

Fig. 1.5 The d50 probe size vs image-side half angle for a 30 keV landing energy helium beam. The two graphs are for optimal conditions **a** for a 0.5 pA helium ion beam, and **b** for a 20 pA beam

$$d_C = 0.34 C_C \frac{\Delta V}{V_p} \alpha_i \tag{1.4}$$

where C_c is the chromatic aberration coefficient of the column at a given column magnification, and ΔV is the energy spread of the ions emitted from the gas field ion source.

The four components are then combined together to form the overall d_{50} probe size d_p:

$$d_p = \sqrt{(((d_A^4 + d_s^4)^{\frac{1.3}{4}} + d_I^{1.3})^{\frac{2}{1.3}} + d_C^2)} \tag{1.5}$$

From (1.5) we can calculate the theoretical probe size (or resolution) at a given probe current, and at a given column magnification.

From (1.1) through (1.5) it is clear that the source properties have a very high impact on the probe size. The gas field ion source is unique compared to other sources in that it has a very high brightness, an atomic-size virtual source size, low energy spread, and an extremely short de Broglie wavelength. Specifically, the helium ion source is characterized by the optical properties presented Table 1.1.

For a given current, I_p (which relates to the source-side half angle by the angular intensity), one can calculate the d_{50} probe size as a function of the image-side half angle, α_i. Figure 1.5 shows some typical d_{50} probe sizes versus α_i plots for helium beams with a 30 keV landing energy. As we can see in these two cases (either 0.5 pA or 20 pA), the probe size of the helium ion beam is primarily limited by source brightness and chromatic aberration.

All four components are also plotted along with the total probe size, and from the plot we can see the optimal probe size for the 30 kV 0.5 pA probe is about 0.35 nm, achieved at an α_i of 0.35 mrad. The corresponding column magnification for this half angle can be calculated using the following equation:

$$M = \frac{\alpha_o}{\alpha_i} \sqrt{\frac{V_{ext}}{V_p}} \tag{1.6}$$

where α_o is the source-side half angle, V_{ext} is the extraction voltage, and V_p is the landing energy of the probe. For the 30 kV 0.5 pA probe considered here, the optimal probe size is achieved with the column magnification of 0.72.

As we can see in these two cases (either 0.5 pA or 20 pA), the probe size of the helium ion beam is primarily limited by source brightness and chromatic aberration.

One important implication from the d_{50} analysis above is that the optimal probe size for helium beam is achieved at a relatively high column magnification (close to 1), as compared to other commonly used charged particle sources (Schottky field emitter has an average source size of 25 nm, Ga source has a source size from 35 to 50 nm; they all operate with a much lower column magnification). If there is any mechanical vibration on the source, the magnitude of the vibration will be imaged

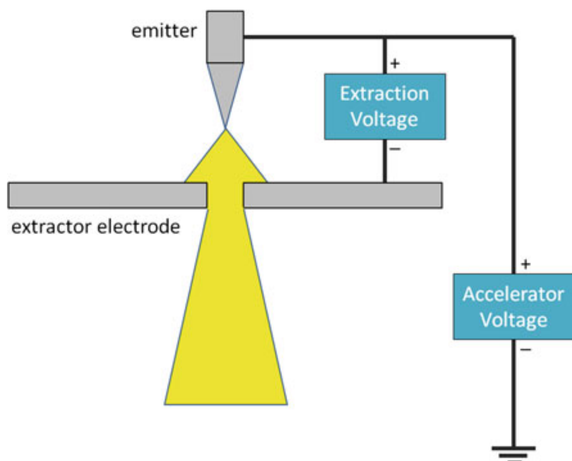

Fig. 1.6 Beam extraction

onto the specimen plane by the column magnification factor. A higher optimal column magnification means higher sensitivity to source vibration. Great care and engineering effort are therefore expended to minimize the source vibrations within the HIM (see Sect. 1.9).

In summary, a working optical column for GFIS needs to be able to provide a focusing property with a column magnification factor in the neighborhood of 1 (typical range of 0.3–2) in order to cover the optimal focusing for a range of probe currents. The column should be relatively immune to mechanical vibration, and the entire column resides in high to ultra high vacuum. In actual implementation, electrostatic lenses are often the lenses of choice because of the weak effect magnetic fields on ions in the energy range in question. In addition to the DC focusing property, the column needs to be able to provide AC forces to deflect the beam to different locations on the specimen plane.

Beam Extraction

In order to ionize the gas atoms and extract them away from the emitter, the gas field ion source is placed at a close distance in front of an extraction electrode (often called the extractor). The extractor is biased to a negative potential with respect to the source in order to generate the electric field needed for ion emission (Fig. 1.6). For helium ions, the field at the apex of the source needs to be at least 4.4 V/Å, and for neon ions, the field is 3.3 V/Å.

The extractor also generates the field needed to select a certain atomic configuration at the source apex for emission site by field evaporating the substrate atoms. This field is typically higher than the extraction field for the imaging gases. After the preferred atomic configuration is achieved, the extraction potential is adjusted to maximize the field only at the selected atomic sites (such as the trimer), and to minimize emission from elsewhere for optimal source brightness.

In implementing the high voltage for the extraction, there are several different topologies available. A commonly used one is floating the extraction power supply

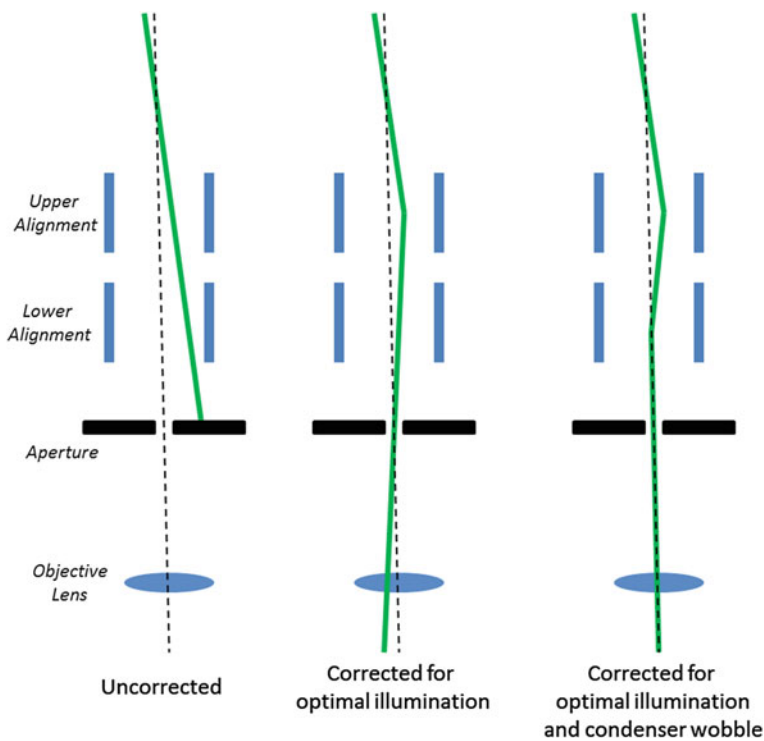

Fig. 1.7 Example of electronic beam alignment with deflectors. The optical axis of the objective lens is shown as a *dotted line*, while the beam is shown as a *solid green line*

on the accelerating voltage power supply for the source. Alternatively, a ground-based extraction supply could also be used. In either case, it is important to prevent the source arcing to any neighboring ground potential in the GFIS gun, because that would momentarily turn on the source into an electron emitter (rather than ion emitter). A safety interlock that locks the extractor potential to remain negative with respect to ground would effectively prevent electron emission due to arcing.

The extractor electrode must be fabricated with mirror finish, with materials that are compatible with high voltage and ultra-high vacuum. Materials with low ion sputtering yield are preferred. The angle that the extractor aperture subtends with respect to the source should be adjusted based on practical operating voltage, effective gas pressure at the apex of the source, distance-pressure-product between the apex and the exit of the aperture, and the exposure to sputtering ions and neutrals.

Beam Alignment

In principle, to achieve the best optical probe size, the ion beam should travel along the optical axis of the column. In reality, the beam emitted from the source may not be aligned with the axis of the condenser lens, and the axis of the condenser lens

may not overlap with the axis of the objective lens due to mechanical tolerances. Therefore, mechanisms are provided within the column to align the beam with the optical axes (Fig. 1.7).

The first alignment typically is to align the beam emerging from the source to the optical axis of the condenser lens. This can be done mechanically with tilt and shift mechanisms, or electronically with beam deflectors, or a combination of both. The alignment criteria of this step would be to minimize image movement while varying the strength of the condenser. The alignment position varies slightly from one atomic configuration of the source to another; therefore, realignment is needed after a new trimer formation or emission site is selected.

The second alignment is to align the beam emerging from the condenser to the axis of the objective lens. A double deflection system above the aperture plane achieves this goal. The upper and lower deflector sets (each with X and Y components) allow the outgoing beam to be correctly aligned to the axis of the objective lens. For convenience, the controls are mapped to provide virtual pivot points which are not necessarily at the planes of the deflectors. This allows the operator to first optimize for illumination, and then for optimize for minimal beam motion with objective lens modulation ("wobble").

Aperture Mechanism

The aperture radius defines the maximum ray angle for a given ray path. Combined with the position of the cross-over point, it defines the probe size and probe current. Therefore, when deciding where to put the aperture and what size should be used, there are two general considerations. First, the aperture plane should be positioned as far away from the condenser lens as possible for maximum probe current adjustment range (while the condenser is positioned as close to the source as possible). There are practical constraints that would not allow positioning the aperture plane immediately before the objective lens. If a double condenser system is used, then the aperture plane should be positioned in between the two condenser lenses, and far away from the first condenser. Secondly, the size of the aperture used for a particular probe current should be optimized. This is done by first computing the optimal ray path for that probe current, and from the position of the aperture plane we can calculate the diameter of the beam on that plane. Such diameter becomes the optimal aperture size for that probe current.

In terms of aperture materials, for the helium beam it is found that the gold thin film type apertures helps improve resolution because of reduced beam-aperture scattering and reduced contamination. The lifetime of this type of thin aperture is however shorter because helium sputters away the aperture over time. For the neon beam, the preferred aperture material is molybdenum for longer lifetime.

Deflection System

The column components mentioned above, extractor, lenses, beam alignment and aperture, all strive to provide a finely focused probe at a given current on the specimen plane. In order to acquire a 2-dimensional image, this probe needs to be

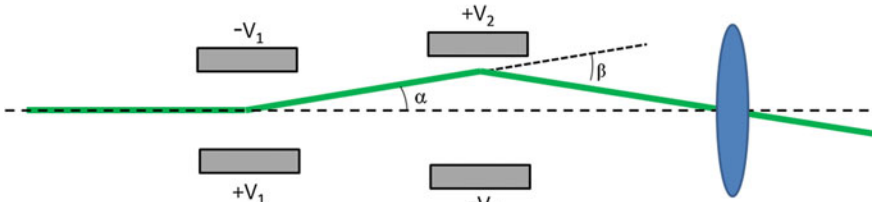

Fig. 1.8 Deflection with a double deflector together with the final lens

deflected to an array of locations on the specimen plane corresponding to the pixels in the final image. This task is accomplished with the deflection system.

There are many ways to deflect an ion beam. For the same reason as in the focusing system, an electrostatic field is a convenient way to implement such deflection. Choices of the deflection could be single deflection, double deflection, or multiple-levels of deflection serving different field of views. The position of the deflection system could also be quite flexible. It could be located before the objective lens (pre-lens deflection) or after the lens (post-lens deflection). Pre-lens deflection has a smaller field of view, but allows a shorter working distance between the lens and the specimen. Post-lens deflection on the other hand can give higher field of view at the expense of working distance.

A pre-lens, double deflection system is shown in Fig. 1.8 as an example. The incoming beam is first deflected by an angle α by the upper deflector, followed by a second deflection to the opposite direction by an angle β by the lower deflector. In the passage of each deflector, the following equation applies:

$$\mathit{deflection\,angle} = \frac{qVL}{2ED} \tag{1.7}$$

where the deflection angle is α or β corresponding to the upper or lower deflection plates, and q is the charge, V is the voltage across the deflector, E is the energy of the particle, L is the length of the deflector and D is the distance between the opposite plates. By applying the appropriate voltages on the double deflection system, the beam should cross the optic axis again after two deflections at an angle of $\beta - \alpha$. The field of view therefore is:

$$FOV = 2(\beta - \alpha)P \tag{1.8}$$

where P is the distance between the pivot point and the specimen. When the microscope changes its magnification, what is changing is the amplitude of the voltage ramps applied to the deflectors, which causes the range of deflection angles to change.

Varying the voltage ratio on the upper and lower deflectors moves the pivot point up and down along the optic axis. There are applications requiring putting the pivot points at various of locations, but typically this pivot point should be located

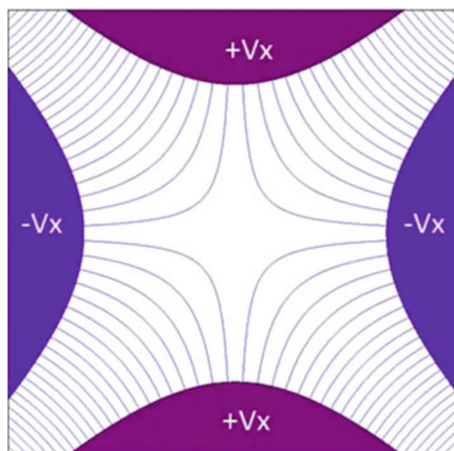

Fig. 1.9 Quadrupole fields for astigmatism correction

at the distortion-free point of the objective lens to minimize the beam blur due to deflection aberrations. By having the pivot point at the distortion-free point also help reduce "barrel" distortion (a result of the pivot point located in front of the distortion-free point) and "pincushsion" distortion (a result of the pivot point located behind the distortion-free point). A side effect of having a pivot point not at the distortion-free point of the lens is, as the focus value varies, the ray is refracted in the lens and results in different field of views.

From a practical engineering point of view, the design of the deflection system requires a complex balance of several often conflicting factors, such as deflection sensitivity, bandwidth, and noise of the driving electronics. For example, for fast patterning applications it is desirable to increase the bandwidth, but that would result in higher noise which would broaden the probe size.

In addition to the dynamic scanning signals discussed above, DC voltages are superimposed on the deflectors to perform static corrections, such as image shift, or astigmatism correction. Image shift or "pan" is the same as scanning, but static. Astigmatism correction is different. Instead of using a dipole field as in the scanning deflection, a stigmator uses a quadrupole field to correct for typical asymmetric beam profiles. An example of quadrupole field is shown in Fig. 1.9. Four electrodes are needed to generate such field. By having two quadrupole fields orientated at an angle (typically 45°), any arbitrary first order astigmatism can be corrected. The sensitivity of the stigmator is proportional to the diameter of the beam at the plane of the stigmator. Therefore for a divergent beam entering the objective lens, the stigmator ideally should be placed close to the final lens. In practice, the stigmator is implemented using the deflection system already in place. When multiple stages of deflection are used, the stigmator should be implemented on the first stage of the deflection, where the beam is closest to the axis.

Dynamic deflection is also used to view the GFIS emission pattern itself, rather than the specimen. The concept is to scan the beam on the aperture plane, and map the angular distribution of rays emitted from the source by correlating the ray that

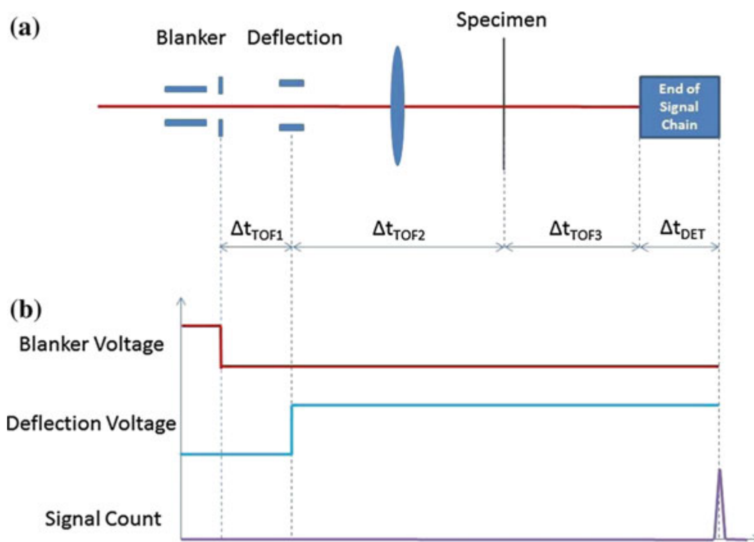

Fig. 1.10 **a** Time of flight of ions through the column to detector; **b** Timing of dynamic components in column and signal collection

passes through the aperture with the deflection angle. As a result, the emission pattern of the GFIS can be obtained. The magnification of such recorded emission pattern is determined by the amplitude of the deflection and position of the cross-over point.

Beam Blanking

The Ion beam can be blanked with a sufficiently large deflection field and a blanking aperture, or "beam stop". Therefore (1.7) also describes the angular deflection of an electrostatic blanker. The primary consideration for a beam blanker is the speed. The blanking or unblanking time is related to the rate at which a required voltage put on the blanker electrodes, and the required voltage is determined by the blanker sensitivity. Consideration must be given to the geometric design of the blanker in order to provide the speed demanded by the specific applications.

A secondary consideration in blanker design is to manage the blanking tail. The term, blanking tail, refers to the beam movement on the specimen while the blanker changes states (from unblanked to blanked or vice versa) which often results in an unwanted partial beam exposure in an adjacent area. Increasing the blanking speed (e.g. increasing the voltage slew rate) can help to minimize this effect. But even for an infinitely fast blanking, there are also cases in which the transition occurs while the ion is within or adjacent to the blanker during the transition. These effect can be largely mitigated by choosing the location of the blanker so that its center is at or near the cross-over position of the beam. The effects can also be mitigated by increasing the blanking sensitivity so that only a small voltage is required to deflect the beam into the beam stop and prevent it from reaching the sample.

Table 1.2 Time-of-flight of He, Ne and Ga ions through 100 mm at various beam energies

Ion species	30 keV	10 keV	1 keV
He	83 ns	144 ns	455 ns
Ne	187 ns	323 ns	1020 ns
Ga	347 ns	600 ns	1900 ns

Time Delays in Ion Columns

To form an accurate image or to perform precise patterning, the applied deflection voltage corresponding to a pixel in the image needs to be precisely matched to the physical landing position of the ions. Further, the corresponding landing position needs to be matched to the signal collected in the detector (in imaging applications). Various of dynamic components in the column and signal chain should be precisely orchestrated in time to achieve this spatial–temporal accuracy.

Ions have finite mass and kinetic energy and therefore their time-of-flight (TOF) through the column are non-negligible and often dictate the timing of various dynamic components. In Fig. 1.10a, an ion is shown to start from the end of the blanker, first reaching the center of the scanning deflector after Δt_{TOF1}, then landing on the specimen after another Δt_{TOF2}, then the secondary electrons reaching the detector after another Δt_{TOF3}, and finally a pulse of signal is received at the end of signal chain after a detector delay Δt_{DET}. In some column designs where the length of the deflector itself is quite long, the TOF through the different deflection stages should also be considered.

A timing diagram of three key dynamic components in the column and signal chain is shown in Fig. 1.10b to show how these TOFs are used in controlling component timing. As an example, suppose the clock starts when the blanker is unblanked. Then after a delay of Δt_{TOF1}, the deflection voltage is applied. (For

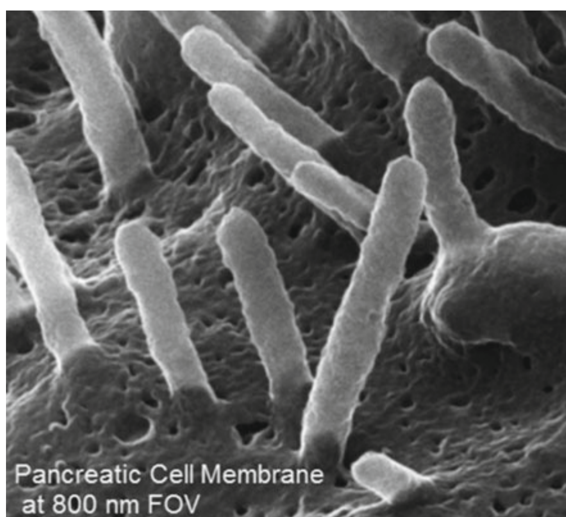

Fig. 1.11 HIM image of the surface of a pancreatic cell membrane (courtesy of Prof. Paul Walther of the Univ. of Ulm, Germany)

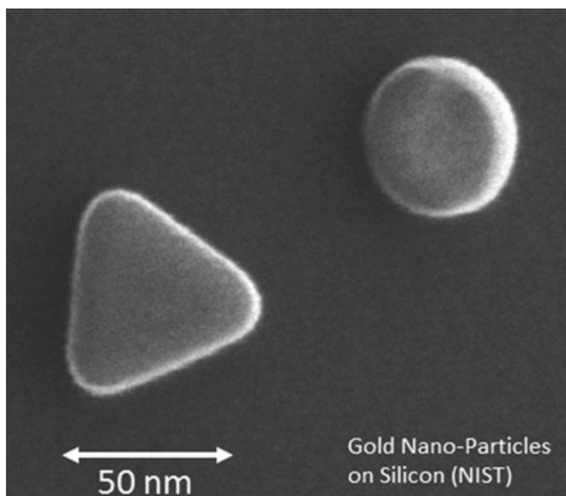

Fig. 1.12 Gold nanoparticles on a silicon substrate (courtesy of Mike Postek, NIST, Gaitherburg, MD, USA)

simplicity of discussion, the rise time of the deflection voltage itself is ignored.) Then after another delay of $\Delta t_{TOF2} + \Delta t_{TOF3} + \Delta t_{DET}$, the signal received at the end of signal chain is counted as the pixel intensity corresponding to the applied deflection signal. In the patterning application, it is important that the particles going through the deflection see a constant deflection voltage, meaning the pixel dwell time cannot be lower than the TOF through the deflector.

Table 1.2 shows some example TOFs of He, Ne and Ga ions travelling a distance of 100 mm. It is clear the for heavier species, such as Ne or Ga, the TOFs at medium to low energy is quite signification. Careful timing control is needed to accurately manipulate the landing positions of those beams.

1.7 Beam Induced Damage

The HIM is known to provide valuable images because of its small focused probe size, its long depth of focus, and the variety of detectable particles which convey unique contrast mechanisms. Figures 1.11 and 1.12 below show some of the high quality, high magnification images.

On the sample surface and beneath the surface, the helium beam is known to produce damage (surface sputtering, charge transfer, implantation, and lattice damage) [19]. In light of this, it is regarded as very important that the imaging system be optimized to gather the most information for a given exposed dosage of ions. In most circumstances, the adverse effects accumulate with each incident ion and are dependent upon an *areal* dosage, σ, (sometimes just called dosage) with units of ions/cm^2. Some effects that dissipate with time (e.g. charging or thermal effects) may have dependence upon the areal dose *rate* which usually expressed in

ions cm^{-2} s^{-1}, but it is generally understood that most adverse effects are rate independent. Thus, for the GFIS imaging systems, the goal of optimizing the detector's efficiency is described as maximizing the signal to noise ratio SNR for a given areal dose, or maximizing the "information to damage ratio". The same goal applies to detectors for SEMs and TEMs, but the damage there is less pervasive due to the lower mass of the incident particle. The same goal applies to gallium FIBs, but is less critical since these instruments are used explicitly for their damage capabilities and are seldom employed for high resolution imaging. So we find that for the HIM, the efficiency of the detector, and the signal chain, are matters of special importance and worthy of optimization.

Regardless of the type of detected particle (e.g. secondary electron, secondary ion, backscattered helium, transmitted helium, etc.), producing a "good" image requires that there be a sufficient number, N_d, of detected particles per pixel in the final image. There are several probabilistic factors that contribute to the detection of the N_d detected particles: The arrival of ions from the source is believed to follow Poisson statistics. The emission of many secondary particles (such as secondary electrons or secondary ions) is also governed by Poisson processes. Further, the detectability of the particle and the signal generation process all introduce their own probability functions. Appealing to the central limit theorem, we suppose that all of these random factors can be combined to give an overall image signal that is roughly Gaussian with a mean value that is proportional to N_d and a standard deviation that is proportional to $\sqrt{N_d}$. Thus, the signal to noise ratio, *SNR* is presumed to follow the general form:

$$SNR = \frac{signal}{noise} \sim \frac{N_d}{\sqrt{N_d}} = \sqrt{N_d}. \tag{1.9}$$

If we define Ni as the average number of incident ions per pixel, and Y as the effective yield of the detected particle per incident ion, such that $Y = N_d/N_i,$ then

$$SNR \sim \sqrt{N_i}\sqrt{\frac{Y}{1+Y}}. \tag{1.10}$$

The simple interpretation of this result is that the SNR ratio is principally limited by the smallest number in the chain of events that leads to the detected signal. For example, if the yield, Y, is appreciably larger than 1, as for secondary electrons, then the SNR is primarily determined by the Poisson statistics of the ion arrival events, and further increases in the yield do not significantly affect the SNR. Whereas in another situation, if the yield of backscattered ions is much less than one, then the sensitivity to yield is still significant.

As a rule of thumb, the SNR should be about 5 to have an easy to interpret image. In the case of SE imaging, where Y is typically 3–5, then this requires about $N_i \sim 25$ incident ions per pixel. Alternately, if the backscatter yield is 0.1, then the SNR rule of thumb would suggest that 250 incident ions are required per pixel. The dependence of areal dosage, σ, on the field of view, *FOV*, is expressed as:

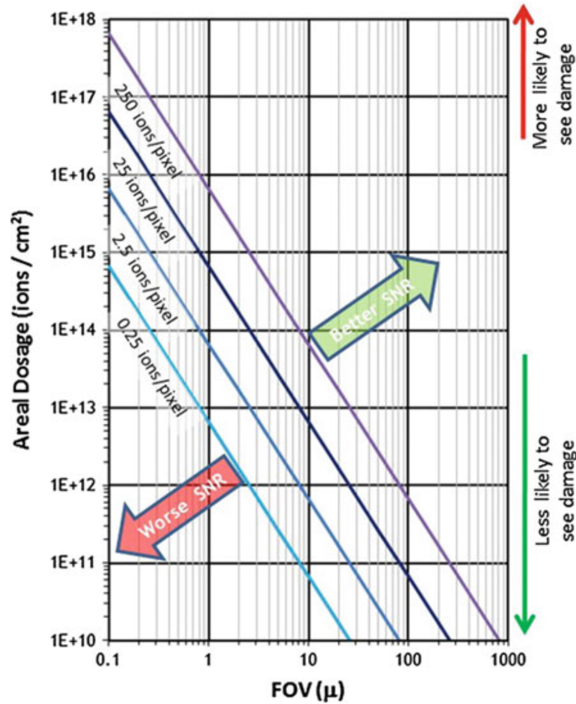

Fig. 1.13 Lines corresponding to a fixed number of incident ions per pixel, are graphed on axes representing the FOV (horizontal axis), and the areal dosage (vertical axis)

$$\sigma = \frac{N_i}{FOV^2}. \tag{1.11}$$

The general scaling of this relation is shown in Fig. 1.13. Eliminating N_i in favor of the *SNR* with help of (1.10) we can arrive at a form which is arguably more important to the microscopist:

$$\sigma = \frac{(SNR)^2}{FOV^2}\left(1 + \frac{1}{Y}\right). \tag{1.12}$$

The microscopist must satisfy the condition, $\sigma < \sigma_{critical,}$ so that the areal dosage is kept below the level that will result in undesired effects. The threshold, $\sigma_{critical}$, depends very much on the materials in question, but even more so upon the particular application's tolerance to damage. For example, for materials that are already amorphous, it is probably not important if they are amorphised by the incident ion flux. And when imaging thin sections, sub surface implantation is not a concern.

From the previous equation, it is now relatively plain to see that decreasing the FOV by a factor of 3 (say from a 3 to 1 μm) will subject the sample to about 10× more areal dosage if the SNR is to be maintained. Similarly, it is also evident from the above equation that generating images from low yield particles (secondary ions,

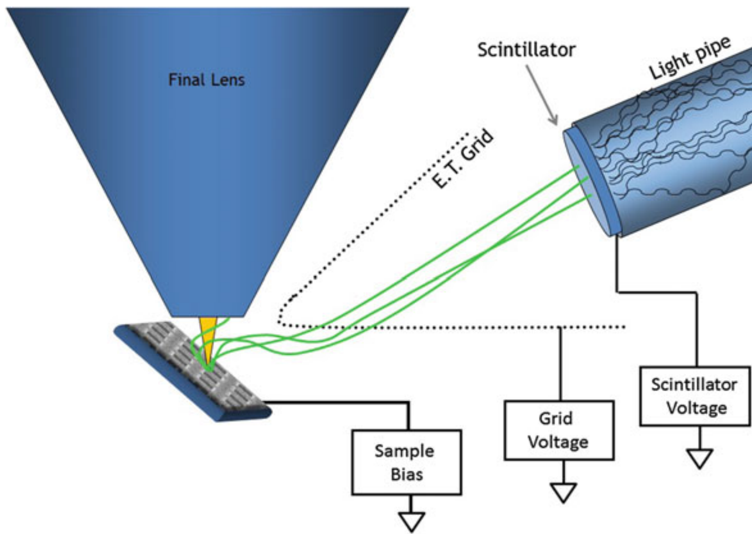

Fig. 1.14 The in-vacuum portion of the Everhart-Thornley detector as adapted to the helium ion microscope. For the collection of secondary electrons, typically the sample is biased to +5 V, the grid is biased to +500 V, and the scintillator is biased to +10,000 V

or backscattered helium for example), where Y $\ll$ 1 will require either larger fields of view, or lower SNR, or higher areal dosages. Note that averaging techniques, such as line averaging or frame averaging, offer no advantage (with the aforementioned provision that dose rate is irrelevant). Note also, that for very small FOVs, the relevant term in the denominator must be increased to reflect the characteristic width of the damage mechanism, w_{dmg}:

$$\sigma = \frac{(SNR)^2}{FOV^2 + w_{dmg}^2}\left(1 + \frac{1}{Y}\right) \tag{1.13}$$

1.8 Detectors and Signal Chain

The above analysis serves to motivate the instrument designer and the operator to ensure that all available information is acquired for a given areal dosage, e.g. maximizing the information to damage ratio. Since secondary electrons (SEs) are known to be produced in abundance from the helium ion beam, and because they can be used to generate high resolution with valuable contrast, the ET detector which collects them should operate with high efficiency. What sets this apart from the same exercise in the SEM is the relatively high helium induced SE yield (typically 3–5), the relatively low probe currents (often 0.5 pA or less), the lower

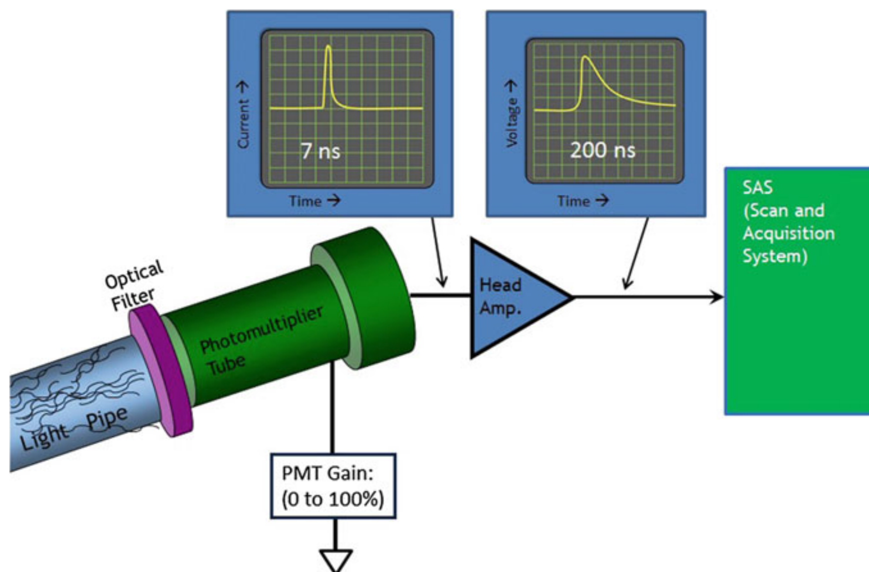

Fig. 1.15 The out-of-vacuum components of the ET detector. The PMT provides the necessary gain, and the head amplifier converts the signal to an easily measured voltage pulse

SE energy distribution (FWHM < 2 eV) [20], and distinctly different nature of the sample charging, and the relatively low contribution of SE2 and SE3 (which rely upon backscattering as an intermediate step).

The in-vacuum components of the HIM's ET detector are only slightly different from the equivalent detector in an SEM. The distinctions include an ET grid which has a fine and highly transparent mesh, and a scintillator that is more consistent and uniform in terms of its photon yield. The grid is commonly biased to +500 V, and the scintillator is usually set to +10 kV (Fig. 1.14). Modeling and experiments confirm that the collection efficiency can be as high as 90%. The ET grid is also designed to be biased negatively to repel the electron flood beam when it is periodically used to dissipate the accumulated positive surface charging encountered with insulating samples. Generally, the best collection occurs when the electric field from the ET grid is strongest at the beam's landing position. This occurs for example when the sample is tilted somewhat, and when sample being imaged is at the nearest the edge of the sample holder. Biasing the sample to several volts positive often has an appreciable benefit.

For each electron striking the scintillator it is expected that over 100 photons are sent through the light pipe, and a significant fraction of these are transferred to the opposite end, outside the vacuum chamber (Fig. 1.15). The light is filtered to eliminate any low wavelength components which represent stray light from the flood gun's filament or the stage encoders. Beyond this, the PMT is selected for its high quantum efficiency photocathode to minimize the chance that any information

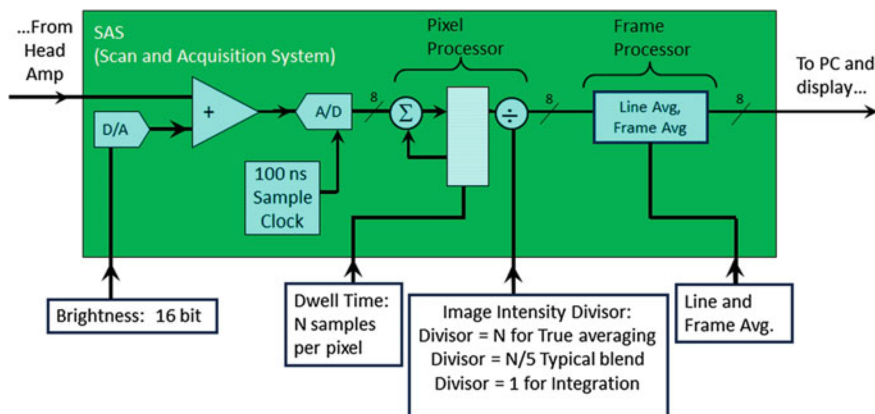

Fig. 1.16 The scan and acquisition system electronics

will be lost at the first strike. The output of the PMT is in the form of a single current pulse (~7 ns width) corresponding to each SE arriving at the scintillator. After passing through a trans-resistance amplifier, the pulse is stretched to about 200 ns FWHM so that it is shaped appropriately for the subsequent sampling at regular time intervals. Since a single incident ion will usually generate a few SEs, and since they arrive at nearly the same time, the resulting pulse height is largely an indicator of the varying SE yield across the sample. Considering that the SE yield is nearly always greater than unity, pulse counting is not of much practical benefit—except to study the emission statistics of the source! So of the two complimentary schemes, pulse frequency provides almost no information about the sample, whereas pulse amplitude provides the richest sample information.

The signal output from the head amplifier is passed to the Scan and Acquisition System (SAS) board where it is first offset with the adjustable brightness (Fig. 1.16). The analog signal is *always* sampled with a 100 ns sample clock and converted to an 8 bit digital value. This is where it is critical that the pulse shape is well chosen. If the pulse shape is too narrow it could fall between the consecutive samples, and convey no information. If the pulse shape is too wide it will result in too many consecutive samples, possibly causing a smearing in the resulting images. The pixel processor collects all the 8 bit sampled values which fall within the chosen pixel dwell and combine them by either averaging, or integration, or some intermediate blend. For example, if the pixel dwell is chosen to be 20 μs, then 200 samples will be acquired at the 100 ns sample clock and combined to produce a single 8 bit number. The parameter "image intensity" allows the user to determine if the computed result for each pixel is more alike to an average value, or more like an integral. The computed result for the indicated pixel is then stored to memory where it will be transferred to the PC and its displayed image. Optionally, with line averaging or frame averaging enabled, the signal measured for repeated beam visits to the same sample location can be averaged to progressively reduce the overall noise for the corresponding pixel

in the image. Once the image is transferred to the PC, further digital analysis is available via the histogram, and further manipulations can be conducted via look up tables. When saved, each TIFF image has an integrated metafile that contains all the instrument settings that might be helpful for documenting the imaging conditions.

It is sometimes suggested that the 8 bit analog to digital conversion is not sufficient to represent the dynamic information presented in a given 100 ns interval. But it is important to recognize that each pulse that is converted conveys only one piece of information: the number of secondary electrons arriving at that 100 ns interval. And given the very low probe currents (say 0.5 pA), the vast majority of the 100 ns intervals contain zero signal. When a non-zero signal is eventually measured, the gain would nominally be set so that the largest possible conversion (255) corresponds to an extreme event where say 10 secondary electrons were detected within a single 100 ns interval. By this analysis, the 8 bit A/D conversion is seen to be adequate. The subsequent pixel processing is conducted with 24 bit resolution for each pixel, before yielding the final result that is again reduced to 8 bits. While these final 8 bits are adequate for most static and linear viewing situations, there is a growing desire allow for more dynamic range—beyond what can be conveyed in 8 bits.

Finally, the importance of the "image intensity" can easily be overlooked, but it has considerable impact in the final image quality. And because the typical SEM has no equivalent imaging parameter, it will be described in detail here. The circumstances that are unique to the HIM and require image intensity are (a) the very low probe currents that cause the ions to arrive at an average interval that is much longer than the sample clock, and (b) the secondary electron yield which is normally appreciably larger than unity. Consider the case where the pixel dwell is set to 20 μs, and image intensity is set to 0, so that pixel processor computes a *true average* of the 200 samples for that pixel. Given the low probe currents, it is likely that perhaps only 40 samples will have measurable pulses. And if the PMT gain is chosen so that the average pulse height is converted to the intermediate digital value of 128, then a true average would give a grey level of just 26 (= 40 × 128/200). The operator seeing this image, would of course increase the gain by a factor of about 5, causing the signal to rise above the maximum A/D conversion level—effectively saturating the A/D convertor, but providing no evidence in the image to the operator. An astute instrument operator could also interrogate the raw signal by briefly changing the dwell to 100 ns, and the image intensity to 0, so the PMT gain can be properly set to avoid the now visible saturation. The image intensity serves to boost the result of the pixel processor to make the operator more likely to recognize the onset of saturation. Given the low probe currents, it is not uncommon to choose a default image intensity of "23.3%" which corresponds to a signal boost of about 5×. For less frequently detected particles, it is not uncommon to choose higher value of image intensity. Whereas for very high currents (e.g. when the detector pulses are overlapping) it is acceptable to set the image intensity to 0 for a true average.

1.9 Vibrational Considerations

All charged particle microscopes (CPM) that use a scanned, focused probe are susceptible to image vibrations because the image is acquired one pixel at a time. Image vibrations can be caused by all effects that cause the emitted beam to land in the wrong location by some time-varying amount. Given the very small probe size of the HIM (0.35 nm for example), it is important that the system vibrations be small enough to permit the expected high magnification images. For any scanned probe microscope like the HIM, vibrations that are evident in the images are always the result of three necessary factors: There must be (a) a source of energy that feeds the vibrations, (b) a flexing element between source and sample, and (c) a transmission pathway between the energy source and the flexing element. Eliminating any one of these three factors will eliminate that particular image vibration.

For the GFIS gun in particular, vibrations at the source are a significant issue since the total emitted current and the angular current density are relatively low, and hence the option of discarding current to achieve source demagnification is generally not viable. Under typical conditions, the overall column magnification from source to sample is in the range of 0.3–1.5 meaning that vibrations at the emitter are directly visible in the images, just as sample vibrations would be. (In contrast, this situation is quite different for a Schottky thermal field emitter where the source is typically demagnified by $\times 20$ or more.)

The first approach for vibration immunity is to design the GFIS gun, column, and sample stage to be as rigid as possible. Unfortunately, the GFIS gun cannot be rigidly mounted to the underlying vacuum chamber, but rather is attached with the flexible vacuum seals to allow it to be shifted and tilted in order to aim the emitted beam along the axis of the column. In effect, the GFIS emitter is mounted on a translation and tilt stage with four degrees of freedom at the top of the microscope. At the opposite end of the microscope, the sample is usually mounted on its own 5 axis stage making a total of 9 degrees of freedom from source to sample, and leaving the system vulnerable to flexing components. As a further engineering challenge, the GFIS gun must be supported by relatively long, thin, thermally insulating supports to reduce the heat transport from the outside world (at room temperature) to the GFIS emitter (at about 70 K).

Addressing the energy sources is another approach. A good microscope will avoid having sources of vibrational energy too close to the critical components of the microscope. Cooling fans, circulated cooling water, 50 or 60 Hz power, and boiling cryogens can be avoided. However the demanding requirements for ultra-high vacuum despite a high flux of noble gases requires the use of turbo pumps. These necessarily introduce vibrations into the system at either the rotor spin frequency (typically 800 Hz to 1 kHz), or its harmonics. The newer models of magnetically levitated turbo pumps are generally preferred, but tend to introduce additional vibrations across a broader frequency range. Energy sources that arise from the environment in the form of floor vibrations, AC fields, and acoustic energy are additional risks. The instrument has a limited tolerance for these, since they can

excite image vibrations, so the installation requirements strictly prescribe a site with low energy levels to achieve the highest image quality.

As a last resort, there is the general approach of interrupting the energy source before it can excite the flexible element between the source and the sample. The commercial HIM instruments have all been built upon a massive granite slabs that are floated on an air isolation system. This helps to intercept and attenuate any floor vibrations, and helps to add inertia to the microscope making it less susceptible to acoustic energy sources. In turn, the granite supports the chamber/column/gun stack by way of another air isolation system. If the site survey measurements indicate that the desired installation site is unsuitable, the customer has other options to help mitigate the facility's problems. If 50 or 60 Hz magnetic fields are an issue, there are commercial packages that can apply opposing magnetic fields to create a field-free region in the vicinity of the column. If floor vibrations are a problem, they can generally be attenuated by introducing an intervening passive or active support structure that is commercially available through third parties. And if the acoustics are deemed to be unacceptable at a specific site, there are acoustic enclosures already designed for the HIM that can greatly diminish to the sound pressure waves and their impact on the image.

1.10 Conclusion

Like the proverbial reference to "shoulders of giants" the HIM relies upon a foundation of several key technologies and sub-systems. The HIM concept was certainly recognized by Muller shortly after 1955 when he recognized that the spots of light on his phosphor corresponded to the individual atoms on the apex of his pointy needle. For the next half century, the critical sub-systems and enabling technologies matured to they could sufficiently support the instrument we've come to call the HIM. These critical technologies outlines in this chapter include cryogenics, high vacuum, gas purity, vibration control, ion optics, and detectors.

References

1. The HIM is presently commercialized by Carl Zeiss Microscopy LLC, as the ORION, ORION Plus, and ORION NanoFab
2. R. Hill, J. Notte, B. Ward, The ALIS He Ion source and its application to high resolution microscopy. Phys. Procedia **1**, 135–141 (2008)
3. R. Ramachandra, B. Griffin, D. Joy, A model of secondary electron imaging in the helium ion scanning microscope. Ultramicroscopy **109**(6), 748–757 (2009)
4. C. Rodenburg, M.A.E. Jepson, B.J. Inkson, X. Liu, Dopant contrast in the helium ion microscope: contrast mechanism. J. Phys: Conf. Ser. **241**, 012076 (2010)
5. J. Notte, R. Hill, S.M. McVey, R. Ramachandra, B. Griffin, D. Joy, Diffraction imaging in a He + Ion beam scanning transmission microscope. Microsc. Microanal. **16**, 599–603 (2010)

6. D. Winston, B. Cord, B. Ming, D. Bell, W. DiNatale, L. Stern, A. Vladar, M. Postek, M. Mondol, J. Yang, K. Berggren, Scanning-helium-ion-beam lithography with hydrogen silsesquioxane resist. J. Vac. Sci. Technol. B **27**(6), 2702–2706 (2009)
7. S.A. Cybart, E.Y. Cho, T.J. Wong, B.H. Wehlin, M.K. Ma, C. Huynh, R.C. Dynes, Nano Josephson superconducting tunnel junctions in YBaCuO directly patterned with a focused helium ion beam. Nat. NanoTechnol. Lett. **76** (2015)
8. J. Yang, D.C. Ferranti, L.A. Stern, C.A. Sanford, J. Huang, Z. Ren, L.C. Qin, A.R. Hall, Rapid and precise scanning helium microscope milling of solid-state nanopores for biomolecule detection. Nanotechnology **22**(28), 285310 (2011)
9. W.J. Arora, S. Sijbrandij, L. Stern, J. Notte, H.I. Smith, G. Barbastathis, Membrane folding by helium ion implantation for three-dimensional device fabrication. J. Vac. Sci. Technol. B **25**(6) (2007)
10. S. Sijbrandij, B. Thompson, J. Notte, B.W. Ward, N.P. Economou, Elemental analysis with the helium ion microscope. J. Vac. Sci. Technol. B **26**(6), 2103–2106 (2008)
11. J. Notte, F.H.M. Faridur Rahman, S. McVey, S. Tan, R.H. Livengood, Neon gas field ion source—stability and lifetime. Microsc. Microanal. **16**(2), 28–29 (2010)
12. J. Notte, Charged particle microscopy: why mass matters. Microsc. Today. 16–21 (2012)
13. L. Pillatsch, N. Vanhove, D. Dowsett, S. Sijbrandij, J. Notte, T. Wirtz, Study and optimization of SIMS performed with He+ and Ne+ Bombardment. Appl. Surf. Sci. **282**, 908–913 (2013)
14. A.J. Melmed, Recollections of Erwin Müller's laboratory: the development of FIM (1951–1956). Appl. Surf. Sci. **94**(95), 17–25 (1996)
15. E.W. Müller, K. Bahadur, Field ionization of gases at a metal surface and the resolution of the field ion microscope. Phys. Rev. **102**(3), 624–631 (1956)
16. In the world of GFIS, the imaging species are regarded as noble and good, while the residual vacuum constituents which corrupt the emission process are jokingly regarded as "peasant atoms". Hence the idiom, "adatoms are bad atoms".
17. R. Gomer, *Field Emission and Field Ionization*. Reprinted as part of the American Vacuum Society Classics Series (American Institute of Physics, New York, NY, 1993)
18. J.E. Barth, P. Kruit, Addition of different contributions to the charged particle probe size. Optik **101**, 101–109 (1996)
19. R. Livengood, S. Tan, Y. Greenzweig, J. Notte, S. McVey, Subsurface damage from helium ions as a function of dose, beam energy, and dose rate. J. Vac. Sci. Technol. B **27**(6), 3244–3249 (2009)
20. Y.V. Petrov, O.F. Vyvenko, A.S. Bondarenko, Scanning helium ion microscope: distribution of secondary electrons and ion channeling. J. Surf. Invest. X-ray Synchrotron Neutron Tech. **4** (5), 792–795 (2010)

Chapter 2
Single Atom Gas Field Ion Sources for Scanning Ion Microscopy

Radovan Urban, Robert A. Wolkow and Jason L. Pitters

Abstract This chapter discusses fabrication and experimental evaluation of W(111) single atom tips (SATs) for gas field ion source applications. Firstly, a brief history of field ion microscopy (FIM) will be given since it will be heavily relied on throughout the text. We will discuss ion current generation in FIM and carry that knowledge over to fabricated SATs. Secondly, gas assisted etching and evaporation process will be discussed in detail. It will be shown that nanotip shape, and therefore SAT characteristics, can be controlled and modified to achieve desirable ion beam properties. Lastly, we will evaluate ion beam width as a function of tip voltage and temperature as examples of experimental efforts to better understand gas field ion source performance.

2.1 Introduction

This chapter will briefly review a history of field ion microscopy as well as scanning ion microscopy. Various methods to fabricate gas field ion sources based on atomically defined nanotips will be covered. Nitrogen assisted etching and evaporation processes will be described in detail as a method to prepare robust single atom tips (SATs).

Scanning ion microscopy (SIM) is a modern imaging technique similar to scanning electron microscopy (SEM). In SIM, however, an electron beam is replaced by positive ions. When helium is used in SIM, it is often referred to as helium ion microscopy (HIM).

R. Urban · R.A. Wolkow (✉)
Department of Physics, University of Alberta, Edmonton, AB, Canada
e-mail: rwolkow@ualberta.ca

R. Urban
e-mail: radovan@ualberta.ca

R. Urban · R.A. Wolkow · J.L. Pitters
National Institute for Nanotechnology, Edmonton, AB, Canada
e-mail: jason.pitters@nrc-cnrc.gc.ca

© Springer International Publishing Switzerland 2016

G. Hlawacek and A. Gölzhäuser (eds.), *Helium Ion Microscopy*,
NanoScience and Technology, DOI 10.1007/978-3-319-41990-9_2

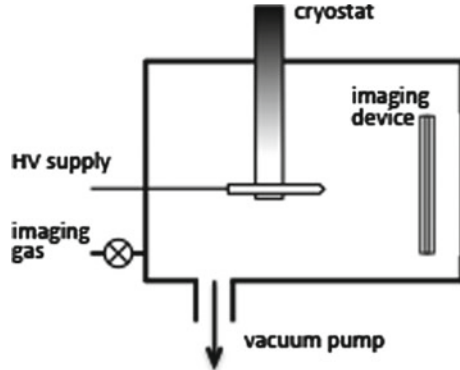

Fig. 2.1 A schematic diagram of a typical FIM apparatus

There are several advantages that SIM offers over conventional SEM, namely (i) large depth of focus due to low beam divergence, (ii) greater surface and element specificity due to lower interaction volume, and (iii) better ion lithography due to minimal proximity effects. The overall instrument design is very similar to SEM or focused ion beam (FIB) instruments. The key difference is in the charge particle source. The SIM uses a gas field ion source (GFIS) to generate gas ions. A historical perspective of the development of a commercial SIM is presented in a review by Economou [1] while more recent advances are covered in the chapter by John Notte.

The principle of He^+ and Ne^+ ion beam generation has been known for many decades and is based on the field ion microscopy (FIM) technique developed by Erwin W. Müller and Tien T. Tsong in the late fifties and early sixties. In a typical FIM system, see Fig. 2.1, a sharp tip is placed in a vacuum system while positive voltage is applied. Typically, several tens of kilovolts is needed to achieve sufficient electric field at the tip apex to ionize imaging gas, typically helium. As imaging gas atoms become ionized near the tip the resulting ions are projected away from the tip by the strong field towards an imaging device, such as a phosphorous screen. The resulting image consists of tens or hundreds of spots each created by an individual tip apex atom. As the understanding and applications of FIM improved, simple metals to complex alloys as well as diffusion studies of ad-atoms and molecules were studied. Further field evaporation studies led to the development of atom probe microscopy which mass spectrally identifies each field evaporated ion to create a 3D map of the tip [2, 3].

In a sense, each spot in an FIM image is due to an ion beam created at a single surface atom of the tip under study. However, in the case of large tips (and hundreds of spots), because the total ion current draws upon a finite source of adsorbed neutral He atoms, the ion current in each beam is too small to be useful for imaging. Over the next several decades since FIM discovery, researches pursued the creation of sharp nanotips to dramatically decrease the number of emitting atoms and thus increase ion current per atom. Several methods were established to create nanotips which are terminated by only a few atoms. These methods include depositing atoms on the

apex [2, 4–6], supertip formation [7–11], annealing in the presence of an electric field [12–17], gas atom facet induced reactions involving gas adsorption [18–24], faceting with thin metallic overlayers [25–37] or field controlled chemical etching [38–46]. With all these nanotips, adsorbed helium is ionized at only a few atoms at the apex (or one atom in the case of a single atom tip) increasing the current density and source brightness required for a working scanning ion microscope.

Source brightness is a key defining characteristic for usable GFIS in a SIM. The source brightness is defined as [55, 56]

$$B = \lim_{\Delta A \to 0} \lim_{\Delta\Omega \to 0} \frac{\Delta I}{\Delta A \cdot \Delta\Omega}, \tag{2.1}$$

where ΔI is an emission current per element area ΔA at the source plane, radiated into a solid angle $\Delta\Omega$. Similarly, angular current density j_a is defined as

$$j_\mathrm{a} = \lim_{\Delta\Omega \to 0} \frac{\Delta I}{\Delta\Omega}. \tag{2.2}$$

The above definitions represent a mathematical limit which is hard to measure experimentally. More recently, *practical brightness* was discussed theoretically by Bronsgeest et al. [57]. They suggested using a solid angle defining aperture that allows half of total current through. Typically, angular current density, or rather *averaged* angular current density, is evaluated by measuring ion current through an aperture of known size. Therefore, averaged values, $\bar{B}$ and $\bar{j}_\mathrm{a}$, are measured

$$\bar{B} = \frac{1}{A_\mathrm{s}} \frac{\Delta I}{\Delta\Omega} = \frac{1}{A_\mathrm{s}} \bar{j}_\mathrm{a}, \tag{2.3}$$

$$\bar{j}_\mathrm{a} = \frac{\Delta I}{\Delta\Omega}, \tag{2.4}$$

where A_s is virtual source size. In available literature where average brightness is evaluated, emission area ΔA from (2.1) is replaced by a virtual source size A_s. Unfortunately, virtual source size has not been measured for single atom gas field ion sources and the values found in literature are based on certain assumptions and are typically <5 Å in diameter [32, 47, 52]. To avoid additional uncertainties we will concentrate on angular current density evaluation rather than brightness which can be well defined.

Definitions (2.3) and (2.4) of beam brightness and angular current density represent average quantities which depend on a particular experimental geometry. This is due to inherent inhomogeneity of the ion beam profile across a finite size aperture defined by a solid angle. It is possible to approximate a uniform aperture illumination for inhomogeneous beam profiles by allowing only a small fraction of total current through the aperture in the limit $\Delta\Omega \to 0$, which corresponds to definitions (2.1) and (2.2) discussed above. This can be approximated in systems with large total currents. However, for GFISs with limited current supply this is a difficult approach since measured current though the aperture would be negligible.

Table 2.1 Compilation of measured *averaged* angular current density available in literature

Measured current	Average angular current density	Helium pressure	Tip voltage	Tip temperature	References
5 nA	5 μA/sr	1×10^{-5} Torr	n/r	5 K	[a]
10 nA	8 μA/sr	$\sim 5 \times 10^{-4}$ mbar	~20 kV	16 K	[b]
4.8 nA	20 μA/sr	5×10^{-4} mbar	n/r	22 K	[c]
n/r	2.2 μA/sr	2.5×10^{-4} Pa	13.3 kV	20 K	[d]
30 pA	1 μ/sr	1 Pa	n/r	LHe	[e]
n/r	1.98 μA/sr	0.019 mTorr	16.6 kV	9 K	[f]
n/r	2.5 μA/sr	n/r	20 kV	n/r	[g]
11 pA	170 μA/sr/Torr	1×10^{-4} Torr	8 kV	20 K	[h]
27 pA	3.5 μA/sr/Pa	1.3×10^{-2} Pa	~7 kV	20 K	[i]
2.52 pA	7.5 nA/sr	1×10^{-2} Pa	6.5 kV	20 K	[j]
0.92 pA	2.98 nA/sr	1×10^{-2} Pa	6.6 kV	20 K	[j]

[a] There was no specifics of the method in this paper. However, there are earlier publications [47] suggesting ion current measurement through the fixed aperture with half-angle of 7.5–10 mrad [48]
[b] Undisclosed method [11]
[c] Current was measured through a square aperture equivalent to 0.3 msr [7]
[d] Current was measured through MCP using predetermined calibration. Determination of solid angle was not discussed [49]
[e] Current was measured by Faraday cup behind aperture with half-acceptance angle of 3.3 mrad. He pressure was estimated around the emitter using differential pumping. Temperature was not specified [50]
[f] Current was measured through a probe hole corresponding to solid angle of 62 μsr [51]
[g] [52] Undisclosed method [52]
[h] Current was measured using multichannel plate gain collecting entire current. Determination of solid angle is not specified [27]
[i] Current was measured using multichannel plate gain collecting entire current. Determination of solid angle is not specified [53]
[j] Current was measured through a fixed size aperture (size was not specified). FIM pattern was used to measure beam width to determine solid angle [54]

Typical measurements of *averaged* angular current density, $\bar{j}_a$, compiled from different publications are summarized in Table 2.1. From the values in the Table it is clear, that angular current densities vary significantly between tip materials, fabrication and experimental methods. The key parameters affecting angular current density are: tip temperature, tip voltage, and gas (helium) pressure which can be measured directly. However, the *averaged* angular current densities are difficult to compare because of the inhomogeneous illumination of the chosen apertures.

It is useful to analyze information that can be obtained from FIM spot measurement of the ion beam intensity profile at a detector plane by a 2-D Gaussian surface[1] [58] defined as

[1] This is also true for an atomically defined (point) electron source.

$$G(r) = A \exp\left\{-\frac{r^2}{2\sigma^2}\right\} , \tag{2.5}$$

where A is spot amplitude and σ^2 is a variance. Although 1-D Gaussian profiles have been used to characterize FIM spots [58], the 2-D representation of the recorded profile is preferred as it can account for asymmetries in the ion beam. In the following discussion, only symmetric FIM spots will be considered since accounting for asymmetries adds unnecessary complexity and does not change the conclusions. The typical FIM pattern of the single atom is presented in Fig. 2.2 along with the calculated 2-D Gaussian profile.

By integrating recorded spot intensity given in (2.5) one obtains the volume under the Gaussian curve (FIM intensity)

$$I_{\text{total}}^{\text{Gauss}} = 2\pi \int_0^{+\infty} G(r) r \, \mathrm{d}r = 2\pi A\sigma^2 , \tag{2.6}$$

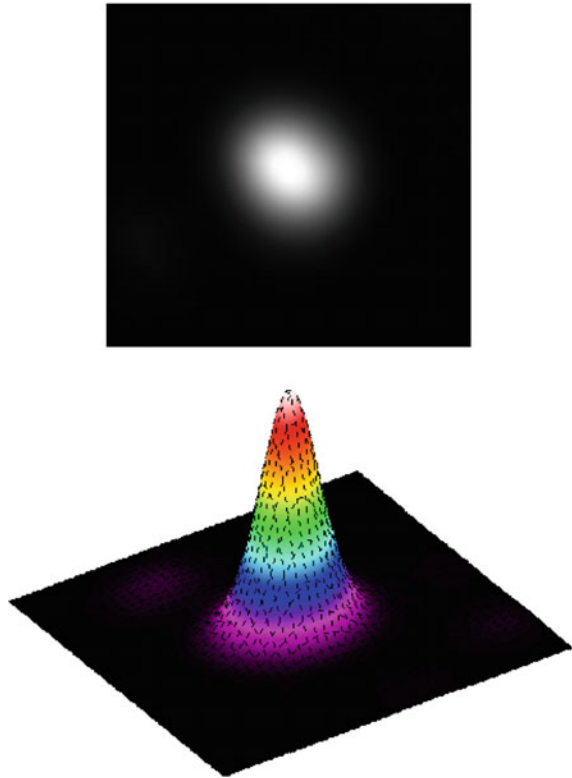

Fig. 2.2 *Top* FIM pattern of a single atom recorded using a multichannel plate and digital camera. *Bottom* 3-D representation of the same spot fitted with the Gaussian surface according to (2.5)

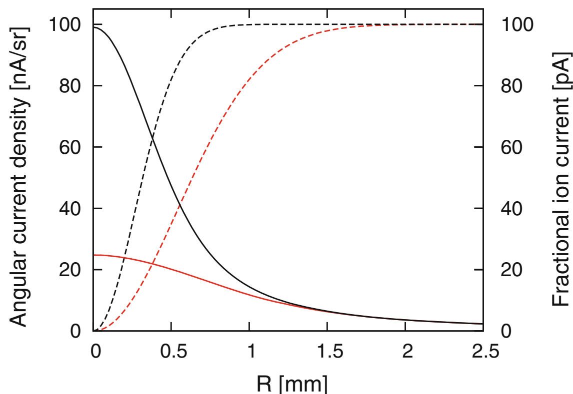

Fig. 2.3 Simulated angular current density (*solid lines*) assuming constant total beam current of 100 pA for two different beam widths $\sigma = 0.25$ mm (*black lines*) and 0.50 mm (*red lines*), respectively as measured on the detector 21 mm away. The *dashed lines* represent corresponding fractional current $I(R)$, see equation (2.8)

which is directly proportional to the total ion current, I_0, emitted by a source

$$I_0 = \gamma I_{\text{total}}^{\text{Gauss}} \tag{2.7}$$

assuming that the entire ion current is measured independently (e.g. by a Faraday cup) and there are no additional FIM spots. Additional FIM spots would result in lowering ion current carried by the central beam and thus skewing the measurements. Once the proportionality constant γ is determined it can be used to evaluate ion current by simply integrating the ion beam profile obtained by FIM. This is particularly useful when measuring low ion currents since MCPs provide large gain. However, one needs to ensure that multichannel plate gain[2] and camera exposure (exposure time, lens aperture, and camera settings) are consistent to obtain reliable data.

The fraction of ion current, see dashed lines in Fig. 2.3, passing through a circular aperture of radius R is given by

$$I(R) = I_0 \left\{ 1 - \exp\left[-\frac{R^2}{2\sigma^2} \right] \right\} \tag{2.8}$$

and the solid angle Ω can be expressed as

$$\Omega = 4\pi \frac{\pi R^2}{4\pi D^2} = \pi \frac{R^2}{D^2} , \tag{2.9}$$

where D is the tip-detector distance (see Fig. 2.4). Strictly speaking, distance D should be evaluated as distance between the virtual source and the detector. However, since the virtual source is located in close vicinity of the tip apex [59, 60], using tip-detector distance instead introduces negligible error.

[2]It should be noted that MCP gain can change (decreases) over time so the calibration should be performed periodically.

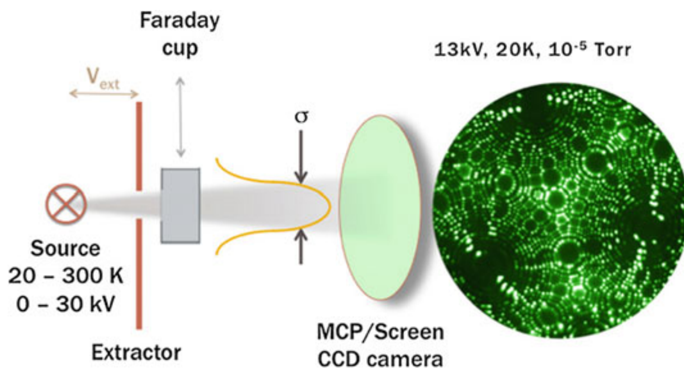

Fig. 2.4 A schematic diagram a custom built UHV FIM system. The movable Faraday cup collects all emitted ions imaged by the micro channel plate

Finally, *averaged* angular current density, see solid lines in Fig. 2.3 is evaluated by

$$\bar{j}_a(R) = \frac{I(R)}{\Omega} = \frac{I_0 D^2}{\pi R^2}\left\{1 - \exp\left[-\frac{R^2}{2\sigma^2}\right]\right\} . \tag{2.10}$$

This is the key equation of our analysis. It explicitly shows the *averaged* angular current density dependence on the solid angle for a given imaging gas pressure and tip temperature.

There are great advantages to measuring ion current from a FIM image. Beam shape is constantly monitored and any changes and/or instabilities are detected. Moreover, knowledge of beam profile (beam width) and total ion current allows one to evaluate both angular current density and averaged angular current density, for arbitrarily sized aperture.

2.2 FIM Details

The majority of the studies presented here were performed in a custom built ultra high vacuum (UHV) FIM system with base pressure $<10^{-10}$ Torr, see Fig. 2.4. The tip was cooled by a flow-though liquid helium cryostat reaching ~12 K at the coldest point and ~20 K at the tip. Both temperatures were measured independently by a thermocouple to determine precise tip temperature. The positive tip and extractor voltages were controlled and monitored by computer. The FIM pattern was amplified by a Hamamatsu microchannel plate (MCP) and displayed on a phosphor screen. The input stage of the MCP was grounded, while the output was typically biased at +900 to +1200 V to achieve desirable gain. The screen was biased at +2500 V above the MCP output to maintain consistent exposure.

Images were recorded using a PixelFly high sensitivity, 12-bit, 1400×1048 pixel camera to retain sufficient detail for further image analysis. Collected images were stored as 16-bit files to avoid data loss. Running averaging[3] was also applied to improve signal-to-noise ratio and easier image recognition especially for larger tips. Typically five to ten frames were averaged to improve image appearance while maintaining temporal resolution of few seconds.

A movable Faraday cup was placed between an extractor and the MCP to measure total emission current from the tip. The input aperture of the Faraday cup was chosen to be larger than the extractor hole to collect all ions generated by the tip. By comparing an FIM image with current measurements one can obtain a calibration between image brightness and ion current. The proportionality constant can be later used to evaluate ion current without moving the Faraday cup.

An electrochemically etched W(111) tip was supported by a wire loop, for heating, and installed in the FIM. In these studies, W(111) tips were prepared by a dc etching method using 2 molar NaOH solution. The dc power supply was equipped with a fast-acting analog cutoff circuit triggered by the sudden drop in etching current caused by the drop of the submerged portion of tungsten wire. This resulted in sharp tips with typical radius of curvature between 10 and 20 nm as measured by FIM. Furthermore, SEM studies showed that tungsten tips prepared by a dc etched have nearly zero cone angle.

The tips were degassed at 900 °C for 3 min, cooled and field evaporated to prepare the initial tip. During heating the tip temperature was measured directly by a disappearing filament pyrometer. Helium and nitrogen gas pressures were controlled with variable leak valves and monitored by a residual gas analyzer. Helium pressure were typically 2×10^{-5} Torr while nitrogen pressures ranged from 5×10^{-8} to 1×10^{-5} Torr.

2.2.1 *Anatomy of Gas-Assisted Etching*

Effects of non-noble gases such as nitrogen, water, or carbon monoxide on metal surfaces were observed in early FIM experiments [61, 62]. Later, Rezeq et al. [40] discovered that imaging of W(110) tip with mixture of helium and nitrogen while continuously lowering applied tip voltage let to apex sharpening and ultimately to creation of a single atom tip (SAT).

The nitrogen etching of a tungsten surface occurs at an applied tip voltage V_{app} below a critical value, V_{crit}, and above a threshold voltage, V_{min}. In case of helium as an imaging gas

$$V_{fe} > V_{img} > V_{crit} > V_{min} , \qquad (2.11)$$

[3]Once a desired number of frames was collected, the oldest image was discarded and a newly acquired frame was added.

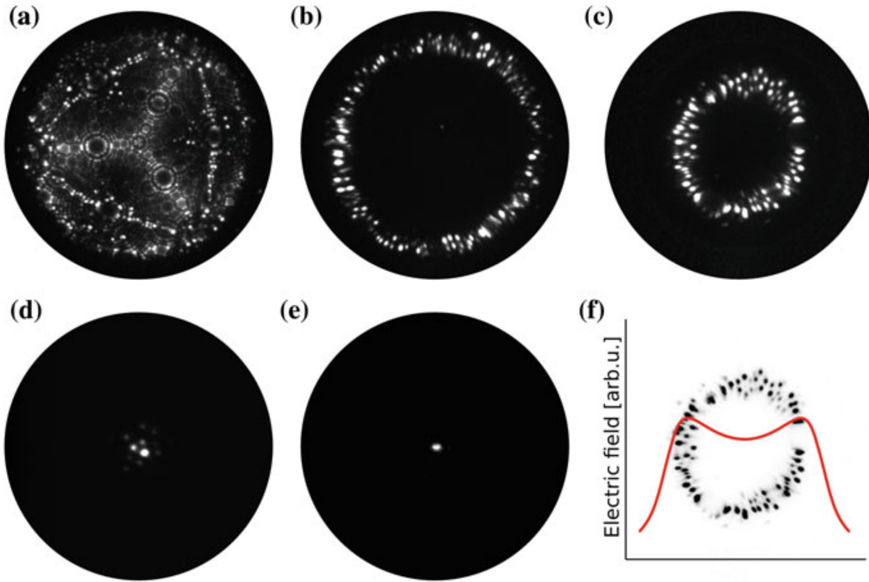

Fig. 2.5 FIM patterns: **a**–**e** Etching sequence of a single crystal W(111) tip from a fully evaporated tip apex (tip radius of 14.4 nm) to a SAT. **f** A schematic diagram representing an electric field profile across the ring structure shown in (**c**)

where V_{img} is the best imaging voltage and V_{fe} is the voltage where field evaporation takes place. V_{crit} is related to ionization probability of a nitrogen molecule while V_{min} corresponds to lowest electric field to remove (field evaporate) *etched* tungsten atom. At the start of etching, tip field (voltage) is selected close to the best imaging voltage. This defines an *etching band* where applied voltage V_{app} satisfies the condition $V_{crit} > V_{app} > V_{min}$. As etching progresses the tip apex becomes protruded and hence local electric field increases and as a consequence tip voltage has to be lowered to prevent field evaporation of apex atoms ($V_{fe} > V_{app}$). Etching/evaporation continues at sharp kinks and eventually the tip apex becomes narrow leaving a single tungsten atom at the apex. A tip prepared with this method is shown in Fig. 2.5.

If the applied field is controlled properly the field at the tip apex protects it from N_2 attack and etching. As etching progresses the FIM pattern changes (see Fig. 2.5). The N_2 etching created a sharp circular edge while the central tip region remained relatively flat. The resulting electric field at the tip apex is not sufficient to ionize He imaging gas leading to a dark region. As the etching progresses the ring of atoms contracts (Fig. 2.5c) indicating further etching. The ring in Fig. 2.5 completely disappears and tip apex atoms become prominent. Various atomic structures are observed depending on the crystal orientation. For W(111) hexamer (not shown) and trimer (Fig. 2.5d) structures are accessible and can be used as ion sources. Subsequent etching further sharpens the tip until only the single apex atom remains (Fig. 2.5e).

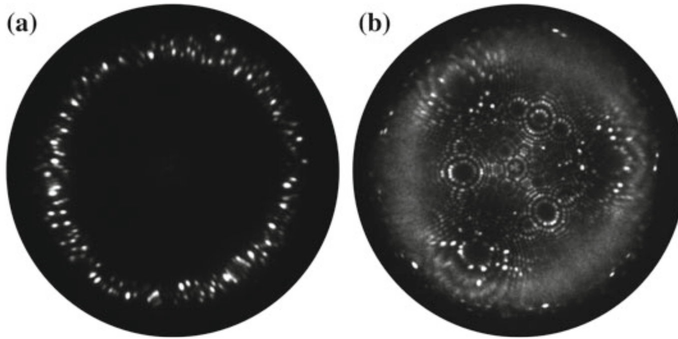

Fig. 2.6 **a** An overexposed FIM pattern partly etched W(111) tip using helium as an imaging gas showing the ring structure. **b** A neon generated FIM pattern of the same tip. The tip voltage in both cases was 15 kV

Table 2.2 Ionization potentials and polarizability for common gases used in FIM [63, 64]

Gas	Ionization potential [eV]	Polarizability [10^{-24} cm^3]
He	24.6	0.20
Ne	21.6	0.29
Ar	15.8	1.63
H_2	15.6	0.80
N_2	14.5	1.74
CO	14.0	1.97
O_2	13.6	1.57
H_2O	12.6	1.43

The flat middle region observed in Fig. 2.5b can be further explored using neon as an imaging gas, while maintaining helium imaging voltage, as seen in Fig. 2.6. Since neon has lower ionization potential than helium, two significant differences in FIM image are observed: (i) the previously black featureless region is revealed to have a clean W(111) crystal structure, (ii) the ring previously seen in the He image no longer reveals atomic structural detail. The ability to image previously inaccessible structure of the tip apex region by introducing neon imaging gas instead of helium is related to its lower ionization potential, see Table 2.2. This allows neon to ionize over the central tip region which was previously not imaged with helium. At the same time, areas with high field, such as the ring visible in the He generated image, become indistinct due to ionization far from the tip surface, reducing the image resolution. The image distortion and large ring separation correspond to high tip curvature where the tip apex connects to the shank of the etched tip. By lowering tip voltage to account for the lower ionization potential of neon imaging gas, the tip apex structure disappears from the neon image; at that point both helium and neon images are nearly identical in appearance. Note, that neon ionization potential is still

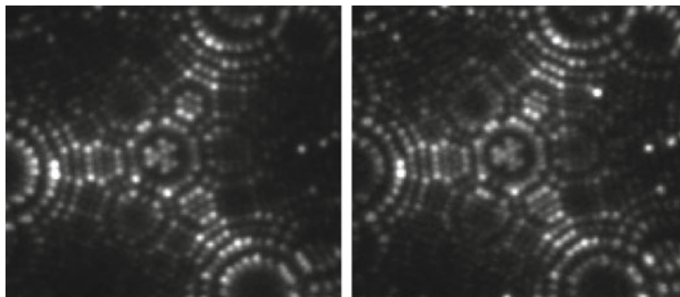

Fig. 2.7 Enlarged portions of He image at $V_{\text{tip}} = 20$ kV (*left*) corresponding to fully evaporated tip with radius of curvature of 14.4 nm and Ne image at $V_{\text{tip}} = 15$ kV (*right*) recorded within the ring structure (Fig. 2.6b). The magnification of Ne image was adjusted to account for different tip voltage. Remarkable similarity is evident

significantly higher than common vacuum contaminants assuring a clean tip apex. Figure 2.7 compares the atomic structure of the partly etched tip shown in Fig. 2.6b with the original unetched tip in Fig. 2.5a. Cropped images are shown to highlight the apex atoms only. It is evident that although significant etching has occurred at the periphery of the tip, virtually no atoms have been removed from the apex showing the remarkable spatial selectivity of the etching process.

Figure 2.7 help to elucidate the mechanism by which nitrogen is delivered to the tip during the etching process. During the etching procedure, the tip apex becomes dark suggesting a lowered electric field insufficient to ionize He imaging gas (Fig. 2.5b, c). However, the field is strong enough to ionize nitrogen and other contaminants before they reach the tungsten surface as the tip apex remains unchanged. Nitrogen is restricted to adsorb on the tungsten surface far back from the apex and migrates along the tip shank towards the apex under the influence of the electric field. As nitrogen molecules reach the high field region at the outside perimeter of the ring structure seen in Fig. 2.5b, c, they can react with the tungsten atoms enabling them to be subsequently field evaporated. In this process, the N_2 molecule is consumed and not available for further reaction as a stable tungsten nitride layer remains. This N_2 delivery mechanism is supported by the fact that the inner region of the observed ring in Fig. 2.5b remains unetched. Only the outer edge atoms are removed despite the fact that the field strength at the outer and inner edges of the ring structure is equivalent (Fig. 2.5b, c, f). This leads to the contraction of the ring structure seen in Fig. 2.5b–d and the eventual formation of a SAT.

FIM imaging with low ionization potential gas such as neon also provides valuable structural information of the SAT, see Fig. 2.8. In the helium generated image only the apex atom is visible with very minor satellite atoms. No other tip structure information is available until the apex atom is removed by either etching or field evaporation. The tip structure can be determined in this manner, but the tip itself is destroyed. By using neon as the imaging gas, but maintaining the helium best imaging voltage, lower field regions can be observed. Figure 2.8 compares both helium

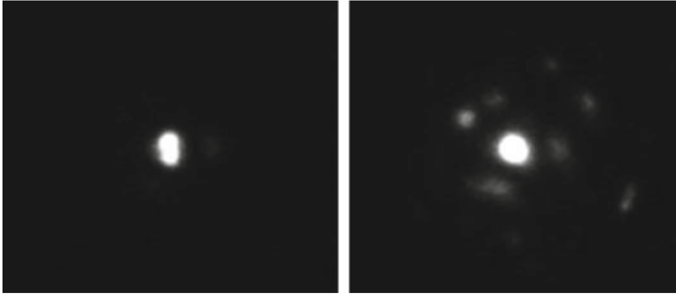

Fig. 2.8 Helium (*left*) and neon (*right*) images of SAT. Lower ionization potential of neon reveals atomic structure of lower atomic planes

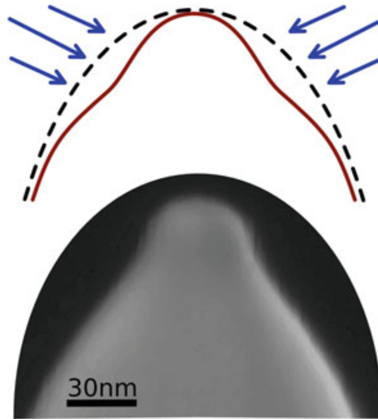

Fig. 2.9 *Top* A schematic diagram of nitrogen assisted etching process. The electric field distribution defines an "etching band" where tungsten atom removal occurs. *Bottom* The overall tip shape was later verified by SEM

(left) and neon (right) images. In this experiment, the neon image reveals an asymmetric support structure reaching only two layers below the apex atom. This indicates that electric field distribution around the apex decreases dramatically over only a few atomic layers.

Based on our observations using helium and neon imaging gases, we can now understand the shaping process that occurs during tip etching. The schematic diagram is shown in Fig. 2.9. The etching occurs outside of the central apex region where the field conditions for etching are satisfied. This creates an etching band which narrows as the etching progresses, indicated by arrows in Fig. 2.9, leading to an extended structure that supports the single atom tip. This structural model is confirmed with a scanning electron microscope image in Fig. 2.9.

2.2.2 *Precursor Tip*

Electrochemically etched tungsten tips are very sharp, but the apex is often fairly irregular. After degassing in UHV, tungsten tips are imaged with He and field evaporated to achieve a nearly spherical tip apex. The tip radius can be determined by the number of rings n between two crystallographic directions in the FIM image separated by angle γ [63]

$$R = \frac{ns}{1 - \cos\gamma} , \tag{2.12}$$

where s is the step height for a particular apex orientation. For bcc tungsten with lattice constant 3.16 corresponding to step height of 0.912 Å for W(111). The [111] and [211] directions are conveniently chosen to determine tip apex radius. For these directions corresponding $1/(1 - \cos\gamma) = 17.5$ Å. Combining all numbers one gets a simple expression for a tip radius

$$R \text{ in Å} = 15.96n . \tag{2.13}$$

In Fig. 2.10, one can count nine rings between [111] and [211] directions indicating tip radius of 14 nm. This is a typical value for electrochemically etched tungsten tips.

Evaluating initial tip radius is very important. It should be noted, that an extraction voltage is not always a good measure of initial tip radius. It is known that overall tip shape plays an important role in determining extraction voltage as well as actual apex curvature. Therefore, it is crucial to carefully measure apex curvature to ensure consistent starting points. Moreover, any tip variations such as defects, imperfections, and grain boundaries can affect field distribution about the tip apex leading to different regions to be etched. They appear as incomplete FIM patterns. In most cases, degassing and field evaporation is sufficient to prepare crystalline tip apexes.

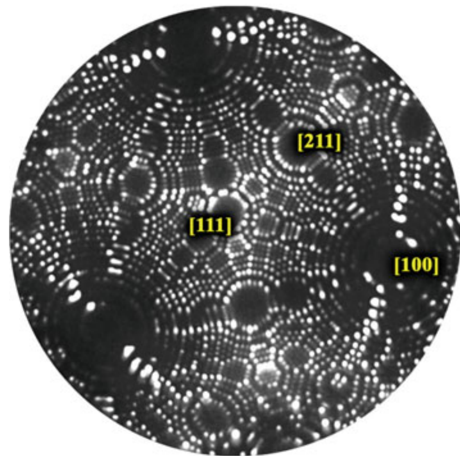

Fig. 2.10 FIM image of W(111) tip showing apex radius of 14 nm recorded at tip voltage of 18 kV. The main crystallographic directions are labeled

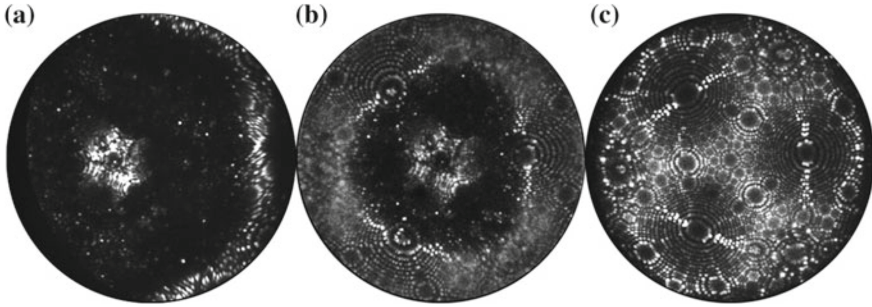

Fig. 2.11 **a** FIM micrographs of insufficiently field evaporated W(111) end form. The tip is shifted towards *left* to reveal *large ring* of atoms surrounding the apex. Applied tip voltage was 23 kV. **b** The same tip after being repeatedly N_2 etched and field evaporated. The FIM pattern is covering most of the screen with a gap still encircling the apex. The tip voltage was 22 kV. **c** FIM pattern showing fully recovered, spherical tip. There are no defects nor imperfections observed. Applied tip voltage was 21 kV. The tip radius was estimated to be 16 nm

However, excessive heating and field evaporation can lead to blunting of the tip creating problems for further processing steps.

In these instances, combination of gas-assisted etching and field evaporation is used to form a symmetric precursor tip. The process includes a saw-tooth voltage profile that cyclically etches the apex, followed by a field evaporation step revealing a clean crystalline understructure, see Fig. 2.11. The number of etching-evaporation cycles is determined by the extent of defects and imperfections. The same process is used to prepare a fresh precursor tip after making a SAT.

2.2.3 SAT Shaping

The main control mechanism to shape the tip apex is by the careful control of the applied tip voltage as the tip etches. Reactive gas pressure and tip temperature typically enhance or reduce etching efficiency uniformly. There are two basic types of etching: (i) constant field, and (ii) forced evaporation [38].

The first method was already described above. The tip voltage is lowered in such a manner that constant field at the apex is maintained. The best imaging field is often chosen since it is sufficiently high to protect the tip apex from random etching and low enough to prevent field evaporation. Typically, a ring structure, as discussed in detail above, is observed using this procedure before a SAT is achieved. SATs prepared in this manner operate at low voltages indicating "taller", large aspect ratio, tips.

In the alternate method, once the initial nitrogen etching is established, the tip voltage is lowered slowly, apex atoms can field evaporate as the tip sharpens. This happens because V_{app} approaches V_{fe} as the tip etches. The evaporation leads to a

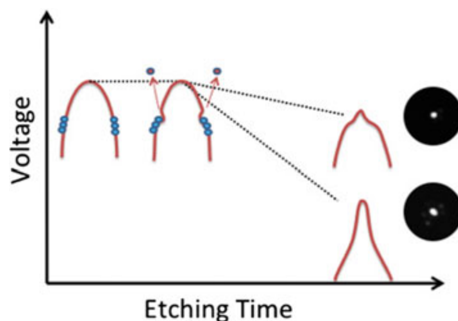

Fig. 2.12 A schematic diagram depicting two etching regimes: (i) constant field, and (ii) forced evaporation depending on a voltage profile. The constant field method leads to "taller" SATs that have a lower operating voltage. The "forced evaporation" method typically results in larger supporting structure and therefore higher extraction voltage

flattening of the overall tip shape. Continued etching and field evaporation will eventually lead to a nanotip with a relatively low aspect ratio, Fig. 2.12.

The overall shape of the tip can be controlled by varying the nitrogen etch rate through the nitrogen pressure and the rate at which the voltage is dropped. If the voltage is dropped more quickly, nitrogen etching is faster than apex field evaporation and a taller nanotip is formed. If the voltage is dropped more slowly, paused or through a custom ramping profile, apex atoms are controllably removed and the tip shape will be controlled through a balance of etching and field evaporation. A tip prepared using the slow voltage drop method is shown in Fig. 2.12.

2.2.4 SAT Reproducibility

The formation of SATs for GFISs needs to be controlled, reproducible and easily aligned in order to be viable as an ion source. Polycrystalline wire is desirable because it is relatively inexpensive compared to single crystal wire, however, the location of the last atom on the (110) plane is unpredictable and poses technological problems for the alignment of the ions beam in a working microscope. For this reason, etching of single crystal W(111) was utilized for the predictable and reproducible formation of SATs.

Figure 2.13 shows a more detailed sequence of events during the formation of the SAT. Figure 2.13a shows a symmetric structure with a central atom. The central atom in the hexamer of Fig. 2.13a will become the single atom tip. This atom is barely visible at this time as the field is quite low at the central atom compared to the out ring atoms where ionization has a high probability. The outer atoms also scavenge incoming helium atoms from the tip shank and shield the central atom from the gas supply. Once the symmetric structure (Fig. 2.13a) is formed, the nitro-

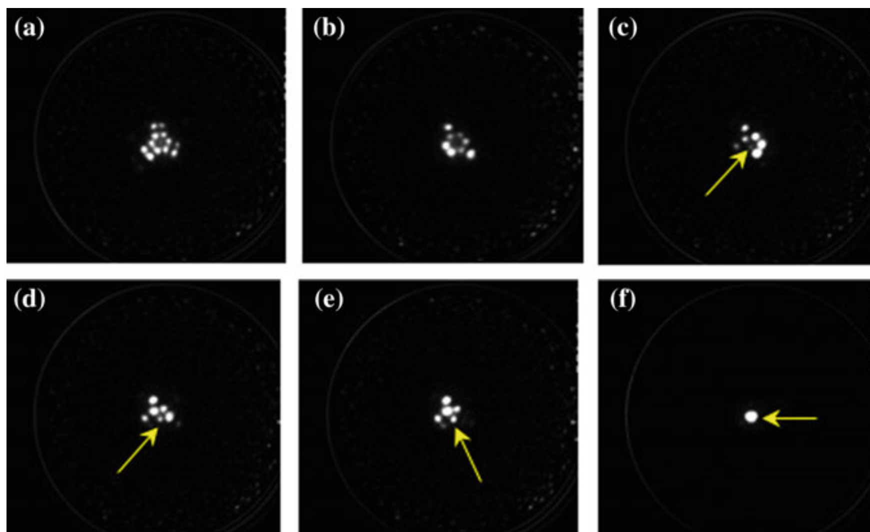

Fig. 2.13 The final stage of SAT formation. Reactive gas (nitrogen) pressure is reduced to 2×10^{-8} Torr and short voltage pulses are applied to promote etching. The symmetry of FIM pattern (*upper right image*) determines the position of the SAT apex atom in the *middle* of the hexagonal structure. Note, that the central atom is barely visible due to lower field; edge atoms are more pronounced. As peripheral atoms are removed, the apex atom, indicated by *arrows*, lights up. Its intensity (ion current) gradually increases until all other atoms are removed and the SAT is created

gen etch gas pressure is reduced by an order of magnitude. This reduces the rate of etching which allows for better control of the tip shape when evaporating the last atoms. Figure 2.13b shows the structure after the etching of several of the perimeter atoms leaving the central atom within the hexamer as well as two satellite atoms. Figure 2.13c shows the structure after removal of two of the hexamer atoms. The central atom now appears as a very small spot as the field is enhanced around the central atom. Figure 2.13e shows the structure with only four atoms surrounding the central atom, after etching of another atom. The central atom is becoming bright as its field is enhanced and a supply of helium gas becomes available from the tip shank. Further atom removal in Fig. 2.13e shows only three remaining atoms from the hexamer. The central atom becomes even brighter. The final atoms were etched in the time of a single movie frame to reveal the SAT shown in Fig. 2.13f. Once the final atom is exposed, the nitrogen etching gas supply is closed. The central atom is indicated with a yellow arrow in Fig. 2.13c–f. The process shown in Fig. 2.13 to create the SAT was completed strictly with the chemical assisted etching method. In other attempts, the process has been completed without the use of nitrogen by using predefined voltage pulses in order to field evaporate the extra atoms.

Figure 2.14 shows the reproducibility of the etching method. A series of single atom tips are prepared. The initial SAT shown in Fig. 2.14a is purposely field evaporated. Three total layers of atoms, including the SAT, are removed to reveal another

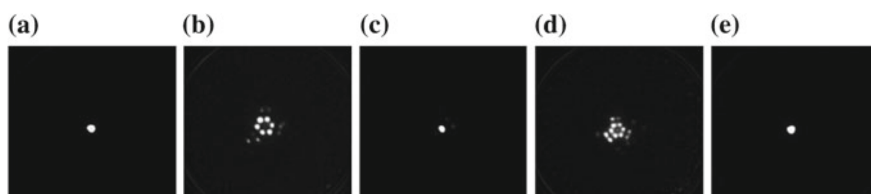

Fig. 2.14 Three SATs (**a**, **c**, and **e**) created and recreated at exactly the same apex position. **b** and **d** figures show symmetric, field evaporated apex forms after three atomic layers were removed

hexamer structure in Fig. 2.14b. This structure is then etched to a SAT in Fig. 2.14c. The time of the etching procedure was 6 min. The process was then repeated and the results are shown in Fig. 2.14c–e, with an etch time of 3.5 min. This process ensures that the final atom is in an identical crystalline position after each reformation, which in turns removes the need for any source alignment after each tip rebuild.

2.2.5 Air Exposure, Thermal Stability, and Faceting

In cases where the SAT must be removed from vacuum, a procedure is required to limit contamination and apex damage. In order to assess the robustness of single-atom tips a series of experiments were performed to evaluate SATs performance with respect to ambient exposure as well as annealing temperatures. Testing required to complete several steps: (i) tip warm-up and voltage ramp down after initial SAT fabrication, (ii) degassing and SAT recovery, and (iii) SAT robustness with respect to annealing temperature which could be either performed during degassing phase or subsequently after SAT recovery. In the following three sections each step is examined to find suitable solutions for maintaining sharp nanotips after ambient exposure.

2.2.5.1 Warm-Up and Voltage Ramp Down

The single-atom tips were prepared in the field ion microscope at nominally liquid nitrogen temperature (approximately 80 K) using the nitrogen etching procedure described above. The first step was to remove high voltage which was applied during the tip etching process as well as to warm the SAT to room temperature (RT). The imaging gas was also removed from the vacuum system to avoid possible contamination due to residual impurities in He imaging gas. After warming to RT overnight, the tip was then cooled down, without any high temperature annealing step, in order to assess any contamination and/or damage from this process. Several scenarios were explored to select an optimal protocol to minimize SAT evaporation or contamination due to condensation on a cold tip or field assisted adsorption and/or diffusion. The tested processes are summarized in Table 2.3. In all cases of tip warming to room

Table 2.3 Summary of voltage ramp-down procedures

Exp	Voltage	Tip temperature	Result
I	BIV	Warming to RT	Filed evaporation occurred
II	85% BIV	Warming to RT	Minimal contamination/tip remaining sharp
III	50% BIV	Warming to RT	Heavy contamination/high voltage required to recover FIM pattern
	50% BIV	LN_2	Minimal contamination/tip remaining sharp
IV	HV off	Warming to RT	Minimal contamination/tip remaining sharp

temperature, the experiments were allowed to occur overnight to assure a warm tip and to allow the vacuum to recover from any cryo-pumped gases.

In experiment I (see Table 2.3), the best imaging voltage for the SAT was maintained during the tip warm up to prevent contamination. However, significant field evaporation occurred effectively destroying the SAT since the field required to remove atoms at RT is lower compare to LN_2 temperature [24]. Although the SAT can be recovered using the gas-assisted etching after the tip was cooled down, this process was far from ideal.

Experiment II resulted in minimal tip apex modification during warm up. After initial warm up under conditions described in Table 2.3, the atomic arrangement was found to be nearly identical after subsequent tip cool down and applying tip voltage. Only two additional adsorbates were observed, which suggests that the electric field at the apex is high enough to protect the apex from contamination but low enough to avoid evaporation.

In order to further evaluate the effect of the voltage application the experiment was repeated, but at a further reduced voltage. In experiment III, during the warm up procedure, the tip voltage was lowered to 50% of the BIV. After cooling to liquid nitrogen temperatures, FIM imaging was again attempted. In this case, while the SAT had originally imaged at 8.9 kV, it was not until the voltage reached 15.8 kV (177% of the SAT) that one could observe the central hexagonal atomic arrangement typical of W(111)-oriented nanotip. Around this arrangement only randomly scattered bright spots (adsorbates) against a black background could be seen; the underlying lattice structure was not visible at all, suggesting substantial apex contamination.

In Experiment IIIB, the tip being maintained at liquid nitrogen temperature overnight while at a voltage of 50% of the BIV, in order to evaluate the effect of raising and lowering the temperature. Upon ramping up the voltage after the overnight vacuum exposure in order to evaluate whether or not the SAT (imaging at 6.5 kV) had undergone any considerable changes, a recognizable crystal pattern (the hexamer) was observed at 7.3 kV, at only 112% of the SAT BIV.

The required increase in operating voltage to image tips is likely due to contamination of the apex. However, the required voltage increase for the RT tip compared to the LN_2 tip suggests that more adsorbates covered the tip at room temperature. This indicates that the majority of contaminants did not arrive from the gas phase. It would

be expected that the cold tip would have more contaminants due to higher sticking coefficient. It was therefore concluded that adsorbates migrated from the shank of the tip (similar to the process of imaging gases) to contaminate the apex. Cold tips would limit migration towards the apex, while during warming to RT contaminants can diffuse towards the tip apex and undergo reaction with tungsten surface atoms.

Experiment IV involved warming of the tip in the absence of any applied voltage. After exposure to the vacuum overnight, the tip was cooled the following day to liquid nitrogen temperature and the voltage was reapplied to the tip. At 9.4 kV an atomic structure is recognized as a hexamer structure which is closely related to the SAT [24]. Further field evaporation to 11.5 kV revealed a larger structure of the tip and showed that the tip was generally undamaged during the exposure.

From these experiments it was determined that removing the voltage from the tip during a warm up period caused a minimal, if any, amount of contamination of the tip. If a voltage is required to be applied during the warming period, the voltage must be lowered to avoid field evaporation, but maintained at a sufficient level to maintain field protection of the apex. It was found that using approximately 85% of BIV caused the least amount of contamination to SAT while low enough to avoid evaporation. Once the tip is warm the HV can be safely removed without introducing additional contamination.

2.2.5.2 Air Exposure

Several SATs were prepared to verify their robustness to air exposure. In one example, the imaging voltage for the single-atom tip was 6.3 kV (Fig. 2.15a). After air exposure, bake-out and tip anneal to dull orange (about 800 °C) the voltage bias applied to the tip was ramped up to 8.3 kV or approximately 130% of the original BIV. After brief etching, a hexamer pattern at 7.5 kV (Fig. 2.15b) which enabled us

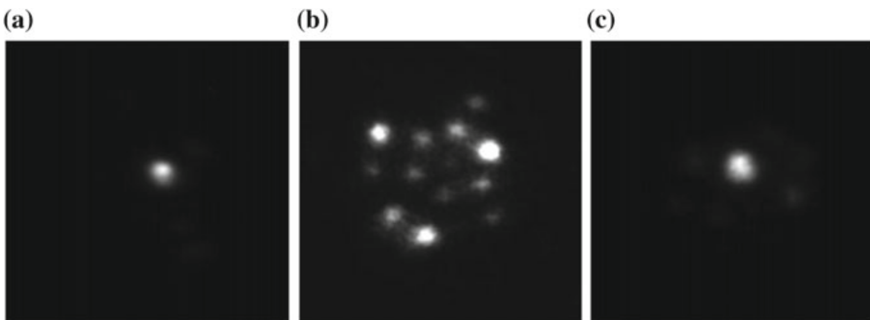

Fig. 2.15 SAT and air exposure. **a** shows the original SAT imaged at 6.3 kV at 77 K. **b** was recorded after air exposure, system bake, and tip degassing at 800 °C. The image was recorded at 8.3 kV and tip temperature 77 K to reveal recognizable FIM pattern. After a brief repair using nitrogen etching and short voltage pulses, the SAT was achieved at 7.5 kV (**c**)

to readily re-etch the tip apex down to a single atom configuration (Fig. 2.15c). The imaging voltage for the resulting single-atom tip was 7.2 kV, only slightly higher than the initial one. This proves that single-atom tips are robust enough to withstand the adsorption of air molecules and that recovery is feasible after air exposure with minimal intervention. While not fully conclusive this series of experiments suggested that the damage to the tips attributable to air exposure was minimal. In all cases, SATs were recovered after a short etching and evaporation process. The imaging voltages of reconstructed SATs were slight higher than the original values indicating only small change to the overall tip shape.

2.2.5.3 Annealing

A series of experiments was performed to determine nanotip robustness with respect to annealing temperature. The same tip, terminated with one or a few atoms, was annealed at an increasingly higher temperature in 100 °C increments starting at 800 °C, which corresponds to a regular degassing/annealing. All annealing steps were performed under vacuum in absence of any other gases. The tip withstood the 1 min long annealing cycles up to 1100 °C with only small change to its apex structure. That is, a nominally single-atom tip could be readily recovered by minimal re-etching after every annealing step.

Annealing temperatures between 1200 and 1300 °C resulted in dramatic changes to the nanotip shape and structure, see Fig. 2.16. Typically the operating voltage doubles from the SAT and obvious faceting of the tip occurs. The faceting reconstructs the tip to flatten the (2 1 1) planes and form ridges along the lines connecting the central [1 1 1] direction with ⟨110⟩ directions. This faceting is similar to that observed for oxygen exposed tips. Wengelnik and Neddermeyer reported on sharp microtip formation correlated with faceting upon heating tungsten tips in an oxygen atmosphere (3.75×10^{-4} Torr) [21]. Szczepkowicz also reported on oxygen-induced tungsten faceting in studies investigating tungsten equilibrium crystal structures [19].

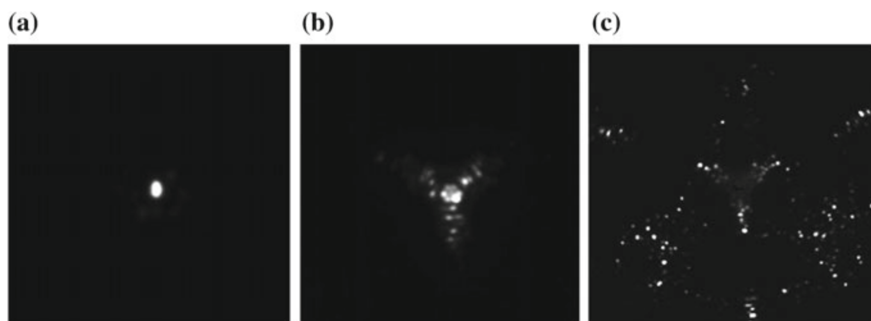

Fig. 2.16 **a** A pristine SAT. **b** A faceted tip apex after an annealing at 1300 °C imaged with **b** helium and **c** neon

In these cases, the presence of oxygen was believed to mediate tungsten atom surface diffusion to reach minimum energy state. It was suspected that the thin layer of nitrogen formed during the etching process causes a similar faceting to that which is observed with oxygen gas.

2.2.6 Iridium and Other Nanotip Materials

Noble metal tips have been proposed because of their potential to operate with more corrosive gases such as nitrogen and oxygen. Nanotips and SATs formed from gold, platinum, palladium and iridium have been prepared on facetted tungsten (111) [26, 27, 29, 33–37] and pure oriented iridium (210) single crystal wire and have been shown to produce helium, hydrogen, nitrogen and oxygen beams at various temperatures [53]. As ion beams of corrosive gases, such as nitrogen, can be created and are stable, one can assume that iridium tips are not affected by these gases. This may be true at low imaging fields, but corrosion can occur when the electric field is raised.

The corrosion mechanism can then be utilized to sharpen and shape iridium tips by the field enhanced etching mechanism. This has been shown by Wood et al. with the caveat that the etching conditions for tungsten were modified in order to etch iridium more easily. Initially, it was found that utilizing helium as the imaging gas with a tip at 77 K (typical conditions for tungsten etching), limited fine control over the etching of the iridium because the evaporation field of iridium (5 V/Å) is close to the best imaging field (BIF) of the imaging gas helium (4.4 V/Å). This created some limits in the ability to controllably etch and observe simultaneously. Switching to neon (3.5 V/Å BIF) as the imaging gas alleviated the issue with field evaporation and etching control and an acceptable etching rate (tip preparation in approximately 1 h) was achieved at room temperature with oxygen as the etchant gas and neon as the imaging gas.

Figure 2.17 shows an Ir(100) tip prior to etching and was obtained at 4.7 kV at room temperature. An approximate ball model of the apex is also shown. The radius of curvature was estimated to be 7.5 nm by counting the number of rings between crystal planes. Figure 2.18a shows a neon image of an iridium tip at room temperature prior to introduction of oxygen. Oxygen was then introduced (5×10^{-6} Torr) allowing the tip to etch. Figure 2.18b shows the tip after some etching. During etching the voltage is lowered in steps of 200 V in order to maintain the best imaging voltage at the apex atoms. Because the tip is sharpening, the voltage must be lowered in order to keep a consistent electric field. The image in Fig. 2.18b was acquired at 3.6 kV. It is evident that the observable iridium atoms have been reduced because of etching of the perimeter atoms. The fuzzy imaging ring observed is due to the oxygen gas in the chamber becoming ionized close to the tip surface. No fuzziness is observed over the apex atoms, indicating that they are substantially protected from oxygen attack because of the high field at the apex. Figure 2.18c, d show snapshots after further etching. The observation of the apex atoms is shrinking. Figure 2.18e shows a very small apex and was acquired at 2.8 kV. The pressure of oxygen was then

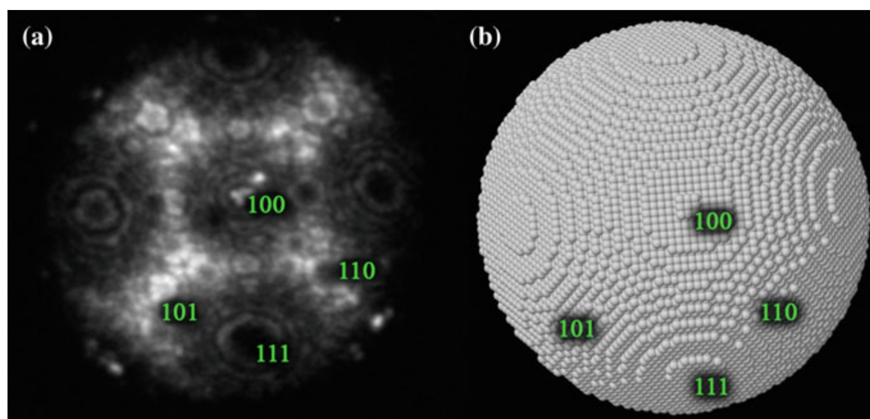

Fig. 2.17 Iridium prior to etching: **a** FIM image using neon, and **b** corresponding ball model

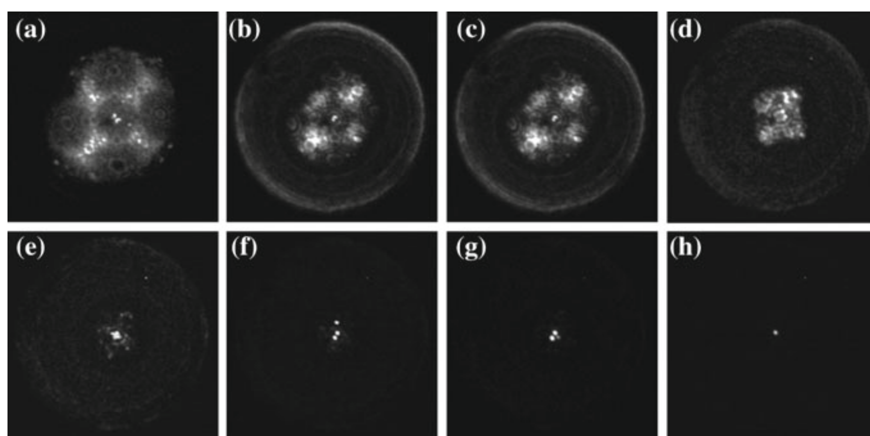

Fig. 2.18 Iridium etching process. All images were collected at room temperature using neon as the imaging gas and oxygen as the etching gas. **a** Iridium nanotip prior to etching, 4.6 kV, tip radius 7.5 nm. **b** after etching, the Iridium tip has been sharpened, 3.6 kV. Oxygen gas ionization can be observed at the perimeter of the image while the apex is protected against oxygen attack. **c**–**e** The apex compresses as the etching of the shank continues. Imaging voltages are 3.4, 3.0 and 2.8 kV respectively. **f**–**h** The oxygen pressure is reduced and the observed oxygen ionization is reduced. **f** three atoms remain at the apex. 2.7 kV. **g** Two atoms, 2.7 kV. **h** Iridium SAT imaged at 2.5 kV

reduced to 1×10^{-8} Torr, and the observation of oxygen gas ionization has almost disappeared in Fig. 2.18f, where only three apex atoms are observed. A single atom is removed resulting in Fig. 2.18g, and the removal of another atom, leaves the SAT in Fig. 2.18h. Some asymmetry of the spots is likely due to gas adsorption near the apex atoms [65]. The Ir SAT can be cooled down to cryogenic temperatures without any issues.

Although it was difficult to control the etching of large tips at LN_2 temperatures, small apex rebuilds could be achieved. In order to perform SAT repairs at LN_2 temperatures, oxygen was reintroduced to a pressure of 10^{-8} Torr and voltage pulses of 1–2 kV with durations of 500 μs were applied. This allowed for removal of satellite atoms. Careful application of the voltage magnitude and duration is required.

2.3 Performance of SATs

In the previous sections we have shown how one can prepare a SAT operating at different extraction voltages by carefully controlling the nanotip formation process. In the following paragraphs we will investigate performance of various SATs in light of GFIS applications. In particular, we will focus our efforts to measure beam width (divergence angle) and total ion current. Note, that the ultimate figure of merit will depend on intended application; for instance, for high resolution imaging a narrow beam is required even at lower total beam (probe) current. On the other hand, higher ion current will be paramount for sputtering and machining applications.

2.3.1 Best Imaging Voltage

Voltage dependence of ion current and beam divergence was studied for multiple SATs. Understanding I-V and σ-V curves is crucial for evaluating the best imaging voltage and ensuring consistent electric field at the tip apex. Interestingly, there is no rigorous definition of BIV in the available literature. Müller and Tsong defined the BIV as:

> The definition of "best image" is somewhat arbitrary as the different regions on the field evaporation end form have varying radii of curvature and, hence, local field strength. However, when it is attempted to repeatedly adjust the voltage of a given tip so that an image with a maximum of details and definition in the region from the (011) plane to about 30 deg off is obtained, it turns out that even different observers arrive at the same voltage to within $\pm 1\%$. When the voltage is gradually reduced from the evaporation range, the "best imaging voltage", BIV, is reached when the overall intensity in the vicinity of the $\{011\}$ region is seen to be drained away towards the more protruding $\{111\}$ and $\{114\}$ regions.

Although this approach is possible for larger tips, where multiple planes are present, it is difficult or even impossible to find BIV by simply looking at "image quality" of a SAT since there is just one spot on an otherwise black screen.

Mathematically, one could analyze FIM images by characterizing spot sizes and contrast or visibility criteria. The spot size is directly corresponds to the beam width σ while visibility is proportional to ion current. Therefore, evaluating voltage dependence using an imaging approach to record both current (image brightness) and σ is invaluable, see Fig. 2.19.

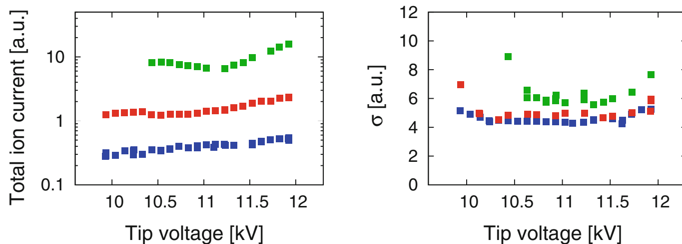

Fig. 2.19 *I-V* (*left*) and σ-V (*right*) curves for a W(111) SAT evaluated at 70 K at different helium pressures: (*blue*) 10^{-6} Torr, (*red*) 10^{-5} Torr, and (*green*) 10^{-4} Torr

There is no significant feature in *I-V* characteristics, measured at 20 K with helium, that would indicate BIV. The upper limit of a voltage range is given by tungsten field evaporation (5.2 V/Å), while the lower limit corresponds to decrease of ionization probability. In some experiments, a kink is observed and described as a transition to the helium supply limited current. It is not related to BIV.

On the other hand, σ-V dependence shows features indicating the presence of a BIV. There is a shallow minimum surrounded by gradual increase of σ for low and high extraction voltage. The increase for higher voltages can be explained by free ionization farther from the tip surface and thus loosing some of its resolution. This increase is rather small before the evaporation field is reached and the apex atom is removed.

At the lower voltage limit, round FIM spots can loose their shape and become irregular. However, the apex structures remains unchanged; once extraction voltage is increased, FIM spots become circular again. It should also be pointed out, that this effect is more prominent at lower temperatures. For liquid nitrogen temperature, these effects are hardly visible; the SAT remains circular and fades out with decreasing voltage. One explanation for the spot size increase is related to the fact that critical distance d_{crit} increases with decreasing extraction voltage [3]

$$d_{crit} = \frac{I - \phi}{eF}\,, \tag{2.14}$$

where I and ϕ are ionization potential of imaging gas and work function of metal, respectively expressed in eV and F is applied electric field in V/m. Since the field at the apex is proportional to the extraction voltage, critical distance will increase as applied voltage decreases, increasing the beam spot size [3].

2.3.2 *Temperature Dependence*

The tip temperature plays a crucial role in the amount of current generated from an SAT as well as the beam shape and size. Simply, colder is better and cooler tips can

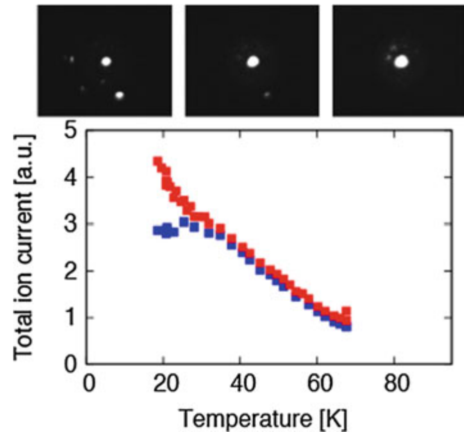

Fig. 2.20 *I-T* curve recorded at extraction voltage of 7.3 kV and helium pressure of 1.3×10^{-5} Torr. *Blue* and *red* symbols represent the SAT current and total current from all atoms respectively. Purposefully over-exposed FIM show surrounding atomic structure with satellites becoming more dominant at lower tip temperatures

generate more current and the beam size is smaller as well. However, lower temperatures also mean higher operating costs and possibly more mechanical vibrations depending on the cooling system. Experimental results were recorded at different temperatures so one can make an informed decision in selecting GFIS operating temperatures.

Figure 2.20 shows ion current recorded at different temperatures. Total ion current, red squares in Fig. 2.20, increases monotonically by almost an order of magnitude between 70 K, at which SAT was formed, and 20 K, the lowest "controllable" temperature. The increase is attributed to capture area increase. Utilizing FIM imaging, instead of the Faraday cup, it is determined that satellite spots become more prominent at lower temperatures. Integrating the current contribution from the SAT only, blue symbols in Fig. 2.20, it is found SAT current flattens as satellites draw some of the helium supply.

Similarly, analysis of the spot size σ can also be evaluated, see Fig. 2.21. The spot size decreases with decreasing temperature. Although temperature dependence of decreasing beam size is qualitatively understood, there is surprisingly little written in the literature regarding SATs. The theory of the FIM beam size is analogous to electron beam resolution evaluated and refined for electron emission microscopy [66–68]. Early studies by Chen and Seidman [69] looked at ion beam spot sizes of large, polycrystalline, (110)-oriented tungsten tips as a function of tip temperature along different crystallographic directions. They showed that atomic resolution, δ, can be written as

$$\delta = \sqrt{\delta_0^2 + \left[\frac{\hbar\beta r_{\mathrm{t}}}{\left(2meV_{\mathrm{t}}\right)^{1/2}}\right] + \left[\frac{16\beta^2 r_{\mathrm{t}}^2}{eV_{\mathrm{t}}}\epsilon_{\mathrm{t}}\right]}, \tag{2.15}$$

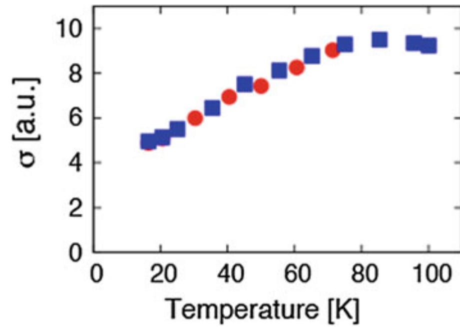

Fig. 2.21 *σ-T* dependence of a SAT. The *blue* and *red symbols* represent cool down and warm up, respectively

where δ_0 is an empirical term related to the ionization disk size [2, 3], the second term comes from the Heisenberg uncertainty principle, and the third term is due to thermal blur. Moreover, it is suggested these terms depend on exact tip shape.

It is clear, that operating GFIS at lower temperature is beneficial in terms ion current. Furthermore, since angular current density is proportional to I_0/σ^2, it increases over an order of magnitude at 20 K compared to LN_2. On the other hand, more efficient, and possibly more expensive, cooling system and mechanical insulation is required.

2.3.3 Shape Dependence

The total ion current that can be generated by a SAT is strongly dependent on tip shape. Since nitrogen-assisted etching offers possibility to vary tip shape it is interesting to measure He^+ ion current for various shaped SATs operating at different extraction voltages. SATs operating at voltages ranging from 3 to 15 kV have been prepared on single crystal W(111) tungsten wires. Each nanotip was reused multiple times preparing SATs using different etching parameters to alter its shape and thus extraction voltage, as well physically different wires were used to examine reproducibility. Experimental results are summarized in Fig. 2.22. Tips used in Fig. 2.22 all have narrow shank angles which are known to produce high ion currents compared to wide ones [7, 70–72].

The current measurement of a trimer nanotip is also interesting. The fact that the total current from both trimer and SAT is the same for tips operating at similar extraction voltages suggests that current is purely a function of tips shape not detailed atomic arrangement at the apex. It also suggests that a single atom at the apex is capable of supplying up to 1 nA of ion current without reaching saturation. This makes total beam current as well as angular current density of the trimer source three times lower since helium supply is equally shared by three atoms compared to an identically prepared SAT.

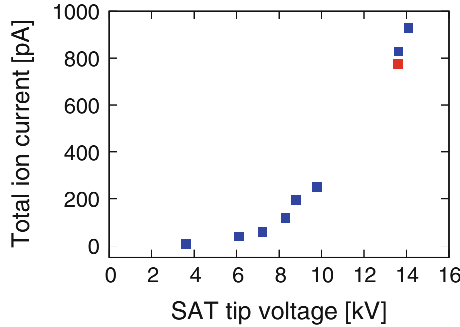

Fig. 2.22 The measured ion current as a function extraction voltage. The extraction voltage was chosen to be close to the BIV. The *blue squares* represent individual SAT builds using three different W(111) wires. The *red square point* is measured total ion current from the trimer tip prepared by field evaporating the SAT apex atom. The tip temperature was 20 K and helium pressure 1×10^{-4} Torr

2.3.4 Current Stability

Trimer tips are generally believed to have better structural stability and greater longevity. Helium beams generated by trimer nanotips are generally very stable. However, utilizing neon, current fluctuations as well as position instabilities were reported [73, 74] when at the neon best imaging voltage, see Fig. 2.23. Abrupt changes in the neon FIM pattern are clearly visible. Remarkably, abrupt increases in ion current from one spot are compensated by reduced current in other FIM spots. The total ion current from the trimer is conserved at all times during the individual

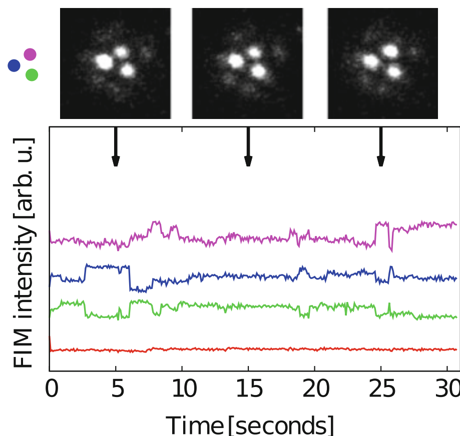

Fig. 2.23 Neon current stability traces of individual apex tungsten atoms. The *bottom red* trace represents the mean intensity of entire trimer structure. The *green*, *blue*, and *purple* traces correspond to average intensities of individual trimer atoms. Significant intensity variations are observed for individual ion-generating sites while averaged ion intensity remains constant. Traces are offset for clarity

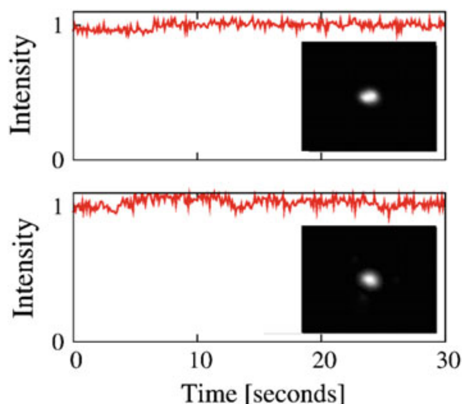

Fig. 2.24 Time traces of mean intensities for a single atom tip for helium (*top*) and neon (*bottom*) imaging gas, respectively. The tip voltage was 6.5 and 5.5 kV for helium and neon to account for different best imaging fields, see Table 2.2. The imaging gas pressures were adjusted to 2×10^{-5} Torr for helium and 2×10^{-6} Torr for neon to maintain same visual appearance on the fluorescent screen

atomic fluctuations; see red trace in Fig. 2.23. This suggests that adsorbed neon or possibly an impurity atom migrates about the trimer structure rendering individual atoms within the trimer inequivalent. At the same time lateral motion is also observed supporting the model of weakly bound adsorbents. This behaviour could be related to a different local field enhancement for adsorbed neon atoms compared to helium as discussed by Suchorski et al. [75, 76]. These instabilities can be diminished when the trimer is operated away from optimal imaging voltage for neon [77].

It is interesting to investigate ion current stability for both helium and neon using a SAT, Fig. 2.24. The SAT was operated at 5.5 kV and 6.5 kV for neon and helium, respectively. Lower tip voltage for neon operation is due to lower ionization potential of Ne atoms. The voltage difference is in a good agreement with ionization potential values presented in Table 2.2. Neon gas pressure was set between 2×10^{-6} and 5×10^{-6} Torr. These pressure values were selected so the FIM image of the SAT had similar visual appearance on the fluorescent screen to an image generated with helium at a typical value of 2×10^{-5} Torr.

In sharp contrast with neon ion current from a trimer structure there is no comparable variation in ion current from the SAT when either helium or neon imaging gases are used. Evidently, excessive neon adsorption and migration does not act here due to different atomic structure of the tip apex. The protruding single tungsten atom at the tip apex results in significantly stronger electric field compared to that at its nearest neighbours. Presumably these effects combined led to stable Ne^+ ion current.

The long term stability of W(111) SATs were also evaluated. Figure 2.25 shows FIM pattern and stability trace of 100 h of continuous operation. The helium partial pressure during the measurement was 1×10^{-5} Torr. The total ion current was not determined. The images were recorded at time zero, midpoint, and then just prior to the intentionally discontinued emission. This indicates that SATs prepared in this manner can result in stable and resilient structures.

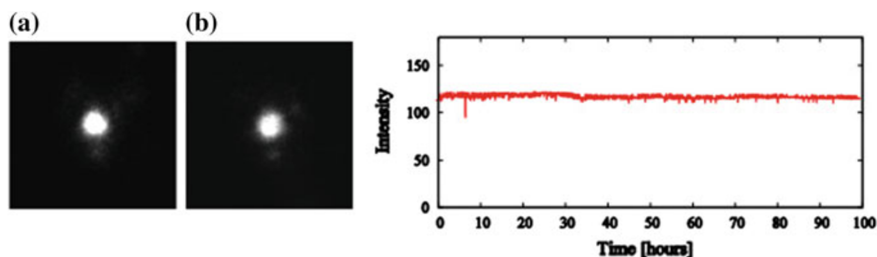

Fig. 2.25 The FIM patterns were captured **a** immediately after SAT formation, and **b** after 100 h of continuous He ion emission at 1×10^{-5} Torr and approximately 80 K. The stability trace (*right*) was evaluated from spot brightness during the experiment

2.4 Conclusions

It has taken decades for the first commercial SIM to come to market and this is due in part to the complexities in developing stable and bright gas field ion sources (GFISs). Different methods have been and are being developed to create improvements to source technologies. This chapter has summarized the method of field assisted chemical gas etching to produce single atom tips for the generation of gas ion beams. These tips can have controlled shapes and can produce stable beams of noble gas ions through a range of temperatures and operating pressures. Development this technology for the generation of noble gas ion beams and other gas ions will continue to help expand the utility of SIM and FIB systems.

Acknowledgments Technical support of Mark Salomons and Martin Cloutier is greatly appreciated.

References

1. N.P. Economou, J.A. Notte, W.B. Thompson, Scanning **34**(2), 83 (2012). doi:10.1002/sca.20239. http://www.ncbi.nlm.nih.gov/pubmed/21611954. N.P. Economou, J.A. Notte, W.B. Thompson, Eng Historical Article 2011/05/26 06:00 Scanning, Mar–Apr 2012, **34**(2):83–89. doi: 10.1002/sca.20239 (Epub 2011 May 24)
2. T.T. Tsong, *Atom-Probe Field Ion Microscopy* (Cambridge University Press, 1990)
3. M. Miller, A. Cerezo, M. Hetherington, G. Smith, *Atom Probe Field Ion Microscopy* (Oxford Science Publications, 2006)
4. H.W. Fink, IBM J. Res. Dev. **30**(5), 460 (1986). doi:10.1147/rd.305.0460
5. H.W. Fink, Phys. Scr. **38**(2), 260 (1988). doi:10.1088/0031-8949/38/2/029. http://stacks.iop.org/1402-4896/38/i=2/a=029
6. G. Antczak, G. Ehrlich, *Surface Diffusion* (Cambridge University Press, 2010). http://dx.doi.org/10.1017/CBO9780511730320. Cambridge Books Online
7. R. Borret, K. Bohringer, S. Kalbitzer, J. Phys. D **23**, 1271 (1990)
8. A. Knoblauch, T. Miller, C. Klatt, S. Kalbitzer, Nucl. Instrum. Methods Phys. Res. Sect. B: Beam Interac. Mater. Atoms **139**(1–4), 20 (1998). doi:10.1016/S0168-583X(97)00960-9. http://www.sciencedirect.com/science/article/pii/S0168583X97009609

9. T. Miller, A. Knoblauch, C. Wilbertz, S. Kalbitzer, Appl. Phys. A **61**, 99 (1995)
10. R. Borret, K. Jousten, K. Bohringer, S. Kalbitzer, J. Phys. D: Appl. Phys. **21**(12), 1835 (1988). http://stacks.iop.org/0022-3727/21/i=12/a=031
11. K. Jousten, K. Bohringer, R. Borret, S. Kalbitzer, Ultramicroscopy **26**(3), 301 (1988)
12. V.T. Binh, J. Marien, Surf. Sci. **202**, L539 (1988)
13. V.T. Binh, S.T. Purcell, App. Surf. Sci. **111**, 157 (1997)
14. V.T. Binh, N. Garcia, Ultramicroscopy **42–44**(Part 1), 80 (1992). doi:10.1016/0304-3991(92)90249-J. http://www.sciencedirect.com/science/article/pii/030439919290249J
15. V.T. Binh, S.T. Purcell, N. Garcia, J. Doglioni, Phys. Rev. Lett. **69**(17), 2527 (1992). http://link.aps.org/doi/10.1103/PhysRevLett.69.2527
16. S.T. Purcell, V.T. Binh, N. García, Appl. Phys. Lett **67**(3), 436 (1995)
17. V. Butenko, Y. Vlasov, O. Golubev, V. Shrednik, Surf. Sci. **266**, 165 (1992)
18. R. Bryl, A. Szczepkowicz, Appl. Surf. Sci. **241**(3–4), 431 (2005). doi:10.1016/j.apsusc.2004.07.041
19. A. Szczepkowicz, Surf. Sci. **605**(17–18), 1719 (2011). doi:10.1016/j.susc.2011.06.005
20. A. Szczepkowicz, R. Bryl, Surf. Sci. **559**(2–3), L169 (2004). doi:10.1016/j.susc.2004.04.035
21. H. Wengelnik, H. Neddermeyer, J. Vac. Sci. Technol. A: Vac. Surf. Films **8**(1), 438 (1990). doi:10.1116/1.576415
22. H.S. Kim, M.L. Yu, U. Staufer, L.P. Muray, D.P. Kern, T.H.P. Chang, J. Vac. Sci. Technol. B **11**(6), 2327 (1993). doi:10.1116/1.586981. http://scitation.aip.org/content/avs/journal/jvstb/11/6/10.1116/1.586981
23. M.L. Yu, B.W. Hussey, H.S. Kim, T.H.P. Chang, J. Vac. Sci. Technol. B **12**(6), 3431 (1994). doi:10.1116/1.587526. http://scitation.aip.org/content/avs/journal/jvstb/12/6/10.1116/1.587526
24. C. Vesa, R. Urban, J.L. Pitters, R.A. Wolkow, Appl. Surf. Sci. **300**, 16 (2014)
25. C.C. Chang, H.S. Kuo, I.S. Hwang, T.T. Tsong, Nanotechnology **20**(11), 115401 (2009). doi:10.1088/0957-4484/20/11/115401. http://www.ncbi.nlm.nih.gov/pubmed/19420438. C.-C. Chang, H.-S. Kuo, I.-S. Hwang, T.T. Tsong, Research Support, Non-U.S. Gov't England 2009/05/08 09:00 Nanotechnology **20**(11), 115401. doi:10.1088/0957-4484/20/11/115401. Epub 2009 Feb 24
26. T.Y. Fu, L.C. Cheng, C.H. Nien, T.T. Tsong, Phys. Rev. B **64**(11) (2001). doi:10.1103/PhysRevB.64.113401
27. H.S. Kuo, I.S. Hwang, T.Y. Fu, Y.H. Lu, C.Y. Lin, T.T. Tsong, Appl. Phys. Lett. **92**, 063106 (2008)
28. H.S. Kuo, I.S. Hwang, T.Y. Fu, J.Y. Wu, C.C. Chang, T.T. Tsong, Nano Lett. **4**(12), 2379 (2004). doi:10.1021/nl048569b. http://dx.doi.org/10.1021/nl048569b
29. K. Nomura, E. Rokuta, T. Itagaki, C. Oshima, H.S. Kuo, T.T. Tsong, e-J. Surf. Sci. Nanotechnol. **6**, 25 (2008)
30. E. Rokuta, T. Itagaki, T. Ishikawa, B.L. Cho, H.S. Kuo, T.T. Tsong, C. Oshima, Appl. Surf. Sci. **252**(10), 3686 (2006). doi:10.1016/j.apsusc.2005.05.075
31. S.T. Purcell, V.T. Binh, Appl. Phys. Lett. **75**(9), 1332 (1999). doi:10.1063/1.124684
32. S. Purcell, V. Binh, P. Thevenard, Nanotechnology **12**, 168 (2001)
33. K. Pelhos, T.E. Madey, R. Blaszczyszyn, Surf. Sci. **426**(1), 61 (1999). doi:10.1016/S0039-6028(99)00196-X. http://www.sciencedirect.com/science/article/pii/S003960289900196X
34. G. Antczak, T.E. Madey, M. Blaszczyszyn, R. Blaszczyszyn, Vacuum **63**(1–2), 43 (2001). doi:10.1016/S0042-207X(01)00169-5. http://www.sciencedirect.com/science/article/pii/S0042207X01001695
35. A. Szczepkowicz, A. Ciszewski, Surf. Sci. **515**(2–3), 441 (2002). doi:10.1016/S0039-6028(02)01960-X. http://www.sciencedirect.com/science/article/pii/S003960280201960X
36. G. Antczak, R. Blaszczyszyn, T.E. Madey, Prog. Surf. Sci. **74**(1–8), 81 (2003). doi:10.1016/j.progsurf.2003.08.007. http://www.sciencedirect.com/science/article/pii/S0079681603000686
37. J. Guan, R.A. Campbell, T.E. Madey, Surf. Sci. **341**(3), 311 (1995). doi:10.1016/0039-6028(95)00741-5. http://www.sciencedirect.com/science/article/pii/0039602895007415

38. J.L. Pitters, R. Urban, C. Vesa, R.A. Wolkow, Ultramicroscopy **131**, 56 (2013). doi:10.1016/j.ultramic.2013.03.013. http://www.sciencedirect.com/science/article/pii/S0304399113000831
39. J.L. Pitters, R. Urban, R.A. Wolkow, J. Chem. Phys. **136**(15) (2012). Artn 154704. doi:10.1063/1.3702209
40. M. Rezeq, J.L. Pitters, R.A. Wolkow, J. Chem. Phys. **124**, 204716 (2006)
41. M. Rezeq, J. Pitters, R. Wolkow, J. Scann. Probe Microsc. **2**(1), 1 (2007). doi:10.1166/jspm.2007.003
42. R. Urban, J.L. Pitters, R.A. Wolkow, Ultramicroscopy **122**, 60 (2012)
43. J. Onoda, S. Mizuno, Appl. Surf. Sci. **257**(20), 8427 (2011). doi:10.1016/j.apsusc.2011.04.124
44. J. Onoda, S. Mizuno, H. Ago, Surf. Sci. **604**(13–14), 1094 (2010). doi:10.1016/j.susc.2010.03.019
45. F. Rahman, J. Onoda, K. Imaizumi, S. Mizuno, Surf. Sci. **602**(12), 2128 (2008). doi:10.1016/j.susc.2008.04.034
46. Y. Sugiura, H. Liu, T. Iwata, S. Nagai, K. Kajiwara, K. Asaka, Y. Saito, K. Hata, e-J. Surf. Sci. Nanotechnol. **9**, 344 (2011). doi:10.1380/ejssnt.2011.344
47. G.R. Hanson, B.M. Siegel, J. Vac. Sci. Technol. **16**, 1875 (1979)
48. P.R. Schwoebel, G.R. Hanson, J. Vac. Sci. Technol. B **3**, 214 (1985)
49. T. Sakata, K. Kumagai, M. Naitou, I. Watanabe, Y. Ohhashi, Yhashi, O. Hosoda, Y. Kokubo, K. Tanaka, J. Vac. Sci. Technol. B **10**, 2842 (1992)
50. H. Hiroshima, M. Komuro, M. Konishi, T. Tsumori, Jpn. J. Appl. Phys. **31**(Part 1, No. 12B), 4492 (1992). doi:10.7567/JJAP.31.4492. http://jjap.jsap.jp/link?JJAP/31/4492/
51. K. Edinger, V. Yun, J. Melngailis, J. Orloff, G. Magera, J. Vac. Sci. Technol. B **15**, 2365 (1997)
52. B. Ward, J. Notte, N. Economou, J. Vac. Sci. Technol. B **24**, 2871 (2006)
53. H.S. Kuo, I.S. Hwang, T.Y. Fu, Y.S. Hwang, Y.H. Lu, C.Y. Lin, J.L. Hou, T.T. Tsong, Nanotechnology **20**, 335701 (2009)
54. Y. Kobayashi, Y. Sugiyama, Y. Morikawa, K. Kajiwara, K. Hata, J. Vac. Sci. Technol. B **28** (2010). doi:10.1116/1.3360302
55. D. Langmuir, Proc. Inst. Radio Eng. **25**(8), 977 (1937). doi:10.1109/JRPROC.1937.228419
56. P. Hawkes, E. Kasper, *Principles of Electron Optics*, Chapter 47, vol. 2 (Academic Press, London, San Diego, 1989)
57. M. Bronsgeest, J. Barth, L. Swanson, P. Kruit, J. Vac. Sci. Technol. B **26**(3), 949 (2008)
58. J. Witt, K. Müller, J. de Physique **47**, c2 (1986)
59. J.C. Wiesner, T.E. Everhart, J. Appl. Phys. **44**, 2140 (1973)
60. J.C.H. Spence, W. Qian, M.P. Silverman, J. Vac. Sci. Technol. A **12**, 542 (1994). doi:10.1116/1.579166
61. J. Mulson, E.W. Müller, J. Chem. Phys. **38**(11), 2615 (1963). doi:10.1063/1.1733560
62. K. Rendulic, Z. Knor, Surf. Sci. **7**, 205 (1967)
63. E.W. Muller, T.T. Tsong, *Field Ion Microscopy* (Elsevier, New York, 1969)
64. E.A. Mason, E.W. McDaniel, *Transport Properties of Ions in Gases*, Chap. Appendix III: Tables of Properties Useful in the Estimation of Ionneutral Interaction Energies (Wiley-VCH Verlag GmbH & Co. KGaA, 2005), pp. 531–539. doi:10.1002/3527602852.app3. http://dx.doi.org/10.1002/3527602852.app3
65. R.T. Lewis, R. Gomer, Surf. Sci. **26**, 197 (1971)
66. M. Benjamin, R. Jenkins, Proc. R. Soc. (London) A **176**(A965), 0262 (1940)
67. R. Gomer, J. Chem. Phys. **20**(11), 1772 (1952)
68. J.D. Rose, J. Appl. Phys. **27**(3), 215 (1956)
69. Y. Chen, D. Seidman, Surf. Sci. **26**, 61 (1971)
70. M. Southon, D. Brandon, Philos. Mag. **8**(88), 579 (1963)
71. G. Gipson, H. Eaton, J. Appl. Phys. **51**(10), 5537 (1980)
72. K. Jousten, K. Bohringer, S. Kalbitzer, Appl. Phys. B **46**, 313 (1988)
73. J. Notte, F. Rahman, S. McVey, S. Tan, R. Livengood, Microsc. Microanal. **16**(Supp. S2), 28 (2010)
74. R. Urban, J.L. Pitters, R.A. Wolkow, Appl. Phys. Lett. **100**, 263105 (2012)
75. N. Ernst, Surf. Sci. **219**(1–2), 1 (1989)
76. Y. Suchorski, W. Schmidt, J. Block, Appl. Surf. Sci. **76–77**(2), 101 (1994)
77. F. Rahman, J. Notte, R. Livengood, S. Tan, Ultramicroscopy **126**, 10 (2013)

Chapter 3
Structural Changes in 2D Materials Due to Scattering of Light Ions

Ossi Lehtinen and Jani Kotakoski

Abstract The family of two–dimensional (2D) materials is an attractive subject for modern microscopy techniques such as helium and neon ion microscopy. In this chapter, we provide a theoretical treatment on the effects of light ion irradiation on the structure of 2D materials, foremost graphene, using methods from the binary collision model to molecular dynamics. While reviewing the current literature on the topic, we point out that helium and neon irradiation can be used to create specifically small point defects (single and double vacancies) or to drill features into graphene. We also point out the current lack of studies involving non-graphene 2D materials.

3.1 Introduction

As described in Chap. 1, imaging in a He/Ne ion microscope is based on the secondary electrons emitted after inelastic collisions between the ions and the target material. In addition, the He ions are also elastically scattered by the target atoms, which can lead to significant structural transformations of the sample. For most samples, this only happens at doses far beyond what is needed for imaging, but in the case of light atoms and thin samples, elastic scattering can alter the structure already at doses much below what is required for images with high signal-to-noise ratio. Despite the typical negative connotation of such “damage”, the ion-induced transformations can also be taken advantage of for manipulating the sample structure at the atomic level. For example, controlled introduction of defects into materials to locally modify their electronic properties can lead to novel solutions for the challenges electronics industry is currently facing with the ever-decreasing devices sizes.

Two-dimensional (2D) materials provide an especially interesting case for structural manipulation, as all their atoms are at the surface and thus equally accessible

O. Lehtinen (✉)
Ulm University, Albert-Einstein-Allee 11, 89081 Ulm, Germany
e-mail: ossi.lehtinen@gmail.com

J. Kotakoski
Faculty of Physics, University of Vienna, Boltzmanngasse 5, 1090 Vienna, Austria
e-mail: jani.kotakoski@univie.ac.at

© Springer International Publishing Switzerland 2016
G. Hlawacek and A. Gölzhäuser (eds.), *Helium Ion Microscopy*,
NanoScience and Technology, DOI 10.1007/978-3-319-41990-9_3

for the ions. Graphene is the best known example from this new class of materials. In this allotrope of carbon, the atoms are arranged in a hexagonal pattern, which visually resembles chicken wire or a honeycomb. Due to the low mass of C atoms (atomic number $Z = 6$), significant amounts of energy can be transferred through elastic collisions with even ions as light as He (atomic number $Z = 2$). This fact, combined with the characteristics of the helium (or neon) ion microscopy (HIM), such as its small probe size, mean that this method is ideally suited for the manipulation of 2D materials. Indeed, experiments have already demonstrated that HIM can be used to draw features both into suspended as well as supported graphene structures. At the same time, much less is known about the non-destructive structural changes that can be achieved with the tool. However, in order to achieve true atomic-level control over these materials via HIM, we need to understand in detail what happens when the ions pass through.

3.2 The Scattering Process

3.2.1 Elastic Scattering

In the simplest model, the elastic scattering process of an energetic ion in a solid can be approximated as an elastic collision of two free point-like particles. The main considerations in this model are the conservation laws of kinetic energy and momentum. For a given geometry (see Fig. 3.1), the energy and momentum transferred from one particle to the other can be worked out exactly if the interaction between the particles is known.

For a two-body system, the interaction can be described by an interatomic potential $\mathscr{U}(r)$ which depends only on the distance r between the particles (i.e., the potential is spherically symmetric). The exact calculation of the potential requires a time-dependent quantum mechanical treatment of the evolution of the electronic systems of the particles once they start overlapping at the smallest r. This approach,

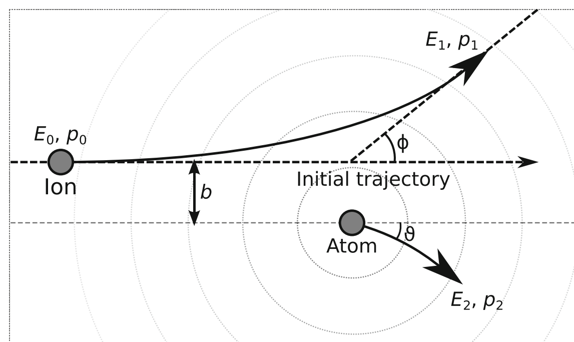

Fig. 3.1 A schematic presentation of the collision geometry for two point-like particles. The spherically symmetric potential between the particles is sketched with the co-centric circles around the atom

however, becomes increasingly complicated as details of, e.g., the velocity dependent excitations of the electronic systems need to be accounted for. Therefore, in practice, approximations are needed.

When two nuclei are close to each other (but not overlapping), the interaction is essentially a Coulombic repulsion of two point charges. At larger distances, however, the electron clouds of the atoms shield the naked interaction of the nuclei. Including this screening leads to the following potential energy function:

$$\mathscr{U}(r) = \frac{1}{4\pi\epsilon_0}\frac{Z_1 Z_2 e^2}{r}\varphi(r/a), \tag{3.1}$$

where the first part describes the Coulombic interaction of the nuclei, dependent on the atomic numbers (Z_1 and Z_2) of the atoms and the interatomic distance r, modulated by a screening function $\varphi(r/a)$, dependent again on r and a screening parameter a. ϵ_0 is the vacuum permittivity and e the unit charge. Such a purely repulsive potential is suitable for modeling interactions between noble gas ions and also other atoms as long as collisions at energies above about 100 eV, below which chemical effects become important [1].

Many formulations for $\varphi(r/a)$ have been proposed, with the universal repulsive potential introduced by Ziegler, Biersack and Littmark being one of the most used ones. Within this potential, often labeled ZBL, a universal $\varphi(r/a)$ is fitted to a large set of *ab-initio* calculations with different atom pairs [2]. The form of the ZBL screening function is

$$\varphi(x) = 0.1818e^{-3.2x} + 0.5099e^{-0.9423x} + 0.2802e^{-0.4029x} + 0.02817e^{-0.2016x}, \tag{3.2}$$

with $x = r/a$, and

$$a = \frac{0.8854a_0}{Z_1^{0.23} + Z_2^{0.23}}, \tag{3.3}$$

where a_0 is the Bohr atomic radius ($a_0 = 0.529$ Å).

Once an interaction model is established, the classical scattering integral can be solved. Here, the equations of motion of the colliding atoms are solved in the presence of the interatomic force with a given initial collision geometry (see Fig. 3.1). In some simple cases an analytical solution can be deduced. However, in practice numerical integration is usually necessary.

One consequence of using a purely repulsive spherically symmetric potential is that a single parameter, that is, the impact parameter (marked as b in Fig. 3.1) is enough to determine the geometry and the energetics of the process. The impact parameter is the distance at which the ion would have passed the atom if it would have continued on a straight trajectory. In general, the smaller the b, the stronger the

interaction, and consequently, the larger the energy transfer and scattering angle ϕ, with the transferred energy monotonously decreasing with increasing b.

Through solving the scattering integral, the energy and momentum transfer to the target atom can be calculated for any collision geometry. Thus the ion-matter interaction can be fully described, as far as an elastic interaction is considered, and one can subsequently focus on what happens *after* the collision.

3.2.2 A Note on Inelastic Scattering

In reality, elastic scattering is not the only process taking place upon the impact of the ions. As mentioned earlier, the electronic systems of the target and the ion can also be excited (which is used for imaging in an ion microscope). If sufficient energy is transferred to the electronic system of the target, this can lead to structural changes through electron-phonon coupling and local heating of the target at the impact point, or possible destabilization of interatomic bonds in an excited state or due to ionization. However, effects severe enough to drastically alter the atomic structure of the sample become important typically only at energies higher than what is relevant for the discussion here (in the MeV range). Similarly, also ion induced excitations of the nuclei take place only at higher energies. Therefore, we concentrate in this chapter on the effects of elastic scattering between the incoming ion and the target atoms.

3.3 Target Evolution Under Ion Impacts

3.3.1 After the Binary Collision

The simple two-body model described in the previous section, so-called binary collision model, describes the momentum transfer from the ion to a target atom. However, in order to understand the effect of irradiation on the atomic structure of the target material, we also need to consider the dynamics *after* the collision. In the case of ion microscopy of free-standing 2D materials, the colliding ion will always retain sufficient kinetic energy in its original direction to escape from the target immediately after the impact. It can hence be discarded from all of the subsequent analysis. However, the relevant question is whether enough energy was transferred during the collision to any of the target atoms to initiate a transformation process.

3.3.1.1 Displacement Threshold, T_d

In general, an irradiation event will only lead to a structural change if one or more target nuclei receive enough kinetic energy to be displaced from their lattice position

to a sufficient distance to prevent immediate recombination of the produced Frenkel pair (a vacancy and an interstitial atom). In the case of 2D materials, the creation of interstitial atoms is rare, however, because the displaced atoms can easily escape into the surrounding vacuum.

Each atom in a crystal resides at the bottom of a potential energy well, defined by the surrounding atoms. At the very least, the energy corresponding to the depth of the well needs to be provided to facilitate a displacement. However, displacement of an atom is a dynamic process, where some of the momentum initially assigned to one atom is transferred to the surrounding atoms. Therefore, the displacement threshold (T_d) tends to be higher than the depth of the well alone. T_d can be either simulated with molecular dynamics (MD; see Sect. 3.3.2) [3] or obtained experimentally [4, 5]. The value for graphene in the out-of-plane direction is approximately 23 eV, and for the chalcogen atoms in transition metal dichalcogenides in the range of 5–7 eV [6].

T_d is sensitive to the local chemical environment of each atom and is therefore material- and configuration-dependant. It is also an anisoptropic quantity in terms of the displacement direction (clearly, displacement into an open crystallographic direction—a crystal channel—is easier than directly against a neighbouring atom). In the case of 2D materials the direction perpendicular to the plane (towards vacuum) tends to have the lowest threshold [3]. However, especially at the higher range of ion energies relevant for ion microscopy, the momentum transfer favors the opposite (in-plane) direction [7].

3.3.1.2 From the Displacement Threshold to a Displacement Cross-Section and a Sputtering Yield

Once the interaction model is defined, the scattering integral is solved, and the displacement threshold is determined, it is straight forward to determine the probability for displacing an atom upon an ion impact. This probability is typically given as a cross-section σ with the dimension of area (typically given in the non-SI units of barn, 10^{-28} m^2), and can be directly expressed in terms of the impact parameter b. In the spherically symmetric case (assuming an isotropic displacement threshold), $\sigma = \pi b_{max}^2$ is the area of a circle with a radius corresponding to the impact parameter b_{max} at which the transferred kinetic energy exceeds the displacement threshold ($E_2 > T_d$). As an example, transferred kinetic energy in a collision of a 30 keV He/Ne ion with a stationary C atom is shown in Fig. 3.2 as a function of the impact parameter b.

In the case of a 2D material, the sputtering yield (the number ejected atoms per ion impact) can be estimated by

$$Y = \frac{\sigma}{A_{atom}} = \sigma \rho_A, \tag{3.4}$$

where A_{atom} is the surface area per atom (in same units as σ) and ρ_A is the atomic areal density of the target ($\rho_A = 1/A_{atom}$). The relationship between b, A_{atom} and σ is

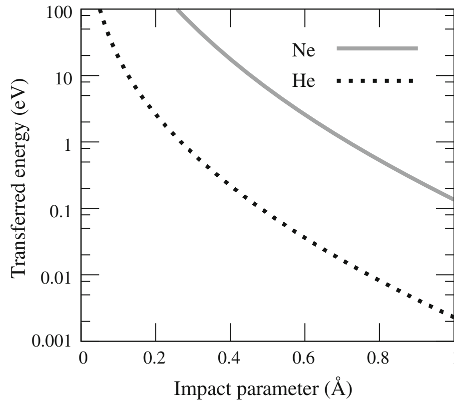

Fig. 3.2 Transferred kinetic energy as a function of the impact parameter for collisions between a 30 keV He/Ne and a C atom, calculated via MD using the ZBL repulsive potential. Notice the logarithmic scale on the *y*-axis

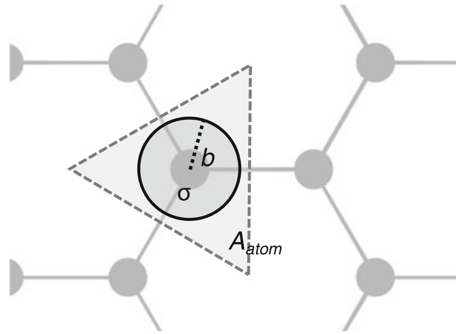

Fig. 3.3 The relation of the displacement cross-section σ and the area per atom A_{atom} exemplified in the case of graphene. If the ion hits the area enclosed by the circle of radius b, the atom is displaced. The ratio of the circular area to the area per atom in the sheet enclosed by the triangle gives the probability of displacing an atom by an ion impact at a random location on the target

illustrated in Fig. 3.3. The vacancy concentration after a given ion exposure (η) can be calculated as

$$c_v = Y\eta = \sigma\rho_A\eta. \tag{3.5}$$

Notice that (3.5) is only valid when η is sufficiently low so that each displacement event can be considered truly independent.

The binary collision model can be used for estimating the sputtering yields in some situations in 2D materials. For example, it has been shown that the sputtering yield is predicted fairly accurately in graphene in the case of Xe ions [7] as compared to MD simulations. The black and red curves in Fig. 3.4 show the sputtering yield

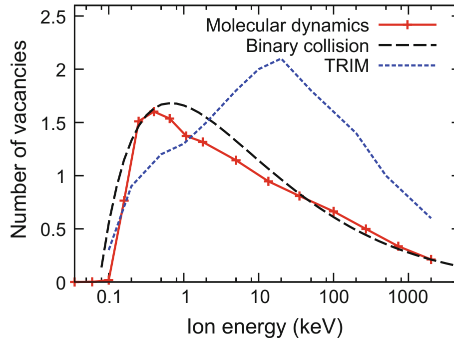

Fig. 3.4 Comparison of different methods for predicting sputtering yields. Impacts of Xe ions on free-standing graphene are calculated by molecular dynamics simulations, the binary collision model, and TRIM simulations. The other two methods can be compared to the more accurate MD simulations. The binary collision model reproduces the MD results with fairly good accuracy, whereas the TRIM simulations fail catastrophically at all the considered energies. Data reproduced from [7]

as estimated by the binary collision method and MD simulations, respectively. In general, the curves are close to each other.

3.3.1.3 Limitations of the Binary Collision Model

It is worth stressing that the binary collision model is a significant simplification of the real situation; Each atom is considered truly independent, sitting in its own potential well (and possibly removed from there through a displacement). In real experiments, displacement events often affect more than just one atom. Such a situation is exemplified in Fig. 3.5. Most of the points discussed below follow from this fact.

For example, when b_{max} is sufficiently large so that an ion can simultaneously displace two atoms, the binary collision model requires that each of the atoms receives kinetic energy which is at least the equivalent to the displacement threshold. However, if the two atoms are bound to each other, it is likely that already a lower energy would suffice because one bond less needs to be broken per atom. Since the T_d even in this case is likely to be only slightly adjusted towards lower values, this error can be considered to be only a slight correction on the model. However, a more significant error is caused by the complete neglect of situations where the ion collides simultaneously with multiple atoms, or where the primary target atoms collides with other target atoms in a collision cascade. Cascades can happen even in 2D materials, when the primary target is displaced in the in-plane direction.

Further, the crystal structure is not accounted for in the simple model, which can be an issue in the case of 2D materials which have some structure in the 3rd dimension, such as transition metal dichalcogenides. In such materials atoms (such

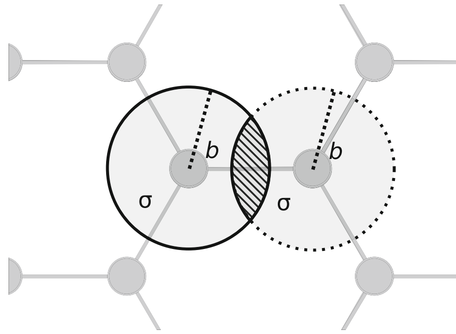

Fig. 3.5 Overlapping cross-sections of neighbouring atoms. If the radius *b*, within which an atom is displaced is so large that the neighbouring cross-sections start overlapping, the assumption of a binary collision is not valid anymore. If an ion hits the shaded area shared by the cross-sections, both of them should be displaced

as the sulphurs in MoS_2) may reside exactly on top of each other, and the lower atom is thus shielded by the upper one. This can be considered an extreme case of ion channeling, which is known to strongly influence damage yields under ion irradiation.

Also one of the basic assumptions behind the binary collision model can cause inaccuracies: as was already mentioned, T_d is in reality not isotropic. In practice, approximating the threshold to be isotropic only leads to significant errors when the typical transferred kinetic energies are similar to T_d. As is seen in the monotonously decreasing curves in Fig. 3.2, there is always a range of impact parameters where the transferred energy is close to T_d. Such a range exists regardless of the ion energy. However, the transferred energy curves have steep slopes (note the logarithmic y-axis), and the variation in the values of a non isotropic T_d is contained within a small impact parameter range, as compared to the total cross-section. Consequently, a suitable statistical average of the nonisotropic T_d can still be used with good confidence.

3.3.2 Molecular Dynamics Simulations of Ion Impacts on 2D Materials

To overcome the limitations of the binary collision model discussed above, one can turn to molecular dynamics (MD) simulations. The basic principle of MD is numerical integration of the equations of motion of the particles in the presence of interatomic forces. The main difference to the binary collision model is that now, in principle, all the atoms in the system interact with each other and the trajectories of all the atoms are followed.

The MD method was developed in the late 1950s to provide a solution for the problem of analytically solving the many-body problem [8, 9]. In the beginning,

it was applied to small systems (i.e., molecules) that consisted of elastic spheres modeled with square-well potentials, from which the method got its name. However, nowadays MD is used to describe atomic (and other) systems with a rich variety of interaction models.

In the heart of MD is the numerical integration of the classical equations of motion for the given system. In Cartesian coordinates, the Hamiltonian equations of motion have the familiar form

$$\dot{\mathbf{R}}_I = \frac{\mathbf{P}_I}{M_I} \tag{3.6}$$

$$\dot{\mathbf{P}}_I = -\nabla_{\mathbf{R}_I} \mathscr{U}\left(\mathbf{R}_1, \mathbf{R}_2, ..., \mathbf{R}_N\right) = \mathbf{f}_I, \tag{3.7}$$

where $\mathbf{R}_I$ are the Cartesian coordinates of atom I, $\mathbf{P}_I$ the corresponding momentum, M_I the mass of the atom, $\mathscr{U}\left(\mathbf{R}_1, \mathbf{R}_2, ..., \mathbf{R}_N\right)$ the potential energy of the system (which depends on the coordinates of all of the atoms, $\mathbf{R}_1, \mathbf{R}_2, ..., \mathbf{R}_N = \{\mathbf{R}_I\}$) and $\mathbf{f}_I$ is the force acting on the atom. The dot represents a time derivative.

It is important to realize that over time any numerical method used to evolve these equations leads to accumulation of error in the trajectories of the particles. However, for a sufficiently short integration step (time advancement between simulation steps), these errors are relatively small. Nevertheless, the results of MD must always be interpreted statistically: For a large enough number of initial conditions, all physically reasonable simulation outcomes will be reached with approximately correct statistical weights.

To understand the justification for using a potential energy function which depends only on the atomic positions in the equations of motion, we need to start with a quantum mechanical description of the atomic structure. According to quantum mechanics, all properties of a system are described by the Schrödinger equation

$$i\hbar \frac{\partial \Psi(\{\mathbf{r}_i\}, \{\mathbf{R}_I\}; t)}{\partial t} = \mathscr{H}\Psi(\{\mathbf{r}_i\}, \{\mathbf{R}_I\}; t), \tag{3.8}$$

where the wave function Ψ is written implicitly to depend on the coordinates of all electrons i in the system $\{\mathbf{r}_i\}$ as well as on the coordinates of all nuclei I $\{\mathbf{R}_I\}$ as well as on time t. $\mathscr{H}$ is the Hamiltonian of the system. In order to carry out MD simulations, we need to establish the connection between this quantum mechanical description of our system and $\mathscr{U}\left(\{\mathbf{R}_I\}\right)$.

By grouping all terms which affect the electronic system into an effective Hamiltonian $\mathscr{H}_e$, the total Hamiltonian can be written as

$$\mathscr{H} = -\sum_I \frac{\hbar^2}{2M_I}\nabla_I^2 + \mathscr{H}_e(\{\mathbf{r}_i\}, \{\mathbf{R}_I\}), \tag{3.9}$$

where the only term which does not depend on the electronic system is the kinetic energy term for the nuclei. $\mathscr{H}_e$ describes the situation assuming static nuclei (clamped-nuclei approximation). If we assume that the exact solution is known for

the corresponding time-independent electronic Schrödinger equation, it is possible to separate hierarchically the light electrons from the heavy nuclei [10] to obtain

$$\left[-\sum_I \frac{\hbar^2}{2M_I}\nabla_I^2 + E_k(\{\mathbf{R}_I\})\right]\chi_k + \sum_l C_{kl}\chi_{kl} = i\hbar\frac{\partial}{\partial t}\chi_k, \tag{3.10}$$

where $E_k(\{\mathbf{R}_I\})$ are the eigenenergies for the time-independent Schrödinger equation for the electronic structure corresponding to the nuclei clamped at $\{\mathbf{R}_I\}$), and the exact nonadiabatic operator C_{kl} couples the electronic and the nucleic systems. χ_k are the wavefunctions corresponding to the nucleic system. Neglecting all but the diagonal terms (C_{kk}) leads to the *adiabatic approximation* to the fully nonadiabatic problem. Assuming that also these terms $C_{kk} \approx 0$, we get

$$\left[-\sum_I \frac{\hbar^2}{2M_I}\nabla_I^2 + E_k(\{\mathbf{R}_I\})\right]\chi_k = i\hbar\frac{\partial}{\partial t}\chi_k, \tag{3.11}$$

which defines the Born-Oppenheimer approximation (BOA). Further assuming that the nuclei can be described as point particles has been shown [10] to lead to the Newtonian equations of motion

$$\dot{\mathbf{P}}_I = -\nabla_I E_k = -\nabla_I \mathscr{U}_k^{\text{BOA}}\left(\{\mathbf{R}_I(t)\}\right) \tag{3.12}$$

for each electronic state k. Therefore, within BOA, the nuclei move in a classical way in an effective potential $\mathscr{U}^{\text{BOA}}$ which is given by the ground state Born-Oppenheimer potential energy surface E_k. Typically it is assumed that the electronic structure reaches its ground state at much shorter time scales than that of the nuclear movement, and the electronic structure is assumed therefore to always correspond to the ground state with respect to the current nuclear coordinates. While other approaches exist for propagating both the electronic and nuclear system in time quantum mechanically in time-dependent effective potentials, in practice BOA is required for collecting any statistics for system sizes which are relevant for ion irradiation experiments.

3.3.2.1 Interatomic Potentials

As described above, the potential for MD simulations $\mathscr{U}\left(\{\mathbf{R}_I\}\right)$ can be interpreted as the Born-Oppenheimer potential energy surface corresponding to the electronic ground state, and it can be calculated with any suitable computational method. The most accurate potential can be reached starting from first principles, utilizing, for example, density functional theory (DFT) or Green's function methods. However, these methods are often computationally too expensive to be practical in the case of ion irradiation simulations. This is especially true in the case of the energetic phase of the irradiation where accurate modeling of the repulsion between the ion and the

target atom requires taking into account the core electrons in the calculations. This renders more efficient pseudo-potential methods unusable, significantly increasing the computational cost.

However, because the ground state potential depends only on the positions of the nuclei, it can be approximated by an analytical function of the form

$$\mathscr{U}^{\mathrm{BOA}}\left(\{\mathbf{R}_I\}\right) = \sum_I \mathscr{U}_1\left(\mathbf{R}_I\right) + \sum_{I>J} \mathscr{U}_2\left(\mathbf{R}_I, \mathbf{R}_J\right) + \sum_{I<J<K} \mathscr{U}_3\left(\mathbf{R}_I, \mathbf{R}_J, \mathbf{R}_K\right) + \ldots, \tag{3.13}$$

where the terms correspond to one-body, two-body, three-body, and higher order terms, respectively. $\sum_{I>J}$ and $\sum_{I<J<K}$ stand for a double sum and a triple sum, respectively. If suitable analytical forms are found for each term, the potential energy function can be fitted to first principles calculation results and/or experiments. Potentials based on this basic idea are often called inter-changeably force fields, empirical potentials or analytical potentials.

In such potentials, the self-energy term ($\mathscr{U}_1$) is often chosen to be zero. Hence, the simplest analytical potentials are described only with the two-body term ($\mathscr{U}_2$), where the only variable is the distance between each atom pair. The repulsive spherically symmetric potentials mentioned in Sect. 3.2.1 are a subset of such potentials. Such potentials typically have a global potential minimum at the desired equilibrium distance for an atom pair, and the slopes of the potential around this point are fitted to reproduce correctly the repulsive and attractive parts of the potential. Because pair-potentials lack any directional dependence of the bonding, they can only be used to described close packed crystals or repulsive interactions.

Covalently bonded materials (such as all known 2D materials) typically show a strong preference for specific bonding directions. Consequently, any potential able to reasonably describe such materials needs to include at least the three-body term ($\mathscr{U}_3$). While there are many approaches to describe covalent bonding, the so-far most successful one is based on the concept of bond order, where the number of bonds an atom has affects the strength of the bonds. Its magnitude is associated both with the bond length as well as the bond angle. The concept dates back to Linus Pauling [11], who proposed the following expression for bond order:

$$s_{IJ} = \exp\left(\frac{R_{IJ} - d_{IJ}}{b}\right), \tag{3.14}$$

where R_{IJ} is the distance between atoms I and J, d_{IJ} the length of the corresponding dimer and b a constant. In a typical nomenclature, a bond order potential is a potential which is based on the dimer properties and where the strength of the potential is affected by the environment. This leads to a general functional form of

$$\mathscr{U}_{IJ} = V_{\mathrm{R}}\left(\mathrm{R}_{IJ}\right) + b_{IJK} V_{\mathrm{A}}\left(\mathbf{R}_{IJ}\right), \tag{3.15}$$

Table 3.1 Analytical interatomic potentials useful for simulating 2D materials. If an established name exists for a potential, that is given, otherwise the name of the first author is given. Note, that this is not by any means an exhaustive list

Material	Author/Name	References
Graphene	Tersoff	[14]
	AIREBO	[13]
	REBO	[12]
	ReaxFF	[15]
h-BN	Albe et al.	[16]
MoS_2	Liang et al.	[17]
	Jiang et al.	[18]
2D-SiO_2	Watanabe et al.	[19]
Black phosphorus	Jiang et al.	[18]

where V_R/V_A is a repulsive/attractive term which depends only on the inter-atomic distance $\mathbf{R}_{IJ}$ and b_{IJK} is a three-body bond order term, which depends on the environment.

In the context of low-dimensional materials, perhaps the most successful implementation of the bond order concept is the Abell-Tersoff formalism adapted by Brenner et al. for solid carbon and hydrocarbon molecules [12]. While a typical potential only describes interactions within a solid or inside a molecule, it cannot properly describe van der Waals type interactions, which can be of importance in the case of 2D materials and other nanostructures. To remedy this issue, Lennard-Jones-type interaction was added by Stuart et al. [13] to an earlier version of Brenner's hydrocarbon potential.

Table 3.1 lists interatomic potentials which the reader might find useful when simulating ion collisions on 2D materials. The list does not intend to be an exhaustive one, and other potentials for simulating the included materials, as well as other (possibly still undiscovered) 2D structures surely exist. As always, special care needs to be taken when employing these potentials in simulations. That is, one should check, for example, how well defect formation energies and/or displacement thresholds are reproduced by the potential to help judge how reliable the simulation results can be expected to be.

3.3.2.2 Special Considerations for Modeling Ion Impacts on Solids

Most computational methods have been developed to describe materials close to the equilibrium and are not therefore well suited for applications in far-of-equilibrium situations such as during ion irradiation. Therefore, one needs to pay attention to several aspects of the simulation which are not important in the typical case.

As an important example, during the energetic phase of the irradiation event, the ion and different atoms in the target material can get atypically close to each other. Because normal solid state simulation methods have not been developed to deal with such short distances, the description of the energetic phase by, for example, DFT implementations with pseudo potentials or analytical potentials is remarkably poor. Therefore, one is advised to obtain accurate data for all of the relevant atom pairs at close interatomic distances to properly model the repulsion. A simpler approach is to use, for example, the ZBL universal repulsive potential (see Sect. 3.2.1).

It should also be kept in mind that the numerical integration is prone to lead to errors in the trajectories of the particles. In a typical simulation this is only a problem over long times. However, for energetic particles which move at high speeds, a too long time step can lead to unphysically close separations between the atoms and thus to spurious behaviour of the system. Because of this, as short a time step as feasible should be used, especially during the energetic phase. To save computational resources, the time step can be increased when the particles have slowed down.

It is also important to consider the size of the simulated system. Only a finite number of atoms can be included in a simulation, and even with the computationally efficient analytical potentials one is limited to millions of atoms, which is quite a small number compared to real targets. Modeling an infinite crystal with a finite simulation target can be accomplished with periodic boundary conditions. That is, the atoms at one edge of the simulation target are made to interact with a mirror image of the opposite edge. Thus the environment of each atom (even at the edges) is as if they were in a perfect infinite crystal. Unfortunately, with periodic boundaries the momentum introduced into the system via irradiation has no way of dissipating, while in reality, phonons generated by an ion impact would simply propagate away from the impact site disappearing into the bulk of the crystal.

To emulate the dissipation of momentum, the system can be connected to an artificial heat bath. One widely used schema for doing this is the Berendsen thermostat [20], where the velocities of selected atoms are scaled in order to drive the total kinetic energy in the system towards a preset value. This can, however, only be done far enough from the impact site so that it does not affect the dynamics of the impact. Therefore, the thermostat is typically applied on the border atoms of a large simulation cell.

Inelastic effects can also be taken into account if necessary. Electronic stopping (see Chap. 5) can be modelled, for example, as a frictional force [21], where the slowing down of the ion due to inelastic scattering is accounted for. However, in a 2D target no significant slowing down can happen as the distance traversed by the ion within the material is minimal. Furthermore, damage production initiates typically only at the MeV range, and thus inelastic scattering is typically not an issue in the context of this chapter.

Here, a word of caution is called for. While MD allows direct studies of the atomic scale dynamics during and after an irradiation process, and in this way provides invaluable insights into what happens during an experiment, direct comparison between the simulations and the experiments can still be challenging. This is partly due to the difference in time scales. In the best case, systems can be modeled

at microsecond time scales, but a more typical simulation ends after some pico- or nanoseconds. Depending on the case, these time scales can be several orders of magnitude shorter than what would be needed to accurately capture some of the experimentally relevant processes (such as defect migration). Given enough time, loosely bound atoms at defects could migrate even at room temperature, and dangling bonds may be saturated by foreign atoms, especially if the sample is not held at ultra high vacuum conditions.

Although there are approaches to try to overcome the time scale issue (such as running multi-scale simulations combining MD and Monte Carlo methods or to carry out MD simulations at elevated temperatures to increase the frequency of rare events), none of them are completely problem free: in Monte Carlo simulations some important processes may be omitted, whereas the relative rates of different processes may be different at elevated temperatures than at normal conditions). In short, one needs to be positively sceptical regarding the final outcomes of any of these simulations when attempting a direct comparison with experiments.

Starting from scratch to implement all the features described above would be a laborious endeavour. Fortunately numerous freely available atomic simulation codes exist. Perhaps the most widely used is the LAMMPS software [22], which is an open source project hosted at the Sandia National Laboratories. The ASE tool-set [23] is another one to mention. Also most DFT codes such as VASP [24], and Quantum Espresso [25] include facilities for conducting dynamical simulations. However, it should be kept in mind that these tools may need to be modified for simulating ion irradiation, as briefly explained above.

3.3.3 Influence of Multiple Impacts

Until now, the discussion has been limited to the case where each ion impact can be considered independent and to occur on a pristine area. At low irradiation doses this is a reasonable assumption, and the effects of prolonged irradiation can be modeled using statistical methods, such as kinetic Monte Carlo (like was done in [1]) and is extensively described in Chap. 5. In such a simulation, damage events are picked from a list of events with rates of occurrence set based on MD simulations (or other criteria). However, this model breaks down when the defects start to overlap since displacing an atom next to a vacancy should be a different process from displacing an atom from a pristine crystal. Another approach is to simulate impacts on targets where damage has already been caused by previous impacts. This can be done by pre-generating such structures, or by running subsequent irradiation simulations on the same target. Unfortunately, because of the demand of large number of repeated simulations to obtain statistically significant results, these approaches are often not feasible.

3.3.4 A Brief Note on the Substrate

While the discussion so far has focused on free-standing 2D materials, in practical situations the 2D membranes may be laying on a substrate material. This can have a strong influence on the ion irradiation effects, as instead of escaping into the vacuum after the impact on the 2D material, the ions collide with the substrate.

In fact, due to the high transparency of 2D materials to energetic ions, the majority of the irradiation-induced effects will happen inside the substrate. This can lead to many effects which affect also the 2D material laying on top: thermal spikes in the substrate can lead to significant local sputtering of atoms and clusters with high enough energies to disrupt the thin membrane, atoms displaced from the 2D structure will be stopped by the substrate and reflected or migrate back and recombine with vacancies, and damaged areas of the membrane are likely to bind to the substrate. Therefore, in the case of ion irradiation of a 2D material on a substrate, the manipulated structure is formed by the interface between the two materials rather than any of the two by themselves.

Accordingly, experiments have confirmed a higher damage rate in supported versus suspended graphene due to sputtering from the substrate [26].

3.4 Results

In the following, simulation studies on ion irradiation of 2D materials, relevant to He and Ne ion microscopy are summarized. In general, graphene is by far the most studied 2D material, and this applies also in the context of this book. Thus, the summary is heavy on graphene, and other materials are visited when results are available.

3.4.1 Graphene

3.4.1.1 Free Standing Graphene

The effect of noble gas ion irradiation of graphene has been comprehensively explored in [1, 7, 27]. All these studies are based on MD simulations, and employ the AIREBO potential (see Sect. 3.3.2) for modeling the carbon-carbon interactions and the ZBL potential (see Sect. 3.2.1) for the ion-carbon interaction.

Figure 3.6 shows the relevant simulation parameters and defect classes into which the resulting structures are categorized. In addition to the ion species and energy, the polar angle θ can be controlled in a typical ion beam experiment. If the in-plane crystal orientation of the sample is known, also the azimuthal angle φ can be controlled. For an MD simulation, these angles can of course be freely set.

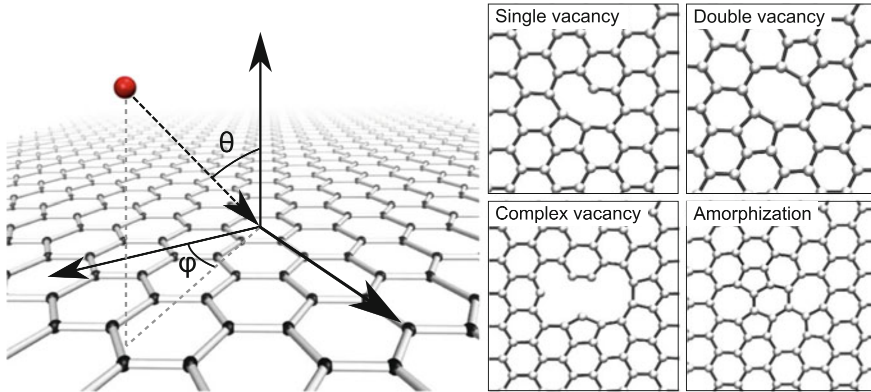

Fig. 3.6 The ion impact geometry on a 2D material, and classes of defects after ion impacts in graphene

Single vacancy is the simplest defect to occur in a material. In a graphene single vacancy, two of the three atoms which have lost a neighbor form a new bond (see Fig. 3.6). Such reconstructions occur frequently in graphene, as the total energy of the defect can be significantly lowered by saturating the dangling bonds [28]. A double vacancy has two missing atoms, and a complex vacancy three or more. Amorphization is defined as a defect where some atoms in the crystal are displaced from their lattice positions but no atoms are sputtered. An example of such a defect is the rotated bond in graphene (so-called Stone-Wales defect [29]), where four hexagons are turned into two pentagons and two heptagons. In principle, also defects with surplus atoms are possible [30], but this would require implanting more carbon into the target [31], which obviously is not possible/relevant in the case of He or Ne ion irradiation.

In practice, the classification of the produced defects has to be automated, as the number of individual simulation runs in a study can reach millions, rendering manual analysis of the cases impossible. The classification can rely on, for example, counting the number of nearest neighbours of each atom, counting the number of carbon rings with different sizes, and of course detecting atoms completely detached from the main target. No universal classification rules can easily be formulated, however, especially when going to more complicated structures, and the task needs to be carefully thought through with the goals of each project in mind.

The 'standard' impact geometry is at the normal direction of the sheet (i.e., $\theta = 0°$). Defect production probabilities in such geometry are shown in Fig. 3.7. The first thing to note is that the sputtering yields have single maxima near 100 eV ion energy, similar to what was shown for Xe earlier in Fig. 3.4, with the maximum position slightly towards higher energies with increasing ion mass.

Second, the sputtering yield is higher with Ne at all the energies as compared to He. This happens because of the higher momentum transfer from the heavier ion. With both He and Ne the sputtering yield remains below one atom per ion, which

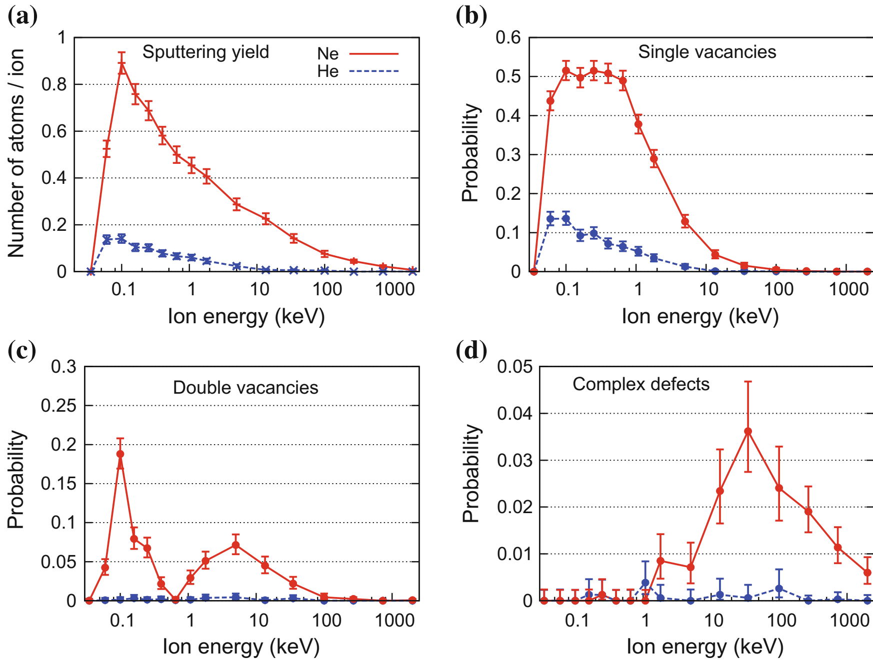

Fig. 3.7 Defect production probabilities in graphene under He and Ne ion irradiation in graphene. **a** Sputtering yields, as in number of removed atoms per ion impact. **b** Probabilities for producing single vacancies in graphene. **c** Probabilities for producing double vacancies. **d** Probabilities for producing complex defects in graphene. The confidence intervals are estimated by the standard error of the mean in a Poisson distribution for the sputtering yield, and as the Clopper-Pearson interval for the probabilities. Data reproduced from [7]

indicates that the binary collision model might remain valid in these cases (only one atom at a time is strongly interacted with). However, sputtering yield is a statistically obtained measure, and it can't be excluded that some cases with more than one sputtered atom per ion are included in the data.

Out of the different defect classes, single vacancies are the most prominent ones (notice the different y-scales in the panels). With He, the picture is quite clear: over the whole simulated energy range, single vacancies are produced almost exclusively, and the sputtering yield, and single vacancy curves are nearly identical. Thus, He ions provide quite a selective tool for modifying the atomic structure of graphene. The situation becomes more complicated only at higher ion energies ($>$10 keV) where complex defects start to appear.

While single vacancies are the most probable defect also with Ne, especially at sub 10 keV energies, double vacancies also appear at significant rates. Interestingly, the double vacancies show two maxima (at 100 eV and 5 keV), with the probability going to zero between them. These peaks can be attributed to two different creation processes: the lower energy case corresponds to the situation sketched in

Fig. 3.5, where the ion simultaneously displaces two target atoms. As is visible also in the sputtering yield plots, the displacement cross-section shrinks with increasing energy, and thus the overlapping area of neighbouring cross-sections also decreases, eventually bringing the probability of this process to zero.

The second peak is explained by a slightly more involved process. Here, the ion interacts strongly only with a single target atom, transferring enough momentum to displace it. However, as the ion moves fast at these energies (as compared to the target atoms), the momentum transfer is nearly symmetrical in the out-of-plane direction. Consequently the initially displaced atom gains momentum in the in-plane direction, having a chance to displace a second atom via a secondary collision.

This process explains also the appearance of the peak in the complex defect class at high energies (note that the complex defect class includes both the complex vacancy and amorphization classes described in Fig. 3.6). The in-plane momentum transfer can lead to a more extensive collision cascade, and the probability and 'violence' of such a cascade increases with increasing ion energy.

At this point it should be noted, that the appearance of the double vacancies and larger defects indicates that the binary collision model is not adequate any more in the case of Ne. However, for He it can still be expected to work correctly.

3.4.1.2 Irradiation at an Angle

The importance of the in-plane cascades occurring in the perpendicular direction to the ion trajectory suggests that the angle of incidence θ plays an important role in the damage production process. This insight is, indeed, verified by simulations run with varying θ [1]. Figure 3.8 shows the probabilities for producing the different types of defects with different angles of incidence. The red lines at $\theta = 0$ corre-

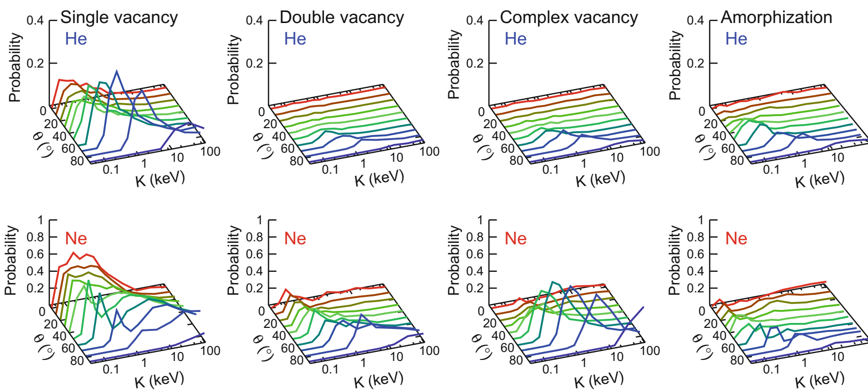

Fig. 3.8 Probabilities for producing different types of defects in graphene by ion impacts at varying angles of incidence. Each curve in the fence plots corresponds to a different polar angle of incidence. The values are averaged over the full range in the azimuth. Data reproduced from [1]

spond to the data in Fig. 3.7 (with the exception of showing the complex vacancy and amorphization classes separately).

One of the effects of tilting is the increased projected atomic density of the target, or in other words, decreased A_{atom} (see Fig. 3.3). With decreasing A_{atom}, the displacement cross-section in (3.4) correspondingly increases, which should lead to an increased damage production probability. This effect is visible in the simulation results of Fig. 3.8. In the case of He, the single vacancy probability increases considerably with increasing θ, and eventually also double vacancies and larger defects start appearing. With Ne the situation is somewhat more complicated, as the different defect classes 'compete' in the graphs. For example, the increasing double and complex vacancy maxima start making a dent in the single vacancy probabilities with increasing θ.

One important feature in the data of Fig. 3.8 is the increasing energy range at low energies where no defects are produced. This is visible as the 'plateau' at the high-θ/low-energy corner of the graphs. This is essentially a channeling effect, where the ion is reflected by a series of minor scattering events with a large number of carbon atoms. In such a process none of the carbon atoms acquire enough energy to be displaced, and the ion is simply redirected back into the vacuum. Such a process is described in more detail, e.g., in [32].

Direct collisions with multiple target atoms are the main process through which also larger defects are produced with high tilt angles, as the cross-sections of even more than two atoms can start overlapping. On the other hand, the circumstances for creating in-plane collision cascades are specific to the normal angle of incidence, and the probability of such events decreases with a tilted angle.

One shortcoming of the previously discussed results is that they only consider impacts on a pristine target, and the evolution of the material during prolonged irradiation is not accounted for.

3.4.1.3 Effect of Continuous Irradiation

To model the effect of earlier damage on the damage rates, MD simulations with previously damaged targets can be conducted. In [27] ion impacts on graphene with varying defect concentrations were simulated. The main finding was that graphene remains stable even at extreme vacancy concentrations of up to 35%, thanks to the ability of the carbon network to reorganize into an interconnected membrane even in the presence of vacancies. However, the increasing vacancy concentration affects the probability for sputtering. As a result, vacancy concentration as a function of dose becomes[1]

$$c_v(\phi) = \frac{1}{\frac{n}{\eta Y_0} + \gamma}, \tag{3.16}$$

[1] The formula has been established for low c_v and shows asymptotically wrong behaviour for $c_v \to 1$. It can therefore only be trusted for $c_v \ll 1$.

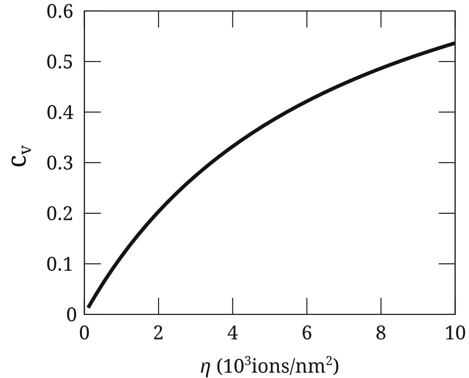

Fig. 3.9 Predicted vacancy concentration c_v in graphene under continuous He irradiation at 30 keV as a function of irradiation dose η assuming $Y_0 \approx 0.005$ and $\gamma = 1.1$

where η is the irradiation dose (ions/nm^2), $n \approx 38.2$ atoms/nm^2 the density of graphene, Y_0 sputtering yield at $c_v = 0$ and γ a constant which can be obtained through simulations [27]. Vacancy concentration is plotted in Fig. 3.9 with values of $Y_0 = 0.005$ and $\gamma = 1.1$, obtained for He irradiation of graphene at 30 keV through MD simulations [27]. Transmission electron microscopy studies have shown that $c_v \approx 10\%$ corresponds to amorphization of graphene [33]. According to Fig. 3.9, this would correspond to a dose of ca. 5×10^2 ions/nm^2 $= 5 \times 10^{16}$ ions/cm^2, whereas three times the amorphization dose should lead to cutting [34].

3.4.2 Experimental Results

Experimental studies on manipulating 2D materials using helium ion microscopy have been relatively rare until very recently. However, it was shown already in 2009 in an application note by Dan Pickard [35] that HIM can be used to carve features into suspended graphene membranes. The smallest demonstrated feature was a 5 nm wide graphene nanoribbon (GNR), but the cuts themselves were significantly larger. According to their results, this was effectively achieved with an irradiation dose of about 3×10^{18} ions/cm^2. This is an order of magnitude higher than what was estimated above, based on MD simulations, to be enough for drilling holes into graphene. One should note, however, that contamination, which is present in all graphene samples, can cause some discrepancy between the MD results and experiments. For example, in a recent graphene amorphization study utilizing a Ga^+ focused ion beam the vacancy concentration estimated via MD simulations (similar to above) was more than three times higher than that estimated experimentally [34]. Since 2009, many research groups have also written features on supported graphene using HIM [36–44], while much fewer studies have been published on suspended membranes [45, 46].

While the earlier works mainly demonstrated that He^+ irradiation can be used to write features into graphene, the more recent studies have also explored the effects of

the irradiation on the graphene structure and its properties, typically via Raman spectroscopy [26, 40–42, 44]. One recent study [47] embedded graphene into a hexagonal boron nitride sandwich structure to protect it from substrate-induced damage during irradiation. The authors concluded that such an arrangement enhanced the self-healing capability of graphene and facilitated its efficient nitrogen doping from the boron nitride encapsulation. A significant defect concentration was found, but its quantification was not possible due to hydrocarbon contamination. In [26], it was shown that for graphene on a substrate, an imaging dose of 10^{13} ions/cm^2 is safe as shown by unchanged Raman spectra, whereas clear damage is observable at 5×10^{14} ions/cm^2. Unfortunately, for a good signal to noise imaging a dose of 10^{17} ions/cm^2 is required. The authors also note that the damage is less for suspended graphene because of the lack of sputtering from substrate, which causes damage during irradiation in the case of supported samples.

At the moment, the only work in which the atomic structure has been directly imaged after He^+ irradiation was that of [48]. There, scanning transmission electron microscopy was used to study the atomic structure of defects created by He^+ irradiation at 30 keV and a 30° irradiation angle up to a dose of ca. 10^{16} ions/cm^2. The shown defect structures agree well with the estimate of [42] where Raman spectra was used to conclude that the typical defect size in graphene due to He^+ irradiation is 0.8 nm. Also the doses used in this study agree well with the estimates from MD simulations above, where a similar dose was estimated to lead to amorphization of graphene.

3.4.3 Other 2D Materials

3.4.3.1 2D Hexagonal Boron Nitride

2D hexagonal boron nitride (2D h-BN) is strikingly similar to graphene in terms of crystal structure, lattice constant and atom mass. However, the two different sublattices are occupied one by boron and the other by nitrogen atoms. To date, the only study on ion irradiation of h-BN that could be located is the MD study of [49]. The basic idea there was similar to the graphene MD studies presented above. As expected from the structural resemblance of h-BN to graphene, the results of the former follow closely what was observed with the latter (see Fig. 3.10). The main distinction is that two types of single vacancies are produced in the binary h-BN, as either B or N can be displaced. Similar to graphene, the He ions again produce almost exclusively single vacancies, while Ne irradiation results in a richer zoo of defects. The probability of an amorphization event is lower in h-BN. This is due to the binary nature of the material, and the low stability of B-B and N-N bonds when incorporated into the 2D network, which in turn prevents flexible reorganization of the atomic network typical for graphene.

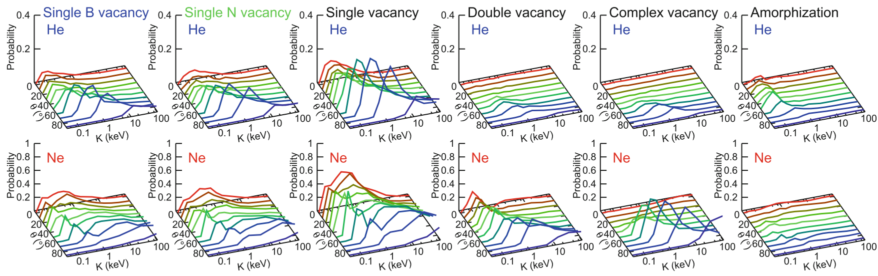

Fig. 3.10 Probabilities for producing different types of defects in 2D hexagonal boron nitride by ion impacts at varying angles of incidence. Each curve in the fence plots corresponds to a different polar angle of incidence. The values are averaged over the full range in the azimuth. Data reproduced from [49]

3.4.3.2 2D Transition Metal Dichalcogenides

2D TMDs have gained much popularity recently. These materials consist of a transition metal atom which is accompanied by two chalcogen atoms. The best known example of such materials is 2D MoS_2. Despite the popularity of these materials, no study exploring the influence of ion irradiation on them could be found. Here, a brief discussion on the requirements of such MD simulations will be given.

As with any MD work, the first issue is to decide on the interaction model. As listed in Sect. 3.3.2, at least two different potentials exist for MoS_2. Since analytical potential development is not a trivial task, these potentials should be used as a starting point. A useful sanity check before running ion impact simulations with this potential (or any new potential) would be to compare the displacement threshold energy against DFT calculations [6], which would indicate whether such dynamic processes are modeled accurately. TMDs which are isoelectronic with MoS_2 (e.g., $MoSe_2$) could be modeled to first approximation with the same interaction potential by simply changing the atom masses. However, special care should be taken when conducting sanity checks and detailed interpretation of the results.

The three dimensional structure within a single layer of a TMDs can be expected to play an important role in defect production under ion impacts. First of all, collision cascades are more easy to initiate, as the primary displacements do not need to happen strictly in the in-plane direction. Second, the angle of incidence will probably influence the defect production even more than in the case of graphene and h-BN: the normal angle of incidence is an easy channeling direction from the point of view of the chalcogen atoms (the bottom chalcogen sits right behind the top one), and once the angle of incidence is tilted, all of the atoms are exposed to the ions.

Classification of defects will be more complicated than in the relatively simple case of graphene. Vacancies should be separately identified for the metal atoms and the chalcogens in the top and bottom layers. Also interstitials can be produced as the displaced atoms could stop inside the layer. The recommendation here would be to limit the detail in which defects are classified, and focus on, e.g., sputtering yields

and the general extent of disorder as in total number of unoccupied lattice sites and interstitial atoms after the impacts. It is also a relatively easy task to calculate the extent of lost structural integrity, for example, by looking at the structure factor for each atom in the structure.

In any case, there is a wealth of research waiting to be carried out in this field.

3.5 Summary

In this chapter, the methodology and published results on the effects of He and Ne ion irradiation of 2D materials were reviewed with a theoretical perspective. Since direct observation of the dynamical atomic scale processes taking place during He/Ne ion microscopy is extremely challenging, simulation methods are currently the only feasible route for understanding and predicting the response of the target to ion bombardment.

To this end, a well-established theoretical framework for modeling the ion-matter interaction was presented. First, the simplest approximation, i.e., the binary collision model was described, after which the discussion was expanded towards more realistic methods, mainly concentrating on MD. The aim of the chapter is to be thorough enough to enable the reader to start conducting his own simulations, typically employing one of the many freely available simulation codes.

When reviewing the existing results, most of the discussion was focused on graphene. This due to the simple fact, that out of the class of 2D materials, graphene is, by far, the most studied one. It was shown that by tuning the experimental setup via selecting the ion species, the ion energy or the irradiation angle can all be separately used to gain detailed control over the dynamical processes that take place in graphene. Very similar behaviour of 2D h-BN to graphene was observed under ion irradiation, which is not that surprising, taking the similarity of the materials into account. As no simulation studies of ion irradiation 2D TMDs are available, the discussion was limited to how such simulations could be conducted, and what are the important considerations in such studies.

While the discussion was focused on free-standing 2D-materials, it was noted that a possible substrate plays a crucial role in ion irradiation of 2D materials by stopping atoms from sputtering from the 2D material, and also via leading to more damage due to sputtering of the substrate atoms. Unfortunately, due to space limitations, this topic was not explored in any detail in this chapter. However, the interested reader is directed to the following references, where combined simulation and experimental research has been carried out on irradiation of graphene on metal and SiO_2 substrates with (typically) heavier ions than He or Ne [32, 50–52].

To conclude, although HIM has until now been mostly used to simply etch features into graphene, this method holds great promise also for more delicate tailoring of the atomic structure of 2D materials, in similar way to what was presented in [34] with

Ga^+ irradiation. An important advantage of using light ions (He or Ne) is the fine control over the induced transformations and feature sizes and, indeed, by correct parametrization, He or Ne beams can be used to produce exclusively, e.g., single vacancies in a 2D material with good spatial resolution.

References

1. O. Lehtinen, J. Kotakoski, A. Krasheninnikov, J. Keinonen, Nanotechnology **22**(17), 175306 (2011)
2. J.F. Ziegler, J. Appl. Phys. **85**(3), 1249 (1999). doi:10.1063/1.369844. http://scitation.aip.org/content/aip/journal/jap/85/3/10.1063/1.369844
3. A. Zobelli, A. Gloter, C. Ewels, G. Seifert, C. Colliex, Phys. Rev. B **75**(24), 245402 (2007). doi:10.1103/PhysRevB.75.245402. http://link.aps.org/doi/10.1103/PhysRevB.75.245402
4. J.C. Meyer, F. Eder, S. Kurasch, V. Skakalova, J. Kotakoski, H.J. Park, A. Chuvilin, G. Benner, A.V. Krasheninnikov, U. Kaiser, S. Roth, S. Eyhusen, Phys. Rev. Lett. **108**(19), 196102 (2012). doi:10.1103/PhysRevLett.108.196102. http://link.aps.org/doi/10.1103/PhysRevLett.108.196102
5. J.C. Meyer, F. Eder, S. Kurasch, V. Skakalova, J. Kotakoski, H.J. Park, S. Roth, A. Chuvilin, S. Eyhusen, G. Benner, A.V. Krasheninnikov, U. Kaiser, Phys. Rev. Lett. **110**(23), 239902 (2013). doi:10.1103/PhysRevLett.110.239902. http://link.aps.org/doi/10.1103/PhysRevLett.110.239902
6. H.P. Komsa, J. Kotakoski, S. Kurasch, O. Lehtinen, U. Kaiser, A.V. Krasheninnikov, Phys. Rev. Lett. **109**(3), 035503 (2012)
7. O. Lehtinen, J. Kotakoski, A. Krasheninnikov, A. Tolvanen, K. Nordlund, J. Keinonen, Phys. Rev. B **81**(15), 153401 (2010)
8. B.J. Alder, T.E. Wainwright, J. Chem. Phys. **31**(2), 459 (1959). doi:10.1063/1.1730376. http://link.aip.org/link/JCPSA6/v31/i2/p459/s1ŹAgg=doi
9. B. Alder, T. Wainwright, J. Chem. Phys. **33**(5), 1439 (1960). http://link.aip.org/link/?JCPSA6/33/1439/1
10. D. Marx, J. Hutter, in *Modern Methods and Algorithms of Quantum Chemistry*, *NIC series*, vol. 1 (2000), *NIC series*, pp. 301–449. http://www.theochem.ruhr-uni-bochum.de/research/marx/marx.pdf
11. L. Pauling, J. Am. Chem. Soc. **69**(3), 542 (1947). doi:10.1021/ja01195a024. http://dx.doi.org/10.1021/ja01195a024
12. D. Brenner, O. Shenderova, J. Harrison, S. Stuart, B. Ni, S. Sinnott, J. Phys. Cond. Matt. **14**, 783 (2002). http://iopscience.iop.org/0953-8984/14/4/312
13. S.J. Stuart, A.B. Tutein, J.A. Harrison, J. Chem. Phys. **112**(14), 6472 (2000). doi:10.1063/1.481208. http://link.aip.org/link/JCPSA6/v112/i14/p6472/s1ŹAgg=doi
14. J. Tersoff, Phys. Rev. Lett. **61**, 2879 (1988). doi:10.1103/PhysRevLett.61. http://link.aps.org/doi/10.1103/PhysRevLett.61.2879
15. K. Chenoweth, A.C.T. van Duin, W.A. Goddard, J. Phys. Chem. A **112**(5), 1040 (2008). doi:10.1021/jp709896w. http://dx.doi.org/10.1021/jp709896w
16. K. Albe, W. Möller, Comput. Mater. Sci. **10**(1), 111 (1998)
17. T. Liang, S.R. Phillpot, S.B. Sinnott, Phys. Rev. B **79**, 245110 (2009). doi:10.1103/PhysRevB.79.245110. http://link.aps.org/doi/10.1103/PhysRevB.79.245110
18. J.W. Jiang, Nanotechnology **26**(31), 315706 (2015). doi:10.1088/0957-4484/26/31/315706. http://iopscience.iop.org/0957-4484/26/31/315706
19. T. Watanabe, H. Fujiwara, H. Noguchi, T. Hoshino, I. Ohdomari, Japan. J. Appl. Phys. **38**(4A), L366 (1999)
20. H.J. Berendsen, J.P.M. Postma, W.F. van Gunsteren, A. DiNola, J. Haak, J. Chem. Phys. **81**(8), 3684 (1984)

21. K. Nordlund, Comput. Mater. Sci. **3**(4), 448 (1995). doi:10.1016/0927-0256(94)00085-Q. http://www.sciencedirect.com/science/article/pii/092702569400085Q
22. LAMMPS Molecular Dynamics Simulator. http://lammps.sandia.gov/
23. ASE, Atomic Simulation Environment. https://wiki.fysik.dtu.dk/ase/
24. VASP, Vienna Ab Initio Simulation Package. https://www.vasp.at/
25. Quantum Espresso. http://www.quantum-espresso.org/
26. D. Fox, Y.B. Zhou, A. O'Neill, S. Kumar, J.J. Wang, J.N. Coleman, G.S. Duesberg, J.F. Donegan, H.Z. Zhang. Nanotechnology **24**(33), 335702 (2013). doi:10.1088/0957-4484/24/33/335702. http://iopscience.iop.org/0957-4484/24/33/335702
27. E. Åhlgren, J. Kotakoski, O. Lehtinen, A. Krasheninnikov, Appl. Phys. Lett. **100**(23), 233108 (2012)
28. B.R.K. Nanda, M. Sherafati, Z.S. Popović, S. Satpathy, New J. Phys. **14**(8), 083004 (2012). http://stacks.iop.org/1367-2630/14/i=8/a=083004
29. A. Stone, D. Wales, Chemical Physics Letters **128**(5–6), 501 (1986). http://dx.doi.org/10.1016/0009-2614(86)80661-3. http://www.sciencedirect.com/science/article/pii/0009261486806613
30. P.O. Lehtinen, A.S. Foster, A. Ayuela, A. Krasheninnikov, K. Nordlund, R.M. Nieminen, Phys. Rev. Lett. **91**, 017202 (2003). doi:10.1103/PhysRevLett.91.017202. http://link.aps.org/doi/10.1103/PhysRevLett.91.017202
31. O. Lehtinen, N. Vats, G. Algara-Siller, P. Knyrim, U. Kaiser, Nano Lett. **15**(1), 235 (2014)
32. S. Standop, O. Lehtinen, C. Herbig, G. Lewes-Malandrakis, F. Craes, J. Kotakoski, T. Michely, A.V. Krasheninnikov, C. Busse, Nano Lett. **13**(5), 1948 (2013)
33. F.R. Eder, J. Kotakoski, U. Kaiser, J.C. Meyer, Sci. Rep. **4**, 4060 (2014). doi:10.1038/srep04060. http://www.nature.com/srep/2014/140211/srep04060/full/srep04060.html
34. J. Kotakoski, C. Brand, Y. Lilach, O. Cheshnovsky, C. Mangler, M. Arndt, J.C. Meyer, Nano Lett. (2015). doi:10.1021/acs.nanolett.5b02063. http://dx.doi.org/10.1021/acs.nanolett.5b02063
35. D. Pickard, L. Scipioni, Zeiss application note (2009). http://wwwha.tcd.ie/Physics/ultramicroscopy/teaching/PY5019/HIM/AN_ORION_PLUS_Graphene.pdf
36. D.C. Bell, M.C. Lemme, L.a. Stern, J.R. Williams, C.M. Marcus. Nanotechnology **20**(45), 455301 (2009). doi:10.1088/0957-4484/20/45/455301. http://www.ncbi.nlm.nih.gov/pubmed/19822934
37. S.A. Boden, Z. Moktadir, D.M. Bagnall, H. Mizuta, H.N. Rutt, Microelectron. Eng. **88**(8), 2452 (2011). doi:10.1016/j.mee.2010.11.041. http://www.sciencedirect.com/science/article/pii/S0167931710004624
38. S. Nakaharai, T. Iijima, S. Ogawa, S. Suzuki, S. Li, K. Tsukagoshi, S. Sato, N. Yokoyama ACS Nano **7**, 5694 (2013). http://pubs.acs.org/doi/abs/10.1021/nn401992q?journalCode=ancac3ŹquickLinkVolume=7ŹquickLinkPage=5694ŹselectedTab=citationŹvolume=7
39. N. Kalhor, S.A. Boden, H. Mizuta, Microelectron. Eng. **114**, 70 (2014). doi:10.1016/j.mee.2013.09.018. http://www.sciencedirect.com/science/article/pii/S0167931713006229
40. A.N. Abbas, G. Liu, B. Liu, L. Zhang, H. Liu, D. Ohlberg, W. Wu, C. Zhou, ACS Nano **8**(2), 1538 (2014). doi:10.1021/nn405759v. http://dx.doi.org/10.1021/nn405759v
41. S. Hang, Z. Moktadir, H. Mizuta, Carbon **72**, 233 (2014). doi:10.1016/j.carbon.2014.01.071. http://www.sciencedirect.com/science/article/pii/S0008622314001298
42. B.S. Archanjo, B. Fragneaud, L.G. Cançado, D. Winston, F. Miao, C.A. Achete, G. Medeiros-Ribeiro, Appl. Phys. Lett. **104**(19), 193114 (2014). doi:10.1063/1.4878407. http://scitation.aip.org/content/aip/journal/apl/104/19/10.1063/1.4878407
43. Y. Naitou, T. Iijima, S. Ogawa, Appl. Phys. Lett. **106**(3), 033103 (2015). doi:10.1063/1.4906415. http://scitation.aip.org/content/aip/journal/apl/106/3/10.1063/1.4906415
44. E.N.D. Araujo, J.C. Brant, B.S. Archanjo, G. Medeiros-Ribeiro, F. Plentz, E.S. Alves, Phys. Rev. B **91**(24), 245414 (2015). doi:10.1103/PhysRevB.91.245414. http://link.aps.org/doi/10.1103/PhysRevB.91.245414
45. M.C. Lemme, D.C. Bell, J.R. Williams, L.a. Stern, B.W.H. Baugher, P. Jarillo-Herrero, C.M. Marcus. ACS nano **3**(9), 2674 (2009). doi:10.1021/nn900744z. http://www.ncbi.nlm.nih.gov/pubmed/19769403

46. M. Annamalai, S. Mathew, V. Viswanathan, C. Fang, D. Pickard, M. Palaniapan, in *Solid-State Sensors, Actuators and Microsystems Conference (TRANSDUCERS), 2011 16th International* (2011), pp. 2578–2581. doi:10.1109/TRANSDUCERS.2011.5969824
47. G. Nanda, S. Goswami, K. Watanabe, T. Taniguchi, P.F.A. Alkemade, Nano Lett. **15**(6), 4006 (2015). doi:10.1021/acs.nanolett.5b00939. http://dx.doi.org/10.1021/acs.nanolett.5b00939
48. C.T. Pan, J.A. Hinks, Q.M. Ramasse, G. Greaves, U. Bangert, S.E. Donnelly, S.J. Haigh, Sci. Rep. **4**, 6334 (2014). doi:10.1038/srep06334. http://www.nature.com/srep/2014/140911/srep06334/full/srep06334.html
49. O. Lehtinen, E. Dumur, J. Kotakoski, A. Krasheninnikov, K. Nordlund, J. Keinonen, Nucl. Instrum. Methods Phys. Res., Sect. A **269**(11), 1327 (2011)
50. E. Åhlgren, S. Hämäläinen, O. Lehtinen, P. Liljeroth, J. Kotakoski, Phys. Rev. B **88**(15), 155419 (2013)
51. C. Herbig, E.H. Åhlgren, W. Jolie, C. Busse, J. Kotakoski, A.V. Krasheninnikov, T. Michely, ACS Nano **8**, 12208 (2014). doi:10.1021/nn503874n. http://pubs.acs.org/doi/abs/10.1021/nn503874n
52. C. Herbig, E.H. Åhlgren, U.A. Schröder, A.J. Martínez-Galera, M.A. Arman, W. Jolie, C. Busse, J. Kotakoski, J. Knudsen, A.V. Krasheninnikov, T. Michely. ACS Nano **9**(5), 4664 (2015). doi:10.1021/acsnano.5b02303. http://dx.doi.org/10.1021/acsnano.5b02303

Chapter 4
Monte Carlo Simulations of Focused Ion Beam Induced Processing

Rajendra Timilsina and Philip D. Rack

Abstract Focused ion beam technologies have revolutionized the modern material research, development and production. It has offered new possibilities for materials modification and fabrication with a higher spatial resolution by using helium and neon ions. In recent years, various experimental and numerical simulation approaches have been developed and implemented to broaden the applications of focused ion beam technology. The Monte Carlo (MC) simulation approach is one of the useful techniques to study the ion-solid interactions which provides crucial quantitative information which cannot be achieved, in some cases, from the experiments. The MC approaches have a number of advantages over analytical calculations. It allows a more rigorous treatment of scattering events, energy distribution of incident ions, recoil target atoms or molecules and secondary electrons as well as their angular distributions. This chapter presents a brief introduction of a Monte Carlo simulator called EnvizION and some simulation results related to focused ion beam induced physical sputtering, Extreme Ultraviolet (EUV) mask repairs, and sputtering-limiting as well as resolution-limiting effects.

4.1 Introduction

Although focused ion beam processing was mainly focused on traditionally used Ga^+ liquid ion source in the past several decades, it has garnered much attention towards the higher resolution gas field ion sources such as He^+ and Ne^+ since the past decade.

R. Timilsina (✉)
Department of Mechanical, Aerospace and Biomedical Engineering,
The University of Tennessee Knoxville, 1512 Middle Drive, Knoxville 37996, USA
e-mail: rtimilsi@utk.edu

P.D. Rack
Department of Materials Science and Engineering, The University of Tennessee
Knoxville, 1508 Middle Dr, Knoxville 37996, USA
e-mail: prack@utk.edu

P.D. Rack
Oak Ridge National Laboratory, Center for Nanophase Materials Sciences,
Oak Ridge 37831, USA

© Springer International Publishing Switzerland 2016
G. Hlawacek and A. Gölzhäuser (eds.), *Helium Ion Microscopy*,
NanoScience and Technology, DOI 10.1007/978-3-319-41990-9_4

Several experimental and simulation efforts have been devoted in the area of focused ion beam induced processing such as precursor gas assisted deposition, etching and sputtering by using helium and neon ions. The advantage of simulation process is not only improvements in the fundamental understanding of the relevant ion-solid interactions but they also provide a predictive power for further advancement. The most popular ion-solid interaction simulator to date is SRIM/TRIM, a Monte Carlo simulator, developed by Ziegler et al. [1, 2]. While the simulator has several advantages for a myriad of applications, it is lagging in providing the understanding of the nanoscale evolution related to ion beam nano-machining because it does not capture the substrate evolution during the sputtering process. The other simulators such as SDTrimSP [3], MCSIM [4] and Geant4 [5] are mainly used to calculate ion trajectories and energy loss for energetic ion solid interactions. These simulators include recoil algorithms, and thus can determine the energy-dependent sputtered yield information for flat surfaces, but do not evolve with the topography changes associated with the sputtering. However, other programs such as AMADEUS [6], IONSHAPER [7] and FIBSIM [8] have been used to calculate the evolution of the surface. Most of these methods combine ion angular and spatial distribution data from Monte Carlo ion-solid simulations and evolve surface topography in a continuum or cellular manner. For example, the IONSHAPER simulator [7] needs input information such as angular distribution and sputtered yields of sputtered atoms and backscattered ions for the subsequent topography modeling. Nellen et al. [9] used SRIM/TRIM [1, 2] and Geant4 [5] ion-solid Monte Carlo data to study linear trench and prototyping of silicon milling with focused ion beams (Ga ions). In their approach they input the Monte Carlo sputter yields and sputtered ion and backscatter ion distributions as well as experimental re-deposition information into the IONSHAPER software [7]. The IONSHAPER software mimics the natural erosion process by a surface velocity vector normal to a discrete surface where the surface shape is a fully continuous derivative. Additionally, Kunder et al. [10] studied the structural changes in sputtering in a similar way by integrating the Monte Carlo ion implantation program (MCSIM) into a three-dimensional topography simulator called ANETCH [10]. Furthermore, Moller developed a computer program called "TRI3DYN" that allows the simulation of the evolution of the shape and the composition of three dimensional nano-structures [11].

Recently, Timilsina et al. [12, 13] have developed a three dimensional Monte Carlo simulator of focused ion beam induced sputtering, called the EnvizION simulator. Although it has a wide range of capabilities to simulate nanoscale deposition [14] and etching, the physical sputtering mechanism is focused in this context. The main goal of their approach is to develop a program that directly simulates the topography evolution due to sputtering in the Monte Carlo environment. In this way it can be directly studied in a wide range of ions and target combinations without prior knowledge about the sputtered yields. The only tuning parameter per se in the simulator is the surface binding energy of the target material. As a starting point the authors have simply used the heat of sublimation for each material, which perhaps fortuitously has yielded very good agreement with the energy-dependent sputter yields. The simulator is capable of tracking sputtered and re-deposited species, illustrat-

ing the evolution of etched nanostructures and sputtered structures, and the evolving energy loss distribution and implantation distributions which are very important in understanding the sub-surface damage [15] for a wide range of ion species. Initially, the authors were missing the angle dependent information of sputtered atoms [14] which essentially contributes and even limits the sputter process for high aspect ratio applications, finally they have implemented it in the EnvizION simulator [12] and comparisons to experiments prove excellent agreement. Furthermore, the authors are devoted to add collision cascade models and capture the information of interstitial atoms as well. It should be noted that the utility of this simulator is ideal for nanoscale focused ion beam induced processing because tractable numbers of ions can reveal important information for experiments. Larger scale simulations become problematic for large numbers of ions and thus the other approaches described above are more appropriate for microscale applications.

In this chapter, a brief introduction of how the fundamental concepts of ion-solid interactions are implemented in EnvizION simulator is presented. Furthermore, some simulation results related to physical sputtering of aluminum, tungsten and copper targets by bombarding neon ions at different energy scales, and a very short discussion of extreme ultraviolet (EUV) mask repair and resolution limiting effects are presented.

4.2 An Example of Monte Carlo Simulation: EnvizION Simulator

The initial development of EnvizION simulator was started by Smith et al. [16] to study focused helium ion beam induced deposition. The simulator was developed by integrating trajectory calculation routines and electron and nuclear energy loss routines from SRIM/TRIM simulator [1, 2], secondary electron routines from IONiSE simulator [17] and precursor gas handling routines from EBID (electron beam induced deposition) simulator [18, 19]. The authors studied nanoscale deposition of PtC_5 target using precursor gas and helium ions beam [16]. Then, it was realized that simulation of heavy ions such as neon is very important to study the nanoscale deposition and to understand the results from experimental Neon Gas Field Ion Source (GFIS). Timilsina et al. [14, 20] developed the necessary routines for the heavy ions, implemented them and performed a study of neon ion beam induced deposition of PtC_5. Furthermore, the simulator has the capabilities of simulating not only single elemental materials (Cu, Al, W etc.) but also the compound target materials such as SiO_2 and a stack of different materials. Over the course of time, Timilsina et al. [12, 13] also developed the simulator with several capabilities such as physical sputtering, gas assisted etching, energy loss and implant concentration calculations, secondary electron and recoil atom re-entries in vias etc. Likewise in other simulation programs the EnvizION simulator has following assumptions.

1. The target material is amorphous.
2. The interaction of an energetic ion and a target material is based on a binary collision approximation.
3. Initially one of the two colliding particles is at rest.
4. The target material is discretized based on three dimensional voxels derived from the density of the material.
5. The scattering step length of ions, recoil atoms and secondary electrons are adjusted by subtracting the corresponding empty space along their paths.
6. Instead of considering a collision cascade the recoil atom has a single trajectory at each scattering step and the atom moves until it is sputtered or it has energy greater than a cutoff energy.
7. The ion cutoff energy is considered as 250eV—50eV depending on the simulation where the recoil atom cutoff energy is equivalent to a heat of sublimation energy of the target material.

Let's take an example of how a scattering step is calculated in EnvizION simulator as shown in Fig. 4.1. While an ion strikes at position 1 as shown in Fig. 4.1a, its initial location (x, y, z) co-ordinates, initial energy and angle of incidence are provided. After having scattered the ion reaches at position 2. The position 2 is determined by calculating a scattering angle (θ) and an azimuthal angle (ψ), and their calculations are described later. Similarly, the ion reaches at position 3 in the next scattering step. The energy loss while approaching the ion from location 1 to location 2, is used to generate the recoil trajectory as shown in Fig. 4.1b. The scattering and azimuthal angles (θ_1 and ψ_1 respectively) are calculated as same as the ion.

After occurring several scattering events the ion follows a random trajectory as shown in Fig. 4.2a. In each scattering step, several quantities (initial x, y and z co-ordinates, final x,y and z co-ordinates, scattering and azimuthal angles, initial and final energies of the ion, scattering length, etc.) should be calculated. Furthermore, recoil atom trajectories in each scattering step as well as secondary electron trajectories as shown in Fig. 4.2b, c respectively need to be calculated. It is to be noted that the secondary electron trajectories are generated along the step length based on

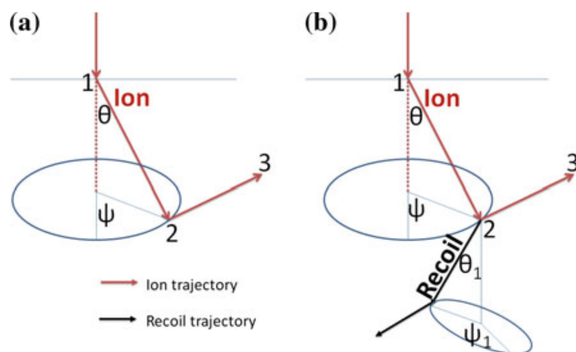

Fig. 4.1 Schematic diagrams of **a** ion and **b** ion and recoil trajectories

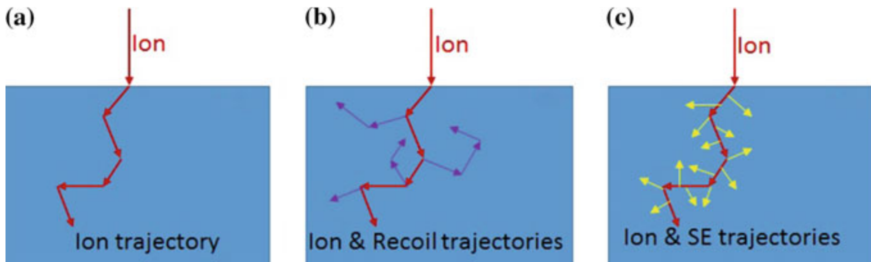

Fig. 4.2 Schematic diagrams of **a** ion trajectory, **b** ion and recoil trajectories, and **c** ion and secondary electron trajectories

secondary electron yields whereas the recoil atom trajectories are generated at the end of each step length. To provide a complete picture of the simulator, some of the important routines are described in the following subsections.

4.2.1 Material Database

The database consists of materials properties of energetic ions and target materials. The properties include atomic number, density, mass, fermi energy, work function, proton stopping coefficient, etc. and they are taken from various experimental and theoretical calculations.

4.2.2 Ion Beam Profile

Focused ion beam technology requires the higher image resolution and increased machining precision for comprehensive analysis. Tuning of ion beam profile overcomes the limitations of older techniques such as edge resolution analysis and ion beam spot burns. For this purpose, the EnvizION simulator has a capability to include jitter in pure Gaussian, cylindrical, or conical distributions of the incident beam. It can superimpose multiple Gaussian beams and add beam tails on it. It has also a capability of scanning the target materials in a spot and raster modes in one and two dimensions. Also, the beam profile has a feasibility of varying geometries to generate the beam distributions of interest.

4.2.3 Nuclear Energy Loss

When an energetic ion strikes a solid, it undergoes a series of collisions with target atoms and electrons. Depending on the energy, mass, density and atomic number

of both incident ion and target material the incident particle loses its energy during these collisions as shown in Fig. 4.2. The energy loss and trajectories of ions, secondary electrons and recoil atoms follow the random process. As a result, Monte Carlo approaches are one of the best methods to understand the mechanism of ion solid interaction. The energy loss rate, $\frac{dE}{dx}$, can be understood separately as (a) nuclear energy loss and (b) electronic energy loss. In a nuclear energy loss, the energy of an incident ion is transmitted as translatory motion to a target atom as a whole and the moving ion excites or ejects atomic electrons in electronic collisions. One of the approximations is to calculate electronic and nuclear energy loss separately and superimpose them as below [21, 22].

$$\left(\frac{dE}{dx}\right)_{total} = \left(\frac{dE}{dx}\right)_{Nu.} + \left(\frac{dE}{dx}\right)_{Elec.} \tag{4.1}$$

Most simulators use this approximation to calculate the energy loss during the collisions and the EnvizION simulator also does the same. The nuclear energy loss can be calculated as

$$\left(\frac{dE}{dx}\right)_{Nu.} = \frac{4M_1M_2}{(M_1+M_2)^2} sin^2\left(\frac{\theta}{2}\right)E. \tag{4.2}$$

where M_1 is mass of an incident ion, M_2 is mass of the target atom, θ is a scattering angle and E is the energy of the ion respectively. The scattering angle can be calculated in two ways based on the ZBL (Ziegler, Biersack, and Littmark) reduced energy (ε) [23].

$$\varepsilon = \frac{32.53M_2E}{Z_1Z_2(M_1+M_2)(Z_1^{0.23}+Z_2^{0.23})} \tag{4.3}$$

If the reduced energy, $\varepsilon \geq 10$ the Rutheford scattering formula is used as follow.

$$sin^2\left(\frac{\theta}{2}\right) = \frac{1}{1+(1+b(1+b))(2\varepsilon b)^2} \tag{4.4}$$

where b is an impact parameter. If $\varepsilon < 10$, the magic formula of scattering is used. The impact parameter calculations and Magic formula for scattering can be found elsewhere in literature [1, 2, 21, 22].

4.2.3.1 Nuclear Stopping Power and Cross-Section

Nuclear stopping power is an average nuclear energy lost by a moving ion due to elastic collisions per unit length travelled in the target [21]. Figure 4.3 depicts the nuclear, electronic and total stopping power of helium ion. In 1985, Ziegler, Biersack, and Littmark (ZBL) developed an expression for the nuclear stopping cross-section as follow [22]

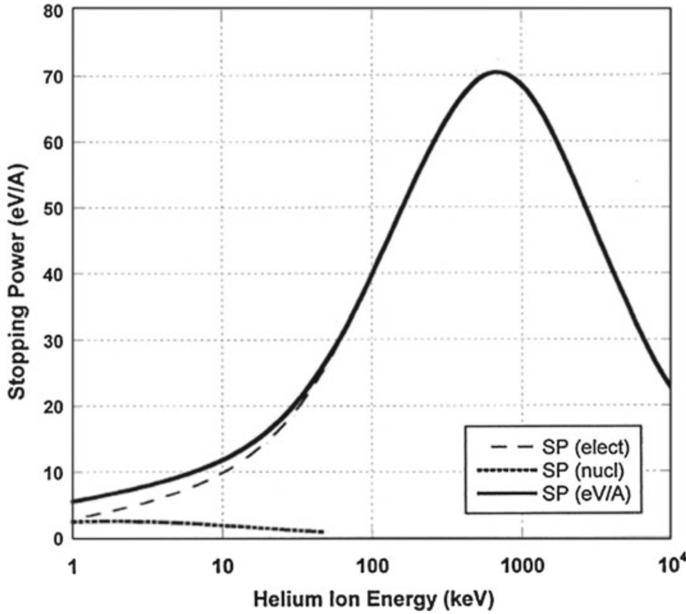

Fig. 4.3 Stopping power of helium ions. This figure is taken from [24] with permission

$$S_n(\varepsilon) = \frac{0.5ln(1 + 1.1383\varepsilon)}{(\varepsilon + 0.01321\varepsilon^{0.21226} + 0.19593\varepsilon^{0.5})} \tag{4.5}$$

for $\varepsilon \leq 30$, otherwise,

$$S_n(\varepsilon) = \frac{ln(\varepsilon)}{2\varepsilon} \tag{4.6}$$

where ε, the reduced energy, is calculated in 4.3. For practical calculations, the ZBL universal nuclear stopping power for an ion with energy E_o is [22, 23] calculated as follow.

$$S_n(E_o) = \frac{8.462 \times 10^{-15} Z_1 Z_2 M_1 S_n(\varepsilon)}{(M_1 + M_2)(Z_1^{0.23} + Z_2^{0.23})}(eVcm^2)atom^{-1} \tag{4.7}$$

4.2.4 Electronic Energy Loss and Stopping Cross-Section

The energy transferred by the ion to the target electrons during the collision mostly depends on the ion velocity and on the charges of the ion and target atoms. The electronic energy loss for high energies are given by Nastasi et al. [21] as

$$-\left(\frac{dE}{dx}\right)_{Elec.} = \frac{2\pi Z_1^2 e^4}{E} N Z_2 \left(\frac{M_1}{m_e}\right) ln \frac{2 m_e v^2}{I} \tag{4.8}$$

where I is an average excitation energy in electron-volts, Z_1 and Z_2 are atomic numbers of ion and target atoms, M_1 and m_e are masses of ion and electron respectively, e is the electronic charge and v is the velocity of the ion. For the low energy, the electronic energy loss can be approximated from Linhard and Scharff [21]. For the practical calculation purposes, the Linhard-Scharff stopping cross-section [22] can be written as

$$S_e(E) = 3.83 \frac{Z_1^{7/6} Z_2}{(Z_1^{2/3} + Z_2^{2/3})^{3/2}} \left(\frac{E}{M_1}\right)^{1/2} = K_L E^{1/2} \tag{4.9}$$

where

$$K_L = 3.83 \frac{Z_1^{7/6} Z_2}{(Z_1^{2/3} + Z_2^{2/3})^{3/2}} \tag{4.10}$$

and $S_e(E)$ is in the units of 10^{-15} eV cm^2 for the ion of energy E in keV and M_1 in atomic mass unit. After multiplying the electronic stopping power by atomic density the electronic energy loss can be calculated.

4.2.5 Ion and Recoil Trajectories

In order to calculate the ion trajectories, the simulator needs initial x,y and z-positions of an ion, an incident energy and an angle of incidence. Then, after having a collision it takes a random path to the next step which depends on the angle of incidence, a scattering angle calculated by either from the Rutherford scattering or from the magic formula scattering, an azimuthal angle ($2\pi RAND$) where $RAND$ is a random number [0–1], a step length calculated from stopping powers and an energy dependent mean free path of the ion for a given target material.

Timilsina et al. [14] presented helium and neon ion trajectories of ten thousands ions at 25 keV on PtC_5 target as shown in Fig. 4.4. The color code in the figures represent the energy associated with the step lengths. The ion trajectories terminated if they have either the lower energy than the cutoff energy (250 eV in this case) or they are back scattered from the surface. These trajectories demonstrate that the neon has a very small interaction region as compared to helium in the same target material. It shows that the neon ion is suitable for sputtering purpose rather than the helium.

While calculating the recoil trajectories, the simulator takes the nuclear energy loss as its starting point and a new direction of a recoil is calculated based on the direction cosines of the preceding step length of the ion. The scattering and azimuthal angles for the next step are calculated likewise in the ion trajectories and they proceed unless they are either backscattered or they have the energy less than the heat of sublimation of the target material. In Fig. 4.5, ten neon ion and associated recoil

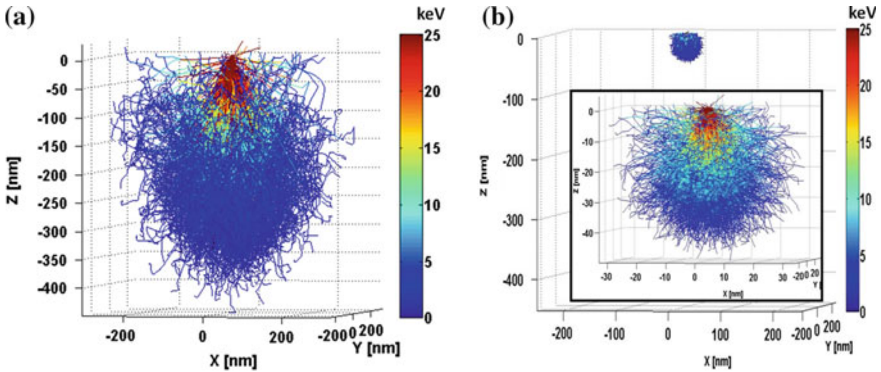

Fig. 4.4 Simulated ten thousands ion trajectories in PtC_5 target at 25 keV. The inner plot is a zoomed version of the outer plot on the *right*. The figure is taken from [14] with permission

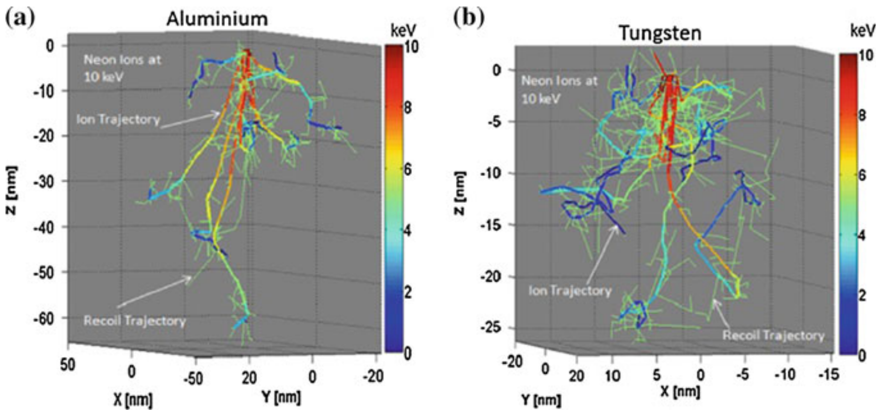

Fig. 4.5 Simulated ten neon ion (*bold*) and associated recoil atom trajectories at **a** aluminum and **b** tungsten targets respectively. The incident beam energy was 10 keV in both cases. The figure is taken from [12] with permission

trajectories are presented for (a) aluminum and (b) tungsten respectively [12]. It is to be noted that the total nuclear energy loss at the particular step is used to generate a single recoil trajectory rather than divided to form a collision cascade. Although a conservation of the nuclear energy loss is implemented while generating the single recoil trajectory, it is to be further investigated. However, the simulator will include collision cascade models of recoil atoms and the authors will study the difference between these two approaches in the near future.

4.2.6 Secondary Electrons

Smith et al. [16] developed a secondary electron generation model in EnvizION simulator after modifying the approach developed by Ramachandran et al. [17]. First

of all, likewise the ions the secondary electrons are treated as a binary collision approximation events where the electronic and nuclear stopping powers are separately handled. The authors used Bethe's stopping power equation to approximate the number of secondary electron generation at each scattering step. To be consistent with IONiSE simulation developed by Ramachandran et al. [17], the electronic energy loss component of the ion is used to generate the secondary electrons. The number of secondary electrons in each scattering step can be approximated from the following expression [16],

$$N_{SE} = -\left(\frac{1}{\varepsilon}\right)\left(\frac{dE}{ds}\right)_{Elec.} \tag{4.11}$$

where ε is the energy required to generate a secondary electron. It is a tunable parameter and it is determined based on the experimental secondary electron yields of the target materials. The authors use inelastic mean free paths of secondary electrons as described in [25] and the energy of secondary electrons according to Kotera et al. [26].

4.2.7 Precursor Gas Handling

The precursor gas handing is one of the important features of the EnvizION simulator. The target material is discretized in several voxels based on its density. Smith et al. [16, 19] developed the necessary routines for a gas handing process while studying the electron beam induced deposition (EBID) and it is well documented in References [16, 18, 19]. However, an important piece of information in the context of ion beam induced deposition is provided here. When an energetic ion or a secondary electron completes its trajectory, the simulator checks for gas desorption and then adsorption of new gas molecules from the precursor flux. Based on the ion and electron dissociation cross-sections the simulator decides whether the gas molecule does deposit or etch on the material surface. Furthermore, the following equation determines a number of gas molecules/atoms deposited in the surface [19].

$$N_{gas} = \Gamma_{gas} N_{sites} \Delta x^2 t \tag{4.12}$$

where N_{gas} is a number of gas atoms deposited, Γ_{gas} is the gas flux (calculated from kinetic theory of gas and pressure), N_{sites} is a number of available gas surface sites on the structure, Δx is the linear dimension of voxel and t is the time between electrons or ions based on the beam current. The simulator updates the position of each gas molecules by a three dimensional surface diffusion algorithm after running the gas adsorption and desorption algorithms. Furthermore, the simulator tracks and updates of the possible adsorption sites after the deposition or etching events and the gas molecules move along the vacant sites by a random walk motion approach. It is to be noted that the motion of a gas is restricted to empty sites only so that no two

gas molecules can occupy the same empty site. Finally, the surface diffusion coefficient, the time for a gas molecule to move and the discrete pixel separation distance determine the number of gas jumps [19].

4.2.8 Deposition and Etching

When an ion or a secondary electron approaches to a gas site in a surface then based on a dissociation cross-section probability of a precursor gas it is decided whether the gas is deposited on the surface or it is etched from the surface. Obtaining an appropriate dissociation cross-section of ions and electrons is one of the challenging tasks for many materials to date. However, Van Dorp et al. [27] have provided some measurements for $(CH3)_3Pt(CpCH_3)$ precursor on amorphous carbon. The electron-beam induced dissociation cross-section as a function of energy and ion beam cross-section of helium ions [28] are presented in Fig. 4.6. It is to be noted that the ion beam dissociation cross-section was obtained by scaling the electron beam cross-section [29] via the ratio of the electronic stopping power of $Pt_{20}C_{80}$ substrate as mentioned in Reference [28]. The EnvizION simulator uses the same electron and ion dissociation cross-section approach as described by Chen et al. [28] (shown in Fig. 4.6). The histograms in the figure are the secondary electron energy spectrum generated from 10×10^3 helium ions on a flat $Pt_{20}C_{80}$ substrate. Recently, a comparison of helium and neon ion deposition was conducted by Timilsina et al. [12] by using EnvizION

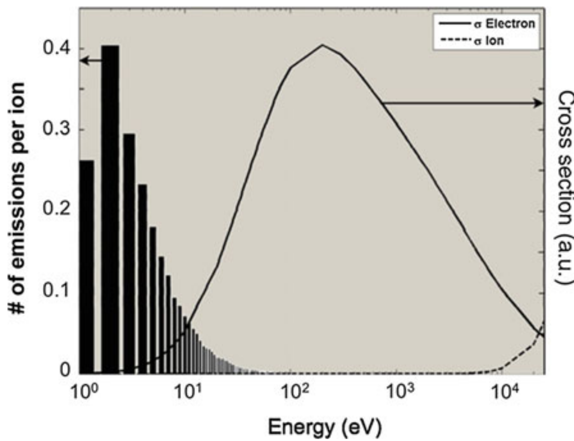

Fig. 4.6 Electron-and ion-induced dissociation cross sections of $(CH_3)_3Pt(C_PCH_3)$. The electron data are a fit to the data in [27]. The ion data are derived from the latter by scaling via the stopping power at the same velocity. The histogram is the simulated secondary electron energy distribution, adjusted to a secondary electron coefficient of 2.9 for a flat $Pt_{20}C_{80}$ substrate of [29]. The figure is taken from [28] with permission

simulator on PtC_5 target material. In their studies the neon deposited nanopillars are narrower as compared to the helium nanopillars. However, more studies are expected in future because the gas-field neon ion sources are available in these days.

4.2.9 Sputtering Algorithms

While developing the sputtering algorithms a number of quantities such as the nuclear energy transferred to a recoil atom, surface binding energy of a target material, sputtering probability and a direction of a recoil path is to be considered. These quantities are very sensitive for the sputtering process. Furthermore, sputtered species have the lower energies as compared to the incident ions and it is to be addressed while calculating the stopping powers and mean free paths of ions and recoil atoms at low energy (especially below 40 eV). SRIM/TRIM [2] is one of the widely used simulators to study the sputtering process in a Monte Carlo fashion. However, it has limitations to study the sputtered structure evolution which is already mentioned in this chapter.

The EnvizION simulator [13] consists of recoil atoms generation and sputtering routines that can capture different sputtering species such as sputtered atoms, re-deposited atoms and the empty voxels left behind after the re-deposition. When a via evolves, the ion and recoil atoms re-enter in the via surface. These re-entries require an adjustment of their paths by subtracting the travelled path in the empty regions (no material region). The concepts of re-entry of ion and recoil trajectories in a via and different sputtering species such as sputtered and re-deposited atoms, and the empty voxels left behind after being re-deposited are presented in Fig. 4.7. When an ion strikes at the surface of the via as shown in Fig. 4.7a it travels in the target material and re-enters in the via and causes a sputtering (the voxel 3). In the similar fashion, a recoil atom re-enters in a via and re-deposited in a side wall (voxel 5) by leaving an empty voxel (voxel 4). These can be further understood by conducting an actual simulation (see Fig. 4.7b, c). The figures consist of two simulated vias and two representative ion trajectories bombarded at different locations. The red and blue lines represent an ion and a recoil atom trajectories. In addition, the red, blue and green spheres represent sputtered, re-deposited and empty voxels in those plots. The following expression is used to calculate the probability of sputtering.

$$P = Ae^{(-d/\lambda)} \tag{4.13}$$

where P is the probability of an atom to be sputtered, A is a constant which is determined based on 2π or 4π space (in this case A =1, because the sputtering is considered at 4π space), d is the step length travelled by the ion or recoil in a particular step length and λ is the mean free path of an ion or a recoil atom depending on the species. The mean free path of the ion or recoil is derived from the stopping cross-section and the density of the materials and it is an energy dependent quantity rather than a constant value. It is to be noted that to generate a recoil atom trajectory the

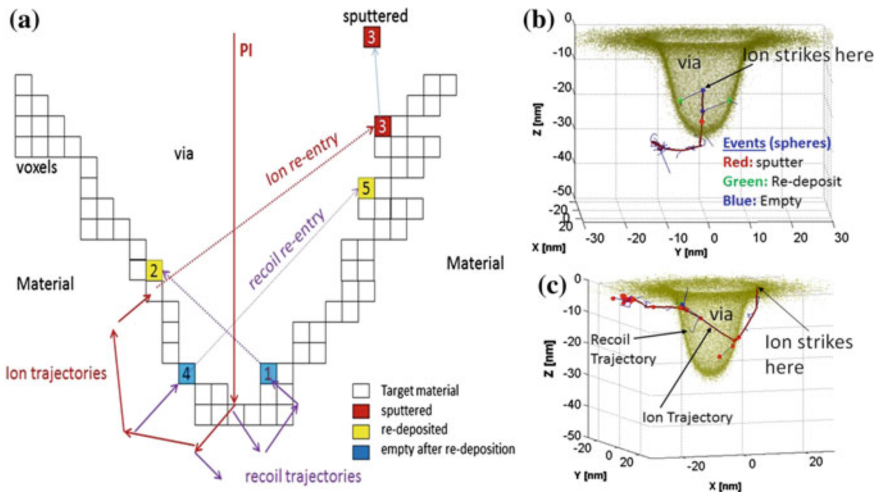

Fig. 4.7 **a** A schematic diagram of ion and recoil trajectories and their re-entries in the via. **b** and **c** The simulated ion (*red*) and recoil (*blue*) trajectories, and sputtered species (sputtered-*red* spheres, re-deposited-*green* spheres and the empty voxel *left behind after* a re-deposition occurs in the next location—*blue* spheres)

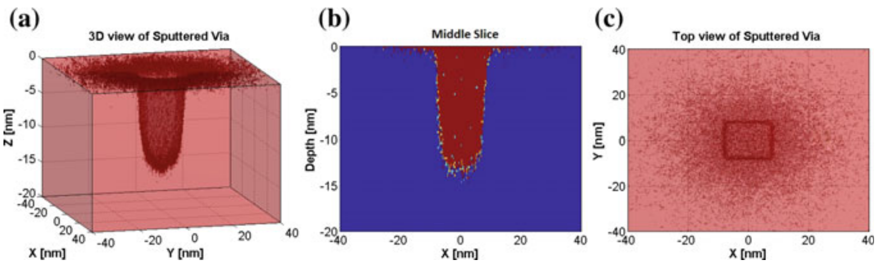

Fig. 4.8 Simulated sputtered structures of Cu target by bombarding Neon ions at 20 keV. **a** Three dimensional structure of a via **b** the *middle* slice of the via and **c** the *top view* of the via. The scan area of the the neon beam was 15 nm × 15 nm. The *red*, *yellow*, *cyan* and blue voxels in the middle slice figure (**b**) are sputtered, re-deposited, empty voxels after the re-deposition and unsputtered target material voxels respectively

nuclear energy loss should be greater than the threshold energy (an energy required to remove the atom from the surface, it is ∼25 eV (for Cu)). If a recoil atom has energy greater than the surface binding energy and a random number [0–1] is less than the sputtering probability then the atom is supposed to be sputtered. However, if the atom does not satisfy the condition of sputtering probability but it has an energy greater than the surface binding energy and there is an empty voxel along the step length in its path then the recoil atom is supposed to be re-deposited by leaving an empty voxel in its origin.

In order to study the structure (via) evolution during the sputtering process, 300,000 neon ions are simulated by using EnvizION simulator [13] on copper target at 20 keV. The Gaussian beam of 1 nm full-width-at-half-maxima is used to raster scan the material at $15 \times 15\ \mathrm{nm}^2$ area with pixel spacing of 1 nm in both x and y-directions. Figure 4.8 presents (a) a full three dimensional structure of a via, (b) the middle slice of the via and (c) the top view of the via surface. A detailed of the sputtering process are discussed in the following sections.

4.3 Monte Carlo Simulations of Physical Sputtering

After conducting several experimental and theoretical studies over the years it is realized that many materials cannot be removed by chemically assisted processes alone. Therefore, extensive studies of physical sputtering are needed to understand the structural evolutions during the sputtering process. It is a statistical process caused by surface erosion on an atomic scale while transferring kinetic energy from incident ion to target atoms. One of the measures of the physical sputtering process is a calculation of sputtered yield, which is defined as the number of ejected species per incident ion. The sputtered yield depends on several factors such as energy and incident angles of energetic ions as well as densities and surface binding energies of target materials etc. Furthermore, it is very sensitive with the shape and size of the via during the sputtered structure evolution process. Another important aspect is re-deposition of sputtered atoms in the side wall of the via that controls the sputtering especially at high aspect ratio. Sigmund [30] provided the following analytical equation to calculate the sputtered yield of the materials. Matsunami et al. [31] and Yamamura et al. [32] also studied the sputtering yields by updating the Sigmund equation for small Z_t materials.

$$Y = \frac{3.56}{U} \frac{Z_t Z_p}{(Z_t^{2/3} + Z_p^{2/3})^{1/2}} \frac{M_p}{M_t + M_p} \alpha(M_t/M_p) S_n(E/E_{tp}) \tag{4.14}$$

where U is a surface binding energy, Z_t and Z_p are atomic numbers of a target and a projectile, M_p and M_t are masses of a target and a projectile, α is a function of (M_t/M_p) and angle of incidence of the ions, and $S_n(E/E_{tp})$ is a universal function of a nuclear stopping cross-section. The constant E_{tp} is given by the following equation [21].

$$E_{tp} = 0.0308(1 + M_p/M_t) Z_t Z_p (Z_t^{2/3} + Z_p^{2/3})^{1/2} (KeV) \tag{4.15}$$

Although the above mentioned expression is one of the best ways to calculate the sputtered yield of the material in ideal conditions it is rather a complex process to obtained the correct sputtered yields in a real situation. For example, during the sputtered structure evolution the target materials have amorphous structures in the vicin-

ity of the vias that will decrease the density of target material as a result the sputtered yield decreases. Similarly at high aspect ratio via (deeper via) the re-deposition controls the sputtered yields significantly. Therefore, more simulation efforts are needed to address these types of issues.

The EnvizION simulator [12, 13] has attempted to address these issues in some extend, however, it still requires to adjust a density of a material in the amorphous regions which are damaged by the ion bombardments. It has both options to calculate the sputtered yield in a flat surface condition (without etching) and a real surface condition (with etching). The sputtered yields calculated with out considering the etching process can be compared with the analytical expression given by Sigmund [21] as well as with the sputtered yields obtained from SRIM/TRIM simulator [2]. However, the sputtered yields of the materials with a consideration of an etching process are always less than the sputtered yields at flat surfaces and they are highly dependent on a width and a depth (or aspect ratio) of vias.

A sputtering process can be understood from a flow chart of EnvizION simulator [12, 13] as shown in Fig. 4.9. The simulation of the sputtering process proceeds as follows. First, the target material is divided into voxels, where each voxel contains one target atom (or molecule) based on the atomic volume (atomic weight/density) [16]. An incident ion with a prescribed energy impinges on the target material at a position governed by the given beam shape (in this case a radially symmetric Gaussian beam). The nuclear and electronic stopping powers and ion trajectories are

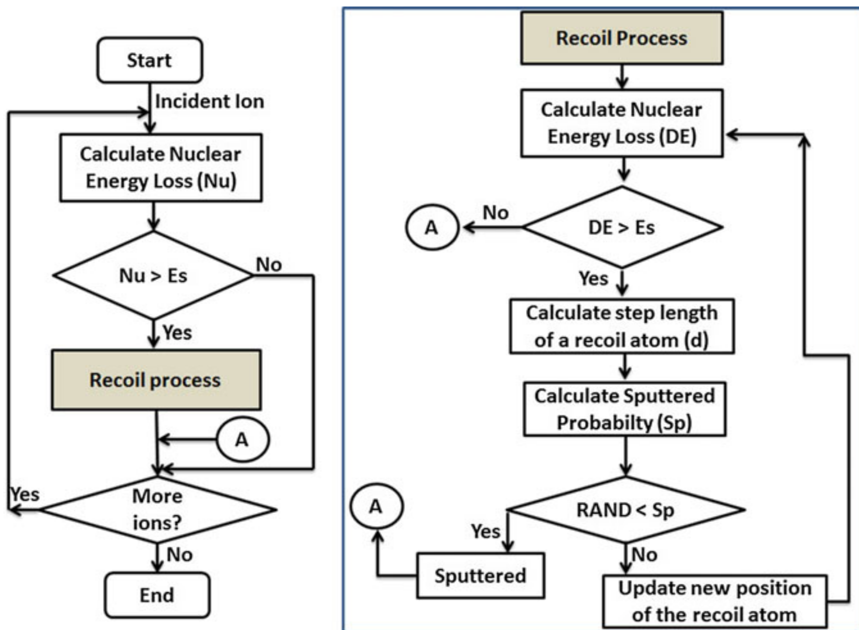

Fig. 4.9 A flow chart of a Monte Carlo program for sputtering. The figure is taken from [12] with permission

estimated based on algorithms similar to the SRIM/TRIM simulation, but extended to three dimensions. If the nuclear energy loss (E_{Nu}) for a scattering event is greater than the surface binding energy (here taken as the heat of sublimation, Es, ~8.68 eV for tungsten and ~3.36 eV for aluminum) [33], then the recoil process routine is executed. In that routine, the nuclear energy loss between two recoil atoms after a collision is calculated. The recoil trajectory is determined and the projected path length to the surface is calculated (d). If the path length includes empty voxels (from previously sputtered atoms) the path length is reduced appropriately.

Then the sputtered probability is calculated by using the expression $e^{-(d-\Delta d)/\lambda}$ where λ is the mean free path of the recoil atom and Δd is the adjusted path length for empty voxels [12, 13]. Finally, if the recoil atom has a sputtering probability less than a random number chosen between 0 and 1, then the atom is removed from the lattice. The recoil process occurs until a atom/molecule is sputtered or it has energy less than the surface binding energy (Es). To simulate re-deposition in the resultant nanostructured vias, atoms that fail the sputter test with a path length extended all the way to the top surface, but passing through the via, are re-tested with the path length to the via interface. If this test is passed, then the atom is transferred from its original position and re-deposited on the surface of the via. Thus, as the via evolves and the aspect ratio increases, we can track both sputtered atoms and re-deposited atoms and determine how many sputtering events are necessary to remove atoms from the vias as a function of their origin [12].

Let's take a simple example as shown in Fig. 4.10 where the black spheres are target atoms and white spheres are empty spaces after the sputtering occurred. In Fig. 4.10a, an ion strikes at the topmost layer of the target material and it follows a random path (red trajectory). Four atoms are ejected during the process as shown in Fig. 4.10b. The next ion strikes at the second layer of the target material and take another random path as shown in Fig. 4.10c. At this time, it ejects five more atoms from the target as shown in Fig. 4.10d. Now the sputtered yields become 4.5 while bombarding two ions. The sputtering occurs in this fashion and after a few number of ions strikes the structure looks like Fig. 4.10e.

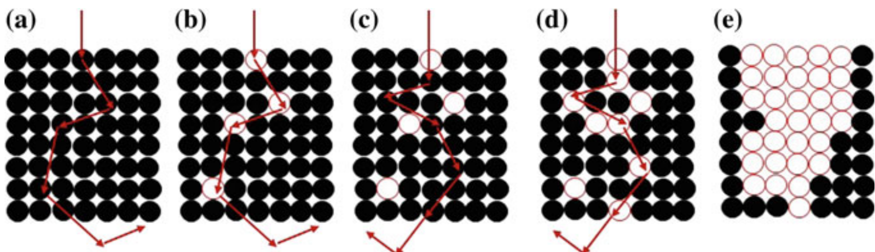

Fig. 4.10 Schematic diagrams of the first eight layers of a target material. **a** An ion (*red solid line*) strikes at the first layer of the target material and propagates in it. **b** The ion sputtered four atoms while travelling in the material. **c** An another ion strikes at the second layer of the material and it does propagate. **d** The ion sputters five more atoms from its scattering steps. **e** The sputtered (*red spheres*) and unsputtered (*black spheres*) after striking a few number of ions

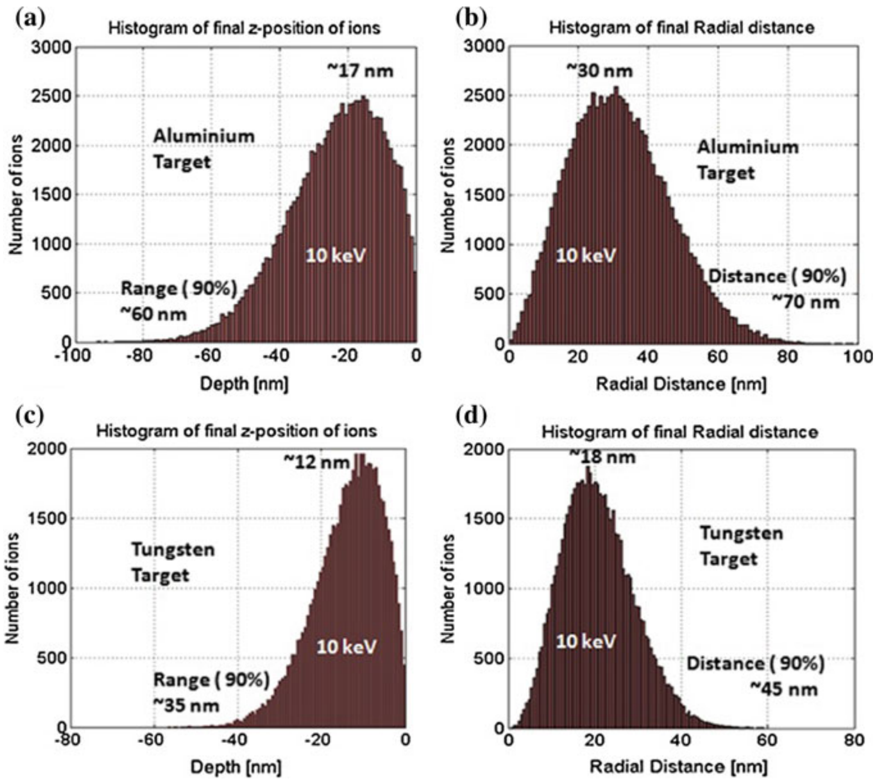

Fig. 4.11 Histograms of final z-positions and the corresponding radial positions of ten thousands terminated neon ions for aluminum (**a** and **b**) and for tungsten (**c** and **d**) respectively. The etching process is ignored for the comparison purpose with SRIM/TRIM. The figure was taken from [12] with permission

4.3.1 Sputtering of Aluminum and Tungsten

Timilsina et al. [12] conducted a study of focused ion beam induced sputtering of aluminum and tungsten by using neon ion beams. The aim of their study was to investigate implant ion distribution, sputtered yield calculation, evolution of nanostructured vias, and temporal behavior of sputtered and re-deposited events with respect to number of incident ions. Figure 4.11 depicts histograms of final z-positions and corresponding radial positions for 100,000 neon ions impinging on aluminum and tungsten at 10 keV beam energy, in this case they ignored the etching process to compare their results with SRIM/TRIM simulator. The maximum peaks of the histograms ((a) and (c)) lie at ∼17 nm for aluminum and ∼12 nm for tungsten. These results are consistent with SRIM/TRIM results [2], in which the maximum peaks lie at ∼21 nm and ∼10 nm for aluminum and tungsten targets respectively. In addition, the 90% range (90% of terminated ions lie within it) is also estimated for both alu-

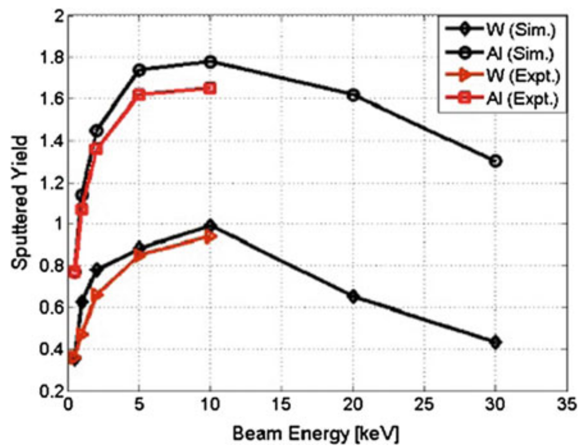

Fig. 4.12 Simulated and experimental sputtered yields of aluminum and tungsten at different beam energies and a constant beam diameter of 20 nm Gaussian. The figure was taken from [12] with permission

minum (~60 nm) and tungsten (~35 nm) materials. Furthermore, the histograms of radial distances (where the ions terminated) are presented in Fig. 4.11b, d for aluminum and tungsten, respectively [12]. The maximum peaks and the distances are also presented in the plots. These observations show that aluminum has maximum peaks and 90% ranges at greater depths than tungsten because of the lower density of aluminum and its smaller nuclear stopping power.

Authors also simulated sputter yields of neon ions for aluminum and tungsten as a function of beam energy [12] compared with the experimental data (National Physical Laboratory database [34]). As shown in Fig. 4.12, the simulation accurately reproduces both the sputter yield magnitudes and the energy dependence. The energy dependence of both materials can be understood by the energy dependence of the nuclear versus electronic stopping power. For instance, at high energy, the nuclear stopping power decreases, thus less nuclear energy loss near the surface occurs, which is responsible for the sputtering of the target material [33]. Finally, if one compares the sputter yield of aluminum to tungsten, both show similar energy functionality, with aluminum having a higher sputter yield over all energies. The increase in the aluminum sputter yield is dominated by the lower heat of sublimation and overcomes the fact that tungsten has a higher energy loss density because of its higher density and atomic number.

Figure 4.13 illustrates the resultant sputtered nanostructures of aluminum (top) and tungsten (bottom) by 100,000 neon ions at various beam energies (0.5, 1, 2, 5, 10, 20 and 30 keV) with a constant beam diameter of 1 nm (full-width-at-half-maximum (FWHM) Gaussian beam). The different colored voxels represent atoms that are sputtered (red), re-deposited (yellow), sputtered but re-deposited (cyan) and original target material (blue). In Fig. 4.13, the horizontal and vertical lines represent the FWHM and maximum depth, respectively. The simulated nanostructures reveal that, in both materials, with increasing beam energy the depth and aspect ratio increases. The absolute full-width-at-half-maxima of the structures increases

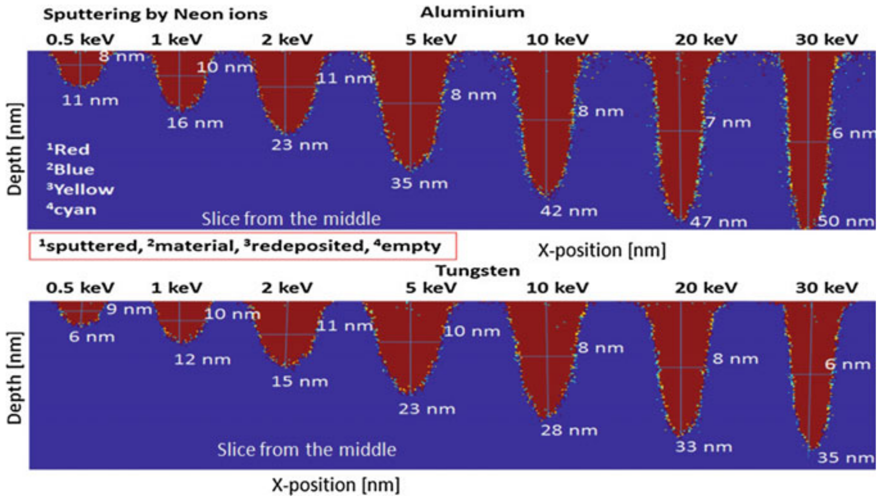

Fig. 4.13 Neon ions simulated nanostructures with different beam energies at a beam diameter of 1 nm. The nanostructures of aluminum and tungsten are presented in the *top* and *bottom* panels respectively. The horizontal and vertical lines represent the FWHM and the maximum depths of the structures respectively. The figure was taken from [12] with permission

to a maximum at 2 keV and then decreases up to 30 keV (~6 nm). The nanostructure depths are larger for aluminum at all beam energies as compared to tungsten because aluminum has a comparatively higher sputter yield relative to tungsten [12].

The sputtering mechanism can be further understood by studying the temporal behavior (demonstrated as a function of the number of ions) of the via depth and aspect ratio versus the number of incident ions [12], as demonstrated in Fig. 4.14 for aluminum (a) and tungsten (b). The plots consist of depth profiles (left y-axes) at 1, 5, 10 and 20 keV, with the aspect ratio in the secondary (right) axes. Both plots of Fig. 4.14 demonstrate that with an increasing number of ions the depth of nanostructures increases; however, the growth rate (slope of the depth versus number of ions) decreases and this decrease scales with the aspect ratio. In both materials, the aspect ratio increases faster initially, then increases gradually with an increasing number of ions.

While the aspect ratio for aluminum is higher at the end of each 100,000 ion simulation, it is an artifact that the aluminum sputter yield is higher and thus the sputter depth is higher [12]. For comparable depths, however, tungsten has a comparable or slightly higher aspect ratio, which is attributed to the shorter ion range. The temporal behavior of the number of sputtered and re-deposited atoms with respect to the number of incident ions at the beam energy of 10 keV is shown in Fig. 4.15. The figure consists of the incremental number of sputtered and re-deposited atoms sampled every 10,000 ions up to 100,000 ions for aluminum (left) and tungsten (right). As shown, the number of sputtered atoms per 10000 ions decreases and the re-deposited atoms increases with the number of ions (increasing depth and aspect

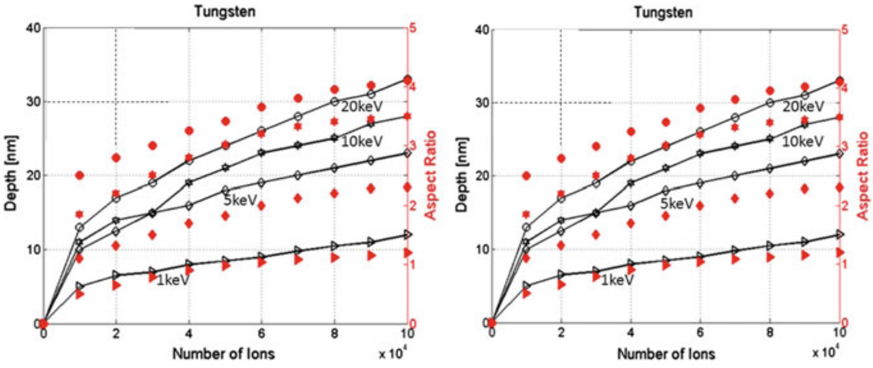

Fig. 4.14 Temporal behavior of the depth profiles with respect to the number of incident ions for aluminum (*left*) and tungsten (*right*). Aspect ratios (AR) are presented on the secondary axes (*red*) in both the plots. The figure was taken from [12] with permission

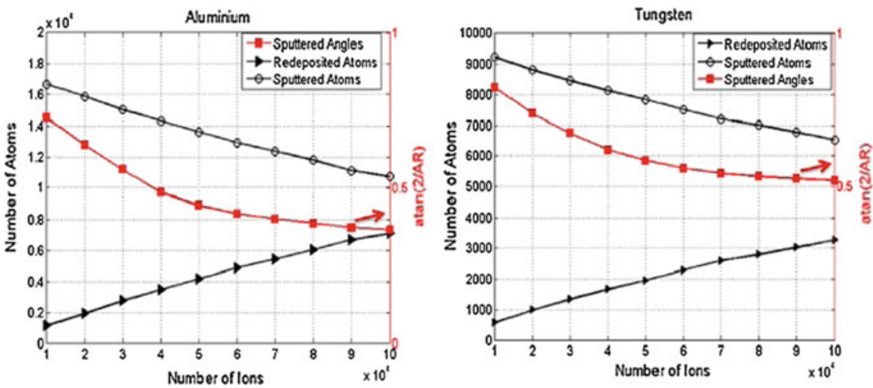

Fig. 4.15 Temporal behavior of sputtered and re-deposited events versus the number of incident ions for aluminum (*left*) and tungsten (*right*) at a beam energy of 10 keV. Both plots consist of tan⁻ (2/aspect ratio) in the secondary axes. The symbol AR represents the aspect ratio in the plots. The figure was taken from [12] with permission

ratio). Thus, as the via develops, the sputtering process is retarded because the beam interaction region is pushed farther from the solid; thus decreasing the escape possibility of the recoiled target atoms [12]. Thus, for sputtering to proceed, directly sputtered species are limited by the open angle of the via and a multi-event sputtering from re-deposited species. This trend can be understood by the fact that the open angle for directly sputtered material decreases with increasing aspect ratio. Furthermore, Fig. 4.15 estimates the sputtered angle, tan^{-1} (2/aspect ratio), on the secondary (right) axis which is the angle of the allowable directly sputtered path [12]. As shown, the functionality of the sputtered angle correlates reasonably with the decrease in the sputtered atoms.

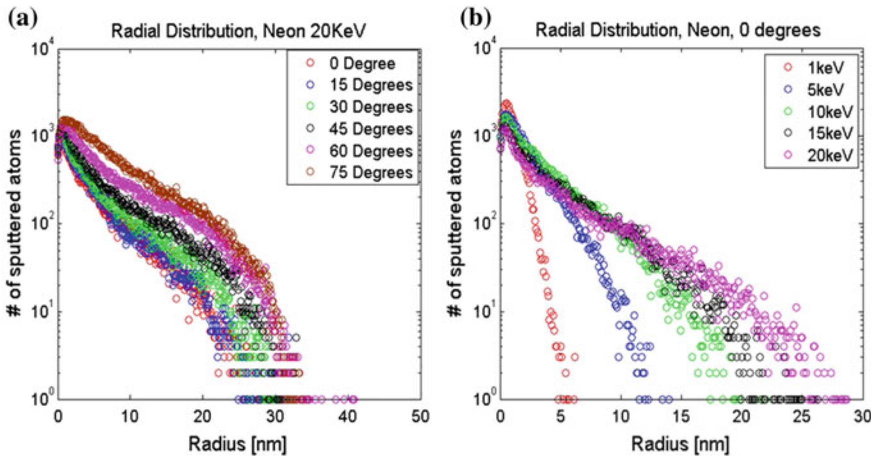

Fig. 4.16 Radial distribution of sputtered Cu atoms **a** 20 keV beam energy at different incident angles and **b** normal incidence with different beam energies

4.3.2 Sputtering of Copper

Tan et al. [35] performed a preliminary study of nanomachining with a focused neon beam by using copper and silicon dioxide target. To understand further their experimental results and to provide more information related to neon ion beam interactions with copper, Timilsina et al. [13] conducted a simulation study by using EnvizION simulator. First of all, the authors calculated the distribution of sputtered atoms without considering an etching process and using a point source. It enabled them to compare their results with SRIM/TRIM [2] in which a structure evolution during the sputtering was ignored. Figure 4.16 depicts radial distributions of sputtered Cu atoms at 20keV neon with different angles of incidence and normal incidence with different neon beam energies respectively. The radial distances in the figures were calculated along the target surface. These radial distributions of the sputtered atoms can be also correlated with the energy dependent and angle dependent sputtered yields as shown in Fig. 4.17.

The angle dependent sputtered yield gradually increases with increase in angle of incidence and it starts to decrease at approximately 80 degree as shown in Fig. 4.17a. Similarly, the energy dependent sputtered yields follow the similar trend as SRIM/TRIM simulator as shown in Fig. 4.17b.

However, with a consideration of the etching in target materials, the sputtered yield becomes limited due to the nature of nanostructure evolution such as aspect ratio of via and re-deposition of atom in the side wall of the via. For this purpose, the authors [13] simulated the neon beam in three different doses (a) $1.5 \times 10^{18} Ne^{+}/cm^{2}$ (b) $3.0 \times 10^{18} Ne^{+}/cm^{2}$ and (c) $6.0 \times 10^{18} Ne^{+}/cm^{2}$. Figure 4.18a demonstrates the temporal evolutions of sputtered (red), re-deposited (blue) and the sum of the sputtered and re-deposited species (black) of copper during the process. The number

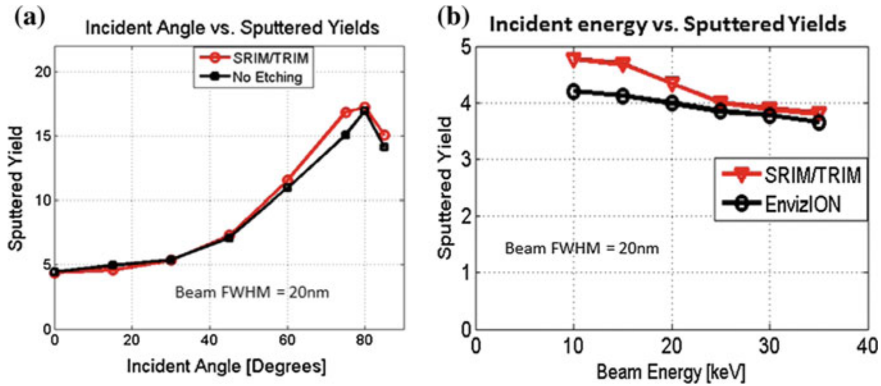

Fig. 4.17 **a** Angle dependent sputtered yields at 20 keV neon beam energy, and **b** energy dependent sputtered yields at normal incidents

of sputtered atoms decreases and the re-deposited atoms increases with increasing aspect ratio of the etching via. This observation is correlated to the effective escape angle of the sputtered species. The sputtered versus re-deposited fraction depends on the trajectory of the copper atom. The open-angle varies approximately as 2 $\times \tan^{-1}[(W/2)/d]$ where W represents the top of the via width and d is the depth [13]. The sputter yield does scale different than the simple open-angle function due to the typical cosine distribution of sputtered species in which the angular distribution of sputtered species is a maximum normal to the substrate. In order to further understand the re-deposited process the via depths are calculated after every one million ions run and the number of re-deposited atoms versus the corresponding depths are presented in Fig. 4.18b. These observation clearly show that the re-deposition events are increasing with increasing depths of the via. Clearly, the rate of re-deposition starts to increase dramatically at ∼150 nm and begins to saturate at the ∼250 nm depth where the re-deposited yield approaches the sputter yield with only a small fraction of the atoms being removed [13].

To understand the nanostructure evolution the sputtered vias are presented in Fig. 4.19. The figure demonstrates the middle slices at three different doses as mentioned above. The simulated via depths at the three doses are ∼152 nm (a), ∼205 nm (b) and ∼272 nm (c), respectively. The corresponding via widths at FWHM are ∼24 nm (a),∼27 nm (b) and ∼35 nm (c), respectively. The summation of the 15 $\times$ 15 1 nm FWHM beam profiles to the sputter cross-sections (white dotted Gaussian beam) are also included in the figure. These observations are in reasonable agreement with the experimental study conducted by Tan et al. [35].

Energy loss, surface damage and implant concentrations are another set of information that play very important role to understand the ion solid interactions. In order to investigate the cumulative nuclear energy loss and implant concentrations, Timilsina et al. [13] conducted a study. In their study, 3.0×10^5 neon ions were simulated using the sputtering algorithm at primary beam energies of 9, 12, 20, 25 and 34 keV

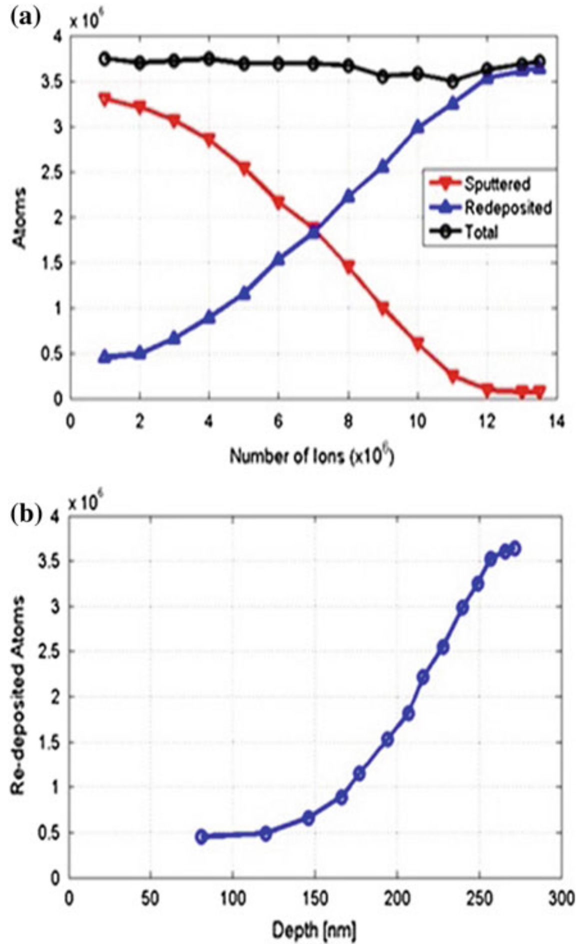

Fig. 4.18 **a** Temporal behavior of sputtered, re-deposited and the sum or total of copper atoms that are displaced as a function of the cumulative number of Ne ions (each data point is sampled every one million ions). **b** Number of re-deposited atoms sampled at every one million ions versus the corresponding via depths. These plots are taken from [13] with permission

on copper substrate in the 15 nm × 15 nm raster scanned area. In these simulations the nuclear, and electronic energy loss, and the implanted ion positions (which are the ion locations when the ion energy drops below the cutoff energy of 250 eV), are stored for each scattering event.

A collage of simulation results for the 20 keV simulation compared to an experimental image of the 20 keV damage profile [13] are illustrated in Fig. 4.20. A TEM micrograph Fig. 4.20a of the bottom of a copper film etched by a neon beam at $1.6 \times 10^{18} Ne^{+}/cm^{2}$ dose shows a noticeable damage region ~49 nm beneath the etched nanostructure. The sub-surface radiation damage is characterized by a high concentration of nano bubbles that are associated with copper vacancy coalescence which likely act as a sink for the implanted neon. Figure 4.20b demonstrates the simulated central sputtered etch slice that illustrates an etch depth of ~13 nm (and a FWHM of ~16 nm). Figure 4.20c is a plot of the radially averaged nuclear energy

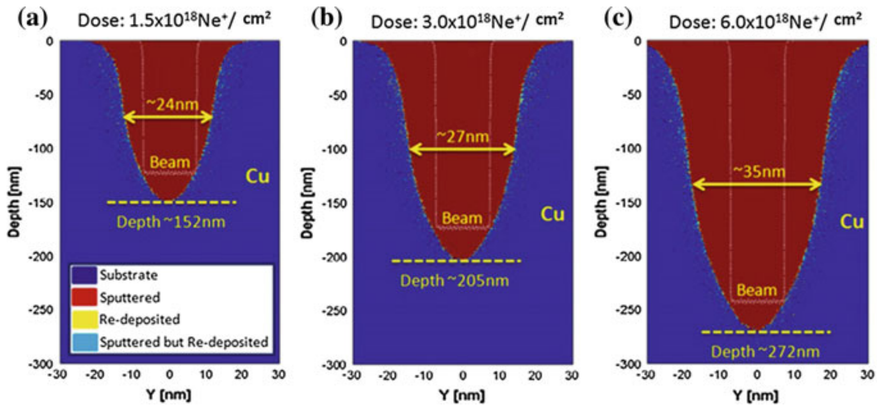

Fig. 4.19 Simulated via structures of Cu at the doses of **a** $1.5 \times 10^{18}\mathrm{Ne}^{+}/\mathrm{cm}^{2}$ **b** $3.0 \times 10^{18}\mathrm{Ne}^{+}/\mathrm{cm}^{2}$ and **c** $6.0 \times 10^{18}\mathrm{Ne}^{+}/\mathrm{cm}^{2}$ and the beam energy of 20 keV. The color code: *blue* (substrate), *red* (sputtered), *yellow* (re-deposited) and *cyan* (sputtered but re-deposited) depict different species. The dotted curves inside the vias represent the summation of 15 × 15 Gaussian beams (of 1 nm FWHM) in each plot. The figure was taken from [13] with permission

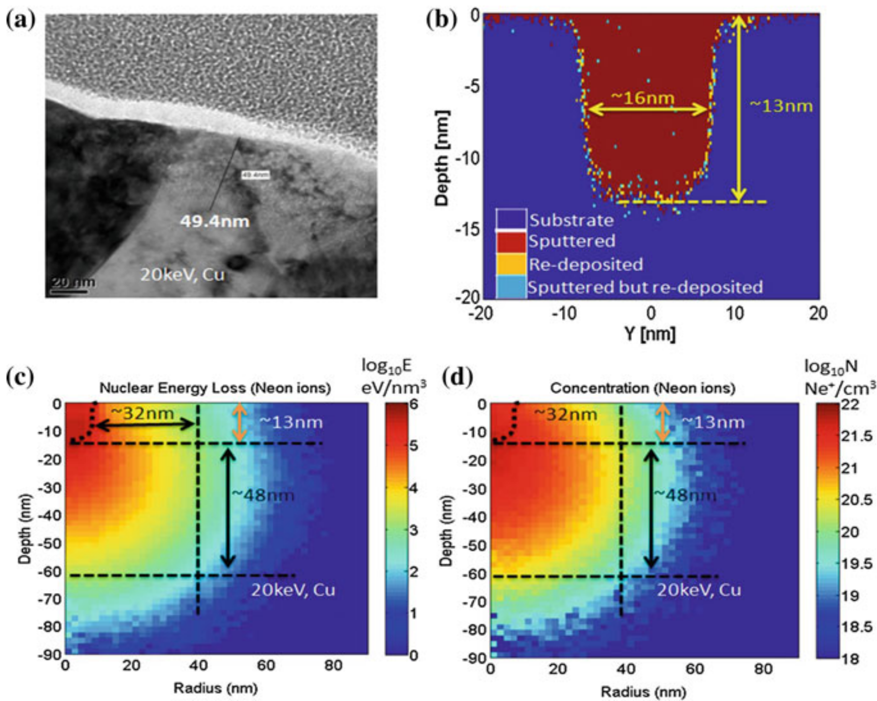

Fig. 4.20 **a** TEM micrograph, **b** middle slice of the via, **c** nuclear energy density, **d** implant neon concentration for 20 keV beam energy on copper. The *dotted black curves* represents the sputtered area of copper in figures (**c**) and (**d**) respectively. The affected area in TEM micrograph (**a**) is also highlighted. The figure was taken from [13] with permission

loss density as a function of position for the 20 keV simulation, where the color scale represents the logarithm of the nuclear energy loss per volume (eV nm^{-3}). Finally, Fig. 4.20d illustrates the logarithm of the radially averaged implant concentration as a function of position [13]. The etched material in Fig. 4.20c, d are denoted by the black dotted curves. To correlate the observed damage profile observed in the TEM micrograph (~49 nm), we note the simulated nuclear energy loss and implant concentration at the experimentally observed damage profile at ~49 nm below the bottom of the simulated etched via is ~1 keV nm^{-3} and $\sim 4 \times 10^{20}$ $Ne^{+}cm^{-3}$, respectively [13]. Note that the implant concentration scale less than or equal to 10^{18} $Ne^{+}cm^{-3}$ is given by the same color (dark blue).

4.4 EUV Mask Repair

Extreme Ultraviolet (EUV) lithography is a next generation lithographic technique of miniaturization in the nanoelectronics industries. However, it requires reflective masks which consist of multilayer dielectric mirror of two different materials with alternating refractive indices. Molybdenum-silicon multilayer system is one of the choices due to its ability to act as a mirror in 13.5 nm wavelength region which has a reflectivity of approximately 70% [36]. Tantalum nitride (TaN) is the most commonly used and studied absorber layer. However, it spontaneously etches during the exposure of XeF_2 while performing mask repair. Therefore, nickel can be an alternative candidate of EUV absorber layer because it has superior EUV absorption over TaN [36].

Carlos et al. [36, 37] conducted a study by using the new gas field ion microscope as a possible strategy for repairing opaque nickel EUV defects. They investigated helium and neon ion beam induced etching of nickel at different doses and energies. The authors used the EnvizION simulator to study sputtering of nickel by using helium and neon ions and correlated observed damage and bubble formation to nuclear energy loss and the implanted inert gas concentration in Molybdenum-silicon stacks. In order to understand the observed damage induced by the helium irradiation, the authors simulated the energy loss at 16 and 30 keV. The simulation was performed by bombarding 100,000 helium ions with a raster scan over a 10 nm by 10 nm area which corresponds to an experimental dose of 1×10^{17} ions/cm^2. Figure 4.21a depicts nuclear and helium ion concentration profiles with TEM image at 16keV simulation. The damage can be seen up to ~140 nm depth, where the thickness of nickel layer is 50 nm. From Fig. 4.21a, the nuclear energy threshold can be calculated and it is ~80 eV/nm^3. This energy correlates well with the damage threshold for 1×10^{17} helium ions/cm^2 dose. From Fig. 4.21b at 30 keV helium ion simulation, a clear damage up to ~180 nm is observed. Their observation shows that the most significant nuclear energy loss remains close to the top surface and with in the nickel layer. Furthermore, their study [36] presents the nuclear energy loss

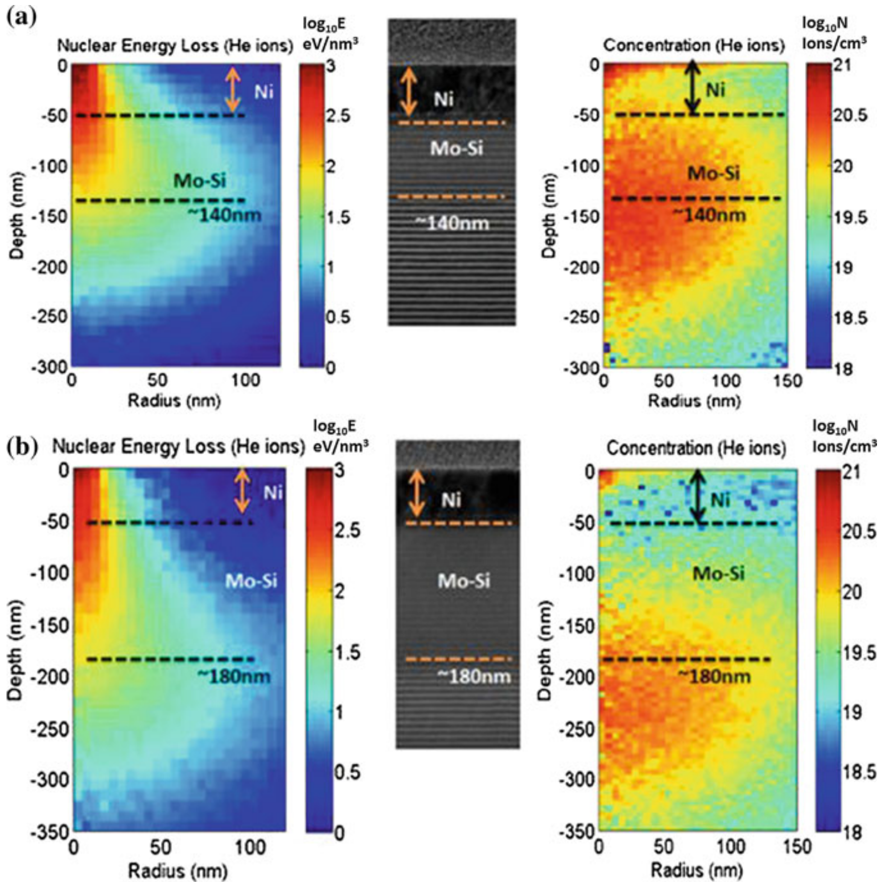

Fig. 4.21 **a** Simulated nuclear energy loss (*left*) and the resultant neon implant concentrations (on *right*) are compared to the experimental TEM micrograph (*middle*) exposed to 16 keV for He ions at a dose of $2 \times 10^{17} Ne^{+}/cm^{2}$. **b** the same as (**a**), but for 30 keV Helium ions. This figure is taken from [36] with permission

near the top of the MO/Si stack is still sufficient to induced some intermixing of silicon and molybdenum. A critical energy density in this region is approximated ~(80–100) eV/nm^3.

Although the EnvizION simulations [12, 13] do not show a discernible etching of nickel with helium at 16 and 30 keVs, it can be observed while using neon ions. Carlos et al. [36] showed the etching of approximately 32 nm depth of nickel by bombarding 150,000 neon ions at 10 nm by 10 nm area with an experimental equivalent dose of ~2×10^{17} Ne^{+}/cm^{2} at 30 keV. In Fig. 4.22, the volumetric nuclear energy loss and final concentrations for neon at 30 keV are compared side by side with the actual TEM cross section micrograph at the same dose. In this case, it is notable that a high nuclear energy loss region extends beyond the nickel layer into the Mo/Si

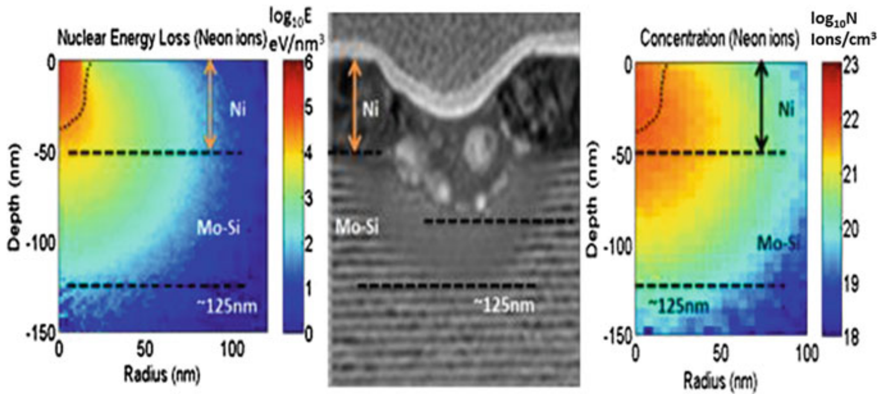

Fig. 4.22 Simulated nuclear energy loss (*left*) and the resultant neon implant concentrations (on *right*) are compared to the experimental TEM micrograph (*middle*) exposed to 30 kV at a dose of $2 \times 10^{17} Ne^{+}/cm^{2}$. This figure is taken from [36] with permission

multilayer. Figure 4.22a depicts the damaged region at $\sim 2 \times 10^{17}$ Ne^{+}/cm^{2} includes nanobubbles in the nickel, but concentrated near the interface of the Mo/Si stack within the stack to a shallow depth of about 50 nm as shown in Fig. 4.22b. Here, it is clear that the peak energy loss is taking place within the Ni, where it causes physical sputtering, yet substantial nuclear energy loss also extends into the Mo/Si region down to $\sim$100 nm from the original top surface of the nickel (experimentally, the halo extends to $\sim$116 nm). For etching in nickel to take place, the simulation [36] predicts a minimum nuclear energy density of $\sim$30 keV/nm^3. Bubbling is observed and is attributed to the implanted neon at concentrations on the order of 1×10^{21} Ne^{+}/cm^{3}; while conversely, no damage is again discernable below 80 eV/nm^3.

4.5 Resolution Limiting and Sputtering Limiting Effects

The resolution limiting and sputtering limiting effects are some of the important issues to be addressed in focused ion beam technology. The study conducted by Timilsina et al. [13] has provided some remarkable information that can be achieved from EnvizION simulations, however, more woks have to be done in this field. For example, changing various beam profile such as point source, cylindrical with different radius, Gaussian beams and addition of beam tails on the original Gaussian beams etc. can provide valuable information about the sputtering and resolution limiting effects. The authors have commented on both sputtering rate-limiting and resolution-limiting effects by performing neon ion beam sputtering simulation on copper [13]. Their studies demonstrated that the damage evolved in copper target effectively decreases the density of the material as a result the sputter yield of the material also decreases. Furthermore, the re-deposition of copper at high aspect ratios which

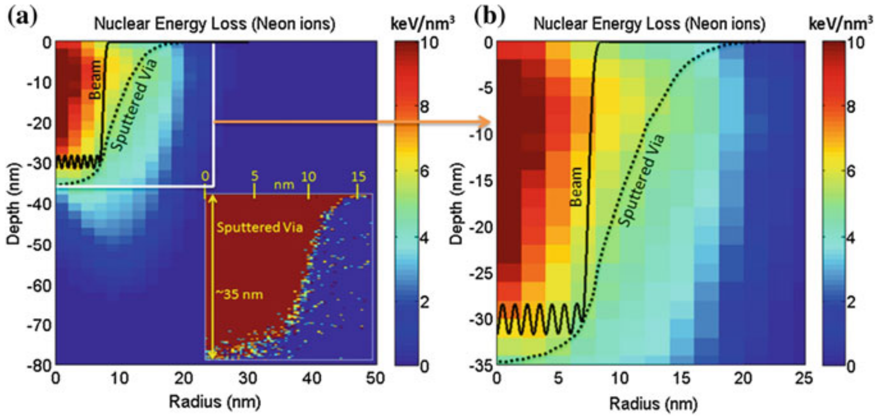

Fig. 4.23 Nuclear energy loss density at Cu target with 702,000 neon ions (a dose of $3.12 \times 10^{17} Ne^+ cm^{-2}$) of 20 keV. The inner plot of (**a**) depicts the sputtering profile and (**b**) is a zoomed region of the rectangle shown in (**a**). The *dark blue color* of figure (**b**) represents nuclear energy loss of 1 keV nm^3 or less. This figure is taken from [13] with permission

lowers the amount of material that is sputtered from the via. The resolution-limiting effects can be illustrated by comparing a simulation of the sputter profile and the resultant energy loss density as shown in Fig. 4.23. Figure 4.23a consists of a plot of nuclear energy loss at 20 keV neon beam at copper target. The sputtered structure of approximately 35 nm depth is also included in the plot. The solid black and dotted black lines in the figure represent a resultant two dimensional beam after superimposing Gaussian beams of 1 nm full-width-at-half maxima (FWHM) raster at 15×15 nm^2 area and boundary line of the sputtered via structure respectively. Figure 4.23b is a zoomed portion of a square region shown in Fig. 4.23a.

Figure 4.23 compares the sputter profile and the energy loss for a 702,000 neon ions simulation, an equivalent dose of $\sim 3.12 \times 10^{17} Ne^+ cm^{-2}$, assuming a 1 nm pixel spacing and the 15×15 1 nm FWHM. Although their energy loss algorithm is computationally demanding it would be significant if more ions can be simulated for this purpose. The authors have also included the resultant incident beams (the summation of the 15×15 Gaussian beams) for comparison to demonstrate the ideal resolution (dotted line indicated as beam in Fig. 4.23a). For clarity, the etched profile is overlaid in Fig. 4.23a on the energy loss density plot. Basically the resolution is limited first of all by the lateral straggle and energy loss of the ion beam. Thus the energy loss distribution is critical to the resolution of the resultant profile and both the vertical and lateral threshold for sputtering appears to be ~ 5.5 keV nm^{-3} as shown in Fig. 4.23b. The dark blue color in Fig. 4.23b represents the energy loss density which is less or equal to 1 keV nm^{-3}. Secondly, as the rate decreases due to re-deposition, the beam tails of the Gaussian are effectively amplified (or the peaks decreased), which can further compromise the resolution at high-aspect ratios [13].

4.6 Summary

Focused ion beam technologies have offered new possibilities for materials modification and fabrication with the higher spatial resolution by using helium and neon ions. Several experimental and simulation efforts are being devoted in this field since the past decades. The EnvizIOn is one of the simulators for simulating the ion-solid interactions. It has several capabilities of simulating gas assisted deposition, physical sputtering and etching. While SRIM/TRIM is very useful for a myriad of applications, it is not applicable for the understanding of the nanoscale evolution associated with ion beam nano-machining as the substrate does not evolve with the sputtering process. As a solution for this problem, a new, adapted simulation code (EnvizION) is briefly overviewed. From this simulator, experimentally observed Ne^+ beam sputter profiles can be explained from a fundamental point of view. Furthermore, the EnvizION simulator contains the potential for computer aided optimization towards predictable sputter processes for different nanotechnology applications. Due to these benefits, the discussed simulation approach represents an enormous step towards a computer based master tool for adaptable ion beam applications in the context of industrial applications.

References

1. J.F. Ziegler, M.D. Ziegler, J.P. Biersack, Nucl. Instrum. Methods B **268**, 1818–1823 (2010)
2. https://www.srim.org
3. J.P. Biersack, W. Eckstein, Appl. Phys. A **34**, 73 (1984)
4. M. Ullrich, A. Burenkov, 1.H. Rysse, Nucl. Instrum. Methods B **228**, 373–377 (2005)
5. http://Geant4.web.cern.ch/Geant4/
6. H.B. Kim, G. Hobler, A. Steiger, A. Lugstein, E. Bertagnolli, Nanotechnology **18**, 245303 (2007)
7. E. Platzgummer et al., Microelectron. Eng. **83**, 936–9 (2006)
8. W. Boxleitner, G. Hobler, Nucl. Instrum. Methods B **180**, 125–9 (2001)
9. P.M. Nellen, V. Callegari, J. Hoftmann, E. Platzgummer, C. Klein, Mater. Res. Soc. Symp. Proc. **960**, 0960–N10-03-LL06-03 (2007)
10. D. Kunder, E. Baer, M. Sekowski, P. Pichler, M. Romme, Microelectron. Eng. **87**, 1597–1599 (2010)
11. W. Moller, Nucl. Instrum. Methods Phys. Res. B **322**, 23–33 (2014)
12. R. Timilsina, P.D. Rack, Nanotechnology **24**, 495303 (2013)
13. R. Timilsina, S. Tan, R.H. Livengood, P.D. Rack, Nanotechnology **24**, 485704 (2014)
14. R. Timilsina, D.A. Smith, P.D. Rack, Nanotechnology **24**, 115302 (2013)
15. R.H. Livengood, S. Tan, R. Hallstein, J. Notte, S. McVey, F.H.M.F. Rahman, Nucl. Instrum. Methods Phys. Res. A **645**, 136 (2010)
16. D.A. Smith, D.C. Joy, P.D. Rack, Nanotechnology **21**, 175302 (2010)
17. R. Ramachandra, B. Griffin, D.C. Joy, Ultramicroscopy **109**, 748 (2009)
18. J.D. Fowlkes, P.D. Rack, ACS Nano. **4**, 1619 (2010)
19. D.A. Smith, J.D. Fowlkes, P.D. Rack, Nanotechnology **19**, 265308 (2007)
20. H.M. Wu, L.A. Stern, J.H. Chen, C.H. Schwalb, M. Winhold, F. Porrati, C.M. Gonzalez, R. Timilsina, P.D. Rack, Nanotechnology **24**, 175302 (2013)
21. M. Nastasi, Cambridge Solid State Science Series (1996)

22. M. Nastasi, J.W. Mayer, Springer, Berlin, Heidelberg (2006)
23. J.F. Ziegler, J.P. Biersack, U. Littmark, Pergamon Press, New York (1985)
24. http://www.nist.gov/pml/data/star/
25. S. Tanuma, T. Shiratori, T. Kimura, K. Goto, S. Ichimura, C.J. Powell, Surf. Interface Anal. **37**, 833–845 (2005)
26. M. Kotera, J. Appl. Phys. **65**, 3991 (1989)
27. W.F. van Dorp, J.D. Wnuk, J.M. Gorham, D.H. Fairbrother, T.E. Madey, C.W. Hagen, J. Appl. Phys **106**, 074903 (2009)
28. P. Chen, E. van Veldhoven, C.A. Sanford, H.W.M. Salemink, D.J. Maas, D.A. Smith, P.D. Rack, P.A.F. Alkemade, Nanotechnology **21**, 455302 (2010)
29. E.R. Cawthron, Aust. J. Phys. **24**, 859 (1971)
30. P. Sigmund, Phys. Rev. **184**, 383 (1969)
31. N. Matsunami, Y. Yamamura, Y. Itikawa, N. Itoh, Y. Kazumata, S. Miyagawa, K. Morita, R. Shimizu, H. Tawara, At. Data Nucl. Data Tables **31**, 1–80 (1984)
32. Y. Yamamura, H. Tawara, At. Data Nucl. Data Tables **62**, 149–253 (1996)
33. R. Behrisch, W. Eckstein, Springer, Berlin (2007)
34. National Physical Laboratory. https://www.resource.npl.co.uk
35. S.D. Tan, R.H. Livengood, P. Hack, R. Hallstein, D. Shima, J. Notte, S. McVey, J. Vac. Sci. Technol. B **29**, 06F604 (2011)
36. C.M. Gonzalez, R. Timilsina, W. Slingenbergh, J.H. Noh, M.G. Standford, B.B. Lewis, K.K. Klein, T. Liang, J.D. Fowlkes, P.D. Rack, J. Vac. Sci. Technol. B **32**, 021602 (2014)
37. C.M. Gonzalez, W. Slingenbergh, R. Timilsina, J.H. Noh, M.G. Standford, B.B. Lewis, K.K. Klein, T. Liang, J.D. Fowlkes, P.D. Rack, in *SPIE Proceeding, Extreme Ultraviolet (EUV) Lithography*, vol. 9048, p. 90480M

Chapter 5
Secondary Electron Generation in the Helium Ion Microscope: Basics and Imaging

Yuri V. Petrov and Oleg F. Vyvenko

Abstract The theories, modeling and experiments of the processes of secondary electron (SE) generation and SE usage in helium ion microscopy (HIM) are reviewed and discussed. Conventional and recently introduced SE imaging modes in HIM utilizing SE energy filtering and ion-to-SE conversion, such as scanning transmission ion microscopy and reflection ion microscopy, are described.

5.1 Introduction

The detection of secondary electrons (SEs) has been the most widely used node of operation in scanning electron microscopy (SEM) since the middle of the last century, when a sensitive SE detector was developed by Everhart and Tornley [1]. The SE detection mode has a number of advantages, including a low lateral spread of the electron escape volume and a simple analytical shape of the dependence of SE yield on the angle of incidence, providing high resolution and easily interpretable SE images. Physical processes related to the electron emission from samples and its application for image formation in SEM have been extensively investigated and their detailed description has been published in books [2, 3] and reviews [4, 5].

SEs can be excited not only by electrons but also by any other primary particles (ions, atoms, electromagnetic quants) that are able to transfer a sufficient amount of their energy to electrons in solids. In scanning ion microscopy, SEs are excited by the focused beam of accelerated ions. By convention, an SE is assumed to have a kinetic energy less than 50 eV. This restriction was introduced to distinguish SEs

Y.V. Petrov · O.F. Vyvenko (✉)
St. Petersburg State University, Faculty of Physics, Ulyanovskaya 1, 198504
Saint-Petersburg, Petrodvoretz, Russia
e-mail: vyvenko@nano.spbu.ru

Y.V. Petrov
e-mail: y.petrov@spbu.ru

© Springer International Publishing Switzerland 2016

G. Hlawacek and A. Gölzhäuser (eds.), *Helium Ion Microscopy*,
NanoScience and Technology, DOI 10.1007/978-3-319-41990-9_5

from scattered electrons of the primary beam in SEMs operating with accelerating voltages above hundreds of volts. In scanning ion microscopes, all electrons excited by the ion beam are secondary.

SE emission is characterized by the number of SEs per primary particle, known as SE yield (SEY), and by SE energy distribution (SEED). The angular dependence of the total SEY provides the main base of topography contrast formation in scanning electron or ion microscopy. The SEY value and the shape of the SEED depend on both the kind of excitation and on the material. Exact knowledge of the particular SEED parameters has been shown to be very useful for correct interpretation of SEM images [5] as well as for electron or ion assisted lithography [6].

In this chapter we present a brief review of available state-of-the-art results of the main properties of SEs excited in the helium ion microscope (HIM) and their use in diverse HIM imaging modes.

5.2 The Processes of Secondary Electron Generation in the Helium Ion Microscope

The process of SE emission can be divided into three consecutive processes: an instant energy transfer from primary particles to electrons in any point of the sample, transport of excited electrons to the surface and their escape through the surface barrier. The mechanisms of the last two processes are independent of the kind of exciting particle or of radiation and are related only to material properties. SE escape from the sample into the vacuum is limited by a barrier at the surface that is determined by the work function of the sample, whereas the transport is usually described as electron diffusion characterized by the electron mean free path (MFP) of a solid.

The energy transfer from primary particles to the electrons of the sample is a multistage process that includes many channels of initial energy dissipation. An important difference between electron-induced and ion-induced SE generation is that ion-induced generation can take two distinct forms: potential electron emission and kinetic electron emission.

Potential emission occurs when the potential energy released on neutralization of the incident ion can provide the energy required to free electrons from the solid [7]. This process has no lower energy threshold but is significant only when the primary ion is slow enough [8] that it corresponds to the kinetic energy of helium ions of few hundred eV [9]. In this case, the potential energy of an ion at the surface can be transferred to an Auger electron in the solid via a two-step process as illustrated in Fig. 5.1. The first step is the tunneling of an electron from the solid to the ion (marked **1** in Fig. 5.1) resulting in its neutralization. The second step is the excess energy transfer to another electron of the solid via the Auger process (marked **2** in Fig. 5.1). The maximum kinetic energy of SE in that case is $I-2\Phi$, where I is the ionization potential of the primary ion and Φ is the work function of the material. The relatively high ionization potential of helium ions, 24.5 eV, makes the Auger

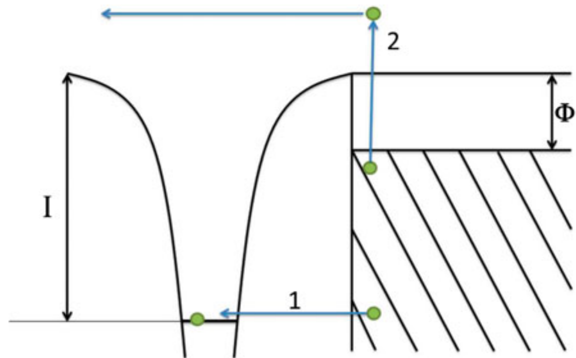

Fig. 5.1 Schematic diagram illustrating the potential electron emission process. The ion is neutralized as the result of the tunneling of an electron from the solid (*arrow* **1**). The energy I-2Φ (*arrow* **2**) is transferred to another electron in the solid via the Auger process. I is the ionization potential of the primary ion and Φ is the work function of the material

mechanism of potential emission possible for the most materials, since in most cases the work function is less than 10 eV.

An additional mechanism of ion–electron interaction at low primary ion energies that might contribute to potential electron emission is potential plasmon excitation [10, 11]. Neutralization of the ion results in the appearance of a hole near the sample surface because of the loss of an electron. Surrounding electrons of the sample move to screen the hole, and oscillations of electron gas can be excited. A detailed review of plasmon excitation in ion–solid interaction can be found elsewhere (see [11] and references therein). Though the contribution of the potential electron emission mechanism to the total SEY in HIM working with accelerating voltages more than 20 kV seems to be insignificant, it should be noted for the following discussion of SEED shape that experimental observations of that mechanism serve as evidence for ion neutralization near the surface.

Kinetic energy transfer takes place when the energy of projectile particles is sufficient for them to penetrate into a solid. There are several mechanisms for the transfer of kinetic energy from projectile particles to the electrons in solids which can result in excitation of secondary electrons. Four of them are depicted in Fig. 5.2. They are direct binary ion–electron collisions, electron cascades generation, excitation by recoil atoms and plasmon excitation.

The resulting impact of all of the processes can be described by stopping power, that is, the rate (in eV/nm) of energy transfer from the primary particles to the sample per unit of the primary path. The instant rate of SE generation is proportional to the stopping power. For electrons the stopping power increases rapidly with increasing energy E reaching a maximum value of about 60 eV/nm at an energy on the order of hundreds of eVs and then falls away at about 1/E following Bethe's law [3]. As a result, the mean free path (MFP) of the SEs (which are the electrons with energies below the stopping power maximum) decreases with their energy, providing behavior similar to SE escape depths in a range from a few to tens of nanometers. Accordingly, the latter values are defined as the values of the depth which are relevant to the ion–electron energy transfer for SE generation.

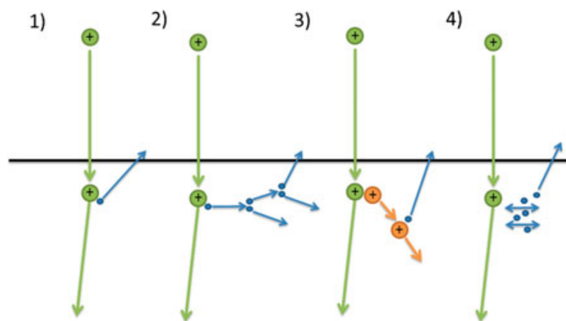

Fig. 5.2 Schematic presentation of the processes of kinetic energy transfer from a projectile to the electrons in solids, resulting in kinetic electron emission: *1* direct binary ion–electron collisions, *2* Electron cascades generation, *3* Excitation by recoil atoms and *4* Plasmon excitation. Green, blue and red arrows show trajectories of the ions, electrons and recoils, respectively

For the helium ions, however, the stopping power stays relatively low until the energy reaches about 5 keV, then increases steadily to reach a maximum value of about 700 eV/nm at an energy of about 800–1000 keV before starting to fall. These distinctly different behaviors might appear to suggest that electrons and helium ions interact with the target in completely different ways, but this conclusion is incorrect because comparing ions and electrons on the basis of their energy is not appropriate. In fact, the interaction of swift particles with a solid depends on their velocity but not on their energy, since according to momentum and energy conservation laws the maximum momentum transfer from any particle to an electron cannot exceed the value 2 mv, where m is the electron rest mass and v is the velocity of the projectile.

The latter value for a helium ion as a function of energy can be calculated as:

$$v_{He+}(cm/s) = 2.196 \times 10^7 \sqrt{E(keV)} \tag{5.1}$$

which corresponds to approximately 1 % of the velocity of an electron of the same energy.

Figure 5.3 shows the normalized stopping power dependence of helium ions and electrons in chromium as a function of incident particle velocity calculated in the paper by Ramachandra et al. [9]. The helium data were obtained from the SRIM routines of Ziegler et al. [12] and include both nuclear and electronic contributions; the corresponding incident electron stopping profile was taken from previous experimental data [13].

Both particles are seen from the Fig. 5.3 to show rather similar behavior and each reaches its peak value close to the same velocity of about 6 * 10^8 cm/s. The shape of the curve for ions is not identical to the shape of the curve for electrons. It is important to note that the SEY for helium exceeds that for electrons at velocities below the maximum. The energies of He ions in HIM (from 10 to 45 keV) correspond to velocities on the left-hand side of the stopping power maximum, while

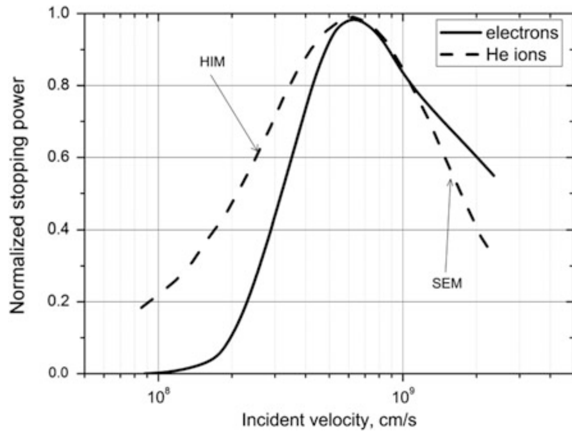

Fig. 5.3 Normalized stopping power (SE yield) dependence of helium ions and electrons as a function of incident particle velocity in chromium replotted using the data calculated in [9]. *Arrows* show helium ion and electron velocities corresponding to usual accelerating voltage values of about 20 kV either in HIM or in SEM

for electrons in SEM their energies (from 0.5 to 30 keV) represent velocities that fall on the right-hand side of the stopping power peak. Thus, increasing the energy of the helium beam in HIM increases the stopping power, leading to an increase in SE production, while increasing the energy of the electron beam results in a fall in stopping power, i.e. in a reduction of SE emission.

The stopping power of He ions is an order of magnitude higher than that of electrons, which corresponds to a higher number of secondary electrons (i.e. to a higher SEY) in HIM. The available experimental data collected during past decades [8, 14, 15,] and obtained recently [16] show that SEY values increase with the ion energy within the energy ranges of interest, and above energies of 5–20 keV (depending on the element) can well exceed unity. SEY values measured in HIM at 20 kV were found to be between 2 and 5 for different metals and reached 7.9 for platinum [17]. Several methods of SEY calculations have been developed using analytical approaches [18–20] as well as Monte Carlo simulations [9, 21, 22]. The results of two SEY calculation routines developed independently by Ramachandra et al. [9] and Inai et al. [22] are in good agreement.

5.3 SE Energy Distribution in HIM

SEY discussed in the previous section is a value independent of the SE energy value which counts the total number of SEs produced by an ion. Secondary electron energy distribution (SEED) describes the number of secondary electrons as a function of their energy. Generally, this function is non-monotonic and can be characterized by its shape and maximum value. The integral of SEED over the energy gives the total SEY. For electron excitation the shape of SEED is known to be essentially independent of the energy of the primary electron beam [4]. It is characterized by most probable energy, $E_{max,}$ and the full width at half maximum

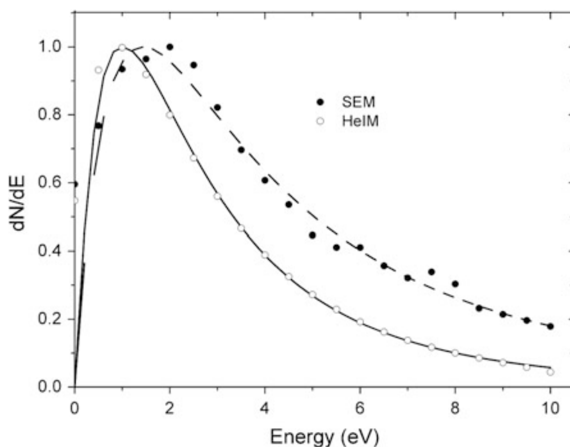

Fig. 5.4 Energy distribution of secondary electrons for Mo excited in SEM (*black closed dots*) and in HIM (*open dots*) working at acceleration voltages of 30 kV and of 32 kV, respectively. *Dashed and solid lines* represent the theoretical shapes of SEED for SEM and for HIM according to (5.2) and (5.10), respectively

(HW). Both E_{max} and HW depend on the surface material of the specimen, so HW is smaller for insulators than for metals [4]. Among numerous papers devoted to theoretical explanations or simulations of SEED shape, the most commonly accepted and used one is the result of Chung and Everhart [23], which suggested a simple equation for SEED as follows:

$$\frac{dN}{dE} = K\frac{E}{(E+\Phi)^4} \tag{5.2}$$

where K is a constant dependent on SEY value, E is the kinetic energy of emitted SE and Φ is a material work function. Equation (5.2) predicts that the SEED maximum corresponds to an SE energy of one-third of the material work function.

SEED in the helium ion microscope was experimentally investigated in [24, 25] by the retarding potential method with a hemispherical analyzer that was also used for SEED measurements in conventional SEM. Black open and closed dots in Fig. 5.4 represent the results of such measurements for molybdenum in SEM and in HIM, respectively. The dashed line in Fig. 5.4 was calculated theoretically with (5.2) of Chung and Everhart taking the known work function value for Mo. One can see that experimental data of SEED shape in SEM can be well-fitted with the theory whereas the data for HIM cannot, because the maximum of SEED in HIM is situated at somewhat lower energy than that in SEM and the high energy tail of SEED for HIM decays more rapidly with the energy than that for SE.

SEED measurements in HIM performed on different metals confirmed the general trend which was well established for electron excitation, that the SEED peak position energy follows the changes of the material work function value (see Fig. 5.5).

To describe the shape of SEED in HIM, a modified Chung-Everhart model was suggested in [25] that used the same formalism to describe the transport of excited electrons to the surface and their escape through the surface barrier, but introduced

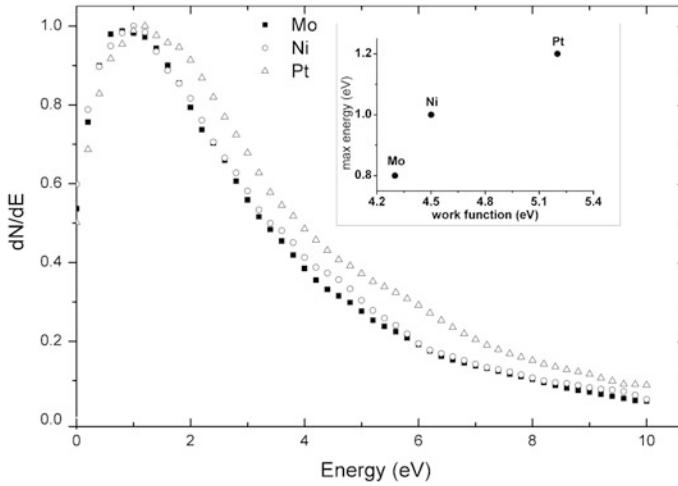

Fig. 5.5 Secondary electron energy distribution measured in HIM for three metals [25]. *Inset* shows the dependence of SEED maximum position on the metal work function

another function for the description of the energy transfer from primary ion to secondary electron. The number of secondary electrons excited per unit energy in the energy interval between E and E + dE at a depth of z from the surface is designated as S(*E*, *z*).

Following Chung and Everhard, S(*E, z*) SEED can be obtained by integrating the product S(*E*, *z*) P(*E*, *θ*, *z*) over all possible θ and z, where P(*E*, *θ, z*) is the probability for secondary electrons to reach the surface moving in the direction θ with the normal:

$$P(E,\theta,z) = \exp\left\{-\frac{z}{\lambda(E)\cos\theta}\right\} \tag{5.3}$$

Here λ (E) is the electron MFP in the solid. SEs can escape the surface if their energy exceeds a critical value of Ecr = Ef + Φ, measured from the bottom of the conduction band. Ef is the Fermi energy, and the relationship $\theta < \arccos(p_{cr}/p)$ is used, where p is a momentum of electron and $p_{cr} = \sqrt{2mE_{cr}}$ [23].

Using the fact that most SEs have energy at most 5–7 eV above the Fermi level, one can estimate the electron MFP to be between 1 and 5 nm according to the results of [26]. According to SRIM calculations [12], helium ion stopping power for most metals remains constant within the first 50 nm from the surface, being as low as about 100–300 eV/nm. Accordingly, the helium ion energy losses at the maximum depth of SE escape are not more than 5% of the initial ion energy and can be considered to be constant within the electron MFP, making the number of secondary electrons excited per unit energy independent of the depth, i.e. S(*E,z*) = S(E). Under these assumptions, SEED is given by the same expression as that obtained in [23]:

$$\frac{dN}{dE} = \frac{S(E)\lambda(E)}{4}\left[1 + \left(\frac{E_f + \Phi}{E}\right)\right] \tag{5.4}$$

where E is measured from the bottom of the conduction band.

Since the transport mechanism of excited electrons to the surface is independent of the kind of excitation, the common expression for MFP obtained in [26] can be used:

$$\lambda(E) \sim \frac{E}{\left(E - E_f\right)^2} \tag{5.5}$$

Inserting (5.5) in (5.4) and denoting SE energy in a vacuum as Ese = E – Ef − Φ, one obtains:

$$\frac{dN}{dE} \sim S(E_{se})\frac{E_{se}}{\left(E_{se} + \Phi\right)^2} \tag{5.6}$$

Energy distribution for excited electrons inside the solid S(E) depends on excitation mechanisms.

Chung and Everhart used the equation calculated by Baroody [27] for electrons to describe S(E):

$$S(E) \sim \frac{1}{\left(E_{se} + \Phi\right)^2} \tag{5.7}$$

which resulted in the dependence (5.2).

Because an explicit form S(E) for excitation of SEs by helium ions in HIM similar to (5.7) is not known, it was suggested in [25] to retrieve the shape of S(E) function S(E) from SEED experimental data. Since MFP of SE does not depend on the excitation mechanism, the function S(E) can be calculated as:

$$S(E) \sim \frac{dN}{dE}\frac{\left(E_{se} + \Phi\right)^2}{E_{se}} \tag{5.8}$$

The S(E) dependence calculated from experimental data [25] is presented in Fig. 5.6 on a double logarithmic scale where energy is measured from the Fermi level.

One can see from Fig. 5.6 that, for all three metals, the dependences show a linear behavior in double logarithmic scale, reflecting a power dependence of:

$$S(E) \sim \frac{1}{\left(E_{se} + \Phi\right)^a} \tag{5.9}$$

where a = 3.3 ± 1 irrespective of material [25].

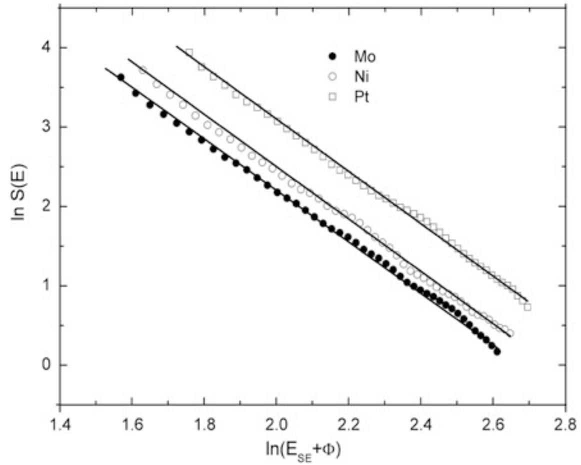

Fig. 5.6 Energy distribution for electrons excited by helium ions inside three metals in HIM at 32 kV [25]

Thus, for SEED:

$$\frac{dN}{dE} \sim \frac{E_{se}}{(E_{se} + \Phi)^{5.3}} \tag{5.10}$$

Solid lines in Fig. 5.5 represent the theoretical shape of SEED for SEM according to (5.2) and for HIM according to (5.10) with **b** = 5.3. A good correspondence between the experimental data and the approximated formulas is evident.

The suggested phenomenological model describing the shape of the SEED for metals can be useful in different applications due to its explicit and simple analytic form.

The difference in the shape of the energy distribution for excited electrons inside a solid and the energy distribution for ions might be explained qualitatively by the distinguishing mechanism of ion–electron interaction. In fact, Monte Carlo simulation of SEED in the case of HIM performed by Ohya et al. [21] showed that SEED for HIM was narrower than SEED for SEM, which is in qualitative agreement with experimental results described before. However, direct comparison of SEED calculated in [21] with experimental data of [25] presented in one plot (Fig. 5.7) shows two noticeable discrepancies.

Firstly, the experimentally obtained SEED is narrower than the calculated one, and secondly, calculated SEED decreases to zero at 10 eV, whereas experimentally obtained SEED has a tail up to 15 eV.

The authors of [21] performed their calculations in the framework of a kinetic ion–electron emission model that included the processes of binary ion–electron collisions, of excitation of electrons by recoiled atoms and of electron cascades. But other ion–electron interaction processes, such as potential emission or Auger

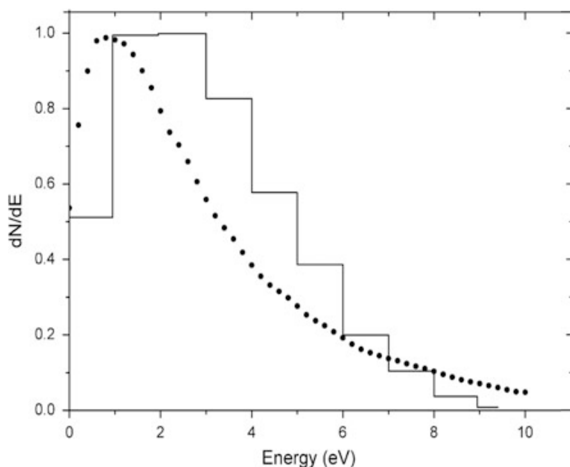

Fig. 5.7 Comparison of experimental SEED [25] (*dots*) and simulation results from [21] (*solid line*)

neutralization discussed above, were not taken into account, since in the ranges of ion energy in HIM, the kinetic emission is commonly understood to dominate [8].

Meanwhile, for the investigated materials, the work function values are about 5 eV, which gives an energy release in the Auger process of helium neutralization at the surface of about 15 eV, so the released energy is enough to excite SE. Thus, the tail of SEED extending up to 15 eV is expected.

In addition, such a processes can result in neutralization of helium ions even before entering the solid. Recent experiments of the impact of voltage bias on the spectra of backscattered ions in HIM [28] confirmed the existence of this neutralization process. This serves as an indirect confirmation of the presence of a potential emission mechanism at the surface of the metals in HIM. In addition, when neutral atoms penetrate into the solid they can also excite secondary electrons. Neutral atoms were shown to generate SEs, though with a lower mean energy than that of ions [29]. Thus, the fact that the experimentally observed SEED shape is narrower and shifted towards lower energies than that calculated based on a kinetic emission model [21] can also be explained as a result of ion neutralization.

Though potential emission and excitation of SE by neutrals are minor processes in ion–electron interaction, their contribution to SEED shape should be taken into account in future accurate calculations.

5.4 Imaging with SE

5.4.1 Topographic Yield

The most important application of SE imaging—revealing surface topography—is made possible because of the variation of SEY with the angle of incidence of the incoming beam to the surface. For electron irradiation, the SEY at some angle of

incidence can be approximately related to the yield at normal incidence by the secant law [4]. This is valid for primary particles of sufficiently high energy when the electronic stopping power along the particle trajectory of SE generation is constant and there are no angular changes in the particle scattering or in the recoil atoms.

The topographic yield behavior in HIM was calculated in [9, 21, 22, 30] using somewhat different algorithms of Monte Carlo simulations. Earlier experimental data for some elements in the helium ion energy ranges of interest are also available [31, 32]. It has been shown that the shape of the angular dependence of the ion-induced SE yield varies with the ion primary energy and with the material atomic number and exactly follows the secant law only for light elements. Thus, special attention to the SE topography treatment is required to retrieve reliable data for metrological measurements of heavy elements in HIM.

5.4.2 SE2/SE1 Ratio

Secondary electrons can be excited by primary ions as well as by backscattered ions (BSI). The ratio of SE excited by BSI is known as SE2. The presence of SE2 is the one of the main factors limiting the spatial resolution of SEM and HIM, because SE2 escapes from the region defined by the width of the interaction volume. In general, the SE2/SE1 ratio depends on the specimen material and on the ion energy. When energy of the primary ions increases, BSI energy also increases. As pointed out in the Sect. 5.2 of this chapter, the stopping power of the ions in HIM increases with energy, so the number of SE2 excited by BSI increases similarly to the number of SE1. At the same time, according to SRIM calculations the number of BSI decreases with the primary ion energy [12]. As a result of the two competitive processes, the energy dependence of SE2/SE1 ratio exhibits a maximum in the range from 10 to 100 keV [9]. According to numerical simulations, the value of this ratio for light elements is far below a unit, but for gold and heavier elements it can exceed one [9]. The latter fact seems to be in contradiction with the suggested energy dependence of SEY, because the energy of backscattered ions is less than the energy of primary ions and backscattering ion yield never exceeds unity. It can be explained due to particular trajectories of BSI (see Fig. 5.8). The number of SE2 per unit path of BSI is less than number of SE1 per unit path of primary ions, but the total length of BSI paths in the SE generation layer is longer due to deviation of those directions from normal. Thus, the number of SE2 which can escape from the sample (red arrows in Fig. 5.8) increases due to the distortion of the trajectories of backscattered ions.

In general, SE1 and SE2 might have different energy distributions. An attempt to investigate this difference experimentally was performed by V. Mikhailovskii et al. [42]. SEED was measured from thin Pt films of different thicknesses deposited on a silicon substrate. The thickness of the Pt film was varied from 5 to 160 nm, which according to SRIM calculations [12] corresponds to the variation of backscattered

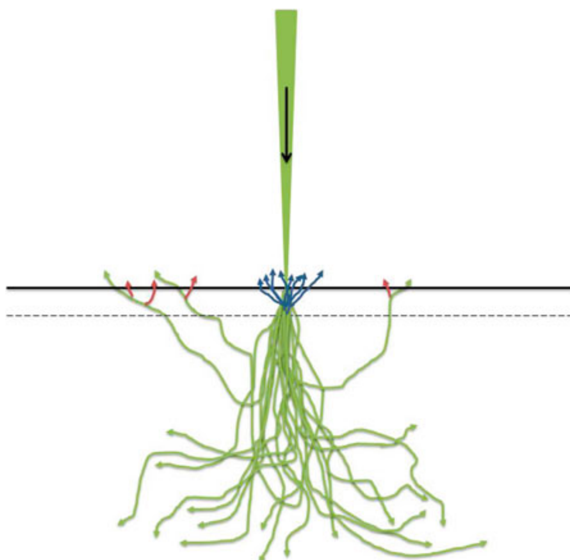

Fig. 5.8 Schematic of the trajectories of helium ions (*green lines*) and secondary electrons in solids. *Blue and red arrows* correspond to SE1 and SE2, respectively

ion yield by an order of magnitude. Experimentally, the measured SEED shape was found to be identical for films of different thicknesses within the measurement error indicating that SEED shape for SE2 does not significantly differ from that for SE1.

5.4.3 SE3

In addition to SE1 excited by primary ions and SE2 excited by BSI, the third kind of SE, SE3, is generated by the ions backscattered from the sample that reach the chamber walls. Some amount of the BSI can immediately reach the SE detector window, but their contribution to the SE detector signal cannot be separated from the signal of SE3, and is formally included in the latter. Thus, the total signal from the ET detector, S, is proportional to the sum:

$$S = S_{SE1} + S_{SE2} + S_{SE3} = f_1(\gamma_1 + \gamma_2\eta) + f_3\gamma_3\eta \tag{5.11}$$

where γ_1, γ_2 and γ_3 are the SEY of SE1, SE2 and SE3, respectively; η is the backscattering ion (BSI) yield of the sample; and f_1 and f_3 are the collection efficiency of SE1, SE2 and of SE3 with the detector; γ_1 and γ_2 are dependent on the material, while γ_3 is not defined by the chamber material.

The SE detector collection efficiencies f_1, f_3 are largely defined, and can be varied, by the potential difference between the particular point of SE sources and ET detector, as well as, in part, by the local electric field configuration of the SE emitted surface.

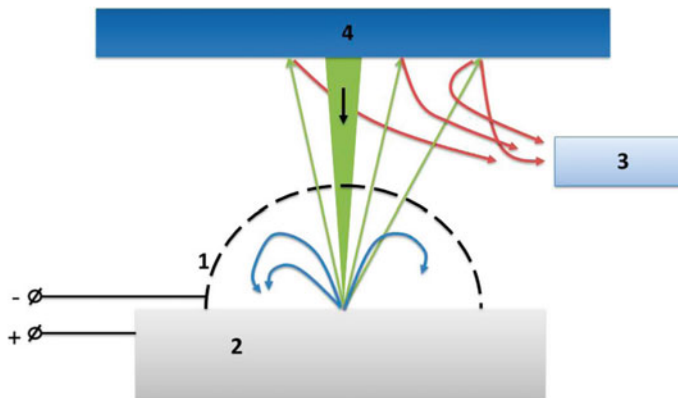

Fig. 5.9 Schematic diagram of an SE3 detection set-up. Semi-spherical grid electrode **1** is installed above the positively biased specimen **2**. Secondary electrons emitted from the specimen (*blue arrows* in Fig. 5.9) are attracted to the sample and do not reach the detector **3**. Backscattered ions (*green arrows* in Fig. 5.9) can escape through the grid electrode due to their energy, and reach chamber walls and objective lens polar piece **4**. Excited SE3 are detected with an ET detector whose signal is proportional to the number of backscattered ions

Experimental measurements of the SE3 ratio were performed in [33] by means of the retarding field method, utilizing the fact that at sufficiently high retarding potential, the collection efficiency f_1 can be eliminated, since SEs generated by the sample (SE1 and SE2) come to be blocked, as schematically depicted in Fig. 5.9.

According to (5.11), the contribution of SE3 to the detected signal depends on both BSI and SE yields of materials and increases with the atomic number of elements.

When comparing SE3 generation in SEM and HIM, one should note that variation in BSE yield with atomic number does not exceed a factor of 5 (it is typically from 0.1 to 0.5), whereas BSI yield can vary in significantly wider ranges, from 0.01 to 0.2. In addition, BSI yield in crystalline materials is affected more strongly by the channeling than that for electrons. As a result, the SE3 ratio can vary more strongly in HIM than in SEM, depending on the element and on the crystalline orientation.

The dependence of the ET detector signal on the retarding grid potential for two heavy polycrystalline metals is presented in Fig. 5.10.

One can see from Fig. 5.10 that with the increase of the electron retarding potential, the SE signal measured by the ET detector tends to a constant value that is as high as about 10% of the total signal for both metals, despite one being twice the other in atomic mass and a corresponding difference in BSI yield. The nearly equal ratios of SE3 signals for Pt and Mo to the total SE signal can be explained by the similar character of the yield changes for BSI and for SE1 (but not of SE2) with the element atomic number resulting in a nearly constant value of the yield's ratio. This assumption is valid until the product of the BSI yield and of the sum of SE and SE2 yields is less than that for SE1, as follows from:

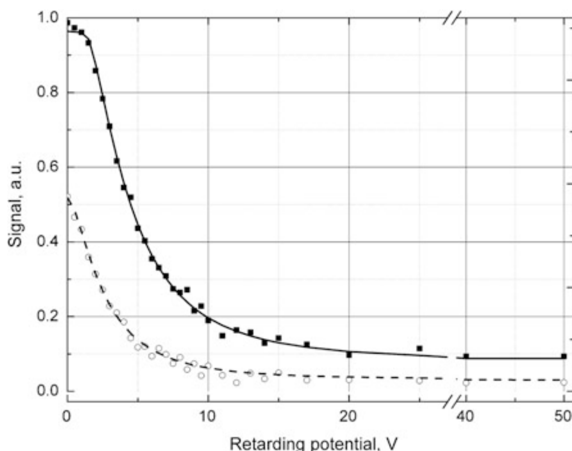

Fig. 5.10 Dependence of ET detector signal on retarding bias for Pt and Mo from [33]

$$\frac{S_{SE3}}{S} = \frac{\gamma_3 \eta}{\gamma_1(Z) + \gamma_2(Z)\eta + \gamma_3 \eta} = \frac{\gamma_3}{\gamma_1(Z)/\eta + \gamma_2(Z) + \gamma_3} \approx \frac{\gamma_3}{\gamma_1(Z)/\eta} \tag{5.12}$$

It seems to be that 10% is a roughly universal ratio value of SE3 signals in HIM for many materials.

A large ratio of SE3 signal to the total detected SE signal requires a careful interpretation of SE images. The impact of SE3 on imaging with the ET detector was demonstrated in [33] on a polycrystalline molybdenum sample. The result is presented in Fig. 5.11. An examination of the images of the same sample region obtained in HIM with the detection of all SEs, with the detection of SE3 (SEs with energies above 50 eV) and direct BSI detection with the standard HIM MCP detector reveals a striking resemblance.

The SE3 (Fig. 5.11b) and MCP (Fig. 5.11a) images are practically identical, confirming that the origin of SEs with energies above 50 eV was indeed caused the

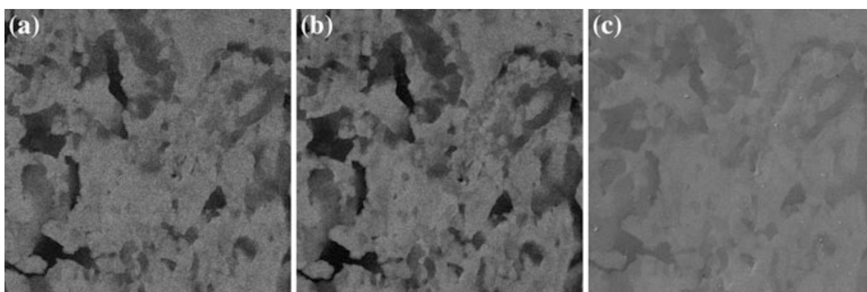

Fig. 5.11 HIM images of Mo with different detectors [30]: **a** MCP detector; **b**, **c** ET detector with 50 V or 0 V retarding potential on the retarding grid sphere, respectively. Field of view is 10 × 10 μm

BSI converted to SEs in the HIM stainless steel chamber beyond the retarding grid sphere. It was pointed out in [33] that the SE3 image exhibited an even better signal-to-noise ratio than the one obtained with MCP detector. Besides, the fact of high efficiency BSI-to-SE conversion by metals can be and was already used for the development of additional operation modes for HIM that will be discussed below.

Dark–bright contrasts on BSI images of the polished metal surface in Fig. 5.11 are believed to be due to the effect of ion channeling on the grain of different crystal orientations. Similar features can be also recognized on the SE image in Fig. 5.11c, indicating that the image obtained with the ET detector in the usual way is a composition of morphological and material contrasts. The contribution of SE3 to the SE image is expected to decrease with a decrease of atomic number and becomes negligible for $Z < 10$.

5.4.4 Material Characterization by SE Contrast Measurements with Energy Filtering

As shown above, the energy distribution of the SEs produced by the interaction of helium ions with a material can be described by an analytical function that depends mainly on two material parameters: its total ion-induced SEY and its work function. The value of the work function can be retrieved from fitting the experimentally obtained function shape with only one adjustable parameter. Unfortunately, the procedure of SEED data acquisition is time consuming and requires a rather big sample area with uniform properties to avoid carbon contamination during multiple scans with different retarding potential values. The common approach to characterize material properties microscopically is to evaluate the SE image contrast between two closely spaced sample regions with different values of surface potentials, as used in SEM [5, 34, 35] and recently, as well, in HIM [33, 36, 37]. SE contrast investigations in SEM have shown that SE energy filtration could increase the sensitivity and the precision of the potential measurements (for a recent review see [5]).

The explicit form describing the SEED shape (5.10) and the possibility of measuring SE3 contrast independently allow us to obtain analytical descriptions of the SE contrast changes between two materials [33] as a function of retarding grid potential, of material work function and of SEY. The energy-filtered SE signal under the application of retarding grid potential $\boldsymbol{V}$ can be calculated by the integration of:

$$S(\Phi, \gamma, V) = \int_{eV + \Delta\Phi}^{\infty} \frac{dN}{dE} dE \quad (5.13)$$

where $\frac{dN}{dE}$ is SEED normalized to the total SEY, $\Delta\Phi = \Phi_r - \Phi$, $\mathbf{\Phi}$, $\mathbf{\Phi_r}$—material and retarding grid work function. SEED normalization factor can be calculated as the number of ions N_i multiplied by the total SEY γ:

$$N_i\gamma = c\int_0^\infty \frac{E}{(E+\Phi)^a}dE \tag{5.14}$$

where a = 5.3 in HIM for metals [25], but may have another value for insulators or semiconductors (note that in SEM a = 2 for metals [23] and a = 1 for insulators [38]).

That gives the final expression for SEED:

$$\frac{dN}{dE} = N_i\gamma(a-1)(a-2)\Phi^{a-2}\frac{E}{(E+\Phi)^a} \tag{5.15}$$

and the final expression for SE signal generated by the specimen:

$$S(\Phi,\gamma,V) = N_i\gamma\left(\Phi^{a-2}\frac{(a-1)(eV+\Delta\Phi)+\Phi}{(eV+\Phi_r)^{a-1}}\cdot\Theta(eV+\Delta\Phi)+\Theta(-eV-\Delta\Phi)\right) \tag{5.16}$$

where $\Theta(eV+\Delta\Phi)$ is the Heaviside function that is used to take into account that $\frac{dN}{dE} = 0$ for $E < 0$.

The detected SE signal also contains the contribution of SE3 that is proportional to the number of backscattered ions that should be added to the SE signal (5.16) for further calculations:

$$S(\Phi,\gamma,\eta,V) = S(\Phi,\gamma,V) + N_i\eta k \tag{5.17}$$

where $\boldsymbol{\eta}$ is the backscattered ions yield of the sample and $\boldsymbol{k}$ is the SE3 excitation and collection efficiency that depends on detection geometry and the materials that the chamber is made of.

The SE contrast between two different materials with work functions Φ_1, Φ_2, SE yields γ_1 and γ_2, and BSI yields η_1 and η_2 is defined as:

$$C = \frac{S(\Phi_1,\gamma_1,\eta_1,V) - S(\Phi_2,\gamma_2,\eta_2,V)}{S(\Phi_1,\gamma_1,\eta_1,V)} \tag{5.18}$$

The shape of the SE contrast dependence on the retarding grid potential calculated according to (5.18) for $\gamma_1 > \gamma_2$, $\Phi_1 > \Phi_2$ is shown in Fig. 5.12. In the absence of SE3 electrons generated by BSI from the sample, the SE contrast is due to SE1

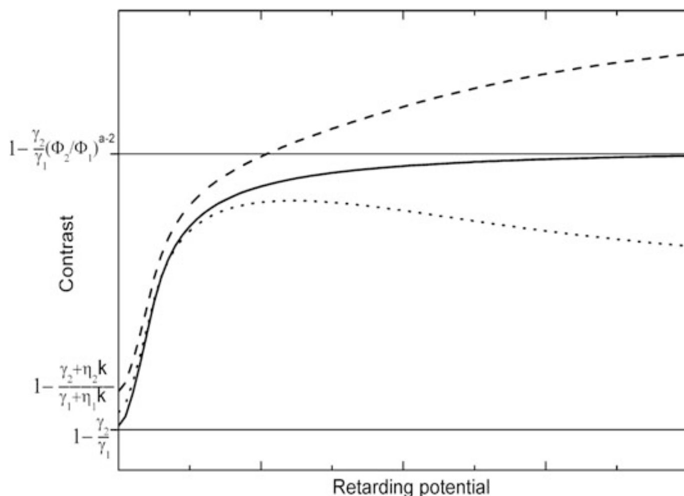

Fig. 5.12 SE contrast between two different materials ($\gamma_1 > \gamma_2$, $\Phi_1 > \Phi_2$) as a function of retarding potential calculated with (5.18) for three cases: $\eta_1 = \eta_2 = 0$, SE1 contrast calculated with (1.16)—*solid line*; $\eta_2/\eta_1 < \gamma_2/\gamma_1(\Phi_2/\Phi_1)^{a-2}$—*dotted line*, $\eta_2/\eta_1 > \gamma_2/\gamma_1(\Phi_2/\Phi_1)^{a-2}$—*dashed line*

electrons. It monotonically increases with the applied grid voltage and saturates at the value defined by the ratio of SEY and work function. At low retarding bias voltages, SE contrast behavior is similar to the SE1 contrast (solid line). In the presence of SE3, depending on the backscattered ion yield values and the ratio between the materials, two kind of the behavior might be distinguished. If $\eta_2/\eta_1 > \gamma_2/\gamma_1(\Phi_2/\Phi_1)^{a-2}$, then the contrast can reach a higher value than for SE1 (dashed line in Fig. 5.12), otherwise a non-monotonic contrast behavior can be observed (dotted line in Fig. 5.12).

The comparison of the experimentally determined dependence of the detected SE contrast between Pt and Mo polycrystalline samples vs. retarding potential with the theoretically calculated dependence was presented in [33] and is shown in Fig. 5.13. The ratio of SE3 and SE total yields were obtained from measurements with the applied bias voltage of 50 V and 0 V, respectively.

Good agreement with experimental data was demonstrated and work function values $\Phi_{Pt} = 4.9$ eV and $\Phi_{Mo} = 4.5$ eV obtained from fitting with (5.17) (solid line in Fig. 5.14) coincide well with handbook values.

Energy-filtered images of Pt film (bottom part of the figure) on polycrystalline Mo (top part of the figure) are shown in Fig. 5.14. It is evident that the relative contrast between Pt and Mo is enhanced when a retarding bias of 10 V is applied. In addition, under the bias within the area of polycrystalline Mo, the contrast of different grains becomes more pronounced. This enhancement results from the ion channeling effect which decreases the number of BSI and consequently decreases

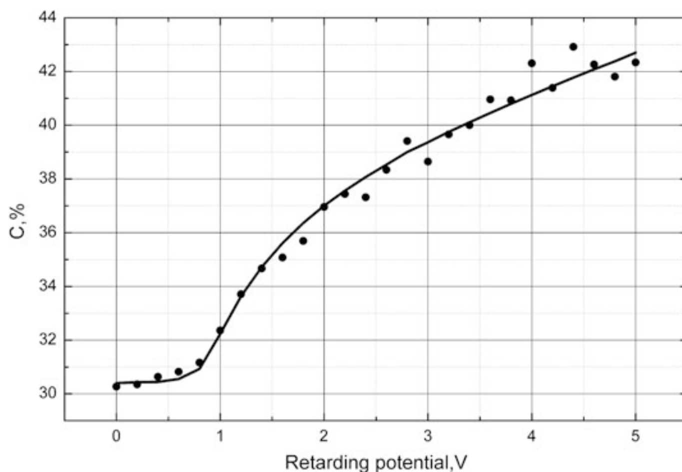

Fig. 5.13 Relative contrast between Pt and Mo from [33], *dots*—experiment, *solid line*—fitting with (1.18)

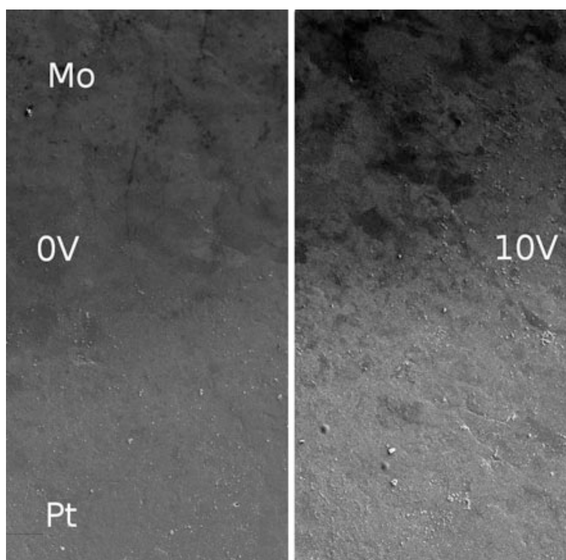

Fig. 5.14 HIM SE images of Pt film on Mo taken with 0 V (*left*) or with 10 V (*right*) retarding potential on the retarding grid. Field of view of each is 22.5 × 45 μm

the number of SE3. In the case of Pt film, grain size is much smaller than that of Mo, so a channeling contrast is not observed. It should be noted that relative contrast values between Pt and Mo plotted in Fig. 5.13 were obtained by averaging the signal over the large area of the sample.

5.5 Imaging Utilizing a High SE Yield in HIM: Ion-to-SE Conversion

A high helium ion-induced SEY from a heavy metal surface provides the possibility to effectively convert BSI to SE, and that in combination with conventional SE detectors can be used for developing new operating modes in HIM. The idea of utilizing such a conversion was described for the first time for backscattered electrons in SEM by Reimer [39]. Obviously, not only backscattered ions can be detected by means of conversion to secondary electrons but so can any ions scattered by the sample or transmitted through it. Recently, two new HIM imaging techniques were realized by using ion-to-electron conversion.

5.5.1 Scanning Transmission Ion Microscopy (STIM) with SE Detector

The sketch of the scanning transmission ion microscope that was recently proposed and realized by A. Hall [40] is depicted in Fig. 15.

Thin sample **1** is installed inside the shield **2** with an aperture **5** under the sample. The surface under the aperture **3** is covered with a material having a high secondary electron yield (for instance, platinum) and tilted towards the ET detector **4** to increase the number of SE and detection efficiency. Transmitted ions (green ray in Fig. 5.15) come through the aperture and excite SEs from the surface (right arrows in Fig. 5.15). The number of this SE is proportional to the number of transmitted ions. Secondary electrons excited from the sample are stopped with the shield around the sample. A retarding field can be applied between the sample and the shield to improve the efficiency of the shield.

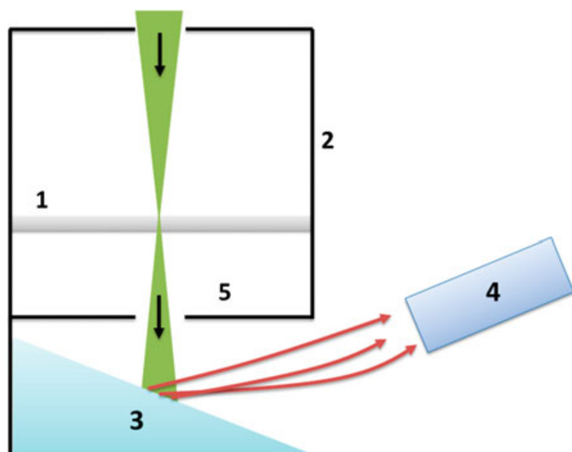

Fig. 5.15 Schematic diagram of scanning transmission ion microscope. See text for detailed description of the comprising elements

The working principle of STIM is similar to STEM. The incident well-collimated ion beam goes through the thin sample without noticeable energy losses but changes the initial ion directions due to elastic scattering in the foil. The output aperture 5 limits spatial angle of the detected transmitted ions and, together with I-to-SE convertor 3, works as a bright field detector. This method of STIM detection was used for the imaging and for the in situ thickness definition of silicon nitride membranes [40]. It was shown that STIM was extremely sensitive for the thin film thickness measurements. The minimum thickness for silicon nitride that could be detected with STIM was about 5 nm, which corresponds to a surface density of 1.5×10^{-6} gcm^{-2}.

5.5.2 *Reflection Ion Microscopy*

Another method utilizing conversion of scattered ions to secondary electrons that was introduced recently is scanning reflection ion microscopy (RIM) [41]. Reflection microscopy is a method that uses low angle scattered particles to form an image of a surface. The best results from reflection microscopy can be obtained in an ideal case of a strictly parallel incident beam. One of the main features of the HIM is a narrow beam convergence angle of about 0.5 mrad that is ten times less than the optimal beam convergence angle in SEM. That makes HIM very suitable for scanning reflection microscopy.

The RIM scheme suggested in [41] is depicted in Fig. 5.16.

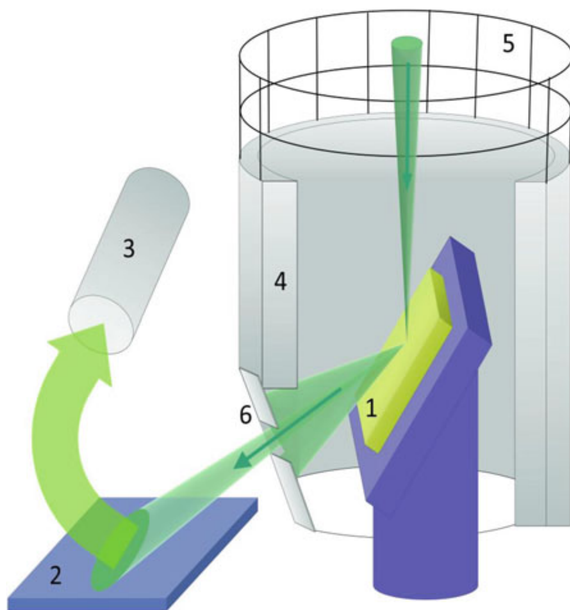

Fig. 5.16 Scheme of detection of reflected ions in the helium ion microscope [41]: 1—sample, 2—Pt-coated surface, 3—secondary electron detector, 4—SE grounded shield, 5—SE3 shield, 6—slit diaphragm

Similarly to the case of STIM, reflected ions come through the aperture **6** and excite secondary electrons which, in turn, are detected with the ET detector **3**. Platinum-coated surface **2** is used for RI-to-SE conversion. SE excited from the sample **1** and SE3 are stopped with the shields **4** and **5**.

Numerous examples of STIM applications were presented in [41]. It was shown that imaging using an incident ion beam at low grazing angles is insensitive to the atomic number or to the density as well as to the resistivity of materials, and RIM contrast is determined by surface morphology only. In particular, it was shown [41] that RIM can be used for imaging of an insulating surface without charge compensation, as demonstrated by the RIM image of a mica surface (Fig. 5.17).

The reason for the insensitivity of RIM to surface charging is not exactly known. One can speculate that some amount of reflected ions neutralize during interaction with the sample surface, so reflected neutrals are not affected by the electric field of the charged surface. At the same time, the probability of neutralization at a charged insulating surface is less than that of a conductive surface because of the low concentration of electrons.

A simple theory of RIM image formation was developed that, in particular, enables us to quantify surface step heights from experimental data. Below is a short version of this theory. The incident beam is considered as an infinitely narrow one.

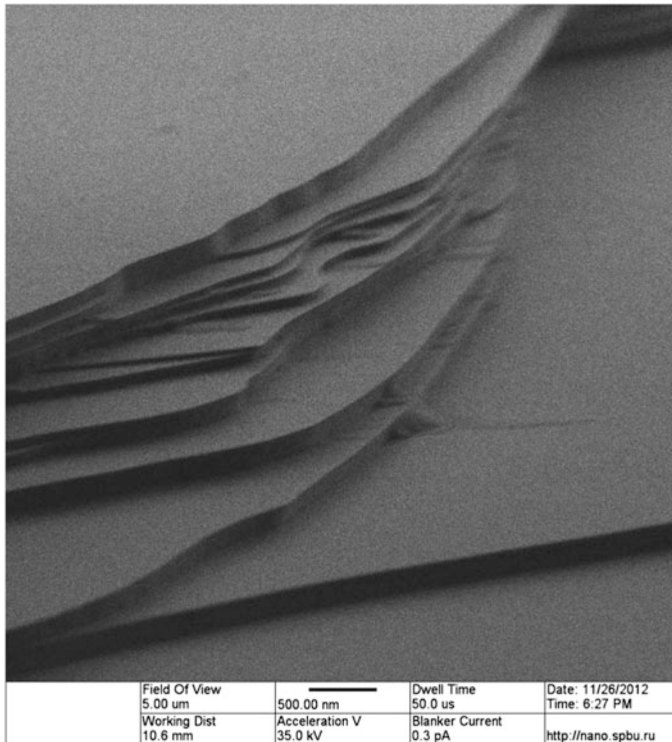

Fig. 5.17 RIM image of a cleaved mica surface

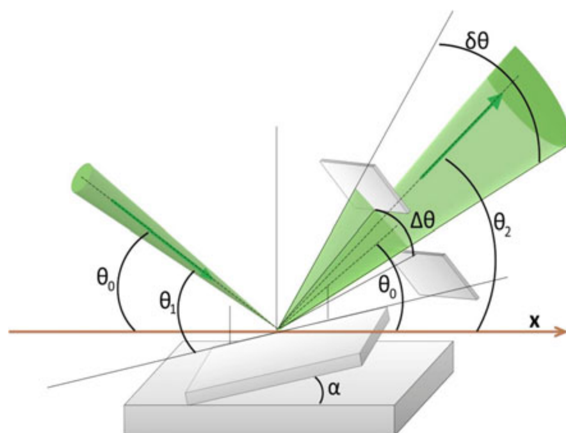

Fig. 5.18 Schematic diagram of incident and reflected ion paths from [41]. α is the angle between the specimen holder plane and a local detail of the specimen surface, Θ_0 is the grazing angle between the incident beam and the specimen plane, Θ_1 is the angle between the incident beam and a local detail of the specimen surface ($\Theta_1 = \Theta_0 + \alpha$), Θ_2 is the angle between the reflected beam and the specimen plane, $\Delta\Theta$ is the angular aperture of RI detection, $\delta\Theta$ is the half width of the angular divergence of RI

Figure 5.18 represents the paths of incident and reflected ion beams in RIM and the designations in the figure caption are used in the following calculations.

In RIM, the reflection coefficient, or reflected ion yield (RIY), is defined as the number of reflected ions per incident ion, which depends on the incident and reflected angles, and will be notated as $\eta(\Theta_1, \Theta_2)$. Note that BSI yield is just RIY at the fixed angles of 90°. It was shown [41] that the RI signal, which is the number of SE per second measured by the ET detector, is determined by RIY, and its angular dependence, the angular distribution of the reflected ions and the angular aperture of the diaphragm can be expressed as follows:

$$S(\alpha) = \frac{N_I \gamma_0}{2} \int_{\Theta_0 - \frac{\Delta\Theta}{2}}^{\Theta_0 + \frac{\Delta\Theta}{2}} \eta(\Theta_0 + \alpha,\ \Theta_2) \sin\, \Theta_2 d\Theta_2 \tag{5.19}$$

where N_I is the number of primary ions per second, $\gamma_0(\Theta_2)$—secondary electron yield for a Pt-coated surface.

The dependence $\eta(\Theta_1)$ for different materials as obtained [41] by Monte Carlo simulation with SRIM software [12] is presented in Fig. 5.19.

As can be seen from Fig. 5.19, the RIY is a monotonic decreasing function of the grazing angle that tends to constant values and depends on the material atomic number when the grazing angle approaches 90°. In contrast, when Θ_1 approaches zero the RIY tends to unity independent of the material. This is because nearly all of the incident ions pass over the specimen surface.

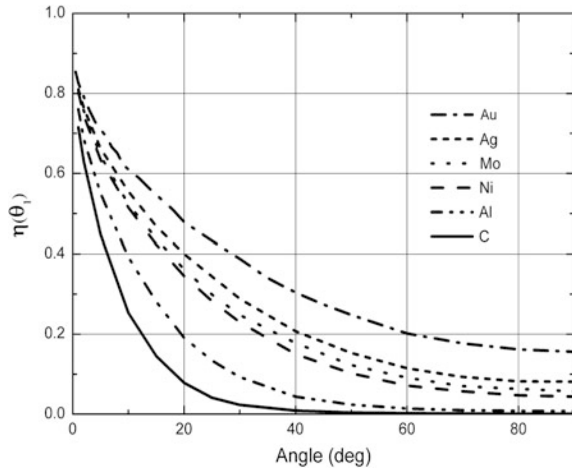

Fig. 5.19 Dependence of reflection coefficient of 35 keV He^{+} on the grazing angle for different materials calculated in [41] by Monte Carlo simulation with SRIM software [12]

When the sample surface is sufficiently smooth, i.e. the angular deviations of the reflected ions are so small that all of the reflected ions pass through the output diaphragm aperture and are collected with the ET detector, RI contrast is determined by the angular dependence of the reflection coefficient only. Under these conditions, the expression for the RI signal can be simplified as:

$$S(\Theta_1) = N_I \gamma_0 \eta_0(\Theta_1) \tag{5.20}$$

where $\eta_0(\Theta_1)$ is the RI reflection coefficient as a function of the grazing angle.

In the case of a rough surface, where the angle between the incident beam and local points on the surface varies across a wide range, some part of the RI are stopped by the diaphragm or by the elements of the specimen surface (shadowing effect). An example of such a situation is presented in Fig. 5.20, where the SE and RI signal profiles taken across the eminence of a square bar shape of a height of 20 nm are shown.

The edges of the bar are marked with arrows: the upward step and the edge of the downward step are marked with “u” and “d” correspondingly. The comparison of the SE profile (dashed line in Fig. 5.20a) and RI profile (solid line in Fig. 5.20a) reveal that the dark area in the RI image of the upward step was broader than the dark area in the SE image of the same step. The width of the bright area in the RI image of the downward step was found to be equal to the width of this area in the SE image.

A detailed calculation of the RI contrast at the upward and downward surface steps was presented in [41]. The shadowing effect and a finite aperture size result in dark areas on the image. These dark areas appear in the regions of a sample where $\alpha > \frac{\delta\Theta}{2} + \frac{\Delta\Theta}{4}$. It was shown that the height of the surface step could be calculated from the width of dark contrast in the RI image and the half width of the slit aperture as follows:

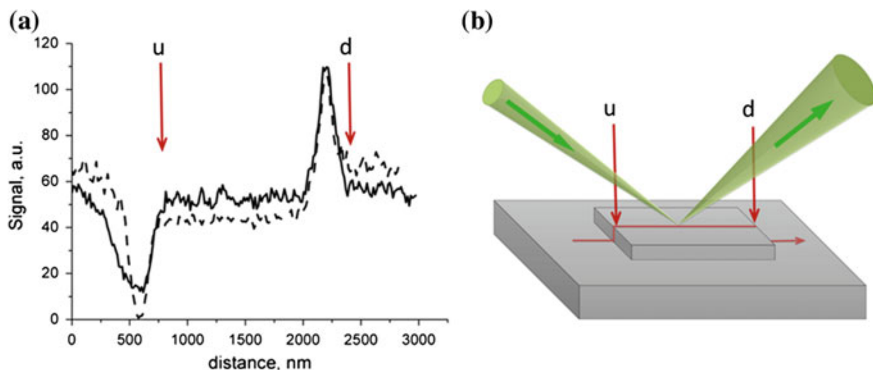

Fig. 5.20 **a**—signal profiles of secondary electrons (*dashed line*) and of reflected ions (*solid line*) across the silicon dioxide bar on silicon substrate measured as schematically shown in (**b**); *red arrows* mark the positions of upward (u) and downward (d) steps

$$h = \frac{d}{\cos\Theta_0 + \frac{\sin\Theta_0}{tg(\Theta_0 + \Delta\Theta)}} \tag{5.21}$$

where *d*—is the width of the dark contrast.

The shadowing contrast formation mechanism describes the RI signal from particular parts of the sample which faced towards the incident ion beam. In the opposite case the primary beam does not hit the surface immediately and, accordingly, no RI signal can be obtained from the scattered ions, except in the vicinity of knobs with sharp edges where the ion transmission may contribute to the image contrast formation. The idea of transmission contrast formation is described in [41]. The reflection coefficient of the primary beam from the upper surface is denoted as $\eta^*(\Theta_1, \Theta_2)$. The asterisk is used to emphasize that the reflection coefficient near the step edge differs from the reflection coefficient of the thick sample surface. Near the step edge, some part of the incident beam penetrates through it with the probability $\rho(\Theta_1, \Theta_3)$ and hits the substrate at an angle Θ_3 that is assumed to be close to the angle of incidence, i.e. $\Theta_3 \approx \Theta_1$. The transmitted ions are reflected from the substrate with reflection coefficient $\eta(\Theta_3, \Theta_2)$. Using these designations, the total reflection coefficient can be written as:

$$\eta_{edge}(\Theta_1, \Theta_2) = \eta^*(\Theta_1, \Theta_2) + \rho(\Theta_1, \Theta_3)\eta(\Theta_3, \Theta_2) \tag{5.22}$$

Figure 5.21 shows dependence of reflection and transmission coefficients as functions of the distance from the rectangular step edge along the top surface from [41]. The ion transmission probability (dotted line in Fig. 5.21) decreases from unity when the ion beam is just at the step edge. On the other side, the ratio of the ions reflected from the upper surface (dashed line in Fig. 5.21) increases with the distance from step edge. The total reflection coefficient calculated with (5.22) (solid

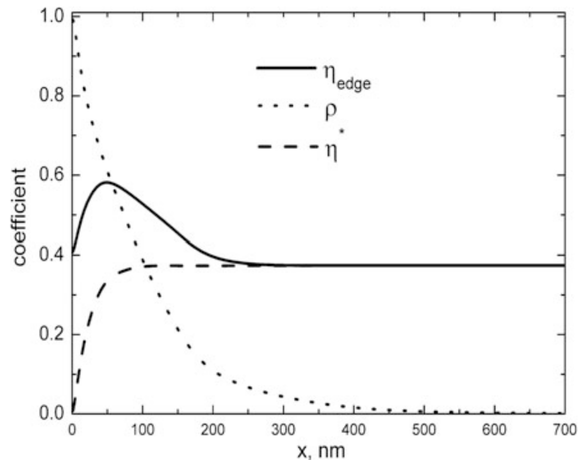

Fig. 5.21 Dependence of coefficients on the distance from the edge of the step: reflection coefficient from upper surface (*dashed line*), ion transmission probability (*dotted line*) and total reflection coefficient calculated with (5.10) (*solid line*) (angle of incidence is 10°) [41]

line in Fig. 5.21) exhibits a maximum at a distance of about 50 nm from the edge of the step, giving the bright contrast in the RI-image. The step height must be higher than $h > x_{\min} \tan \Theta_1$ to observe edge contrast.

The RI image formation mechanisms described above originate from ion scattering by the specimen relief and do not consider a possible impact of the surface potential produced by the interaction of the ions with the sample. Positive charging makes it impossible to use SE detection for imaging at both normal and at glancing ion incidence, but RI detection can be successfully used in this case. Generally, the angle of incidence changes due to the surface charging, so it should be taken into account for the metrology of the surface relief. As for accurate calculation of the step height from shadowing contrasts, it should be noted that the dependence of the width of a shadow on the angle of incidence according to (5.21) is rather weak for the experimental parameters used in RIM. In fact, a variation of the angle of incidence from 0° to 10° results in relative variation of the width of a shadow within few percentage points and does not affect the accuracy of the measurements.

5.6 Summary

Secondary electron generation is a very important process under both electron and helium ion bombardment, as their detection is the main imaging operation mode in SEM and HIM. In this chapter it was shown that there are several distinguishing features of that process in HIM caused by particular properties of ion–electron interaction in solids, such as a high total SE generation yield that might significantly exceed unity, a narrow SEED, and a low ratio of SE generated by backscattered ions, at least for the elements with atomic number less than that of gold. The

properties give rise to enhanced potential contrast sensitivity, enabling easy conversion of incident helium ion fluxes into electron current that has been used to characterize samples in transmission and reflection ion microscopy.

The number of examples of the application of these properties is not very large, to date. In addition, there is a lack of experimental data about SEED in many materials, including semiconductors and insulators. There are also many issues that are due to be solved in the future, such as a theory of SE generation which could satisfactorily explain the shape of the SEED in HIM, quantitative understanding of neutralization processes of the ions of the energy ranges of interest and many others. Obviously it will take time…

References

1. T.E. Everhart, R.F.M. Thornley, Wide-band detector for micro-microampere low-energy electron currents. J. Sci. Instrum. **37**(7), 246 (1960)
2. L. Reimer, *Scanning Eelectron Microscopy*, vol. 42 (Springer, Springer Series In Optical Science, 1985)
3. J. Goldstein, D.E. Newbury, D.C. Joy, C.E. Lyman, P. Echlin, E. Lifshin, L. Sawyer, J.R. Michael, *Scanning Electron Microscopy and X-ray Microanalysis* (Springer, US, 2003)
4. Seiler, H.: Secondary electron emission in the scanning electron microscope. J. Appl. Phys. **54**(11), R1−R18 (1983). doi:http://dx.doi.org/10.1063/1.332840
5. J. Cazaux, From the physics of secondary electron emission to image contrasts in scanning electron microscopy. J. Electron Microsc. **61**(5), 261–284 (2012). doi:10.1093/jmicro/dfs048
6. V. Sidorkin, E. van Veldhoven, E. van der Drift, P. Alkemade, H. Salemink, D. Maas, Sub-10-nm nanolithography with a scanning helium beam. J. Vac. Sci. Technol. B **27**(4), L18−L20 (2009). doi:http://dx.doi.org/10.1116/1.3182742
7. H.D. Hagstrum, Theory of auger ejection of electrons from metals by ions. Phys. Rev. **96**(2), 336–365 (1954)
8. R.A. Baragiola, E.V. Alonso, A.O. Florio, Electron emission from clean metal surfaces induced by low-energy light ions. Phys. Rev. B **19**(1), 121–129 (1979)
9. R. Ramachandra, B. Griffin, D. Joy, A model of secondary electron imaging in the helium ion scanning microscope. Ultramicroscopy **109**(6), 748–757 (2009). doi:http://dx.doi.org/10.1016/j.ultramic.2009.01.013
10. S.M. Ritzau, R.A. Baragiola, R.C. Monreal, Proton-induced kinetic plasmon excitation in Al and Mg. Phys. Rev. B **59**(23), 15506–15512 (1999)
11. R.A. Baragiola, C.A. Dukes, Plasmon excitation in ion–solid interactions. Nucl. Instrum. Methods Phys. Res., Sect. B **182**(1–4), 73–83 (2001). doi:http://dx.doi.org/10.1016/S0168-583X(01)00723-6
12. J.F. Ziegler, M.D. Ziegler, J.P. Biersack, SRIM—The stopping and range of ions in matter (2010). Nucl. Instrum. Methods Phys. Res. Sect. B-Beam Interact. Mater. Atoms **268**(11–12), 1818−1823 (2010). doi:10.1016/j.nimb.2010.02.091
13. D.C. Joy, S. Luo, R. Gauvin, P. Hovington, N. Evans, Experimental measurements of electron stopping power at low energies. Scanning Microsc. **10**(3), 653–666 (1996)
14. G. Lakits, F. Aumayr, M. Heim, H. Winter, Threshold of ion-induced kinetic electron emission from a clean metal surface. Phys. Rev. A **42**(9), 5780–5783 (1990)
15. P.C. Zalm, L.J. Beckers, Secondary electron yields from clean polycrystalline metal surfaces bombarded by 5−20 kev hydrogen or noble gas ions. Philips J. Res. **39**(3), 61–76 (1984)
16. J. Morgan, J. Notte, R. Hill, B. Ward, An introduction to the helium ion microscopy. Microsc. Today 24–31 (2006)

17. J. Morgan, J. Notte, R. Hill, B. Ward, An introduction to the helium ion microscopy. Microsc. Today 24–31 (2006)
18. T. Kaneko, Energy distribution of secondary electrons emitted from solid surfaces under electron bombardment: I. Theory. Surf. Sci. **237**(1–3), 327–336 (1990). doi:http://dx.doi.org/10.1016/0039-6028(90)90545-J
19. T. Kaneko, Secondary electron emission from metal surfaces by ion impact. Nucl. Instrum. Methods Phys. Res., Sect. B **67**(1–4), 655–658 (1992). doi:http://dx.doi.org/10.1016/0168-583X(92)95893-V
20. E.J. Sternglass, Theory of secondary electron emission by high-speed ions. Phys. Rev. **108**(1), 1–12 (1957)
21. K. Ohya, T. Yamanaka, K. Inai, T. Ishitani, Comparison of secondary electron emission in helium ion microscope with gallium ion and electron microscopes. Nucl. Instrum. Methods Phys. Res., Sect. B **267**(4), 584–589 (2009). doi:http://dx.doi.org/10.1016/j.nimb.2008.11.003
22. K. Inai, K. Ohya, T. Ishitani, Simulation study on image contrast and spatial resolution in helium ion microscope. J. Electron Microsc. (2007). doi:10.1093/jmicro/dfm024
23. M.S. Chung, T.E. Everhart, Simple calculation of energy distribution of low-energy secondary electrons emitted from metals under electron bombardment. J. Appl. Phys. **45**(2), 707–709 (1974). doi:10.1063/1.1663306
24. Yu.V. Petrov, O.F. Vyvenko, A.S. Bondarenko, Scanning helium ion microscope: distribution of secondary electrons and ion channeling. J. Surf. Inv. **4**(5), 792–795 (2010)
25. Yu. Petrov, O. Vyvenko, Secondary electron emission spectra and energy selective imaging in helium ion microscope. In: M.T. Postek, D.E. Newbury, S.F. Platek, D.C. Joy, T.K. Maugel (eds.) Scanning Microscopies 2011: Advanced Microscopy Technologies for Defense, Homeland Security, Forensic, Life, Environmental, and Industrial Sciences, Orlando, Florida, USA 2011, pp. 80360O-80310. SPIE
26. H. Kanter, Slow-electron mean free paths in aluminum, silver, and gold. Phys. Rev. B **1**(2), 522–536 (1970)
27. E.M. Baroody, A theory of secondary electron emission from metals. Phys. Rev. **78**(6), 780–787 (1950)
28. G. Behan, J.F. Feng, H.Z. Zhang, P.N. Nirmalraj, J.J. Boland, Effect of sample bias on backscattered ion spectroscopy in the helium ion microscope. J. Vac.Sci. Technol. A **28**(6), 1377–1380 (2010). doi:http://dx.doi.org/10.1116/1.3502667
29. J.I. Juaristi, R. Díez Muiño, A. Dubus, M. Rösler, Charge-state dependence of kinetic electron emission induced by slow ions in metals. Phys. Rev. A **68**(1), 012902 (2003)
30. K. Ohya, J. Kawata, Monte Carlo study of incident-angle dependence of ion-induced kinetic electron emission from solids. Nucl. Instrum. Methods Phys. Res., Sect. B **90**(1–4), 552–555 (1994). doi:http://dx.doi.org/10.1016/0168-583X(94)95612-X
31. J. Ferrón, E.V. Alonso, R.A. Baragiola, A. Oliva-Florio, Dependence of ion-electron emission from clean metals on the incidence angle of the projectile. Phys. Rev. B **24**(8), 4412–4419 (1981)
32. I.N. Evdokimov, E.S. Mashkova, V.A. Molchanov, D.D. Odintsov, Dependence of the Ion-electron emission coefficient on the angle of incidence. Phys.Status Solidi B **19**(1), 407–415 (1967). doi:10.1002/pssb.19670190141
33. V.Yu. Mikhailovskii, Yu.V. Petrov, O.F. Vyvenko, Energy filtration of secondary and backscattered electrons by the method of the retarding potential in scanning electron and ion microscopy. J. Synch. Investig. **9**(1), 196–202 (2015). doi:10.1134/s1027451014060378
34. C. Rodenburg, M.A.E. Jepson, B.J. Inkson, E. Bosch, A.K.W. Chee, C.J. Humphreys, Energy filtered scanning electron microscopy: Applications to dopant contrast. J. Phys: Conf. Ser. **209**(1), 012053 (2010)
35. O. Jbara, M. Belhaj, S. Odof, K. Msellak, E.I. Rau, M.V. Andrianov, Surface potential measurements of electron-irradiated insulators using backscattered and secondary electron spectra from an electrostatic toroidal spectrometer adapted for scanning electron microscope applications. Rev. Sci. Instrum. **72**(3), 1788–1795 (2001). doi:10.1063/1.1344596

36. C. Rodenburg, M.A.E. Jepson, B.J. Inkson, X. Liu, Dopant contrast in the helium ion microscope: contrast mechanism. In: R.T. Baker, (ed.) Electron Microscopy and Analysis Group Conference 2009, vol. 241 (2010). J. Phys. Conf. Ser.
37. C. Rodenburg, M.A.E. Jepson, A.B. Stuart, M.B. Darren, Helium ion microscopy and energy selective scanning electron microscopy—two advanced microscopy techniques with complementary applications. J. Phys: Conf. Ser. **522**(1), 012049 (2014)
38. B.L. Henke, J. Liesegang, S.D. Smith, Soft-x-ray-induced secondary-electron emission from semiconductors and insulators: models and measurements. Phys. Rev. B **19**(6), 3004–3021 (1979)
39. L. Reimer, B. Volbert, Detector system for backscattered electrons by conversion to secondary electrons. Scanning **2**(4), 238–248 (1979). doi:10.1002/sca.4950020406
40. A.R. Hall, In situ thickness assessment during ion milling of a free-standing membrane using transmission helium ion microscopy. Microsc. Microanal. **19**(03), 740–744 (2013). doi:10.1017/S1431927613000500
41. Yu.V. Petrov, O.F. Vyvenko, Scanning reflection ion microscopy in a helium ion microscope. Beilstein J. Nanotechnol. **6**, 1125–1137 (2015). doi:10.3762/bjnano.6.114
42. V.Yu. Mihkailovki, Yu.V. Petrov, unpublished

Part II
Microscopy

Chapter 6
Introduction to Imaging Techniques in the HIM

Stuart A. Boden

Abstract The helium ion microscope (HIM), as the name implies, is primarily an imaging tool. This chapter serves as an introduction to imaging with the HIM and explores the various ways this is implemented by first describing the numerous imaging signals and contrast mechanisms available and then giving an overview of some practical HIM imaging techniques. Several examples from the literature are used to illustrate the important imaging modes including high resolution secondary electron imaging, backscattered ion imaging, ionoluminescence imaging and imaging with transmitted or reflected ions. Key concepts such as ion channeling, charge neutralization and utilizing the large depth of field are introduced, setting the scene for the subsequent chapters in this section that focus on particular aspects of HIM imaging.

6.1 Introduction

The primary use of the helium ion microscope is as a high resolution surface imaging tool with similar applications to the more established scanning electron microscope (SEM). Over recent years, the application space for the HIM has expanded into the territory of focused ion beam (FIB) tools and some remarkable nanoengineering capabilities have been demonstrated. These will be covered later in the book (see Part IV). The focus for this chapter will be on the imaging capabilities of the HIM.

In the HIM, helium atoms are ionized in the high electric field concentrated around three tungsten atoms (the ‘trimer’) at the tip of source. This creates three ‘beamlets’, one of which is directed, by tilting the gun housing, down the column, through an aperture and various beam steering and focusing optics to be brought to focus on the surface of a sample in the main chamber. The atomic size and high brightness of the helium ion source together with the large momentum (and so smaller de Broglie wavelength) of helium ions compared to electrons, means that the resultant probe size on the sample is smaller than what can be achieved with a focused electron beam in a scanning electron microscope. This, coupled with the

S.A. Boden (✉)
Electronics and Computer Science, University of Southampton, Highfield, Southampton, UK
e-mail: sb1@ecs.soton.ac.uk

© Springer International Publishing Switzerland 2016

G. Hlawacek and A. Gölzhäuser (eds.), *Helium Ion Microscopy*,
NanoScience and Technology, DOI 10.1007/978-3-319-41990-9_6

reduced lateral and back-scattering of the beam as it enters a sample leads to a small interaction volume and hence high resolution images. Furthermore, the beam divergence angle is 5–10 times smaller than in an SEM, leading to a larger depth of field and so the ability to capture in sharp focus highly structured three dimensional (3D) surfaces. Charge neutralization can be achieved through the use of an integrated electron flood gun so that the benefits of high resolution and large depth of field can be realized in images of insulating samples.

This chapter begins with a survey of the different signals generated by the helium beam when it interacts with a sample, with a overview of the contrast mechanisms involved when images are formed from these signals and some examples illustrating practical applications of the concepts discussed. Various imaging techniques that have been developed for the HIM are then described, where more detail is given on using the system for high resolution imaging, achieving effective charge neutralization and taking full advantage of the large depth of field to extract 3D information from highly structured samples. The aim is to give an overview of imaging with the HIM, setting the scene for more in-depth analysis of particular techniques in the other chapters of this section.

6.2 Imaging Signals and Contrast Mechanisms

The process of image formation in the HIM follows the same principle as for an SEM: The primary beam is directed onto a point on the sample surface, a signal is measured whilst the beam dwells on this point and then this is converted to a grey scale value to display as a pixel on the viewing screen. The beam is then shifted to an adjacent point on the sample and the process is repeated. Thus, the image is constructed, pixel-by-pixel, as a two dimensional map of the intensity of a signal generated by the interaction of the beam with the sample. There are a number of different signals emitted as a result of the interaction of the focused helium beam with a sample and these can be used to form images that reveal or highlight different aspects of the sample structure and composition. These signals include secondary electrons, backscattered ions, transmitted ions, reflected ions and photons.

6.2.1 Secondary Electrons

By far the most commonly used signal for imaging in scanning beam microscopes is that of secondary electrons (SEs) and the helium ion microscope is no exception. Secondary electrons are sample electrons that are excited through energy transfer from the primary beam. They generally have energies less than 50 eV and those that are generated close to the surface and with sufficient energy will escape from the sample and can be detected. Detection of secondary electrons is achieved with an Everhart Thornley (ET) detector mounted in the HIM chamber in a similar configuration to an SEM. Some of the advantages of HIM over SEM lie in the differences in the nature of the detected secondary electron signal. Differences between HIM and

SEM arise in the overall SE yield, the contribution of SEs generated by backscattered particles and the interaction volume from which the SE signal originates. An overview of these concepts is given below. For a more detailed discussion of these concepts, see Chap. 5.

SE Yield

The rate of secondary electron generation is proportional to the instantaneous stopping power of the sample material on the beam, i.e. the rate that energy is lost from the beam as it travels through the material. The stopping power for helium ions (and ions in general) is greater than for electrons and so more SEs are generated per unit path length. This results in an increase in the SE yield for HIM compared to SEM. In practice this leads to a higher signal-to-noise ratio for a given beam current or lower beam currents being required to achieve a reasonable signal-to-noise ratio. The SE yield is also known to vary considerably depending on the target material, much more so than for SEM. For example, Morgan et al. showed experimental HIM SE yield variations of between 2 and 8 for a range of different target materials, highlighting the enhanced compositional contrast this provides [1].

Backscattered Contribution

In SEM, SEs generated by backscattered electrons, termed the 'SE_2 component', comprise a significant proportion of the total SE signal, increasingly so as the beam energy is increased. These SE_2s can be generated some distance away from the primary beam impact zone, resulting in a delocalization of the signal and consequently a reduction in resolution. In HIM, the backscattered contribution is small and so the total SE signal is dominated by SEs that are generated by the primary beam. This ensures that the high resolution afforded by the small probe size transfers into the detected SE signal and therefore into the image.

Interaction Volume

Upon entering the sample, the helium beam initially loses energy through interactions with the sample electrons. Due to the higher mass of a helium ion, large angle scattering events are rare in this region and there is little divergence of the beam within the first few tens of nanometers from the surface. There are various freely-available Monte Carlo simulation programs which reveal the differences in interaction volumes for electron and helium ion beams. As an example, Fig. 6.1 presents Monte Carlo results of a 1 keV electron beam and a 30 keV helium beam interacting with an infinitely-thick silicon target. (The reason that a 30 keV helium ion beam is often compared with a 1 keV electron beam is discussed in the Sect. 6.2.1.1). The electron beam data is calculated from CASINO v2.48 [2] and the helium ion beam data from SRIM 2008 [3]. The plots show that the helium beam scatters far less and so remains more tightly focused as it travels through the first few tens of nanometers of material. For more information on Monte Carlo simulations applied to helium ion microscopy, see Chap. 4.

Secondary electrons are generated along the path of the beam but the probability, $P_{esc}(z)$, that an SE will be generated with sufficient energy to escape the sample

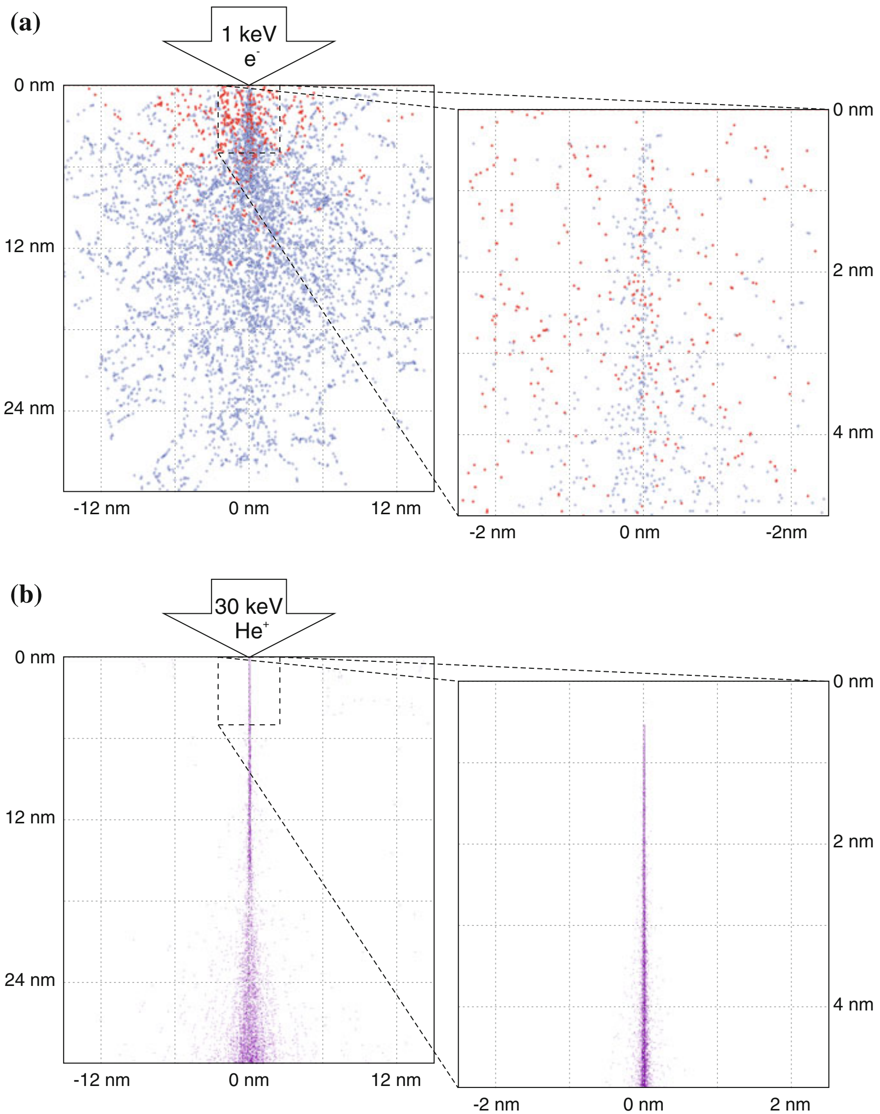

Fig. 6.1 Monte Carlo simulations illustrating scattering events of 1000 particles entering a silicon substrate for **a** a 1 keV electron beam (CASINO v2.48 [2]), where *red* indicates backscattering collisions and *blue* indicates forward scattering collisions and **b** a 30 keV helium ion beam (SRIM 2008)

decreases exponentially with the distance, z, from the point of generation to the surface [4], i.e.

$$P_{esc}(z) = C \exp(-z/\lambda) \tag{6.1}$$

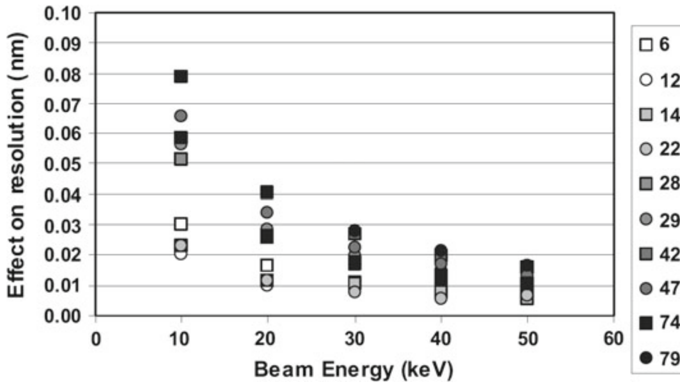

Fig. 6.2 Effect on image resolution of helium ion beam spread due to scattering of beam as it enters a sample versus beam energy for various target materials, indicated by atomic number shown in the legend. (Reprinted with permission from [5]. Copyright 2010, American Vacuum Society.)

where C is a constant and λ, the effective diffusion length for SEs, is around 1 nm for most solids [5]. The result is a cylindrical interaction volume from which the SE signal originates, restricted in radius by the small probe size and in depth by the SE escape depth. Sijbrandij et al. demonstrated through SRIM calculations that the effect of beam spread on image resolution in the HIM is dependent on beam energy and target atomic number (see Fig. 6.2) but is approximately one order of magnitude smaller than the resolution limit for the tool [5]. The effect decreases further as beam energy is increased. In contrast, for SEM, there is considerable scattering of the primary beam as it interacts with sample electrons near to the surface. This results in a larger interaction volume and therefore a lower resolution compared to HIM.

6.2.1.1 Contrast Mechanisms for SE Images

We have established that a SE signal is emitted from a sample due to interaction with a helium ion beam and that the characteristics of this process results in higher resolution images. In this section, we will examine how variations in the sample can lead to differences in the SE signal and hence contrast in the image.

Topographic Contrast

Topographic contrast arises in an image as the beam scans over areas of a surface with varying local degrees of tilt with respect to the incident beam and the ET detector. It produces images that are easily interpretable by the untrained eye as a three dimensional representation of the surface of a sample, despite the rather abstract way in which the image is formed. It is therefore the contrast mechanism exploited in most HIM images, as it is with SEM.

In SEM, the secant law is used to describe the variation of SE yield, δ, with surface tilt angle and hence the origin of topographic contrast, θ, i.e.

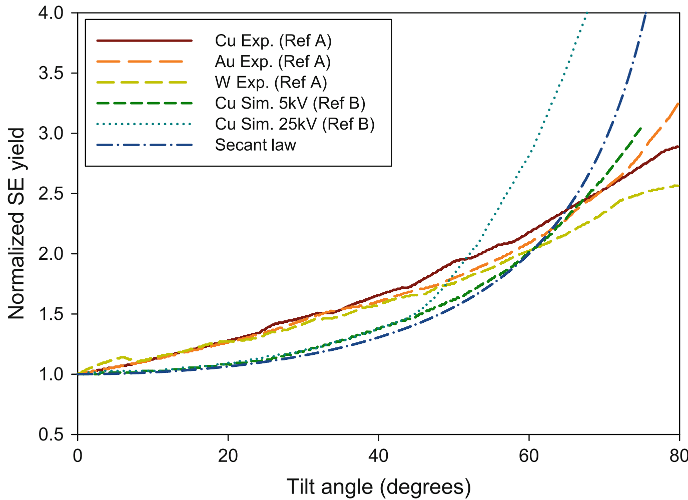

Fig. 6.3 Plot of normalized SE yield versus tilt angle for various sample materials with data taken from two sources: Ref A. is experimental data from Bell [6] (beam energy unspecified) and Ref B is simulation data taken from Ramachandra et al. [7]. The secant relationship is also plotted

$$\delta = \delta_0 \sec(\theta) \tag{6.2}$$

where δ_0 is the SE yield at zero tilt. It has been shown experimentally that for HIM, the trend differs somewhat from the secant law [6] (see Fig. 6.3). There are variations with material but the general trend is more linear than that described by (6.2), with higher SE yields at low angles and lower yields at high angles. In another study, simulations predict that the trend also varies with beam energy and can exhibit a steeper yield versus angle curve than described by the secant law [7]. In general, the variation of SE yield with angle, although often less dramatic than with SEM, is still sufficient to generate clear topographic contrast.

The appearance of an SE image depends on from how deep in the sample the detected SEs originate. Due to the higher stopping power and negligible SE_2 contribution associated with HIM, a greater proportion of the detected SEs are generated near to the surface, resulting in an enhancement in surface detail compared to SEM. Surface sensitivity in SEM is increased by reducing beam energy and therefore HIM images resemble low voltage SEM images, with the advantage of a higher resolution. This is clearly seen in Fig. 6.4 where 15 and 1 keV SEM images of a highly textured 'black' silicon surface are shown alongside a 30 keV HIM image. The 30 keV HIM image shows a superior level of surface detail compared to the 15 keV SEM image and is similar in appearance to the 1 keV SEM image, but with noticeably sharper features due to the smaller probe size and smaller number of high angle scattering events as the beam interacts with the sample.

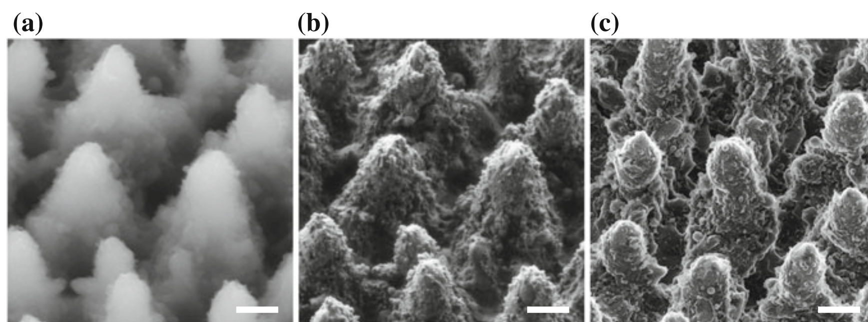

Fig. 6.4 Two SEM images (captured using a Carl Zeiss NVision40 with Gemini FEGSEM column) and one HIM image (captured using a Carl Zeiss Orion Plus HIM) of a highly textured silicon surface, taken with a specimen tilt angle of 42°: **a** SEM at 15 keV, **b** SEM at 1 keV and **c** HIM at 30 keV. All three scale bars are 1 µm

Compositional/Elemental Contrast

Secondary electron yield varies more strongly with target material for an incident ion beam compared to an incident electron beam. Consequently, compared to those from SEM, HIM images tend to exhibit greater contrast range when several different materials are present [8]. Modelling work carried out by Ramachadra et al. supports this with Monte Carlo simulations (IONiSE) predicting an SE yield for HIM that varies with sample composition to a greater extent than in SEM [4]. This is also seen in the experimental data in Fig. 6.3 where the degree of deviation from the secant rule of SE yield versus tilt angle differs depending on the target material. In combination with the high surface sensitivity of the technique, this can be exploited to reveal differences in composition at the monolayer level. Examples include observing contrast between areas of patterned self-assembled monolayer films where the only compositional difference is a reduction of the NO_2 to NH_3 in the top surface terminal group [8] and visualizing different surface terminations (Si or Ti) on epitaxial Ti_3SiC_2 films (Fig. 6.5) [9].

Ion Channeling Contrast

Although mostly a topic for backscattered ion imaging, crystallographic orientation can also provide contrast in HIM secondary electron images. Polycrystalline metal surfaces appear as a patchwork of grains with different greyscale levels in a HIM SE image due to their different crystallographic orientations with respect to the incident beam [10]. The mechanism behind the observed contrast involves the reduction in hard collisions with the lattice atoms necessary to excite SE when the ions are incident along low index planes of the crystalline lattice. Ions traveling through grains oriented in channeling directions will undergo fewer collisions per unit path length and therefore the SE yield from these grains will be low. Conversely, grains oriented away from channeling directions will present a more densely-packed projection of lattice atoms to the incident beam, resulting in more SE generating collisions within the escape depth and so a higher SE yield. Veligura et al. demonstrated that contrast

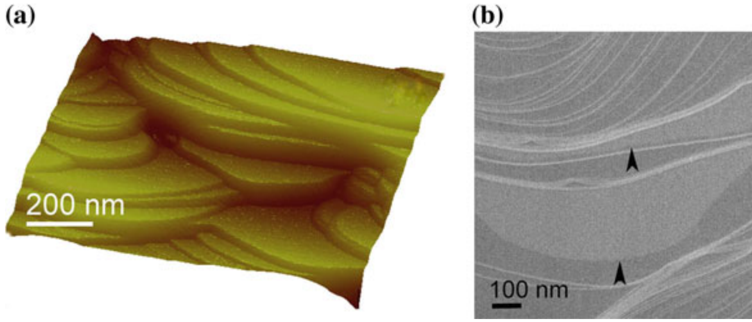

Fig. 6.5 Steps on an epitaxial Ti_3SiC_2 film grown on SiC: **a** AFM image showing step heights as multiples of unit cells or half unit cells, **b** HIM SE image demonstrating strong compositional contrast and surface sensitivity, with the *arrows* showing changes in contrast due to changes in surface termination from Si to Ti, as expected for half or full unit cells of Ti_3SiC_2 (Reprinted from [9], Copyright 2011, with permission from Elsevier)

variations with grain orientation can be accurately predicted using a simple geometric projection model and that this can lead to mapping of grain orientation from an azimuthal series of SE images (see Fig. 6.6). For more details on ion channeling contrast in SE mode, see Sect. 9.2.

Dopant Contrast

Contrast due to variations in doping concentration across a sample surface has been studied in low voltage SEM instruments for many years, however the resolution limits of the SEM mean that dopant distributions in modern nanoscale devices are beyond its capabilities. The contrast mechanism here relies on differences in built-in potential at a p-n junction due to differences in dopant concentration either side of

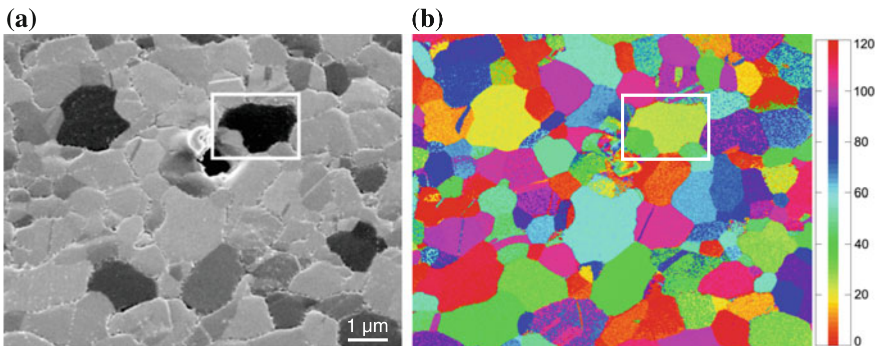

Fig. 6.6 **a** HIM SE image of annealed polycrystalline gold film taken with a 14 keV primary beam energy and an ion dose of 4.9×10^{14} cm^{-2}, with a 35° sample tilt angle at which the $\langle 110 \rangle$ direction is aligned with the incoming beam; **b** colour-coded map of grain orientation determined from an azimuthal series of SE images, an example from which is shown in (**a**) (adapted from [10] under the Creative Commons Attribution License 2.0)

the junction. This affects the probability of SEs escaping from the surface and so the number reaching the detector. Dopant contrast has also been studied in the HIM, driven by the promise of higher resolution images of dopant variations [11–13]. It was found that whilst less sensitive to low concentrations of dopant, HIM provided improved sensitivity to changes in high concentrations of dopant compared with the low voltage SEM technique [12]. Some degree of quantification was also demonstrated with a linear relationship observed at high doping levels between the logarithm of the dopant concentration difference and the observed contrast. Differences in dopant contrast between HIM and SEM were assigned to differences in sensitivity to the influence of surface states and associated band bending. Later studies revealed however that resolution in images exploiting dopant contrast is often limited by the depletion region width of the p-n junction rather than the probe size of the instrument and so the smaller probe size of the HIM would provide higher resolution images of dopant contrast only where the depletion region is very thin. An alternative approach that utilizes the difference in oxidation rates of p and n type silicon to convert differences in dopant concentration to differences in oxide thickness has also been developed [13]. This process uses the integrated plasma cleaner present in many HIM instruments to perform in-situ oxidation of the surface and effectively convert dopant contrast to materials contrast. The resolution is then limited by the sharpness of the interface between different thicknesses of oxide and not by the depletion region width.

Static Capacitive Contrast

Another contrast mechanism involving changes to the surface fields and their subsequent effect on SE emission is that of static capacitive contrast (SCC) [14, 15]. Again, this effect has been observed in SEM and, along with the closely related technique of capacitive coupling voltage contrast, is used for characterizing conducting lines buried beneath an insulating layer in integrated circuits [16]. The surface field present on an insulating surface is reduced by the presence of a buried conducting line below it, allowing more SEs to escape from this region and therefore this region to appear brighter in the image. Furthermore, the effect is dependent on the capacitance and so on the depth of the buried line from the surface. Preliminary studies suggest that SCC is more prominent in HIM compared to SEM due to the fact that the SE energy distribution has a peak at lower energies for HIM and therefore the generated SEs are more sensitive to subtle local variations in surface fields [14]. More information on this is available in Chap. 19. This 'through dielectric imaging' has been demonstrated on conductive lines buried as deep as 200 nm below the surface [17], although the exact mechanism for the observed contrast is not yet fully understood.

6.2.2 Backscattered Ions

Using light ions such as helium in a scanning beam microscope enables images to be formed from the ions that are scattered back out of the sample after collision

with a heavier sample atom (Rutherford scattering). Such backscattered ion imaging is not useful with gallium FIB instruments because the heavy gallium ions rarely encounter a heavier atom in the sample off which to backscatter. This imaging mode is analogous to backscattered electron imaging in SEM and likewise can be used in the helium ion microscope to give greater compositional contrast and to probe to greater depths in a sample. However, this is at the expense of topographic contrast, surface sensitivity and resolution.

The yield of backscattered helium ions (BSHe) is typically several orders of magnitude less than the yield of SEs. As mentioned previously, this is advantageous for SE imaging because it means that the SE_2 contribution that often limits resolution in SEM is much smaller in HIM. However, this also means that when attempting to use the BSHe signal for imaging, the detector efficiency is key to maximizing the useful information available from this relatively weak signal [18, 19]. An annular microchannel plate (MCP) is employed on most HIM systems to detect backscattered ions. This is attached to a retractable arm so that it can be inserted between the sample and the pole piece, with the beam passing through the centre. The wide collection angle of the MCP and the gain mechanism achieved by secondary electron avalanches through the chevron configuration of the microchannels ensures efficient detection of the backscattered ions. Nevertheless, due to the low yield from the sample, BSHe images tend to be noisier than their corresponding SE images. An overview of the various contrast mechanisms available for backscattered ions is given below. For a more detailed discussion of these mechanisms, see Sect. 9.3.

6.2.2.1 Elemental/Compositional Contrast

The BSHe imaging mode provides greater compositional contrast than the SE mode due to the strong dependance of the backscattered coefficient on the size of the target nuclei. Topographic contrast is not so strong in BSHe mode because the nature of ion-nucleus interaction is less dependent on surface slope. Studies have shown that BSHe yield does not monotonically increase with target material atomic number, as may be expected from a simple treatment of scattering from increasingly large nuclei [14, 20]. Rather, the BHSe yield versus atomic number trend exhibits oscillations that map well to rows of the periodic table but mean that unambiguous identification of target material through BSHe contrast alone is not possible.

Channeling Contrast

Channeling contrast is often exploited in ion and electron microscopy to reveal information on the relative crystallographic orientation of grains within a polycrystalline sample. In Sect. 6.2.1.1, this was described for SE imaging in the HIM but it is also used in backscatter mode. The mechanism arises from the variation in how far an ion can travel through a sample when it is moving in different directions with respect to the columns of atoms in the target lattice. When the beam is aligned to a crystallographic axis, the cross-section for nuclear scattering is reduced and so fewer ions are scattered back out of the sample. Conversely, in other orientations, the projection of sample atoms to the incoming beam is such that it increases scattering probability

and the BSHe yield increases as a result. This effect has been demonstrated on polished metallographic samples [6], where it is comparable to channeling contrast in SEM and FIB, and in nanoparticle imaging where, in one example, areas thought to be separated by a twin grain boundary on a single nanoparticle were distinguished [18].

The possibility of exploiting this channeling effect for quantitative crystallographic orientation mapping using the BSHe signal has also been discussed [21]. In an approach analogous to Electron Backscatter Diffraction (EBSD) in SEM, it has been suggested that ion blocking patterns formed by imaging exiting BSHe ions from a tilted sample could be used in the same way as Kikuchi Patterns are used in EBSD to map out grain orientation. However, to the author's knowledge, this has not yet been practically implemented.

Bulk Versus Surface Imaging

The BSHe signal includes information from deeper in the sample when compared with the SE signal which originates from only the top few nanometers. The maximum depth at which helium ions can be backscattered and still reach the detector varies considerably with sample material and beam energy but is typically 10–100 s of nanometers below the surface. BSHe yield increases as beam energy is decreased, as does the depth to which He ions penetrate and therefore the depth from which the BSHe signal originates. Therefore, lower beam energies tend to be used for BSHe imaging compared to imaging in SE mode where higher energies increase SE yield. The larger bulk signal in BSHe can be used to reveal the presence of heavier structures buried under material of a lower atomic weight [6]. Furthermore, this can be used to complement SE images captured of the same area to distinguish between surface and sub-surface features. In one example, Hlawacek et al. used this method to distinguish between the gold core and a lighter ~1.5 nm cetryltrimethylammonium-bromide coating in agglomerations of nanorods [18].

Although, as discussed, BSHe imaging is usually associated with signals from deeper within a sample, there are certain circumstances in which imaging in backscattered mode can be used to characterize very thin surface layers. Hlawacek et al. demonstrated that sub-monolayer coverage can be detected in a BSHe image through a dechanneling mechanism whereby the thin layer decreases the channeling probability and therefore increases the BSHe yield [22]. This particular study was made possible because the chamber was modified in order to reduce the base pressure to UHV levels (10^{-9} mbar) and so significantly reduce surface hydrocarbon contamination compared to standard HIM systems.

A more detailed exploration of BSHe imaging and channeling effects can be found in Chap. 9.

6.2.3 Transmitted and Reflected Ions

If an appropriately-designed sample holder is used and a sufficiently thin specimen is examined then the HIM can be operated in scanning transmission ion microscopy

(STIM) mode. The simplest realization of this is to mount a thin sample on a TEM grid and then position a metallic plate, coated with a high SE yielding material, underneath the sample, with the plate's surface normal tilted towards the ET detector. Helium ions that penetrate through the sample will generate SEs in the plate causing the resulting area of the image to appear brighter. This approach has been used to monitor the milling of nano-sized pores through thin gold films and to image the resulting nanopores in order to confirm complete penetration (Fig. 6.7a) [23]. It has also been demonstrated on arrays of 5 nm diameter pores milled in silicon nitride membranes for biomolecule detection applications (see Chap. 18) [24].

With a more sophisticated STIM detector design, it is possible to distinguish between bright field and dark field transmitted ion signals and secondary electron signals from the top side or rear side of the sample [14]. This was used to image MgO crystals in transmission mode, revealing thickness fringes analogous to those observed in transmission electron microscopy (TEM) and the presence of dislocations within the crystal lattice (Fig. 6.7b, c) [25]. These features in STIM are however more difficult to interpret and analyze than in TEM due to the greater number of Bragg diffraction events and smaller Bragg angles resulting from the ion beam interaction with the sample.

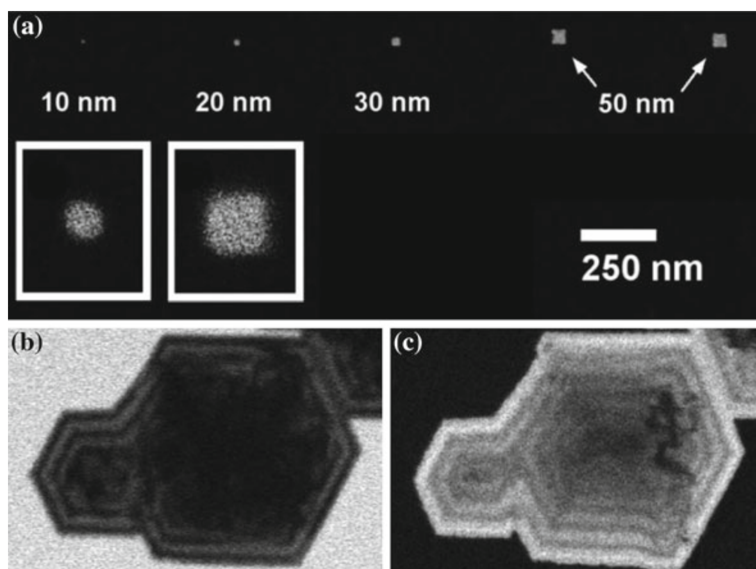

Fig. 6.7 Examples of helium ion microscopy images taken in transmission mode: **a** Image of vias milled through a thin gold film. The insets show ×10 magnified views, captured separately, of the 10 and 20 nm vias [23]; **b** Bright-field image of MgO crystal (FOV = 200 nm) [25]; **c** Dark-field image of MgO crystal shown in (**b**) [25]. (Image **a** is reprinted with permission from [23]. Copyright 2010, American Vacuum Society. Images **b** and **c** are reproduced with permission from [25].)

Another change in sample mount configuration can facilitate the operation of the helium ion microscope in reflection ion microscope (RIM) mode. Here, the sample is tilted so that the primary ion beam is incident at grazing incidence and an aperture is positioned to allow only the reflected ions to hit a platinum coated surface and produce an SE signal. This approach is partly motivated by the ability of the electron equivalent technique (reflection electron microscopy) to resolve atomic steps on surfaces [26]. An investigation by Petrov et al. revealed that RIM imaging is not sensitive to composition but rather topographic contrast dominates [27]. The technique can be used to produce sharp images of an insulating surface without charge compensation and whilst atomic resolution of surface steps was not demonstrated, further developments in the sample mount and detector design, together with a higher vacuum in the chamber, could make this possible in the future. More information on using the HIM in reflection and transmission modes can be found in Chap. 5.

6.2.4 Photons

Ionoluminescence (IL) in HIM is the emission of light as a result of electron energy transitions caused by the helium ion beam interacting with certain types of sample. The emission can be extrinsic, i.e. resulting from energy transitions in impurities within a sample such as rare-earth ions, or intrinsic, i.e. from the bulk of the sample itself in the form of interband transitions or emission from defects. This phenomenon was first observed in crystals of NaCl [28] and further studies revealed the mechanism involved the ion induced formation and then subsequent relaxation of defects known as colour centres within the crystals [29]. Ionoluminescence in the HIM has been demonstrated with a wide range of samples including thin film direct band gap semiconductors [19], agglomerations of semiconductor quantum dots, rare earth doped bulk and nanocrystal samples [30], SiO_2 [31] and even mouse teeth impregnated with organic fluorophores [32].

Ionoluminescence can be studied with the same type of detectors used for cathodoluminescence detection and analysis in SEM. To illustrate the various modes available for IL, the example of cerium/terbium doped lanthanum phosphate nanocrystals is presented in Fig. 6.8 [30]. In panchromatic imaging mode, light from the sample is coupled into a photomultiplier tube and an image generated pixel-by-pixel of the variation in luminescent intensity with position on the sample (Fig. 6.8b). Filters can be inserted to image over restricted spectral regions and these can be combined with a simultaneously-collected SE image to produce a composite colour image of luminescence from a sample (Fig. 6.8 c). Alternatively, the emitted light can be directed through a spectrometer for spectral analysis (Fig. 6.8d).

In addition to fundamental studies of beam-sample interactions and modifications, the technique has potential for use in immunofluorescence imaging with higher resolution compared to photon or electron based methods. More detail on the generation and analysis of ionoluminescence in HIM is given in Chap. 14.

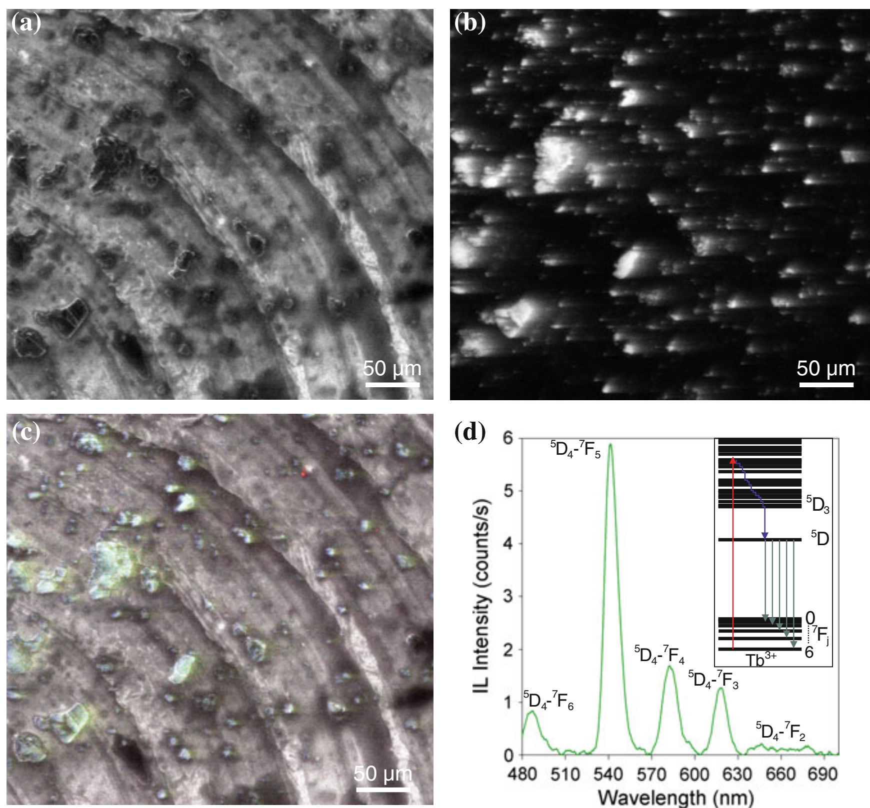

Fig. 6.8 HIM images and IL spectrum from agglomerated Ce/Tb doped $LaPO_4$ nanocrystals: **a** SE image, **b** panchromatic IL image, **c** composite image constructed from filtered IL images and SE image, **d** IL spectrum showing peaks due to f electron transitions in the Tb^{3+} dopant ions (adapted with permission from [30])

6.3 HIM Imaging Techniques

This section explores examples of imaging techniques that exploit one or more of the contrast mechanisms described previously, giving details on their practical implementation.

6.3.1 High Resolution Imaging

When discussing HIM, often the first benefit mentioned is its high resolution imaging capability. The sub-nm probe size and limited number of high angle scattering events experienced as the beam travels through the first few 10 s of nanometers of the sample

restricts the interaction volume in the lateral direction and the low energy spread of the generated SEs restricts it in the vertical direction. The result is that detected SEs originate from only a small volume near the surface of a sample and therefore the technique is capable of high resolution imaging. Note that the same argument does not apply in backscattered imaging mode because unlike SEs, BSHe that reach the detector can originate from collisions 10 to 100 s of nanometers below the surface, resulting in a larger interaction volume and therefore a lower resolution. For this reason, the highest resolution images in HIM are obtained in SE mode.

For the highest resolution images, the primary beam energy should be maximized and the beam current minimized, whilst ensuring that the signal to noise ratio is still sufficiently high. For best results in the Zeiss Orion HIM, a beam current of <0.2 pA is used. This is generally done by using a small mid-column aperture (typically 10 μm) and a high spot control, which has the effect of positioning the beam cross-over point further up the column, away from the aperture, so that less of the beam passes through the aperture. There are two reasons to minimize beam current when attempting high resolution imaging. Firstly, sample sputtering rates and damage due to implanted helium scale with the areal dose. High resolution imaging requires high magnifications (small fields of view); a low beam current minimizes areal dose and therefore damage to the sample during image capture. Secondly, the level of hydrocarbon contamination build-up in the area being imaged also scales with dose. This problem is well know in SEM, particularly for low primary beam energies, and is thought to result from field-enhanced mobility of hydrocarbons towards the area being imaged and subsequent 'cracking' of the hydrocarbons, forming a thin layer [33]. Using a He ion beam exasperates this problem because contamination layer growth is faster and, with the high surface sensitivity of the technique, the unwanted material has a more pronounced effect on the image and can quickly obscure features of interest.

Hydrocarbon contamination is the main enemy when attempting sub-nm resolution imaging in the HIM. Therefore, in addition to using a small beam current, sample cleanliness is of paramount importance to achieving good results. If possible, solvent cleans and vacuum bakes should be performed prior to loading samples into the HIM. Often, an in-situ remote plasma cleaner is used on the sample in the load lock during the loading procedure. This attachment regulates the load lock pressure at $\sim$0.5 Torr and generates a low power ($\sim$10 W) plasma from an air feed. The oxygen radicals generated in the plasma diffuse around the load lock, reacting with hydrocarbon contamination and creating volatile organic molecules that are pumped away by the vacuum system. The technique can also be used periodically on the chamber itself, where an overnight series of plasma cleans and nitrogen purges can ensure hydrocarbon contamination in the chamber is minimized [34]. For some samples it is necessary to perform multiple remote plasma cleans but care should be taken with delicate samples to ensure that the plasma does not significantly damage/modify features of interest. On the other hand, for some samples, it is possible to use the plasma cleaner to controllably modify surfaces, revealing more detail in the nanostructure. An example of this is the visualization of the nanoscale compositional variation in organic photovoltaic polymer thin films reported by Pearson et

al.. Here, in-situ plasma cleans were used to remove material from the surface and gain access to the bulk nanostructure [35].

Quantification of image resolution in HIM can be performed using an edge resolution technique. The edge of an atomically-sharp graphene flake protruding from a HOPG (Highly Ordered Pyrolytic Graphite) sample is imaged at a high magnification and line profiles showing the contrast change with distance cutting across the edge are extracted. The distance over which the contrast changes from 25 to 75% of its final value is measured and given as the edge resolution. If the flake edge is sufficiently sharp then this gives a measure of the probe size of the beam. An example of this is shown in Fig. 6.9a, where an edge resolution of 0.3 nm is measured as an average using 132 locations along the edge. As a comparison, high performance SEMs are typically capable of achieving an edge resolution of ∼1 nm whereas TEM can achieve sub-angstrom edge resolution. HIM therefore sits in between these two techniques in terms of probe size. More detail on imaging 2D materials such as graphene can be found in Chaps. 11 and 12.

Quantification and comparisons of resolution in surface images of thick specimens is more tricky because it is often dependent on the sample. Resolution standards such as gold particles on a carbon substrate are often presented to show high surface resolution [8, 37, 38]. An example of high resolution HIM imaging on a non-standard sample is shown in Fig. 6.9b, where a mesoporous silica film fabricated by electrochemically assisted surfactant assembly (EASA) is imaged in SE mode [36]. The image shows clearly resolved pores which run perpendicular to the sample surface with diameters of only 2–3 nm.

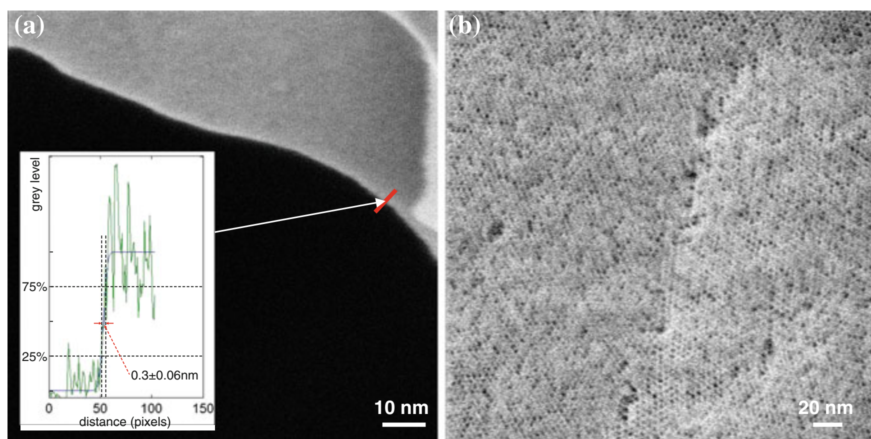

Fig. 6.9 High resolution HIM images of **a** a graphene flake protruding from HOPG with an inset showing an edge resolution measurement; **b** porous silica sample, with pore pitch of 2–3 nm. Details of the sample can be found in [36]

6.3.2 Charge Neutralization

In SEM, imaging of electrically insulating materials is complicated by the accumulation of surface charge. This is caused by an imbalance in the negative charge arriving at the surface in the form of the incident beam and that which leaves through the emission of SEs. This changes the local potential of the area under the beam, which can affect the emission of SEs and the trajectories of the electrons in the primary beam. This gives rise to various charging artifacts in an image, obscuring the true surface structure of the sample. Methods to mitigate charging in SEM include coating the sample with a thin conductive layer, using low voltages and currents to balance the charges entering and exiting the sample and the introduction of an inert gas into the chamber in a so-called 'environmental' or 'variable/extended pressure' mode.

Insulating samples also charge up under the beam in HIM but as the incident beam is positively charged and the exiting species is negative secondary electrons, then the surface charge is always positive. This has the effect of creating a larger potential barrier for the SEs to overcome in order to be emitted from the sample and so results in a low signal and dark images. Fortunately, the fact that only positive charge develops means that an electron flood gun can be used to neutralize the charge accumulated on insulating samples in HIM. An electron flood gun is a standard attachment in most HIM systems. It directs a diffuse beam of low energy electrons onto the sample area being imaged in pulses that can be interlaced with the ion beam scan by line or by frame. By carefully adjusting the energy, pulse duration and positioning of the flood gun beam, charge build up on a sample can be prevented and high signal-to-noise images of uncoated insulating samples can be captured.

An example of charge neutralization with the electron flood gun is shown in Fig. 6.10 where the silicon core of an optical fibre is imaged with and without the flood gun operating. The core is clad in an insulating silica material and so is electrical isolated from the ground. Under the helium beam, the surface develops a positive charge and the resultant image appears dark due to suppression of SE emission (Fig. 6.10a). With the flood gun operating, the positive charge is neutralized and a clear image is acquired (Fig. 6.10b). The inset to Fig. 6.10b illustrates that high resolution imaging is possible in this mode, with sub 10 nm features clearly resolvable.

Charge neutralization with the electron flood gun in the HIM is particularly useful for imaging biological samples where structures tend to be made from non-conductive materials such as the polymer chitin. These specimens can be coating with thin layers of metal but this may obscure fine features on the surface. Likewise, low voltage and environmental modes used for charge neutralization in SEM often sacrifice resolution for mitigation of charging effects. The electron flood gun approach in the HIM enables high resolution imaging of the native sample surface and has been used to study various specimens from the biological world ranging from butterfly wing scales [39] (see Fig. 6.11) and blood clot microstructures [40] to

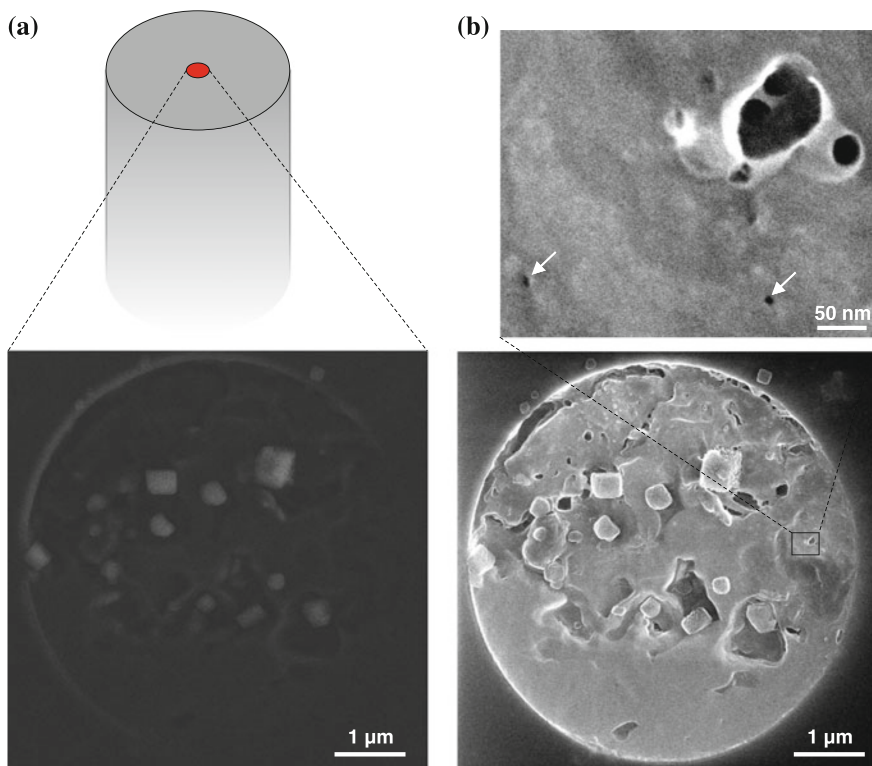

Fig. 6.10 Images illustrating that charge neutralization during HIM imaging of insulating materials can be achieved using the electron flood gun: **a** an image of the end of an optical fibre comprising a silicon core clad in silica; **b** the same area with the flood gun operating and optimized. The inset is a zoom on an area of the silicon core, revealing sub-10 nm features (indicated by *white arrows*) and so demonstrating that high resolution imaging is possible when using the electron flood gun

human cancer cells [41], predator nematodes (roundworms) [42] and parasites invading kidney cells [43]. A more detailed exploration of HIM on biological samples is presented in Chap. 7.

6.3.3 Imaging with a Large Depth of Field

One striking feature of HIM SE images is the large depth of field—a result of the small convergence angle of the helium beam afforded by the atomic scale source. This allows features over a wide range of working distances to be captured in sharp focus within a single image. SEM is considered to be an imaging technique with a large depth of field compared to optical microscopy but blurring of features in the background compared to those in the foreground is still observed, increasingly so

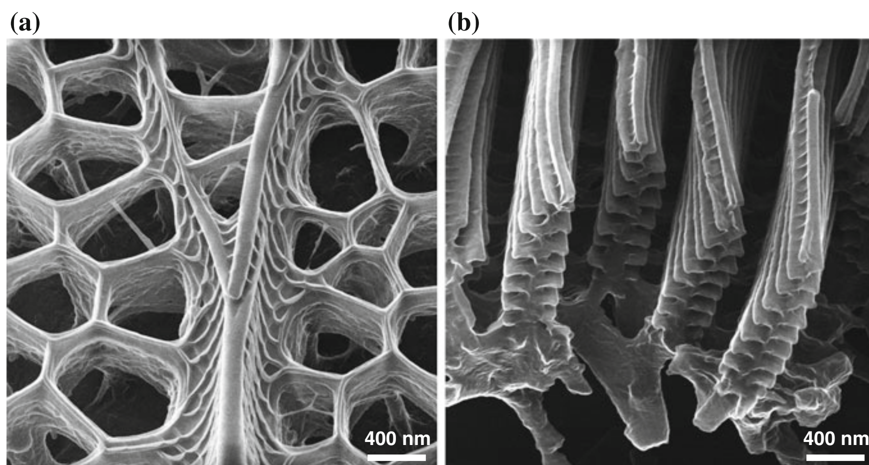

Fig. 6.11 HIM SE images of uncoated wing scale structures of two species of butterfly where the electron flood gun was used to neutralize surface charge during imaging: **a** *Papilio ulysses* (reproduced with permission from [39]); **b** *Morpho rhetenor*

when imaging at high tilt angles and with low accelerating voltages. With a depth of field of 5–10 times that of SEM, HIM images are less prone to this. This has proven to be particularly useful in imaging of biological specimens which tend to be highly structured in three dimensions [42].

The HIM's large depth of field has also proven to been advantageous in the extraction of three dimensional information using a stereo imaging approach [39]. This method, which has been used in photography and SEM for many years, involves collecting two images of the same area at different tilt angles. These form a 'stereo pair', i.e. two images that when placed side-by-side and viewed using a stereoscope (or relaxing the eyes and focusing 'beyond' the plane), allow the viewer to perceive a three dimensional effect [44]. Alternatively, by applying different coloured filters to each image in the pair, an anaglyph can be generated and viewed using filtered spectacles. The large depth of field of the HIM results in a stronger 3D effect because the features remain in focus as the viewer observes different parts of the image. Furthermore, heights or depths of features can be quantified by analyzing lateral separations in each image of the stereo pair. This technique was demonstrated on image pairs taken of an area of a butterfly wing and the calculated heights were shown to compare well with direct measurements using cross-sectional TEM [39]. Examples of HIM stereo pairs and anaglyphs for two different biological samples, a blood clot microstructure and a cancer cell trapped in a micro-cavity, are presented in Figs. 6.12 and 6.13. Another example of where the large depth and high resolution of the HIM is put to good use is presented in Chap. 8, where a study of nascent soot particles is described.

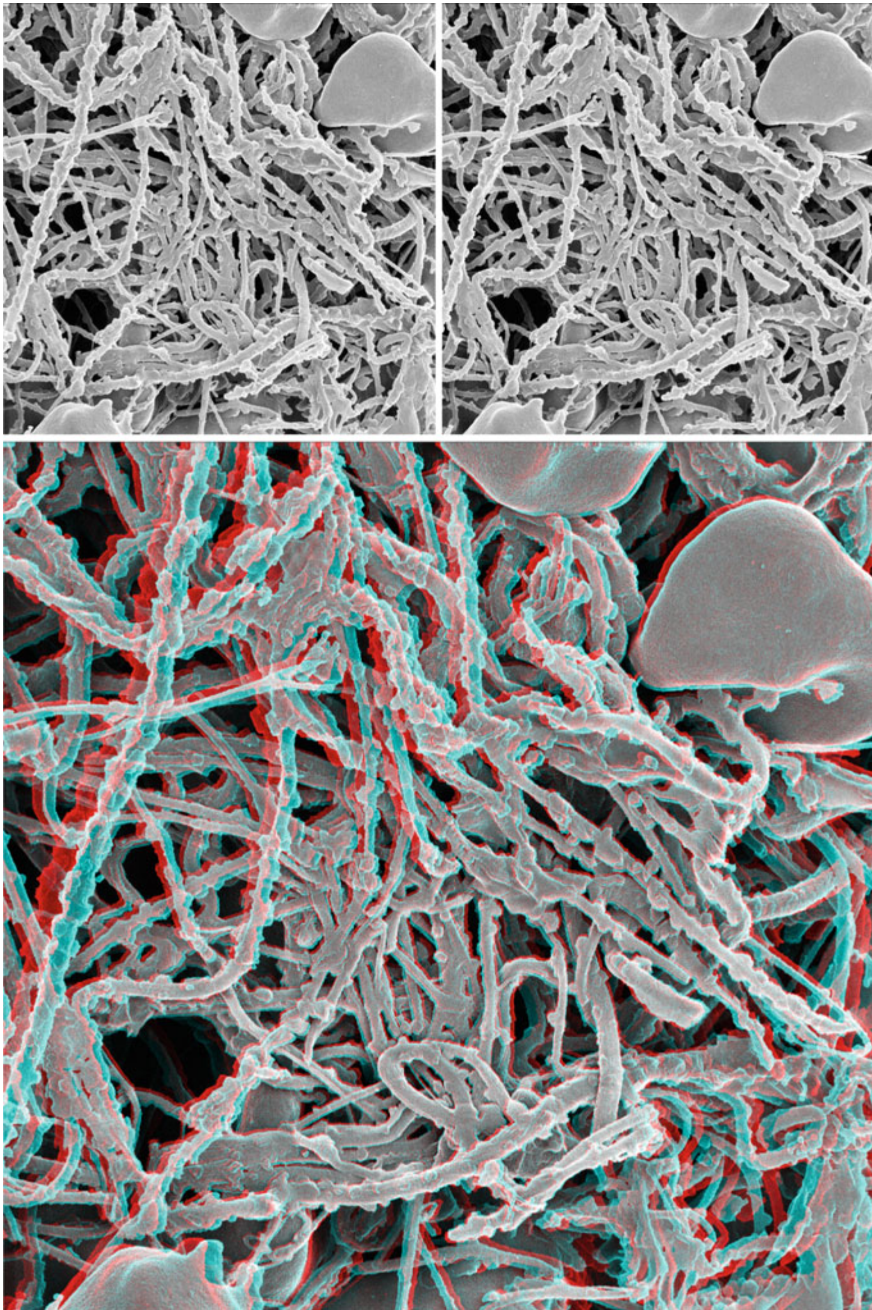

Fig. 6.12 HIM SE images of blood clot microstructure (details of the sample can be found in [40]). The *top* two images form a stereo pair and were captured with a tilt angle difference of 6° and a field of view of 14 μm. The *bottom* image is a *red-cyan* anaglyph formed as a composite of the stereo pair. The 3D effect can be observed using *red/cyan* filtered spectacles (*left eye cyan*, *right eye red*)

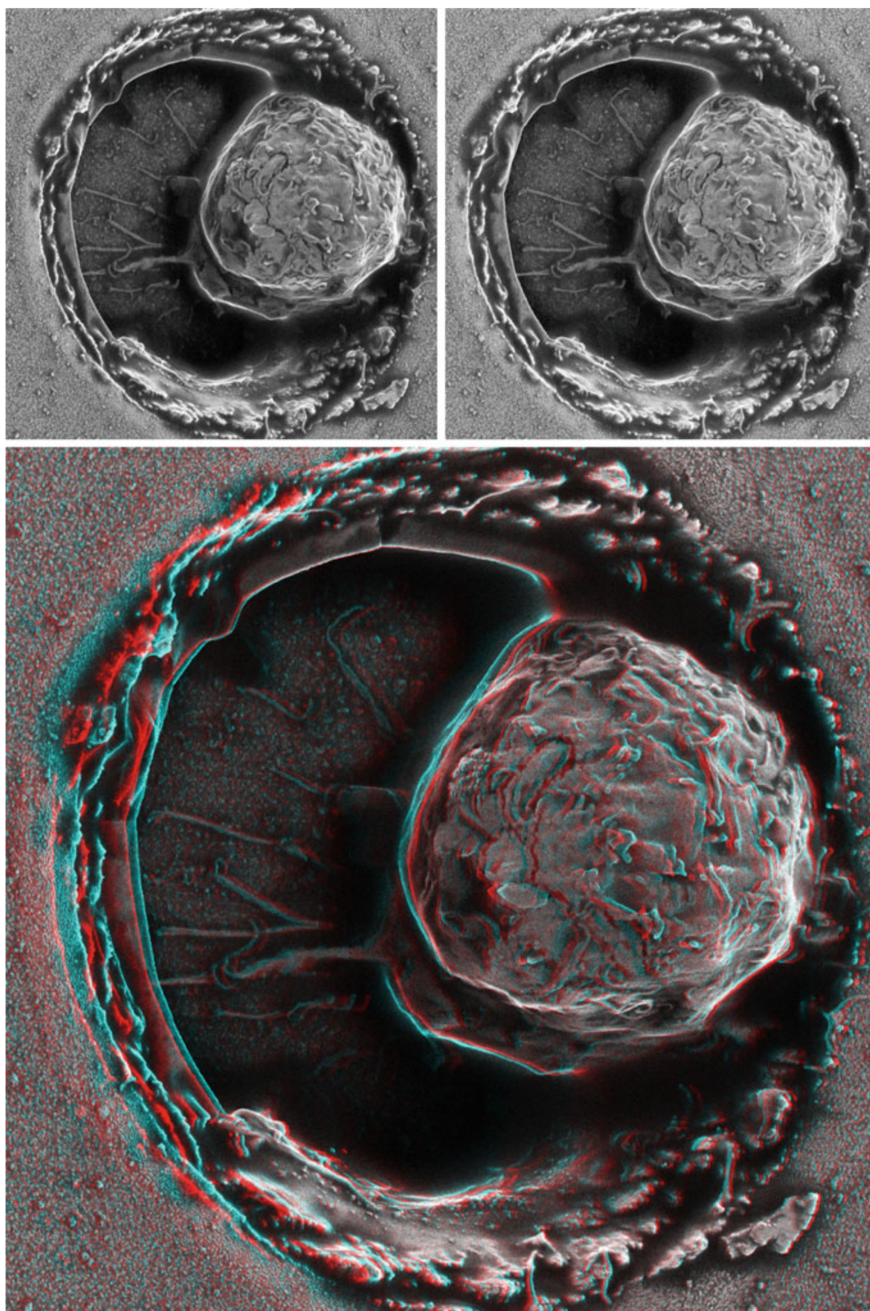

Fig. 6.13 HIM SE images of a Ramos B cell trapped within a polymer micro-cavity (details of the sample can be found in [45]). The *top* two images form a stereo pair and were captured with a tilt angle difference of 6° and a field of view of 20 μm. The *bottom* image is a *red-cyan* anaglyph formed as a composite of the stereo pair. The 3D effect can be observed using *red*/*cyan* filtered spectacles (*left eye cyan*, *right eye red*)

6.4 Conclusions

The emergence of helium ion microscopy as a surface imaging technique has seen it applied in a wide range of fields over a relatively short period of time. Researchers have explored ways of exploiting the variety of different signals and contrast mechanisms available with the technique to produce information-rich images, reaching beyond what is possible with more-established electron beam methods. Secondary electron imaging in HIM takes advantage of the sub-nm probe size and subsequent minimal interaction volume to resolve ultra-fine surface features. Backscattered ion imaging can reveal further information on differences in composition and grain orientation. Imaging with and analysis of ions transmitted through thin samples, or of photons emitted during helium ion bombardment of luminescent samples, can provide further insights into sample characteristics. Moreover, the ability to neutralize surface charge and the large depth of field capabilities make HIM highly suitable for imaging samples from the natural world. Subsequent chapters in this section will delve into more detail concerning particular imaging modes and applications developed over recent years. However, the technique is still in its infancy and it is expected that with further developments in instrumentation and with the increasing availability of systems, HIM imaging will find applications in many more research fields in the years to come.

References

1. J. Morgan, J. Notte, R. Hill, B. Ward, Microsc. Today **14**(4), 24 (2006)
2. D. Drouin, A.R. Couture, D. Joly, X. Tastet, V. Aimez, R. Gauvin, Scanning **29**(3), 92 (2007)
3. J.F. Ziegler, J.P. Biersack, M.D. Ziegler, *SRIM—The Stopping and Range of Ions in Matter* (SRIM Co., 2008). http://www.srim.org
4. R. Ramachandra, B. Griffin, D. Joy, Ultramicroscopy **109**(6), 748 (2009). doi:10.1016/j.ultramic.2009.01.013
5. S. Sijbrandij, J. Notte, C. Sanford, R. Hill, J. Vacuum Sci. Technol. B: Microelectron. Nanometer Struct. **28**(6), C6F6 (2010). doi:10.1116/1.3497012
6. D.C. Bell, Microsc. Microanal. **15**(2), 147 (2009). doi:10.1017/S1431927609090138
7. R. Ramachandra, B.J. Griffin, D.C. Joy, in *Proceedings of SPIE*, vol. 6922, ed. by J.A. Allgair, C.J. Raymond (2008), pp. 69,221W–69,228W. doi:10.1117/12.772300
8. L. Scipioni, L.A. Stern, J. Notte, S. Sijbrandij, B. Griffin, Adv. Mater. Process. **166**(6), 27 (2008)
9. K. Buchholt, P. Eklund, J. Jensen, J. Lu, A.L. Spetz, L. Hultman, Scripta Materialia **64**(12), 1141 (2011). doi:10.1016/j.scriptamat.2011.03.013
10. V. Veligura, G. Hlawacek, R. van Gastel, H.J.W. Zandvliet, B. Poelsema, Beilstein J. Nanotechnol. **3**, 501 (2012). doi:10.3762/bjnano.3.57
11. M.A.E. Jepson, B.J. Inkson, C. Rodenburg, D.C. Bell, EPL (Europhys. Lett.) **85**(4), 46001 (2009). doi:10.1209/0295-5075/85/46001
12. M. Jepson, B. Inkson, X. Liu, L. Scipioni, C. Rodenburg, EPL (Europhys. Lett.) **86**(April), 26005 (2009). doi:10.1209/0295-5075/86/26005
13. M. Jepson, X. Liu, D. Bell, D. Ferranti, B. Inkson, C. Rodenburg, Microsc. Microanal. **17**, 637 (2011). doi:10.1017/S1431927611000365

14. L. Scipioni, C.A. Sanford, J.A. Notte, B. Thompson, S. McVey, J. Vac. Sci. Technol. B: Microelectron. Nanometer Struct. **27**(6), 3250 (2009). doi:10.1116/1.3258634
15. R.H. Livengood, M. Grumski, Y. Greenzweig, T. Liang, R. Jamison, Q. Xie, Physics Procedia **1**(1), 143 (2008). doi:10.1016/j.phpro.2008.07.089
16. R.J. Feng, H.B. Zhang, K. Ura, J. Electron Microsc. **52**(5), 455 (2003)
17. S. Ogawa, W. Thompson, L. Stern, L. Scipioni, J. Notte, L. Farkas, L. Barriss, Jpn. J. Appl. Phys. **49**(4), 04DB12 (2010). doi:10.1143/JJAP.49.04DB12
18. G. Hlawacek, I. Ahmad, M.A. Smithers, E.S. Kooij, Ultramicroscopy **135**, 89 (2013). doi:10.1016/j.ultramic.2013.07.010
19. G. Hlawacek, V. Veligura, R. van Gastel, B. Poelsema, J. Vac. Sci. Technol. B: Microelectron. Nanometer Struct. **32**(2), 020801 (2014). doi:10.1116/1.4863676
20. S. Sijbrandij, B. Thompson, J.A. Notte, B.W. Ward, N.P. Economou, J. Vac. Sci. Technol. B: Microelectron. Nanometer Struct. **26**(6), 2103 (2008). doi:10.1116/1.2993262
21. R.A. Schwarzer, Microsc. Today **16**(1), 34 (2008)
22. G. Hlawacek, V. Veligura, S. Lorbek, T.F. Mocking, A. George, R. van Gastel, H.J.W. Zandvliet, B. Poelsema, Beilstein J. Nanotechnol. **3**, 507 (2012). doi:10.3762/bjnano.3.58
23. L. Scipioni, D.C. Ferranti, V.S. Smentkowski, R.A. Potyrailo, J. Vac. Sci. Technol. B: Microelectron. Nanometer Struct. **28**(6), C6P18 (2010). doi:10.1116/1.3517514
24. J. Yang, D.C. Ferranti, L.A. Stern, C.A. Sanford, J. Huang, Z. Ren, L.C. Qin, A.R. Hall, Nanotechnology **22**(28), 285310 (2011). doi:10.1088/0957-4484/22/28/285310
25. J.A. Notte, R. Hill, S.M. McVey, R. Ramachandra, B.J. Griffin, D.C. Joy, Microsc. Microanal. **16**(05), 599 (2010). doi:10.1017/S1431927610093682
26. A.V. Latyshev, A.L. Aseev, A.B. Krasilnikov, S.I. Stenin, Surf. Sci. **213**(1), 157 (1989)
27. Y.V. Petrov, O.F. Vyvenko, Beilstein J. Nanotechnol. **6**, 1125 (2015). doi:10.3762/bjnano.6.114
28. L. Scipioni, L. Stern, J.A. Notte, Microsc. Today **15**(6), 12 (2007)
29. V. Veligura, G. Hlawacek, R. van Gastel, H.J.W. Zandvliet, B. Poelsema, Journal of Physics. Condens. Matter: Inst. Phys. J. **26**(16), 165401 (2014). doi:10.1088/0953-8984/26/16/165401
30. S.A. Boden, T.M.W. Franklin, L. Scipioni, D.M. Bagnall, H.N. Rutt, Microsc. Microanal. **18**(6), 1253 (2012)
31. S. Ogawa, T. Iijima, S. Awata, R. Sugie, N. Kawasaki, Y. Otsuka, Microsc. Microanal. **18**(Supplement S2), 814 (2012). doi:10.1017/S1431927612005922
32. T.M.W. Franklin, Scanning Ionoluminescence Microscopy with a Helium Ion Microscope. Ph.D. thesis (University of Southampton, 2012)
33. J.I. Goldstein, D.E. Newbury, D.C. Joy, C.E. Lyman, P. Echlin, E. Lifshin, L. Sawyer, J.R. Michael, in *Scanning Electron Microscopy and X-ray Microanalysis*, 3rd edn. (Springer Science + Business Media, Inc., New York, 2003), chap. 5, p. 203
34. D.C. Bell, M.C. Lemme, L.A. Stern, C.M. Marcus, J. Vac. Sci. Technol. B: Microelectron. Nanometer Struct. **27**(6), 2755 (2009). doi:10.1116/1.3237113
35. A.J. Pearson, S.A. Boden, D.M. Bagnall, D.G. Lidzey, C. Rodenburg, Nano Lett. **11**(10), 4275 (2011). doi:10.1021/nl202269n
36. C. Robertson, R. Beanland, S.A. Boden, A.L. Hector, R.J. Kashtiban, J. Sloan, D.C. Smith, A. Walcarius, Phys. Chem. Chem. Phys. **17**(6), 4763 (2015). doi:10.1039/C4CP05730A
37. M.T. Postek, A.E. Vladár, Scanning **30**(6), 457 (2008). doi:10.1002/sca.20129
38. D. Joy, *Helium Ion Microscopy: Principles and Applications*, 1st edn. (Springer, New York, 2013)
39. S.A. Boden, A. Asadollahbaik, H.N. Rutt, D.M. Bagnall, Scanning **34**(2), 107 (2011). doi:10.1002/sca.20267
40. M.J. Lawrence, S. Kumar, K. Hawkins, S. Boden, H. Rutt, G. Mills, A. Sabra, R.H.K. Morris, S.J. Davidson, N. Badiei, M.R. Brown, P.R. Williams, P.A. Evans, Thromb. Res. (2014). doi:10.1016/j.thromres.2014.05.039
41. D. Bazou, G. Behan, C. Reid, J.J. Boland, H.Z. Zhang, J. Microsc. **242**(3), 290 (2011). doi:10.1111/j.1365-2818.2010.03467.x

42. M.S. Joens, C. Huynh, J.M. Kasuboski, D. Ferranti, Y.J. Sigal, F. Zeitvogel, M. Obst, C.J. Burkhardt, K.P. Curran, S.H. Chalasani, L.A. Stern, B. Goetze, J.A.J. Fitzpatrick, Sci. Rep. **3**, 3514 (2013). doi:10.1038/srep03514
43. W. de Souza, M. Attias, J. Struct. Biol. **191**(1), 76 (2015). doi:10.1016/j.jsb.2015.05.003
44. J.I. Goldstein, D.E. Newbury, P. Echlin, D.C. Joy, C.E. Lyman, E. Lifshin, L. Sawyer, J.R. Michael, *Scanning Electron Microscopy and X-ray Microanalysis*, 3rd edn. (Springer Science + Business Media Inc, New York, 2003)
45. K.S. Kiang, J. Zekonyte, D.A. Johnston, S.A. Beers, M.S. Cragg, S.A. Boden, I.M. Anteney, H.M.H. Chong, in *Proceedings of the 40th Conference on Micro and Nano Engineering* (Lausanne, CH, 2014)

Chapter 7
HIM of Biological Samples

Armin Gölzhäuser and Gregor Hlawacek

Abstract Due to its charge compensation capabilities the imaging of insulating sample is a natural application of Helium Ion Microscopy. The imaging of biological samples often requires complicated sample preparation methods who's influence on the sample structure is not always fully understood. In this chapter we will present a number of recent studies from the aforementioned field that make use and demonstrate the benefits of Helium Ion Microscopy for these research topics. These examples also demonstrate the large depth of focus that distinguishes the method.

7.1 Introduction

Since the early days of medicine and life science, the analysis of organs, tissue, and cells was aided by microscopic investigations to determine their structure and to discriminate between functional and dysfunctional biological matter. For this, the structure of membranes, the morphology of tissue and the distribution of proteins therein play important roles. Since the invention of the light microscope, biological samples have been analysed with the help of magnified images. The development of electron microscopy since the 1930s was consequently accompanied by the utilization of electron micrographs in biology. Nowadays, fluorescence microscopy is the most frequently used tool for the imaging of tissue and cells, followed by electron microscopy. Both fluorescence an electron microscopy have their drawbacks: fluoresce microscopy requires a labelling of the biomaterial, which allows the identification of specific binding sites and provides superb resolution. However, labelling

A. Gölzhäuser (✉)
Physics of Supramolecular Systems and Surfaces, Bielefeld University,
33615 Bielefeld, Germany
e-mail: ag@uni-bielefeld.de

G. Hlawacek
Institute for Ion Beam Physics and Materials Research,
Helmholtz–Zentrum Dresden–Rossendorf,
Bautzner Landstr. 400, 01328 Dresden, Germany
e-mail: g.hlawacek@hzdr.de

© Springer International Publishing Switzerland 2016

G. Hlawacek and A. Gölzhäuser (eds.), *Helium Ion Microscopy*,
NanoScience and Technology, DOI 10.1007/978-3-319-41990-9_7

also requires additional preparation steps and fluorescence micrographs only show the position of the labels and not the overall morphology of a cell. Transmission electron microscopy that routinely used in medicine also needs special preparation (thin cuts) and only provides a view through two-dimensional slices of tissue. Conversely, the scanning electron microscope offers a view on the complete cell morphology. However, SEM images of insulating biomaterials often show blur, as the trajectories of secondary electrons are affected by electrostatic charging. This can be avoided by coating the entire cell surface by a conductive (metal or carbon) coating. However, at high magnification a conductive coating changes the cell's appearance and morphology and is thus not adequate for an imaging of cell surfaces.

7.2 Large Depth of Field Bioimaging

A Helium Ion Microscope can provide sharp images from electrically insulating biological samples without a conductive coating. This is achieved by a special charge compensation, in which the positive charge that is deposited by the He^+ beam is neutralized by a simultaneous deposition of electrons that is balancing the charge of the incoming helium ions and the outgoing secondary electrons.

This has been visualized by Schürmann et al. [1], who compared HIM images of coated and uncoated biological samples at different magnifications. In Fig. 7.1 an example of neural crest-derived stem cells (NCSCs) from the human respiratory mucosa [2] is shown. Figure 7.1a–c shows images of NCSC-derived human neurons with and Fig. 7.1d–f without an initial gold coating.

In specimens sputter–coated with gold (Au) with a typical thickness of approx. 10 nm, the cell membrane is covered with clustered Au, masking the cell surface. Conversely, HIM images of uncoated, native–state cell membranes revealed numerous pit–like membrane inhomogeneities or domains with varying diameters that are not visible in coated cells. This is best seen by comparing the high magnification HIM images in Fig. 7.1c, f. The conductive coating is completely covering the nanoscale morphology of the cell surface; hence, in SEM images of coated samples, details seen at high resolution (beyond 100 nm) can simply not be trusted.

Armed with the capability of charge compensation, the HIM is well suited to successfully image complex biological specimen with sub–nanometer resolution. Figure 7.1f shows that the outer surface of the cell is not homogeneous but contains circular (or almost circular) nanodomains with diameters between 10 and 100 nm. To understand the origin of these nanodomains, Schürmann et al. further looked at the membranes of the same cell type with Atomic Force Microscopy and Fluorescence Microscopy. In a comparative study, they could demonstrate that the pit–like structures revealed in helium ion microscopy images of mammalian cell membranes represent both lipid raft–like membrane nanodomains and caveolae [1]. This study shows that the HIM is a well–suited microscopic tool for the exploration of nanoscale details of biological membranes and other biomaterial surfaces.

After the introduction of commercial helium ion microscopes, there have been a number of exploratory studies of all types of biological samples [3, 4], most of them

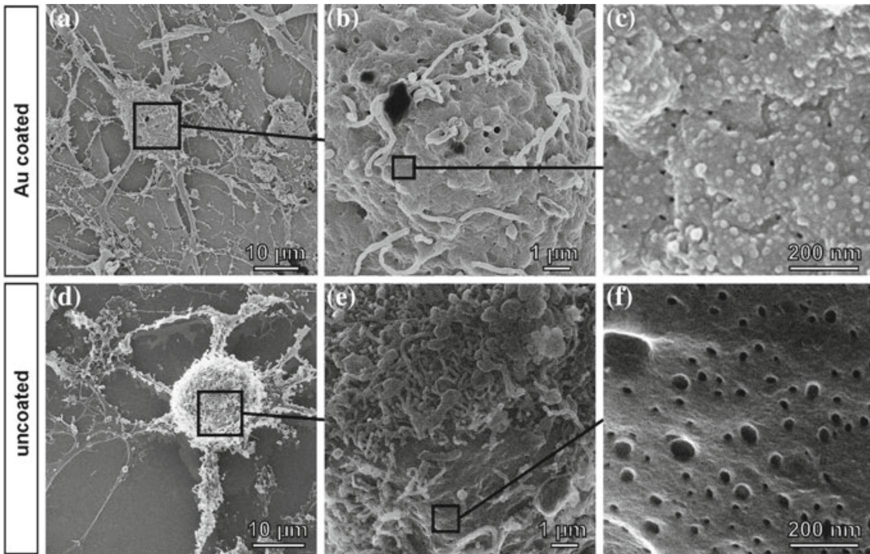

Fig. 7.1 Helium ion microscopic images of critical point dried stem cells with and without gold coating. **a**, **d** Human neural crest–derived stem cells differentiated to neurons with a round and defined cell body and numerous thin, slender, branching and long projections with small diameter representing neurites. **b**, **e** Cell membrane of soma. **c** In specimens sputter coated with gold (Au) with standard thickness of approx. 10 nm the cell membrane is covered with clustered Au, masking the true cell surface. **f** Helium ion microscopy allows high resolution inspection of uncoated cell surface in the native state. Numerous nano-domains with a roundish circumference and of varying diameter become discernible. Reproduces with permission from [1]

are utilizing the charge compensation to visualize fine surface details that remain unresolved in SEM images. Rice et al. [3] used a HIM to image parts of the epithelium of the rat kidney. They evaluated different preparation methods, such as in–situ fixation of kidney tissue with glutaraldehyde or modified paraformaldehyde lysine periodate, critical point drying and sectioning into 500 μm thick slices for easier handling. They imaged the glomerulus, a network of capillaries at the beginning of a nephron, which is a basic structural unit in the kidney that serves as a stage in the filtering process of the blood. Figure 7.2 displays high-magnification images of glomerular structures; the length of the scale bars is 120 nm (Fig. 7.2a) and 100 nm (Fig. 7.2b–f). Figure 7.2a shows a part of a filamentous nano–protrusion with bulbous ends (white arrows); the surrounding podocyte cells tissue (foot process) that wraps around the capillaries of the glomerulus, shows an irregular structure of the membrane surface (black arrows), comparable to those observed by Schürmann et al. [1]. It is thus likely that such nanodomains are common to mammalian cells, and originate from lipid rafts and caveolae. Figure 7.2b shows a higher magnification image of the actual "filtration" regions (slit diaphragms) between five adjacent podocyte foot processes [3]. One can clearly recognize a ladder–like structure of cross–bridging filaments with pore widths of 22 nm ±8 nm. For comparison, in con-

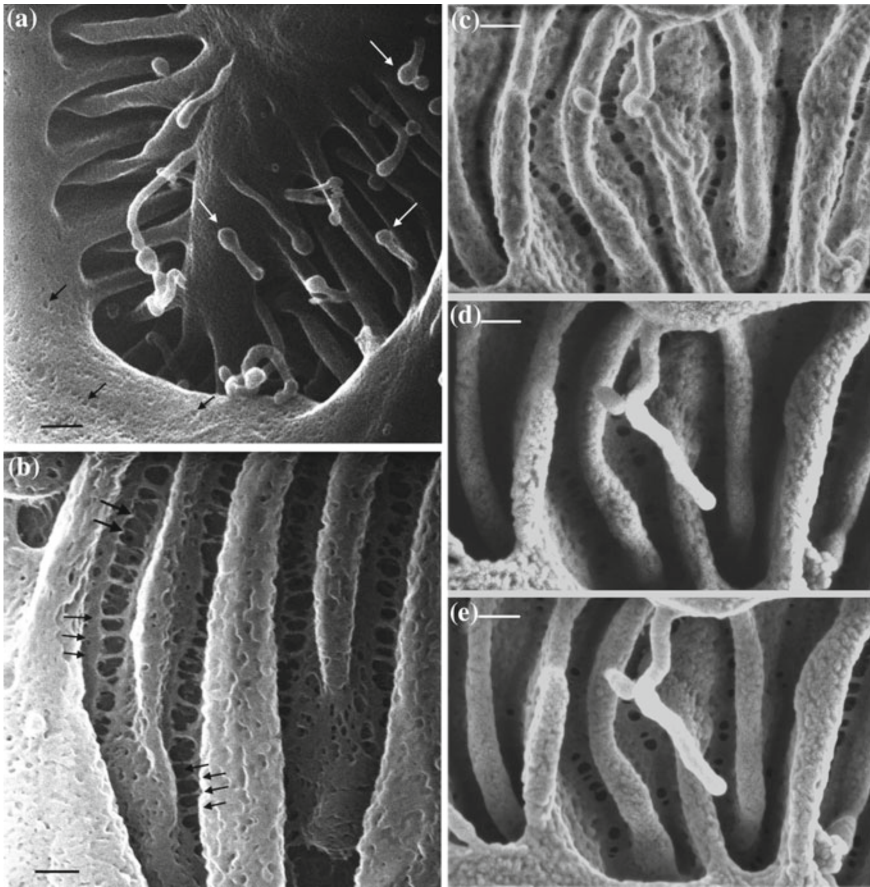

Fig. 7.2 Comparison of SEM versus uncoated HIM images. **a** Detail of a glomerular podocyte (HIM, no–coating). Bar 120 nm (**b**) Detail of four *filtration* regions (slit diaphragms) between five adjacent podocyte foot processes. Bar 100 nm (HIM, no–coating) (**c**) Sample imaged by SEM without sputter coating, using an in-lens detector. **c**, **d** Coated samples imaged by SEM using either the standard SE2 detector (**d**) or an in-lens detector (**e**). Bar 100 nm. Reproduced from [3]

ventional SEM images of an uncoated (Fig. 7.2c) and Pt sputter coated (Fig. 7.2d, e) slit diaphragms, these fine filaments are much harder to see and their diameter is not so simply measured. The HIM images show much more contrast and a higher magnification, which is further confirmed by looking at the SEM images of an earlier low voltage field emission scanning electron microscope (LVFESEM) study of the slit diaphragm [5]. Bioimaging with HIM and SEM have not only been compared in studies of mammalian tissue, Joens et al. [4] used LVFESEM and HIM to compare the images of Arabidopsis thaliana plants. Figure 7.3 shows 10 HIM and corresponding LVFESEM images of Arabidopsis thaliana sepal cuticle structures; the field of view (FOV) is increasing from 274 μm to 478 nm. The samples have been critical

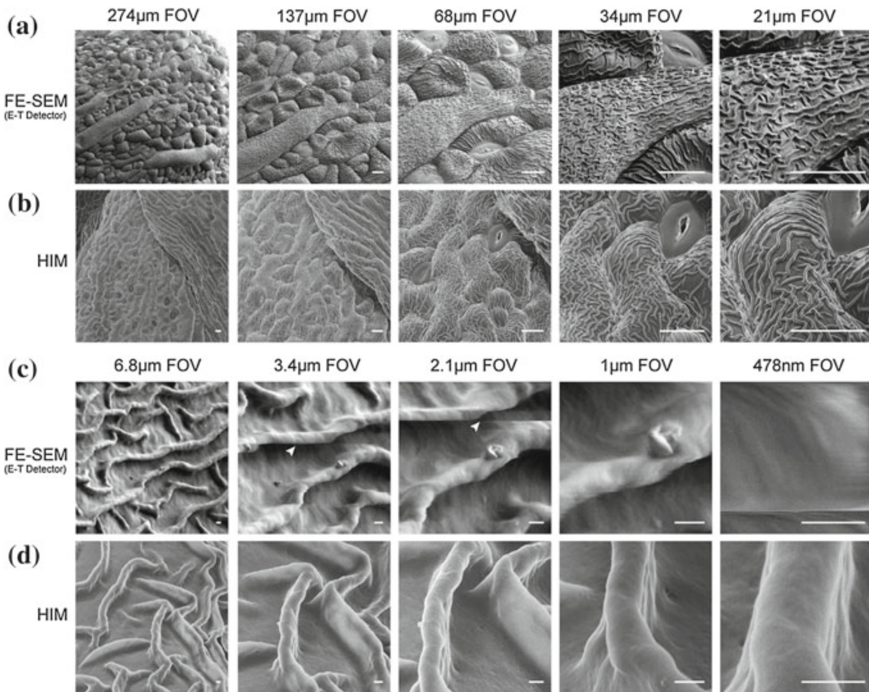

Fig. 7.3 Comparison of HIM and LVFESEM using Arabidopsis thaliana. **a** Low and **c** high magnification of uncoated samples. **b** Low and **d** high magnification using HIM. No artefacts are visible and even at the highest magnification cuticle structures are visible. *Bars* **a**, **b** 10 μm **c**, **d** 200 nm. Reproduced from [4]

point dried and were uncoated. At low magnification, Fig. 7.3a, b HIM and LVFESEM images are comparable with respect to resolution, contrast and depth of field. At higher magnification (Fig. 7.3c, d) this changes. At a FOV of 3.4 μm, charging artefacts (streaks, see arrow) become visible in the LVFESEM images. At a FOV of 2.1 μm, the sample surface appears textured and, compared to the corresponding HIM image, the LVFESEM image appears more blurred. At a FOV 478 nm, details can no longer be resolved in the LVFESEM, while the HIM image still clearly displays edges and surface structures of Arabidopsis thaliana sepal cuticle. At this magnification, the HIM image has no charging artefacts; hence there charge compensation by a simultaneous operation of the helium ion beam and an electron flood gun clearly reveals fine details in the images of plant cells. The article by Joens et al. [4] contains a number of plastically images of biological objects. An example is shown in Fig. 7.4, where a predator nematode (roundworm) pristionchus pacificus, has been investigated with the HIM. Figure 7.4a shows a low magnification image of the pristine nematode that shows a little cavity behind which the mouth and teeth structure is hidden. In Fig. 7.4b, this cavity has been enlarged and the primary teeth structures become visible. This "capping" of the nematode has been performed by neon milling

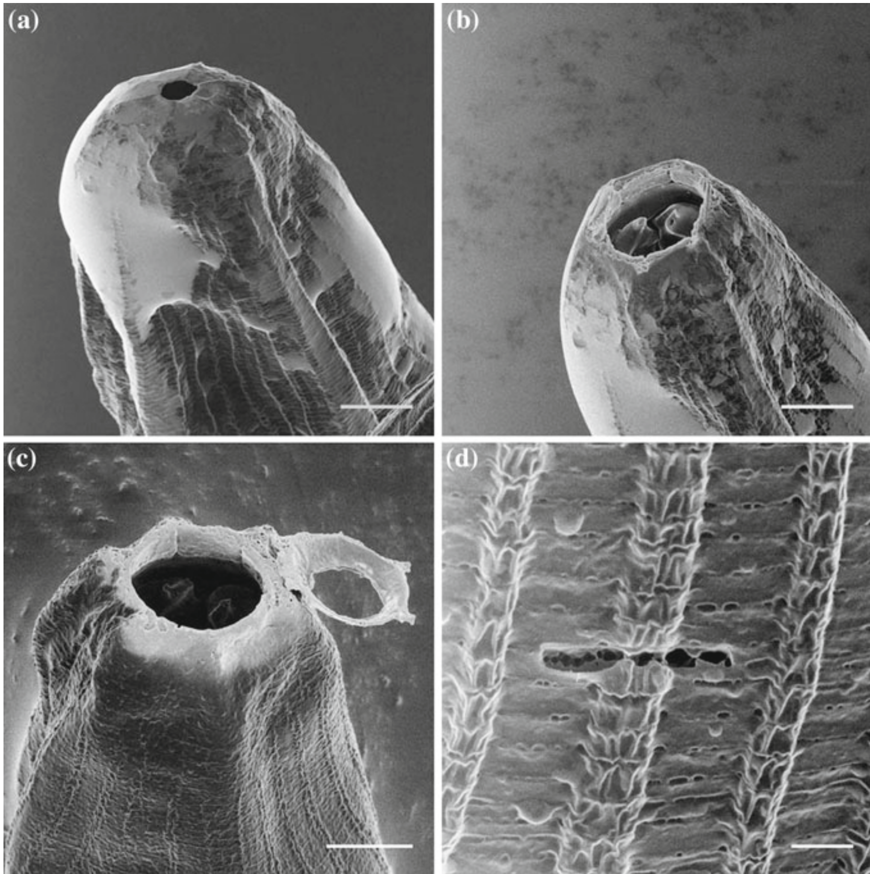

Fig. 7.4 HIM images of predator worms demonstrating the high depth of focus and the nano–machining capabilities of the Orion NanoFab. **a** Native sample, **b** neon milling reveals the primary tooth, **c** removed outer sheath and **d** patterned line using a low fluence. *Bars* **a–c** 5 μm **d** 1 μm. Reproduced from [4]

with the HIM, i.e. by operating the HIM with neon ions and focussing their beam to remove the outer sheath. A snapshot of this process is seen in Fig. 7.4c, where the outer sheath is almost removed, and in Fig. 7.4d where a small line was written in the outer cuticle of the nematode with a neon ion dose of 0.3 nC/μm^3.

Fascinating examples of bioimaging with the HIM have been accomplished by Boden et al. [6] who investigated the structures of differently coloured butterfly wings. Like in the other studies discussed so far, a comparison with electron microscopy has been made. Figure 7.5 shows Variable Pressure (VP) SEM and HIM image of a wing structure of uncoated Papilio Ulysses. The HIM image is much sharper and shows finer details. Looking into closer detail, an analysis of the edge sharpness, a common measure of resolution, yields in this case a surprisingly

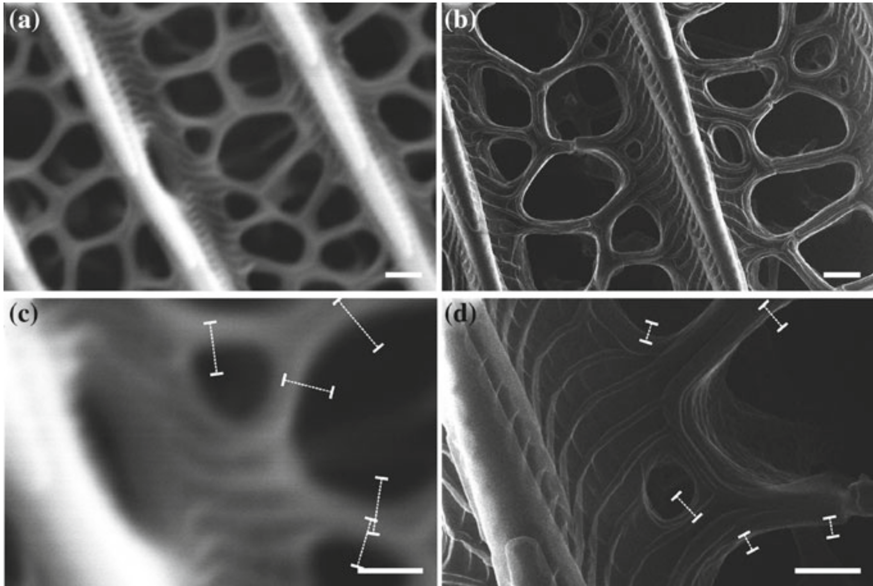

Fig. 7.5 Comparison of VP SEM (**a**, **c**) and HIM (**b**, **d**) using uncoated Papilio ulysses black dorsal scales. *Scale bars* **a**, **b** 500 nm, **c**, **d** 300 nm. Reproduced with permission from [6]

large (16x) difference between the resolution of the VP–SEM (55 nm) and the HIM (3.4 nm). This discrepancy is much larger than for the previously discussed examples. In this case, the better performance of the HIM is most likely caused by a special combination of depth–of–focus and charging. The fact that a VP–SEM instead of a LVFESEM was employed may also explain the low resolution in the electron micrographs of the insulating and spatially extended wing structures. This example also shows that under certain circumstances only helium ion microscopy is capable to provide reasonable images of insulating nanostructures. The study by Boden et al. [6] also contains stereo anaglyphs (or 3D) images of biological samples, an uncoated wing of Papilio Ulysses is here used an example. Stereo Imaging can be achieved because of the combination of a high depth of field and a high resolution that allows the imaging of a stereo–pair under different angles. This is practically done by recording two pictures of the same object with incoming helium ion beams at different angles. Experimentally this is simply performed by imaging at two slightly different stage tilts. When the images are then viewed with filtered spectacles, three-dimensional images can be seen and trigonometry can be used to reconstruct the distance in the depth of field. In Fig. 7.6 a sequences of HIM images of a Papilio Ulysses wing imaged under tilt angles that vary between 0 and 26° is presented. Figure 7.7 shows a stereo pair of Papilio Ulysses wing images taken at tilts of 10 and 15°. The height of the structures can be calculated from measuring the distances A and B. To validate the HIM values have also been compared with values for A and B obtained from TEM images [7]. In general this shows that 3D–HIM can obtain

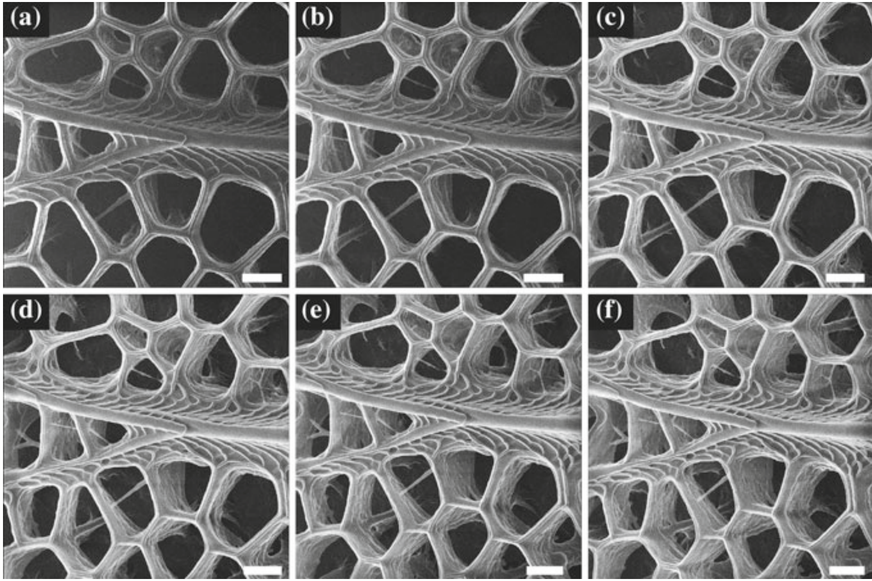

Fig. 7.6 Tilt series obtained from black Papilio ulysses ground scales used to reconstruct anaglyphs and for 3D reconstruction. Stage tilt angles: **a** 0°, **b** 5°, **c** 10°, **d** 15°, **e** 21°, and **f** 26°. All scale bars are 400 nm. Reproduced with permission from [6]

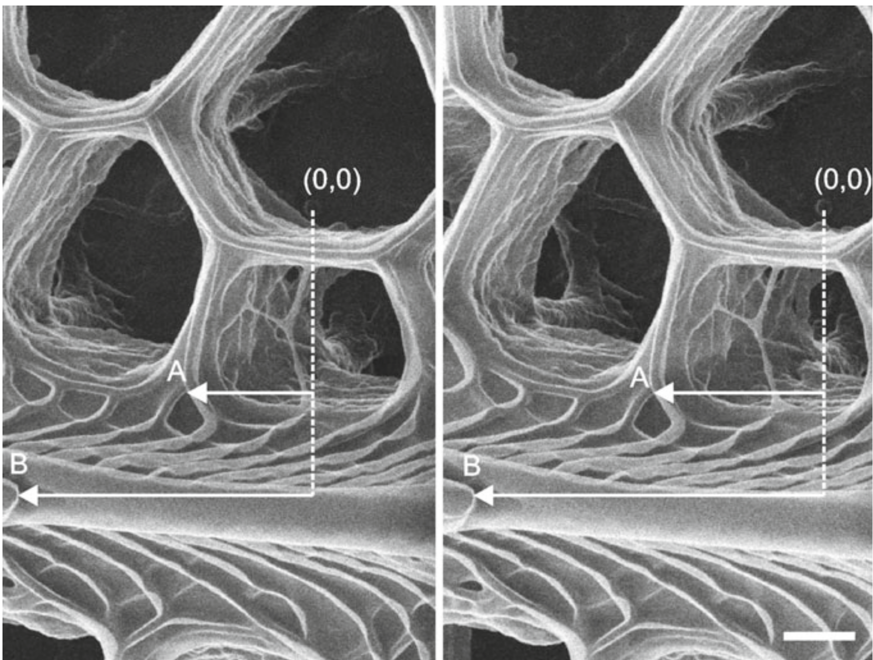

Fig. 7.7 Height calculations based on Fig. 7.6. The distance between (0, 0) and *a* and *b* is 1.5 and 1.9 μm respectively. *Scale bar* 200 nm. Reproduced with permission from [6]

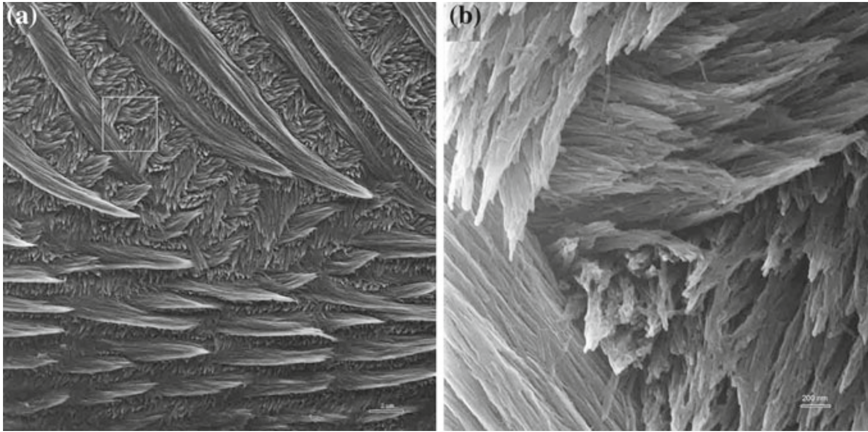

Fig. 7.8 High depth of field imaging of mouse incisor enamel. Reproduced from [8]

a quantitative precision in length measurements, comparable to TEM, but without the very time consuming TEM sample preparation. More examples of butterfly wing structures are also shown in Chap. 6 of this book.

Teeth contain both mineral and organic phases in a well–defined three–dimensional organisation. Bidlack et al. [8] investigated mouse incisor enamel crystallites and the extracellular tooth matrix with HIM and FE–SEM for comparison. Figure 7.8 shows a HIM micrograph of uncoated mouse incisor enamel that exhibits high resolution at low magnifications and a large depth of field.

An other example where the high depth of focus is a surplus to the ability to use uncoated specimens and achieve very high lateral resolution is presented in Fig. 7.9. Paunescu et al. investigated the interaction of mouse epithelial cells with spermazota [9]. The head of a mouse spermatozon which is well anchored in the principal cell stereocilia presented in Fig. 7.9a. More details can be observed in Fig. 7.9b which shows ring—and vesicle–like structures on the surface of a cytosolic droplet found close to the mid–principal junction. This vesicle–like features can be seen in more detail in Fig. 7.9c–d. While confirming older results on the presence of microplicae or small membrane ruffles on the surface of clear cells, it also could shed new light on the interaction of the spermazotoa during the epididymal transit. The fact that the sperm cytoplasmic droplet is covered with spherical features with a size of approximately 90 nm indicates an indirect interaction. The authors conclude that this images can be interpreted as showing epididymosomes while fusing with the sprematozoon membrane. This allows to deliver proteins originating from the epithelium during epididymal maturation.

In the previous study sophisticated preparation protocols have been used to ensure that the selected tissue is preserved. However, for the magnification series presented in Fig. 7.10 no special preparation has been used with the exception of a 5 h drying at room temperature in a high vacuum vessel. The sample has than been directly

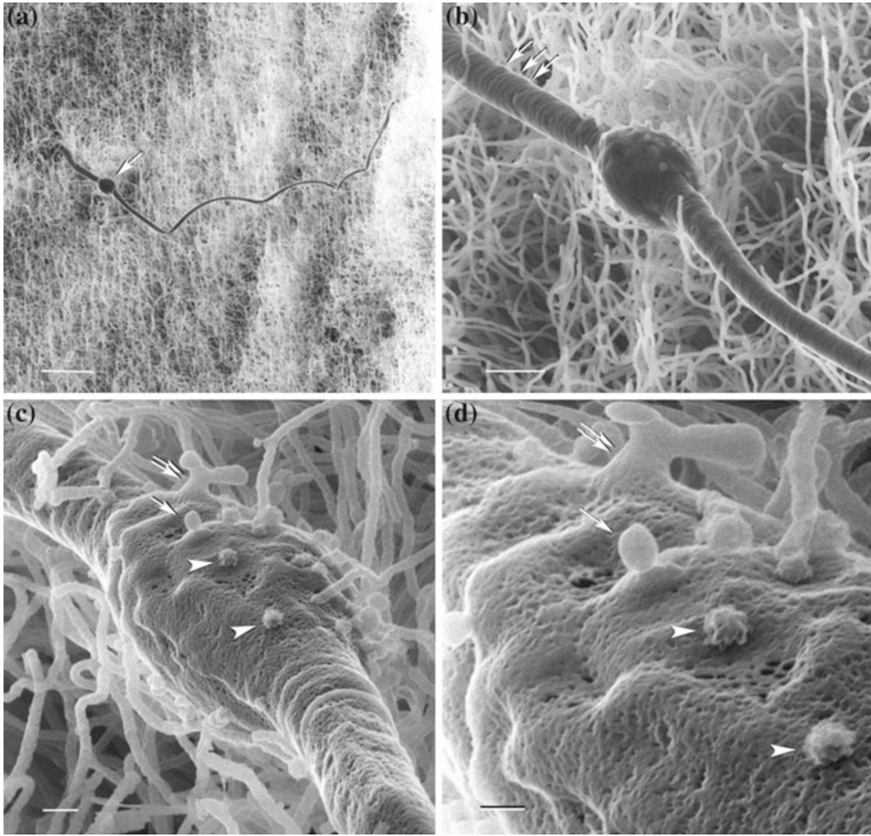

Fig. 7.9 HIM images of mouse cauda spermatozoon. **a** Low magnification image showing the head embedded in the epididymal epithelium. **b** Intermediate and **c**, **d** High magnification of the same sperm cell. *Scale bars* **a** 5 mm; **b** 1 mm; **c** 200 nm; **d** 100 nm. Reproduced from [9]

inserted into the sample chamber of the HIM. The series shows details of a leave surface with increasing resolution. The epicuticular wax platelets shown at high magnification in Fig. 7.10d are approximately 50 nm thick. Attempts to use critical point drying to prepare the leave surface failed as the sensitive wax layer has been removed or at least severely damaged.

A similar preparation approach [11] has been chosen to image [12] the leaves of Pinus densiflora and Pinus rigida (see Fig. 7.11). The complex network formed by the epicuticular waxes found in the stoma of Pinus rigida is presented in Fig. 7.11d.

The ability to image the structure of biological specimens also comes in handy for a variety of correlative imaging approaches. Schürmann et al. used a combination of direct stochastic optical reconstruction microscopy (dSTORM) and helium ion microscopy to identify the nature of pit like structures revealed by HIM on the surface of mammalian cell membranes [1]. From their correlative study it becomes clear that

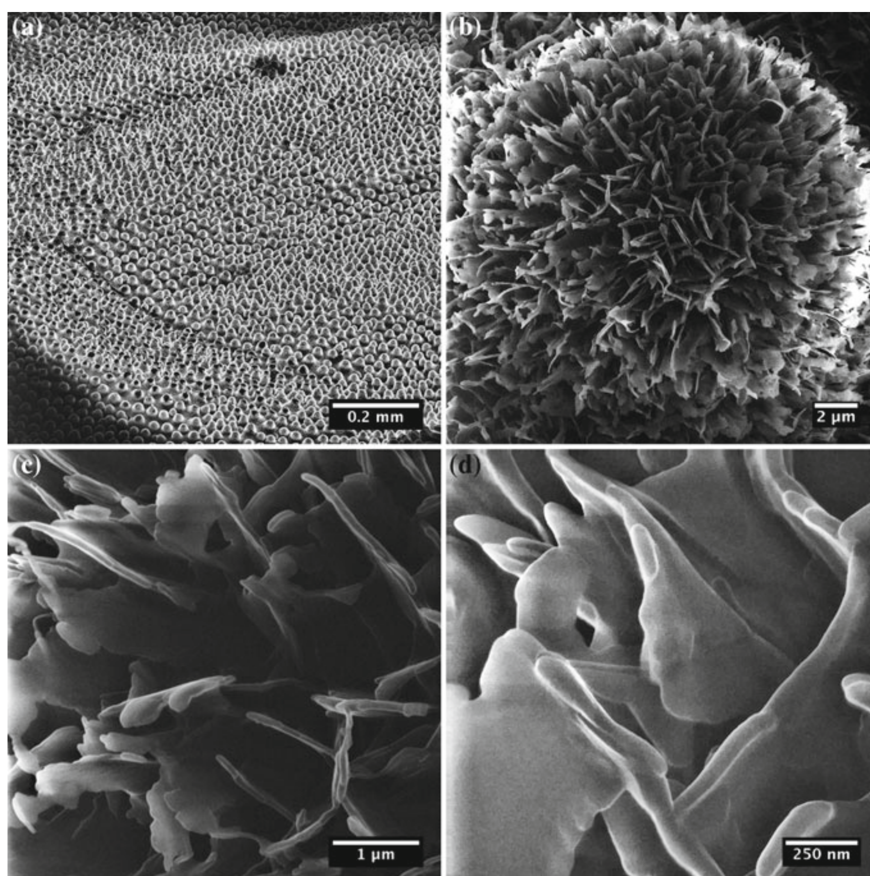

Fig. 7.10 HIM images of uncoated Euphorbia myrsinites leaves. Samples courtesy of N. Hornsveld [10]

at least the densely spaced (<50 nm) domains represent lipid rafts. Lipid rafts are subject of ongoing discussion as they are difficult to visualize in cells. The above mentioned study based on HIM and dSTORM allowed to identify and image these structures in uncoated and unstained samples.

Given the fact that HIM provides a large number of different signal path's correlative imaging can also be performed in–situ. Although some of these path's are still under development (see for example the chapters on SIMS 13, backscatter spectrometry 12 and IL 14) first results are obtained. A biological relevant example is presented in Fig. 14.1 of Chap. 14 where SE and IL images of Alexa Fluor® 488 are compared. While the IL images allows to identify the region of interest the charge compensation capabilities of the HIM could be used to obtain high resolution data from the target sites.

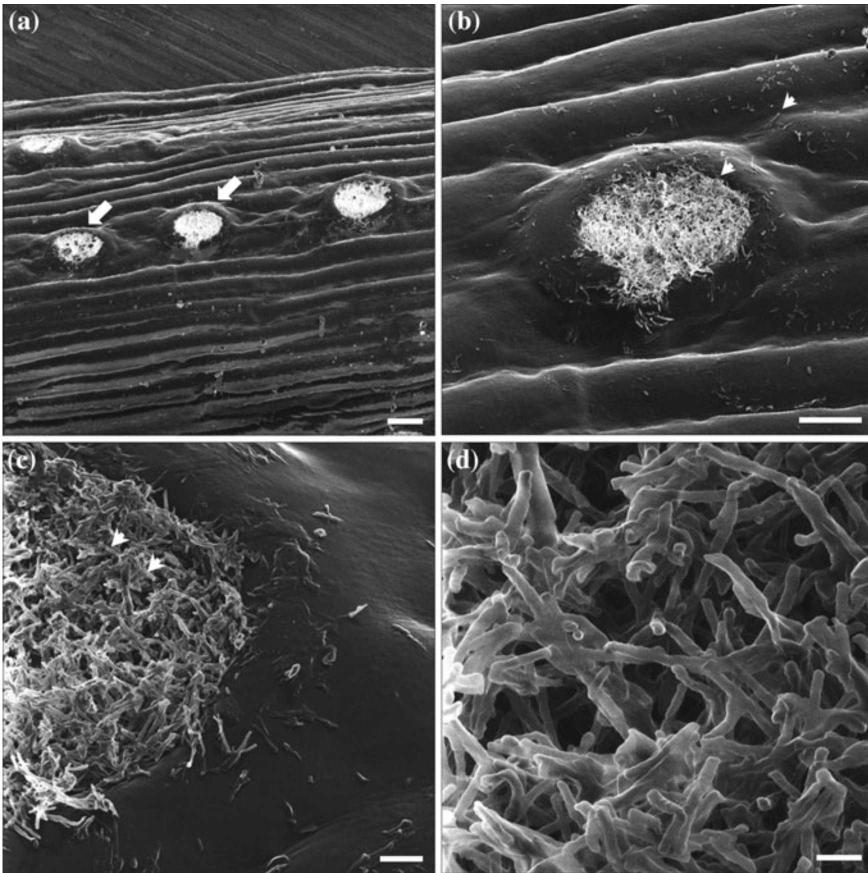

Fig. 7.11 HIM magnification series showing the surface of Pinus rigida. The complex network of formed by the epicuticular wax inside the Stoma is shown. (*scale bar* 20 µm (**a**), 10 µm (**b**), 2 µm (**c**), and 500 nm (**d**)). Reproduced from [12]

7.3 Summary

In conclusion, we have seen that the biological studies in the first 10 years are mainly focused on a comparison of ion and electron microscopy. From the numerous examples presented above it becomes obvious that the charge compensated results obtained by HIM provide a higher resolution, contrast and more details in comparison with standard electron microscopy methods used in biology and medicine. Besides this clear advantages the large depth of focus is a big surplus for the investigation of the morphology of unstained and unlabelled cells.

HIM has evolved into a tool that can be used for the investigation of biological and medical samples, but is still far away from being accepted as a main stream method in these fields. In the next years it needs microscopists skilled in ion microscopy

as well as the established optical methods to perform more in depth studies which will reveal new insights into the underlying biological mechanisms. In particular the investigation of the influence of labeling will provide a holistic view on the possible influence of standard sample preparation methods onto biological systems.

References

1. M. Schürmann, N. Frese, A. Beyer, P. Heimann, D. Widera, V. Mönkemöller, T. Huser, B. Kaltschmidt, C. Kaltschmidt, A. Gölzhäuser, Small **11**(43), 5781 (2015). doi:10.1002/smll.201501540. http://doi.wiley.com/10.1002/smll.201501540
2. S. Hauser, D. Widera, F. Qunneis, J. Müller, C. Zander, J. Greiner, C. Strauss, P. Lüningschrör, P. Heimann, H. Schwarze, J. Ebmeyer, H. Sudhoff, M.J. Araúzo-Bravo, B. Greber, H. Zaehres, H. Schöler, C. Kaltschmidt, B. Kaltschmidt, Stem Cells Dev. **21**(5), 742 (2012). doi:10.1089/scd.2011.0419. http://online.liebertpub.com/doi/abs/10.1089/scd.2011.0419
3. W.L. Rice, A.N. Van Hoek, T.G. Păunescu, C. Huynh, B. Goetze, B. Singh, L. Scipioni, L.A. Stern, D. Brown, PLoS One **8**(3), e57051 (2013). doi:10.1371/journal.pone.0057051. http://dx.plos.org/10.1371/journal.pone.0057051
4. M.S. Joens, C. Huynh, J.M. Kasuboski, D.C. Ferranti, Y.J. Sigal, F. Zeitvogel, M. Obst, C.J. Burkhardt, K.P. Curran, S.H. Chalasani, L.A. Stern, B. Goetze, J.A.J. Fitzpatrick, Sci. Rep. **3**, 3514 (2013). doi:10.1038/srep03514. http://www.ncbi.nlm.nih.gov/pubmed/24343236
5. E. Gagliardini, S. Conti, A. Benigni, G. Remuzzi, A. Remuzzi, J. Am. Soc. Nephrol. **21**(12), 2081 (2010). doi:10.1681/ASN.2010020199. http://www.pubmedcentral.nih.gov/articlerender.fcgi?artid=3014021&tool=pmcentrez&rendertype=abstract, http://www.jasn.org/cgi/doi/10.1681/ASN.2010020199
6. S.A. Boden, A. Asadollahbaik, H.N. Rutt, D.M. Bagnall, Scanning **34**(2), 107 (2012). doi:10.1002/sca.20267. http://www.ncbi.nlm.nih.gov/pubmed/21796646
7. P. Vukusic, J.R. Sambles, C.R. Lawrence, Proc. R. Soc. B Biol. Sci. **271**(Suppl_4), S237 (2004). doi:10.1098/rsbl.2003.0150. http://rspb.royalsocietypublishing.org/cgi/doi/10.1098/rsbl.2003.0150
8. F.B. Bidlack, C. Huynh, J. Marshman, B. Goetze, Front. Physiol. **5**(October), 1 (2014). doi:10.3389/fphys.2014.00395. http://journal.frontiersin.org/article/10.3389/fphys.2014.00395/abstract
9. T.G. Păunescu, W.W.C. Shum, C. Huynh, L. Lechner, B. Goetze, D. Brown, S. Breton, Mol. Hum. Reprod. **20**(10), 929 (2014). doi:10.1093/molehr/gau052. http://www.molehr.oxfordjournals.org/cgi/doi/10.1093/molehr/gau052
10. N. Hornsveld, Characterization of natural epicuticular wax. Master Thesis, University of Twente (2014). http://essay.utwente.nl/65872/
11. K.W. Kim, I.J. Lee, C.S. Kim, D.K. Lee, E.W. Park, Microsc. Microanal. **17**, 118 (2011)
12. K.W. Kim, Korean. J. Microsc. **42**(3), 147 (2012). doi:10.9729/AM.2012.42.3.147. http://koreascience.or.kr/journal/view.jsp?kj=JJHMBC&py=2012&vnc=v42n3&sp=147

Chapter 8
HIM Applications in Combustion Science: Imaging of Catalyst Surfaces and Nascent Soot

Henning Vieker and André Beyer

Abstract In this chapter, selected applications of helium ion microscopy are presented which demonstrate the strength of this method in characterizing systems relevant for the field of combustion science: nascent soot and transition metal oxide catalysts. Soot consists of carbon-based nanoparticles which were generated in flames. The knowledge about soot growth at very early stages is of high interest in combustion science, where HIM yields a new lower size limit for imaging such particles with high contrast. In fact, the contrast on samples composed of light elements, in combination with the high lateral resolution, are key advantages of HIM which are relevant for studying soot. HIM allowed time efficient probing of a high number of particles with sizes and shapes down to 2 nm. In the first part of this chapter, this is demonstrated for soot from different flames. Their sizes and shapes were simultaneously analyzed for typically 1000 particles per sample. Due to the high resolution and high depth of focus, HIM is also well suited to investigate the surface morphology of highly corrugated catalysts, which is shown here for transition metal oxide films grown by pulse spray evaporation CVD. In the second part of this chapter, examples of such catalyst surfaces are presented. In particular, the morphologie of oxides of iron, iron-cobalt and iron-copper films are characterized by HIM with high resolution.

H. Vieker · A. Beyer (✉)
Physics of Supramolecular Systems and Surfaces, Bielefeld University,
Bielefeld, Germany
e-mail: andre.beyer@uni-bielefeld.de

H. Vieker
e-mail: h.vieker@physik.uni-bielefeld.de

H. Vieker
CNM Technologies GmbH, Herforder Straße 155a, 33609 Bielefeld, Germany

© Springer International Publishing Switzerland 2016

G. Hlawacek and A. Gölzhäuser (eds.), *Helium Ion Microscopy*,
NanoScience and Technology, DOI 10.1007/978-3-319-41990-9_8

8.1 Introduction

In this chapter, selected applications of helium ion microscopy are presented which demonstrate the strength of this method in characterizing systems relevant for the field of combustion science: nascent soot and transition metal oxide catalysts.

Soot consists of carbon-based nanoparticles which were generated in flames. The knowledge about soot growth at very early stages is of high interest in combustion science, where HIM yields a new lower size limit for imaging such particles with high contrast. In fact, the contrast on samples composed of light elements, in combination with the high lateral resolution, are key advantages of HIM which are relevant for studying soot. HIM allowed time efficient probing of a high number of particles with sizes and shapes down to 2 nm. In the first part of this chapter, this is demonstrated for soot from different flames. Their sizes and shapes were simultaneously analyzed for typically 1000 particles per sample.

Due to the high resolution and depth of focus, HIM is also well suited to investigate the surface morphology of highly corrugated catalysts which is shown here for transition metal oxide films grown by pulse spray evaporation CVD. In the second part of this chapter, examples of such catalyst surfaces are presented. In particular, the morphologies of oxides of iron, iron-cobalt and iron-copper films are characterized by HIM with high resolution.

8.2 Organic Nanoparticles: Nascent Soot Analysis

This section reports a study about nascent soot particles. The high resolution of HIM is used to gain a better understanding of combustion, leading to more accurate models which eventually aid the development of more efficient combustion processes. This section starts with one model ethylene flame [1], followed by studies where the flame conditions [2], and the model fuels [3] were varied.

8.2.1 Introduction: Soot

Soot is a particulate matter resulting from incomplete combustion processes of hydrocarbons. It is a known human carcinogen [4] and has considerable negative effect on global climate change [5]. Thus, the understanding of the fundamental growth processes is of high scientific interest. Mature soot is known to consist of aggregates of nearly spherical particles, 20–50 nm in diameter, composed of large polycyclic aromatic hydrocarbons (PAHs) [6]. The formation of soot in flames starts from the reaction of PAHs into small particles (see Fig. 8.1). Young nascent soot is mostly aromatic in nature. Mass and size of the particles are growing quickly in flames. Experimentally, this nascent soot is difficult to characterize. However, it

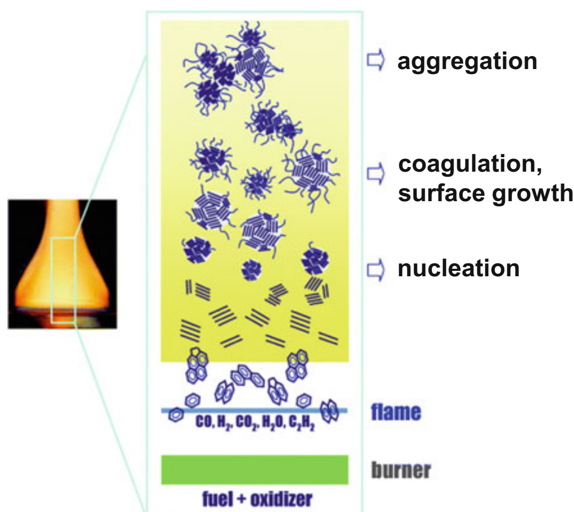

Fig. 8.1 Schematic illustration of soot growth in a flat flame. Stacks of lines represent stacked aromatic structures, and the wiggly lines represents aliphatic components. (Illustration reprinted with permission [7], text on the *right side* is added to understand the chosen soot sampling heights that correspond to different stages of soot formation

is this soot that undergoes the most rapid growth in a flame and is eventually responsible for the emission of particulates into the atmosphere from fossil-fuel combustion. A better understanding of these early growth stages is necessary to identify and fill in the gaps of current kinetic descriptions of soot formation. Detailed reviews about the current knowledge of soot growth processes were published by Wang in 2011 [7] and more recently by Kohse-Höinghaus [8].

A standard method to analyze soot is transmission electron microscopy (TEM), in which the beam penetrates the particle of interest as well as an underlying support film. This support can reduce the image signal-to-noise ratio substantially. In fact, the smallest soot particles detectable trough TEM are usually around 10 nm in diameter [9, 10]. Note that an improvement in the signal-to-noise ratio by simply increasing the beam dose is limited by sample damage. This TEM image contrast limitation may be lifted in future by new developments like dynamic TEM [11] or by depositing soot on thinner substrates, e.g. the carbon nanomembranes discussed in a Chap. 10. After the detection of a particle, TEM is able to reveal the inner structure down to atomic resolution, whereas HIM provides detailed information about the outer shape.

In HIM, SEM, and AFM, imaging is possible on almost all sufficiently flat, bulk surfaces. In comparison, low-voltage SEM provides similar contrast as HIM, but the achievable resolution is substantially lower. AFM can detect particles smaller than 10 nm, but the probe tip is usually larger than the particle size; therefore, the particle image must be geometrically reconstructed with assumptions that are often difficult to verify. Also, fine features on a particle surface cannot be revealed easily in AFM, again owing to the finite tip size [12]. An additional advantage of HIM is the substantially faster imaging process, which allows the investigation of a sufficiently large number of particles for statistical analysis.

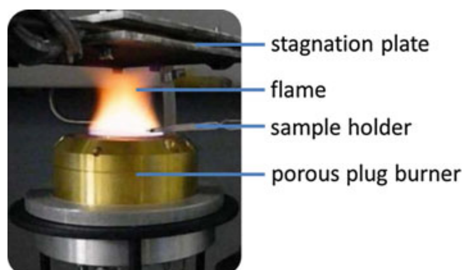

Fig. 8.2 Sampling procedure. Stagnation flow ethylene flame, stabilized on porous plug burner. To deposit soot particles on Si-wafers, the sample holder is quickly moved through the flame. Reprinted from Supporting Information of [1]

8.2.2 *Soot Sampling*

Soot sampling was carried out as shown in Fig. 8.2. A premixed, burner-stabilized stagnation-flow flame was used for the production of nascent soot. Samples were probed by thermophoretic sampling, where a cold, flat surface is quickly swiped through the flame. The substrate was affixed on a sample holder mounted on a stepper motor. The exposure time to the flame is typically ~16 ms. We used standard p-doped silicon wafer pieces without further cleaning as substrate for the HIM measurements. Breaking and handling the silicon pieces was done in a clean room. To ensure clean substrates, reference samples were measured for each batch. Note that all additionally tested "cleaning" methods yielded more particle contaminated surfaces than pristine silicon wafer pieces.

Samples were collected at specific distances from the burner surface, which coincided with the three important stages of soot formation: nucleation, early mass growth, and aggregation (see Fig. 8.1).

8.2.3 *Imaging of Soot*

For HIM imaging of sensitive samples such as nascent soot, the level of damage caused by the probing beam is a crucial parameter. Herein, we discuss the procedures for identifying reliable HIM operating parameters to achieve optimal results. Figure 8.3 shows consecutive HIM images of two soot samples. The top panels represent images collected with a very high ion dose density of 2182 ions/nm^2 per image. The bottom panel shows consecutive images collected with a lower ion dose density of 262 ions/nm^2.

Exposing the samples to the ion beam causes no discernible degradation of the particles. Changes in the contrast were only observed at the higher dosage, but no change in particle size or shape occurred. The observed changes are attributed to condensation of evaporated organics onto the sample as discussed by Stuart Boden in Sect. 6.3.1. Please note that for the highest doses also substrate swelling is occurring. All these sample modifications occur at higher ion doses than used for

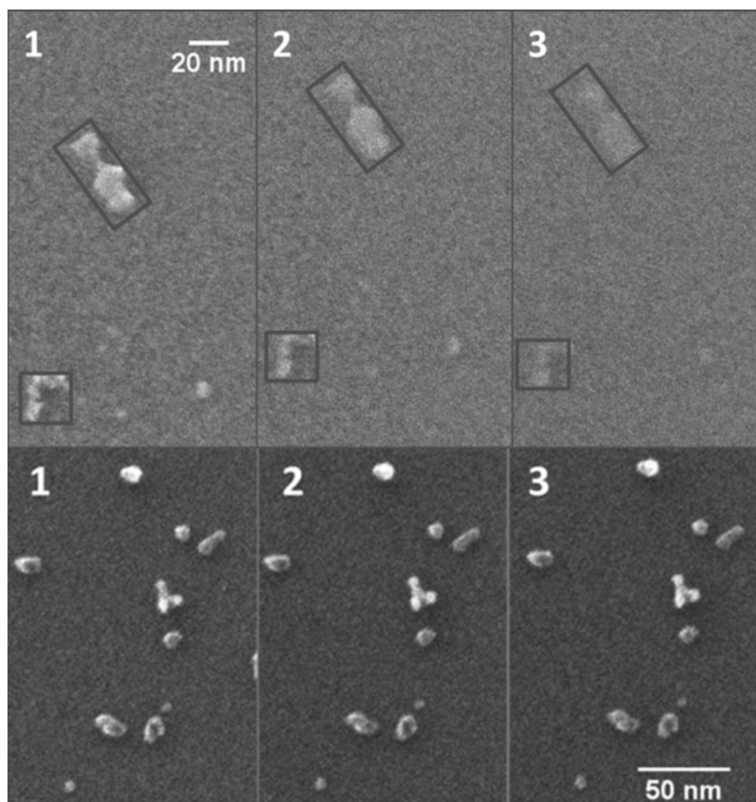

Fig. 8.3 Beam damage evaluation: Series of consecutive HIM images of soot collected from an ethylene C3 flame. *Top panels* sample collected at 1.0 cm from the burner surface with an ion dose density of 2182 ions/nm^2. *Bottom panels* sample collected at 0.8 cm from the burner surface and probed by exposing it to an ion dose density of 262 ions/nm^2. Reprinted with permission [1]

evaluated images. All other images shown or used for analysis are taken from sample positions which have not been scanned before.

As shown in Fig. 8.4, HIM is able to identify nascent soot particles as small as 2 nm. For larger particles (>5 nm), HIM detects particles with high contrast, allowing the accurate characterization of both size and morphology.

8.2.4 Analysis of Soot from Ethylene Flames

Figure 8.5 shows typical HIM images of nascent soot which were collected at the three different heights in the flame. The particle size is growing with the distance from the burner as the soot has a longer residence time in the flame.

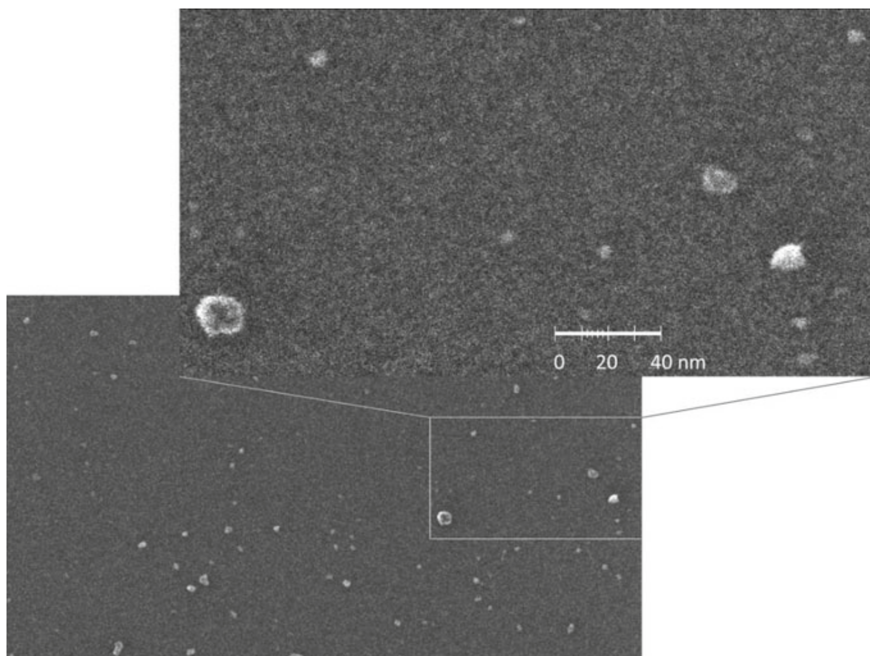

Fig. 8.4 HIM image of soot particles collected at 0.5 cm distance from the burner, showing the capability of the technique for imaging nascent particles of 2–3 nm in size. Reprinted from supporting information of [1]

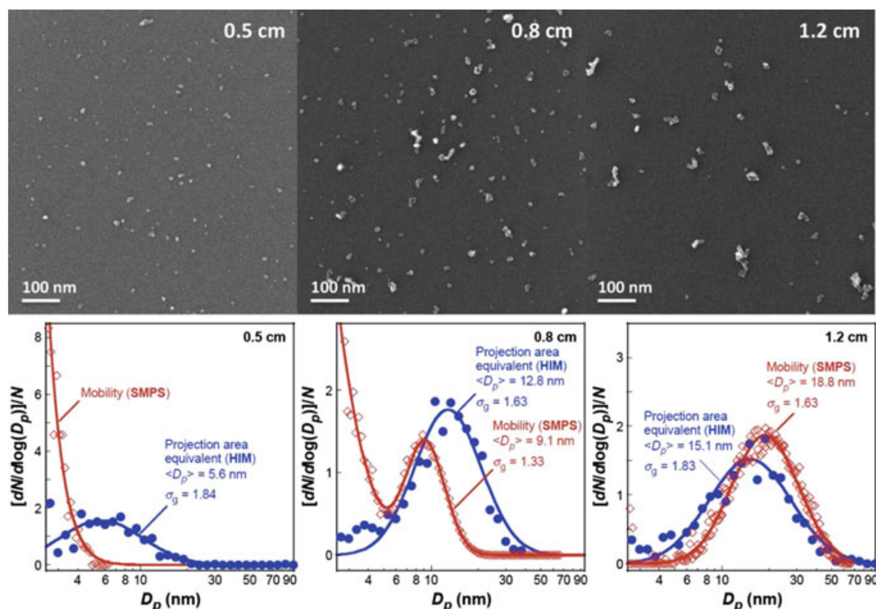

Fig. 8.5 HIM images of nascent soot from an ethylene C3 flame. Particle size and morphology change as a function of the distance from the burner surface. Reprinted with permission [1]

From these images primary particle size distributions can be determined from the projected areas of the particles. Distribution functions of the particle size are plotted in Fig. 8.5. They are superimposed by mobility diameter (scanning mobility particle size, SMPS) distributions of the same flame conditions which were determined in the gas phase in a previous study by Hai Wang and coworkers [13]. The measured physical value is different in both techniques as SMPS measures the surface area whereas HIM measures the 2D projection (the outline) of a particle. In a following publication this study was extended to a variety of ethylene flame conditions [2].

An additional unique strength of HIM is its ability to probe size and morphology of particles at the same time and at sizes that have previously been impossible. Figure 8.6 shows morphological variations of soot sampled in different heights. Particles sampled at 0.5 cm from the burner surface are spheroidals with a characteristic size of less than 10 nm. At 0.8 cm from the burner surface a notable number of aggregated particles are observed although the number of apparent spheroids exceeds that of aggregates, and the apparent primary particle diameter is around 10 nm. Images obtained at 1.2 cm from the burner show that the primary particles have grown to around 20 nm, and the number of aggregates greatly exceeds the number of primary particles.

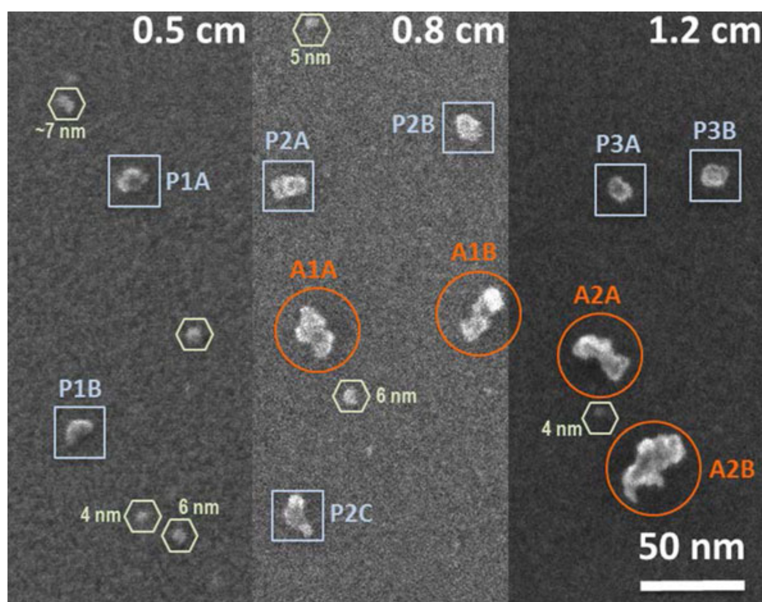

Fig. 8.6 Morphological variations of nascent soot collected from the ethylene C3 flame at heights of 0.5, 0.8 and 1.2 cm and imaged by HIM showing representative primary and aggregate structures. Particles shown in the hexagons are in the apparent size range of 4–8 nm; those in the squares are 14–18 nm. Particles shown in the circles are apparent aggregates. Reprinted with permission [1]

The morphology of soot from ethylene flames is discussed and analyzed in terms of sphericity, circularity, and fractal dimension. These parameters do not vary much over the collected samples, but a comparison to representative real particle shapes indicates that the nascent soot particles have no simple or general shape.

8.2.5 Imaging of Soot from Different C_4 Fuels

To analyze the influence of the fuel chemistry on the soot morphology the following C_4 fuels were analyzed: n-butane, i-butane, i-butene, and i-butanol.

HIM micrographs of soot from n-butane, i-butane, i-butene are very similar, therefore, Fig. 8.7 compares HIM micrographs of only n-butane and i-butanol. In both flames, relatively small particles with sizes smaller than 10 nm are detected. However, the structure of the aggregates differs notably. The soot from i-butanol is

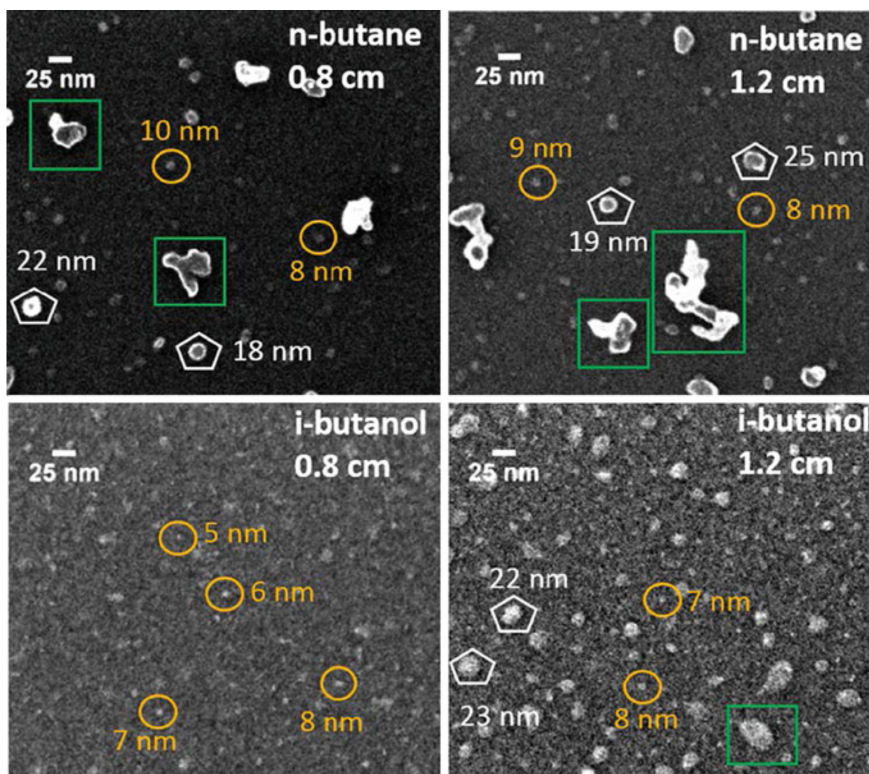

Fig. 8.7 HIM micrographs for soot probed from atmospheric-pressure flames of n-butane (*upper row*) and i-butanol (*bottom*). For near-spherical particles (circles and pentagons), the diameter is given. Reprinted with permission [3]

at the lower height of 0.8 cm close to the detection limit, whereas the n-butane flame is already producing branched structures. Soot from i-butanol is almost spherical whereas n-butane soot is agglomerating to bigger structures.

This difference might indicate an influence of the fuel structure on the morphology of nascent soot particles. This could be caused by the different C/O ratios or the chemical structure of the fuel itself.

8.2.6 Summary: Imaging of Nascent Soot

For imaging of soot, HIM yields images with exceptional contrast even for smallest nanoparticles. This allows the unambiguous recognition of smaller nascent soot particles than those observed in previous electron microscopy studies. The results indicate that HIM is ideal for rapid and reliable probing of the morphology of nascent soot. Particles as small as 2 nm are detectable. The results also show that nascent soot is structurally inhomogeneous, and even the smallest particles can have shapes that deviate notably from a perfect sphere.

8.3 CVD-Grown Films of Transition Metal Oxides

In the field of combustion, catalytically active films are of high interest for e.g. cleaner exhaust gases. One type of such films is characterized by HIM in an exemplary study which is presented in this section. The investigated transition metal oxide (TMO) films were produced by pulsed spray evaporation chemical vapor deposition (PSE-CVD). With its high depth of focus at full resolution, HIM is well suited to investigate the morphology of these highly corrugated films. At the end, a variety of analytical techniques were combined to obtain thorough information about the samples. Special focus of this study were transition metals and their oxides, especially iron, [14, 15] cobalt, [16] copper, [17, 18] and mixtures there of [19–21].

8.3.1 Introduction

The scientific goal of this study was the development of functional catalytic surfaces which are suitable for better and cleaner combustion processes. Burning organic material produces not only soot as discussed in the previous chapter, but also volatile organic compounds (VOCs). These are linked to a variety of environmental issues and negative effects on human health [22]. Many currently employed catalysts are, on one hand, quiet effective, but, on the other hand, made from noble metals, so they are generally expensive. A potential alternative candidate are

transition metal oxides (TMOs), as they are quite inexpensive and show a promising functionality as catalyst [23].

Chemical vapor deposition (CVD) is a deposition technique to produce thin films. The substrate is exposed to a precursor in the vapor phase. The film is then formed by decomposition or chemical reaction of this precursor on or near the vicinity of the heated substrate surface. This method can provide pure materials, and it allows a high control of film structure and composition.

In this study pulse spray evaporation chemical vapor deposition (PSE-CVD) is used. In PSE-CVD, the precursor is dissolved in a solvent, and this mixture is directly injected in the process chamber (evaporation zone, see Fig. 8.8). Only small amounts (~μL) are sprayed with every pulse, so the solution immediately evaporates. A gas flow then transports this vapor to the heated substrate. PSE-CVD has advantages over conventional techniques due to its simple (thus inexpensive) setup, high flexibility, good growth rate control, and high number of parameters for tuning the properties of the final surface [24, 25].

The catalytic functionality of the prepared films were tested in a flow reactor as depicted in Fig. 8.9. The oxidation of several model pollutants like carbon monoxide (CO), propene (C_3H_6) and others were studied and compared to known catalysts. In detail, a catalyst-coated steel mesh was placed inside a flow chamber and the exhaust pollutant concentration was measured. Good catalysts reduce the necessary temperature and are long-term stable. A typical “light-off curve” of such a measurement on α-Fe_2O_3 grown at 300 °C is presented in Fig. 8.9b.

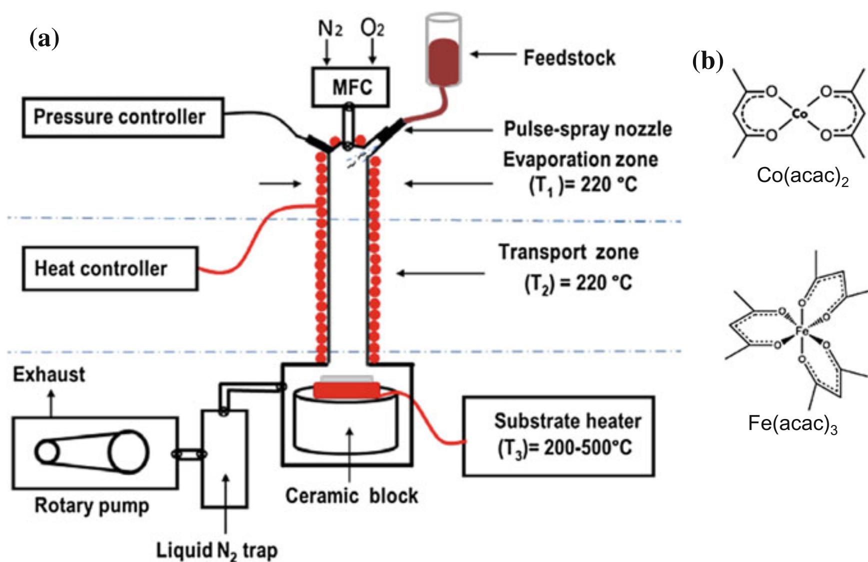

Fig. 8.8 **a** Schematic of the PSE-CVD reactor used to prepare the functional films. **b** Structure of typical acetylacetonate (acac) precursors. (Reprinted from supporting information of [14])

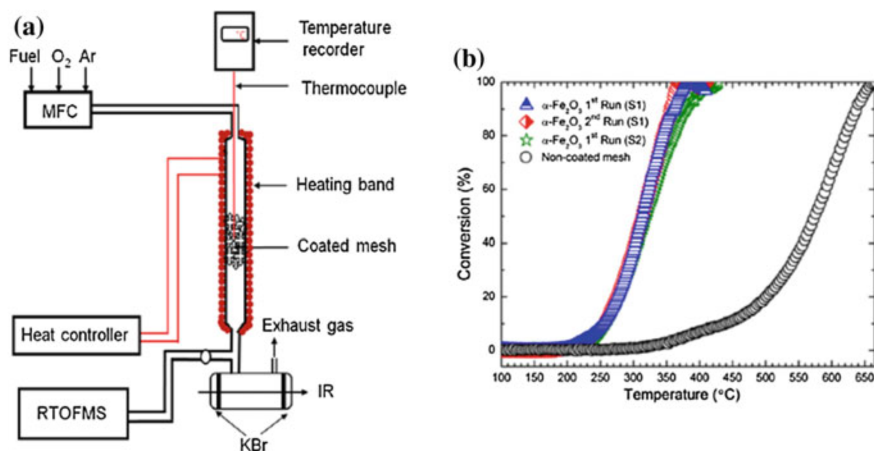

Fig. 8.9 Testing of the catalytic functionality. **a** Schematic representation of the flow-reactor used for catalytic tests. **b** A typical test curve where the mesh temperature is plotted against the conversion rate. This example is α-Fe_2O_3 grown at 300 °C substrate temperature. Reprinted with permission [15]

Layers with promising catalytic activity were then comprehensively characterized by X-ray diffraction (XRD), emission Fourier transform infrared (FTIR) and Raman spectroscopy, scanning electron microscopy (SEM), energy-dispersive X-ray spectroscopy (EDX), ultraviolet–visible (UV–Vis) spectroscopy, and X-ray photoelectron spectroscopy (XPS).

Helium ion microscopy (HIM) was used to obtain the morphology of the catalyst surfaces in more detail. One advantage of this instrument is the depth of focus which is demonstrated in Fig. 8.10. Therein typical HIM micrographs are shown

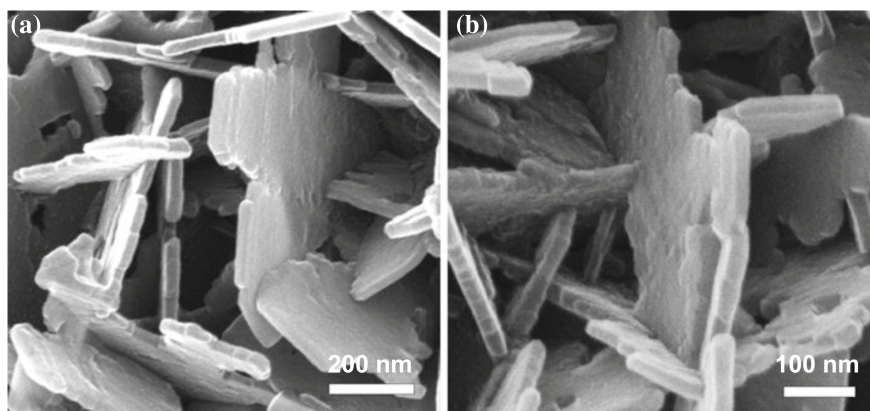

Fig. 8.10 Surface micrographs of α-Fe_2O_3 grown at 300 °C substrate temperature

which allow the identification of small surface features on very steep surfaces. These images clearly reveal that the film is composed of a large quantity of nanoplate-like structures with random orientations. In literature, such a morphology is linked to a higher mechanical strength and a lower pressure drop in catalytic processes which allows higher reactant gas flow rates in comparison to fine powder catalysts. The observed morphology may therefore be related with the catalytic performance of the deposited α-Fe_2O_3 [26]. These images are good examples for the extraordinary depth of focus in the HIM having all features in focus despite height differences of some micrometers.

8.3.2 Binary Mixtures of TMOs

To further enhance the catalytic properties of the iron oxide films, cobalt containing precursor molecules were mixed to the CVD process. Figures 8.11 and 8.12 show significant differences in film morphology as the composition changes. The precursor was varied from 100% $Fe(acac)_3$ to 100% $Co(acac)_2$ providing mixed cobalt-iron oxide films. For both figures only samples grown at 400 °C substrate temperature were selected.

The pure cobalt oxide (Fig. 8.12h) forms closed layer of cubic crystals growing into each other in numerous orientations. On the other hand, pure iron oxide (Fig. 8.11a) presents a uniform densely packed microstructure in hexagon shape. It consists of pallet-shaped crystals which are stacked on each other with equal orientation. Increasing the amount of cobalt in the precursor to 5% (Fig. 8.11b) leads to comparable, but somehow “disturbed” structures. At 10% Co, the morphology is totally different. Small grain sizes with a particular open, porous structure dominate the sample. Already at 30% Co there is a better defined crystal structure with a pyramidal shape embedded in a matrix consisting of small cubic grains. The step to 50:50 precursor mixing ratio gives films composed of large grains which exhibit a cauliflower structure. These films show apparent open porosity, where the amount of rectangular angles like in the pure cobalt film is increasing.

In most cases the surface morphology was characterized by imaging the top side which is the catalytically active area. To obtain more information about the whole growth process some samples were also grown on silicon wafers. These wafers are broken apart and the edges were imaged. This view allows more information on the growth process and a deep view inside the layer. An example is given in Fig. 8.13 which shows an iron-copper oxide layer. This film consists of pallet shaped crystals that grew from the Si substrate to the top of the layer.

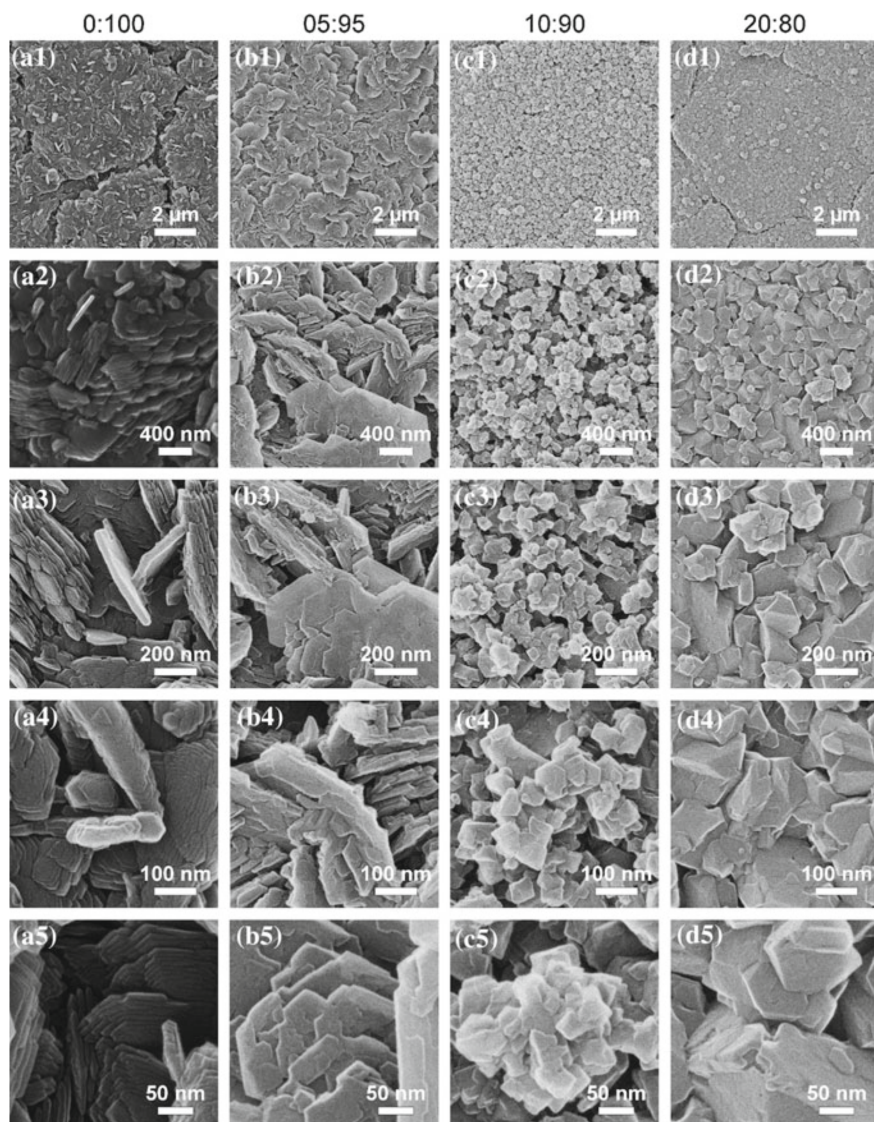

Fig. 8.11 PSE-CVD grown films of iron and cobalt mixed oxides, Part 1. The precursor mixing ratio ($Co(acac)_2$:$Fe(acac)_3$) is given on top of the figure. The field of view of the images increases from 10 µm (*first row*) to 2 µm, 1 µm, 500 nm until 300 nm (*last row*). (Continued in next figure)

8.3.3 Summary: Imaging PSE-CVD Grown Films

Here we presented the use of helium ion microscopy for imaging CVD films. The influences of changes in deposition parameters like temperature and composition

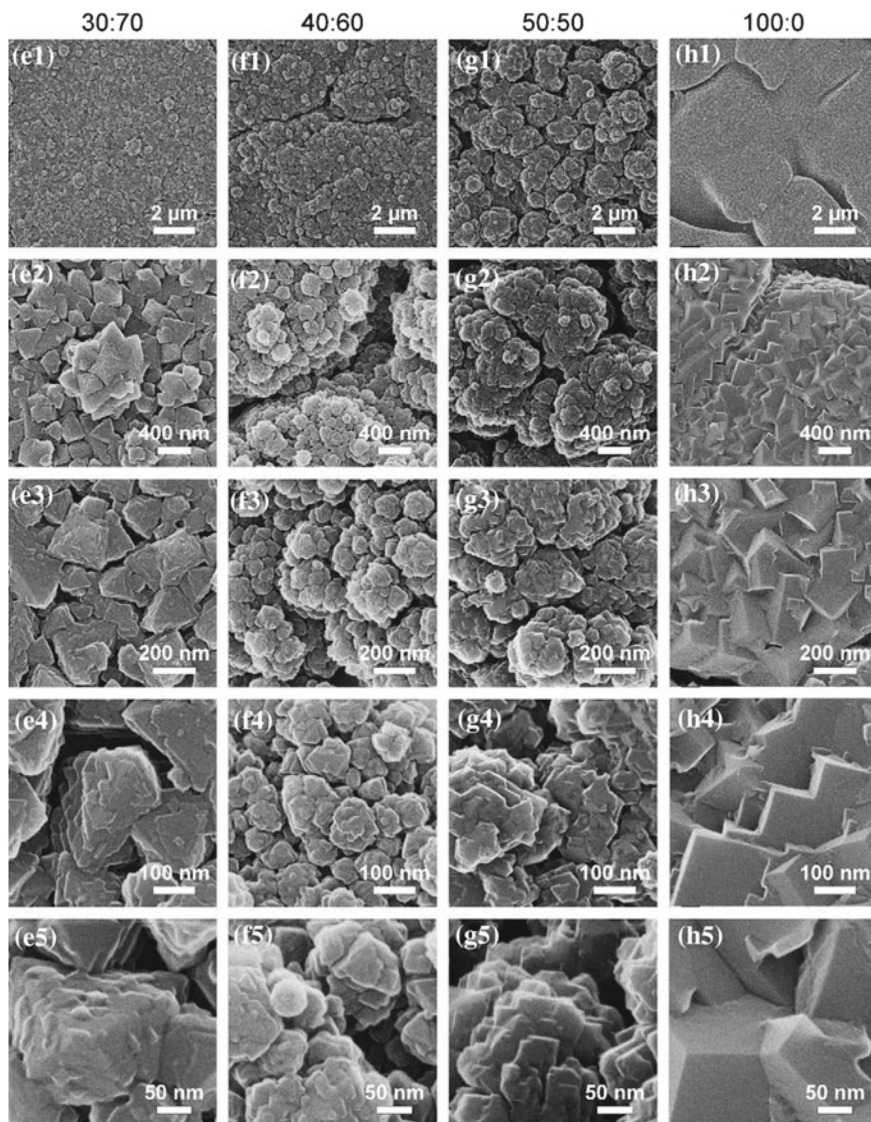

Fig. 8.12 PSE-CVD grown films of iron and cobalt mixed oxides, Part 2. All films are grown at 400 °C substrate temperature (some of the micrographs are already published [14, 19, 20])

are investigated. These changes affect all aspects of the films—not only the surface structure. There is no simple connection of catalytic activity to surface structure. However, in the light of all analytical tools it was possible to gain answers on growth process and details of the catalytic activity itself.

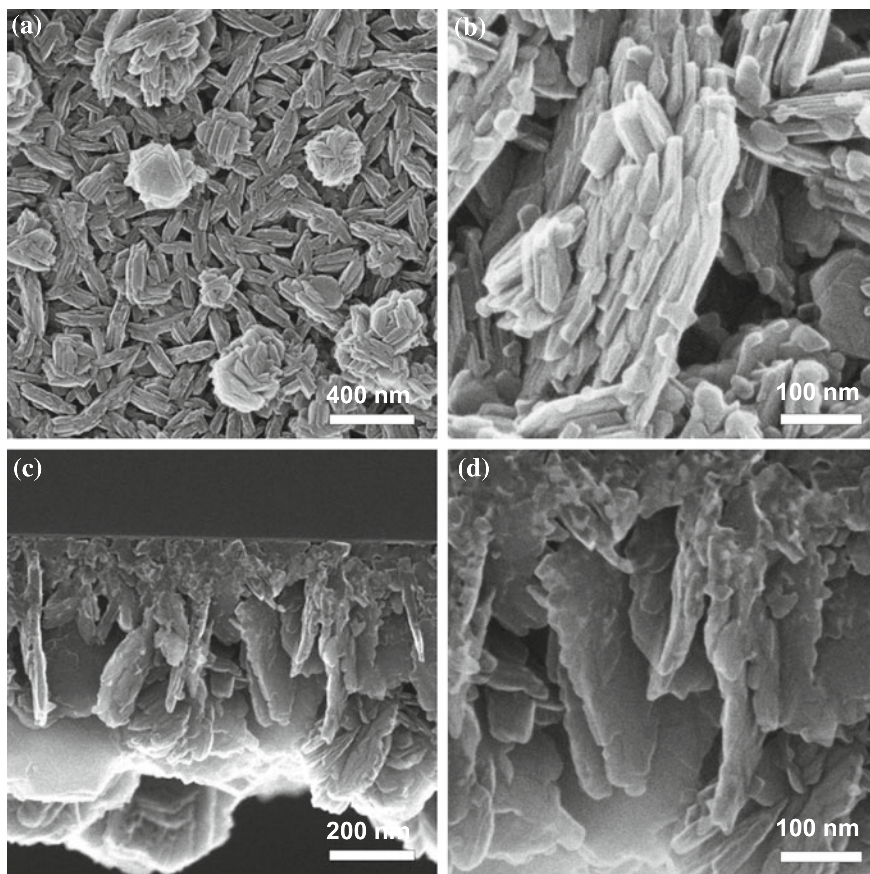

Fig. 8.13 HIM micrographs of iron-copper oxide films on a silicon wafer. **a**, **b** Images of the top surface. **c**, **d** Cross-section images. The silicon wafer was freshly cleaved and the sample was mounted at an angle of 90° in the HIM chamber. A part of the Si wafer is located in the upper part in (**c**) (*dark area*). The Fe-Cu film grow direction in both cross-section images points downwards. The precursor ratio was 50:50 ($Fe(acac)_3$:$Cu(acac)_2$) at a substrate temperature of 400 °C

Due to the high resolution of the HIM it was possible to image very fine surface details. At the same time, the whole sample is in focus due to the high depth of field. These two aspects of the helium ion microscope were especially useful for the analysis of CVD grown films.

8.4 Summary and Conclusions

In this chapter, two examples of the use of helium ion microscopy (HIM) in combustion science are presented. We showed advantages of HIM compared to the established techniques. For both cases, the extraordinary small spot size and thus the achieved high lateral resolution were crucial.

For nascent soot particles, the high contrast on samples composed of light elements, in combination with the high lateral resolution, are key advantages of using HIM. This microscopy method allows time efficient probing of a high number of particles for sizes and shapes down to 2 nm. Therewith, a reasonable effort was sufficient to obtain a thoroughly statistical analysis. Furthermore, the hypothesis that nascent soot is often not spherically could be supported.

A variety of transition metal oxide (TMO) films were imaged, where the high depth of field provided well resolved images on these highly corrugated films. The understanding of the growth and the catalytic activity of such films was enhanced by the use of HIM. These films were found to be potential candidates for better and cheaper catalysts in combustion processes.

Acknowledgments We thank the Physical Chemistry 1 at Bielefeld University where all samples were prepared. In particular, we are thankful to Prof. Katharina Kohse-Höinghaus who did inspire and supervise most of these experiments, as well as Prof. Armin Gölzhäuser who supported this work from the physics side.

In the soot project we thank Marina Schenk (Bielefeld) as well as Prof. Hai Wang and Sydnie Lieb from USC California and Nils Hansen (Sandia National Laboratories). The CVD-Team consisted of Patrick Mountapmbeme Koutou, Achraf El-Kasmi, Patrick Hervé Tchoua Ngamou, Hans-Jakob Herrenbrück and Zhen-Yu Tian—thank you all.

References

1. M. Schenk, S. Lieb, H. Vieker, A. Beyer, A. Gölzhäuser, H. Wang, K. Kohse-Höinghaus, ChemPhysChem **14**, 3248 (2013)
2. M. Schenk, S. Lieb, H. Vieker, A. Beyer, A. Gölzhäuser, H. Wang, K. Kohse-Höinghaus, Proc. Combust. Inst. (2014). doi:10.1016/j.proci.2014.05.009
3. M. Schenk, N. Hansen, H. Vieker, A. Beyer, A. Gölzhäuser, K. Kohse-Höinghaus, Proc. Combust. Inst. (2014). doi:10.1016/j.proci.2014.06.139
4. B. Kumfer, I. Kennedy, *Combustion Generated Fine Carbonaceous Part* (KIT Scientific Publishing, 2009)
5. T.C. Bond, S.J. Doherty, D.W. Fahey, P.M. Forster, T. Berntsen, B.J. DeAngelo, M.G. Flanner, S. Ghan, B. Kärcher, D. Koch, S. Kinne, Y. Kondo, P.K. Quinn, M.C. Sarofim, M.G. Schultz, M. Schulz, C. Venkataraman, H. Zhang, S. Zhang, N. Bellouin, S.K. Guttikunda, P.K. Hopke, M.Z. Jacobson, J.W. Kaiser, Z. Klimont, U. Lohmann, J.P. Schwarz, D. Shindell, T. Storelvmo, S.G. Warren, C.S. Zender, J. Geophys. Res. Atmos. **118**, 5380 (2013)
6. J.B. Donnet, Carbon **20**, 267 (1982)
7. H. Wang, Proc. Combust. Inst. **33**, 41 (2011)
8. K. Kohse-Höinghaus, *Reference Module in Chemistry, Molecular Science and Chemical Engineering* (Elsevier, 2015)

9. B. Zhao, K. Uchikawa, H. Wang, Proc. Combust. Inst. **31**, 851 (2007)
10. H. Wang, B. Zhao, B. Wyslouzil, K. Streletzky, Proc. Combust. Inst. **29**, 2749 (2002)
11. W.E. King, G.H. Campbell, A. Frank, B. Reed, J.F. Schmerge, B.J. Siwick, B.C. Stuart, P.M. Weber, J. Appl. Phys. **97**, 111101 (2005)
12. S. Lieb, Experimental Investigation of Nascent Soot Physical Properties and The Influence on Particle Morphology and Growth, Dissertation, University of Southern California, 2014
13. A.D. Abid, N. Heinz, E.D. Tolmachoff, D.J. Phares, C.S. Campbell, H. Wang, Combust. Flame **154**, 775 (2008)
14. P.M. Kouotou, Z.-Y. Tian, H. Vieker, A. Beyer, A. Gölzhäuser, K. Kohse-Höinghaus, J. Mater. Chem. A **1**, 10495 (2013)
15. P.M. Kouotou, Z.-Y. Tian, H. Vieker, K. Kohse-Höinghaus, Surf. Coat. Technol. **230**, 59 (2013)
16. P.H. Tchoua Ngamou, A. El Kasmi, T. Weiss, H. Vieker, A. Beyer, V. Zielasek, K. Kohse-Höinghaus, M. Bäumer, Z. Phys. Chem. **229** (2015)
17. Z.-Y. Tian, H.J. Herrenbrück, P.M. Kouotou, H. Vieker, A. Beyer, A. Gölzhäuser, K. Kohse-Höinghaus, Surf. Coat. Technol. **230**, 33 (2013)
18. A. El Kasmi, Z.-Y. Tian, H. Vieker, A. Beyer, T. Chafik, Appl. Catal. B Environ. **186**, 10 (2016)
19. P.M. Kouotou, H. Vieker, Z.-Y. Tian, P.T. Ngamou, A.E. Kasmi, A. Beyer, A. Gölzhäuser, K. Kohse-Höinghaus, Catal. Sci. Technol. **4**, 3359 (2014)
20. Z.-Y. Tian, P. Mountapmbeme Kouotou, A. El Kasmi, P. H. Tchoua Ngamou, K. Kohse-Höinghaus, H. Vieker, A. Beyer, A. Gölzhäuser, Proc. Combust. Inst. **35**, 2207 (2015)
21. Z.Y. Tian, H. Vieker, P.M. Kouotou, A. Beyer, Faraday Discuss. **177**, 249 (2015)
22. A.J. McMichael, R.E. Woodruff, S. Hales, The Lancet **367**, 859 (2006)
23. H.H. Kung, *Transition Metal Oxides: Surface Chemistry and Catalysis* (Elsevier, 1989)
24. J.-P. Sénateur, C. Dubourdieu, F. Weiss, M. Rosina, A. Abrutis, Adv. Mater. Opt. Electron. **10**, 155 (2000)
25. P. M. Kouotou, Synthesis and Catalytic Application of Functional Transition Metal Oxides, Dissertation, Universität Bielefeld, 2014
26. J. Ma, J. Teo, L. Mei, Z. Zhong, Q. Li, T. Wang, X. Duan, J. Lian, W. Zheng, J. Mater. Chem. **22**, 11694 (2012)

Chapter 9
Channeling and Backscatter Imaging

Gregor Hlawacek, Vasilisa Veligura, Raoul van Gastel and Bene Poelsema

Abstract While the default imaging mode in HIM uses secondary electrons, backscattered helium or neon contains valuable information about the sample composition and structure. In this chapter, we will discuss how backscattered helium can be used to obtain information about buried structures and provide qualitative elemental contrast. The discussion is extended to the use of channeling to increase image quality and obtain crystallographic information. As an example, we demonstrate that the period of a dislocation network in a film only two monolayers thick can be obtained with atomic precision.

9.1 Introduction

Typically, secondary electrons are used for image creation in the HIM. However, as will be explained in more detail in Chap. 12, backscattered helium or neon atoms contain valuable information on the sample composition. We will show examples that make use of backscattered helium to obtain qualitative elemental contrast, which is often sufficient to understand processes in a specimen. This is especially true for well-defined samples with a known composition and where the user is only interested in knowing the location of the heavy or light elements present.

Although this works well, there is an important simplification that is rarely mentioned or discussed. For nearly all imaging applications—and, in fact, practically all

G. Hlawacek(✉)
Institute for Ion Beam Physics and Materials Research,
Helmholtz–Zentrum Dresden-Rossendorf, Bautzner Landstr. 400,
01328 Dresden, Germany
e-mail: g.hlawacek@hzdr.de

V. Veligura · R. van Gastel · B. Poelsema
Physics of Interfaces and Nanomaterials, Univerity of Twente,
Enschede, The Netherlands

© Springer International Publishing Switzerland 2016

G. Hlawacek and A. Gölzhäuser (eds.), *Helium Ion Microscopy*,
NanoScience and Technology, DOI 10.1007/978-3-319-41990-9_9

theoretical work—the sample is considered to be an amorphous solid without a crystal structure. In reality, for both the secondary electrons and the backscattered ions, directional effects rooted in the crystal structure of the sample play an important role. In this chapter we will begin by summarizing the theoretical foundations of ion channeling and how it affects the secondary electron generation. We will show how this can be used to obtain crystallographic information in a way similar to electron backscatter diffraction. After a brief discussion of imaging with backscattered ions and how it can be used to obtain information on buried structures, we demonstrate how channeling can be exploited to obtain contrast from thin surface layers. The last example presented is a powerful demonstration of the high-resolution imaging capabilities of HIM. By exploiting the dechanneling from lattice defects present in an ultrathin silver layer deposited onto a platinum crystal, we reveal a dislocation network formed at the interface between the substrate and the adlayer. While the ability to image this network is an achievement in itself, the periodicity of this network can be measured with atomic precision. This demonstrates that the combination of high-resolution HIM imaging with channeling can provide new insight into sample structure.

9.2 Directional Effects in Ion Solid Interaction

9.2.1 Ion Channeling

Channeling of ion beams into crystalline solids is a well-understood effect that is often exploited in ion beam analysis [1]. The phenomenon was extensively described by Lindhard [2] in the 1960s and has been used for ion beam analysis ever since [3]. Although it is often used at high energies typical for Rutherford backscattering spectrometry, it is also effective at lower energies. In fact, the probability for channeling is even higher at low energies E. This becomes evident by considering the equation for the critical angle

$$\Psi_c = \Psi_1 = \sqrt{\frac{U_a(r_{min})}{E}}. \tag{9.1}$$

Here, $U_a(r_{min})$ is the average potential at a distance r from the string of atoms, with r_{min} being the distance of closest approach of the ion with atomic number Z_1 to the string. Assuming a Thomas–Fermi type potential, we can calculate the potential of a string of atoms with atomic number Z_2 [4]

$$U_a(r_{min}) = \frac{Z_1 Z_2 e^2}{4\pi\epsilon_0 d} \ln\left[\left(\frac{Ca_{TF}}{r}\right)^2 + 1\right]. \tag{9.2}$$

Here, d is the spacing between the atoms in the string, Z_1 and Z_2 are the atomic number of the projectile and the impinging particle, ϵ_0 is the vacuum permittivity, e

is the unit charge, and C^2 is usually taken to be 3 [2]. However, particularly for the low energies relevant for ion microscopy, other screening functions can be used. We stick with the Thomas–Fermi screening length, which is given by

$$a = a_{TF} = \frac{0.885 a_0}{(Z_1^{1/2} + Z_2^{1/2})^{2/3}} \tag{9.3}$$

where $a_0 = 0.053\,\text{nm}$ is the Bohr radius. As a result of the relation (9.1), the acceptance angle for channeling increases with decreasing energy. However, in the low-energy regime Ψ_c is proportional to $E^{1/4}$ instead of $E^{1/2}$. This low-energy regime is entered when [2]

$$E < E' = \frac{2 Z_1 Z_2 e^2}{4\pi\epsilon_0} \frac{d}{a^2}. \tag{9.4}$$

For the energies used in the HIM, this condition is always fulfilled[1] and the critical angle has to be modified to [2]

$$\Psi_2 = \left(\frac{Ca}{d\sqrt{2}} \Psi_1 \right)^{1/2}. \tag{9.5}$$

For even lower energies, this approximation breaks down, and the critical angle begins to decrease rapidly. For the example of He into tungsten, this occurs at roughly 1 keV [5].

From this short discussion it becomes clear that channeling occurs easily in the HIM.

9.2.2 *Directional Effects in Secondary Electron Emission*

However, in the HIM, one seldom records data based on the collection of either transmitted or backscattered helium atoms. In the HIM, the standard imaging mode is based on the collection of secondary electrons. These electrons are excited by the impinging energetic atom and emitted from the sample. Two possible processes for the generation of secondary electrons are typically discussed. The first—potential emission via Auger neutralization—is effective only at energies smaller than those used in the HIM [6, 7]. The other process—kinetic electron emission—is based on the direct knock-on collision of the moving atom with electrons of the sample atoms. In a first-order approximation, the rate of secondary electron generation δ_{iSE} is proportional to the electronic stopping power $\frac{\mathrm{d}E}{\mathrm{d}s}$ in eV/Å [8, 9] .

---

[1]For 30 keV He into Au $E' = 1.3\,\text{MeV}$, and for Si $E' = 0.12\,\text{MeV}$.

$$\delta_{iSE} = -\frac{1}{\epsilon}\frac{\mathrm{d}E}{\mathrm{d}s} \tag{9.6}$$

ϵ is a scaling constant. Once secondary electrons have been generated, they still need to escape from the solid. This can be described as a diffusion process. The characteristic length scale of this diffusion process—the effective diffusion length of secondary electrons λ_d is on the order of 1 nm for nearly all materials [6]. This leads to the fact that only the first few nanometers of the material add to the emitted SEs. As a consequence, HIM is very surface-sensitive [10]. Measurements of the effective SE yield in HIM show variations from 1 for carbon to values as high as 8 for platinum [11].

A number of theories have been proposed for predicting SE yields. Although this has been the topic of numerous investigations over several decades, no simple theoretical model is capable of predicting the SE yield for all possible ion/sample combinations with satisfactory precision. Baragiola et al. have analyzed several models for predicting iSE yields and have compared them to experimental results [12]. They conclude that the iSE yield can be calculated with sufficient accuracy for the energy range important in HIM using

$$\delta_{iSE} = \frac{PLS_i(v_i)}{2J}. \tag{9.7}$$

Here, v_i is the velocity of the impinging particle, P is the surface escape probability, L is the electron mean free path, $S_i(v_i)$ is the velocity-dependent total inelastic stopping power, and J is the average energy required to form an electron–hole pair with an energy above the vacuum level. This already includes the simplification wherein S_i does not change much over the distance of L. By comparing experimental results to (9.7), they found that for velocities above 7×10^5 m/s,

$$\delta_{iSE} = 0.1 S_i(v) \tag{9.8}$$

within 40% if $S_i(v)$ is given in Å/eV. This condition is easily fulfilled in the HIM for energies above 10 keV.

An attempt to find an empirical formula by fitting existing yield data was made by Ramachandra et al. [6] (see also Chap. 4 and in particular Sect. 4.2.6 and references therein). However, this approach requires prior knowledge of experimental yields. On the other hand, it could be used for elemental targets as well as complex mixtures. Furthermore, the Monte Carlo code used is also able to predict δ_{iSE} changes with morphology.

Similar to the approach discussed above, most of the theoretical descriptions of δ_{iSE} deal with amorphous materials and do not take into account the crystal structure of the solids. Several attempts have been made to do so [13]. Initial results—relevant for the energies and ion masses used in GFIS-based ion microscopy—used the shadow cone of the surface atoms and considered the change in stopping power across the channel, which is determined by the impact parameter [14]. More recent

work has explicitly attempted to calculate the electron density within the channel, and has achieved good agreement with experiments [15]. For the practitioner, these approaches have in common that they require detailed knowledge of the analytical models and are computationally expensive. As a consequence, this model cannot be *quickly* checked against experimental data. However, a *transparency model* was introduced much earlier—first for sputtering—that has led to useful qualitative agreement with measured data [16–18].

This transparency model [16] is based on the following assumptions

1. Secondary electrons are ejected due to kinetic electron emission
2. A collision happens close to the surface or does not play a role for the electron emission
3. The escape probability is independent of orientation
4. The ion–electron ejection coefficient is proportional to the probability for a collision.

While (1) and (2) are easy to understand, considering the energy range of interest and the mean free path of electrons within the material, the remaining assumptions require more attention. If one assumes that the work function of the surface plays no role in the SE emission (3), special care must be taken. In particular, HIM has been shown to be a very surface-sensitive imaging technique that allows the detection of small changes in work function [19, 20]. However, some results are obtained with less sensitive techniques, and simulations indicate that the variation in work function between different crystallographic surface terminations might be too small to be detected [21]. In addition, the possibility that electron emission channeling [22] influences the observed (directional) iSE yield must be considered. However, the effect of channeling seems to be stronger than the changes in work function. One also should keep in mind that iSE yield and work function for a specific surface do not correlate directly. From (4) we can derive that for large enough energies where the cross sections of the atoms for iSE production do not overlap, the ratio of the blocked area to the total area is the same as the ratio of the iSE yields. A similar approach based on the transparency of the crystal has been used to understand the channeling-related change in X-ray emission from metals and organic crystals [23, 24].

More recent descriptions are based on molecular dynamics simulations [21]. Using the Oen–Robinson [25] inelastic loss function, they attempt to mimic the electron density around the target nuclei. Good agreement is reached for both random orientation and the directional dependency of the iSE emission coefficient.

In the following section we will describe the effect of crystal orientation on the backscatter yield and the secondary electron yield as it is observed specifically in the HIM. The examples presented will highlight how channeling can be used to obtain crystallographic information and how dechanneling can reveal information on thin organic and inorganic surface layers. As will become clear, a qualitative transparency model is sufficiently accurate for understanding the observed changes in SE yield. We will further show that backscattered helium can be used to obtain information on buried interfaces perpendicular to the surface.

9.3 Mapping of Crystal Orientation in the Ion Microscope

As discussed above, channeling of He ions leads to a change in the backscatter yield. Using a micro-channel plate (MCP), backscattered helium (BSHe) images can be recorded. The contrast in such an image depends on the amount of backscattered particles that hit the annular MCP mounted above the sample. Although yields are usually small, the large solid angle of the detector and the high sensitivity of the MCP results in good signal-to-noise ratios. Such a BSHe image of a polycrystalline gold sample is presented in Fig. 9.1. The individual gold grains can be distinguished, as their random orientation results in different channeling conditions [26, 27]. The surface normal of the dark grain at the top of the image is a low index or close to a low index direction. This allows the ions to penetrate deep into the sample, and when they are finally backscattered, only a small number of them have sufficient energy to reach the surface and be detected. For bright grains the situation is reversed. Their orientation is not close to a low index direction, and channeling does not occur. The amount of BSHe is high, as the ions will very likely undergo at least one small impact parameter collision close to the surface. The resulting lower average penetration depth will allow more backscattered helium to reach the surface. While the sample has an overall $\langle 1\,1\,1 \rangle$ texture, the orientation of the grains has a 3.5° wide angular distribution. Keeping in mind that the axial half angle Ψ_2 (9.5) for He into Au at 20 keV is around 3°, one can understand the rich contrast in the image.

The standard imaging mode in HIM is the secondary electron (SE) mode. Here, the emitted electrons and not the backscattered primary particles are used for image generation. In Fig. 9.2 three images obtained in SE mode from the same polycrys-

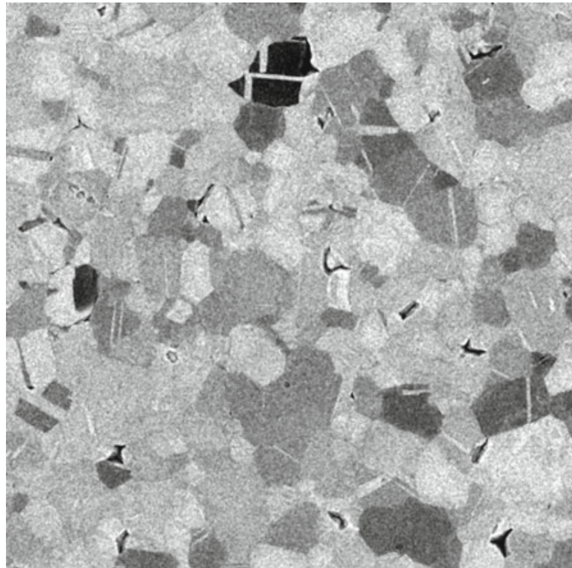

Fig. 9.1 BSHe image of a polycrystalline gold sample. The image was recorded using 1.11×10^{15} cm^{-2} 20 keV He ions under normal incidence. The FOV is 15 μm. Reproduced from [26]

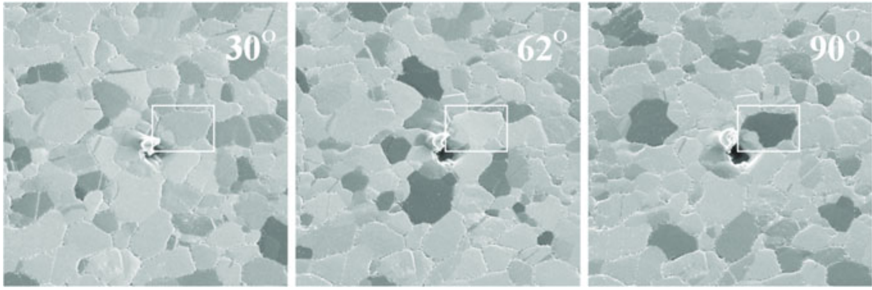

Fig. 9.2 Surface of a polycrystalline Au sample. The image was recorded in SE mode using 4.9×10^{14} cm^{-2} He ions at a primary energy of 15 keV. The FOV is 10 μm. Reproduced from [26]

talline gold sample are presented. Around a central defect, the different gold grains can be identified by their difference in brightness. This particular image series was obtained under a polar angle of 35°. The grains in the film all have a $\langle 1\,1\,1 \rangle$ texture, but their in-plane orientation is random. As a result, some of them will be in a channeling condition while others will not. This results in a strong channeling contrast [28, 29].

Rotating the sample around its surface normal, intensity curves similar to the ones shown in Fig. 9.3a can be obtained. Azimuthal rotation around the [1 1 1] surface normal of the sample will eventually align the beam along the $[\bar{1}\,\bar{4}\,\bar{1}]$ and the $[\bar{1}\,\bar{1}\,0]$ direction. Alignment of the beam with these low index directions leads to the dips in the SE intensity curves. Views of the crystal along these directions are shown as inserts in Fig. 9.3a. A strong energy dependence of the depth of the channeling dip is observed here. However, this is not directly related to the minimum yield for dechanneling of the primary projectile (χ_{min}), which should be independent of energy and should depend solely on the properties of the target crystal [4].

A model similar to the earlier mentioned *transparency model* [16–18] was used in [26] to obtain the simulated curve presented in Fig. 9.3b. A model of an fcc crystal was created using a lattice parameter of 4.078 Å and an atom diameter of 0.68 Å. The slab thickness was restricted to 14 layers. This corresponds to roughly three times the effective diffusion length for the secondary electrons [6] . As a result, deeper lying collisions will not contribute significantly to the SE yield. This model crystal was than rotated and tilted, and the blocked area fraction (opacity) calculated. The results show excellent agreement with respect to the position of the minima, and can to a certain extent also reproduce the relative depth of the minima. The latter in particular is very sensitive to choice of atom diameter. As others have shown, a sensible choice of this diameter can be made.

Using the above method, opacity/transparency values can be obtained for the entire hemisphere. The result of such calculations for both fcc and bcc are presented in Fig. 9.4. The results obtained agree well in terms of dip position with calculations based on code from B. Doyle. In contrast to the approach presented here, he evaluates the well-known equations based on the original paper by Lindhard [2], with

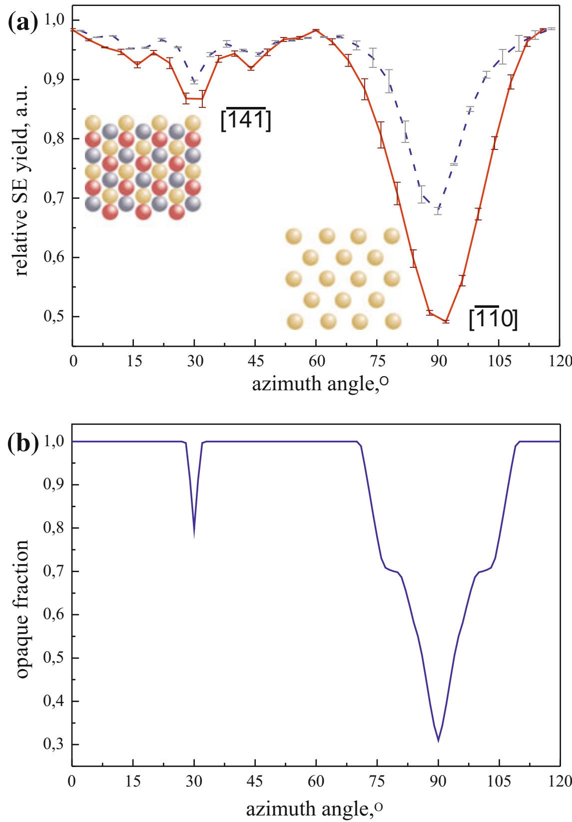

Fig. 9.3 SE yield plotted against the rotation around the surface normal for a {111} textured polycrystalline gold film. **a** Experimental data: Results for two different energies (15 keV: *red*, *solid line*; 33.6 keV: *blue*, *dashed line*) are shown. The *insets* show the view along the indicated directions. Color coding of atoms is as follows: *gold* 1st layer, *silver* 2nd layer, and *red* 3rd layer. **b** Simulated intensity variation obtained using the transparency model

some modifications that account for low and high energy deviations [30]. Using this approach, the calculated width of the channeling dip for 15 keV He along Au[$\overline{1}\,\overline{1}\,0$] corresponds to $2\Psi_2 = 12.44°$. This is slightly smaller than the value of 15° obtained in the simulation (see Fig. 9.3b) and also smaller than the measured (Fig. 9.3a) value of 17°. However, one must keep in mind that the calculation is for the channeling-induced reduction of the backscatter yield. What was measured by Veligura et al. [26] was the change in secondary electron yield. As discussed above, these two phenomena are related to one another, but not the same. Furthermore, a somewhat higher angular resolution in the measurement would result in a deeper minimum and consequently a smaller Ψ_2.

The above-mentioned calculations are easily performed with a recently developed program that allows for the calculation of channeling parameters for arbitrary direction [31]. Unlike the earlier-presented transparency models, this code is based on

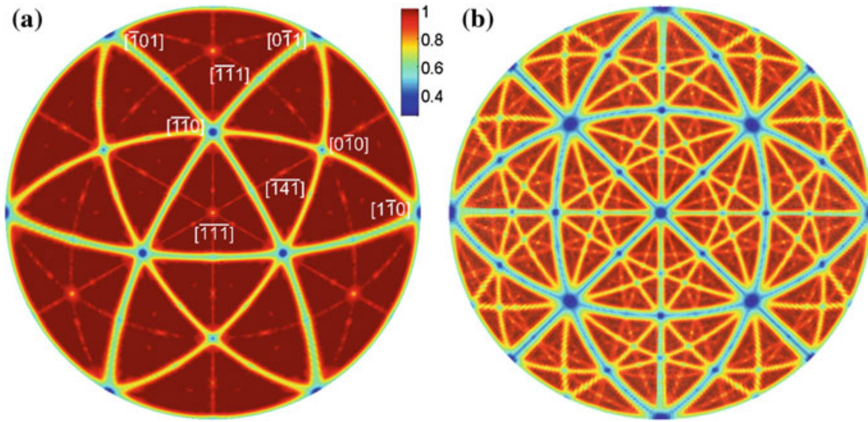

Fig. 9.4 Channeling maps for fcc (*left*, reproduced from [26]) and bcc (*right*). Both maps are centered around ⟨1 1 1⟩. While *red* corresponds to a blocking direction, *blue* indicates maximum transparency

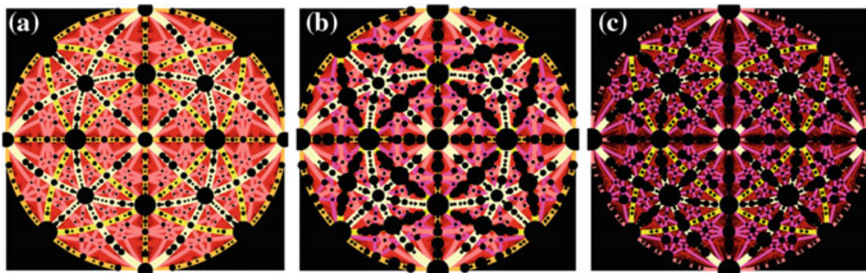

Fig. 9.5 Stereographic projections of channeling maps for 10 keV He into **a** Si diamond lattice, **b** Cu fcc lattice and **c** Fe bcc lattice. In all three plots, the ⟨0 0 1⟩ direction is located at the center. Calculation and image courtesy of B.L. Doyle, Sandia National Lab [31–33]

analytically derived formulas. However, the agreement is very good, and the resulting channeling maps are presented in Fig. 9.5 [32, 33].

For determination of the orientation of the underlying crystal, the absolute depth and width of the channeling dips is of minor importance. As long as the positions can be predicted with sufficient accuracy, maps like the ones presented in Fig. 9.4 can be used to obtain orientation information. This was done for the polycrystalline gold film presented in Fig. 9.2. For each pixel, the intensity versus angle graph is compared to the calculated map. Provided that the measured data covers a sufficiently large angular range, a single solution exists that will map the measured minima positions to the expected ones in the map. The result is presented in Fig. 9.6.

A related effect can be seen during the in situ observation of He-induced blister formation in metals [34]. In Fig. 9.7a, b, He-induced blistering in gold and tungsten can be seen. The blisters show characteristic patterns of dark lines, which reflect

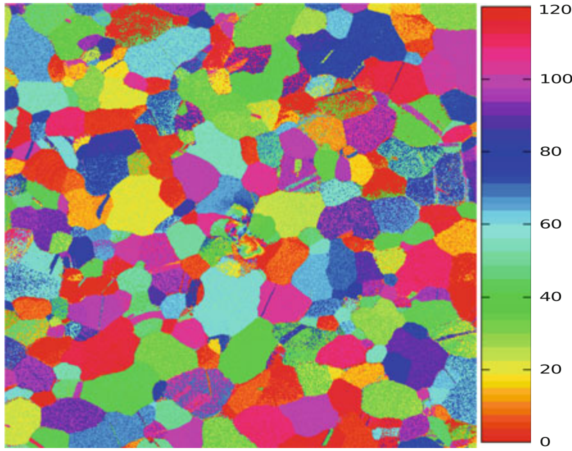

Fig. 9.6 Color-coded orientation map of the polycrystalline gold film presented in Fig. 9.2. The color code corresponds to the in-plane rotation of the grains. All grains have the ⟨1 1 1⟩ direction perpendicular to the surface. Reproduced from [26]

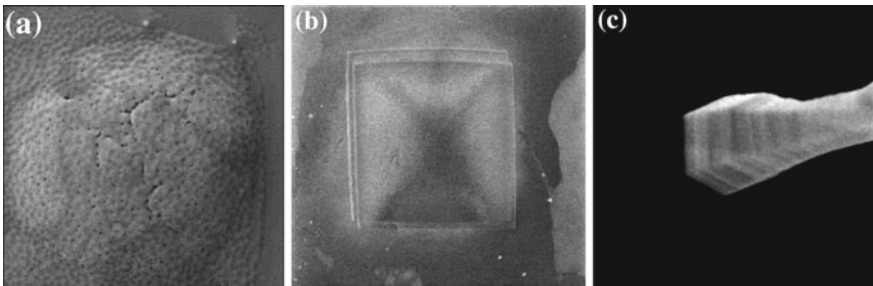

Fig. 9.7 Channeling effects. **a** Helium-filled blister in gold. Reproduced from [34]. **b** Blister in tungsten created by high-fluence He implantation. The triangular (Au) or diagonal (W) arrangement of *dark lines* is the result of the channeling-related reduction in SE yield. **c** Twins in a GaAs nanowire. The alternating *dark* and *bright* stripes are the result of twinning and the related change in channeling conditions

their crystalline structure. In the case of gold, parts of the bent crystalline surface of the blister fulfill the channeling condition for the {1 1 1} planes. The angle between these planes when they intersect the (1 1 1) surface is 120°, which results in the characteristic arrangement of the dark lines (compare the fcc map in Fig. 9.4). For the bcc metal tungsten, the dark lines most likely correspond to the intersection of the {1 1 0} planes with the surface.

A further example demonstrating the usefulness of channeling is presented in Fig. 9.7c. The alternating pattern of dark and bright stripes on the surface of the hexagonal-shaped nanorod is the result of twins present in the GaAs nanowire. A twin leads to a flip of the crystal structure. Consequently, if one part of the crystal fulfills the channeling condition, the other part of the twin typically will not.

9.4 Imaging with Ions

9.4.1 Backscattered Helium Versus Electrons for Image Generation

Although SE are mostly used for image generation in the HIM, the use of backscattered helium (BSHe) offers several interesting options not available with electrons. On the other hand, there are clearly some drawbacks to using BSHe for image formation:

1. Low yield. Only a small fraction of the impinging helium will be backscattered, not all of which will hit the detector. For secondary electrons multiplication of the incoming beam by a factor of 2–8 occurs, and nearly all emitted electrons will eventually be sucked into the Everhart–Thornley detector.
2. Lower lateral resolution. While the secondary electrons are generated in only a very small volume close to the surface, backscattered helium originates from various depths and a large lateral area proportional to the radial range of the ions.

The first of these in particular requires longer integration times and higher total fluence, which will lead to greater sample damage.

However, the backscatter yield has a square root dependence on the atomic number of the target atom. This can be exploited to distinguish heavy (high backscatter yield) from light elements (low backscatter yield). An example is presented in Fig. 9.8

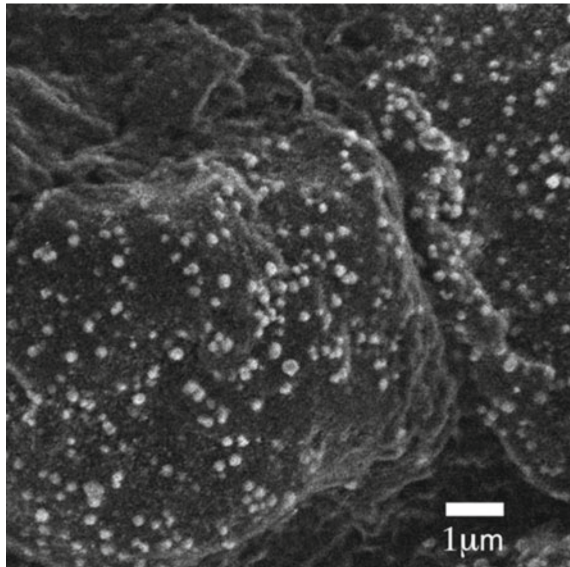

Fig. 9.8 BSHe image of carbon-black toner particles with embedded metal nanoparticles. Thanks to the difference in atomic number, the metal particles are clearly discernible. Reproduced with permission from [27]

A BSHe image of metallic nanoparticles on a carbon support is shown [27]. Because of their higher atomic number, the backscatter yield from the nanoparticles is higher than for the carbon support, which appears dark. In general, higher atomic numbers will lead to increased backscattering. However, a more detailed analysis reveals an oscillatory behavior of the backscatter yield [35–37], which further complicates a quantitative analysis of this signal.

9.4.2 Subsurface Imaging

Subsurface imaging is a useful imaging mode that can be substantially enhanced if channeling is considered. It provides the potential for revealing buried structures formed by heavy elements. Van Gastel et al. present an approach for visualizing the buried diffusion front of an electric contact made of a Pd_2Si alloy [38]. This contact is formed in an annealing step below a silicon oxide with a thickness exceeding 100 nm [39]. The advantage of this imaging method over classical cross sectioning [40] is clear from the data presented in Fig. 9.9.

The bright areas at the top and bottom of the figure are the deposited Pd reservoirs on the sample surface. Particularly in the right BSHe image, these deposits appear bright, due to their high content of heavy Pd. While in the left SE-mode image, the two Pd reservoirs are separated by a rough polycrystalline oxide film, a faint contrast can be observed in the right BSHe image. These areas are separated by a dark, Pd-free area. Although the contrast for the buried Pd_2Si is weak, the rough nature of the diffusion front is clearly visible. Accessing the roughness of the diffusion front is not easy in classical cross section-based methods.

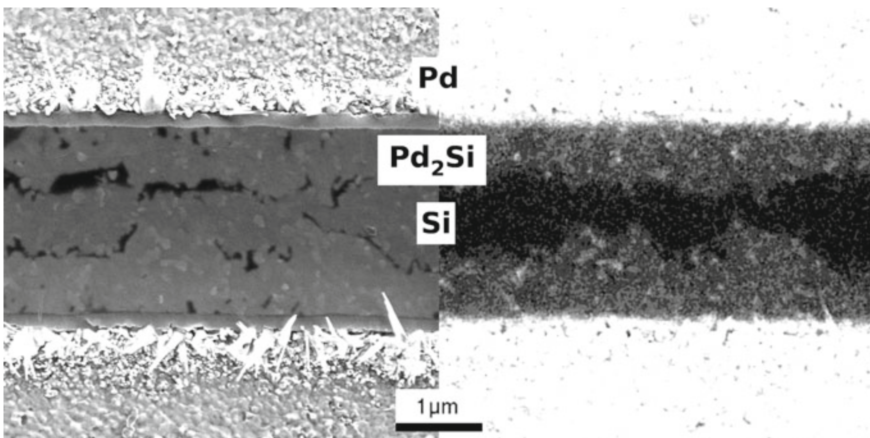

Fig. 9.9 Imaging a buried diffusion front. The buried Pd_2Si electrical contact is visible only in the *right* BSHe image, and not in the *left* SE mode image. Reproduced with permission from [38]

Another possibility for subsurface imaging is through the use of static capacitative contrast [41] to reveal hidden features. This approach is similar to the often used dopant contrast, which yields excellent quantitative results in the HIM [42].

9.5 Dechanneling Contrast

One practical application of the channeling contrast mechanism described in Sect. 9.3 is to exploit the dechanneling that is caused by either defects or adlayers on the surface. This is often performed using medium- or high-energy beams to resolve the structure of surface reconstructions and epitaxial layers [43–45]. However, in an imaging device like the HIM, simple changes in backscattering probability due to blocking can already reveal information on the outermost surface layer. In this section, we will first (Sect. 9.5.1) present examples where a simple amorphous layer results in an enhanced backscattering probability for BSHe. In Sect. 9.5.2, we will then use changes in the SE yield to resolve the surface reconstruction of a thin metallic adlayer.

9.5.1 Dechanneling by Thin Films

An SE mode image of a silicon(001) wafer patterned with two different self-assembled monolayers is presented in Fig. 9.10a [46]. Two different molecules have been used to create the stripe pattern [20]. Because of their different work functions,

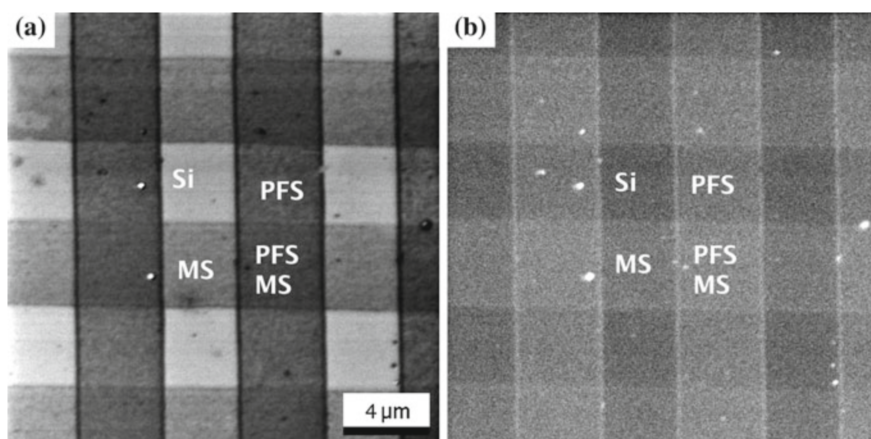

Fig. 9.10 Self-assembly monolayers on silicon. Two different SAMs have been patterned in vertical and horizontal stripes onto a Si (001) wafer. **a** SE-mode image. **b** BSHe image. Reproduced from [46]

one can conclude that the vertical stripes are formed by triethoxy(1H,1H,2H,2H-tridecafluoro-n-octyl)silane (short perflourosilane, PFS, $\Phi = 6.6$ eV [46, 47]). They appear darker than the horizontal stripes formed by (3-mercaptopropyl) trimethoxysilane (short mercaptosilane, MS, $\Phi = 5.3$ eV [48]). However, our main point of interest here is the corresponding BSHe image presented in Fig. 9.10b. Interestingly, the SAM stripes are also visible here and can be distinguished. While the empty Si patches backscatter a minimal amount of He atoms, significantly more He is backscattered from the areas covered by PFS and MS.

The increased backscattering is a result of the enhanced dechanneling due to the additional carbon atoms, reducing the channeling probability into the underlying Si(001) crystal. From the channeling map presented in Fig. 9.5b, it is clear that the $\langle 0\,0\,1 \rangle$ direction is one of the strongest available in the diamond lattice. Therefore, in the uncovered areas, dechanneling is minimal, and occurs only due to the thin native oxide on the Si. The addition of several tens of Ångströms of carbon very effectively blocks the channels and increases the backscatter probability. Calculations for Si$\langle 0\,0\,1 \rangle$ with and without overlayer show a threefold increase of χ_{min} after the addition of a 3 nm carbon overlayer. The observed increase in backscatter probability between the Si patches and the carbon covered patches is somewhat smaller, as an additional thin SiO_x layer is present everywhere on the substrate.

A clear thickness dependence can be observed in this experiment. The edges of the SAM stripes are slightly thicker due to the preparation process, which leads to an enhanced dechanneling and higher signal from these areas. This is most visible for the edges of the vertical PFS stripes, and is also confirmed by the χ_{min} calculations. Increasing the carbon adlayer from 3 to 6 nm further decreases the channeled fraction by a factor of 2. Similar effects have been observed for monolayer-thick islands of organic semiconductor molecules [46] and cobalt germanide nanocrystals on germanium (001) [49]. The former result is presented in Fig. 9.11. The left column presents a para-sexiphenyl (6P) island observed under normal incident, which corresponds to the $\langle 0\,0\,1 \rangle$ channeling direction into the silicon substrate. The island is clearly visible in both the SE-mode image 9.11a and the BSHe-mode image 9.11b. A small nucleus of the second layer is visible in the center of the island and is marked by an arrow. Similar to Fig. 9.10b, the second layer becomes visible due to the increased dechanneling as a result of the greater thickness. The right part of the panel shows a similar island observed using a 10° tilt angle. While the island is clearly visible in the SE image, only noise is observed in the BSHe data. Now the beam experiences a high backscattering probability over the entire field of view, as the underlying bulk sample is in a blocking orientation.

9.5.2 Dechanneling by Lattice Distortions

As shown above, dechanneling can be used in the HIM to investigate thin adlayers. On the other hand, channeling has traditionally been used to investigate lattice defects such as dislocations and point defects including both interstitial and substi-

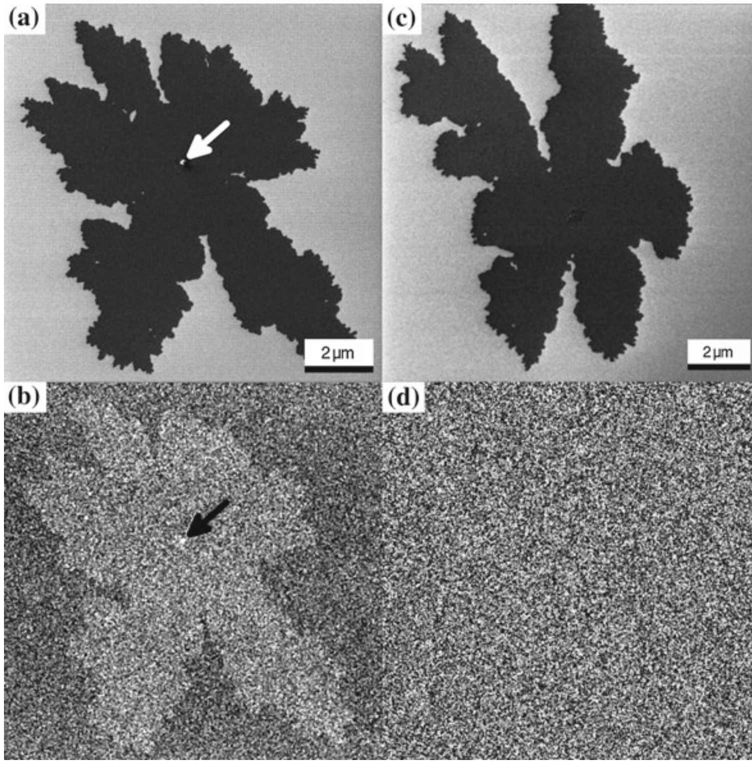

Fig. 9.11 Para-sexiphenyl islands deposited onto a silicon wafer. The SE-mode image (**a**) and the corresponding BSHe image (**b**) obtained in a channeling condition clearly show the 6P island. If the substrate is oriented in a blocking condition, the island stays visible in the unaffected SE image (**c**), but disappears in the BSHe image (**d**). Reproduced from [46]

tute atoms in bulk crystals. In this section we will show how channeling in the HIM can be exploited to reveal changes in the atomic lattice that are confined to the first atomic layers. While this is another demonstration of the high surface sensitivity that can be achieved in the HIM [10, 46, 50], it also makes use of channeling to reveal information about the crystal structure.

In Fig. 9.12a, a high-resolution HIM image of a two-layer-thick silver film on Pt$\langle 1\,1\,1 \rangle$ is shown. Using characteristics of the surface morphology, the sample has been aligned with its $[\bar{1}\,\bar{1}\,0]$ direction parallel to the beam. As is evident from Fig. 9.4a, b, this is the strongest channeling direction for fcc crystals. Consequently, the interaction of the incoming He with the sample Pt atoms is minimized, resulting in reduced iSE yield, provided that the channeling is not disturbed. A careful analysis based on the fast Fourier transform (FFT) of Fig. 9.12a presented in Fig. 9.12b reveals the presence of a regular sixfold symmetric line pattern. From the FFT one can deduce a spacing of 6.65 nm along the $\langle \bar{1}\,\bar{1}\,2 \rangle$ direction. A mask based on the

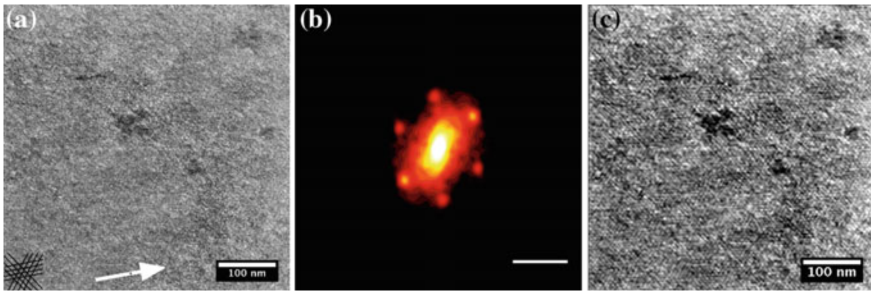

Fig. 9.12 High-resolution HIM-based analysis of two layers of silver on Pt(1 1 1). **a** High-resolution HIM image of the surface. The *white arrow points* in the $[1\,\bar{1}\,0]$ direction. **b** FFT of (**a**). **c** The data from (**a**) filtered in the frequency domain using a filter based on (**b**). Reproduced with permission from [19]

FFT presented in Fig. 9.12b has been used as a bandpass filter in the Fourier space, removing all unwanted high-frequency noise. The remaining FFT has then been converted back into real space to obtain Fig. 9.12c, which clearly shows the sixfold symmetric line pattern. The dark areas in the center and upper right part of the image are pure Pt precipitates in the otherwise Ag-rich surface, which, thanks to the reduced dechanneling and the higher work function, appear dark.

A closer inspection of the silver on the Pt(1 1 1) system reveals that a complicated network of dislocations is formed at the interface between the Pt(1 1 1) and the deposited silver layers once a coverage of more than two layers is reached [51]. This is related to a local change in stacking. The normal ABC stacking of the fcc lattice is locally replaced by a CAC stacking. As seen from Fig. 9.13a, this locally closes the channels. The helium atoms (green) entering the crystal along the $[\bar{1}\,\bar{1}\,0]$ direction in the fcc area in the center of Fig. 9.13a can easily channel from the silver (yellow) into the supporting Pt (magenta) crystal. However, in the hcp areas at the left and right sides of the figure, the Pt atom column sits right in the center of the channel formed by the surface Ag layer. A significant localized increase in the electronic stopping can be expected due to the very likely small-impact-factor collisions, which will occur in the hcp areas.

The local differences across the surface become clear from Fig. 9.13b. Observing the crystal surface along the $[\bar{1}\,\bar{1}\,0]$ direction reveals that the fcc areas are much more open than the hcp areas. The latter areas allow for a more intense interaction of the incoming He atoms with the electronic system of the substrate crystal, and hence one expects a higher iSE yield. The expected distribution of the iSE yield is shown in Fig. 9.13c. Please note that Fig. 9.13c is obtained only by blurring of Fig. 9.13b. The image is thought of as an illustration and not as a correct physical representation of the iSE yield. However, it does show the projected atom density in the first few layers, which in a rough approximation is proportional to the stopping power. As we can see from (9.6) and (9.8), a simple relation exists between the stopping power and the expected iSE yield.

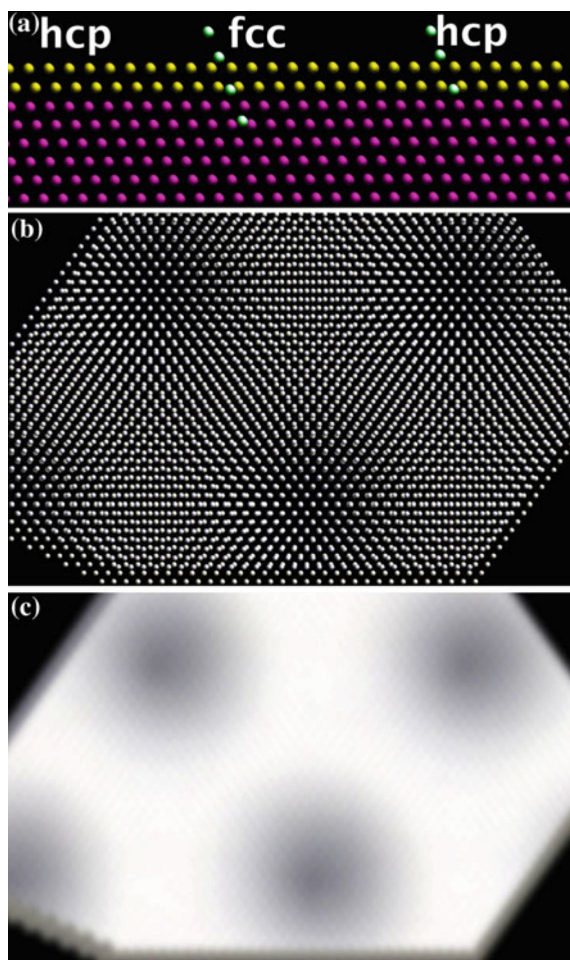

Fig. 9.13 Model explaining the dechanneling induced by a surface reconstruction. **a** Side view along $[\bar{1}\,1\,0]$ of 2 ML Ag (*yellow*) on Pt(1 1 1) (*magenta*). Helium atoms entering the crystal along $[\bar{1}\,\bar{1}\,0]$ at different lateral locations are depicted in green. **b** *Top* view of the crystal surface along $[\bar{1}\,\bar{1}\,0]$. **c** Expected qualitative electron density and SE yield. Adapted with permission from [19]

Here, it is important to understand that the obtained result is caused by a shift of the atoms in the two outermost layers by $1/\sqrt{3}$ of the nearest-neighbor distance. This corresponds to a movement from the default lattice site to the center of the threefold hollow position (without moving out of the plane). The unique combination of high lateral resolution and the resolving power of channeling-based ion beam analysis make this result possible. The precision and accuracy that is reached is outstanding. Spot profile analysis low-energy electron diffraction (SPA-LEED) measurements obtained a periodicity of 6.55 nm for the same system [52]. The calibration of the HIM is better than 1%, and the obtained distance agrees with a configuration where 23 silver atoms sit on top of 24 Pt atoms with an accuracy of 0.03%.

9.6 Summary

In this chapter we have shown that not only does channeling occur in the HIM, but that it can also be exploited to enhance or create new imaging modalities. We demonstrated in Sect. 9.3 that it is possible to identify the orientation of crystals with high-accuracy by recording channeling maps and comparing them to existing maps for known crystal structures. Imaging with backscattered ions (Sect. 9.4.1) and sub-surface imaging with backscattered helium were also introduced (Sect. 9.4.2). We further showed in Sect. 9.5.1 how channeling can and should be used to enhance the contrast when imaging thin adlayers. Finally, in Sect. 9.5.2 we presented results demonstrating that in the HIM, changes in the crystal structure such as defects or, in the presented case, surface reconstructions can be resolved with atomic precision.

These results are also promising in the sense that automated routines for orientation mapping will become standard in the HIM, and are competitive in terms of time and resolution with SEM-based techniques, providing similar results [53]. Another interesting area where channeling plays an important role is STIM. In principle, transmission channeling should allow the simultaneous characterization of mass density and crystallographic properties of a sample [54, 55], providing in-depth information on the sample structure.

Acknowledgments We want to thank B. Doyle for providing the channeling figures and the texts he shared with us, as well as for the insightful discussions. We also acknowledge support from the Dutch Technology Foundation STW, which is part of the Netherlands Organization for Scientific Research (NWO), and which is funded in part by the Dutch Ministry of Economic Affairs.

References

1. I. Stensgaard, Reports. Prog. Phys. **55**(7), 989 (1992). doi:10.1088/0034-4885/55/7/003
2. J. Lindhard, Mat. Fys. Medd. Dan. Vid. Selsk. **34**(14), 1 (1965)
3. L.C. Feldman, J.W. Mayer, S.T. Picraux, *Materials Analysis by Ion Channeling* (Academic Press, New York, 1982)
4. M. Nastasi, J. Mayer, Y. Wang, *Ion Beam Analysis* (CRC Press, 2014). doi:10.1201/b17310
5. A.A. van Gorkum, Phys. Lett. A **75**(1–2), 134 (1979). doi:10.1016/0375-9601(79)90302-5
6. R. Ramachandra, B.J. Griffin, D.C. Joy, Ultramicroscopy **109**(6), 748 (2009). doi:10.1016/j.ultramic.2009.01.013
7. J. Ferrón, E. Alonso, R.A. Baragiola, A. Oliva-Florio, Phys. Rev. B **24**(8), 4412 (1981). doi:10.1103/PhysRevB.24.4412
8. H.A. Bethe, Phys. Rev. **59**(11), 913 (1941). doi:10.1103/PhysRev.59.913
9. R.A. Baragiola, E.V. Alonso, A.O. Florio, Phys. Rev. B **19**(1), 121 (1979). doi:10.1103/PhysRevB.19.121
10. G. Hlawacek, I. Ahmad, M.A. Smithers, E.S. Kooij, Ultramicroscopy **135C**, 89 (2013). doi:10.1016/j.ultramic.2013.07.010
11. J.A. Notte, B.W. Ward, N.P. Economou, R. Hill, R. Percival, L. Farkas, S. McVey, D.G. Seiler, A.C. Diebold, R. McDonald, C.M. Garner, D. Herr, R.P. Khosla, E.M. Secula, in *AIP Conference Proceedings*, vol. 931, ed. by D.G. Seiler, A.C. Diebold, R. McDonald, C.M. Garner, D. Herr, R.P. Khosla, E.M. Secula (AIP, 2007), vol. 931, pp. 489–496. doi:10.1063/1.2799423

12. R.A. Baragiola, E. Alonso, J. Ferron, A. Oliva-Florio, Surf. Sci. **90**(2), 240 (1979). doi:10.1016/0039-6028(79)90341-8
13. B. Brusilovsky, Vacuum **35**(12), 595 (1985). doi:10.1016/0042-207X(85)90322-7
14. S. Drentje, Phys. Lett. A **24**(1), 12 (1967). doi:10.1016/0375-9601(67)90169-7
15. J.S. Briggs, A.P. Pathak, J. Phys. C Solid State Phys. **7**(11), 1929 (2001). doi:10.1088/0022-3719/7/11/009
16. G.D. Magnuson, C.E. Carlston, Phys. Rev. **129**(6), 2403 (1963). doi:10.1103/PhysRev.129.2403
17. M.T. Robinson, in *Sputtering by Part. Bombard. I*, ed. by R. Behrisch (Springer, Berlin, 1981), pp. 73–144. doi:10.1007/3540105212_8
18. U. Von Gemmingen, Surf. Sci. **120**(2), 334 (1982). doi:10.1016/0039-6028(82)90154-6
19. G. Hlawacek, M. Jankowski, H. Wormeester, R. van Gastel, H.J. Zandvliet, B. Poelsema, Ultramicroscopy **162**, 17 (2015). doi:10.1016/j.ultramic.2015.11.009
20. A. George, M. Knez, G. Hlawacek, D. Hagedoorn, H.H.J. Verputten, R. van Gastel, J.E. ten Elshof, Langmuir **28**(5), 3045 (2012). doi:10.1021/la204437r
21. M.A. Karolewski, R.G. Cavell, Surf. Sci. **605**(19–20), 1842 (2011). doi:10.1016/j.susc.2011.06.022
22. M. Nègre, J. Mischler, N. Bénazeth, C. Noguera, D. Spanjaard, Surf. Sci. **78**, 174 (1978)
23. W. Brandt, R. Dobrin, H. Jack Jr., R. Laubert, S. Roth, Can. J. Phys. **46**(6), 537 (1968). doi:10.1139/p68-067
24. W. Brandt, J.M. Khan, D.L. Potter, R.D. Worley, H.P. Smith, Phys. Rev. Lett. **14**(2), 42 (1965). doi:10.1103/PhysRevLett.14.42
25. O.S. Oen, M.T. Robinson, Nucl. Inst. Meth. **132**(3), 647 (1976). doi:10.1016/0029-554X(76)90806-5
26. V. Veligura, G. Hlawacek, R. van Gastel, H.J.W. Zandvliet, B. Poelsema, Beilstein J. Nanotechnol. **3**, 501 (2012). doi:10.3762/bjnano.3.57
27. D.C. Bell, Microsc. Microanal. **15**(2), 147 (2009). doi:10.1017/S1431927609090138
28. R.E. Franklin, E.C.G. Kirk, J.R.A. Cleaver, H. Ahmed, J. Mater. Sci. Lett. **7**(1), 39 (1988). doi:10.1007/BF01729909
29. R. Levi-Setti, T.R. Fox, K. Lam, Nucl. Inst. Meth. Phys. Res. **205**(1–2), 299 (1983). doi:10.1016/0167-5087(83)90201-6
30. M.L. Swanson, in *Handbook of Modern Ion Beam Material Analysis: Materials Research Society Handbook*, ed. by J.R. Tesmer, M.A. Nastasi (Materials Research Society, Pittsburgh, 1995), chap. 10, pp. 231–300
31. B.L. Doyle, Nucl. Instrum. Methods Phys. Res. Sect. B Beam Interact. Mater. Atoms (2015). doi:10.1016/j.nimb.2015.08.047
32. B.L. Doyle, Channeling (2015). http://www.sandia.gov/pcnsc/departments/iba/ibatable.html
33. B.L. Doyle, A. Corona, A.Q. Nguyen, Ion Channeling Revisited. Technical Report, Radiation Solid Interactions Department 01111, Sandia National Labs, Albuquerque (2015)
34. V. Veligura, G. Hlawacek, R.P. Berkelaar, R. van Gastel, H.J.W. Zandvliet, B. Poelsema, Beilstein J. Nanotechnol. **4**, 453 (2013). doi:10.3762/bjnano.4.53
35. S. Sijbrandij, B. Thompson, J.A. Notte, B.W. Ward, N.P. Economou, J. Vac. Sci. Technol. B Microelectron. Nanom. Struct. **26**(6), 2103 (2008). doi:10.1116/1.2993262
36. G. Hlawacek, V. Veligura, R. van Gastel, B. Poelsema, J. Vac. Sci. Technol. B Microelectron. Nanom. Struct. **32**(2), 020801 (2014). doi:10.1116/1.4863676
37. I. Gertner, M. Meron, B. Rosner, Phys. Rev. A **21**(4), 1191 (1980). doi:10.1103/PhysRevA.21.1191
38. R. van Gastel, G. Hlawacek, H.J. Zandvliet, B. Poelsema, Microelectron. Reliab. **52**(9–10), 2104 (2012). doi:10.1016/j.microrel.2012.06.130
39. E.J. Faber, R.A.M. Wolters, J. Schmitz, I.E.E.E. Trans, Semicond. Manuf. **25**(3), 339 (2012). doi:10.1109/TSM.2012.2202793
40. A.C. Diebold (ed.), *Handbook of Silicon Semiconductor Metrology* (CRC Press, 2001)
41. K. Ura, S. Aoyagi, J. Electron Microsc. (Tokyo). **49**(1), 157 (2000). doi:10.1093/oxfordjournals.jmicro.a023780

42. M.A.E. Jepson, B.J. Inkson, X. Liu, L. Scipioni, C. Rodenburg, EPL Europhysics Lett. **86**(2), 26005 (2009). doi:10.1209/0295-5075/86/26005
43. L.C. Feldman, Phys. Scr. **28**(3), 303 (2006). doi:10.1088/0031-8949/28/3/007
44. J. Knapp, D. Follstaedt, B. Doyle, Nucl. Instrum. Methods Phys. Res. Sect. B Beam Interact. Mater. Atoms **7–8**, 38 (1985). doi:10.1016/0168-583X(85)90526-9
45. J. Davies, P. Norton, Nucl. Inst. Meth. **168**(1–3), 611 (1980). doi:10.1016/0029-554X(80)91319-1
46. G. Hlawacek, V. Veligura, S. Lorbek, T.F. Mocking, A. George, R. van Gastel, H.J.W. Zandvliet, B. Poelsema, Beilstein J. Nanotechnol. **3**, 507 (2012). doi:10.3762/bjnano.3.58
47. K.Y. Wu, S.Y. Yu, Y.T. Tao, Langmuir **25**(11), 6232 (2009). doi:10.1021/la900046b
48. J. Singh, J.E. Whitten, J. Phys. Chem. C **112**(48), 19088 (2008). doi:10.1021/jp807536z
49. T.F. Mocking, G. Hlawacek, H.J.W. Zandvliet, Surf. Sci. **606**(11–12), 924 (2012). doi:10.1016/j.susc.2012.02.007
50. K. Buchholt, P. Eklund, J. Jensen, J. Lu, A.L. Spetz, L. Hultman, Scr. Mater. **64**(12), 1141 (2011). doi:10.1016/j.scriptamat.2011.03.013
51. K. Aït-Mansour, H. Brune, D. Passerone, M. Schmid, W. Xiao, P. Ruffieux, A. Buchsbaum, P. Varga, R. Fasel, O. Gröning, Phys. Rev. B **86**(8), 085404 (2012). doi:10.1103/PhysRevB.86.085404
52. M. Jankowski, H. Wormeester, H.J.W. Zandvliet, B. Poelsema, Phys. Rev. B **89**(23), 235402 (2014). doi:10.1103/PhysRevB.89.235402
53. C. Langlois, T. Douillard, H. Yuan, N. Blanchard, A. Descamps-Mandine, B. Van de Moortèle, C. Rigotti, T. Epicier, Ultramicroscopy **157**, 65 (2015). doi:10.1016/j.ultramic.2015.05.023
54. A. D'Alfonso, B. Forbes, L. Allen, Ultramicroscopy **134**, 18 (2013). doi:10.1016/j.ultramic.2013.06.019
55. J.A. Notte, R. Hill, S.M. McVey, R. Ramachandra, B.J. Griffin, D.C. Joy, Microsc. Microanal. **16**(05), 599 (2010). doi:10.1017/S1431927610093682

Chapter 10
Helium Ion Microscopy of Carbon Nanomembranes

Armin Gölzhäuser

Abstract Carbon Nanomembranes (CNMs) are extremely thin (0.5–3.0 nm), synthetic two-dimensional (2D) layers or sheets with tailored physical, chemical or biological function. With two opposing surfaces they interface and link different environments by their distinct physical and chemical properties, which depend on their thickness, molecular composition, structure and the environment on either side. Due to their nanometer thickness and 2D architecture, they can be regarded as "surfaces without bulk" separating regions with different gaseous, liquid or solid components and controlling any materials exchange between them. Helium Ion Microscopy is very well suited to investigate CNMs. Its main advantage is its high surface sensitivity that generates high contrast images, even in samples where there is very little material available. It is shown that HIM imaging is an effective tool for the characterization of "free-standing" as well as "supported" CNMs. Effects of sample charging, the imaging of multilayer-CNMs and the identification of image artefacts are discussed. It will be shown that at even low magnification, single sheets of CNM can be clearly detected and HIM images show a lot of detail. Folds, wrinkles and pores in the membrane are clearly seen and can be used to characterize the quality of CNMs. In addition, the high depth of focus eases the HIM operation. CNMs can also be milled with the HIM, and nanopores of very small diameter (down to 1.3 nm) have been fabricated.

10.1 Introduction

Two-dimensional (2D) materials are atomically or molecularly thin sheets or membranes with tailored physical, chemical and biological function [1–3]. They interface and link different gaseous, liquid or solid surroundings. Their physical, chemical and biological properties depend on their thickness, molecular composi-

A. Gölzhäuser (✉)
Physics of Supramolecular Systems and Surfaces, Bielefeld University,
33615 Bielefeld, Germany
e-mail: ag@uni-bielefeld.de

© Springer International Publishing Switzerland 2016

G. Hlawacek and A. Gölzhäuser (eds.), *Helium Ion Microscopy*,
NanoScience and Technology, DOI 10.1007/978-3-319-41990-9_10

tion, and internal structure. They can be utilized as membranes or layers that separate regions with different components and control the materials exchange between them.

In the 2000s, the field of 2D materials was shaped by new discoveries, novel technical breakthroughs and industrial demands. A prominent example for this development is "The rise of graphene", which had major impacts on science and technology. Physicists, chemists and engineers have intensively explored graphene, a 2D material with the thickness of only one carbon atom [4]. Its unique electronic, mechanical and optical properties gave fascinating insights into graphene and lead to innovative technology in the investigation and handling of two-dimensional systems.

This turned out to be beneficial for a number of other materials; layers, sheets and membranes did not only receive much more attention, but also benefited from new preparative and analytical procedures and the awareness of applications. In the efforts to understand and apply 2D materials, the Helium Ion Microscope plays an important role as a tool for imaging and structuring. This chapter will demonstrate the capabilities of the HIM for characterizing 2D materials using images of graphene and carbon nanomembranes as representative examples.

Perfect graphene is a homogeneous and chemically inert material, and it is difficult to functionalize its surface for specific applications. Carbon nanomembranes (CNMs) are 2D materials with a thickness of one molecule (0.5–2 nm) [5]. CNMs were invented at about the same time than graphene [6], they are as thin as graphene, allow a chemical functionalization and can easy to be produced in large areas. CNMs are made from self-assembled monolayers (SAMs), monomolecular films formed by the self-assembly of amphiphilic molecules on solid surfaces. SAMs were first prepared in the late 1970s and were, since then used to coat and modify the surfaces of a diversity of materials: metals, semiconductors and ceramics.

CNMs are fabricated by exposing a SAM of aromatic molecules to low energy electrons [7] or to soft X-rays [8]. The radiation results in the cross-linking of neighbouring molecules into a CNM with molecular thickness. CNMs can also be fabricated by crosslinking with a helium ion beam [9]. The CNM is then released as a free-standing foil by dissolving the substrate and then transferring the CNM onto a support [10]. Figure 10.1 shows a scheme of CNM fabrication.

CNMs are composed of molecules that assemble on a solid surface, where they are then cross-linked into a two-dimensional film that is released as a free-standing sheet. Its thickness, homogeneity, porosity and surface chemistry are determined by the nature of the initial molecular layer. Hence, the choice of the initial molecular layer sallows flexibility in the properties and applicability of the resulting CNMs, which makes CNMs a platform technology for building 2D materials. Scientists from physics, chemistry, and biology create and investigate new CNMs with the goal to understand their formation, to study their properties and to utilize them for applications.

In these efforts, Helium Ion Microscopy does not only provide superb resolution but also offers high materials contrast and surface sensitivity. There are a number of publications on HIM imaging of ultrathin membranes. Many of them place a focus on the lithographic modification and production of small structures and circuits [11]. Graphene and boron nitride (h-BN), an insulating 2D material whose

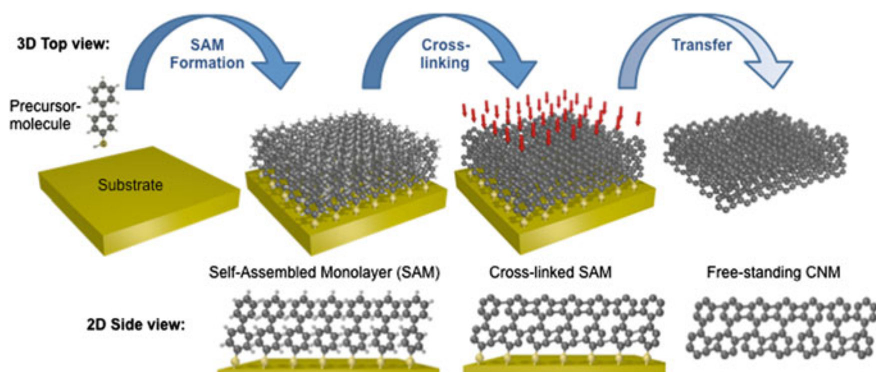

Fig. 10.1 a Fabrication scheme of CNMs made from aromatic self-assembled monolayers (biphenylthiol in this case)

hexagonal structure is similar to graphene, were imaged in a comparative study [12]. Therein, it is shown that HIM is more sensitive and consistent than SEM for characterizing the number of layers and the morphology of 2D materials. It was also shown that HIM is very sensitive in characterizing supported, thin organic layers due to its high surface sensitivity [13, 14]. In a recent study Beyer et al. studied HIM imaging of CNMs in detail [15].

10.2 A Comparison Between HIM and SEM

At the beginning of our chapter on HIM imaging of 2D materials stands a comparison of a HIM image of a CNM with the corresponding SEM image. Figure 10.2 shows HIM (left) and SEM (right) images of the same CNM. The 1 nm thick CNM is placed on a 15 nm thick perforated carbon foil with a regular pattern of 2 µm holes (Quantifoil, Jena) that covers a TEM grid with 40 µm square openings. One clearly recognizes that the HIM image resolves many more details than the SEM image and provides a much higher contrast between the different materials. In both images, the squared opening of the supporting metal frame and the regular holey pattern in the 15 nm thick carbon foil are clearly visible. In addition, the HIM image also shows the 1 nm thick carbon nanomembrane that is present in the right half of the image; we clearly see that the CNM is folded, its appearance resembles a piece of cloth or silk. Contrariwise, in the SEM image, it needs skill to correctly guess where the CNM is located. Without the HIM image as a *guide to the eye*, it is difficult to exactly locate the CNM. Hence, in a first and intuitive comparison of both images, the HIM clearly generates a “better” image. It is noteworthy that the HIM is somewhat easier to operate, i.e. for the extremely thin CNMs, it took longer to focus and to find the best imaging parameters for the SEM than for the HIM.

Figure 10.3 displays a series of HIM images of CNMs. Figure 10.3a is a large area overview image of a CNM transferred onto a TEM grid with hexagonal

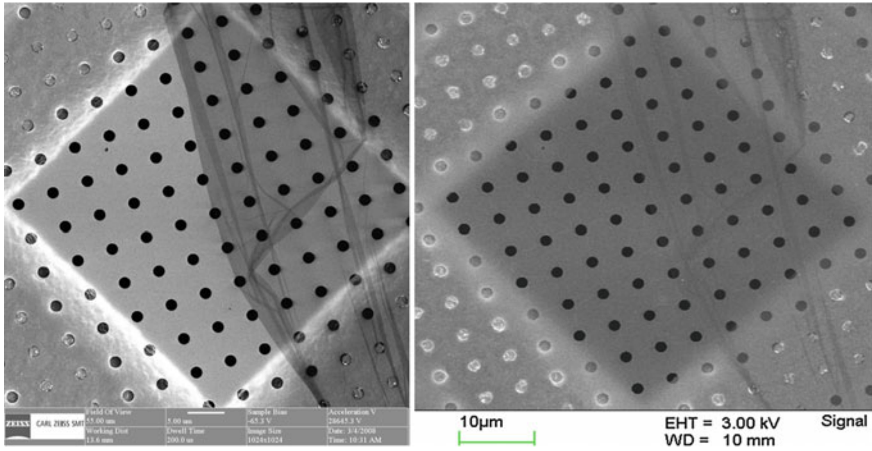

Fig. 10.2 HIM image (*left*) and SEM image (*right*) of a Carbon Nanomembrane placed on a perforated carbon foil with 2 μm holes (quantifoil) that is spanned over a TEM grid with 40 μm squared openings. The HIM images shows many more details of the CNM

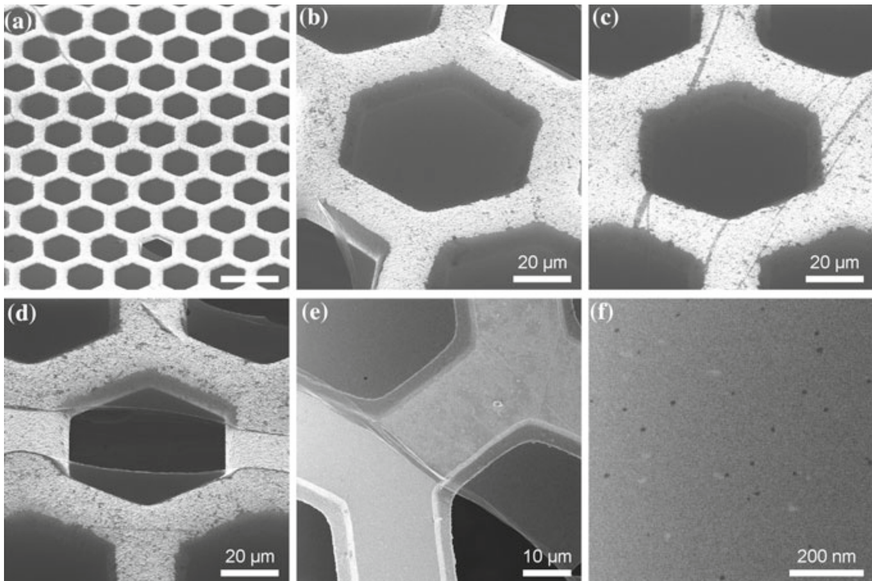

Fig. 10.3 HIM images of CNMs supported by TEM grids. **a** Large area of intact membranes. Only one ruptured membrane is found in this area. Scale bar is 100 μm. **b** Intact membrane. **c** Intact membrane with foldings. **d** Ruptured membrane. **e** Improved contrast with charge compensation. **f** Nanopores in large free-standing CNMs imaged with charge compensation. The nanopores appear as *dark spots* in the CNM

openings. It is easily seen that almost the entire grid is covered by the CNM, only a single hexagonal opening in the lower part of the image is not covered because there the CNM is ruptured. Hence, whether or not a CNM covers an opening and the state of its structural integrity is easily comprehended from its HIM image. The characterization of CNMs concerning cleanliness, the presence of ruptures and the amount of folding of the CNMs is also straightforwardly elucidated from HIM images; Fig. 10.3b–d shows examples. In the imaging of 2D materials is a general observation that, the secondary electron signal in HIM imaging has a higher intensity than in comparable SEM images.

Imaging the electrically insulating CNMs at higher helium ion beam current leads to sample charging which prevents secondary electrons from reaching the detector. However, the charge compensation system allows a further increase of the CNM signal intensity in the HIM image. Figure 10.3e displays an image in which the free-standing CNMs is simultaneously exposed with low energy electrons (charge compensation), which leads to a higher secondary electron intensity and a brighter appearance of the CNM. This clearly demonstrates that charge compensation is a quite useful tool in the HIM imaging of insulating thin 2D objects. Figure 10.3f shows a charge compensated high magnification secondary electron HIM image of a CNM. Within a grey background, generated by SE's from the CNM, a number of small black spots are seen. These spots originate from small holes within the membrane and show that a CNM is not always a homogeneous monomolecular film; it can contain "nanopores". By HIM imaging of CNMs from different precursor molecules, Angelova et al. [16] could show that the size and the number of nanopores are determined by the size of the parenting molecules as well as by the film properties of the parenting SAM.

10.3 CNMs on Solid Supports

CNMs are made by cross-linking molecular monolayers on solid substrates. A CNM can then be transferred from the surface, where the initial monolayer was formed, onto other solid substrates. An commonly occurring example is a transfer from gold onto a silicon surfaces [17], for which transfer procedures with polymeric media are well-established [18]. The CNM can be imaged with HIM on its original and on its new substrate. HIM images of CNMs on flat surfaces often provide high contrast and good visibility of features of the membrane. Figure 10.4 shows six different substrates with transferred CNMs at magnifications ranging from overview images with fields of views (FOV) of 4–1 mm down to higher magnification images (1 μm FOV). The areas covered by the CNM are labelled with yellow letters, stating "CNM". One would expect that a CNM on a flat substrate would not show a good contrast. However, the first visual inspection allows a clear identification of the nanomembranes. This is mainly due to defect features that serve as guide to the eye. Most of the contrast in the HIM images of Fig. 10.4 originates from ruptures, folds or edges of the membranes or the supports. In Fig. 10.4a

(1.6 mm FOV), the edge of a CNM is imaged on oxidized silicon, together with a scratch in the substrate that was made as a marker when the sample is imaged with different techniques. Defects and folds are frequently observed at edges of transferred CNMs, together with contaminations, also very well visible in a CNM that was transferred onto mica (2 mm FOV, Fig. 10.4b). Imaging the CNM at higher magnification (90 μm FOV, Fig. 10.4e) shows a small scratch in the middle, and some double-layers of CNMs in the upper part. These are very typical for non-perfect transfer, and HIM image can clearly identify these defects. Figure 10.4c (3.75 mm FOV) shows a CNM double-layer that has been transferred on a silicon nitride surface. At higher magnification (10 μm FOV, Fig. 10.4f) defects, folds and contaminations are clearly seen and can be assessed in great detail. The number of folded sheets can be calculated from the number of grey values in the CNM's image and the thickness of a supported multilayer CNM can thus be quantitatively analysed. A similar behaviour is found for a CNM on silicon carbide (Fig. 10.4g, 2.5 mm FOV; Fig. 10.4j 1 μm FOV).

CNMs have also been transferred on soft supports; polymers for example. Here CNMs are tested as ultrathin filter membranes in gas and liquid permeation measurements. For the use of a nanomembrane as a filter, the amount of defective area is a very important factor in the performance [19]. Figure 10.4h (2.5 mm FOV) and Fig. 10.4k (400 μm FOV) show HIM images of CNMs that were transferred on polydimethylsiloxane (PDMS). The images were made for a study on gas permeation through such "hybrid" membranes. For permeation experiments it is of importance to exactly know the "active area" of the CNM. This can be achieved by quantitatively analysing HIM images. An example is shown in Fig. 10.4k, where a defect is clearly seen in the center; the area where the CNM is "missing" can be directly calculated from the HIM image and enters the calculations of the permeability [19].

Figure 10.4i (1.8 mm FOV) and Fig. 10.4l (80 μm FOV) show CNM on a Teflon substrate with a pore. Teflon is much rougher than PDMS, however, a successful transfer has been achieved. In all examples shown in Fig. 10.4, the CNM lowers the SE-intensity compared to the bare substrates. This can be understood by the fact that the insulating CNMs lead to slightly higher surface charging, as compared to the conducting surface.

10.4 HIM Imaging of Free-Standing CNMs (Porous Supports and TEM Grids)

Another goal of CNM fabrication is to produce membranes that are homogeneous and mechanically stable and that can span large areas as 2D free-standing sheets. To achieve this, CNMs are transferred onto holey supports. The size of the holes then determines the free-standing area. Transmission electron microscopy grids (TEM grids) are commercially available microstructures with standardized openings of well-defined size and shape ranging from 1 μm to 1 mm, they are also perfect holey

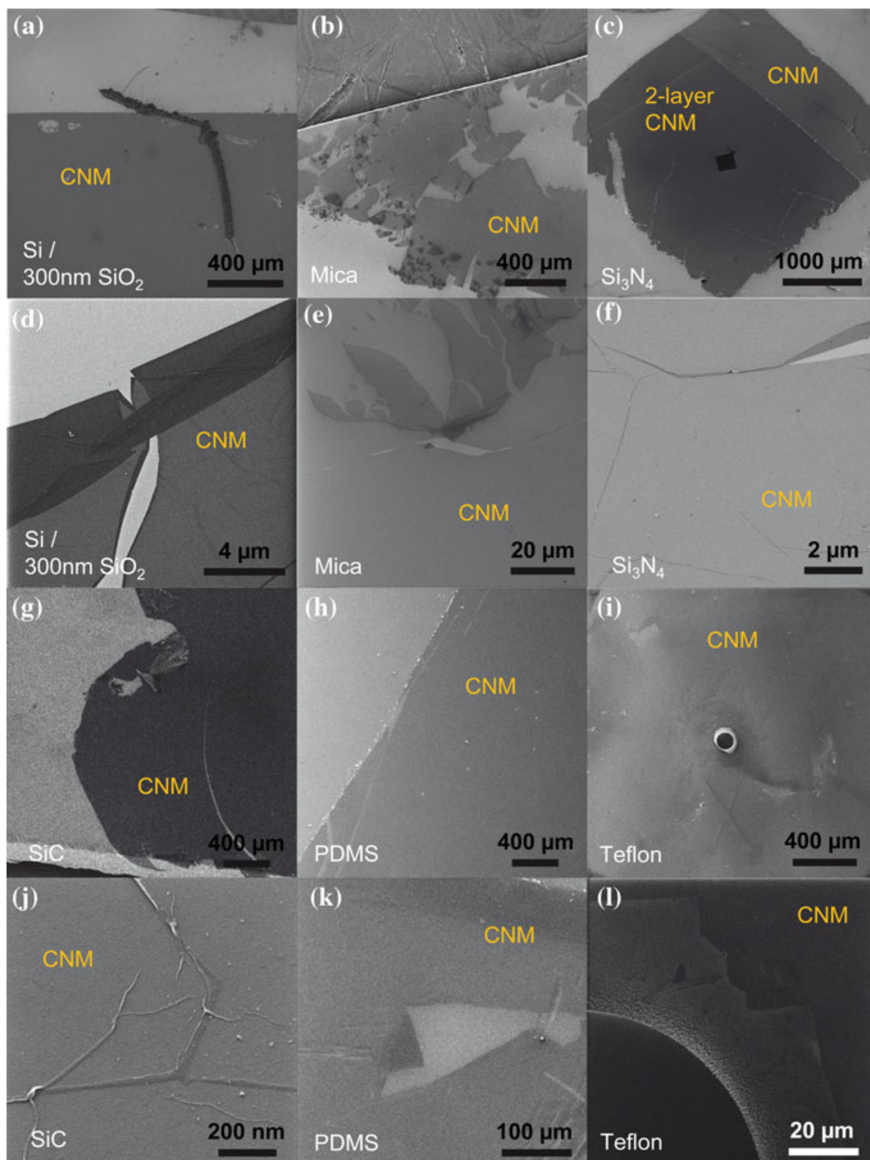

Fig. 10.4 HIM images of CNMs supported by different materials. **a**, **d** SiO_2. **b**, **e** Mica. **c**, **f** Si_3N_4. **g**, **j** SiC. **h**, **k** PDMS. **i**, **l** Teflon

supports for CNMs. The stability and quality of a specific CNM can simply be evaluated after a transfer onto a TEM grid and the subsequent observation of the number and the size of defects in the transferred CNM. For this task, the HIM has proven to be a very useful instrument. Beyer et al. [15] investigated the imaging of

different CNMs with HIM, and in the following section here we review parts of their work. For imaging with the HIM, the most important characteristics of CNMs are that they are ultrathin (≈1 nm) and electrically insulating. Because of its high surface sensitivity, the helium ion microscope is well suited to image CNM with a high signal-to-noise-ratio. The helium beam easily penetrates the CNM and can also interact with other objects below the freestanding film. Figure 10.5 displays an example of this effect. The HIM images in Fig. 10.5a, b show the same object: a hexagonal TEM grid that is mounted in a sample stage with a mm-sized, circular opening (visible in the four corners of the images). The CNM that has been transferred on the grid is partly ruptured; only 20 % of the hexagonal meshes of the TEM grid are covered by CNM, most of the grid is not. White arrows indicate CNM-covered regions. Both HIM images were taken with the same ion acceleration voltage and ion current; however, their contrast appears almost inverted. This difference relates to the background: In Fig. 10.5a, the grid is placed closely over the metal surface of the sample stage. An edge of the sample holder surface is visible as a bright strip running from the top to the lower right of the image. Background features are visible as helium ions impinge upon the sample stage and eject secondary electrons that reach the SE detector without being blocked. In Fig. 10.5b, the sample stage is removed from the grid, so the secondary electrons from the stage are blocked and cannot reach the detector. Thus, in Fig. 10.5b, uncovered meshes of the grid appear dark in all parts of this image. The arrows in Fig. 10.5a, b depict the same locations in both images. Note that regardless of the mounting and stage position, the large field of view (2.25 mm) together with the high depth of view and contrast between bare and CNM-covered grid meshes allow a fast quantitative evaluation of the area of intact CNMs. The recording time of these images is less than 1 min.

CNM images are further affected by electrostatic charging. In Fig. 10.5c, d HIM images of CNMs with and without electrostatic charging are compared. A cross-section of the sample together with a line profile of the grey values in Fig. 10.5c (dotted line) is given in Fig. 10.5e. Along the dotted line are three meshes: an empty one followed by a partially and a fully CNM covered mesh. The helium ion impact and the secondary electrons emission can only result in a positive charging, regardless of the secondary electron yield of the CNMs. A positively charged CNM will hinder the emission of secondary electrons and, thus, appear darker in HIM images. This is observed in Fig. 10.5c where the freestanding regions of the CNM are dark, while the regions in contact with the copper grid appear much brighter. In the latter, secondary electrons are also emitted from the underlying copper grid and charges in the CNM are neutralised by the metallic support. This yields the high contrast between the CNM-covered and non-covered regions. However, structural details of the CNMs can hardly be investigated under these imaging conditions. In the partially covered mesh the edges of freestanding CNMs appear brighter than the intact CNMs. As schematically depicted in Fig. 10.5e, this can be explained by secondary electrons from the sample support whose path to the detector is blocked by intact CNMs, while partially ruptured CNMs do not. A reduction of the beam current (dwell time per pixel), frame

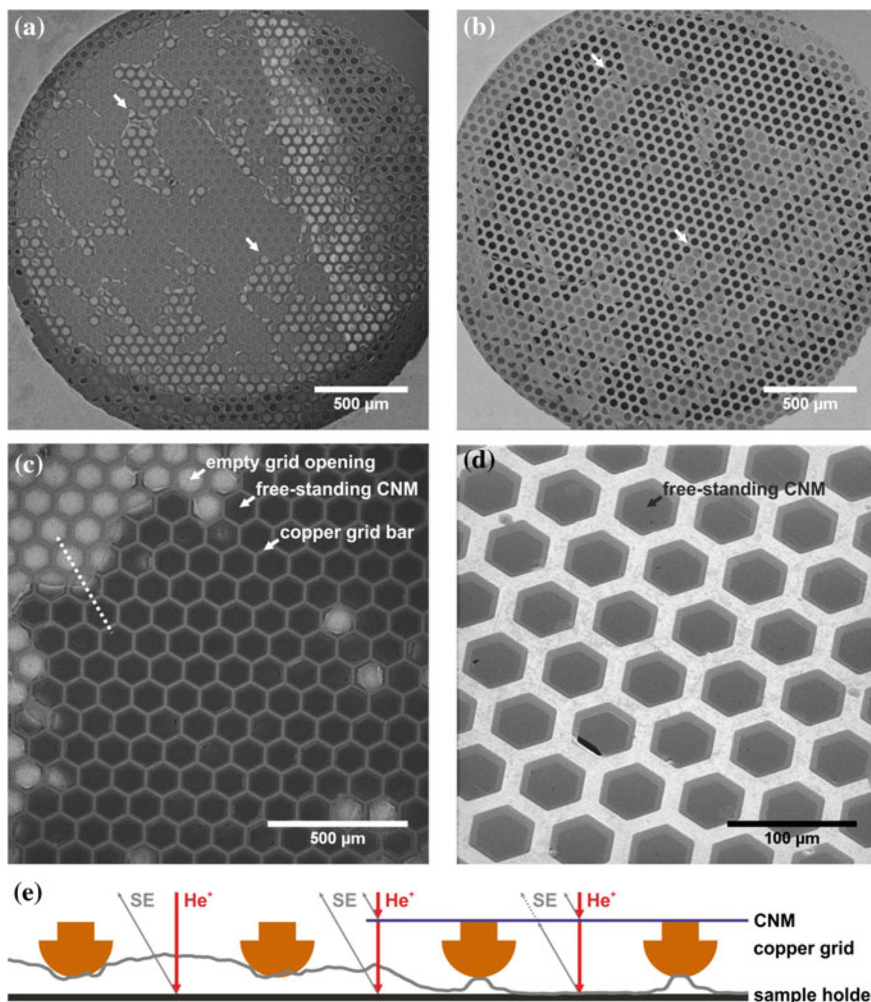

Fig. 10.5 **a**, **b** HIM images of freestanding CNMs on TEM grids, illustrating the importance of the background. Both images show the same sample mounted differently. The *arrows* point to the same positions as a guide to the eye. **c** CNMs on a TEM grid with a *bright* background and substantial membrane charging. **d** CNMs are imaged on a *dark* background with negligible membrane charging. **e** Schematic cross-section and superimposed line profile of the image greyscale values along the *dotted line* in (**c**) with the primary He^+ beam and secondary electrons emitted from the CNM and the sample holder depicted at three exemplary locations. The values of the line profile (*grey curve*) are a measure of the amount of detected secondary electrons. (from [15])

averaging as well as charge compensation can reduce or avoid electrostatic charging. In Fig. 10.5d the sample was mounted in a way that no secondary electrons from the sample stage could reach the detector. The image does not show

notable charging, small ruptures in the CNM show the high contrast between the bright CNM and its surrounding. Under these conditions, small details (pores, folds, contaminants) of the freestanding CNM and the support grid are clearly visible.

Different CNMs on copper TEM grids with hexagonal meshes are shown in Fig. 10.6. From these, one can identify different features that are clearly visible in HIM images. In Fig. 10.6a larger folds on the upper side of the image and one rupture in the centre are visible. The grey features the copper mesh most likely result from adsorbed hydrocarbons, indicating that the surface of commercial TEM grids is not contamination free. Figure 10.6b is an example of a membrane that rolls up after a rupture, showing the high flexibility of CNMs. Small folds like those in Fig. 10.6c are frequently observed, while wrinkling of the free-standing membrane

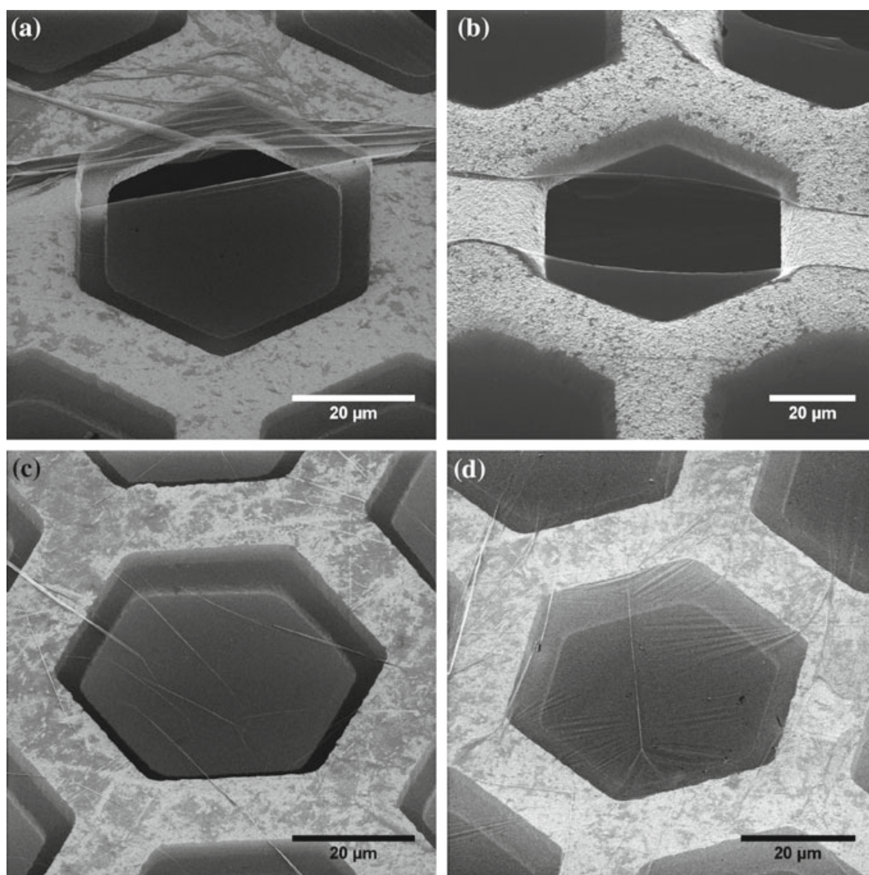

Fig. 10.6 Low magnification HIM images of CNM transferred onto TEM grids with hexagonal mesh. **a**, **b** show partly ruptured CNMs, **c**, **d** intact ones. Despite the low magnification minute details, such as wrinkles and folds within the CNM are clearly visible, which allows a quick inspection of the CNM's quality. Reproduced from [15]

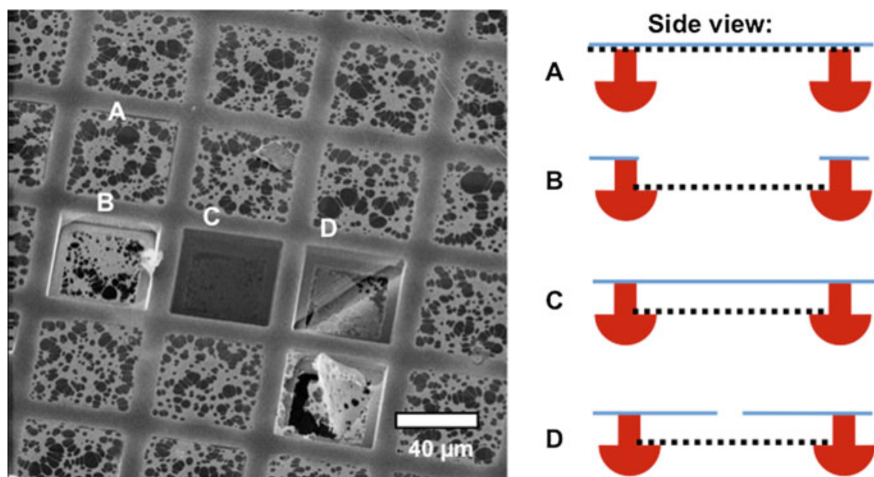

Fig. 10.7 Low magnification HIM image of a lacey carbon TEM grid covered with a CNM. The schematic side view on the *right* shows 4 different configurations (*A*–*D*) of lacey carbon and CNM visible in the image: *A* CNM and carbon foil are in close contact. *B* CNM ruptured. *C* CNM and lacey carbon are at a distance from each other. *D* CNM with a small rupture at a distance from lacey carbon

(Fig. 10.6d) is less often observed. These HIM images of free-standing, folded and ruptured CNMs on copper grids are very helpful to intuitively understand 2D materials, they serve as an inspiration for potential application as they transmit the —true—picture that nanomembranes almost look like plastic foils.

Figure 10.7 shows an instructive HIM image of a CNM that was transferred onto a copper grid with square meshes that covered with a holey carbon film. Within this hybrid structure of three different objects, the copper grid provides the supporting frame on which the holey carbon film is mounted. A CNM was then transferred onto the holey carbon film. In the upper right corner some small wrinkles within the CNM are visible; in most of the squares the CNM does not fold and one can see that the holey carbon film touches the CNM forming a double layer, for example in the square A and side view A. However, in the center of the HIM image defects are visible within squares B, C and D that show distinct contrast features. In square B the CNM is removed, the holey carbon is on the other side of the TEM grid. Secondary electrons emitted from holey carbon film and the walls of the grid reach the detector without being attenuated by the CNM. Holey carbon film and the walls of the copper square thus appear brighter than in surrounding squares. In square C, the holey carbon is also on the other side of the grid and the CNM is free-standing above the holey carbon foil without touching. Secondary electrons from beneath the CNM are blocked, leading to a darker appearance. Finally, the CNM at square D is also not touching the holey carbon film, but it has a large diagonal crack. Secondary electrons from beneath the CNM escape through this crack providing a brighter appearance of features the closer these are to the crack. The defects evaluated in

squares B, C, D are basically caused by the transfer of the CNM, and Fig. 10.7 is a good example how Helium Ion Microscopy helps to identify the nature and the origin of defects in 2D materials.

10.5 Visualization of Large Area CNMs

Another specialty of imaging 2D materials with the Helium Ion Microscopy is that the HIM can visualize ultrathin objects over large areas. Figure 10.8 shows examples of freestanding CNMs on a TEM grid with a hexagonal mesh. Note that the 1 nm thick membranes are self-supporting over distances of up to 0.5 mm. An overview image (Fig. 10.8a, 1 mm FOV) shows three intact freestanding CNMs, their neighbouring hexagons contain remnants of ruptured membranes. The top of

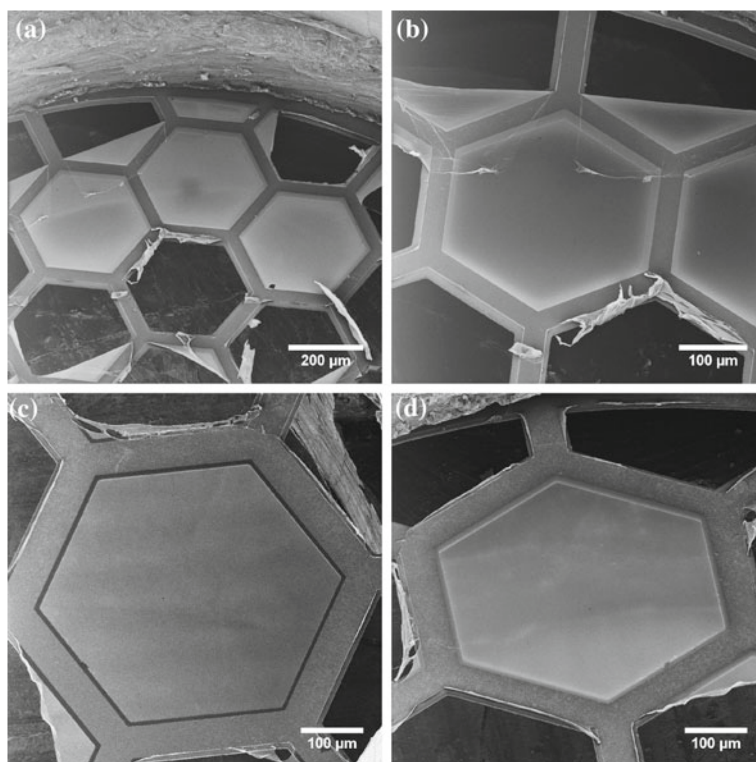

Fig. 10.8 HIM images of CNMs spanned over a TEM grid with a large area (diameter 500 µm) hexagonal openings. The slight intensity variations in (**a**–**d**) result from background illumination from SE of the grid (**a**, **b**) and the sample stage (**c**, **d**). The CNMs in (**c**) and (**d**) show no folds, indicating a high homogeneity of production as well as a high precision of the transfer. Reproduced from [15]

the sample stage is visible at the upper rim of the image and its bottom can be seen through the empty hexagons. Hence, this overall view that is due to the high focal depth of the HIM, allows a good overall inspection of extended objects as a starting point for more detailed investigations.

Figure 10.8b shows the left CNM of Fig. 10.8a at higher magnification. Two membrane fragments from a neighbouring ruptured membrane are flipped over and cover part of the intact CNM. The edges of the fragments appear very bright, which is due to a topographical contrast and which allows a clear identification of even the small defects and contaminants on the CNM. A further large CNM is presented in Fig. 10.8c, d. The HIM images were taken at different scanning orientations and sample tilt angles; the intensity variations of the CNM's surfaces originate mostly from secondary electrons emitted by the sample stage.

10.6 Imaging of Hybrid and Composite Systems

The ability of the HIM to visualize complex 2D systems can be well studied in Fig. 10.9 that shows an "unusual" composite structure consisting of a copper mesh, a holey carbon film and single layer graphene. A schematic view of the structure is shown in Fig. 10.9: the holey carbon film is connected to the TEM grid at the

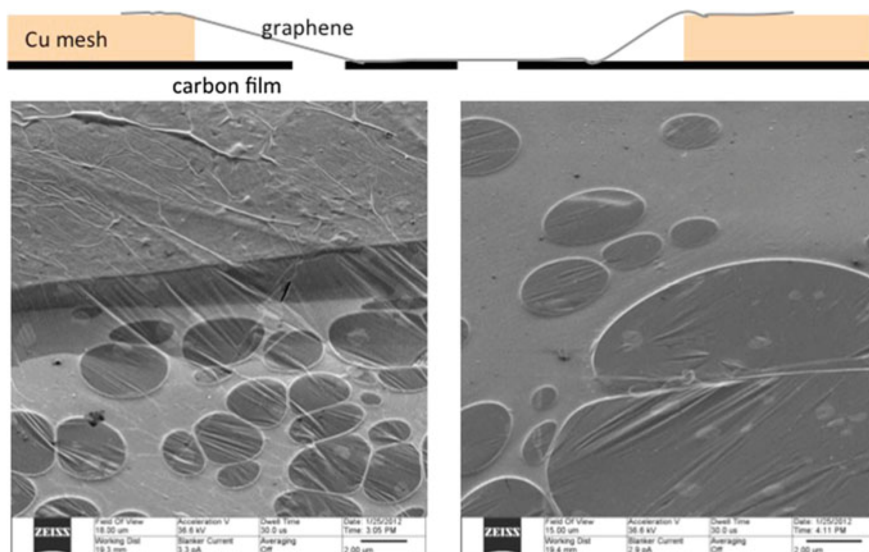

Fig. 10.9 HIM images of an "unusual" composite structure schematically shown at the *top*. A graphene sheet is placed on the back side of a copper grid covered with a lacey carbon film. The graphene freely suspends over the copper bar until it touches the carbon film. The image plastically shows folds and wrinkles within the graphene and lacey carbon sheets

bottom of the rectangular shaped cooper rod; a layer of graphene has been transferred to its opposite side. Both, the holey carbon film and the graphene are isolated in the proximity of the copper rod, however after about 4 μm away from the rod, they touch each other and form a sandwich layer. Figure 10.9 shows this with great detail. In upper third of the left HIM image the rectangular copper rod is seen covered by a layer of graphene. In the middle of the image, the graphene suspends over the edge of the bar as a freestanding foil that exhibits some folds resembling a piece of drape or a film of saran wrap. One also sees the line along which the graphene film touches the holey carbon. Finally, in the bottom part of the image, as well as in the right HIM image, a bilayer of graphene and holey carbon is seen. One can detect folds and wrinkles in the openings of the holey carbon, as well as bright patches within the graphene sheets. The bright patches originate from regions of double layer graphene that contain more carbon atoms and, consequently, generate more secondary electrons. Figure 10.9 contains a many details in a single image with also has a very large field of view, which is unmatched by other charge particle microscopies. Images from TEM, SEM, or STM/AFM would either show fine details or a less resolved overview. The HIM is unique in the sense that it combines a large field of view, material contrast and high resolution.

The imaging of nanomaterials with high resolution in a field of view below 1 μm allows to study the position and morphology of their defects in high detail. Figure 10.10 shows a sequence of HIM images in which different amounts of gold were deposited on silicon nanospheres. The spheres are gold coated only on top providing so-called "janus nanoparticles" that are used as substrate in surface enhanced Raman spectroscopy (SERS). The morphology of these spheres was studied in detail with HIM; in Fig. 10.10, the growth of a continuous gold film on the silicon spheres is seen [20].

In Fig. 10.11, a CNM was transferred onto these "gold-capped" nanoparticles. An immediate question is whether the CNM stays intact after the transfer process and how is the morphology of the nanomembrane on this heterogeneous and rough substrate. Figure 10.11a shows that the CNM lays over large areas intact on the nanospheres. Due to its high flexibility it follows the shape of the particles very well. However, Fig. 10.11b shows a group of nanoparticles that are only partly covered; arrows indicate the edge of the CNM.

10.7 Imaging of Perforated CNMs

Perforated CNMs posses a high potential to be utilized as filters for the separation of liquids or gases. This can be simply understood by the fact that the mass flow through a thin 2D sheet is much more faster than the diffusion through a filter with macroscopic thickness. To understand and model the mass transport through specific 2D materials performance, one firstly needs to quantitatively determine the number and the size of pores in a given 2D membrane. Here Helium Ion

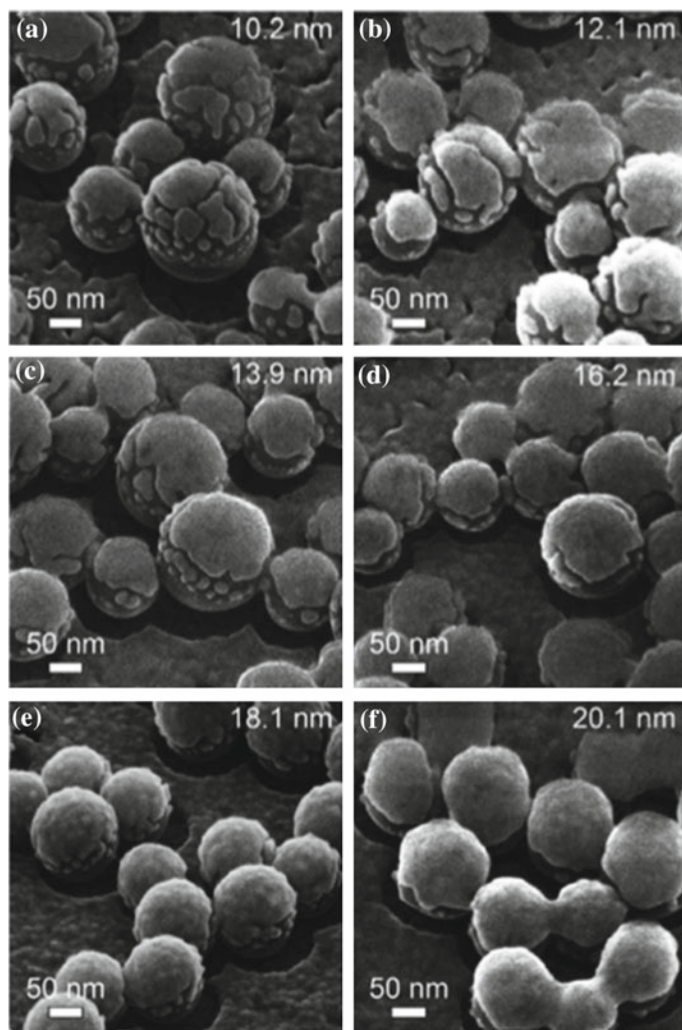

Fig. 10.10 Janus nanoparticles: Silicon nanospheres covered (capped) with different amounts of gold (*thickness* shown in the *upper right corner*), to be used in surface enhanced Raman spectroscopy (from [20])

Microscopy can provide qualitative and quantitative information on the shape and size of pores in 2D materials.

Figure 10.12 shows a series of images of pores in CNMs that were created by the impact of slow highly charged ions (HCI) [21], i.e. ions where a large number of electrons have been removed. Upon irradiation with Xe^{40+} and Xe^{35+}, i.e. Xenon atoms with 40 or 35 electrons removed, every HCI hitting the CNM produces a single hole. The perforated membranes were them investigated by four different imaging techniques: HIM (10.12a, b), TEM (10.12c, d), SEM (10.12e, f),

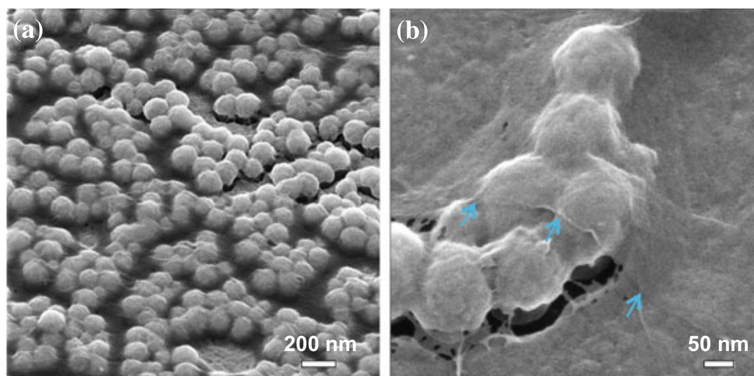

Fig. 10.11 Gold capped silicon nanoparticles covered with a CNM

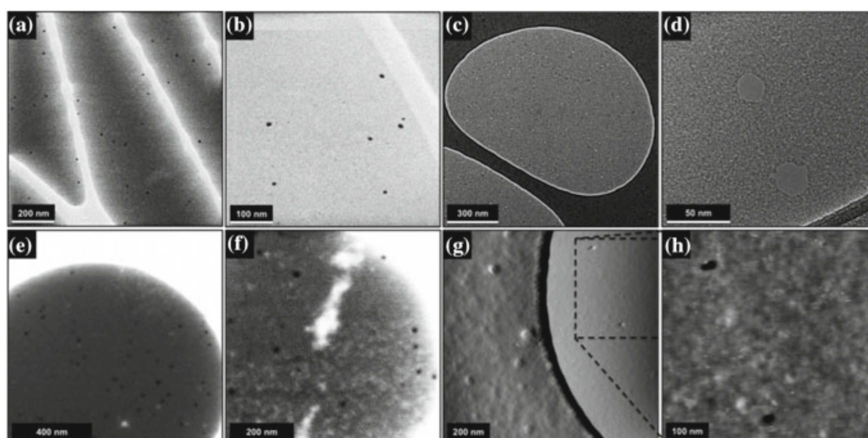

Fig. 10.12 Pores in CNMs imaged with different microscopy techniques after irradiation with slow highly charged ions: **a** HIM image of pores induced by Xe^{40+} (kinetic energy: 180 keV). **b** HIM image, Xe^{40+} (4 keV). **c** TEM image, Xe^{40+} (180 keV). **d** TEM image, Xe^{40+} (40 keV). **e**, **f** SEM images, Xe^{40+} (12 keV). **g** AFM amplitude image, Xe^{35+} (12 keV). **h** AFM height image (zoomed in from (**g**)). While the TEM images pores as bright spots, with all other techniques (HIM, SEM, and AFM), they appear as dark spots. (from [21])

AFM (10.12g, h). The comparison of these images shows that HIM provides the highest contrast of the pores, even at low magnification. This eases an automatic and quantitative analysis the images when large areas of a CNM have to be characterized.

Many properties of CNMs (thickness, chemical composition, density, etc.) are determined by the precursor molecules, the substrate and preparation conditions. In an extended study [16], aromatic molecules were studied for their ability to form CNMs.

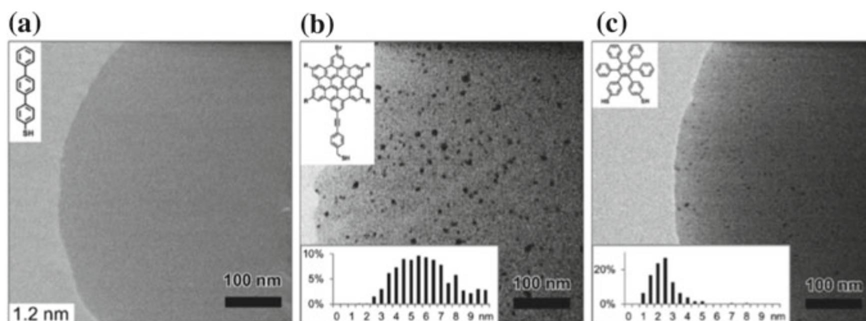

Fig. 10.13 HIM micrographs of free-standing CNMs. After cross-linking the nanomembranes were transferred onto TEM grids. CNMs were prepared from: **a** TPT **b** HBC **c** HPB; the *upper left insets* show the precursor molecules. The number in the *lower left corner* in (**a**) is the TPT CNM thickness. HIM images (**b** and **c**) show CNMs with nanopores, the *lower insets* show the respective distributions (in %) of pore diameters (in nm) [16]

It could be shown that a perforation of the CNMs can also be achieved by creating pores from defects in the molecular layers that after cross-linking became pores.

HIM was used to quantitatively analyse the porosity of the different CNMs. Figure 10.13 shows medium magnification images (500 nm FOV) of CNMs made from Terphenylthiol (TPT, 13a), hexa-peri-benzocoronene derivatives (HBC, 13b) and hexaphenylbenzene derivatives (HPB,13c). While the TPT CNM did not show any visible pores, the CNMs made from HBC and HPB showed pores that could be quantitatively analysed. The histograms at the bottom of Fig. 10.13b, c show the distributions of pore sizes. We can see that the HPB CNM has a very sharp (full width at half maximum 2 nm) pore distribution with a peak at pore diameters of 2.5 nm. Conversely, the HBC CNM has a much broader distribution centred at ca. 5 nm with a full width at half maximum of about 5 nm. Both histograms average data from many images; between 550 and 1300 pores were counted for every graph. Hence, the HIM images clearly show the differences between the CNMs and also show the capability of the HIM for a quantitative analysis of 2D materials. During this type of analysis, aspects to be considered are charging, deposition of contaminations and sputtering. The CNMs in Figs. 10.12 and 10.13 were transferred onto conductive supports, so charging is low and imaging is well possible without any charge compensation. Contamination deposit and sputtering effects are somehow compensating each other. On contaminated samples pores are sometimes closed by scanning, however, a skilled operator easily observes this. High scanning doses can increase pore sizes, so optimized scanning strategies have to used to avoid systematic errors in the pore size determinations. It is important to note that in the presented work, all positions are only scanned once.

10.8 Lithography with Nanomembranes

This chapter ends with an example of the controlled modification of nanomembranes with the help of the HIM. As will be further elaborated in Part IV of this book, Helium Ion Lithography (HIL) is a very powerful tool for micro fabrication and 2D materials have been particularly explored. An recent example is the work of Emmrich et al. [22], who explored the drilling of nanopores with helium ions in three different 2D materials: SiN, Graphene and CNMs. Figure 10.14a shows a HIM image of an array of 100 nanopores written with the focused helium ion beam in graphene. In the writing process, the ion beam was kept focused at a specific location until the 2D material was sputtered away. In each 2D material, a variation in nanoporesize was achieved by adjusting the current between 0.6 and 6 pA and

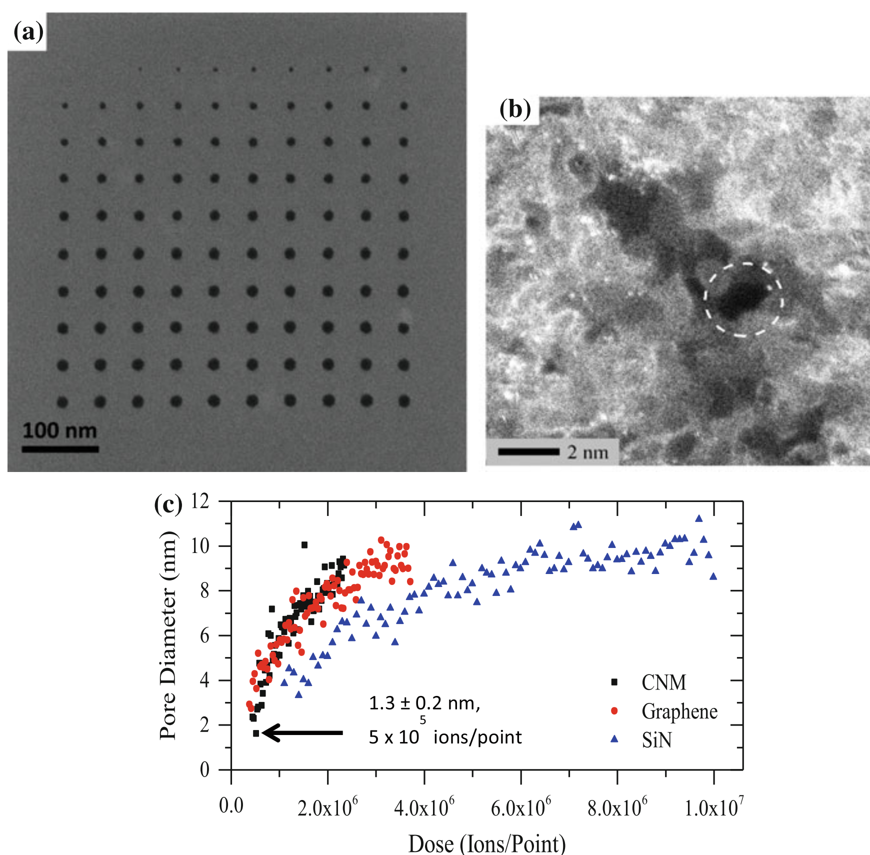

Fig. 10.14 **a** HIM image of a nanopore array milled in a graphene sheet by HIL. Different pore sizes were obtained by varying the dwell times while keeping the beam position fixed. **b** scanning transmission electron micrograph of a 1.3 nm diameter nanopore milled in a CNM by HIL. **c** Plot of measured pore diameters as a function of ion dose for different 2D materials. (from [22])

Table 10.1 Minimal pore sizes and corresponding "breakthrough doses" for the milling of nanopores with the HIM in different 2D materials

2D material	Thickness (nm)	Smallest nanopore diameter (nm)	Breakthrough dose (ions/point)
Graphene	0.34	2.9	3.7×10^5
CNM	1	1.3	4.5×10^5
SiN	30	3.8	1.1×10^6

the dwell times to values between 5 and 500 ms. Table 10.1 shows the resulting minimal pore sizes and corresponding ion doses. The smallest nanopore was written in a CNM with a dose of 4.5×10^5 ions/point. It had a diameter of 1.3 nm, which could not be resolved by HIM. Figure 10.14c shows a scanning transmission micrograph of a 1.3 nm pore, demonstrating the power of the HIM as an ultrafine drilling tool that creates molecular sized nanopores in 2D materials.

10.9 Summary

In summary, the helium ion microscope is an imaging tool that is very well suited to investigate 2D materials. A main advantage is the high surface sensitivity that generates high contrast images, even in samples where there is very little 2D material available. This is particularly useful at low or medium magnification, when single sheets of graphene or CNM are to be clearly detected within other structures. In this magnification range, HIM images already show a lot of detail: folds, wrinkles and pores in the 2D material are seen and can be used to characterize its quality and its performance. This all can be done without too many efforts in sample preparation; the high depth of focus further eases the operation of the HIM, so the microscope may become a routine tool in the observation of technological devices containing 2D materials.

Acknowledgments The reviewed work was financially supported the Volkswagenstiftung, the Deutsche Forschungsgemeinschaft, the German Bundesministeriumfür Bildung und Forschung (BMBF), and the German Bundesministeriumfür Wirtschaft (BMWi). This work was further conducted within the framework of the COST Action CM1301 (CELINA). The research leading to these results also received funding from the European Union Seventh Framework Programme under grant agreement no. 604391 Graphene Flagship.

References

1. J.A. Rogers, M.G. Lagally, R.G. Nuzzo, Synthesis, assembly and applications of semiconductor nanomembranes. Nature **477**, 45–53 (2011)
2. D. Anselmetti, A. Gölzhäuser, Converting molecular monolayers into functional membranes. Angewandte Chemie-International Edition **53**, 12300–12302 (2014)

3. J. Sakamoto, J. van Heijst, O. Lukin, A.D. Schlüter, Two-dimensional polymers: just a dream of synthetic chemists? Angewandte Chemie-International Edition **48**, 1030–1069 (2009)
4. A.K. Geim, K.S. Novoselov, The rise of graphene. Nat. Mater. **6**, 183–191 (2007)
5. A. Turchanin, A. Gölzhäuser, Carbon nanomembranes from self-assembled monolayers: functional surfaces without bulk. Prog. Surf. Sci. **87**, 108–162 (2012)
6. W. Eck, A. Küller, M. Grunze, B. Völkel, A. Gölzhäuser, Freestanding nanosheets from crosslinked biphenyl self-assembled monolayers. Adv. Mater. **17**, 2583–2587 (2005)
7. A. Turchanin, D. Käfer, M. El-Desawy, C. Wöll, G. Witte, A. Gölzhäuser, Molecular mechnisms of electron-induced cross-linking in aromatic sams. Langmuir **25**, 7342–7352 (2009)
8. A. Turchanin, M. Schnietz, M. El-Desawy, H.H. Solak, C. David, A. Gölzhäuser, Fabrication of molecular nanotemplates in self-assembled monolayers by extreme-ultraviolet-induced chemical lithography. Small **3**, 2114–2119 (2007)
9. X. Zhang, H. Vieker, A. Beyer, A. Gölzhäuser, Fabrication of carbon nanomembranes by helium ion beam lithography. Beilstein J. Nanotechnol. **5**, 188–194 (2014)
10. A. Turchanin, A. Beyer, C. Nottbohm, X. Zhang, R. Stosch, A. Sologubenko, J. Mayer, P. Hinze, T. Weimann, A. Gölzhäuser, 1 nm thin carbon nanosheets with tunable conductivity and stiffness. Adv. Mater. **21**, 1233–1237 (2009)
11. K. Celebi, J. Buchheim, R.M. Wyss, A. Droudian, P. Gasser, I. Shorubalko, J.I. Kye, C. Lee, H.G. Park, Ultimate permeation across atomically thin porous graphene. Science **344**, 289–292 (2014)
12. H. Guo, J. Gao, N. Ishida, M. Xu, D. Fujita, Characterization of two-dimensional hexagonal boron nitride using scanning electron and scanning helium ion microscopy. Appl. Phys. Lett. **104**, 031607 (2015)
13. G. Hlawacek, V. Veligura, S. Lorbek, T.F. Mocking, A. George, R. van Gastel, H.J.W. Zandvliet, B. Poelsema, Imaging ultra thin layers with helium ion microscopy: utilizing the channeling contrast mechanism. Beilstein J. Nanotechnol. **3**, 507–512 (2012)
14. G. Hlawacek, I. Ahmad, M.A. Smithers, E.S. Kooij, To see or not to see: imaging surfactant coated nano-particles using him and sem. Ultramicroscopy **135**, 89–94 (2013)
15. A. Beyer, H. Vieker, R. Klett, H.M.Z. Theenhausen, P. Angelova, A. Gölzhäuser, Imaging of carbon nanomembranes with helium ion microscopy. Beilstein J. Nanotechnol. **6**, 1712–1720 (2015)
16. P. Angelova et al., A universal scheme to convert aromatic molecular monolayers into functional carbon nanomembranes. ACS Nano **7**, 6489–6497 (2013)
17. C.T. Nottbohm, A. Turchanin, A. Beyer, R. Stosch, A. Gölzhäuser, Mechanically stacked 1-Nm-thick carbon nanosheets: ultrathin layered materials with tunable optical, chemical, and electrical properties. Small **7**, 874–883 (2011)
18. C.T. Nottbohm, A. Beyer, A.S. Sologubenko, I. Ennen, A. Hütten, H. Rösner, W. Eck, J. Mayer, A. Gölzhäuser, Novel carbon nanosheets as support for ultrahigh-resolution structural analysis of nanoparticles. Ultramicroscopy **108**, 885–892 (2008)
19. M. Ai et al., Carbon nanomembranes (CNMs) supported by polymer: mechanics and gas permeation. Adv. Mater. **26**, 3421–3426 (2014)
20. H. Takei, N. Bessho, A. Ishii, T. Okamoto, A. Beyer, H. Vieker, A. Gölzhäuser, Enhanced infrared LSPR sensitivity of cap-shaped gold nanoparticles coupled to a metallic film. Langmuir **30**, 2297–2305 (2014)
21. R. Ritter et al., Fabrication of nanopores in 1 Nm thick carbon nanomembranes with slow highly charged ions. Appl. Phys. Lett. **102**, 063112 (2013)
22. D. Emmrich, A. Beyer, A. Nadzeyka, S. Bauerdick, J.C. Meyer, J. Kotakoski, A. Gölzhäuser, Nanopore fabrication and characterization by helium ion microscopy. Appl. Phys. Lett. **108**, 163103 (2016)

Chapter 11
Helium Ion Microscopy for Two-Dimensional Materials

Yangbo Zhou, Daniel S. Fox and Hongzhou Zhang

Abstract The ability to modify materials at the atomic scale is crucial for the fabrication of functional nanoscale building blocks for novel nanodevices. Consistency and reproducibility of modifications represent the greatest technical challenges, which demand finer structuring capability than the currently available methods. In this chapter, we will present our recent results of sub-nanometer characterization and modification of two-dimensional (2D) materials enabled by an ultrafine helium ion beam. Characterization will be presented not only in terms of lateral dimension measurement, but also with quantitative thickness and work function extraction. This information is obtained from secondary electron imaging. The effect of contamination and charging on our ability to extract such quantitative information will also be assessed. We will demonstrate that structural defects and stoichiometry modification can be controllably introduced in a few-layer molybdenum disulfide (MoS_2) sample at a few-nanometer scale. Consequently, localized tuning of the physical properties of MoS_2 can be realized. Fabrication of MoS_2 nanostructures with 7-nm dimensions and pristine crystal structure has also been achieved, and the effects of beam dose and profile on the modification will be clarified. This nanoscale modification technique is a generalized approach which can be applied to various 2D materials to produce a new range of 2D metamaterials.

HIM images can reveal surface morphology of a sample. This will be of great importance for the imaging of 2D layered materials (e.g. graphene). The lateral dimensions of these layered structures can vary from nanometer to micrometer scale. The layer thickness of 2D materials may also change, resulting in variation in electronic properties (e.g. work function variations in few-layer graphene). The

Y. Zhou (✉) · D.S. Fox · H. Zhang
School of Physics and CRANN, Trinity College Dublin, Dublin, Ireland
e-mail: yzhou@tcd.ie

D.S. Fox
e-mail: foxda@tcd.ie

H. Zhang
e-mail: hozhang@tcd.ie

© Springer International Publishing Switzerland 2016

G. Hlawacek and A. Gölzhäuser (eds.), *Helium Ion Microscopy*,
NanoScience and Technology, DOI 10.1007/978-3-319-41990-9_11

remarkable resolution and surface sensitivity of HIM can provide detailed information regarding surface contamination, local defects, smoothness, uniformity and thickness, which may be invisible in other microscopy methods. In addition, there is a charge compensator system in HIM that reduces the beam-induced charging on an insulating substrate. In conventional fabrication processes (i.e. mechanical exfoliation) 2D materials are transferred to an insulating substrate. HIM will therefore be an ideal tool to image their structure with minimal substrate charging influence.

The ability to modify materials at the atomic scale is crucial to fabrication of functional nanoscale building blocks for novel nanodevices. Consistency and reproducibility of modification represent the greatest technical challenges which demand finer structuring capability than the currently available methods. The delivery of a precise quantity of ions to a sub-nanometer area on the surface of a sample provides the most convincing way of achieving this capability.

In this chapter, we will first discuss the application of high-resolution HIM imaging in 2D material characterization, especially graphene. We start with the lateral dimension measurement and then introduce the thickness contrast of 2D materials observed in HIM. This will be followed by a brief introduction to quantitative extraction of the work function of graphene using secondary electron imaging in the helium ion microscope. The discussion of HIM imaging will be concluded by introducing its unique charge compensation mechanism and the influence of beam-induced contamination on the imaging of graphene. In the second section, we will present our recent results of sub-nanometer modification enabled by an ultrafine helium ion beam and discuss the effects of beam dose and profile on the modification. We will demonstrate that structural defects and stoichiometry modification can be controllably introduced in a few-layer MoS_2 sample at a few-nanometer scale. Consequently, localized tuning of the electrical properties of MoS_2 can be realized. This nanoscale modification technique is a generalized approach which can be applied to various 2D materials to produce a new range of 2D metamaterials.

11.1 Graphene Characterization

The morphology of graphene determines its physical properties. For example, the electronic structure of few-layer graphene is different from that of single-layer graphene [1, 2]. Unique physics appear as the lateral dimensions of graphene are reduced, i.e. the opening of a band gap in graphene ribbons [3] and tuning of plasmon resonance in graphene quantum dots [4]. Understanding the properties of graphene normally requires knowledge of its dimensions at the sub-nanometer scale. This poses an extreme challenge for the task of surface characterization. HIM imaging is a promising technique to address this challenge.

11.1.1 Lateral Dimension

The imaging resolution of lateral dimensions is crucial for the characterization of 2D materials. HIM can produce a sub-nanometer sized ultrafine probe, which is an ideal tool for high-resolution lateral dimension characterization. The dimension of the focused He^+ probe can be evaluated from the measurement of probe size. A freestanding flake of a 2D material with a perfectly sharp edge is usually selected, and a series of SE images that go across the in-focus state are obtained. The SE intensity drop-off over the edge of the flake in the image can be attributed to the Gaussian distribution of the ions in the probe. Therefore, an in-focus SE image represents the finest probe size. For example, see Fig. 6.10, in which a 0.3-nm edge resolution in a HIM image is presented. We can also compare this 30-keV He^+ probe size with the optimized probe size of the e-beam for different beam energies, which were obtained from a Zeiss Ultra SEM. As shown in Fig. 11.1, the electron probe size monotonically decreases from 2.7 $\pm$ 0.2 nm to 1.6 $\pm$ 0.1 nm as the e-beam energy increases from 0.5 to 20 keV. The smallest e-beam probe is more than five times the size of the He^+ probe (0.3 nm).

HIM, with its sub-nanometer He^+ probe, can provide a well-defined edge contrast, which is useful for accurate dimensional analysis when compared to electron microscopes [5]. Figure 11.2 shows images from three different microscopes, obtained by SEM in-lens mode, STEM-HAADF mode and HIM, respectively. The HIM image exhibits a much more clearly defined edge profile than the SEM or STEM images. In the SEM and STEM profiles, the edges are somewhat rounded, making it difficult to identify the exact edge of the flake. However, in the HIM profile, the edge has an increase in intensity with a sharp peak, which is due to the enhanced sensitivity of secondary electron (SE) yield on incidence angle in HIM. Therefore, HIM imaging can provide more accurate measurement of the dimensions of nanostructures.

HIM can also show the extension of a graphene domain boundary with a high spatial resolution. Figure 11.3a shows an image of the domain boundary between the substrate-supported monolayer and bilayer graphene acquired in a HIM. The intensity profile across this atomically sharp boundary is presented in Fig. 11.3b. The boundary revealed in the HIM image extends ca. 10 nm. Although the value is larger than the

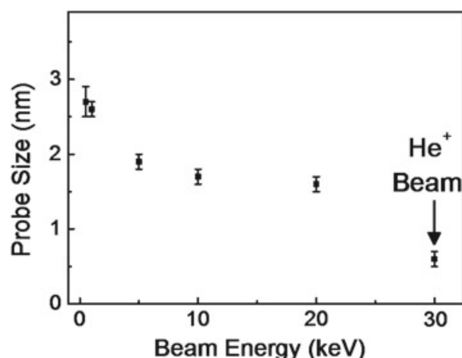

Fig. 11.1 The relationship between beam probe size and beam energy. The data points are all from SEM images, except the smallest probe size, which is from a HIM image

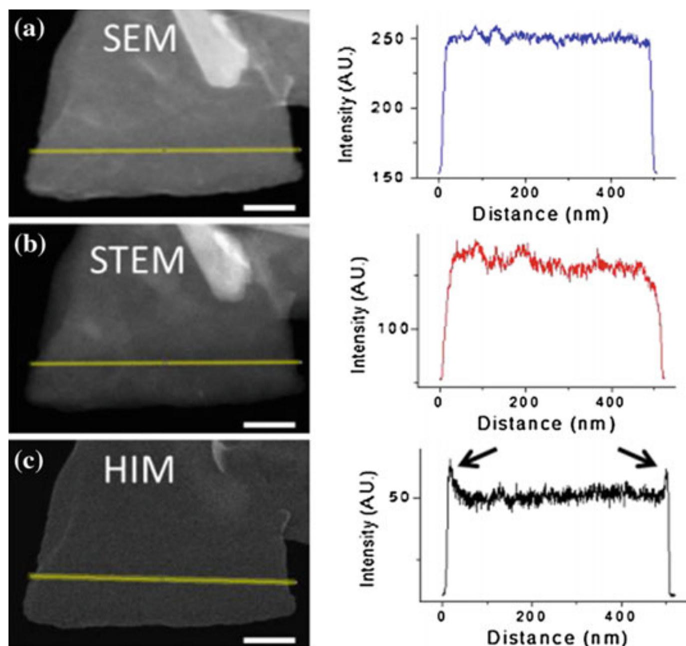

Fig. 11.2 **a** SEM in-lens image of a graphene flake. An intensity profile across the flake is shown adjacent. **b** STEM-HAADF image of the same graphene. The intensity profile from the same region of the flake is shown adjacent to the image. **c** HIM image of the same flake, with the intensity profile from the same region also plotted. The well-defined flake edges in the HIM intensity profile are indicated by two *arrows*

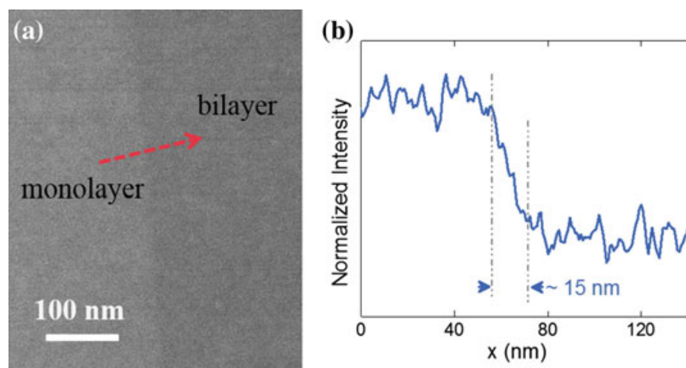

Fig. 11.3 **a** High-resolution HIM-SE image of 1–2-layer graphene boundary. **b** Intensity profile across in boundary in **a**

physical dimension, it is much smaller than the diffraction-limited value of ~680 nm in an optical image. Therefore, HIM imaging provides a much higher lateral spatial resolution than the optical imaging typically used in high-throughput measurement of graphene flake dimensions. This enables us to investigate the properties of graphene that correlate with HIM imaging at the nanometer scale.

HIM is a relatively new surface imaging technique, complementary to the well-established SEM. Many HIM publications have shown the values of the ultrafine probe (~0.2 nm) of the tool. However, no lattice resolution has been demonstrated. This might be due to beam damage, sample orientation, contamination, etc. (see Chap. 3, Sect. 3.4). Similar to electron microscopes, the chromatic and spherical aberrations in HIM are important issues that can limit its resolution. By applying correcting octopoles to the quadrupole doublet objective lens in the HIM, the resolution is expected to be improved from 3 to 0.3 Å [6]. Thus, atomic-level resolution of HIM becomes possible. A recent report predicts that the resolution of HIM could be competitive to HRTEM [7]. The first principles simulations show that when a highly focused He^+ beam is irradiated on freestanding graphene, the amount of emitted SEs strongly depends on the impact point of the He^+ ions. Within the graphene lattice, the higher the valence charge density becomes, the more SEs will be emitted during the He^+–graphene interaction process. The charge density distribution in graphene can be revealed in the corresponding HIM image (see [7], Fig. 11.3a). Therefore, measuring a lattice image of suspended graphene by HIM is feasible. This may provide a high-throughput and non-destructive method for imaging nanostructures at atomic-level resolution.

11.1.2 Thickness and Work Function

HIM is well-suited to high-lateral-resolution SE imaging. The SE imaging in HIM also provides a thickness-dependent contrast for 2D layered materials, which reveals their layer thickness information as well as other quantitative information. The SE imaging in SEM has been used to investigate the layer thickness information of graphene [8]. Mechanically exfoliated few-layer graphene flakes on thick insulating substrates (e.g. SiO_2, sapphire, mica) were observed by using the SEM with various beam energies. The researchers found a linear relationship between the SE intensity and graphene thickness. A practical method for determining the number of graphene layers was proposed in the paper. Compared with conventional optical observation, the benefits of this method are the characterization of sub-micrometer graphene samples on various insulating substrates. The mechanism of graphene thickness contrast has also been discussed but remains controversial. Various mechanisms including work function effect [9] and attenuation effect have been proposed [8]. HIM can provide a different excitation source for us to investigate the graphene layer thickness and contrast mechanism. Furthermore, graphene has been reported to have a layer-dependent work function, which increases from 4.3 eV to a saturated value of 4.6 eV as its layer numbers increase from one to

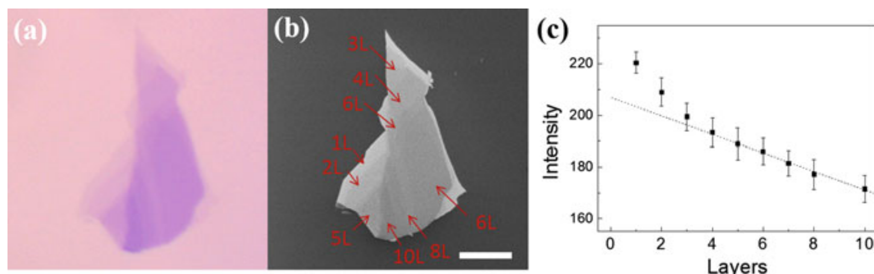

Fig. 11.4 **a** Optical image of a few-layer graphene flake. The graphene flake has different thickness from 1 to 8 layers and 10 layers; the scale bar is 10 µm. **b** A 30-keV HIM image of the corresponding graphene flake. **c** The relationship between SE intensities and graphene layer thickness

more than four [10, 11]. The SE contrast of graphene may therefore also be able to reveal its work function variations.

We recently investigated the thickness contrast in HIM SE imaging. Figure 11.4a, b shows optical and HIM images of a few-layer graphene flake on a Si substrate covered by a 285-nm SiO_2 layer. The HIM image clearly shows the existence of a graphene flake, which appears "brighter" than the substrate, indicating a larger SE emission from the graphene surface. A non-uniform SE contrast can also be observed on the graphene flake, which corresponds to the different graphene layer thicknesses observed in the optical image. As the graphene layer number increases, the SE intensities from grapheme are reduced. Figure 11.4c shows the relationship between the SE intensity and graphene layer thickness. It was found that the SE intensity decreases rapidly for a few (1–4) graphene layers, then follows an almost linear decrease to at least ten layers. Therefore, up to ten layers can be identified from the HIM image. In addition to the layer thickness information, the HIM image reveals the work function effect. The linear relationship we observed in Fig. 11.4c can be attributed to the SE attenuation effect, while the large deviation for one to four layers shows the change of graphene work function for few graphene layers.

The thickness contrast in HIM is not limited to few-layer graphene flakes, but can be extended to a wider variety of 2D materials. Recently, the thickness contrast of a few-layer hexagonal boron nitride (h-BN) nanosheet in HIM was also reported by Guo et al. [12]. Figure 11.5 shows a HIM SE image of an h-BN flake on an Fe–Cr-Ni substrate. SE images similar to those of graphene in HIM are observed, and the HIM imaging of h-BN also shows a larger SE emission from the BN surface. However, the SE intensity increases with increased h-BN layer thickness, which is quite different from HIM imaging of graphene. Up to seven layers of h-BN can be identified from the obtained SE image. The relationship between SE intensity and h-BN layer thickness shows a non-linear increase, and can be well-fitted by an exponential curve based on an attenuation model. This indicates that the attenuation effect dominates the SE contrast, while the work function variation between h-BN layers can be ignored.

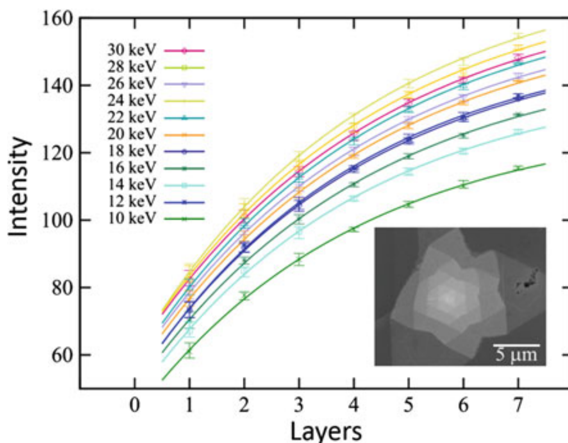

Fig. 11.5 SE Intensities of h-BN nanosheets observed using HIM (scattered points) with a theoretical fitting based on an attenuation model. The *inset* shows the morphology of typical h-BN nanosheets observed by HIM [12]

In conclusion, we show that HIM can be used to detect the layer thickness information of 2D materials. Combined with its high spatial resolution, it may also be able to distinguish variations in layer thickness at the nanometer scale.

11.1.3 Surface Contamination

The fabrication of graphene nanodevices normally involves transferring graphene onto a suitable substrate (e.g. SiO_2/Si wafers) and defining electrodes. Wet chemistry with organic species is often unavoidable, for example the use of resists exemplified by polymethyl methacrylate (PMMA) in electron beam lithography. Therefore, surface residues will arise during the process, and degrade the electronic properties of graphene devices. A fundamental understanding of the residue morphology is still absent due to a lack of high-throughput and high-resolution surface characterization methods. We recently demonstrated that SE imaging in the SEM and HIM could provide sub-nanometer information of a graphene surface and reveal the morphology of surface contaminants[13].

Figure 11.6a is a HIM image of freestanding graphene, with 35-keV He^+ beam irradiation and 400-nm field of view (FOV). The freestanding graphene was fabricated by a transfer process with the assistance of a PMMA film. The PMMA residues on the graphene surface are visible in the HIM image, which exhibits a non-uniform contrast. The typical features include bright spots (~10 nm in diameter), less bright clusters (several hundred nanometers) and relatively dark areas surrounding these clusters. The darkest regions appear as dot-like features with an average size of 2.7 ± 0.4 nm (inset of Fig. 11.6a). These featured structures can also be identified in the SEM images (Fig. 11.6b–d). However, their visibility

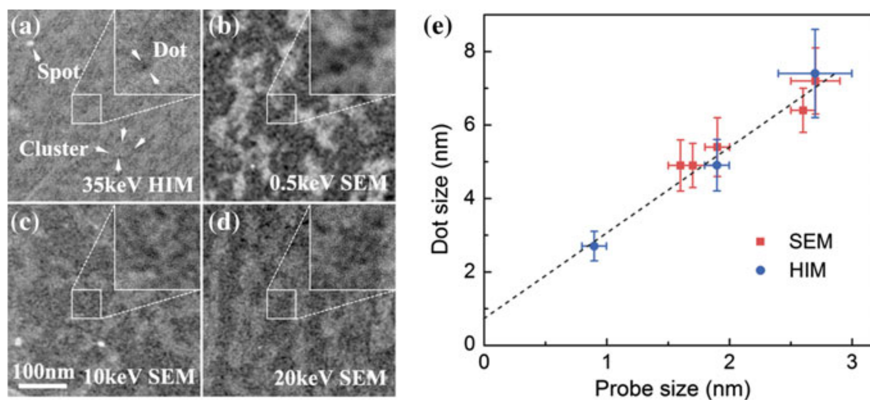

Fig. 11.6 High magnification SE images of freestanding graphene under **a** 35-keV He^+ irradiation. **b** 0.5-keV e-beam irradiation **c** 10-keV e-beam irradiation **d** 20-keV e-beam irradiation. **e** The relationship between the beam probe size and the *dark dot* size

varies with e-beam energies. The lower the e-beam energy becomes, the higher the contrast exhibited in the corresponding image. Another significant difference among these images is the dimension of the dark dots. Under the 0.5-keV e-beam imaging, these dots have the largest apparent size of 7.2 ± 0.9 nm, while their average size is reduced to 4.9 ± 0.7 nm under the 20-keV e-beam imaging, which is twice as large as that in the HIM images.

The morphology difference observed in Fig. 11.6a–d can be attributed to the image resolution, which is revealed in the variation in beam probe size. We found that the size of the dark dots measured from a SEM image was linearly dependent on the size of the electron beam probe that was used to acquire the image (Fig. 11.6e). The linear relationship is valid for the e-beam energies that we tested (from 0.5 to 20 keV, which corresponds to a monotonous decrease in electron probe size from 2.7 ± 0.2 nm to 1.6 ± 0.1 nm). A striking feature is that the measured He^+ probe fits the linear relationship as well (0.9 ± 0.1 nm). The He^+ probe size was tuned using defocus to values comparable to the e-beam probe size (e.g. ~2.6 nm). The featured structures were still visible in the defocused image, and their size distributions matched well with those obtained from 0.5-keV SEM images with a similar probe size. This correlation indicates that the measured size of the dark dots depends on the probe size and is independent of the beam type. When the probe size decreases to zero (i.e. the y-intercept), the real physical size of these dots is revealed to be 0.7 ± 0.3 nm, which is beyond the resolution limits of SEM and HIM. Nevertheless, compared with SEM, HIM imaging reveals the surface morphology with higher fidelity and surface sensitivity due to its finer sub-nanometer probe.

11.1.4 Charge Compensation Effect on Graphene Imaging

Graphene and other 2D materials are usually mechanically exfoliated on a dielectric substrate (i.e. a Si substrate with 285 nm thickness of the SiO_2 layer), which are suitable for further device fabrication. However, this kind of substrate is not suitable for imaging in charged particle microscopes. This is because during the scanning process in SEM or HIM, energetic charged particles (electrons or He^+) will be injected into the substrate. The SiO_2 layer is an insulator, which means that this charged particle will stay within the layer and cannot be conducted to the ground. Meanwhile, the beam irradiation will also cause the SE emission process, resulting in a charged region near the surface. The SiO_2 layer will therefore be charged during the irradiation process which will influence the SE imaging. In SEM, substrate charging can only be controlled by varying the e-beam energy, which changes the SE emission yield from the surface. Charge neutralization can only be achieved at a certain e-beam energy where the SE emission yield is around 1. Figure 11.7 shows the SEM images of few-layer graphene flakes irradiated by e-beams with different energies. It can be seen that at a low e-beam energy of 0.5 keV, the SE image appears similar to HIM images, i.e. graphene becomes “brighter” than the substrate. However, due to the substrate charging the contrast is not uniform on the substrate or on the graphene flake, even with the same layer thickness. The charging-induced non-uniform SE contrast is greatly reduced at higher e-beam energies, e.g. 5 keV (Fig. 11.7b). Although the 20-keV SEM image (Fig. 11.7c) still shows an almost charge-neutralized substrate, the contrast of graphene becomes worse, which means the high energy is not ideal for graphene imaging. Therefore, it becomes difficult to obtain a balance between high resolution and less substrate charging for imaging graphene on an insulating substrate.

In HIM, both the He^+ irradiation and SE emission cause positive charging to the SiO_2 layer. Therefore, we can use a charge compensator in HIM to reduce positive substrate charging. The charge compensator, which is called an electron flood gun,

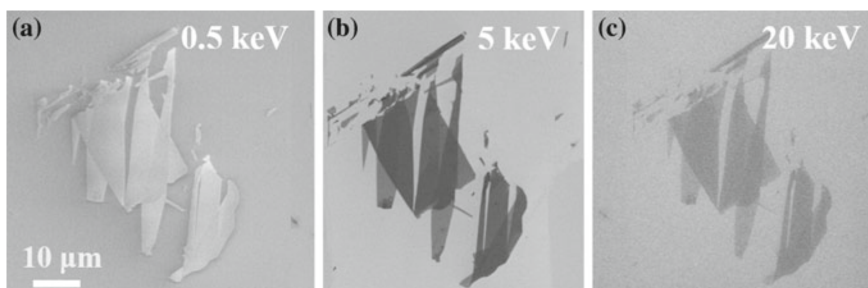

Fig. 11.7 SEM images of graphene with the irradiation of different e-beam energies of **a** 0.5 keV, **b** 5 keV and **c** 20 keV. The scale bar is 10 μm

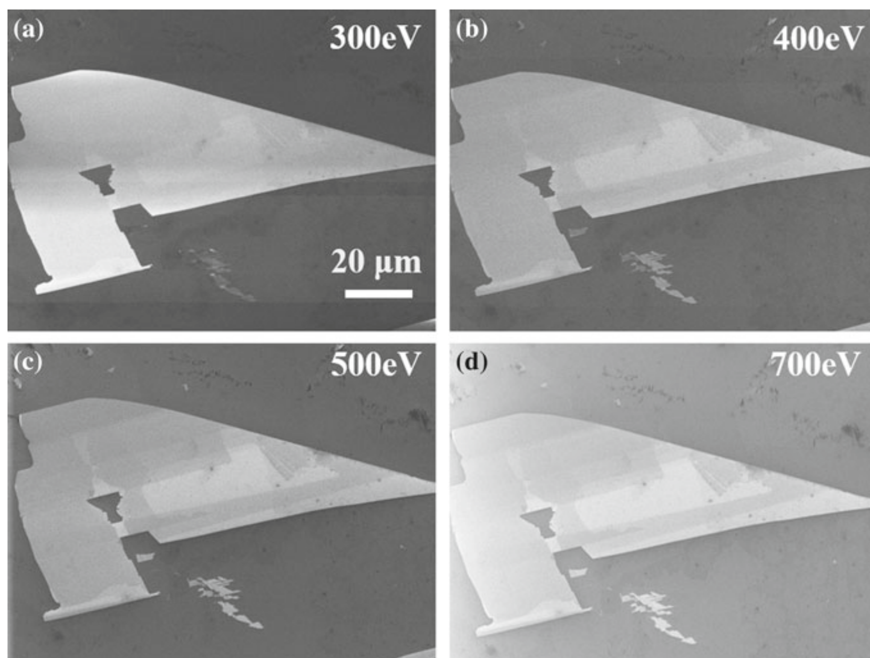

Fig. 11.8 HIM images of a graphene flake acquired with a He^+ beam energy of 35 keV but with different flood energies of 300, 400, 500 and 700 eV in **a**–**d**, respectively

provides a broad low-energy electron beam that can effectively neutralize the positive charge near the surface. The electron flood gun provides various controls to tune the charge compensation process, for example, flood time (compensation time) and flood energy (compensation depth). Figure 11.8 shows the influence of varying the flood energy on the He^+ imaging of graphene. When the graphene flake is imaged by a constant 35-keV He^+ beam and neutralized by a low flood energy (Fig. 11.8a, 300 eV, constant flood time of 10 µs), a non-uniform contrast can be observed in the scanned area, which indicates the existence of strong positive charging. This can be explained by the penetration depth of a 300-eV electron not fully penetrating the positively charged region near the surface. Strong positive charging still exists and affects the SE imaging. A higher flood energy (Fig. 11.8b and c, 400 and 500 eV, respectively) significantly reduces the positive charging, but the contrast difference between graphene layers is much improved at 500-eV flood energy compared to 400 eV. However, at a much higher flood energy of 700 eV (Fig. 11.8d), the contrast of the image again becomes non-uniform, indicating charging of the substrate by the flooding electron beam. Therefore, by tuning the

charge neutralization parameters, the charging of graphene on a non-conductive substrate can be minimized at any given beam energy. High-resolution images can then be obtained.

11.1.5 Influence of Beam-Induced Contamination

The contamination issue is also very important to SE imaging. Hydrocarbon contamination is known to be generated on graphene surfaces in both the e-beam and He^+ beam irradiation processes. The formed contamination layer will reduce the SE emission of the underlying surface, therefore the real surface information of graphene might not be obtained. The contamination issue can be more serious in HIM, because He^+ imaging results in a lower SE energy distribution. The SE emission will be more sensitive to the cleanliness of the surface.

In the previous section we showed that HIM can be used to detect the layer thickness information of graphene. However, during the scanning process hydrocarbon contamination will be accumulated on the surface and thus influence the thickness information of graphene. Figure 11.9a is a HIM image of a freshly exfoliated few-layer graphene flake. Different thicknesses of graphene layers can be clearly identified from the different SE contrast on the graphene surface. The sample was then scanned repeatedly (~20 images, total irradiation dose $\sim 10^{16}$ He^+/cm^2) and stored in air for approximately one week. Repeat measurements showed a reduced contrast difference between graphene layers. It became difficult to distinguish even the few graphene layers (Fig. 11.9b). On the contrary, the SEM imaging of this He^+ irradiated graphene flake still reveals the contrast difference between graphene layers (Fig. 11.9c). The results show that HIM imaging is very sensitive to the beam-induced surface contaminants, while the existence of these contaminants does not obviously affect the SEM imaging. A clean graphene surface is therefore very important for HIM imaging.

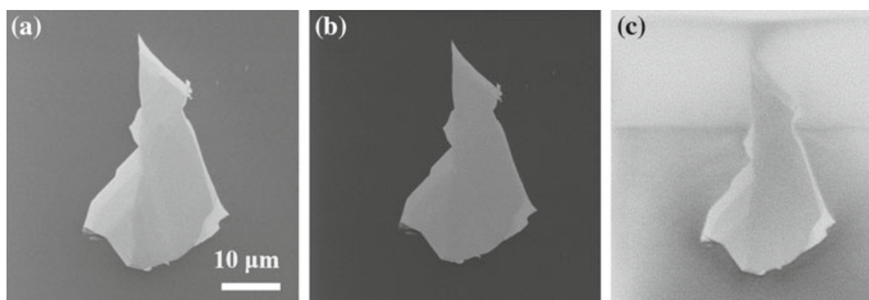

Fig. 11.9 30-keV HIM image of a graphene flake after **a** being freshly exfoliated, and **b** after being kept in air for one week. **c** A 3-keV SEM image of this graphene flake after He^+ imaging

11.2 HIM Modification of Two-Dimensional Materials

The nature of the ion source in HIM indicates that it is not only an imaging tool, but can also act as a fabrication tool for modifying nanostructures[14]. Similar to traditional and well-developed fabrication tools such as the gallium ion focused ion beam (FIB), the focused He^+ beam can fabricate and modify nanostructures by sputtering away materials [15]. HIM can produce structures an order of magnitude smaller than the Ga^+ FIB while also avoiding contamination caused by the injection of metallic gallium ions [16]. The highly localized and precise modification capabilities of HIM do have the disadvantage of a low sputtering yield. Therefore, it will be most suitable for the modification and fabrication of 2D layered materials [17].

In this section, we will first briefly discuss defect generation in 2D materials by He^+ irradiation and the influence on the properties of these materials. We will then introduce the nanometer-scale structure fabrication on 2D materials by He^+ milling.

11.2.1 Controllable Defect Creation in 2D Materials

Defects in 2D materials can influence their properties. The focused He^+ beam in HIM has been used to generate defects in graphene. The relationship between the helium ion dose and the defect density in graphene was recently experimentally established [5, 18]. The Raman spectra in Fig. 11.10 show the change in the structure of a material by HIM irradiation. Doses of less than 10^{13} He^+/cm^2 had a negligible effect on the structure of the material. This was confirmed by the presence of the sharp and well-defined G peak (~1580 cm^{-1}) and 2D peak (~2700 cm^{-1}) associated with pristine graphene. At doses between 10^{13} and 10^{18} He^+/cm^2, the defect-related D peak (~1350 cm^{-1}) intensity increased with dose. At doses above 10^{16} He^+/cm^2, the structure was completely destroyed, as evidenced by the splitting and broadening of the G peak and the complete loss of the 2D peak.

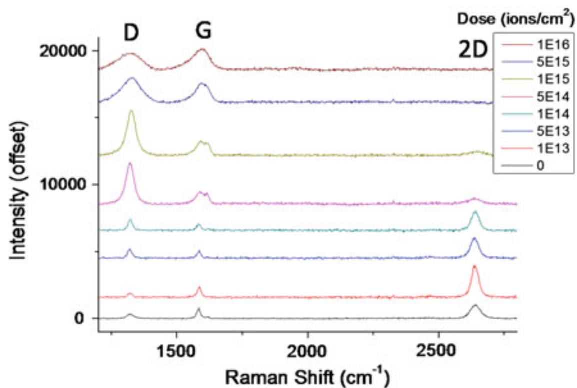

Fig. 11.10 Raman spectra of freestanding graphene samples irradiated with the range of doses shown. In both cases the dose increases from the bottom spectrum up to the top spectrum. The D peak is at ~1350 nm^{-1}, the G peak is at ~1580 nm^{-1} and the 2D peak is at ~2700 nm^{-1}

He^+ irradiation of a 2D material supported on a substrate causes an enhanced rate of damage and a damage extension of hundreds of nanometers from the irradiated area. The damage can be directed to one side by tilting the sample, thus allowing the fabrication of high quality structures. The generation of defects in graphene also tunes the electronic properties of graphene. A low density of defects, which is two orders of magnitude less than the density of carbon atoms, can be used for conduction tuning of graphene [19]. Due to the strong localization of carriers at the defect sites, a high current on-off ratio of two orders of magnitude was observed by back gate modulation at room temperature. When the graphene was cut with a high irradiation dose over 10^{18} He^+/cm^2, which completely removed the materials, the conductance of graphene was dramatically reduced, with just some residual current attributed to hydrocarbon contamination [20]. The observed beam irradiation-induced damage can be reduced by encapsulating graphene between BN layers [21]. An n-type doping was observed, as well as a reduction in damage to the graphene, which can be explained by the exchange between nitrogen and carbon atoms.

Another type of 2D material, MoS_2, also shows defect-dependent properties. Structural defects in MoS_2 can modify its crystal structure [22, 23] and stoichiometry[24–26], thus tuning the electronic transport properties of MoS_2. We recently used a focused He^+ beam to generate defects in few-layer MoS_2 flakes. The sub-nanometer He^+ probe allows us to modify MoS_2 at the atomic scale [27]. Irradiation with highly controllable doses of He^+ allows tuning of both the crystal structure and stoichiometry of MoS_2, with unprecedented spatial resolution. Figure 11.11 shows HRTEM images of few-layer freestanding MoS_2 flakes before and after He^+ irradiation. With no He^+ irradiation, the hexagonal lattice symmetry of pristine MoS_2 can be observed in Fig. 11.11a. With a relatively low irradiation dose of 10^{13} He^+/cm^2, MoS_2 still maintains its high crystal quality, with no significant difference from pristine MoS_2. However, at a higher irradiation dose of 10^{18} He^+/cm^2, the crystal structure of MoS_2 can be seen to have been completely removed in Fig. 11.11c; the sample becomes amorphous.

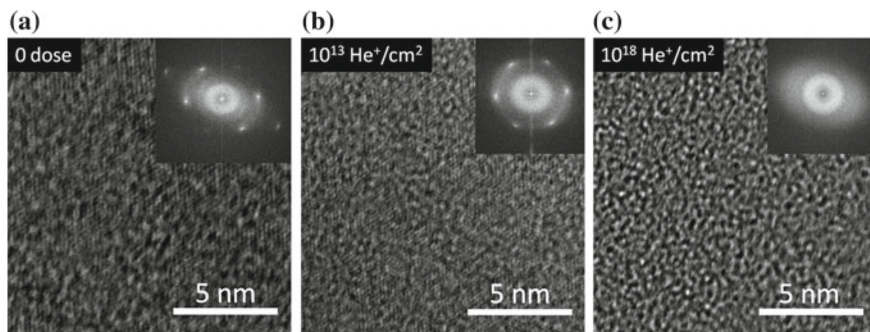

Fig. 11.11 **a** HRTEM image of pristine MoS_2. **b** MoS_2 irradiated with **a** 10^{13} He^+/cm^2 and **b** 10^{18} He^+/cm^2. Only the highest irradiation dose results in observable damage

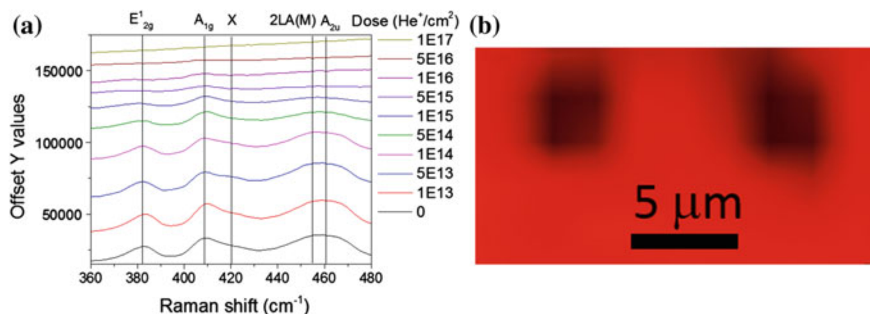

Fig. 11.12 **a** The Raman active modes from our sample in the range from 360 to 480 cm^{-1}. **b** Raman mapping of two areas irradiated with 10^{16} and 5×10^{16} He^+/cm^2 (*left* and *right*, respectively)

The structural modification is also revealed in the Raman spectra for a 4-nm-thick MoS_2 flake under He^+ irradiation, as shown in Fig. 11.12a. The evolution of two characteristic peaks, E^1_{2g} (the in-plane Mo-S vibration) and A_{1g} (the out-of-plane Mo-S vibration) demonstrates the ability of He^+ irradiation to alter the crystal structure by defect introduction and material removal. The Raman mapping of irradiated areas is shown in Fig. 11.12b; a uniform Raman signal decrease is observed in the irradiated region, indicating that the transition to an amorphous structure happens uniformly. These results show that the crystal structure of MoS_2 can be controllably amorphized by the He^+ irradiation process.

The sputtering rates of the molybdenum and sulfur atoms in MoS_2 are different during He^+ irradiation. The sulfur atom can more easily be knocked out during the He^+ specimen interaction process because of its lighter mass. The preferential sputtering of sulfur from MoS_2 not only changes the stoichiometry, but also tunes the electronic properties of MoS_2. Figure 11.13 shows the electrical characterization of a He^+ modified MoS_2 transistor device. Semiconducting, metallic or insulating MoS_2 can be obtained by irradiation with different doses of He^+. The inset shows the lack of gate response, and therefore metallic behavior, of the 10^{17} He^+/cm^2 dose device.

11.2.2 Nano-Patterning of 2D Materials Using HIM

The irradiation of nanostructures with a He^+ beam not only changes their crystal structure and composition, but can also be used to modify their geometry. The sub-nanometer He^+ beam provides a high-efficiency way to tailor the morphology at nanometer scale. For 2D layered materials, such as graphene and MoS_2, geometric modification becomes more important because the materials' properties can also be tuned. For example, by tailoring the 2D graphene sheet to a

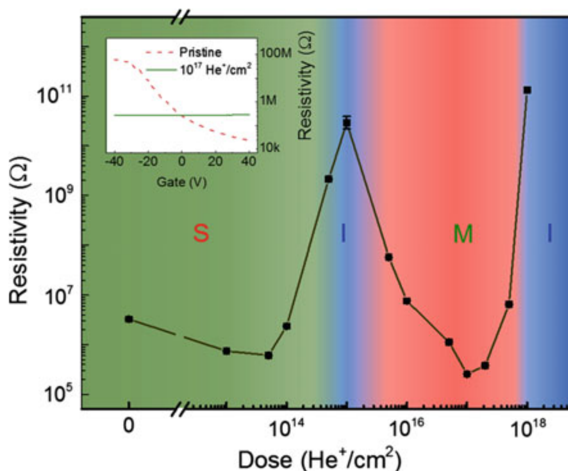

Fig. 11.13 Double log plot of electrical resistivity versus He^+ dose for a substrate supported, mechanically exfoliated bilayer MoS_2 flake. *Inset* Resistivity measurement as a function of gate bias

one-dimensional nanoribbon with a width less than 10 nm, a direct band gap can be opened. Similarly, the MoS_2 nanoribbons with specified edge orientations and widths of ~3 nm can also have extraordinary physical properties, such as ferromagnetic behavior [28, 29].

We have successfully fabricated sub-10-nm nanostructures of 2D materials by using He^+ beams. For example, graphene nanoribbons milled by HIM are shown in Fig. 11.14. This image shows that with a sufficient dose the graphene can be completely removed where required. A large dose of 10^{18} He^+/cm^2 was used to remove two nearby rectangular areas leaving a ribbon in between. The geometry fabricated here is just one example of how such a material can be altered.

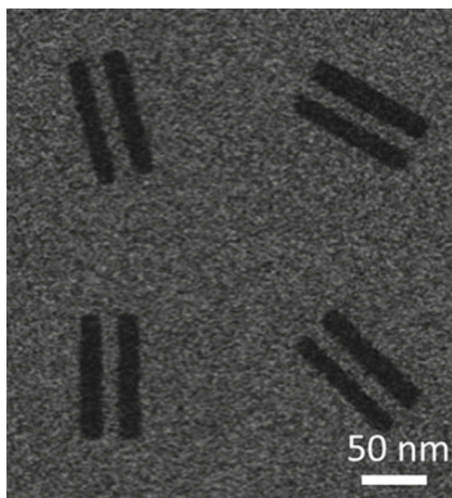

Fig. 11.14 Four graphene nanoribbons milled at various orientations by a HIM

Nanopores or more complex geometries are also possible, with the appropriate beam scan control.

Fabrication of graphene nanoribbons (GNR) is not always achieved without issue. The most common problems are shown in the HIM images in Fig. 11.15. During the GNR fabrication process, when the sample or chamber is not sufficiently clean, hydrocarbon contaminants will be deposited on graphene surface with a faster rate than the milling of graphene. This result in a series of parallel carbon deposits, and no ribbons can be produced (Fig. 11.15a). The milled structure should avoid any unnecessary acquisition of high quality images in HIM, because the sample can be greatly altered by this single image acquisition (Fig. 11.15b, c). When these ribbons are milled in series, the milling of features near one another, the previous area will be affected by the fabrication of a new feature (Fig. 11.15d). The ribbons bend towards the area being patterned by the beam. This can be avoided by milling nearby areas in parallel. The possible damage due to the pre-imaging of

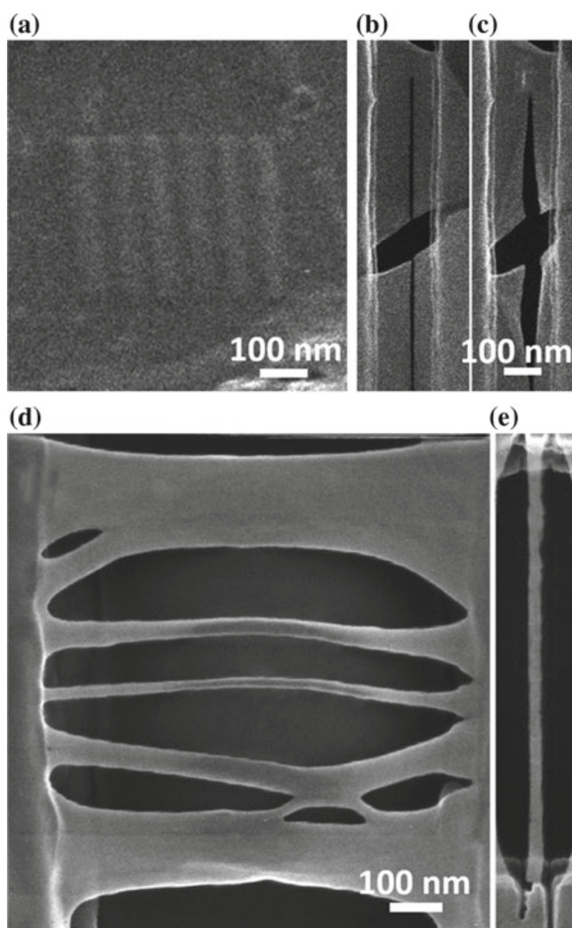

Fig. 11.15 Several issues encountered during the milling process. **a** Deposition of contamination. **b** +**c** Damage caused by imaging after milling. **d** The influence of milling order to the final structure. **e** The pre-imaging might degrade the structure of the milled intact GNR

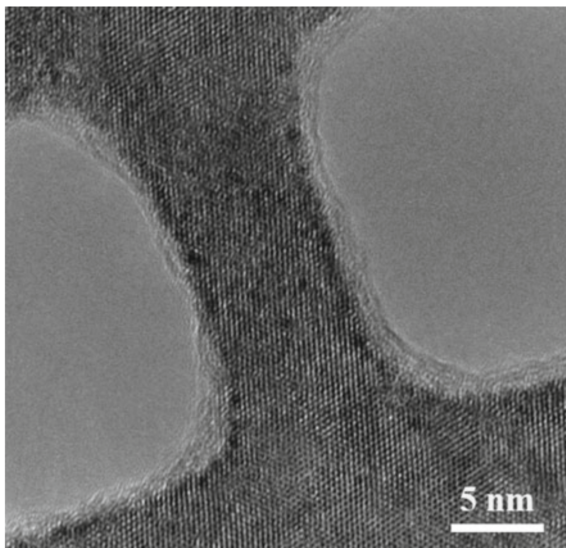

Fig. 11.16 TEM image of an 8-nm-wide milled MoS_2 ribbon. The structure remains pristine with some minor (<1 nm) edge damage

samples should also be considered. The 15-nm-wide GNR in Fig. 11.15e remained intact during the fabrication process. However, it was exposed to a substantial dose of helium ions as images were acquired to position the patterns. Its structure has most likely been severely degraded. This could have been avoided by placing the patterns without having looked at the sample, or at least by imaging with a substantially lower dose.

This nanofabrication technique is not limited to graphene. As an example of the robustness of this method, nanoribbons of MoS_2 were also fabricated in HIM. Figure 11.16 is a TEM image of an MoS_2 nanoribbon with a width of approximately 8 nm. The crystallinity of the material was observed to remain well intact and was not damaged by the fabrication process. This shows how localized and well-controlled He^+ milling is.

References

1. B. Partoens, F.M. Peeters, From graphene to graphite: Electronic structure around the K point. Phys. Rev. B **74** (2006)
2. K.F. Mak, M.Y. Sfeir, J.A. Misewich, T.F. Heinz, The evolution of electronic structure in few-layer graphene revealed by optical spectroscopy. Proc. Natl. Acad. Sci. **107**, 14999–15004 (2010)
3. Y.-W. Son, M.L. Cohen, S.G. Louie, Energy gaps in graphene nanoribbons. Phys. Rev. Lett. **97** (2006)
4. J.D. Cox, F. Javier García de Abajo, Electrically tunable nonlinear plasmonics in graphene nanoislands. Nat. Commun. **5** (2014)

5. D. Fox et al., Helium ion microscopy of graphene: beam damage. Image Qual. Edge Contrast. Nanotechnol. **24**, 335702 (2013)
6. F.W. Martin, A proposal for improved helium microscopy. Microsc. Microanal. **20**, 1619–1622 (2014)
7. H. Zhang, Y. Miyamoto, A. Rubio, Ab initio simulation of helium-ion microscopy images: the case of suspended graphene. Phys. Rev. Lett. **109**, 265505 (2012)
8. H. Hiura, H. Miyazaki, K. Tsukagoshi, Determination of the number of graphene layers: discrete distribution of the secondary electron intensity stemming from individual graphene layers. Appl. Phys. Express **3**, 095101 (2010)
9. J. Cazaux, Calculated dependence of few-layer graphene on secondary electron emissions from SiC. Appl. Phys. Lett. **98**, 013109 (2011)
10. H. Hibino et al., Dependence of electronic properties of epitaxial few-layer graphene on the number of layers investigated by photoelectron emission microscopy. Phys. Rev. B **79**, 125437 (2009)
11. D. Ziegler, et al., Variations in the work function of doped single- and few-layer graphene assessed by Kelvin probe force microscopy and density functional theory. Phys. Rev. B **83** (2011)
12. H. Guo, J. Gao, N. Ishida, M. Xu, D. Fujita, Characterization of two-dimensional hexagonal boron nitride using scanning electron and scanning helium ion microscopy. Appl. Phys. Lett. **104**, 031607 (2014)
13. Y.B. Zhou, R. O'Connell, P. Maguire, H.Z. Zhang, High throughput secondary electron imaging of organic residues on a graphene surface. Sci. Rep. **4**, 7032 (2014)
14. M.M. Marshall, J. Yang, A.R. Hall, Direct and transmission milling of suspended silicon nitride membranes with a focused helium ion beam. Scanning **34**, 101–106 (2012)
15. S.A. Boden, Z. Moktadir, D.M. Bagnall, H. Mizuta, H.N. Rutt, Focused helium ion beam milling and deposition. Microelectron. Eng. **88**, 2452–2455 (2011)
16. M. Huth, A. Golzhauser, Focused particle beam-induced processing. Beilstein J. Nanotechnol. **6**, 1883–1885 (2015)
17. Y. Zhou, K.P. Loh, Making patterns on graphene. Adv. Mater. **22**, 3615–3620 (2010)
18. S. Hang, Z. Moktadir, H. Mizuta, Raman study of damage extent in graphene nanostructures carved by high energy helium ion beam. Carbon
19. S. Nakaharai et al., Conduction tuning of graphene based on defect-induced localization. ACS Nano **7**, 5694–5700 (2013)
20. M.C. Lemme et al., Etching of graphene devices with a helium ion beam. ACS Nano **3**, 2674–2676 (2009)
21. G. Nanda, S. Goswami, K. Watanabe, T. Taniguchi, P.F.A. Alkemade, Defect control and n-doping of encapsulated graphene by helium-ion-beam irradiation. Nano Lett. (2015)
22. M. Ghorbani-Asl, A.N. Enyashin, A. Kuc, G. Seifert, T. Heine, Defect-induced conductivity anisotropy in MoS2 monolayers. Phys. Rev. B **88**, 245440 (2013)
23. W. Zhou et al., Intrinsic structural defects in monolayer molybdenum disulfide. Nano Lett. **13**, 2615–2622 (2013)
24. X. Liu et al., Top-down fabrication of sub-nanometre semiconducting nanoribbons derived from molybdenum disulfide sheets. Nat. Commun. **4**, 1776 (2013)
25. J. Lin et al., Flexible metallic nanowires with self-adaptive contacts to semiconducting transition-metal dichalcogenide monolayers. Nat. Nanotechnol. **9**(436–442), 27 (2014)
26. I.S. Kim et al., Influence of stoichiometry on the optical and electrical properties of chemical vapor deposition derived MoS_2. ACS Nano **8**, 10551–10558 (2014)
27. D.S. Fox et al., Nanopatterning and electrical tuning of MoS_2 layers with a subnanometer helium ion beam. Nano Lett. **15**, 5307–5313 (2015)
28. A.R. Botello-Méndez, F. López-Urías, M. Terrones, H. Terrones, Metallic and ferromagnetic edges in molybdenum disulfide nanoribbons. Nanotechnology **20**, 325703 (2009)
29. Y. Li, Z. Zhou, S. Zhang, Z. Chen, MoS_2 nanoribbons: high stability and unusual electronic and magnetic properties. J. Am. Chem. Soc. **130**, 16739–16744 (2008)

Part III
Analysis

Chapter 12
Backscattering Spectrometry in the Helium Ion Microscope: Imaging Elemental Compositions on the nm Scale

Rene Heller, Nico Klingner and Gregor Hlawacek

Abstract The idea of using backscattered helium particles to access chemical information on the surface in a helium ion microscope came up right from the early days of this relatively young imaging technique. From the basic principles of backscattering spectrometry, ion solid interaction and particle detection it became clear rapidly that this attempt will suffer many difficulties in terms of technical realization and physical limitations. This chapter is about describing those difficulties and working out different scenarios of how to apply backscattering spectrometry to the HIM anyways. It will be shown that an actual technical realization exist enabling laterally resolved chemical analysis in a HIM with a resolution down to 55 nm.

12.1 Introduction

As shown in the previous chapters helium ion microscopy offers excellent imaging properties as well as unique capabilities in materials modifications on the nm scale. However, the secondary electrons can generate great image contrast in a topological sense but they rarely deliver information on the surface chemistry. Since the total SE yield depends on the work function of an element one would expect to gain some elemental contrast in an image as well. In deed this is true under certain circumstances.

Figure 12.1 shows an HIM image of a carbon sample covered with rectangular patches of Si, Ni and Au (This particular sample is described in detail in Sect. 12.5.3). The brightness (the number of SEs) significantly differs within the particular element patches and thus delivers an elemental contrast. Nevertheless, it is not possible to make use of this contrast in terms of element identification because of two reasons.

R. Heller (✉) · N. Klingner · G. Hlawacek
Helmholtz-Zentrum Dresden-Rossendorf,
Bautzner Landstr. 400, 01328 Dresden, Germany
e-mail: r.heller@hzdr.de

N. Klingner
e-mail: n.klingner@hzdr.de

G. Hlawacek
e-mail: g.hlawacek@hzdr.de

© Springer International Publishing Switzerland 2016

G. Hlawacek and A. Gölzhäuser (eds.), *Helium Ion Microscopy*,
NanoScience and Technology, DOI 10.1007/978-3-319-41990-9_12

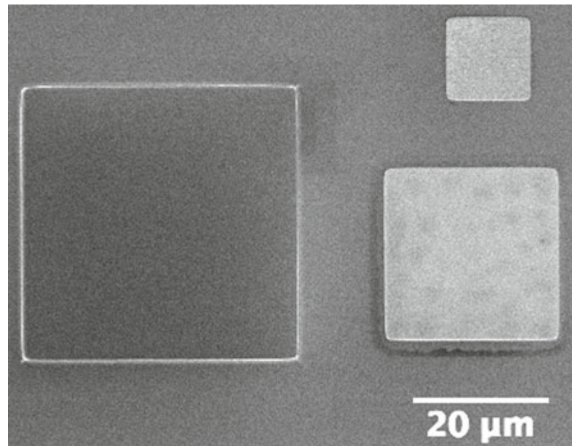

Fig. 12.1 HIM image of a carbon sample covered with rectangular patches of Si, Ni and Au. The variance of brightness between the substrate and the particular patches reveals differences in the SE yield for different elements

On the one hand the number of secondary electrons cannot be expressed as an analytical function of the atomic number Z. The SE yield depends on the electronic stopping which itself shows an oscillating behavior with increasing Z. It thus happens that the SE yield of two different elements may become equal making them indistinguishable in an HIM image [1]. On the other hand the SE yield of compounds (of two or more elements) is not necessarily a linear superposition of the SE yields from the particular constituents. Even if this was true, it would be impossible to recover the elemental composition from measuring the total SE yield of a compound with two or more elements.

Since the early days of Helium ion microscopy the idea came up to make use of the backscattered He ions in order to gain elemental information in a similar way as in Rutherford Backscattering Spectrometry (RBS). Since the primary ion energies in a HIM ($E \leq 40$ keV) are by far lower then those applied in classical RBS (typical 1−3 MeV) several technical difficulties arise. Those are mainly attributed to the fact that most particle detection concepts of classical RBS are not suitable to be applied for keV ion in a HIM. Further, the small beam focus and field of view (nm^2 to μm^2) used in a HIM lead to physical limitation in terms of achievable lateral resolution and sensitivity in RBS mode. Integration of RBS into a HIM presents thus a very challenging task in a technical and in a physical sense.

The present chapter is dedicated to the attempt of applying backscattering spectrometry in a HIM. In the beginning (Sect. 12.2) a brief summary on the basic principles of RBS is given followed by the particular challenges and limitations in bringing RBS into a HIM (Sect. 12.3). In Sect. 12.4 possible concepts for the practical realization are presented and compared to each other. The most promising approach—Time-of-Flight backscattering spectrometry—is described in detail in Sect. 12.5 including the presentation of an actual implementation and results from a current development by the authors [2].

12.2 Principles of Rutherford Backscattering Spectrometry

Rutherford backscattering spectrometry represents one of the most commonly used ion beam analysis techniques for chemical and structural investigations of surfaces and sub-surface regions. RBS is based on the elastic (back)scattering of light ions (H, He, Be) in the Coulomb potential of a target nuclei. Typical primary ion energies vary between 500 keV to some few MeV. The measurement of the backscattered ions energy distribution reveals the classical RBS spectrum containing information on the involved collision partner's masses as well as their distribution in depth (depth profiling). Despite this definition, backscattering with non-Rutherford cross sections and/or forward scattering spectrometry are often also referred as RBS, although they just have in common that the scattered incident particles are analyzed. The observation of the backscattered particles is most suitable for the analysis of heavy elements (see RBS cross sections below). The corresponding ion beam analysis technique of investigating the recoil atoms energy spectra is called elastic recoil detection (ERD) which is commonly used for the analysis of light elements.

Using standard solid state particle detectors, RBS typical delivers depth resolutions in the order of ≈10 nm in the surface proximity. However, modern high resolution magnetic spectrometers allow for sub-nm surface depth resolution [3, 4]. The sensitivity in RBS measurements depends on the particular mass of the element of interest (see RBS cross sections below) and evaluates down to some ppm for heavy elements. The typical analysis depths in RBS is in the order of some μm depending on the primary ion energy.

Although first scattering experiments with alpha particles scattering on a Au foil go back to E. Rutherford in 1909, the idea of applying backscattering spectrometry as an elemental analysis technique was firstly described in literature 1957 by Rubin et al. [5].

Figure 12.2 illustrates the elastic scattering of a charged particle (mass M_1 and energy E_1) in the Coulomb potential of an atomic core initially at rest ($M_2, E_2 = 0$). The scattering process is characterized by a momentum transfer from the projectile to the target which leads to a change in the direction of movement and in the energy of both collision partners. By applying conservation of energy and momentum classical mechanics reveals the relation between the scattering angle Θ and the energy transfer to

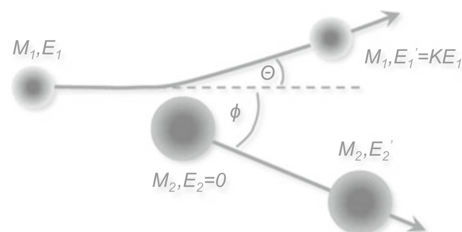

Fig. 12.2 Scattering kinematics of a charged particle of mass M_1 and energy E_1 in the Coulomb potential of a second charged particle of mass M_2 being at rest ($E_2 = 0$)

$$E_1' = \frac{M_1^2}{(M_1 + M_2)^2} \left\{ \cos\Theta \pm \sqrt{\left(\frac{M_2}{M_1}\right)^2 - \sin^2\Theta} \right\}^2 E_1 \equiv KE_1. \tag{12.1}$$

K is referred as the *kinematic factor*. The plus sign in (12.1) is valid for $M_1 < M_2$ whereas in the case of $M_1 \geq M_2$ both solutions of (12.1) become allowed. In the latter case the scattering angle can not exceed a maximum value of

$$\Theta_{\max} = \arcsin\left(\frac{M_2}{M_1}\right). \tag{12.2}$$

From (12.1) the finite energy resolution of a particle detector ΔE can be directly converted into a maximum mass resolution ΔM_2 according to

$$\Delta E = E_1 \frac{\mathrm{dK}}{\mathrm{d}M_2} \Delta M_2. \tag{12.3}$$

Equation (12.3) reveals that the achievable mass resolution in an RBS measurement is determined not only by the detectors energy resolution but also by the slope of the kinematic factor $\frac{\mathrm{dK}}{\mathrm{d}M_2}$.

The K-factor for different projectiles as a function of the target mass M_2 according to (12.1) is plotted in Fig. 12.3. For protons K shows a pronounced slope ($\frac{\mathrm{dK}}{\mathrm{d}M_2}$) at low target masses but rapidly saturates for heavy target masses yielding in a poor mass resolution. Contrary, carbon projectiles reveal a moderate $\frac{\mathrm{dK}}{\mathrm{d}M_2}$ over the whole range of target masses. However, the energy resolution of a solid state detector (and according to (12.3) thus also the mass resolution) drops rapidly with increasing projectile mass. Helium ions reveal a good trade-off and are thus most commonly used in RBS.

The cross section for Rutherford backscattering in cgs units is given by

$$\sigma_{\mathrm{R}} = \left(\frac{\mathrm{Z_1 Z_2} e^2}{4E}\right)^2 \frac{4\left[\sqrt{M_2^2 - M_1^2 \sin^2\Theta} + M_2 \cos\Theta\right]^2}{M_2 \sin^4\Theta \sqrt{M_2^2 - M_1^2 \sin^2\Theta}} \tag{12.4}$$

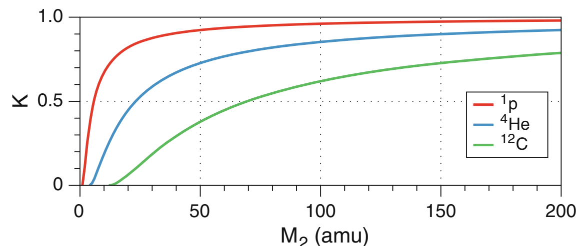

Fig. 12.3 Kinematic factor for protons, helium and carbon ions as a function of the collision partners mass M_2 and for a given scattering angle $\Theta = 170°$

or more handy for practical purposes by

$$\sigma_\mathrm{R}\left[\mathrm{mb/sr}\right] = 5.18374\times10^6\left(\frac{\mathrm{Z}_1\mathrm{Z}_2}{E[\mathrm{keV}]}\right)^2\frac{\left[\sqrt{M_2^2-M_1^2\sin^2\Theta}+M_2\cos\Theta\right]^2}{M_2\sin^4\Theta\sqrt{M_2^2-M_1^2\sin^2\Theta}} \tag{12.5}$$

were E is the primary ion energy and Z_1, Z_2 are representing the ions and targets atomic number, respectively. A detailed derivation of (12.4) can be found elsewhere [6]. Noticeable are the $\frac{1}{E^2}$ dependency on the ions energy and the scaling with the square of the atomic numbers of both projectile and target.

By developing (12.4) into a Taylor series of $\frac{M_1}{M_2}$ and neglecting terms of second and higher orders one obtains a simplified expression being only valid for $M_1 \ll M_2$ which is fulfilled in most RBS experiments

$$\sigma_\mathrm{R} = \left(\frac{\mathrm{Z}_1\mathrm{Z}_2e^2}{4E}\right)^2\frac{1}{\sin^4\left(\frac{\Theta}{2}\right)}. \tag{12.6}$$

In this form it becomes evident that small angle scattering is much more likely to occur ($\sigma \propto \sin^{-4}\left(\frac{\Theta}{2}\right)$) than large angle (back) scattering. However, even if (12.6) points out that RBS at lager scattering angles may not be preferable in terms of efficiency, from a kinematic point of view (see (12.1) and (12.3)) large scattering angles reveal a way better mass resolution.

When ions penetrate into a solid they are losing energy due to electronic and nuclear interactions with target atoms. Thus the primary particle becomes decelerated and the cross section for being backscattered in higher depths increases. The energy of a particle with primary energy E_0 after a certain penetration depth d in a solid is given by

$$E(d) = E_0 - \int_0^d \frac{\mathrm{d}E}{\mathrm{d}x}(E(x))\,\mathrm{d}x. \tag{12.7}$$

$\frac{\mathrm{d}E}{\mathrm{d}x}(E(x)) \equiv S(E)$ is the stopping power and represents the energy loss per path length for a given ion energy. There have been many investigations on the evaluation of $S(E)$ for a given target material, ion species and ion velocity, within the last century. Describing them here would go beyond the scope of this book. Further information on this topic can be found elsewhere [7]. For the particular interest in backscattering spectrometry within this section it is sufficient to know that $S(E)$ can be gained from tabulated values, determined analytically from semi-empirical formulas [7] or obtained by using the program package SRIM [8].

The accuracy of calculated values for $S(E)$ is usually better than 5% for light incident particles (H, He) and $\leq$10% for heavier projectiles (for MeV ion energies). In [10–12] more detailed discussions on the accuracy of tabulated and calculated stopping power values are given.

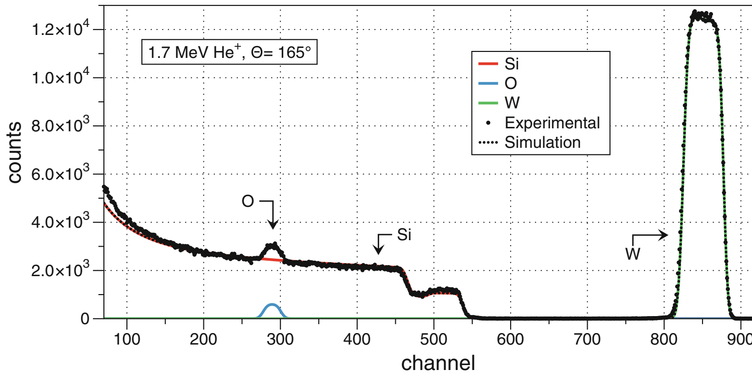

Fig. 12.4 RBS spectrum of He ions backscattered from WSi_2 on SiO_2 on Si. Scattering angle $\Theta = 165°, E = 1700\,\text{keV}$. *Colored lines* and *dotted black line* represent simulation results using SIMNRA code [9]

With (12.7) and formula (12.4) it is possible to evaluate the total number of particles being backscattered towards a detector from a certain element of concentration c in a particular depth d. By dividing the sample virtually into thin slaps, one thus can predict the content of each channel in an RBS spectrum.

Figure 12.4 shows a typical RBS spectrum of a WSi_2 layer on top of a SiO_2 layer on Si. The spectrum was acquired using 1.7 MeV He ions backscattering into a detector at $\Theta = 165°$. The contributions of the single atom species are marked in the figure. The width of the elemental signals reveals the thickness of the layer they belong to and the signal height corresponds to the particular elements concentration. The fit in the figure and the particular contributions from each element were obtained using the SIMNRA code [9].

Further information on the interpretation of RBS spectra and a more detailed description of the basic principles of RBS and related experimental setups can be found in text books e.g. [6, 13].

12.3 Challenges in Performing Rutherford Backscattering Spectrometry in the Helium Ion Microscope

When RBS is applied to low energy projectiles with energies of some 10 keV, as typically used in a HIM, the principles of the backscattering process as described in Sect. 12.2 hold promise in general. However in this energies regime several additional effects have to be taken into consideration being discussed in this section.

12.3.1 Screening Effects and Cross Sections

The cross section for Rutherford scattering as given in (12.4) is deviated by assuming a pure Coulomb interaction potential between the projectile and the target nuclei. To justify this assumption the incident particles velocity has to be high enough to penetrate well inside the target atoms electron orbitals. In this case the scattering is exclusively caused by the interaction of two positively charged nuclei of atomic number Z_1 and Z_2. However, at low projectile velocities the primary ion is not completely penetrating through the electron shells of the target atom and the innermost electrons partially screen the charge of the target nucleus.

For a pure Coulomb interaction potential the distance of closest possible approach d during scattering can be deviated by equating the primary ions kinetic energy to the potential energy at d yielding in

$$d = \frac{Z_1 Z_2 e^2}{E}. \tag{12.8}$$

Using this relation one can estimate the energy where screening effects have to be taken into consideration. Therefor one has to assume that for a pure Coulomb interaction the distance of closest approach has to be smaller than the K shell radius which is given by a_0/Z_2 ($a_0 = 0.053\,\text{nm}$ [Bohr radius]). With (12.8) the lower limit for the primary particles energy evaluates to

$$E = \frac{Z_1 Z_2^2 e^2}{a_0}. \tag{12.9}$$

For primary He ions scattering from silicon ($Z_2 = 14$) this value corresponds to $\approx$10 keV and for scattering from tungsten ($Z_2 = 74$) to $\approx$ 298 keV, respectively. However, (12.10) reveals just the limit for scattering in a completely unscreened Coulomb potential. Actual deviations from Rutherford cross sections will already occur at higher energies since some fraction of the ions trajectory is always located in a partially screened region. Nevertheless at higher energies this fraction becomes rapidly negligible since the major momentum transfer takes place close to the target nucleus.

In RBS analysis screening can be taken into consideration in a first order by applying a screening correction to the unscreened cross sections [14] leading to the *screened Rutherford cross section*

$$\sigma_{\text{sc}} = \text{F}(Z_1, Z_2, E_{\text{CM}})\sigma_{\text{R}}(\Theta). \tag{12.10}$$

E_{CM} represents the energy of the ion in the center of mass (CM) system. For $\theta > 90°$ the correction factor proposed by L'Ecuyer et al. [14] is commonly used:

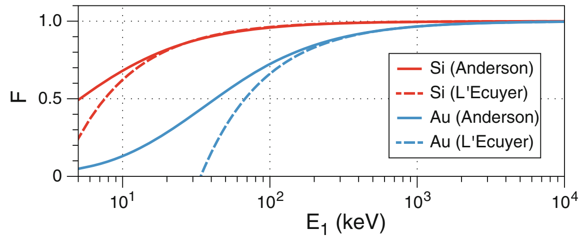

Fig. 12.5 Screening function for He impinging on Si and Au (*red and blue*) according to models by Anderson (*solid lines*) and L'Ecuyer (*dashed lines*) for a scattering angle of $\Theta = 170°$

$$F_{\mathrm{L'Ecuyer}} = 1 - \frac{0.049 Z_1 Z_2^{4/3}}{E_{\mathrm{CM}}}. \tag{12.11}$$

Equation (12.11) represents a first order correction and neglects the influence of the scattering angle Θ. A more precise modeling of the screening factor, taking into account the dependence on Θ, was proposed by Andersen et al. [15]:

$$F_{\mathrm{Andersen}} = \frac{\left(1 + \frac{1}{2}\frac{V_1}{E_{\mathrm{CM}}}\right)^2}{\left\{1 + \frac{V_1}{E_{\mathrm{CM}}} + \left[\frac{V_1}{2E_{\mathrm{CM}} \sin \Theta_{\mathrm{CM}}/2}\right]^2\right\}^2} \tag{12.12}$$

where Θ_{CM} represents the scattering angle in the CM system and expression V_1 is given by

$$V_1[\mathrm{keV}] = 0.04873 Z_1 Z_2 \sqrt{Z_1^{2/3} + Z_2^{2/3}}. \tag{12.13}$$

It reveals more accurate results especially in the low scattering angle regime. The screening function according to both models is plotted exemplarily in Fig. 12.5 for He projectiles backscattering from Si and Au, respectively. It immediately becomes evident that for MeV ions screening can be neglected whereas for energies typically used in the HIM (10–30 keV) screening seriously has to be taken into consideration when RBS spectra are analyzed quantitatively.

12.3.2 Dual, Plural and Multiple Scattering

The evaluation of measured RBS spectra is typically done via comparison to simulation results. In an iterative way the spectrum of a virtual sample of a certain layer structure and a certain elemental composition of each layer in the stack[1] is simulated and the result is subsequently compared to the measured spectrum. The target model is refined until simulation and measured spectra fit each other.

[1]The sum of information on number of layers, layer thicknesses and the particular elemental composition of each layer is referred as *target model*.

Such an approach requires a fast simulation algorithm. Modern analytical simulation codes as RUMP [16], SIMNRA [9], WINDF [17] deliver quiet accurate simulation results for a given target model in very short simulation times (typically some ms). However, they all have in common that for the analytical calculation of the spectrum one single collision per ion is assumed, i.e. a primary particle penetrates the target and travels along a straight trajectory until it is backscattered in a certain depth and leaves the sample towards the detector again on a straight trajectory.

Although this assumption may be justified for MeV projectiles (since the cross section for backscattering are rather low ($\sigma \propto 1/E^2$)), the low energy end of an RBS spectrum may have a measurable contribution of backscattered particles that result from dual or plural scattering. The term *Plural Scattering* (PS) is commonly used when more then one *large angle* scattering events are involved.

In contrast, a quiet similar mechanism is always contributing to an RBS spectrum: *Multiple Scattering* (MS). It accounts for the fact that the path of the incoming and the outgoing ion is not exactly a straight line but a zigzag trajectory caused by numerous small angle scattering events taking place. From (12.6) it is evident that low angle scattering cross sections are rather high in comparison to large angle scattering. Although the contribution to a change of the ions momentum in a small angle scattering event is supposed to be small, it may lead to an angular spread, which finally transfers into an energy spread in the recorded spectra. Figure 12.6 schematically illustrates the trajectories of the ion in dual, plural and multiple scattering. A review and extended information on multiple scattering can be found in [18, 19] and in a more theoretical approach also in [20, 21]. Dual and plural scatting are well summarized and discussed in more detail in [22–26].

Multiple scattering is taken into consideration by almost all of the above mentioned simulation codes. Dual scattering is partially taken into account in SIMNRA and WINDF. However, plural scattering can not be simulated so far. This represents no major drawback in classical MeV RBS (since the cross sections for large angle scattering are rather small, making dual or plural scattering unlikely to occur) but it becomes an issue when ion energies are getting low as in the HIM. Evaluating the

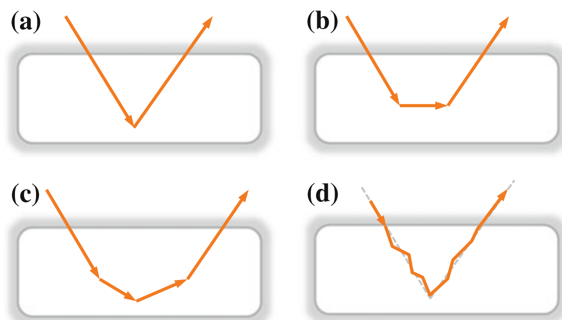

Fig. 12.6 Ion trajectories in single scattering (**a**), dual scattering (**b**), plural scattering (**c**), and multiple scattering (**d**). Incident angle as well as scattering angle are equal in all cases while the ions energy when leaving the sample varies (see description in text)

cross sections for backscattering ($\Theta = 170°$) according to (12.5) and (12.12) yields to $\sigma_R = 2.5 \times 10^2$ mb/sr for 2 MeV and $\sigma_R = 2 \times 10^6$ mb/sr for 20 keV He ions impinging on Si.

Since its contribution is small in the MeV range, multiple scattering as well as dual scattering are determined in analytical approximations and applied as correction to the basic fit evaluated for pure single scattering. However, if energies become low MS/PS causes significant contribution to the spectrum and this approach fails to deliver proper simulation results.

The number of scattering events for the scattering of 30 keV and 2 MeV He ions on Fe derived from a binary collisions simulation using the SRIM code [8] is shown in Fig. 12.7. It illustrates the contribution of single, dual and plural scattering to the total backscattering yield in which a *scattering event* is defined as a collision with an energy transfer of $\Delta E > 1\%$ (a) and $\Delta E > 0.1\%$ (b), respectively. Independent on the choice of the energy transfer threshold both figures show clearly, that almost all ions in the MeV case are undergoing single scattering exclusively whereas in the low energy regime plural scattering is even more likely to occur.

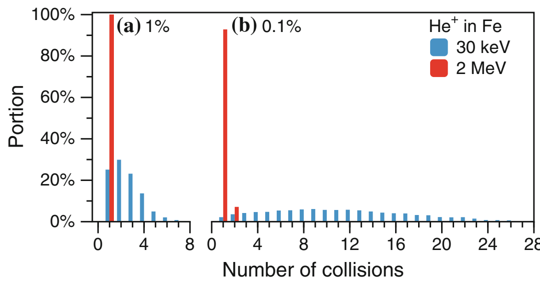

Fig. 12.7 Statistics of the number of scattering events contributing to backscattering of 30 keV (*blue*) and 2 MeV (*red*) He ions from Fe. A collision is registered as *scattering event* if the energy transfer during the collision exceeds 1% (**a**) and 0.1% (**b**) of the ions initial energy

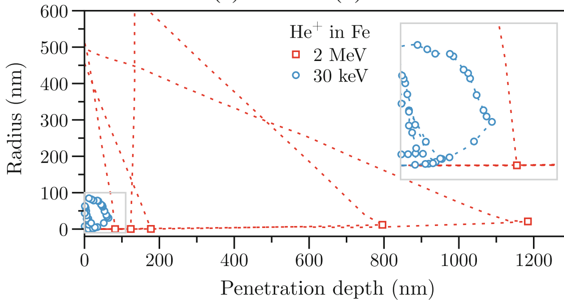

Fig. 12.8 Trajectories (*dotted lines*) and collision events (*squares and circles*) of He ions scattering in Fe as simulated by SRIM for primary ion energies of 30 keV and 2 MeV, respectively. As described in the text for MeV ions backscattering is based on a single large angle collision event. For keV ions plural scattering is dominating the backscattering process. Only collision events with an energy transfer of $\Delta E \geq 1\%$ are indicated as *squares/circles* in the figure

In Fig. 12.8 some selected trajectories[2] of the simulations from Fig. 12.7 are plotted together with the locations of the scattering events. Again it becomes evident that the assumption of a straight in- and out-path and a single scattering event is well justified at MeV energies whereas low energy scattering is dominated by heavy plural scattering.

It thus seems clear that for the quantification of backscattering spectra at keV energies analytical simulation code is not suitable. In contrast binary collision Monte-Carlo simulations (BCMC) allow the precise simulation of each individual ion trajectory. From those one can reconstruct the expected RBS spectrum without the need for any analytical approximations. However simulating the full trajectory of each ion requires a rather high amount of calculation time. Although the cross sections for BS become large at low energies it still requires the simulation of 10^6-10^8 ions to collect a reasonable statistics in the simulated BS spectrum. Some BCMC codes like CORTEO [27] or TRBS [28] have been optimized for the simulation of backscattering spectra and are able to perform a complete spectrum simulation on a time scale of minutes. However, the iterative comparison between simulated and measured spectra is much less convenient and way more time consuming than in MeV Rutherford backscattering spectrometry. The high amount of plural scattering in low energy backscattering additionally leads to a very pronounced low energy tailing in the spectra making it partially very difficult to identify light elements embedded in a heavy matrix.

12.3.3 Charge Fraction

Independent on the scattering process, keV ions rapidly become neutralized when penetrating into a solid surface [29]. Thus only ions scattered at the topmost surface atoms remain charged. In MeV RBS this effect must not be taken into consideration since solid state detectors, as being commonly used, are sensitive to both: ions and neutrals as well. However, in Low Energy Ion Scattering Spectrometry (LEIS) where charged particle detectors are used (most commonly electrostatic analyzers) this effect drastically enhances the surface sensitivity. A typical LEIS spectrum just comprises single distinct peaks arising from the backscattering on the different atom species at the first atomic surface layer.[3] LEIS is thus supposed to be one of the most surface sensitive analysis techniques using ion beams. However, due to a lack of a completely quantitative understanding of the particular charge exchange processes a precise prediction of the ion yields in LEIS is barely available, making the comparison to elemental standards necessary (despite different groups are continuously investigating these processes in ongoing research [31–36]).

[2]For the actual simulation shown in Fig. 12.7 in total 1×10^6 ion trajectories were evaluated. Plotting all of them into Fig. 12.8 would not allow to identify single trajectories.

[3]Despite the surface peaks, LEIS spectra also contain a background that is caused by backscattered neutrals being re-ionized during scattering or on their way back towards the surface (see also [30]).

Since the typical ion energies used in LEIS (1−10 keV) are close to the ones available in a Helium ion microscope (15−35 keV) one could assume making the same benefits in terms of surface sensitivity. However, in LEIS typically a board primary ion beam (on the mm scale) is utilized, while applying backscattering spectrometry to the HIM aims to make use of the high lateral resolution the device offers—meaning probing on the nm scale. As Sect. 12.3.4 will reveal, sample damage in terms of sputtering is representing a major issue in that case, making it unaffordable to observe backscattered charged particles exclusively. This becomes more evident when having a look to some particular values of ion-to-neutral ratios (charge fractions). For energies below 10 keV the charge fraction rapidly drops below 1% for scattering from depths as shallow as 1 nm [30, 37–39]. Even at energies above 30 keV the charge fraction sticks at values well below 10% [40].

The fact that the charge fraction varies with the primary ions energy and depends on the actual elemental composition of the surface, further emphasis the need for a particle detection sensitive to ions *and* neutrals when it comes to an implementation of backscattering spectrometry in a HIM.

12.3.4 Sputtering

As it was described in Sect. 12.3.2 an impinging ion may undergo numerous small angle scattering events when it penetrates into a solid. Although the energy transfer to the target atoms is rather small in such collisions, in some cases it may be sufficient to allow the atom to be to displaced from its original site and to generate a recoil cascade by itself. When such a cascade terminates at the surface, atoms may leave the sample as neutrals or as positive or negative ions. This effect is commonly known as sputtering. The average number of target atoms sputtered during the impact of one single ion is referred as the sputter yield.

Sputtering is a rather complex process and its full description would go beyond the scope of this book. There is no analytical formula predicting the sputter yield for a given sample model. It is a complex function of the masses of the target atom and the incident ion, the kinetic energy of the latter one, the angle of incidence, as well as the chemical composition of the sample and its crystallographic orientation. However, binary collision Monte-Carlo simulations as SRIM [8] or TRYDYN [41] deliver quite accurate sputter yields compared to values determined in measurements.

Sputtering leads to a continuous removal of atoms from the topmost surface layer during ion bombardment which has to be seriously taken into consideration in backscattering spectrometry. This applies for BS in general, but especially becomes an issue when BS is going to be applied in a HIM.

The total number of particles backscattered from a layer with an areal density A_D, which are contributing to an RBS spectrum is given by

$$\mathrm{N}_{\mathrm{det}} = \sigma_R \Omega \mathrm{Q} A_D \tag{12.14}$$

where Ω represents the solid angle of the detector, Q the number of incident particles and σ_R the Rutherford cross section. The number of particles being removed from the layer due to sputtering during the same RBS measurement can be written as.

$$N_{sp} = Y\frac{Q}{F} \tag{12.15}$$

with Y being the sputter yield (sputtered particles per incident ion) and F the area covered by the analyzing beam. To make sure the RBS spectrum is acquired before the layer is completely removed by sputtering, the condition

$$N_{sp} < A_D \tag{12.16}$$

must be fulfilled, which can be converted into a lower limit for Q by using (12.14) leading to

$$Q < \sqrt{\frac{N_{det}F}{2Y\sigma_R\Omega}}. \tag{12.17}$$

Substitution of Q according to (12.15) finally results in an upper limit for A_D according to

$$A_D > \sqrt{\frac{N_{det}Y}{2F\sigma_R\Omega}}. \tag{12.18}$$

Note that by claiming for (12.16) the layer areal density is continuously shrinking down to zero during the measurement which has to be taken into consideration by applying a factor of 2 to the left side of (12.14).[4]

Applying (12.18) to 2 MeV He ions backscattering under an angle of $\Theta = 170°$ from a thin layer of Fe, evaluates to $A_D = 2 \times 10^{14}$ atoms/cm^2. Assuming a mass density of $\rho = 7.9$ g/cm^3 and the number of Fe atoms per mono layer (ML) as 1.85×10^{15} the result converts into 0.1 ML or 0.02 nm, respectively. For this evaluation a sputter yield of $Y_{He}(2\,\text{MeV}) = 0.002$[5] and a beam spot of 1 mm×1 mm were chosen. The solid angle was set to $\Omega = 3 \times 10^{-3}$ sr and the cross section was evaluated using (12.5) and (12.12). Thus realistic conditions of a typical MeV RBS setup are considered. N_{det} was arbitrary chosen to be 1000 revealing reasonable statistics.

A value of $N_{det} = 1000$ may appear a way to high assuming that in MeV RBS the contribution of a thin surface layer corresponds to a very narrow peak in the spectrum. However, for keV ion backscattering the peak becomes rapidly broadened and

[4]The factor of 2 assumes a constant sputter yield and thus a constant layer removal rate, independent on the actual areal density of the layer.

[5]The sputter yield was extracted from TRIM simulations [8] evaluating a minimum of 1×10^6 incident ions.

thus N_{det} is spread over a many channels yielding in a rather poor channel contend and thus bad statistics. Thus the relatively high choice of N_{det} is justified by just being comparable with the following results.

Performing the same calculation for 30 keV He ions under the experimental conditions for backscattering spectrometry in a HIM as they will be described in Sect. 12.5 ($\Theta = 126°$, $\Omega = 10.8 \times 10^{-3}$ sr, $Y_{He}(30\,\text{keV}) = 0.033$) (see footnote 5) and claiming that the the ion beam is scanned homogeneously over an area of 100 nm × 100 nm, the resulting minimum layer thickness becomes $A_D = 6 \times 10^{16}$ atoms/cm^2 corresponding to 32 ML or 7 nm. When using Ne with a much higher sputter yield ($Y_{Ne}(30\,\text{keV}) = 2.1$) (see footnote 5) the result is getting even worse ($A_D = 2.6 \times 10^{17}$ atoms/cm$^2 \mathrel{\hat{=}} 140$ ML $\mathrel{\hat{=}} 30$ nm).

From those numbers it becomes clear that due to the increased sputter yields and the much smaller probing area, keV backscattering spectrometry on the nm scale preformed in a HIM can never reach the sensitivity of classical MeV RBS on a broad scale. To emphasize that point one can adapt the upper equations to determine the minimum beam spot size that is necessary to detect a certain concentration c of an element in a compound layer for a given layer thickness A_D. Therefore (12.14) transforms into

$$N_{det} = \sigma_R \Omega Q A_D c. \tag{12.19}$$

Equations (12.15) and (12.16) remain un-touched. Putting all three together reveals

$$F > \frac{Y N_{det}}{2\sigma_R \Omega A_D^2 c}. \tag{12.20}$$

Assuming a circular beam shape with diameter d (12.22) becomes

$$d > \sqrt{\frac{2 Y N_{det}}{\pi \sigma_R \Omega A_D^2 c}}. \tag{12.21}$$

The only assumption that has been made to derive this result is that the sputter yield of a compound containing element A with concentration c is the same as the one of the pure element A and independent on the actual value of c. This assumption holds true only for compounds containing elements of similar mass. However, for getting a rough estimation it may be justified.

Evaluating (12.21) for 2 MeV and 30 keV He and Ne ions impinging on a compound layer $Fe_c X_{1-c}$ with a thickness of 5 and 20 nm, reveals a minimum beam diameter, as plotted in Fig. 12.9. All other parameters are chosen as in the examples above.

Instead of regarding a minimum necessary beam diameter it is equivalent to state that a structure (a particle or a feature) of a certain height must exceed a particular lateral dimension in order to analyze its elemental composition by means of backscattering spectrometry. As an example, Fig. (12.9) reveals that a nano particle of 20 nm height containing 10% Fe has to be bigger than 125 nm if the Fe content

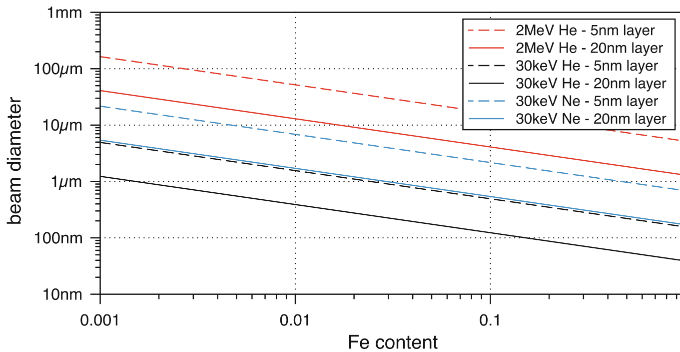

Fig. 12.9 Minimum beam diameter for 2 MeV He (red), 30 keV He (*black*) and 30 keV Ne (*blue*) ions necessary to detect a certain fraction c of Fe in a compound layer Fe_cX_{1-c} of 5 nm (*dashed lines*) and 20 nm (*solid lines*) thickness, respectively. X represents any element with a mass similar to Fe. Using a beam spot smaller than this threshold would lead to a complete removal of the layer due to sputtering just before a certain amount of counts is collected in the spectrum, necessary to identify the Fe concentration

should be determined in a HIM using 30 keV He ions. Remarkably, in classical MeV RBS the limit on the beam size is even higher (≈5μm) than in the keV case. This is mainly attributed to the much lower backscattering cross sections ($\sigma_R \propto 1/E^2$), although the sputter yields are way lower.

From the above estimates it becomes evident that sputtering represents the mayor physical limitation of performing backscattering spectrometry in a HIM. It defines a lower limit for the size of observable objects (≈ some 10 nm, depending on the actual element concentration) independent on the focal size (<1 nm) of the primary beam.

12.4 Experimental Approaches

Apart from the physical constrains in performing backscattering spectrometry in the keV energy range as presented in the previous section, its actual technical implementation reveals additional issues and limitations. The most challenging part thereby may be represented in finding a suitable concept for the determination of the backscattered particles energy. In this section a brief overview on different possible detection concepts is given with emphasis on the applicability for BS spectrometry in a HIM.

12.4.1 Solid State Detectors

Solid state detectors (SSD) are the most commonly used particle detectors in classical RBS. It thus may be plausible to consider their use also for keV ion energies. A SSD in principle represents a reverse biased diode where the depletion area is brought close to the surface being accessible for the incoming particles to be detected. When a particle penetrates the depletion layer it produces a certain number N of electron-hole pairs due to electronic interaction with the solid. N is proportional to the incident particles energy and since the diode is reverse biased the electron-hole pairs are separated from each other generating a small current pulse. Amplification of this signal finally yields in a voltage pulse with a pulse height corresponding to the incoming particles energy.

Although the depletion layer of an SSD is located close to the surface it will be always covered by the p-doped part of the diode which is usually referred as the *dead layer*. Electron-hole pairs generated in this region are not contributing to the charge peak which finally leads to an uncertainty in the peak height. A second source of uncertainty arises from the fact that not the total energy of the incoming particle is consumed by electron-hole pair formation. Some fraction is going into nuclear collisions between the incoming particle and the atoms in the detector (nuclear stopping). Both effects lead to a finite detector resolution which depends on the primary particle energy as well as on the thickness of the dead layer. The latter one is typically in the order of >50 nm. It should be mentioned that additional to these both effects contributions from electronic noise in the amplification electronics lead to a further degradation of the detectors energy resolution.

For 2 MeV He particles SSD typically deliver resolutions of $\Delta E_{\text{det}} \geq 10\,\text{keV}$ corresponding to a relative energy resolution of $\frac{\Delta E}{E} = 5 \times 10^{-3}$. However, for keV particles the fraction of nuclear stopping to the total energy loss raises, yielding in much higher values. Figure 12.10 shows the achievable energy resolution of a solid

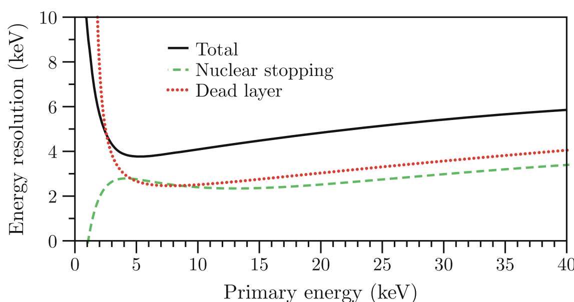

Fig. 12.10 Achievable energy resolution of a *solid* state detector for He particles (*solid line*) as a function of the primary particles energy. Contributions from nuclear stopping and straggling in the dead layer (15 nm) are shown as *dotted* and *dashed lines*. The results are obtained from binary collision approximation Monte Carlo simulations using SRIM code [8]. Contributions from electronic noise are neglected

state detector in the keV energy range assuming only contributions from nuclear stopping and dead layer energy straggling.[6] It reveals slightly better absolute values as low as 5 keV for 30 keV He particles corresponding to a rather poor relative energy resolution of $\frac{\Delta E}{E} = 1.7 \times 10^{-1}$.

According to (12.3) this value transfers into a mass resolution of $\Delta M_2 \approx 10$ amu that is not acceptable in BS spectrometry for practical purposes. However, although it turns out that SSD may not be that suitable for performing BS at keV energies in general, they have been used in the very first experiments carried out by Sijbrandij et al. that demonstrated the general feasibility of backscattering spectrometry in a helium ion microscope [42, 43].

12.4.2 Electrostatic Analyzers

Electrostatic analyzers (ESA) are a commonly used tool to determine the energy of keV ions. Their working principle is rather simple: Particles of an energy E_{pass} enter the electrical field of two opposite electrodes through an entrance aperture and are bended along a certain trajectory towards an exit aperture of a fixed size. Particles with other energies than E_{pass} will follow other trajectories and miss the exit aperture. Thus ESA are also considered as energy filters. There exist many different forms of ESA which basically differ by the geometrical implementation of the electrodes ranging from simple plates to cylindrical, spherical and toroidal shaped ones. However, they work all on the same principle and it would go beyond the scope of this book to describe them all in detail.

ESA are known to deliver excellent energy resolutions of down to $\frac{\Delta E}{E} = 1 \times 10^{-3}$ [44, 45] which is a fixed parameter of the device, not depending on the particles energy as it is in a SSD. Furthermore, in contrast to a solid state detector an ESA suffers no degradation of energy resolution for higher projectile masses.

Nevertheless, energy spectra can only be recorded sequentially in an ESA by stepwise changing its electrical field. During the measurement of one particular energy in a scan all particles arriving with different energies will be discarded. Depending on the actual resolution of the scan the overall efficiency of an ESA thus may drop to values far below 1%. Furthermore, the working principle of an ESA allows the detection of charged particles only. From Sect. 12.3.3 it it is known that only a small fraction of the backscattered particle leave the surface as ions. Most of them are neutrals and thus not detectable with an electrostatic analyzer.

Assuming an ion fraction of ≈1% for 30 keV He ions scattering from a Si surface and an ESA spectrum acquired in 100 steps, reveals an overall efficiency of just 1×10^{-5}. With regard to sample damage in terms of sputtering (see Sect. 12.3.4) it becomes unambiguous that ESA may not represent a suitable detection concept for

[6] In the simulation a dead layer of 15 nm thickness was assumed.

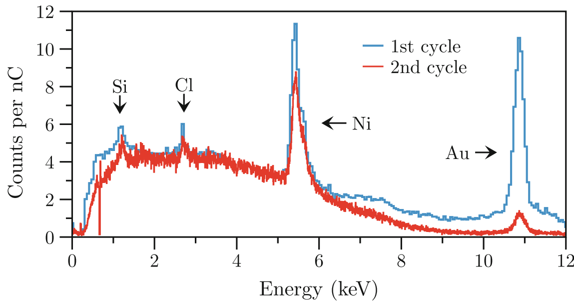

Fig. 12.11 Backscattering spectra of a carbon sample covered with patches of Si, Ni and Au as measured by an electrostatic analyzer in two subsequent cycles. 15 keV Ne ions were used and the applied fluence was 3×10^{17} ions in each cycle. Since the Au patches have a thickness of just 85 nm they are almost completely removed due to sputtering during the first measurement cycle

applying BS spectrometry in a HIM. Since its energy resolution increases for smaller entrance and exit apertures the available solid angle is rather small leading to an even worse overall performance.

Figure 12.11 shows exemplarily spectra of 15 keV Ne ions backscattering from the carbon test sample shown in Fig. 12.1 as recorded with a cylindrical ESA. A broad beam of $\approx 1\,\text{mm}^2$ was used covering all Si, Ni and Au patches on the C sample[7] equally. The spectra were recorded on one and the same surface site and in each cycle a total fluence of 3×10^{17} ions was applied. Both spectra reveal the surface peaks of Au, Ni and Si as well as the corresponding low energy tails from re-ionization in the bulk (see also Sect. 12.3.3). However, it is clearly visible that the Au contribution to the spectrum is nearly vanished in the second measurement cycle which is caused by the massive removal of Au due to sputtering. Since the Au patches have a height of just 85 nm it can be assumed that they are completely removed during the first scan and the signal in the second run arises from Au re-deposited during the sputtering. Of course also the Ni and Si patches are underlaying erosion due to sputtering but since they are much thicker (110 and 300 nm) this effect is less pronounced in the spectra.

Although due to the poor efficiency ESA figure out to be not suitable for being used in BS analysis on the nm-scale in a HIM, they are commonly used in LEIS investigations using a broad beam. Here the fact that in this energy regime the sensitivity to the topmost surface layers is drastically enhanced outbalances the destructive character of the measurement.

[7] See also Sect. 12.5.3 for details on this sample.

12.4.3 Time of Flight Spectrometry

A further technique being considered to determine the backscattered particles energy is the evaluation their time of flight (ToF) from the sample to a detector. Since the mass of the BS projectiles is fixed, the relation between energy and flight time is biunique.

Measuring a time requires a start and a stop signal. The latter one can be accessed rather easily by registering the BS particles hit on a detector. Since the energy is evaluated by the time of flight there is no need for the detector to be energy dispersive. It just has to detect the particles arrival. For this purpose micro channel plates (MCP) are commonly used. They offer two major advantages that are particularly valuable for an implementation in keV BS in the HIM: they can be manufactured in quite large dimensions (up to a couple of cm) revealing large achievable solid angles and they are sensitive to both: neutrals and charged particles as well. This makes them great performing in terms of efficiency.

The acquisition of a proper start signal for ToF measurement represents a more delicate task. The start time must not exactly coincidence with the actual BS event at the sample. Any signal that has a fixed offset time prior or subsequent to the scattering may be suitable. The tree most commonly used techniques are:

- using a start foil,
- using secondary electrons or
- pulsing the primary ion beam.

Figure 12.12 illustrates the first approach. On its way towards the stop detector (5) the backscattered particle has to pass a thin (typically ≤5 nm) carbon foil (3).

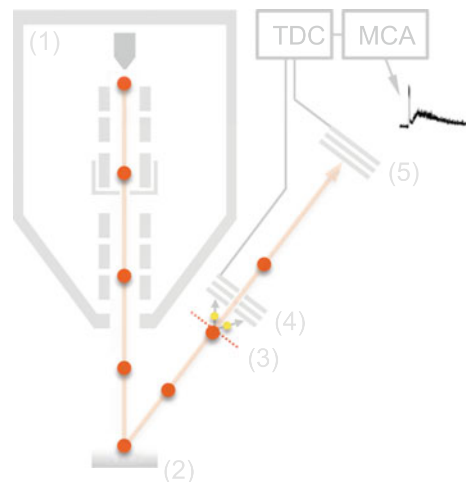

Fig. 12.12 Time-of-Flight setup using a thin carbon foil for start signal generation, comprising the HIM column (*1*), the sample (*2*), a thin carbon foil (*3*), a start detector (*4*) and a stop detector (*5*)

During the interaction with that foil secondary electrons are emitted which may be registered in an additional start MCP (4). The flight path equals the distance between start foil and stop detector.

The over-all efficiency in this approach is limited by three points. (1) As the energies of backscattered particle become low the probability for scattering inside the carbon foil increases and a major fraction of the particles may no longer reach the stop detector. (2) Carbon foils of thicknesses $\leq$5 nm are not available as free-standing sheets covering a size bigger than a few mm. Thus the usable solid angle of the system becomes rather low. Although larger foils are available on supporting grids which could increase the solid angle, the finite transmission of the supporting grid (typically $50-75\%$) is partially compensating this gain. (3) The secondary electron yield in a thin carbon foil becomes relatively low as soon as the projectile energy drops to the keV range. Hence not more than 2–3 electrons are expected to be emitted per passing projectile [46]. In combination with a reduced detection efficiency of the start MCP for low energy electrons it becomes probable that not every passing particle is generating a start signal. Thus it may appear that a stop signal is generated without a proper start signal being present, which finally creates background noise in the ToF spectrum. Weller et al. performed calculations on the overall efficiency of a ToF setup using carbon foils for start signal generation and came up with values in the order of $\approx$1% [46].

Secondary electrons emitted during the impact of the projectile on the target may be also represent a usable start signal for ToF measurements. Actual attempts of applying this approach to the HIM have been reported by Kobayashi et al. [47] and by Xu et al. [48]. A schematic representation of this technique is given in Fig. 12.13. Beside the stop detector (4) only a suitable electron detector (3) is needed which is typically realized by a channeltron detector or another MCP. Even the HIMs existing SE detector (used for imaging in SE mode) could be utilized.

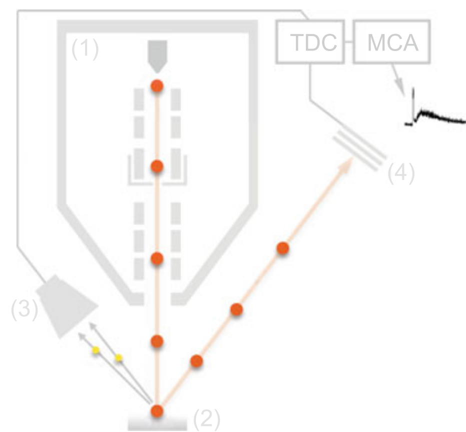

Fig. 12.13 Time-of-Flight setup using secondary electrons for start signal generation, comprising the HIM column (*1*), the sample (*2*), an electron detector (*3*) and a stop detector (*4*)

Despite of its simpleness this technique reveals one mayor drawback: The number of emitted secondary electrons (depending on the target element 1–5 per ion) is considerably higher than the number of backscattered particles (backscattering probability $\approx$0.001 per ion). Thus much more start than stop events are generated leading to a rather poor signal to noise ratio of up to 2:1 in the resulting ToF spectra. Moreover, since the maximum total count rate of the start detector is physically limited to $10^5-10^6\,\mathrm{s}^{-1}$ the primary ion current has to be drastically reduced leading to considerably high measurement times (up to several hours per spectrum) which additionally contribute to a bad signal-to-noise ratio. However, for the identification of (heavy) elements on the sample surface this approach seems suitable especially since its implementation requires just a small amount of equipment.

A third method of deriving a proper start signal for ToF measurements is represented by pulsing the primary ion beam. In this approach no start detector is necessary at all since the start signal is predetermined by an external pulse generator that causes the primary beam to periodically pass towards the sample only for a very short time period t_{pulse}. If the period (repetition rate) of pulsing is larger than the flight time of the backscattered particles towards the stop detector $t_{\mathrm{f\,light}}$ and if

$$t_{\mathrm{pulse}} \ll t_{\mathrm{f\,light}} \tag{12.22}$$

this method may deliver a promising way of performing ToF BS spectrometry in the HIM since there are no mayor drawbacks present as they are in the approaches shown before. Therefore this method is discussed in a more detailed manner in the following section separately.

12.5 Pulsed Primary Beam ToF-BS

Based on experimental work carried out by the authors of this chapter [2] the following section describes the technical implementation of a time-of-flight setup enabling laterally resolved backscattering spectrometry in a HIM. The results will reveal the general feasibility of performing elemental analysis on the nm scale but also point out its limitations.

12.5.1 Experimental Setup

For pulsing the primary helium/neon beam an existing pair of blanking plates within the HIM column is used (2 in Fig. 12.14). In standard secondary electron imaging mode (SE mode) these plates are used to blank the beam into a Faraday cup for determination of the beam current and for stopping the beam on hitting the sample after image acquisition. For this purpose the requirements on the blanking speed are not very high (typical time scale in the order of $50-100\,\mathrm{ns}$).

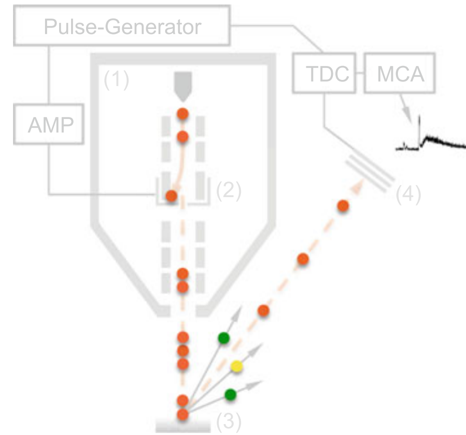

Fig. 12.14 Pulsed beam Time-of-Flight setup comprising the HIM column (*1*), the blanking plates (*2*), the sample (*3*) and the stop detector (*4*)

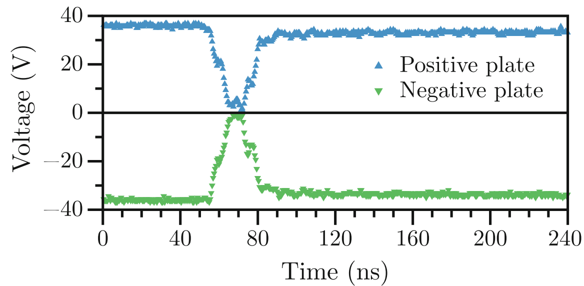

Fig. 12.15 Voltage pulses on both blanking plates in pulsed beam operation as measured by an oscilloscope

For the purpose of generating short beam pulses with ns length, as needed for ToF measurements, the original pulse generating electronics is replaced by a much faster one. This electronics is capable of generating voltage pulses of a few ns on the blanking plates. The pulse generation electronic itself is triggered by a standard TTL signal which is supplied from a pulse generator with typical repetition rates of up to 350 kHz. This TTL signal is also used as the start signal for ToF measurement. Fig. 12.15 shows an oscillograph of the voltage pulses on both blanking plates. Both of them show an equal rise and fall time of ≈8 ns.

The stop signal for the ToF measurement is generated by the detection of the backscattered particles on a micro channel plate (MCP) (4 in Fig. 12.14). The MCP is mounted on one of the HIMs available spare ports under a backscattering angle of 126° at a distance of 358 mm which defines the flight path length for the ToF measurement. With a MCP diameter of 42 mm the effective solid angle for particle detection evaluates to 10.8 msr.

To improve the time resolution in the ToF measurement (and thus the energy resolution in the recorded BS spectra) a longer flight path, related to a longer flight time would be desirable. However, increasing the flight path simultaneously decreases the solid angle which leads to a drastically ($\propto 1/r^2$) reduced solid angle. However,

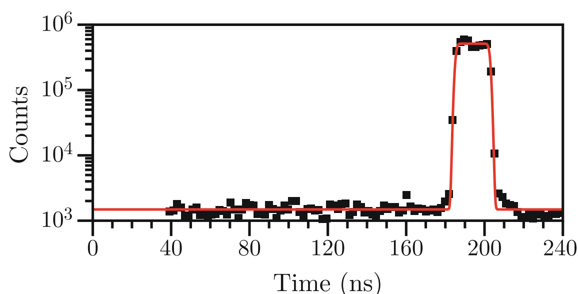

Fig. 12.16 Time of flight spectrum of the primary ion beam as measured by a channeltron detector mounted directly below the ion column of the HIM. *Red curve* presents a box fit with a FWHM of 17 ns

since the HIM offers plenty of spare ports a second MCP stop detector is mounted in a distance of 1023 mm (with a corresponding solid angle of 1.3 msr).

The signal of the stop detector is amplified by a pre-amplifier and discriminated by a constant fraction discriminator. The resulting square wave pulse represents the stop signal of the ToF measurement. Start and stop signal are digitalized in a time-to-digital converter (TDC) which also contains a multi-channel analyzer (MCA) to generate the final ToF spectrum.

Figure 12.16 shows a ToF spectrum measured with the setup described above but with using a simple channeltron detector mounted at the position of the sample as stop detector. Thus the stop signal is generated directly by the primary ions instead of the backscattered particles and the time structure of the beam on the sample can be revealed. Ideally the time structure should be a rectangular pulse with a width as small as possible. For the measurement 30 keV He ions were used and the time spectrum was recorded over 2×10^7 beam pulses. A double error function (very close to a rectangular pulse) with a width of 17 ns and a rise/fall time of ≈1.7 ns reproduces the measured spectrum fairly well.

12.5.2 Backscattering Spectra and Simulation

The ToF spectrum of a 2 nm HfO layer on top of Si substrate measured by using 30 keV He ions is shown in Fig. 12.17. During the measurement the beam was continuously scanned over an area of ≈200 μm^2. The spectrum reveals a sharp peak around 320 ns corresponding to the Hf signal. From around 380 ns the signal of the Si bulk arises. Two smaller peaks at ≈2 and ≈50 ns correspond to the signals from Photons and Electrons emitted during the primary ion impacts at the surface.

Since the HfO layer is very thin, the width of the Hf peak in the ToF spectrum can be assumed to represent the time resolution of the setup. The measured value of $\Delta t = 17.3$ ns corresponds to a relative time resolution of $\Delta t/t \leq 5.4\%$ and thus fairly reproduces the ratio of blanker length (≈20 mm) and flight path length (358 mm). For the second stop detector in a distance of 1023 mm (see text above) the ToF spectrum of the same sample (not shown here) reveals a relative time resolution of $\Delta t/t \leq 2.7\%$.

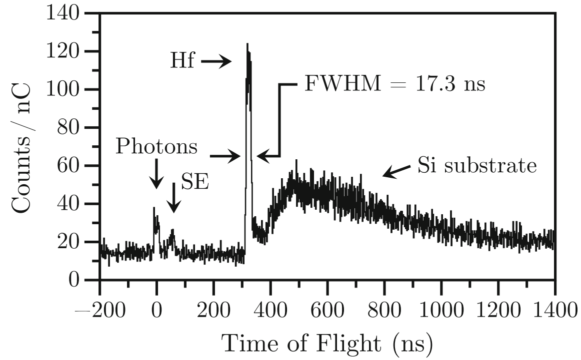

Fig. 12.17 ToF-BS spectrum of 30 keV He on 2 nm HfO_2 layer on *top* of Si. Flight path = 358 mm

A conversion of the time resolution into an energy resolution is not trivial in this energy range since the high amount of multiple scattering and the energy-straggling (see also Sect. 12.3) lead to a rapid decrease of the energy resolution with increasing penetration depth. An exact value can there for just derived directly at the surface and evaluates to $\Delta E \approx 3.2\,\text{keV}$ ($\Delta E \approx 1.6\,\text{keV}$ for the second stop detector with longer flight path).

Taking multiple scattering into consideration (see Sect. 12.3.2) only Monte Carlo simulation codes based on binary collision models like SRIM [8], CORTEO [27], TRBS [28] or TRYDYN [41] can be utilized to simulate backscattering spectra in the keV energy range. However, the comparison of measured ToF-spectra with simulation results makes it necessary to convert the time of flight into an energy spectra or vise versa. Therefore is indispensable to know the exact origin of the ToF spectra time axis.

The time delivered from the TDC refers to the span between start and stop signal. However the actual flight time of the BS particles starts when the BS particle leaves the sample surface. The difference (offset) is obviously determined by electronic delay (actually the generation of the voltage pulses on both blanking plates) as well as the flight time of the ions from the blanking plates to the sample. For the latter case the exact amount can be easily calculated since it just depends on the ions mass, its energy and the distance between blanking plates and the sample. All theses quantities are known.

Contrary, the contribution of electronic delay can not be determined trivially. To determine the offset of the time axis anyway one can make use of photons emitted in the ion-sample interaction. Those are registered by the stop detector as well and contribute to a small peak in the ToF spectra (see also Fig. 12.17). Although the production yield for photons is rather low for primary ion energies $E \leq 30\,\text{keV}$ it is sufficient to collect a few of them in typical measurement time of some minutes. The life time of electronic excitations that radiatively decay is know to be in the order of less than 10 ns [49, 50] and the flight time of a photon from the sample to the stop detector calculates to 2 ns. Thus the offset in the time axis of the ToF spectra can be evaluated fairly accurate.

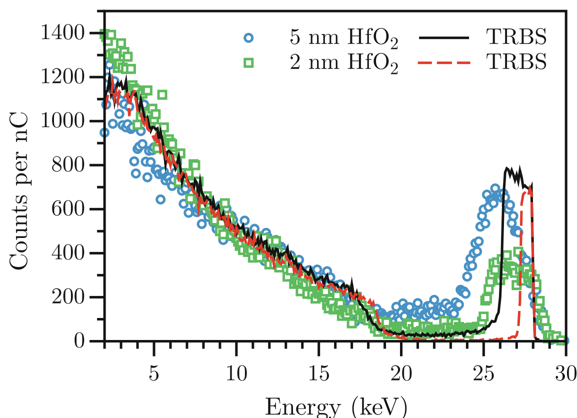

Fig. 12.18 ToF-BS spectrum of 30 keV He on 2 nm HfO_2 layer on *top* of Si converted into energy space. Flight path = 358 mm. Histograms show measured *spectra lines* indicate results from TRBS simulations

The ToF spectra of two different HfO layers are shown in Fig. 12.18. The time axis in the spectra have been converted into energy. The thickness of the HfO layer is 2 nm and 5 nm, respectively. The substrate is Si in both cases. Dots and squares represent measured spectra while the full and dashed lines are results from Monte Carlo simulations using TRBS. The data in Fig. 12.18 clearly show that the energy resolution of the ToF setup within the HIM is sufficient to distinguish between layers of different thicknesses on the nm (depth) scale. The simulations are based on the evaluation of 5×10^7 primary ions. Simulated particles backscattered towards the detector are recorded and sorted into a pulse height spectrum according to their energy. The resulting spectrum was scaled to the solid angle and plotted as counts per nC.

To make the simulated spectra comparable to the measured ones an adoption of the spectrum hight (scaling) has to be applied. This scaling is necessary since the charge measurement during the measurements is not exact. The current measurement in the HIM is designed to measure DC ion currents. Since for the ToF-BS measurements the beam is pulsed the results of the current measurement show significant deviation from the actual value. Even worse, this effect is influenced by the absolute value of the ion current itself as well as by the pulsing repetition rate. Since the spectra shown in Fig. 12.18 are recorded at different ion currents, the scaling factors that had to be applied to fit their height to the simulation results are different.

In both spectra the area between the Hf peak and the Si bulk signal is showing an non-zero offset that is not predicted by the simulations. Such offset has also been reported in literature for focused ion beam based ToF-BS [51, 52]. However, its origin stays unclear so far. Since in the simulation backscattering energies are not convoluted with any finite detector resolution, peak hight and peak width of the Hf peaks are differing partly significant from the measured data.

12.5.3 Imaging in ToF-BS Mode

To enable lateral resolved element analysis in the HIM by applying ToF-BS it is necessary to scan the ion beam and to correlate each backscattering event to the current beam position. Therefor the HIM scan electronics provides an analog input for external beam control (for both x- and y-deflection of the beam). In ToF-BS imaging the beam control is thus applied from an external scan controller that not only does the beam scanning but also records the flight times (read from the TDC) for each BS particle detected. All recorded backscattering events are stored in a list mode file. Thus during post processing flexible regions of interest (ROI) within the scan field (field of view) can be selected and the corresponding local BS spectra can be extracted. All scan parameters of the external scan controller (scan positions, field of view, dwell time, etc.) are adjusted remotely within a control software running on a PC.

Figure 12.19 shows images of a test sample in standard SE-mode (a) as well as in ToF-BS mode (b). This test sample basically comprises a piece of glassy carbon coated with rectangular patches of Si, Ni and Au. The patches have different dimensions of $40\,\mu m \times 40\,\mu m \times 300\,nm$ (Si), $25\,\mu m \times 25\,\mu m \times 110\,nm$ (Ni) and $12\,\mu m \times 12\,\mu m \times 85\,nm$ (Au), respectively. For the contrast generation in Fig. 12.19 for each pixel only the value of the highest registered BS energy was taken into account. This leads to an enhanced elemental contrast in the image. However, the corresponding list mode file contains the whole energy spectrum for each pixel allowing post analysis with different kind of filtering.

ToF-BS spectra within different surface regions from the ToF-BS image shown in Fig. 12.19b are plotted in Fig. 12.20. The colors of the spectra correspond to the the colors of the rectangles in Fig. 12.19b marking the particular region of interest. The latter ones were placed on the different patches of Si, Ni and Au. One region of

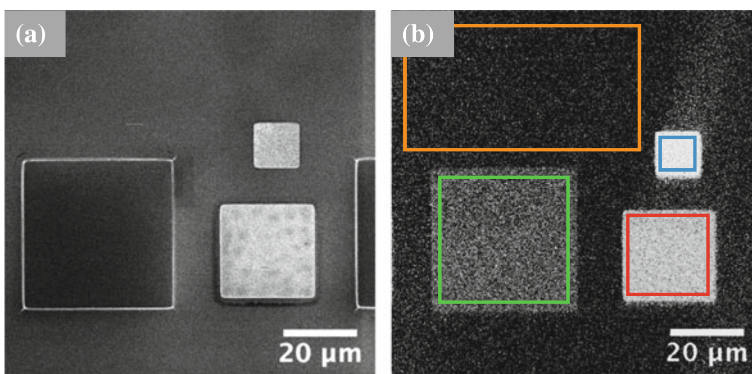

Fig. 12.19 Images of a carbon sample covered with *rectangular* patches of Si, Ni and Au acquired in standard SE mode (**a**) and in ToF-BS mode (**b**). For **b** 30 keV primary He ions have been used in pulse beam mode with 17 ns pulsed width and a repetition rate of 250 kHz

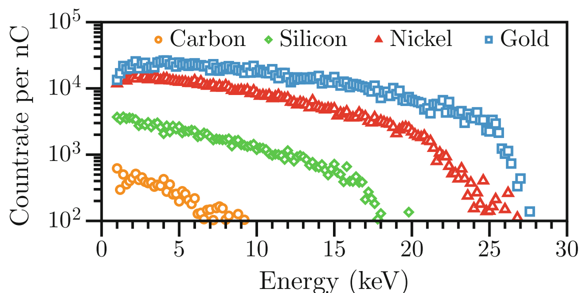

Fig. 12.20 ToF-BS spectra from within different regions of interest in the image shown in Fig. 12.19b. The *color* of spectra correspond to the colors of the rectangles drawn in Fig. 12.19b indicating the particular region of interest

interest was also placed on the Carbon substrate. The energy resolution of the ToF-BS setup is sufficient to distinguish clearly between the different elements. In this way local elemental analysis is introduce to the HIM that was not possible before in classical SE imaging mode.

The lateral resolution for imaging in ToF-BS mode is limited by two disturbing influences: (a) the lateral beam spread due to the pulsing of the primary beam and (b) statistical distributed exit locations of the backscattered He ions after undergoing multiple scattering events below the surface. A primary He ion with an energy of 30 keV needs a flight time of approx. 17 ns to pass through the blanking plates (approx. 20 mm). The ion will pass the blanker in a undisturbed manner if both plates are grounded during this time period. However, for some a part of the incoming ions the blanker will change its state during the ions transition and the ions will be deflected from their aligned trajectories. In the end this leads to a reduced lateral resolution in the order of some nm to several 10 nm depending on the actual blanking time. The contribution of distributed exit locations of the BS He can be estimated from binary collisions to some 10 nm.

An experimental evaluation of the overall lateral resolution in ToF-BS mode is shown in Fig. 12.21. The edge of a Ni patch on the test sample described above is imaged in SE mode without pulsing the primary beam (a) and in pulsed beam ToF-BS mode (b). Figure 12.21c shows averaged line scans across the Ni edge from images (a) and (b). The areas that were used for averaging are indicated as dashed rectangles in (a) and (b) as well as the directions of line profiles (arrows). The blanking direction in these measurements was 52° with respect to the Ni edge. The edge resolution (80%–20°) evaluates to 10.9 nm in SE mode (without pulsing the beam) and 53.7 nm in ToF-RBS mode using beam pulses of 55 ns length.

It has to be emphasized that a variation of the pulse-length has an influence on the lateral resolution, the energy resolution and the signal to noise ratio simultaneously. By adjusting pulse length and the duty cycle one can select between optimum lateral and highest energy resolution. Both have to be adapted according to the particular demands of the actual measurement task.

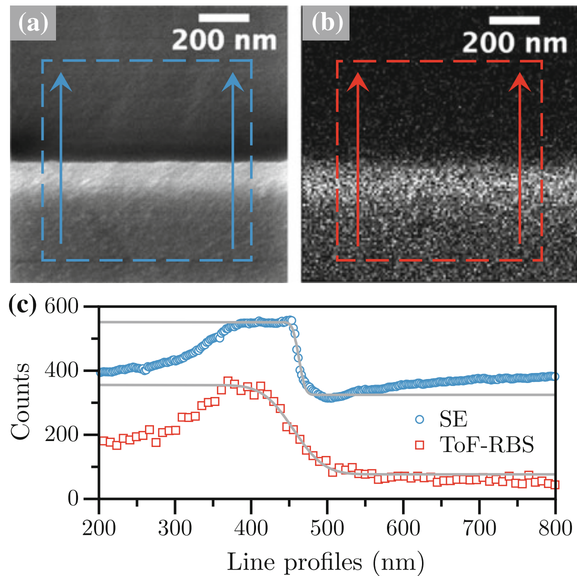

Fig. 12.21 SE image (**a**) and ToF-BS image (**b**) of a Ni patch on the test sample described in the text and derived line profiles of the Ni edge (**c**). Line profiles are measured and averaged across the Ni edge according to the *rectangles plotted* in (**a**) and (**b**) and error functions fitted at the edges. The edge resolutions (80%–20%) was determined to 10.9 nm in SE mode and 53.7 nm in ToF-BS mode using 55 ns beam pulses

12.5.4 Time of Flight Secondary Ion Mass Spectrometry

The concept of beam pulsing to generate the start signal in ToF-BS mode, instantaneously allows for another powerful analysis technique to be applied in the HIM: Time-of-Flight Secondary Ion Mass Spectrometry (ToF-SIMS). However, since ToF-SIMS is discussed separately in Chap. 13 of this book, we just refer to reference [2] at this point.

12.6 Summary

Utilizing backscattered projectiles in a helium ion microscope to gain excess to laterally resolved chemical analysis on the nm scale was figured out to be a challenging task, right at the beginning in the history of helium ion microscopy. Early attempts using a solid state detector revealed the general ability of performing BS spectrometry in the energy regime available in the HIM. However the limited energy resolution and thus the reduced mass separation capabilities of the SSD indicated that more sophisticated detection concepts are required to make this technique suitable for a quantitative elemental analysis on the nm scale.

Different concepts of detecting the BS particles have been discusses in this chapter and it was evaluated that the approach of measuring the particles time of flight seems the most promising attempt. In an experimental study done by the authors it was

demonstrated that by applying pulsed beam ToF backscattering spectrometry, chemical analysis is feasible with a lateral resolution down to 55 nm, being close to the physical limits.

In combination with the outstanding imaging capabilities offered by a helium ion microscope, this technique now allows to gain full information on a sample surface on both topography as well as chemical composition. This technique can easily be adapted to existing devices since it requires only a minimum and affordable amount of additional equipment. Thus a powerful complementary source of information on the sample is introduced that does not influence the excellent imaging capabilities of the device.

Acknowledgments Financial support from the Bundesministerium für Wirtschaft und Energie (BMWi) (Grant 03ET7016) is acknowledged. The authors thank R.Aniol (HZDR) for manufacturing of the mechanical parts for the ToF setup and P. Bauer (JKU Linz) for providing TRBS simulations.

References

1. R. Ramachandra, B. Griffin, D. Joy, Ultramicroscopy **109**(6), 748 (2009). doi:10.1016/j.ultramic.2009.01.013
2. N. Klingner, R. Heller, G. Hlawacek, J. von Borany, J. Notte, J. Huang, S. Facsko, Ultramicroscopy **162**, 91 (2016). doi:10.1016/j.ultramic.2015.12.005
3. M. Vieluf, F. Munnik, C. Neelmeijer, M. Kosmata, S. Teichert, Thin Solid Films **520**(18), 5900 (2012). doi:10.1016/j.tsf.2012.04.086
4. M. Kosmata, F. Munnik, D. Hanf, R. Grötzschel, S. Crocoll, W. Möller, Nucl. Instrum. Methods Phys. Res. Sect. B Beam Interact. Mater. Atoms **337**, 27 (2014). doi:10.1016/j.nimb.2014.07.018
5. S. Rubin, T. Passell, L. Bailey, Anal. Chem. **29**(5), 736 (1957). doi:10.1021/ac60125a001
6. W.K. Chu, J.W. Mayer, M.A. Nicolet, *Backscattering Spectrometry* (Academic Press INC, Boston, 1978)
7. J.F. Ziegler, J. Biersack, U. Littmark, *The Stopping and Range of Ions in Solids*, 3rd edn. (Pergamon Press, New York, 1985)
8. J.F. Ziegler, J.P. Biersack, M.D. Ziegler, *SRIM, the stopping and range of ions in matter* (SRIM Co., Chester, 2008). http://www.worldcat.org/isbn/096542071
9. M. Mayer, in *AIP Conference Proceedings* (AIP, 1999), pp. 541–544. doi:10.1063/1.59188
10. M. Mayer, J. Roth, K. Ertl, Nucl. Instrum. Methods Phys. Res. Sect. B Beam Interact. Mater. Atoms **190**(1–4), 405 (2002). doi:10.1016/S0168-583X(01)01274-5
11. J. Ziegler, Nucl. Instrum. Methods Phys. Res. Sect. B Beam Interact. Mater. Atoms **136–138**, 141 (1998). doi:10.1016/S0168-583X(97)00664-2
12. H. Paul, A. Schinner, Nucl. Instrum. Methods Phys. Res. Sect. B Beam Interact. Mater. Atoms **227**(4), 461 (2005). doi:10.1016/j.nimb.2004.10.007
13. Y. Wang, M. Nastasi (eds.), *Handbook of Modern Ion Beam Analysis*, 2nd edn. (Materials research Society, Warrendale, PA, 2009)
14. J. L'Ecuyer, J.A. Davies, N. Matsunami, Nucl. Instrum. Methods **160**(2), 337 (1979). doi:10.1016/0029-554X(79)90612-8
15. H.H. Andersen, F. Besenbacher, P. Loftager, W. Möller, Phys. Rev. A **21**(6), 1891 (1980). doi:10.1103/PhysRevA.21.1891
16. L.R. Doolittle, Nucl. Instrum. Methods Phys. Res. Sect. B Beam Interact. Mater. Atoms **9**(3), 344 (1985). doi:10.1016/0168-583X(85)90762-1

17. N.P. Barradas, C. Jeynes, R.P. Webb, Appl. Phys. Lett. **71**(2), 291 (1997). doi:10.1063/1.119524
18. E. Szilágyi, F. Pászti, G. Amsel, Nucl. Instrum. Methods Phys. Res. B **100**(1), 103 (1995). doi:10.1016/0168-583X(95)00186-7
19. G. Amsel, G. Battistig, A. L'Hoir, Nucl. Instrum. Methods Phys. Res. Sect. B Beam Interact. Mater. Atoms **201**(2), 325 (2003). doi:10.1016/S0168-583X(02)01740-8
20. P. Sigmund, K.B. Winterbon, Nucl. Instrum. Methods **119**(C), 541 (1974). doi:10.1016/0029-554X(74)90805-2
21. P. Sigmund, K.B. Winterbon, Nucl. Instrum. Methods **126**(C), 317 (1975)
22. A. Weber, H. Mommsen, W. Sarter, A. Weller, Nucl. Instrum. Methods Phys. Res. Sect. B **198**, 527 (1982)
23. A. Weber, H. Mommsen, Nucl. Instrum. Methods Phys. Res. Sect. B **204**, 559 (1983)
24. E. Steinbauer, P. Bauer, J. Biersack, Nucl. Instrum. Methods Phys. Res. Sect. B Beam Interact. Mater. Atoms **45**(1–4), 171 (1990). doi:10.1016/0168-583X(90)90810-H
25. P. Bauer, E. Steinbauer, J. Biersack, Nucl. Instrum. Methods Phys. Res. Sect. B Beam Interact. Mater. Atoms **79**(1–4), 443 (1993). doi:10.1016/0168-583X(93)95383-G
26. W. Eckstein, M. Mayer, Nucl. Instrum. Methods Phys. Res. Sect. B Beam Interact. Mater. Atoms **153**(1–4), 337 (1999). doi:10.1016/S0168-583X(98)01011-8
27. F. Schiettekatte, Nucl. Instrum. Methods Phys. Res. Sect. B **266**(8), 1880 (2008). doi:10.1016/j.nimb.2007.11.075
28. J.P. Biersack, E. Steinbauer, P. Bauer **61**(1), 77 (1991). doi:10.1016/0168-583X(91)95564-T
29. E. Taglauer, W. Englert, W. Heiland, D.P. Jackson, Phys. Rev. Lett. **45**(9), 740 (1980)
30. D. Primetzhofer, M. Spitz, E. Taglauer, P. Bauer, Surf. Sci. **605**(21–22), 1913 (2011). doi:10.1016/j.susc.2011.07.006
31. Y. Bandurin, V. Esaulov, L. Guillemot, R. Monreal, Phys. Rev. Lett. **92**(1), 017601 (2004). doi:10.1103/PhysRevLett.92.017601
32. Y. Bandurin, V.A. Esaulov, L. Guillemot, R.C. Monreal, Phys. Status Solidi (B) Basic Res. **241**(10), 2367 (2004). doi:10.1002/pssb.200404909
33. S. Wethekam, D. Valdés, R.C. Monreal, H. Winter. Phys. Rev. B Condens. Matter Mater. Phys. **78**(7), 1 (2008). doi:10.1103/PhysRevB.78.075423
34. D. Primetzhofer, S.N. Markin, J.I. Juaristi, E. Taglauer, P. Bauer, Phys. Rev. Lett. **100**(21), 1 (2008). doi:10.1103/PhysRevLett.100.213201
35. D. Primetzhofer, S.N. Markin, J.I. Juaristi, E. Taglauer, P. Bauer, Nuclear Instruments and Methods in Physics Research. Section B: Beam Interactions with Materials and Atoms **267**(4), 624 (2009). doi:10.1016/j.nimb.2008.10.050
36. D. Primetzhofer, M. Spitz, S. Markin, E. Taglauer, P. Bauer, Phys. Rev. B **80**(12), 125425 (2009). doi:10.1103/PhysRevB.80.125425
37. T.M. Buck, Y.S. Chen, G.H. Wheatley, W.F.V. der Weg, Surf. Sci. **47**, 244 (1975). http://www.sciencedirect.com/science/article/pii/0029554X76907953
38. M. Draxler, R. Gruber, H.H. Brongersma, P. Bauer, Phys. Rev. Lett. **89**(26), 263201 (2002). doi:10.1103/PhysRevLett.89.263201
39. D. Primetzhofer, S.N. Markin, P. Zeppenfeld, P. Bauer, S. Průša, M. Kolíbal, T. Sikola. Appl. Phys. Lett. **92**(1), 11929 (2008). doi:10.1063/1.2822816
40. T.M. Buck, G.H. Wheatley, L.C. Feldman, Surf. Sci. **35**, 345 (1973). doi:10.1016/0039-6028(73)90224-0
41. W. Möller, W. Eckstein, Nucl. Instrum. Methods Phys. Res. Sect. B **2**(1–3), 814 (1984). doi:10.1016/0168-583X(84)90321-5
42. S. Sijbrandij, B. Thompson, J. Notte, B.W. Ward, N.P. Economou, J. Vac. Sci. Technol. B Microelectron. Nanometer Struct. **26**(6), 2103 (2008). doi:10.1116/1.2993262
43. S. Sijbrandij, J. Notte, L. Scipioni, C. Huynh, C. Sanford, J. Vac. Sci. Technol., B: Microelectron. Nanometer Struct. **28**(1), 73 (2010). doi:10.1116/1.3271254
44. H.R.J. Ter Veen, T. Kim, I.E. Wachs, H.H. Brongersma, Catal. Today **140**(3), 197 (2009). doi:10.1016/j.cattod.2008.10.012

45. H.H. Brongersma, T. Grehl, P.A. van Hal, N.C.W. Kuijpers, S.G.J. Mathijssen, E.R. Schofield, R.A.P. Smith, H.R.J. ter Veen, Vacuum **84**(8), 1005 (2010). doi:10.1016/j.vacuum.2009.11.016
46. R.A. Weller, J.H. Arps, D.D. Pedersen, M.H. Mendenhall, Nucl. Instrum. Methods Phys. Res. Sect. A Accel. Spectrom. Detect. Assoc. Equip. **353**(1994), 579 (1994). doi:10.1016/0168-9002(94)91727-2
47. T. Kobayashi, A. Kamoshida, H. Akiyama, K. Watanabe, T. Ohnishi, K. Takada, T.T. Suzuki, Appl. Phys. Express **7**(10), 106601 (2014). doi:10.7567/APEX.7.106601
48. C. Xu, H.D. Lee, S. Shubeita, G. Liu, Y. Xu, L. Wielunski, J. Bloch, B. Yakshinskiy, E. Garfunkel, T. Gustafsson, L.C. Feldman, in *International Conference on Atomic Collisions in Solids (Conference)*, Debrecen (2014)
49. G. Andersson, H. Morgner, Surf. Sci. **405**(1), 138 (1998). doi:10.1016/S0039-6028(98)00062-4
50. H.D. Hagstrum, *Inelastic Ion-Surface Collisions* (Academic New York, 1976), p. 1. doi:10.1016/B978-0-12-703550-5.50006-6
51. S. Abo, T. Azuma, T. Lohner, F. Wakaya, M. Takai, Nucl. Instrum. Methods Phys. Res. Sect. B **273**, 266 (2012). doi:10.1016/j.nimb.2011.07.091
52. K. Hayashi, H. Takayama, M. Ishikawa, S. Abo, T. Lohner, M. Takai, Nucl. Instrum. Methods Phys. Res. Sect. B **219–220**(1–4), 589 (2004). doi:10.1016/j.nimb.2004.01.125

Chapter 13
SIMS on the Helium Ion Microscope: A Powerful Tool for High-Resolution High-Sensitivity Nano-Analytics

Tom Wirtz, David Dowsett and Patrick Philipp

Abstract Secondary Ion Mass Spectrometry (SIMS) is an extremely powerful technique for analysing surfaces, owing in particular to its excellent sensitivity, high dynamic range, very high mass resolution, and ability to differentiate between isotopes. The combination of He/Ne microscopy and SIMS makes it possible not only to obtain SIMS information limited only by the size of the probe–sample interaction (~10 nm), but also to directly correlate such SIMS images with high-resolution (0.5 nm) secondary electron images of the same zone taken at the same time. This chapter will discuss the feasibility of combining SIMS with Helium Ion Microscopy from a fundamental and instrumental point of view.

13.1 Secondary Ion Mass Spectrometry

13.1.1 Introduction

In Secondary Ion Mass Spectrometry (SIMS), an energetic beam of ions (called primary ions) is used to sputter the sample. The primary ions penetrate the sample and lose all or a part of their energy during collision cascades with the target. Some of these collision cascades will lead to the ejection of one or several target atoms. Amongst the emitted particles, the ions (called secondary ions) are of interest in SIMS. These ions are extracted using an electric field and accelerated into a mass spectrometer, mass filtered, and counted by detectors.

Depending on the primary ion fluence, one distinguishes between static SIMS and dynamic SIMS. In static SIMS, the primary ion fluence is below 10^{13} ions/cm^2.

T. Wirtz (✉) · D. Dowsett · P. Philipp
Advanced Instrumentation for Ion Nano-Analytics, Luxembourg Institute of Science and Technology, 41 rue du Brill, 4422 Belvaux, Luxembourg
e-mail: tom.wirtz@list.lu

D. Dowsett
e-mail: david.dowsett@list.lu

P. Philipp
e-mail: patrick.philipp@list.lu

© Springer International Publishing Switzerland 2016

G. Hlawacek and A. Gölzhäuser (eds.), *Helium Ion Microscopy*,
NanoScience and Technology, DOI 10.1007/978-3-319-41990-9_13

The analysis is therefore limited to the extreme surface, and the fragmentation of target molecules is limited, allowing molecular information to be obtained. In dynamic SIMS, the primary ion fluence is typically much higher (10^{16}–10^{18} ions/cm^2). This results in nearly full fragmentation of molecules, so that only mono-atomic ions or small cluster ions are detected. The high primary ion fluence results in a progressive erosion of the sample surface, such that depth profiling is possible in dynamic SIMS.

There are four main types of SIMS operation modes:

(i) Mass spectra, providing information about the composition of the analysed sample
(ii) Depth profiles, showing the distribution of selected species with respect to depth
(iii) 2D imaging, revealing the 2D spatial distribution over the analysed area
(iv) 3D imaging, providing the distribution of species within the analysed volume

The main strengths of SIMS are its excellent sensitivity (detection limits down to the ppb are possible), its high dynamic range (the detectable concentrations range from matrix elements to trace elements), its good depth resolution (sub-nanometre depth resolution is possible when using low-energy primary ion beams), and its ability to differentiate between isotopes. The main weakness of SIMS is its difficulty in quantifying analyses, which is referred to as the SIMS matrix effect.

13.1.2 Underlying Fundamentals

13.1.2.1 Sputtering Processes

SIMS uses primary ion beams with energies higher than 100 eV. While energies below 1 keV are typically used for depth profiling with high depth resolution, higher beam energies (15–30 keV) are used to finely focus the primary ion beam for imaging with high lateral resolution. The incident primary ion penetrates the sample and loses its energy progressively when colliding with target atoms.

Figure 13.1 illustrates a single impact of Ar on a Si_3N_4 target as simulated using the TRIM code. TRIM is a Monte Carlo code for modelling ion bombardment of an amorphous target using the binary collision approximation (BCA) [1–3]. The impacting ion loses its energy both during collisions with nuclei and as electronic excitation. The ratio of electronic versus nuclear energy loss is dependent on the characteristics of the incident ion (mass and velocity) and of the target (mass of target atoms). The energy transfer to the target atoms can lead to their displacement and the formation of defects. If the energy transfer to a target atom is sufficiently important, it can displace other atoms and hence trigger a collision cascade. Amongst the three categories of collision cascades that one distinguishes (single knock-on regime, linear cascade regime, spike regime), the linear cascade regime is the most relevant for SIMS. Target atoms that are in the vicinity of the sample

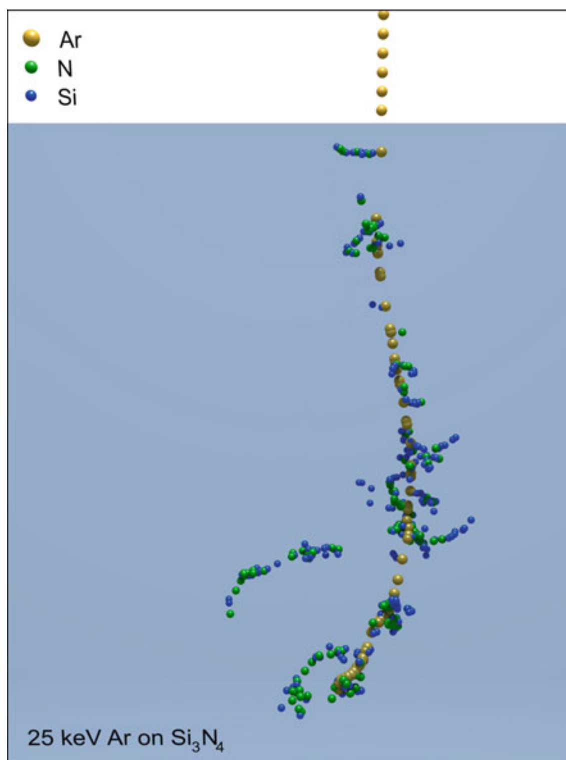

Fig. 13.1 3D view of a collision cascade developing under 25 keV Ar impact on Si_3N_4 at normal incidence. The Ar projectile is shown in *yellow*; displaced Si and N atoms are shown in *blue* and *green*, respectively. The cascade was simulated using TRIM

surface can get enough energy to be ejected during a collision cascade. Such sputtering happens only for atoms that are close to the sample surface: most ejected atoms are initially in one of the two topmost atomic layers. One can therefore conclude that the information depth of SIMS is a priori very shallow.

The energy deposited close to the sample surface is a key parameter in determining sputtering. For very light elements like helium, only a small fraction of the energy is deposited near the surface, thus the resulting sputter yield (defined as the ratio between sputtered particles and incident ions) is low. Considerably higher sputter yields result from the impacts of heavy ions such as Cs or Xe, which are species routinely used in SIMS, as the fraction of energy that is deposited close to the surface is significantly higher. Figure 13.2 shows the evolution with beam energy of the sputter yield obtained at normal incidence for four different primary ion species (He, Ne, Ga, and Cs) impacting on Si. For all ions except He, the sputter yield increases with increasing impact energy. Also note that helium is the only element with a sputter yield well below 1. For Ne, the sputter yield starts to decrease again for energies above 10 keV, as the peak in the energy deposition distribution moves away from the surface with increasing beam energy. The same phenomenon would also occur for the heavier species Ga and Cs, but at higher impact energies than the ones shown in Fig. 13.2. Helium already shows this

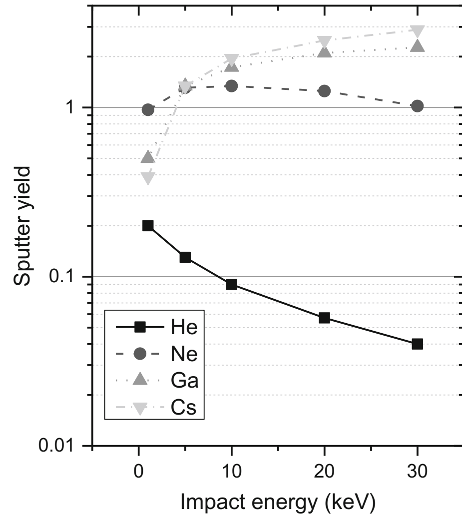

Fig. 13.2 Sputtering yield as a function of impact energy for helium, neon, gallium, and caesium bombardment of silicon at normal incidence. The results were obtained by TRIM. Figure adapted from [4]

behaviour at very low impact energies, resulting in a continuous decrease of the produced sputter yield over the considered energy range.

The angle of incidence of the primary ion beam is another important factor influencing the fraction of energy deposited in the vicinity of the surface, and hence the sputter yield. At a grazing angle of incidence, more energy is deposited close to the sample surface, and the resulting sputter yield will be higher. The sputter yield thus increases with beam angle (defined with respect to the normal to the sample surface), until the primary ions start to be reflected by the surface, whereupon the sputter yield decreases again.

When large primary ion fluences (up to or above 10^{17} ions/cm^2) are used, subsequent collision cascades start to overlap spatially and induce various transport mechanisms. The higher the beam energy, the more important this atomic mixing effect will be. Other relevant parameters determining the extent of atomic mixing are the incidence angle of the primary ion beam, the primary ion species, and the sample composition. Radiation-induced diffusion further contributes to this atomic mixing effect. The effects caused by atomic mixing are illustrated in Fig. 13.3, which shows an example of depth profiling simulated by TRIDYN [5–7]. TRIDYN is based on TRIM, but also allows for the simulation of the system evolution with primary ion fluence giving access to sputtering yields and system composition for transition and steady-state conditions. Due to the BCA approach, only atomic mixing and no diffusion processes are taken into account. The sample consists of silicon with three boron delta layers at depths of 110, 330, and 450 Å (Fig. 13.3a). The depth profiling has been carried out for four different conditions. For 1 keV Cs bombardment, a broadening of the delta layers can be observed, but the three layers are well separated (Fig. 13.3b). For the same impact energy but neon as primary ion, the mixing is increased and the dynamic range of the B signal is reduced (Fig. 13.3c). However, the three layers are still separated. The situation changes for higher impact energies. For 20 keV caesium bombardment, the first boron delta layer is visible but the decay length is significantly increased, reducing the

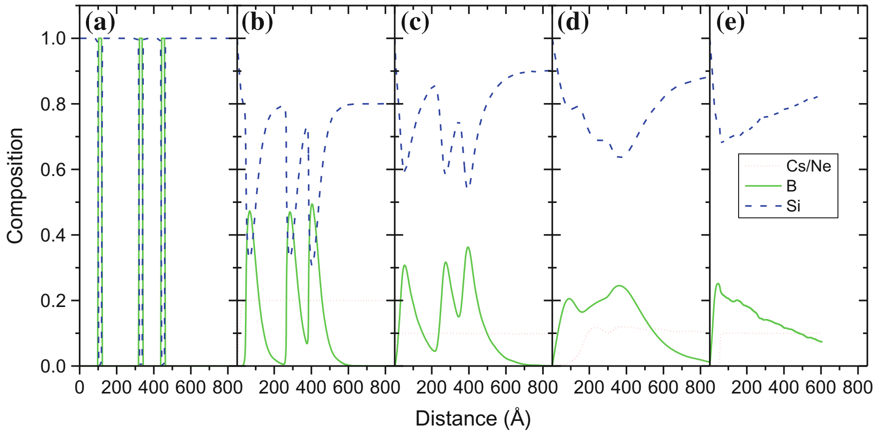

Fig. 13.3 Depth profiling of Si sample containing 3 B delta layers at 110, 330, and 450 Å by TRIDYN. **a** Initial configuration before depth profiling, **b** depth profiling by 1 keV Cs, **c** depth profiling by 1 keV Ne, **d** depth profiling by 20 keV Cs, and **e** depth profiling by 20 keV Ne

separation between the first and the following delta layers (Fig. 13.3d). In addition, the second and third delta layers are no longer separated. The separation between the different delta layers is even less pronounced for the 20 keV neon bombardment. The first boron delta layer is visible, but it is followed by a long and slow decay of the boron intensity (Fig. 13.3e).

13.1.2.2 Ionisation of Sputtered Matter

A study by Lindhard and Scharff [8] regarding the energy transfer from an impacting atom to electronic degrees of freedom showed that emitted particles might be in an excited state when leaving the surface. Additionally, valence electrons might be transferred to or from the surface when the sputtered atom is leaving the surface. While there are a number of models for different classes of materials and impinging ion species and conditions, we will limit our discussion here to two main models explaining the ionisation of sputtered material.

A model based on electron tunnelling is usually used to describe the ionisation processes of atoms sputtered from metallic and semiconductor samples. Electron transfer occurs via an electron tunnelling effect between the atomic level of the sputtered atom and the delocalised state of the valence band of the metal substrate (Fig. 13.4a) [9]. For emission of positive and negative ions, the resulting ionisation probability is given by, respectively:

$$\begin{cases} \beta^{+} = 1,\ if\ \phi > I \\ \beta^{+} = e^{-\left(\frac{I-\phi}{\epsilon_p}\right)},\ if\ \phi < I \end{cases}, \quad \begin{cases} \beta^{-} = 1,\ if\ \phi < A \\ \beta^{-} \propto e^{-\left(\frac{\phi - A}{\epsilon_n}\right)},\ if\ \phi > A \end{cases}$$

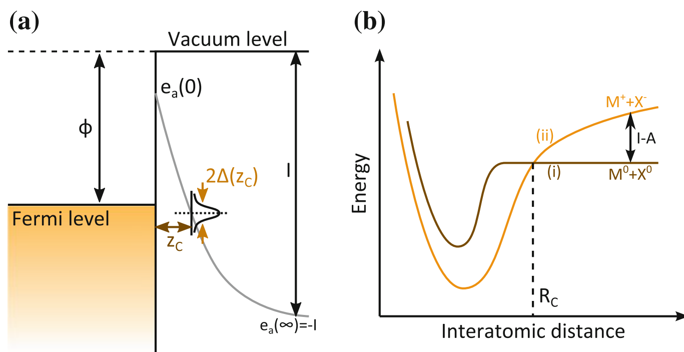

Fig. 13.4 Schematics for ionisation models. **a** Concept of charge exchange illustrated for atom leaving metal surface used for electron tunnelling model, **b** concept of bond breaking model illustrated by potential energy curves for covalent (*i*) and ionic (*ii*) bonding for bond breaking model. Figure adapted from [4]

where I is the ionisation energy of the sputtered atom, A is the electron affinity of the sputtered atom, ϕ is the electron work function of the sample, and ϵ_p and ϵ_n are parameters depending on local properties of the sample [10].

For an explanation of the ionisation probabilities obtained during sputtering processes from oxides, the model developed by Slodzian is widely used [11, 12]. This model is based on the assumption that an ion M^+ leaves the sample during the sputtering process and leaves behind a vacant cation with an electron affinity A. This site will then retain the electron for the duration of the sputtering process ($\sim 10^{-13}$ s). A charge transfer between sample and sputtered ion is possible at a distance R_C above the surface where the curves for ionic potential energy and covalent potential energy are crossing each other (Fig. 13.4b). The probability for such a charge transfer can be deduced from the Landau–Zener formula, which predicts that the ionisation probability rapidly decreases with increasing ionisation energy.

These ionisation models show that the ionisation probability of sputtered atoms strongly depends on the local sample composition. The secondary ion signal detected for a given element A can be written as:

$$I_A = I_p \cdot Y \cdot C_A \cdot \beta_A \cdot \tau$$

where I_p is the primary ion current hitting the analysed area, Y is the sputtering yield, C_A is the concentration of species A, β_A is the ionisation probability of that element, and τ includes the transmission of the mass spectrometer and the detection efficiency [4].

An important parameter for expressing the sensitivity of an analysis is the useful yield (UY), which expresses the ratio between the number of detected ions for a given element A and the number of atoms A that were sputtered from the analysed volume during the analysis:

$$UY = \frac{N_{ions\,detected}}{N_{atoms\,sputtered}}$$

In order to maximise the ionisation probability, and hence the detected secondary ion signal and UY, reactive primary ion species are typically used in SIMS. To enhance the emission of negative secondary ions, electropositive primary ion species (e.g. caesium) are used. Conversely, the use of electronegative primary ion species (e.g. oxygen) favours the emission of positive secondary ions. As described in Sect. 13.1.2.1, the primary ion species are implanted into the sample, and thus load the sample with a given concentration of reactive species, resulting in an advantageous modification of the local chemical composition of the sample in view of enhanced ionisation of emitted atoms and molecules.

Implanting primary ion species is not the only means of changing the local sample composition in order to enhance secondary ion ionisation probabilities. Another solution is the flooding of the sample surface with reactive species during SIMS analysis, i.e. simultaneously with the ion bombardment. The use of reactive gas flooding is of particular importance when sputtering is performed with a non-reactive primary ion beam, e.g. Ga^+, He^+, Ne^+, or Ar^+.

For the enhancement of positive secondary ion ionisation probabilities, oxygen flooding is routinely used [13]. Depending on the element of interest, UY can be increased by several orders of magnitude. Ionisation probabilities of negative secondary ions can be improved by caesium flooding. This method was first used by Bernheim et al. in 1977 [14, 15], and was later improved upon by Wirtz et al. [16, 17]. Studies have shown that Cs flooding can increase UY by up to four orders of magnitude [18, 19].

13.1.2.3 Matrix Effect and Quantification

The strong dependency of the ionisation probability of secondary ions on the local sample composition ("matrix effect") greatly complicates the quantification of the SIMS signal, i.e. the conversion of the secondary ion signal detected for element A to the concentration of the element A in the analysed sample. Several protocols, mostly relying on reference samples, can be used to quantify SIMS data.

One first possibility is calculating the useful yield using a reference sample in order to convert the secondary ion signal into concentration:

$$c_A = \frac{I_A}{UY_A \cdot I_p \cdot Y}$$

where c_A is the concentration of species A, I_A is the secondary ion current of the same species, UY_A its useful yield as defined in Sect. 13.1.2.2, I_p the primary ion current, and Y the sputtering yield.

Instead of calculating the useful yield for the species of interest, it is also possible to use relative sensitivity factors (RSF) [20]. With this method, one calculates the concentration of a trace element X based on the ratio of the secondary ion intensity of this element I_X and the intensity of the matrix signal I_M:

$$c_X = \frac{I_X}{I_M} \cdot RSF_X$$

where RSF_X needs to be determined by analysing a sample of a composition that is known and similar to the sample composition. The benefit of the RSF method is that variations in the primary beam current which change the erosion rate have no influence on the calculated concentration. This RSF protocol only works in the dilute limit for trace elements where it is considered that the ionisation probability does not change with the concentration of the element.

Quantification can also be performed by detecting the so-called MCs^+ secondary ions, where M represents the element of interest. These clusters, which form when sputtering a sample using a Cs^+ primary ion beam or when using caesium flooding, may be detected with a reduced matrix effect [21, 22]. The useful yields for MCs^+ typically lie in the range of 10^{-6} to 10^{-4} [23], which is below the optimal SIMS useful yields that one may achieve by analysing $M^{\pm}$, leading to a poorer detection limit in the MCs^+ mode. For electronegative elements, yields can be improved by detecting MCs_2^+ ions rather than MCs^+ ions [24].

13.1.3 Instrumentation

As a consequence of the secondary ion yield enhancement induced by reactive primary ion species (see Sect. 13.1.2.2), traditional SIMS instruments are typically equipped with a surface ionisation Cs^+ ion source and a plasma source (typically a duoplasmatron or RF plasma source) delivering an $O_2{}^+$ and/or O^- primary ion beam. Modern instruments also often include sources for generating species such as Ga^+, Au^+, and Bi^+, as well as various cluster ions like Ar_n^+, Au_n^+, Bi_n^+, and $C_{60}{}^+$. The latter become relevant when molecular information needs to be obtained from the sample.

Secondary ions are extracted from the sample by applying a voltage difference between the sample and an extraction electrode, and they are subsequently focussed into a mass spectrometer. Depending on the application, three types of mass spectrometers are used in SIMS. Quadrupole mass spectrometers have the lowest mass resolution and transmission, and do not allow parallel detection of several secondary ion signals. Time-of-flight (TOF) mass spectrometers offer an unlimited mass range and are thus used mostly on instruments dedicated to the detection of molecular ions. Such instruments dedicated to gaining molecular information are increasingly equipped with MS/MS capabilities. Mass measurement occurs through measurement of the flight time of the secondary ions between a given origin and the

detector. The flight time is initiated by a pulse of the primary or secondary ion beam. In modern TOF mass spectrometers equipped with electrostatic mirrors for the correction of flight time differences for ions having the same mass but a different energy (arising from the energy distribution of sputtered ions), mass resolutions $\frac{M}{\Delta M}$ of 10,000 are easily obtained. Compared to TOF mass spectrometers, magnetic sector mass spectrometers offer the advantage of continuous analysis, removing the duty cycle induced by beam pulsing, which leads to better overall sensitivities (if the primary ion beam is operated in the DC mode and the secondary ion beam pulsed) or better sensitivities for similar analysis times (if the primary ion beam is pulsed) [4]. However, magnetic sector mass spectrometers have a limited mass range, restricting their application to the analysis of monatomic and small cluster ions. In a double-focussing magnetic sector instrument, achromatic mass filtering (i.e. independent of the initial energy distribution of the secondary ions) is achieved by combining an electrostatic analyser with the magnetic filter. Magnetic sector mass spectrometers can be operated in a scanning mode (in this case, there is typically only one detector, and the magnetic field must be tuned for a selected mass to reach this detector) or in a non-scanning mode. In this latter configuration, parallel mass detection is possible when using the Mattauch–Herzog design, where all masses are focussed in a focal plane containing several detectors. Common designs present mass resolution ranging from several hundred up to several tens of thousands [25].

13.1.4 SIMS Applications

The most basic application of SIMS is the acquisition of mass spectra, which provide information about the surface composition of the analysed sample. If the mass spectra are performed in the static SIMS mode or using cluster primary ion beams, they also reveal molecular information.

Depth profiling is a very common SIMS analysis mode. In this case, selected secondary ion signals are plotted with respect to time. The time scale is then converted to a depth scale using the erosion rate, which can either be calibrated prior to analysis using reference samples, or deduced from crater measurements by profilometry performed on the post-analysis crater. In situ Scanning Probe Microscopy (SPM) analysis has recently become possible, allowing measurement of the crater during analysis, eliminating errors from differences in sputter rates in multilayer/complex samples [26]. Depth profiles are typically used to reveal variations in elemental composition as a function of depth. The interface structure and the diffusion between layered structures can be studied with sub-nanometre depth resolution using low impact energies. SIMS depth profiling has been used extensively for over 35 years by the semiconductor industry [27, 28], in display technology, optoelectronic applications, and memory applications [29], and more recently for

solar cells [30]. In this sector, the quantification of dopants is a key point, which is only possible when using standard reference samples, as discussed previously.

For SIMS imaging, two different modes can be used, the microscope mode and the microprobe mode [4]. In the microprobe mode, the sample surface is sputtered by a finely focussed beam which is raster-scanned over the analysed area. The counting of the secondary ions is synchronised with the raster-scanning of the primary beam in order to reconstruct the mass-filtered secondary ion image pixel by pixel. In this configuration, the lateral resolution does not depend on the capabilities of the mass spectrometer, but only on the focussing of the primary ion beam. In the microscope mode, an unfocussed beam with homogeneous beam density is used to irradiate the sample. The field of view is determined by optical gating. The mass spectrometer acts as a stigmatic microscope and transfers the image of the sample surface on the detector surface. Position sensitive detectors such as a micro-channel plate are used as detector. In the microscope mode, the lateral resolution is determined by the quality of the optics of the mass spectrometer, the image magnification, and the pixel density on the detector. The microscope mode has the advantage of being much faster than the microprobe mode (e.g. 10^6 times faster for a 1 k $\times$ 1 k image at the same current density). A typical level of performance of commercial SIMS instruments in terms of lateral resolution achievable in 2D imaging is 50 nm for the microprobe mode and a few μm in the microscope mode.

Both imaging modes can be used to record one or several frames. For 2D imaging, a single frame can be recorded or the data from several frames can be integrated. For 3D information, several frames are recorded, and the conversion from frame number to depth is carried out applying protocols similar to the ones described earlier for depth profiling, so that a 3D volume reconstruction by image stacking can be obtained. Note that these standard 3D reconstruction protocols do not take into account the topography of the sample, as they assume that the sample surface is flat and the analysed volume is cuboid [26].

2D and 3D elemental imaging by SIMS provides important information on sample composition in many applications [4]. In materials science, SIMS imaging is extensively used in fields such as metallurgy, or polymers, providing, for instance, insights regarding diffusion, ageing, oxidation, corrosion, or kinetics. For biological studies, SIMS became of utmost interest only after the development of the latest generation of instruments allowing for the analysis at the cellular scale with optimised sensitivities. Typical applications in biology include metabolism studies by localising specific elements or isotopes inside cells, investigations in nano-toxicology by tracking nanoparticles within tissues, pharmacological studies, studies of bacterial systems using stable isotopes as markers that can then be mapped at high resolution by SIMS, research in plant and soil sciences, and investigations in the field of biomineralisation. SIMS 2D and 3D imaging is also of great interest in geology (e.g. determining the age of rocks) and astronomy (e.g. insights into the composition and origin of interplanetary dust and meteorites). For these two domains, the capability of SIMS to determine isotope ratios with precision of a few percentage points to a few tenths of a percentage point is of utmost interest.

13.2 Fundamental Aspects of SIMS Performed Under He^+ and Ne^+ Bombardment

13.2.1 Dimensions of Collision Cascades

For SIMS imaging with He^+ and Ne^+ beams, the microprobe mode is clearly the most attractive. As mentioned in Sect. 13.1.4, the imaging resolution in this mode depends primarily on the focussing of the spot size of the ion beam raster-scanning the sample surface. As this spot size can be in the nanometre range in the particular case of He^+ and Ne^+ beams generated by a gas field ion source (GFIS) column, the dimensions of the collision cascade triggered inside the sample upon impact of the He^+ and Ne^+ ions become of utmost importance. More specifically, the dimensions of the collision cascade in the extreme vicinity of the sample surface are relevant, as this will determine the origin of secondary ions and hence contribute to the achievable spatial resolution. A second parameter to investigate is the lateral mixing induced by the primary ion bombardment, but this aspect becomes relevant only if the sample is sputtered down to a depth where atomic mixing occurs.

It is important to note that atoms are mainly sputtered from the first topmost monolayers, while the He^+ and Ne^+ primary ions are implanted much deeper. As illustrated in Fig. 13.5, the collision cascade is much narrower near the sample surface than deeper inside the sample. Hence, the diameter where the sputtered atoms are emitted from (Fig. 13.6) is significantly smaller than the radial range (Fig. 13.7). The area of origin of the sputtered atoms is characterised by the diameter of the area which contains 50% of the sputtering events (FW50) [31]. The FW50 of sputtered particles for helium irradiation is smaller than for neon irradiation. This is the consequence of the He^+ beam initially only experiencing an electronic loss phase, and hence only a weak scattering of the beam when entering into the sample. The nuclear stopping process with elastic scattering starts to play an important role only at energies below 3 keV for He irradiation [32]. The dimensions of the collision cascade triggered by He^+ impacts, therefore, remain very small in the vicinity of the surface, i.e. in the region of interest for sputtering. By contrast, the Ne^+ beam immediately generates collision cascades when entering the substrate as the nuclear collisions are dominant over the entire energy regime. The scattering of the primary ions close to the surface is, therefore, larger for Ne^+ impacts. This leads to a wider FW50 of sputtered particles under Ne irradiation, with values ranging from 26 Å at 1 keV Ne^+ impacts up to 94 Å at 30 keV Ne^+ impacts, compared to values ranging from 22 Å at 1 keV He^+ impacts up to 54 Å at 30 keV He^+ impacts. Traditional projectiles used in SIMS such as Ga^+ and Cs^+ lead to areas of emission that are further reduced in size, as these projectiles are heavier resulting in less scattering of primary ions close to the sample surface (Fig. 13.6).

When sputtering the sample down to a depth where the atomic mixing begins to be important, the radial range of the cascade becomes the relevant parameter. While He^+ and Ne^+ probe sizes of 5 nm and smaller are possible with the GFIS column,

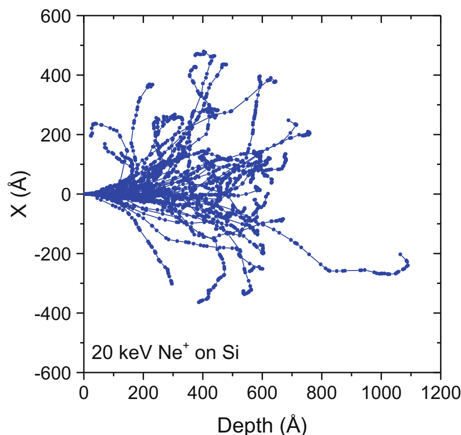

Fig. 13.5 Dimensions of 20 keV Ne^+ cascades in silicon simulated by TRIM

the cascade develops over dimensions larger than that (Fig. 13.5). The lateral dimension of the cascade can be characterised by the diameter of the area, which contains 50% of the implanted atoms. This diameter increases with impact energy and decreases with the mass of the primary ion species (Fig. 13.7). For He^+ bombardment at normal incidence, it changes from 236 Å at 1 keV to 2585 Å at 30 keV. For impacts of the much heavier Cs^+ ions, the same diameter is typically one order of magnitude smaller. Ne^+ is situated approximately half way in between these two extremes, hence offering advantages in terms of resolution compared to He^+ when 3D imaging over a significant depth is required.

In addition to this radial atomic mixing, which becomes relevant when sputtering the sample down to a significant depth, depth resolution must be considered when performing 3D imaging. Depth resolution is typically limited by atomic mixing, diffusion, and segregation processes induced by the primary ion bombardment. In general, better depth resolution is obtained at low impact energies; however, focussing of the primary ion beam is poor for such experimental conditions. In practice, imaging is done with beam energies in the range of 15–30 keV, leading to depth resolution typically worse than 20 nm.

13.2.2 Sensitivity

The secondary ion current and the useful yield will be the important parameters to consider when discussing the sensitivity of the SIMS analysis performed under He^+ and Ne^+ primary ion bombardment. The useful yield, which was defined in Sect. 13.1.2.2, is a global parameter determining the achievable detection limit. In addition, the secondary ion current needs to be sufficiently high to have both a reasonable signal-to-noise ratio and a reasonable analysis duration. For monoatomic secondary ions, the useful yield for a given element A can be written as:

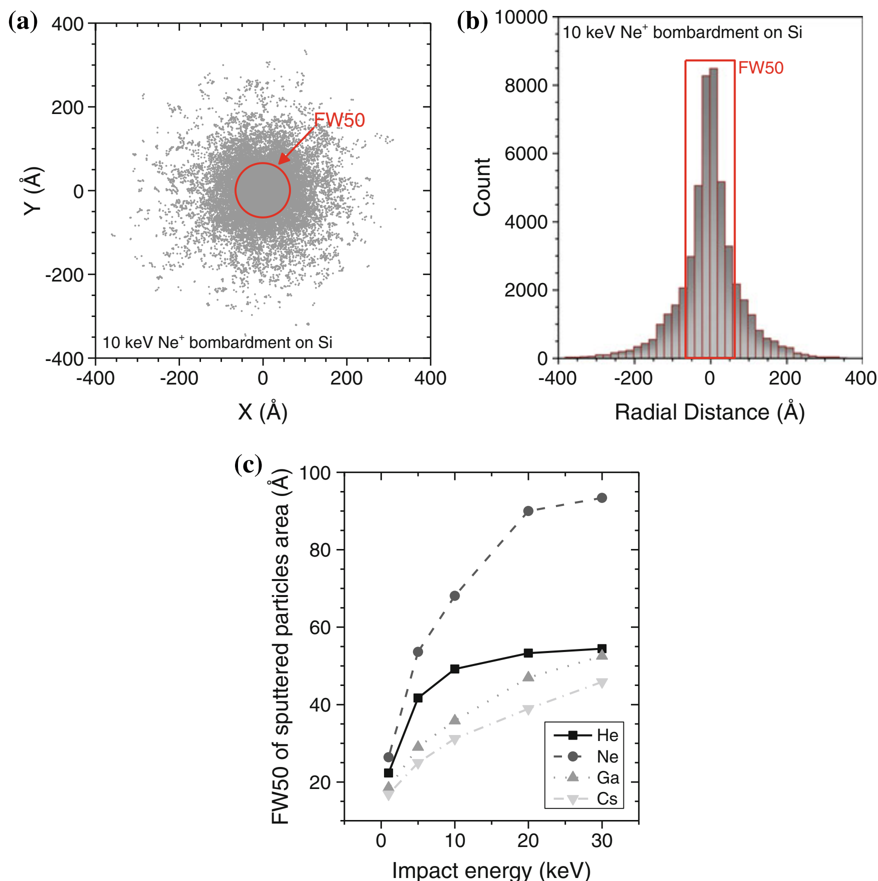

Fig. 13.6 Origin of sputtered atoms for 10 keV Ne^+ impacts on silicon: **a** distribution of sputtered particles with respect to the impact point (0, 0) of the Ne^+ projectile, the red circle containing 50% of the sputtered atoms, and **b** histogram of this distribution. **c** Diameter of area (FW50) where secondary particles are sputtered from as a function of impact energy for He^+, Ne^+, Ga^+ and Cs^+ bombardment on silicon at normal incidence (adapted from [4]). All results were obtained with TRIM

$$UY = \beta_A \cdot \tau$$

where β_A is the ionisation probability of that element and τ includes the transmission of the mass spectrometer and the detection efficiency. While transmission of the mass spectrometer is discussed in Sect. 13.3, this section deals with strategies to maximise the ionisation probability. A second important factor that will be discussed in this section is the sputtering yield, as this one will contribute to the intensity of the secondary ion current (see Sect. 13.1.2.2).

Experimental studies and simulations performed by Pillatsch et al. show that the sputter yields obtained for Ne are on average one order of magnitude higher than those obtained for He [33]. For He and Ne bombardment on Si, for instance, sputter yields of 0.04 and 1.3 were experimentally determined, respectively [33]. While there is thus a huge difference in sputter yield between He and Ne impacts, the difference between sputter yields obtained with Ne^+ primary ions and primary ions typically used in standard SIMS is far less significant. Taking again the example of Si, the sputter yields under O and Cs bombardment are 1.5 and 3.3, respectively, compared to 1.3 obtained with a Ne^+ beam. Considering also that typical currents used in the HIM (e.g. 5–10 pA of He and Ne in a spot size of 10 nm) are significantly higher than in traditional SIMS (e.g. 0.3 pA of Cs in a spot size of 50 nm on the Cameca NanoSIMS 50), the lower sputter yields under He and Ne are more than compensated by the current so that the duration of an analysis on HIM-SIMS is not any longer than the one on traditional SIMS [4].

Regarding ionisation probabilities, experimental studies performed by Wirtz et al. [34] and Pillatsch et al. [33] show that, as expected, the useful yields remain low under pure He and Ne bombardment due to the inertness of these elements. In addition, the useful yields determined for positive and negative secondary ions are very similar for both projectiles (Fig. 13.8). As the useful yield of monoatomic secondary ions is dependent only on the ionisation probability (and the instrumental factor τ), and not on the sputter yield, this proves that identical ionisation mechanisms are relevant under He^+ and Ne^+ ion bombardment. The data in Fig. 13.8 also show the expected trend for electropositive and electronegative elements: the positive ionisation probability, and hence the useful yield, is higher for electropositive elements such as Al, Ni, Ge, Ga, and W, whereas the negative ion formation is more favourable for electronegative ions like P and As. For Si, no significant difference is observed in Fig. 13.8. To increase the ionisation

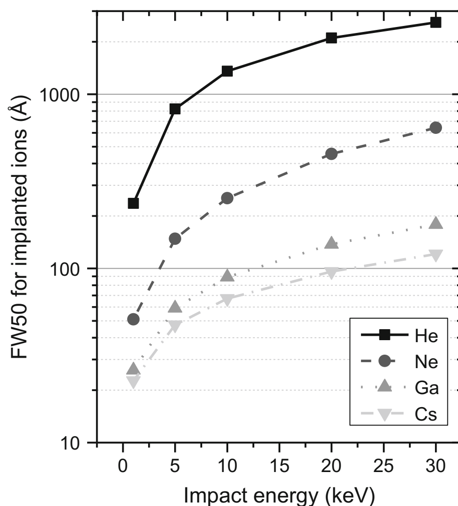

Fig. 13.7 Radial range as a function of impact energy for He^+, Ne^+, Ga^+, and Cs^+ bombardment on silicon at normal incidence. Adapted from [4]

probabilities, and thus to reach better detection limits, Wirtz et al. [34] and Pillatsch et al. [33] applied reactive gas flooding during the analysis, as outlined in Sect. 13.1.2.2. This led to an enhancement in the useful yields by several orders of magnitude, as shown in Fig. 13.8. For Al, Si, Ni, and W, an increase in positive ionisation probability between two and four orders of magnitude was measured when using O_2 flooding. For Si, a useful yield of 5×10^{-2} was reached, which leads to an ionisation probability of 35%, taking into account a transmission factor of about 14% on the instrument used for these experiments [33]. Applying Cs flooding in secondary negative mode resulted in a significant enhancement of the useful yields for all detected elements, i.e. more than four orders of magnitude for Si and three orders of magnitude for P.

13.2.3 Detection Limit Versus Pixel/Voxel Size

While the lateral resolution is fundamentally limited by the characteristics of the collision cascade, the minimum feature size one can detect is also dependent on the sensitivity of the analysis, and thus in particular on the useful yield [35, 36]. According to Orloff et al. [35], the smallest feature that can be detected before being sputtered away is given by:

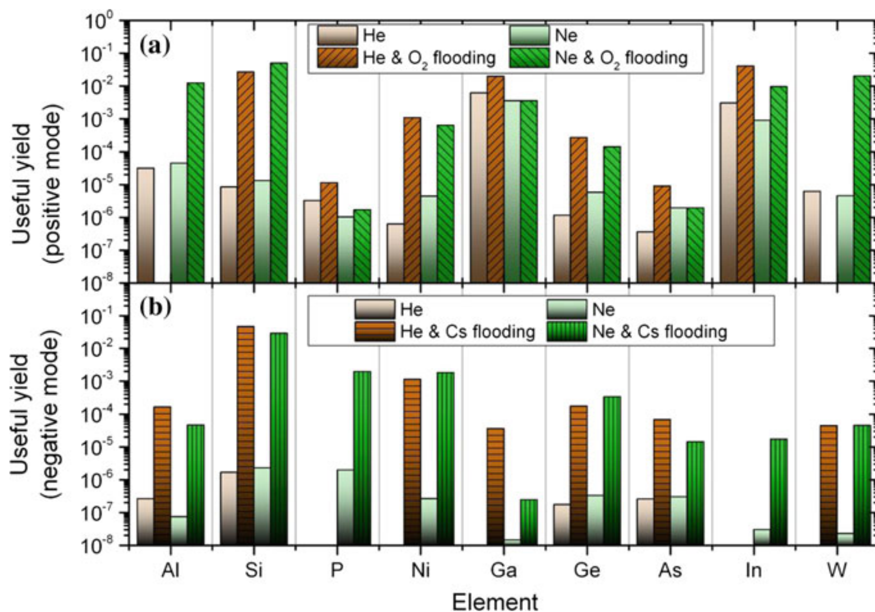

Fig. 13.8 Useful yields for different elements sputtered from the same matrix for He^+ and Ne^+ bombardment: **a** for positive secondary ions with and without oxygen flooding, **b** for negative secondary ions with and without caesium flooding

$$D_{min} = \sqrt[3]{\frac{Y \cdot A \cdot N_i}{(1-\omega)^2 \cdot \rho \cdot N_A}}$$

where D_{min} is the minimum feature size, Y the sputtering yield, A the atomic weight, N_i the number of primary ions per pixel, ω the beam overlap, ρ the target density, and N_A the Avogadro number.

Figure 13.9 shows the evolution of the detection limit of Si^+ under Ne^+ irradiation as a function of feature size D_{min} without and with caesium flooding for cubic voxels. As discussed in Sect. 13.2.1, the dimension of the collision cascade corresponds to roughly 10 nm under these bombardment conditions. For a cubic volume of 10 nm side length, which would hence correspond to the physical limit in spatial resolution, Fig. 13.9 indicates a detection limit of approximately 10^{-3} when using reactive gas flooding. With such reactive gas flooding, a detection limit at the ppm level can be obtained for features of about 100 nm. Without O_2 flooding, detection limits are worsened by three orders of magnitude, as already indicated by Fig. 13.8. Values for other secondary ion species can be deduced by rescaling Fig. 13.9 using data from Fig. 13.8. The data were obtained for a magnetic mass spectrometer with an overall transmission of about 30%. For lower or higher transmissions, the detection limit would change accordingly.

For the same primary ion dose, the detection limit under He^+ bombardment is typically one order of magnitude poorer than under Ne^+ bombardment, due to the lower sputtering yield caused by He compared to Ne, resulting in lower secondary ion yields and thus poorer signal-to-noise ratios, ultimately restricting the detection limit. Similarly, to reach the same detection limit, the He^+ ion fluence needs to be one order of magnitude higher than with Ne^+ bombardment. In general, SIMS measurements with high sensitivity require high ion fluence per pixel, and thus subsequent damage formation and an increase in the minimum detectable feature

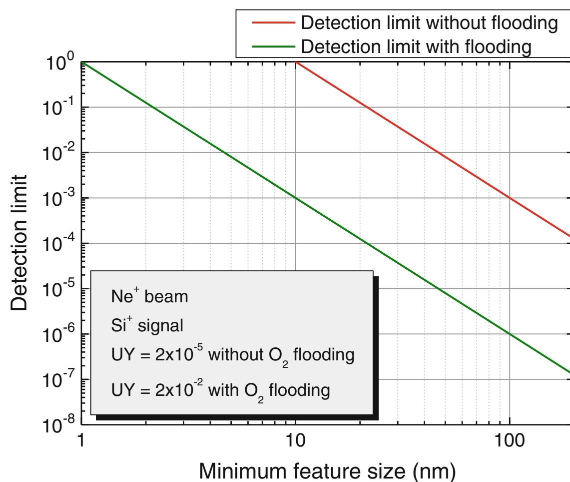

Fig. 13.9 Detection limit for Si^+ as a function of minimum feature size calculated for 25 keV Ne^+ bombardment with and without simultaneous oxygen flooding and for cubic voxels

size will begin to become important. Consequently, the ion fluence per pixel must be chosen carefully in order to find the right trade-off between sensitivity, lateral resolution, and damage formation [31].

The trade-off between detection limits and minimum detectable feature size in SIMS imaging shown in Fig. 13.9 can be overcome using the correlative microscopy approach [4]. With this correlative approach, the SIMS will be run in a mode leading to the required detection limit, the spatial resolution corresponding to this detection limit (as determined by Fig. 13.9) being secondary. The required excellent spatial resolution is obtained in a second step by overlaying the SIMS image with a high-resolution secondary electron image obtained with the He^+ (or Ne^+) ion beam. Different possibilities arise from these in situ instrument combinations [4]. One approach involves imaging the sample in the SIMS mode to localize hot spots (e.g. a high concentration of a given element or a given isotope of interest), and then identifying the feature corresponding to this hot spot in the secondary electron mode. A second approach consists in beginning with a secondary electron image to identify zones or features of interest, and then determining the chemical composition (or the isotopic ratios) of these features or zones by SIMS. Given the destructive nature of SIMS, the second approach is often preferred, especially for small feature sizes.

13.3 Instrumentation for SIMS Performed on the HIM

13.3.1 Instrumental Constraints

The fundamental aspects listed in Sect. 13.2 indicate that performing SIMS on the HIM is not only possible, but it would afford a number of advantages over conventional SIMS in terms of achievable lateral resolution. To realise these advantages practically, special consideration must be given to the type of instrumentation used to perform SIMS on the HIM. The mass spectrometer should have an appropriate mass range and mass resolution. Given that the primary beam will consist of atomic He^+/Ne^+ ions at a significant dose, the analysis will always be in the dynamic regime (see Sect. 13.1.1), and thus molecular information will not be obtained, so a moderate limit for mass range would be sufficient. Additionally, the spectrometer must be designed to work with an existing instrument, placing a number of constraints on its design. The design considerations for performing SIMS on the HIM are listed below in order of priority.

- The size and weight of the spectrometer should be compatible with mounting on the HIM.
- The extraction system should not significantly degrade the probe size of the HIM in SIMS mode.
- The extraction system either should be removable, or should not affect standard imaging/milling operations.

- Detection of positive and negative secondary ions should be possible.
- As the secondary ion current will be low, the extraction efficiency and overall transmission of the spectrometer should be high.
- Parallel detection of secondary ions is important for avoiding a poor sample consumption duty cycle.
- The acquisition time for SIMS images should be similar to that for SE images.
- Reactive gas flooding should be integrated into the SIMS system.

13.3.2 Prototype Instrument for SIMS Performed on the HIM

Addressing all the listed constraints simultaneously is no easy task. The first consideration is choosing which of the types of mass spectrometers described in Sect. 13.1.3 would be the most appropriate given the design considerations above. The condition of parallel detection eliminates the possibility of using a quadrupole, and would suggest the use of either a TOF or a magnetic sector with a long straight focal plane. To perform TOF, it is necessary to pulse either the primary or the secondary beam. Pulsing the He/Ne beam is not possible without degrading the probe size and so can be eliminated. Pulsing of the secondary beam is possible. The most common type of spectrometer that operates in this fashion is the orthogonal TOF (oTOF). oTOFs have the advantages of being compact and relatively simple. They have high mass resolution and an unlimited mass range. However, when coupled to a constant kinetic energy beam such as in this case, the duty cycle of an oTOF is mass-dependent, resulting in a square root variation in the sensitivity [37]. Also, as analysis would be performed in the dynamic regime, the principal components of the secondary beam will be atomic ions or small clusters. Thus, one of the main advantages of a TOF—its unlimited mass range—cannot be exploited in this case. The grids present in a TOF also reduce transmission and can introduce a background when analysing negative ions. Magnetic sector instruments with long focal planes can be used to analyse a wide mass range in parallel, given their high transmission and, if double-focussing designs are used, high mass resolution. They typically have better abundance sensitivity than TOFs. Typical magnetic sector spectrometer designs are large and heavy. However, recent developments in compact design show potential for reducing the size of such spectrometers while maintaining suitable SIMS performance. For these reasons, a compact double-focussing magnetic sector was chosen for use on the HIM.

Typically, magnetic sector instruments require high acceleration voltages to achieve high mass resolution. This is normally accomplished by biasing the sample to high voltage and using a grounded extraction electrode. Were this approach to be

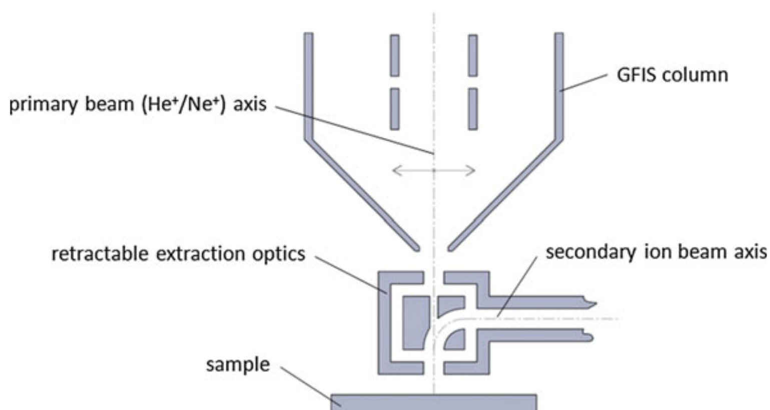

Fig. 13.10 Schematic of the extraction region of the HIM. Some electrodes are simplified or removed for clarity. The entire extraction system is removable so SE imaging and milling operations are unaffected

used on the HIM, the probe size would be severely degraded due to the high extraction field. To avoid this, Dowsett et al. [38] developed a low-field high-efficiency extraction system, with the specific intent of maintaining a sub-10 nm probe size while optimising extraction efficiency. This value of 10 nm was derived from considerations of the dimensions of collision cascades, and hence physical limitations in spatial resolution, as described in Sect. 13.2.1. The secondary ion extraction system designed for the HIM is shown schematically in Fig. 13.10. It is fully retractable, so that the HIM can be used in SE mode without being affected by the extraction system.

Figure 13.11a shows a simulation of the probe size obtained on the sample with this type of system using an extraction voltage of 250 V. Figure 13.11b shows a corresponding total ion image taken by mounting a detector at the exit of such an extraction system. The image was recorded in negative mode; as the image is not mass filtered, the signal comes primarily from secondary electrons (SE). The edge resolution obtained was around 4 nm, demonstrating that probe sizes with dimensions below that of the collision cascade can be obtained with this type of extraction system.

A post-acceleration stage is then used to accelerate the secondary ions to the required voltage for the spectrometer, and a system of transfer lenses transports the beam and focusses it onto the entrance plane of the spectrometer. The spectrometer, shown schematically in Fig. 13.12, is based on a modified Mattauch–Herzog configuration with a 450-mm-long focal plane. In this case the length of the focal plane was optimised to collect ions with m/q up to 250 amu/e with a mass resolution of greater than 400. At lower accelerating voltages ions with m/q up to ~500 can be collected, but at lower mass resolution. A multi-collection system with four

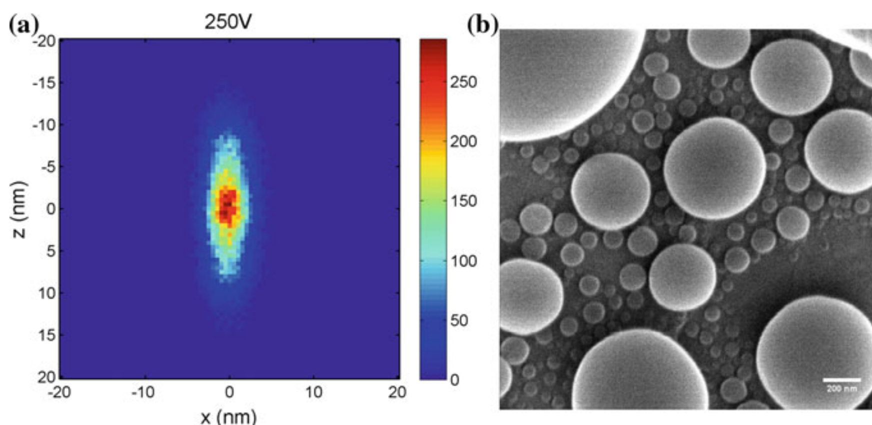

Fig. 13.11 **a** Simulation of probe size at 250 V extraction. The astigmatism is caused by non-rotationally symmetric fields in the extraction system. It may be easily corrected using the HIM's existing stigmator. **b** Negative mode total secondary ion image of a tin on carbon test specimen (Agar AGS1937) with an edge resolution (75–25%) of 4 nm

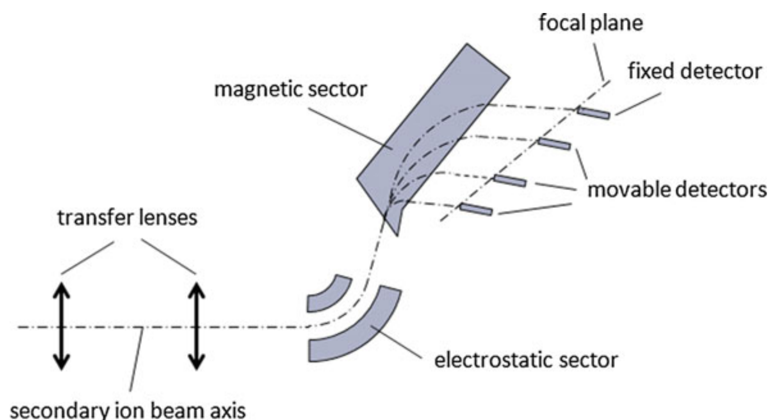

Fig. 13.12 Schematic of the double-focussing magnetic sector spectrometer. The spectrometer has a long straight focal plane, allowing parallel detection of a wide range of masses

detectors (one fixed and three movable) allows parallel detection of up to four masses. Continuous channel electron multipliers are used, as they have high dynamic range (six orders of magnitude) and very low noise (dark noise $\ll 1$ cps). This type of spectrometer is also fully compatible with so-called focal plane detectors. These record the entire mass spectrum in a single shot. However, the demands of high mass resolution, dynamic range, and low noise are not compatible with the pixel resolution and sensitivity of existing detectors.

13.4 SIMS Applications on the HIM

As, at the time of writing, the only existing SIMS spectrometer for the HIM is a prototype still in the development stage, the results presented in this section are somewhat preliminary and do not necessarily represent the limits of performance achievable with the instrument. Nevertheless, they are extremely promising and show that the analytical possibilities offered by performing SIMS on the HIM have great potential.

13.4.1 Mass Spectra

Mass spectra may be acquired either by distributing the detectors over the focal plane and scanning the magnetic field, or by scanning the detectors along the focal plane at fixed magnetic field. In both cases the mass resolution is affected by the speed and step size of the scanning. The rate of scanning is linked to the detector integration time. Short integration times lead to noisier spectra, and trace elements will not be detected if the integration time is not sufficient to generate a count rate above the noise. Typically, integration times of a few hundred milliseconds are used. For high-resolution spectra, step sizes of 0.05 A (which corresponds to approximately 0.18 mT) are used when scanning the magnetic field and 50 μm when scanning the detectors. This leads to acquisition times for a high-resolution spectrum of around 25 min when scanning the field and 8 min when scanning the detectors. Scanning the detectors is faster, because each detector records one third of the mass spectrum. When scanning the magnetic field, each detector records a mass spectrum from mass 1 to mass M, where M is dependent on the detector position, so in this case the spectra overlap, and only the fixed detector records the entire mass spectrum.

Figure 13.13 shows a partial mass spectrum of a lithium titanate and boron nitride nanoparticle mixture on a silicon substrate. The mixture was prepared from an aqueous suspension of the two powders by dropping a few drops onto a silicon wafer and drying. The mass spectrum shows very well separated mass peaks, indicating good mass resolution, with the isotope ratios for both lithium and boron accurate to within 5 and 25% of their respective natural abundance. It should be noted that accuracy limits arising from Poisson statistics for the lithium and boron ratios are 5.2% and 22%, respectively.

The standard mass range is from 1 to 250 amu. However, by operating the spectrometer at reduced accelerating voltage, a wider mass range is accessible, at the cost of mass resolution. Figure 13.14 shows a mass spectrum from an indium phosphide semiconductor wafer. Despite bombardment by a high-energy atomic primary ion, inorganic clusters of several atoms can still be seen in the mass

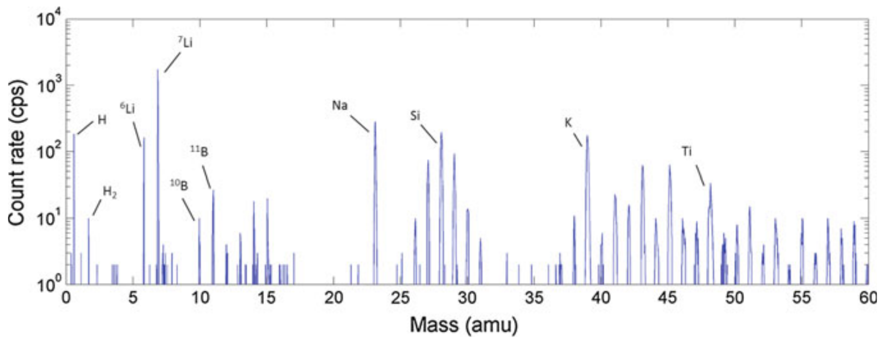

Fig. 13.13 Mass spectrum of a lithium titanate and boron nitride nanoparticle mixture on a silicon substrate (primary beam Ne^+ 25 keV at 6 pA)

spectrum. The mass resolution for each peak was determined by fitting a Gaussian to each peak or, in the case of overlapping peaks, multiple Gaussians. The standard deviation of the Gaussian was then used to determine the full width at half maximum (FWHM) of the peak. Across the complete mass spectrum shown in Fig. 13.14, the average mass resolution was 300.

13.4.2 Depth Profiling

As described in Sect. 13.2.1, the high primary beam energies typically used in the HIM are not ideal for achieving high depth resolution. Nevertheless, the HIM has the unique advantage that depth profiles may be performed on extremely small zones of a few hundred nanometres or less. This can be a particular advantage for

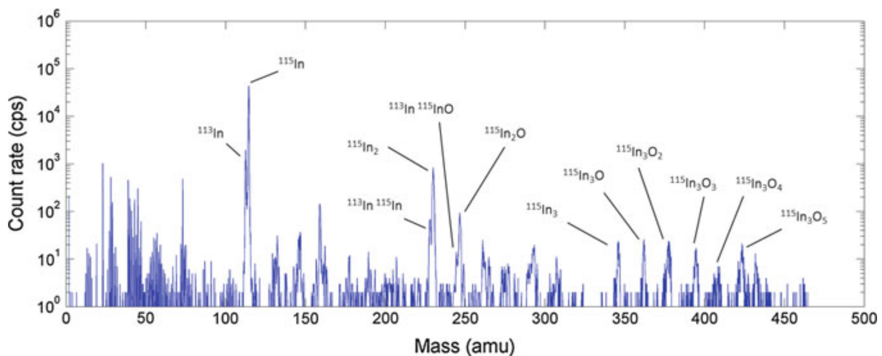

Fig. 13.14 Mass spectrum of an indium phosphide semiconductor wafer under 25 keV Ne^+ bombardment at reduced secondary acceleration voltage. Inorganic clusters up to In_3O_5 (mass 425) have been observed

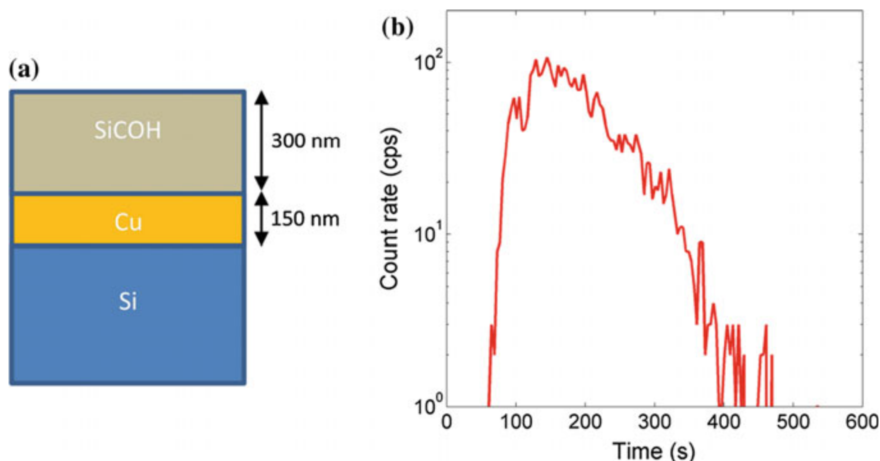

Fig. 13.15 **a** End pointing test structure consisting of a 300 nm thick cap of low-k dielectric (SiCOH) on top of a 150 nm thick copper layer on a silicon substrate. **b** Depth profile through the test structure ($^{63}Cu^{+}$ signal) for a 500 × 500 nm^2 crater

semiconductor end-pointing applications or process control during nano-machining, where the aim is to sputter through the sample and to stop the sputtering immediately upon reaching a certain layer. As an example, Fig. 13.15b shows the depth profile obtained from a test structure described in Fig. 13.15a. The structure consists of a low-k dielectric layer on top of a buried copper layer on a silicon substrate. This depth profile was obtained with a 27 keV Ne^{+} beam raster-scanned over 500 × 500 nm^2. While the depth profile shows a sharp rising edge for the Cu^{+} signal, allowing for a precise definition of the blanking of the primary ion beam in an end-pointing application, the falling edge is much less precisely defined due to mixing taking place during the sputtering of the sample when using high-energy ion beams.

13.4.3 Imaging

Imaging is certainly one of the most interesting applications of SIMS performed on the HIM. As described above, the probe size on the HIM is smaller than the dimensions of the collision cascade, so under the right circumstances (e.g. yield, signal-to-noise ratio, surface concentration), the SIMS images should be the highest resolution possible. Figure 13.16 shows an image of the boron and lithium distributions obtained on a nanoparticle mixture containing 50% lithium titanate ($Li_4Ti_5O_{12}$) and 50% boron nitride. The mixture was prepared by making an aqueous suspension of the two nanoparticle powders, mixing in an ultrasonic bath, and then dropping the solution onto a silicon wafer and drying at ambient

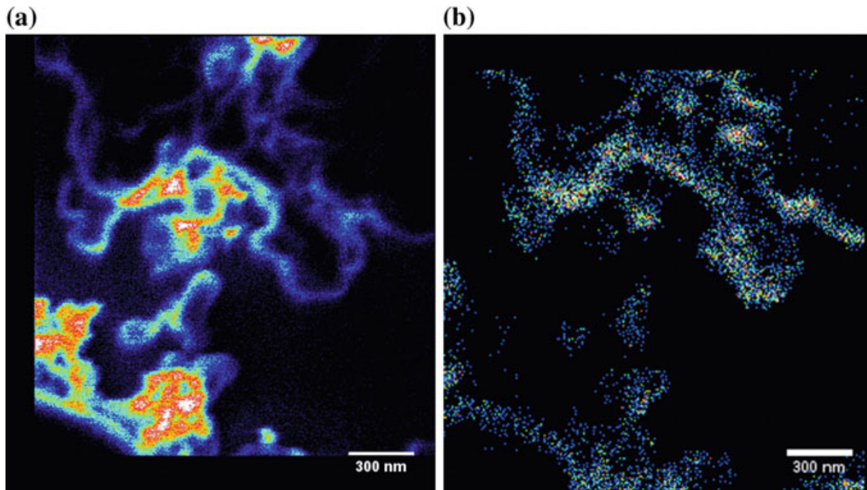

Fig. 13.16 **a** ^{7}Li and **b** ^{11}B distributions for a lithium titanate boron nitride nanoparticle mixture. The field of view is 1.9 μm. Primary beam 27 keV Ne^{+} at 6 pA. The ^{11}B image has been binned by a factor of 2 to aid clarity in the printed reproduction

conditions. The wafer was then imaged at 500 V extraction. The total acquisition time for each mass image was just 53 s (dwell time 50 μs, frame average 4). The edge resolution (75–25%) of the lithium image is around 13 nm.

Figure 13.17 shows an overlay of the ^{48}Ti and ^{39}K distributions of the surface of a TiO_2/Au/TiO_2 photocatalytic multilayer structure produced by plasma-enhanced chemical vapour deposition (PECVD). These multilayer structures allow the wavelength of absorbed UV light to be shifted into the visible spectrum for better performance. High purity of the individual layers is required, and SIMS can be used to track impurities. The ^{48}Ti signal gives an overview of the microstructure of the surface, while the ^{39}K signal shows trace levels of contamination.

13.4.4 Correlative Microscopy

One of the unique features of HIM-SIMS is the capacity to work in an in situ correlative mode, as described in Sect. 13.2.3. Switching between SIMS and SE acquisition can be done in one of two ways. The first consists in simply switching off the sample and extraction voltages, which has the advantage of being nearly instantaneous, but does reduce the SE signal level on the ET detector, as line of sight is partially blocked by the SIMS extraction system. The second involves switching off the sample voltage and retracting the extraction system; this method is only slightly slower (insertion/retraction of the extraction system takes a few seconds), and does require fine alignment of the extraction system upon reinsertion. This

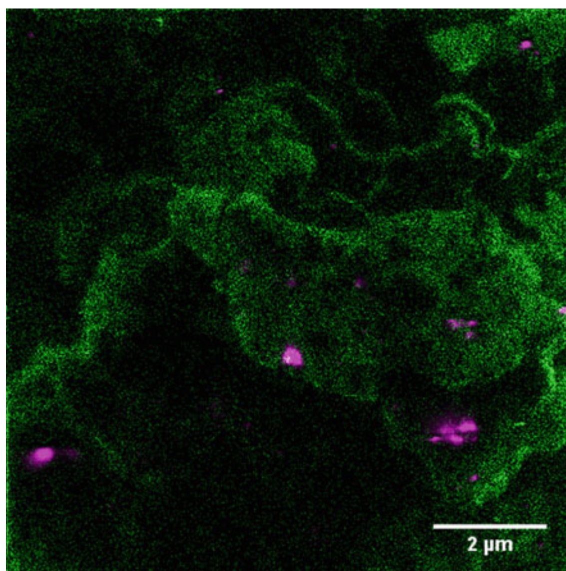

Fig. 13.17 Overlay of ^{48}Ti (*green*) and ^{39}K (*magenta*) distributions of the surface of a TiO_2/Au/TiO_2 photocatalytic multilayer structure

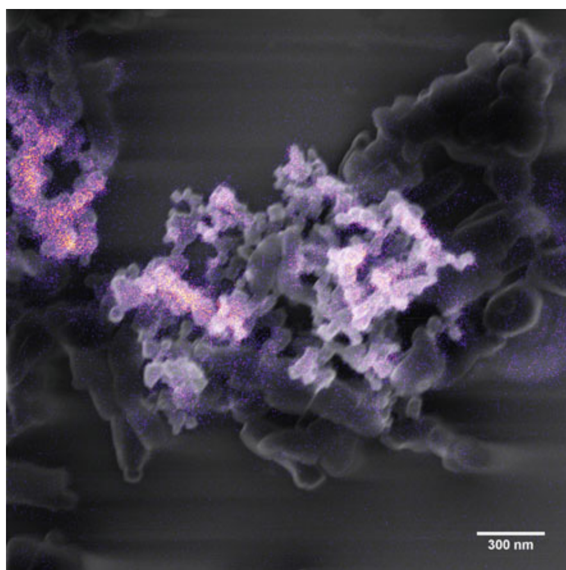

Fig. 13.18 Correlative SE (*grey scale*) and SIMS (^{7}Li) (*magenta*) image. Both the SE and the SIMS images were acquired under 25 keV He^+ bombardment using primary currents of 0.4 pA and 9 pA respectively. Sample: lithium titanate boron nitride nanoparticle mixture on silicon substrate

approach allows SE images of exactly the same zone analysed with SIMS to be acquired easily and rapidly. Figure 13.18 shows a combined SE-SIMS image of the lithium titanate and boron nitride nanoparticle mixture. The SE image has a resolution of a few nanometres, clearly showing the structure of individual nanoparticles, while the SIMS image has a resolution of a few tens of nanometres, and allows unambiguous identification of individual nanoparticles.

The speed with which it is possible to switch between SIMS and SE modes gives rise to a number of novel ways of working. Samples can be imaged in the SE mode both before and after SIMS acquisition to assess the amount of sputtering/sample damage, or multiple images can be acquired, interlacing between SIMS and SE mode to build up 3D volumes with both high-resolution structural information from SEs and high-sensitivity chemical information from SIMS.

13.5 Conclusions

SIMS constitutes an extremely sensitive technique for elemental and chemical analysis. Apart from its excellent sensitivity, advantages of SIMS include high dynamic range and the ability to differentiate between isotopes. Fields of application for SIMS can be found in materials science, life sciences, geology, and cosmo-chemistry. Isotopic labelling plays a major role in many of these applications, as it allows tracing of molecules without the need to minimise fragmentation, enabling one to take advantage of the unique sensitivity and lateral resolution of elemental SIMS imaging.

In general, the lateral resolution in SIMS imaging when using the microprobe mode is limited by (i) the ion probe size, which is dependent on the brightness of the primary ion source, the quality of the optics of the primary ion column, and the electric fields in the near sample region used to extract secondary ions; (ii) the sensitivity of the analysis, as a reasonable secondary ion signal needs to be detected from very tiny voxel sizes and thus from a very limited number of sputtered atoms; and (iii) the physical dimensions of the collision cascade determining the origin of the sputtered ions with respect to the impact site of the incident primary ion probe.

The combination of He/Ne microscopy and SIMS makes it possible not only to obtain SIMS information limited only by the size of the probe–sample interaction ($\sim$10 nm), but also to directly correlate such SIMS images with high-resolution (0.5 nm) secondary electron images of the same zone taken at the same time.

Acknowledgments Some of the work presented in this paper was funded by the National Research Fund of Luxembourg by the grants FNR-MAT-08-01, C09/MS/13, C10/MS/801311 and C13/MS/5951975.

This work was supported in part by the Intelligence Advanced Research Projects Activity (IARPA) via Air Force Research Laboratory (AFRL) contract number FA8650-11-C-7100. The U. S. government is authorised to reproduce and distribute reprints for governmental purposes, notwithstanding any copyright annotation thereon. The views and conclusions contained herein are those of the authors and should not be interpreted as necessarily representing the official policies or endorsements, either expressed or implied, of IARPA, AFRL, or the U.S. government.

References

1. J.P. Biersack, L.G. Haggmark, Nucl. Instrum. Methods **174**, 257 (1980)
2. J.P. Biersack, W. Eckstein, Appl. Phys. A-Matter **34**, 73 (1984)
3. W. Eckstein, W. Möller, Nucl. Instrum. Methods Phys. Res. B **7**(8), 727 (1985)
4. T. Wirtz, P. Philipp, J.-N. Audinot, D. Dowsett, S. Eswara, Nanotechnology **26**, 434001 (2015)
5. W. Moller, W. Eckstein, Nucl. Instrum. Methods Phys. Res. B **230**, 814 (1984)
6. W. Eckstein, J.P. Biersack, Appl. Phys. A-Matter **37**, 95 (1985)
7. W. Moller, W. Eckstein, J.P. Biersack, Comput. Phys. Commun. **51**, 355 (1988)
8. J. Lindhard, M. Scharff, Phys. Rev. **124**, 128 (1961)
9. K. Wittmaack, Surf. Sci. Rep. **68**, 108 (2013)
10. K. Wittmaack, Anal. Chem. **86**, 5962 (2014)
11. G. Slodzian, Surf. Sci. **48**, 161 (1975)
12. G. Slodzian, Phys. Scr. **T6**, 54 (1983)
13. K. Franzreb, J. Lörincik, P. Williams, Surf. Sci. **573**, 291 (2004)
14. M. Bernheim, G. Slodzian, Journal de Physique Lettres **38**, L325 (1977)
15. M. Bernheim, J. Rebière, G. Slodzian, *Proceedings of the Second International Conference on Secondary Ion Mass Spectrometry (SIMS II);*40 (1979)
16. T. Wirtz, H.N. Migeon, Surf. Sci. **557**, 57 (2004)
17. T. Wirtz, H.N. Migeon, Appl. Surf. Sci. **222**, 186 (2004)
18. P. Philipp, T. Wirtz, H.N. Migeon, H. Scherrer, Int. J. Mass Spectrom. **253**, 71 (2006)
19. P. Philipp, T. Wirtz, H.N. Migeon, H. Scherrer, Appl. Surf. Sci. **252**, 7205 (2006)
20. A. Benninghoven, Werner H. Wand, F.G. Rüdenauer, *Secondary ion mass spectrometry: basic concepts, instrumental aspects, applications and trends* (Wiley-Interscience, New York, Chichester, Brisbane, Toronto, Singapore, 1987)
21. Y. Gao, J. Appl. Phys. **64**(7), 3760 (1988)
22. T. Wirtz, H.N. Migeon, H. Scherrer, Int. J. Mass Spectrom. **225**, 135 (2003)
23. H. Gnaser, H. Oechsner, Surf. Interface Anal. **21**, 257 (1994)
24. Y. Gao, Y. Marie, F. Saldi, H.N. Migeon, *Proceedings of the Ninth International Conference on Secondary Ion Mass Spectrometry (SIMS IX)* 406 (1993)
25. W. Compston, S.W.J. Clement, Appl. Surf. Sci. **252**, 7089 (2006)
26. Y. Fleming, T. Wirtz, Beilstein J. Nanotechnol. **6**, 1091 (2015)
27. H. Oechsner, H. Schoof, E. Stumpe, Surf. Sci. **76**, 343 (1978)
28. W. Vandervorst, Appl. Surf. Sci. **255**, 805 (2008)
29. M.Y. Chan, P.S. Lee, V. Ho, H.L. Seng, J. Appl. Phys. **102** (2007)
30. A. Redinger, K. Hönes, X. Fontan, V. Izquierdo-Roca, E. Saucedo, N. Valle, A. Prez-Rodriguez, S. Siebentritt, Appl. Phys. Lett. **98** (2011)
31. T. Wirtz, N. Vanhove, L. Pillatsch, D. Dowsett, S. Sijbrandij, J. Notte, Appl. Phys. Lett. **101**, 041601 (2012)
32. J.F. Ziegler, J. Biersack, U. Pand Littmark, *The Stopping and Range of Ions in Solids* (Pergamon, 1985)
33. L. Pillatsch, N. Vanhove, D. Dowsett, S. Sijbrandij, J. Notte, T. Wirtz, Appl. Surf. Sci. **282**, 908 (2013)
34. T. Wirtz, H.N. Migeon, Appl. Surf. Sci. **231–232**, 940 (2004)
35. J. Orloff, L.W. Swanson, M. Utlaut, J. Vac. Sci. Technol. B **14**(6), 3759 (1996)
36. V. Castaldo, C.W. Hagen, P. Kruit, E. van Veldhoven, D. Maas, J. Vac. Sci. Technol. B **27**, 3196 (2009)
37. M. Guilhaus, D. Selby, V. Mlynski, Mass Spectrom. Rev. **19**, 65 (2005)
38. D. Dowsett, T. Wirtz, N. Vanhove, L. Pillatsch, S. Sijbrandij, J. Notte, J. Vac. Sci. Technol. B **30**, 06F602 (2012)

Chapter 14
Ionoluminescence

Vasilisa Veligura and Gregor Hlawacek

Abstract After a sample has been excited by ion irradiation it has several ways to release the excess energy. One of them is photon emission. This process is called ionoluminescence (IL). The IL signal contains information on the electronic structure of the sample. Furthermore, it can help to reveal the processes occurring in the sample under the influence of an ion beam. Analysis of IL is significantly complicated by the fact that ion beam not only induces light emission, but also modifies the luminescence properties of the material. Several types of materials were investigated in HIM in terms of ionoluminescence: semiconductors, minerals, organic compounds. Analysis of the IL signal and its behavior allowed not only to identify the origin of the signal, but also to study the formation of ion-induced defects, their migration and interaction with each other. The effect of crystal coloration in case of the alkali halides led to a possibility for the creation of nano–scaled luminescent patterns using the He^+ ion beam. Such ionoluminescent patterns allowed the visualization and direct experimental measurements of the ion beam interaction volume.

14.1 Introduction

Ion beam irradiation of a target may lead to photon emission that is beyond thermal radiation. This phenomenon is known as ionoluminescence (IL). Three main stages can be distinguished in any luminescence process [1]:

1. energy absorption and excitation of the electronic system;
2. system relaxation and energy transfer to the emission centers;
3. transition of the system into the ground state by photon emission.

V. Veligura (✉) · G. Hlawacek
Physics of Interfaces and Nanomaterials, University of Twente,
PO Box 217, 7500 Enschede, The Netherlands
e-mail: vaveligura@gmail.com

G. Hlawacek
e-mail: g.hlawacek@hzdr.de

© Springer International Publishing Switzerland 2016

G. Hlawacek and A. Gölzhäuser (eds.), *Helium Ion Microscopy*,
NanoScience and Technology, DOI 10.1007/978-3-319-41990-9_14

While the last two stages mainly depend on the target properties, the first stage is also determined by the type of excitation. Ionoluminescence is rather a general term since there can be several sources of light emission during ion beam interaction with the target. The light can originate from the excited backscattered neutral He atoms [2], from excited sputtered target atoms and molecular complexes, or can be emitted by the sample itself [3]. The emission from the species which leave the target in excited states consists of discrete Doppler - broadened lines and corresponds to the optical transitions within atomic (or molecular) orbitals. This light emission is usually observed in a distance up to a few millimeters from the sample surface [3]. However, one would not expect to observe these types of emission in a HIM. The sputtering rates and He^+ currents in HIM are too low to generate an IL signal sufficient for detection. This has been experimentally verified in the work of Franklin [4].

Both organic and inorganic materials may exhibit luminescence. In the case of organic samples IL reveals the electronic structure of the organic compounds and typically is a result of electronic transitions of π electrons [5].

The physics of light emission from solids is usually described using the sample's electronic band structure or configuration coordinate diagrams [1]. Two general types of luminescence can be distinguished based on its origin: *extrinsic* and *intrinsic* [6]. Extrinsic luminescence is due to the presence of impurity atoms or ions (so called *activators*) in the sample material. Activators are classified by their electronic structure:

1. transition metal ions with d^n electronic configuration (e.g. Ti^{3+}, Cr^{3+}, Mn^{2+});
2. ions with s^2–configuration (e.g. Tl^+, Pb^{2+}, Sb^{3+});
3. rare-earth elements ($REE^{2+/3+}$);
4. actinides (e.g. UO_2^{2+}, Cm^{3+}).

In some cases the presence of a certain impurity (*sensitizer*) is required for the luminescence of an activator (for example Pb^{2+} ions for activation of Mn^{2+} luminescence in calcite). A sensitizer is needed to allow the energy transfer to the activator [1]. In contrast to sensitizers *quenchers* suppress light emission from an activator. As an example, Fe^{2+} ions quench emission from Mn^{2+} in apatite. Furthermore, a high concentration of activators can lead to self–quenching as a result of resonant absorption processes between the active sites.

Emission from the sample material itself is referred to as intrinsic luminescence. First, these are optical transitions from delocalized excited states. In other words, the recombination of excited free electrons in the conduction band with holes in the valence band, including direct and indirect transitions. The radiative recombination of free excitons also falls into this category. Second, optical transitions which involve localized states are also attributed to intrinsic luminescence. This includes the following processes: recombination of excitons trapped at defect sites (so–called, self–trapped excitons (STEs) [7]); emission from excited defects—vacancies, crystal imperfections and distortions, etc. (e.g. nitrogen–vacancy centers in diamond); transitions of charge carriers between delocalized and localized states.

Any light generated in the sample still has to reach a detector. Unfortunately, some loss of signal intensity is unavoidable during this process. First of all, there

are internal losses $A(\lambda)$ within the sample [4]. That includes: light absorption by the sample material, reflection by the sample surface, and total internal reflection. The signal detection is also limited by the detection system efficiency $D(\lambda)$. Therefore, the total detection rate can be expressed as:

$$N(\lambda) = Q(\lambda)\,(1 - A(\lambda))\,D(\lambda) \tag{14.1}$$

where $Q(\lambda)$ is photon yield per incident ion which is proportional to the electronic stopping power.

IL is in many aspects similar to the cathodoluminescence (CL) [8, 9] which is light emission under an electron beam irradiation. Hence, numerous exiting CL studies can be useful for comparison and interpretation of IL results. IL studies are significantly complicated by the fact, that an ion beam not only induces light emission, but also directly influences luminescence properties of the target due to defect creation leading to either coloration or rapid quenching of the IL. Although the IL technique has been used for material characterization for a few decades and several reviews [3, 10] can be found, the field is still not fully established and has plenty of room for research. The ion beam energies typically used for IL generation are in the range of hundreds of keVs or even a few MeVs, whereas a typical He^+ beam energy in HIM is in the 15–35 keV range. Therefore, we will discuss and give an overview of the IL generation and application at this low energy regime available in HIM.

14.2 Ionoluminescence in HIM

The first demonstration of IL in the HIM was done by Boden et al. [11]. The authors investigated a wide variety of samples most of which were found to exhibit IL under He^+ irradiation. However, the IL signal was reported to decay fast under prolonged beam exposures due to defect accumulation. At about the same time Ogawa et al. [12] reported an observation of IL in a HIM from SiO_2 [12]. The IL intensity was found to increase with increasing ion fluence. This could be related to the beam induced formation of defects responsible for the observed luminescence [13]. We have performed extensive studies of IL in the HIM from semiconductors and alkali halides [14–16]. We also applied IL technique to investigate the damage formation caused by the He^+ beam. These and several other up–to–date IL findings obtained by helium ion microscopy are discussed below in detail.

14.2.1 Semiconductors

The CL technique is a common tool for the investigation of semiconductors and semiconductor based devices [8]. It provides a strong light signal due to radiative recombinations of electron–hole pairs that are produced by the primary electron beam.

Since the light emission originates not only from recombinations across the band–gap, but also from recombinations via impurity and defect states, CL provides information on surface and lattice defects. It is also widely applied for imaging crystal lattice distortions [17].

The availability of a sub–nm He^+ ion beam for IL generation resulted in the expectation that it would provide higher resolution capabilities for detailed studies of the properties and defects of semiconductor samples [4, 11, 16, 18]. Although some semiconductors were found to exhibit IL, generally the IL signal is a few magnitudes lower than CL signal. Furthermore, the IL signal degrades fast under ion irradiation. The relative strength and stability of the IL emission depends on the material composition. In addition, it was be shown that the stability of the IL signal depends also on the sample dimensions.

14.2.1.1 Bulk Semiconductors

The first attempts to investigate IL from bulk semiconductors using HIM were not very successful [4, 11]. The authors could not obtain any detectable signal from a series of direct band–gap semiconductor devices, including: GaP, GaN on SiC, InGaN, GaN on sapphire and InGaAlP on GaAs commercial LED dies [4]. The absence of the IL signal was attributed to a combination of the beam induced damage and the presence of a dead layer that the beam could not penetrate through. Additionally, there may simply not be sufficient IL signal generated to obtain images or spectra. However, the authors could image GaN hillock microstructures on sapphire using IL [4]. Moreover, IL and CL images as well as spectra were obtained from GaN on a sapphire wafer (see Fig. 14.1).

The characteristic band–gap emission at around 360 nm (3.4 eV) and the yellow emission around 560 nm (2.2 eV), which is typical for GaN, were observed. The yellow emission has been extensively studied for several decades, but there is still no clear agreement on its exact nature (see Review [19]). It is usually attributed to either Ga vacancies, or to impurities such as C or O.

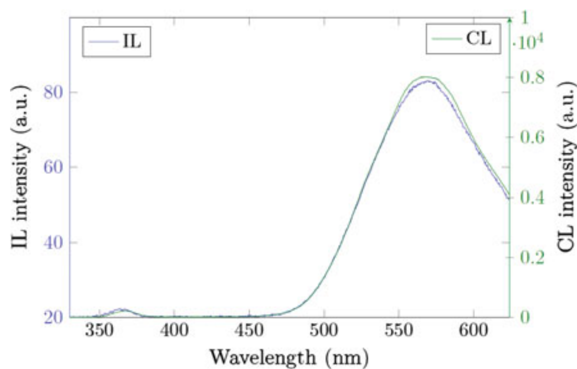

Fig. 14.1 IL (*blue line*) and CL (*green line*) spectra of GaN on a sapphire wafer [4]

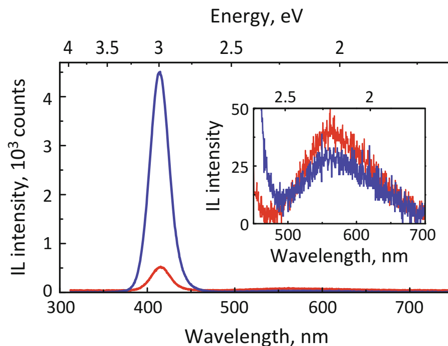

Fig. 14.2 IL spectra of n–type doped GaN film on sapphire obtained at a He^+ beam energy of 10 keV (*red line*) and 35 keV (*blue line*). The spectra are recorded at identical settings [16]

Si–doped GaN films on sapphire were investigated by Veligura et al. [16]. The luminescence from the sample was completely quenched after fluencies of several 10^{13} ions/cm^2 similar to what was reported in [4]. IL spectra were acquired at different He^+ beam energies: 10 keV (red line in Fig. 14.2) and 35 keV (blue line in Fig. 14.2) while leaving the remaining acquisition parameters constant.

The ultraviolet band–gap emission expected from GaN was absent. The intensity of the yellow emission at around 560 nm did not depend on the excitation beam energy (see inset in Fig. 14.2) and was relatively weak compared to the other observed emission at 3 eV. Both spectra show a strong peak at 415 nm (or ∼3 eV), which is nine times stronger at a beam energy of 35 keV compared to the 10 keV irradiation. This blue emission is unlikely to be related to the band–gap transition (typically at 3.4 eV), since a shift of nearly half an electron volt would require a significant modification of the material composition. Blue emission from undoped and Si–doped GaN layers was previously observed in several photoluminescence [19, 20] and CL [20, 21] studies, but its origin is not completely clear [19]. Authors in [20, 21] relate it to structural defects with a deep level.

The SE image in Fig. 14.3 (left image) demonstrates the surface details of the GaN film. The holes in the surface are, so–called V–pits with diameters of 50–90 nm. These defects are formed during film growth and have the shape of hexagonal inverted pyramids with $\{10\bar{1}1\}$ faceted side walls [22]. A simultaneously recorded panchromatic IL image (right in Fig. 14.3) reveals the inhomogeneous distribution of the IL emission. The signal is lower from the defect free areas, whereas the IL emission is enhanced in the vicinity of defect agglomerations. An enhancement of the CL signal at the V–pits was observed in GaN, AlInGaN and Si–doped AlGaN films [22–24] and was attributed to the enhancement of the free carrier recombination at the associated defect sites.

Two other bulk semiconductors were examined in [16] namely InP and S–doped GaP. Their typical IL spectra and signal degradation plots are shown in Fig. 14.4.

Although the signal to noise ratio is low, the peak of the IL emission from InP is clearly discernible and is centered at 1.34 eV (see Fig. 14.4a). That corresponds

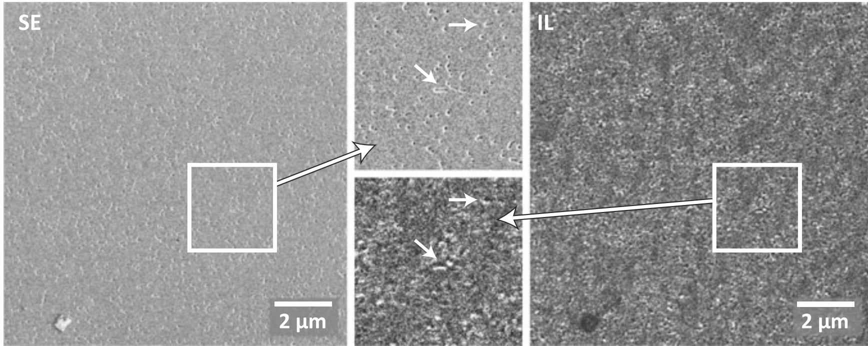

Fig. 14.3 SE (*left*) and panchromatic IL (*right*) images of a Si–doped GaN film [16]. He^+ beam energy is 35 keV. FOV is 12 µm. The inset in the *middle* shows a magnified region of interest (ROI). The size of the ROI is 3 µm × 3 µm. The *arrows* mark prominent features

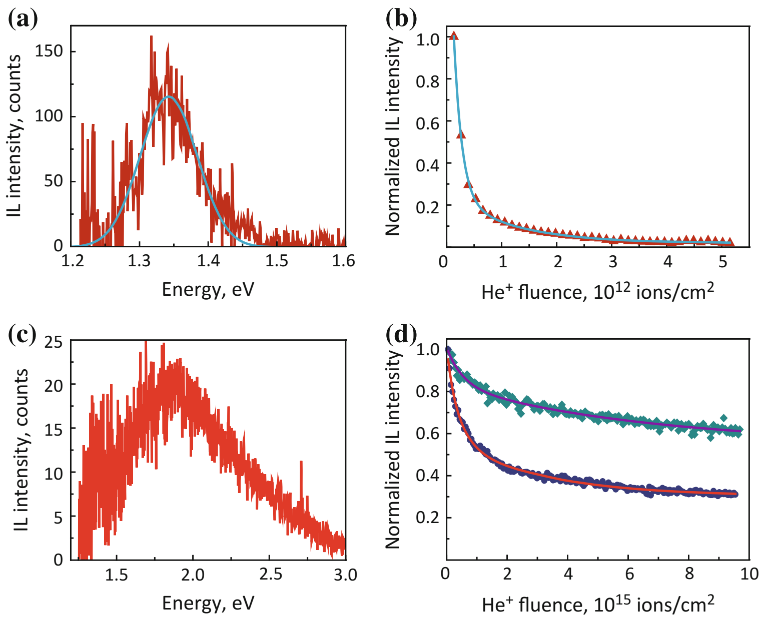

Fig. 14.4 **a** IL spectrum of InP wafer. The peak is fitted by a Gaussian with a center at 1.34 eV. **b** Degradation of the IL signal from InP wafer with increasing He^+ fluence. **c** IL spectrum of S-doped GaP. **d** Degradation of the IL signal from GaP bulk sample (*blue circles*) and NWs (*dark cyan diamonds*) with increasing He^+ fluence. The ion beam energy is 35 keV [16]

to the material's band–gap at RT. As can be seen from Fig. 14.4b, the signal from InP rapidly drops to zero with increasing ion fluence. S–doped GaP showed a broad-band emission with a maximum at 1.9 eV (see Fig. 14.4c). The band–gap emission (2.26 eV) and the near–band–edge emission (2.15–2.33 eV), associated with dopants

and impurities, are suppressed and a new dominant peak at 1.9 eV develops. Similar results were obtained in CL studies of the defects in GaP crystals generated by proton, neutron and gamma ray irradiation [25]. The degradation of the IL signal is shown in Fig. 14.4d by blue circles (lower data set). In contrast to the previously discussed examples, the IL signal from bulk GaP does not vanish completely. However, it has dropped by 70% once a fluence of $\sim 10^{16}$ ions/cm^2 was reached.

Irradiation of semiconductors by light ions leads to the creation of mainly isolated point defects [26–29]. The defects can provide radiationless pathways for electron de–excitation. Moreover, point defects introduce shallow levels in the band–gap, influencing the charge carrier lifetime and mobility [28, 29]. The damage may accumulate and transform into complex defect clusters with increasing ion fluence [26, 27]. Swift heavy ion irradiation studies at RT showed that in the case of GaP the relative defect concentration does not exceed a certain level even at high ion fluences, whereas a continuous amorphous layer develops in InP [30]. This difference in response of materials to the ion irradiation may explain the observed difference in the IL signal degradation (compare Fig. 14.4b and d).

14.2.1.2 Semiconductor Nanowires

As opposed to bulk semiconductors, the IL emission from nanowires (NWs) was found to be remarkably stable under ion beam irradiation [16]. Overgrown GaP–GaAs NWs [31] could be imaged at high resolution using not only SEs, but also the IL signal (see Fig. 14.5). An arrow in the images points at a NW with a thickness of 17 nm, which is clearly resolved—both in the SE and in the IL images.

For the example of GaP NWs with a silicon shell [32] it has been demonstrated that the NWs continue to luminesce even after they were substantially modified [16]. The NWs deformed and bent as a result of an extensive exposure to the He^+ ion beam (fluence of $\sim 10^{17}$ ions/cm^2 at 35 keV), but remained visible in the IL images.

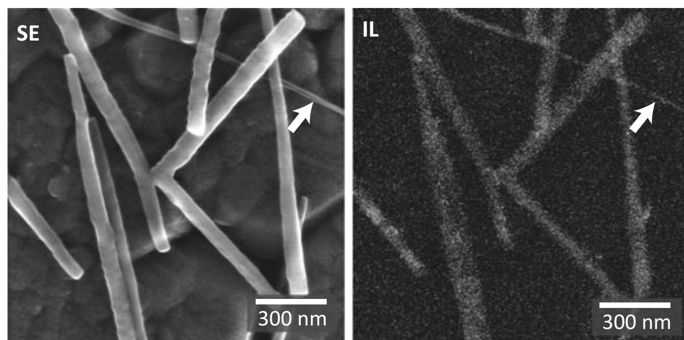

Fig. 14.5 HIM SE and panchromatic IL image of overgrown GaP–GaAs nanowires [16]. The *arrow* points at a nanowire with a thickness of 17 nm, detectable by IL imaging. FOV is 1.42 μm

The IL signal degradation from the GaP NWs is compared to the one from the bulk GaP in Fig. 14.4b (dark cyan diamonds). The curves were obtained under identical conditions. The overall trend is the same. However, after an applied He^+ fluence of $\sim 10^{16}$ ions/cm^2 the IL signal obtained from the NWs decreased by 30% versus a 70% drop of the signal from the bulk sample (Sect. 14.2.1.1).

As proposed in [16], the observed modification of the NWs are mainly caused by sample heating, while no considerable amount of helium was implanted nor substantial amount of crystal defects was created. In the first few tens of nanometers after entering the target—which correspond to the thickness of NWs—electronic stopping is predominant. The hard nuclear collisions—leading to a large number of atomic displacements—occur deeper in the bulk after the ions have been substantially decelerated. For the case of supported NWs this results in helium implantation and damage accumulation in the substrate and not in the structure of interest. Moreover, in the case of He^+ irradiation the sample damage is mostly caused by recoiling target atoms [33]. This damage mechanism is not of importance for the discussed NWs due to their limited size. Additionally, some of the IL signal from GaP originates from the defect states (see spectrum in Fig. 14.4c and discussion in Sect. 14.2.1.1) leading to the presence of IL emission after prolonged ion irradiation. Unfortunately, no IL spectrum could be recorded from GaP NWs to support this statement.

14.2.2 Alkali Halides

In case of certain crystalline materials an ion beam not only induces light emission, but causes coloration of otherwise not luminescent crystal. This happens due to the formation of specific types of defects, so–called color–centers [10]. Color–centers can be produced through electrolysis, heating or by introducing impurities. However, more often they are created under natural or man–made ionizing radiation, which leads to appearance of various electronic and atomic defects, as well as their agglomerates. The group of alkali halides includes some of the best–known examples for crystal coloration [34, 35]. Extensive studies of IL of alkali halides in HIM were performed using the example of NaCl [14, 15].

14.2.2.1 Ionoluminescence of NaCl

NaCl crystals provide a relatively strong IL signal in the HIM [14]. The measurements of NaCl crystals with sizes from several tens to a few hundreds of nanometers allowed us to estimate a minimum crystal volume required for the detection of an optical signal (see Fig. 14.6).

Clearly, the minimum detectable crystal size depends on the ion fluence that is applied during imaging. Unfortunately, there is an upper limit for the allowed ion dose in each particular experiment. At high ion fluencies imaging in HIM can

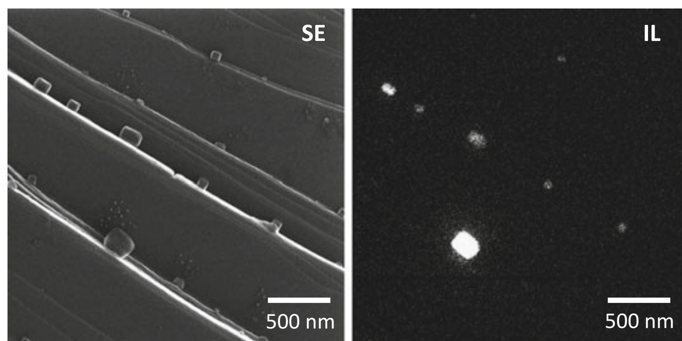

Fig. 14.6 SE (*left*) and IL (*right*) images of NaCl crystals on an HOPG substrate [14]. The strength of the IL signal depends on the crystal volume. The smallest detectable crystal has a size of 50 nm × 50 nm

become destructive and severely modify small crystals even before they can be detected with IL. The smallest NaCl crystal that could be detected by IL had a size of 50 nm × 50 nm × 50 nm [14].

A characteristic spectrum of the emission from NaCl crystals consists of two main emission bands at 2.46 eV and 3.05 eV, and is shown in Fig. 14.7a. As mentioned above, luminescence of alkali halides typically originates from color–centers which are created during ion irradiation. The simplest defects created there are a Frenkel pair of F– and H–centers. An F–center consists of an halide ion vacancy filled with an electron [35, 36]. If an F–center loses an electron, an α–center is formed, which is basically a negative ion vacancy [37]. An H–center is a negative halogen molecular ion ($(\text{halogen})_2^-$) which occupies one anion site [38, 39]. Another kind of primary defect is a self–trapped hole (V_k–center). In this case a $(\text{halogen})_2^-$ ion occupies two adjacent anion sites along the $\langle 1\,1\,0 \rangle$ direction [39–41]. At high defect concentrations clustering and the formation of more complex defects occurs. Also self–trapped

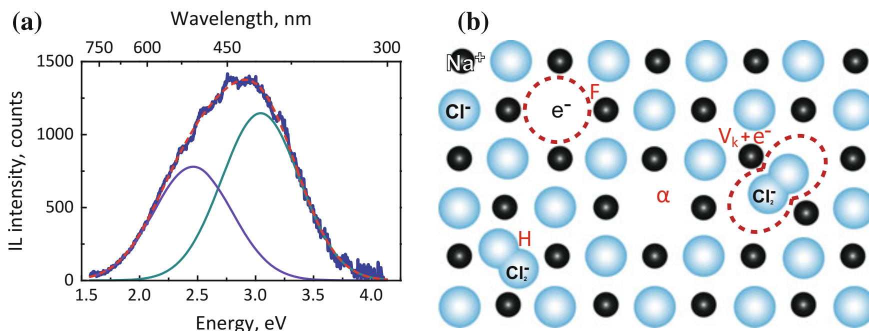

Fig. 14.7 **a** Ionoluminescence spectrum of a NaCl crystal, fitted with two Gaussians. The peaks are centered at 2.46 eV and 3.05 eV. **b** Model of the simplest defects in alkali halides: F–, H–, α–centers and a self–trapped exciton in an on-center configuration [14]

excitons (STEs) are created under ionizing irradiation [34, 36, 41]. An STE can be referred to as a V_k–center with a bound electron [39, 41]. The above discussed crystal defects are schematically shown in Fig. 14.7b.

In the IL studies of NaCl the luminescence peak position was found to vary between samples. Luminescence around 2.4–2.45 eV was consistently observed, and several mechanisms for its origin were proposed [42–45]. However, the most plausible mechanism seems to be a recombination of an electron with a V_F–center (which is a self trapped hole next to a cation vacancy) [14, 46]. The band around 3.05 eV is usually referred to as α–emission [47–50]. This emission originates from the recombination of an F–center electron with a hole (a V_k–center) [37, 46, 50, 51]. This process is equivalent to the recombination luminescence of an STE perturbed by a neighboring α–center [49–51].

14.2.2.2 Tracking Defect Formation Using IL

IL can also be applied to study the dynamics of the defect creation. In order to do so we tracked the IL intensity as a function of ion fluence [14]. The IL signal dependences were recorded at various combinations of beam currents and pixel separations. This can be interpreted as different ion current densities through the sample surface. Typical curves at various beam parameters are presented in Fig. 14.8.

The obtained curves could be divided in two parts. The first one is an initial fast increase. In the second part, the signal either stagnated or slowly increased. Therefore, two regimes were discriminated based on these different behaviours at higher fluencies: stagnation and creep. The experimental curves were fitted using the Weibull growth model [52]. A growth rate equal to 1 was chosen as a criterion for discrimination between the two regimes. Stagnation at a growth rate large than 1, and creep for values smaller than 1. The shape of the curves depends on how the ion

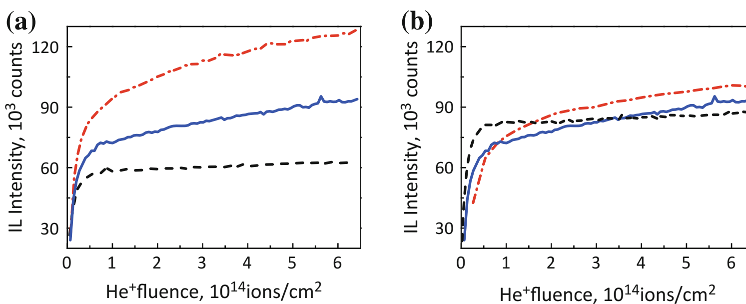

Fig. 14.8 **a** IL signal intensity versus He^+ ion fluence at various currents, but at a fixed 36.7 nm pixel spacing. The He^+ beam currents are 1.9 pA (*dashed black line*), 2.5 pA (*solid blue line*), and 2.8 pA (*dot–dashed red line*). **b** IL intensity versus ion fluence at various pixel spacings, but at a fixed 2.5 pA beam current. The pixel spacings are 64.6 nm (*dashed black line*), 36.7 nm (*solid blue line*), and 18.5 nm (*dot–dashed red line*). In all cases the He^+ beam energy is 35 keV [14]

fluence is delivered to the sample (at which scanning parameters). It was found, that the IL signal stagnated in the case of a low current density, and it demonstrated a creeping behavior for high current densities.

As could be expected, the ultimate IL intensity level was higher for higher ion beam current when all other parameters were fixed. A more careful analysis of the change in the ultimate IL intensity value with increasing beam current revealed that its growth rate was not monotonous. Two linear stages of growth could be easily distinguished. Slower IL intensity growth changed to a more rapid one with increasing beam current. The change of the growth rate occurred at the same experimental conditions at which the above discussed IL intensity vs. fluence curves change their behavior between stagnation and creep.

Recording the fluence dependencies using different color filters placed in the optical beam path helped to verify which emission process is influenced by the variation of the scanning parameters. The intensity of the 2.46 eV band was tracked using a *red* filter (600–700 nm), while the changes in intensity of the 3.05 eV band were observed using a *blue* filter (400–500 nm). The general shape of the IL intensity curve of the 2.46 eV band was not affected by the variation of scanning parameters. However, a clear change in the behavior of the IL signal was observed for the blue 3.05 eV band, which corresponds to α–emission. The fluence dependence switches from *stagnation* to *creep* with increasing beam current. Therefore, α–emission was identified to be responsible for the changes in the behavior of the IL signal.

The intensity of the 3.05 eV band is proportional to the concentration of F–centers [14]. Ion bombardment leads to the creation of F–H Frenkel pairs via both atomic and electronic excitations, and these processes cannot be easily discriminated. In the case of the atomic excitation, a halide ion is displaced in a collision and then an electron is trapped in the formed vacancy. Nevertheless, the color–center production through electronic excitations is more effective [53, 54]. First the exciton relaxation models of the radiation damage in alkali halides were independently suggested by Hersh [34] and Pooley [36] in 1966, and was extensively studied and developed later [41, 55, 56]. During irradiation a Cl^- ion can lose an electron forming a free exciton. A free exciton rapidly transforms into a STE as a result of the bonding of the Cl atom with a neighboring Cl^- ion. An STE in an off–center configuration, where Cl_2^- is displaced along the $\langle 1\,1\,0 \rangle$ direction, subsequently acts as precursor for the F–H pair formation [41, 56]. The radiationless transition of an off–center from an excited state can provide sufficient energy for the displacement of a Cl_2^- ion and the formation of a nearest–neighbor F–H pair. This process of STE conversion into an F–H pair is effective at room temperature [56, 57]. While H–centers are mobile in NaCl already above 80 K [58], F–centers are mobile only above 500 K [59]. Thus, the dynamics of H–centers is key in interpreting the observed results.

Each collision cascade can be considered individually as long as the ion current density is low and the period between two arriving ions is relatively long. With increasing current density the events start to temporally overlap, and the occurring processes are not independent any longer. When the cascade events start to overlap, the high concentration of the H–center, combined with their high mobility, increases the probability for the formation of a Cl_2 molecule [38, 60–62]. This process leads

to a reduction of the number of H–centers. The recombination rate between an F–centers and Cl_2 molecules is much smaller than that between F–H centers. Since the concentration of H–centers that can recombine with F–centers is reduced, the concentration of F–centers is efficiently increased and a subsequent enhancement of the IL signal is observed. A similar effect of enhanced F–center production was observed in the experiments where LiF crystals were irradiated with heavy swift ions [60, 61]. Dislocations are also effective traps for H–centers [47, 62] and can further enhance the F–center formation.

Some discrepancies in the first parts of the curves are apparent in Fig. 14.8b where the pixel separation is varied while the ion beam current is fixed. A shorter distance between neighboring pixels results in the interference of the processes occurring in these areas and complicates the situation. Defects created at the current ion impact position interact with those from the previous one. The balance between F– and H–centers is changed by the H–centers stemming from the previous pixel. They can diffuse into the interaction volume of the current pixel and thereby increase the recombination rate of the F– and H–centers. This suppresses the initial increase of the IL signal.

An overview [see [14] Fig. 7] of the different regimes at various beam currents and pixel separations shows that the transition between the two regimes occurs at increasing pixel spacing with increasing beam current. At higher current the diameter of the volume possessing a high enough H–center concentration is bigger and effects which are a result of the overlap of the interaction volumes start to appear already at large pixel separations.

Thus, HIM allows in–situ monitoring of the defect creation in ionic crystals at high resolution. The defect formation depends on irradiation parameters such as pixel spacing and ion beam current. This is the result of overlap between the interaction volumes of neighboring ion impacts in combination with differences in mobility of the various types of crystal defects.

14.2.3 Other Minerals

Since the first applications of CL in petrology in the middle of the 1960s [63–65], it has been widely used in geosciences [9]. CL is a powerful tool for identification, quantification and localization of trace materials, as well as for characterization of defects and heterogeneities. Ionoluminescence of a selected minerals has been tested in HIM [11, 18].

14.2.3.1 Sapphire

Ionoluminescence of sapphire excited by He^+ ions has been studied previously by Jardin et al. [66] using a 2 MeV ion beam. The authors observed strong IL emission with initially rising intensity with increasing ion fluence due to creation of emission

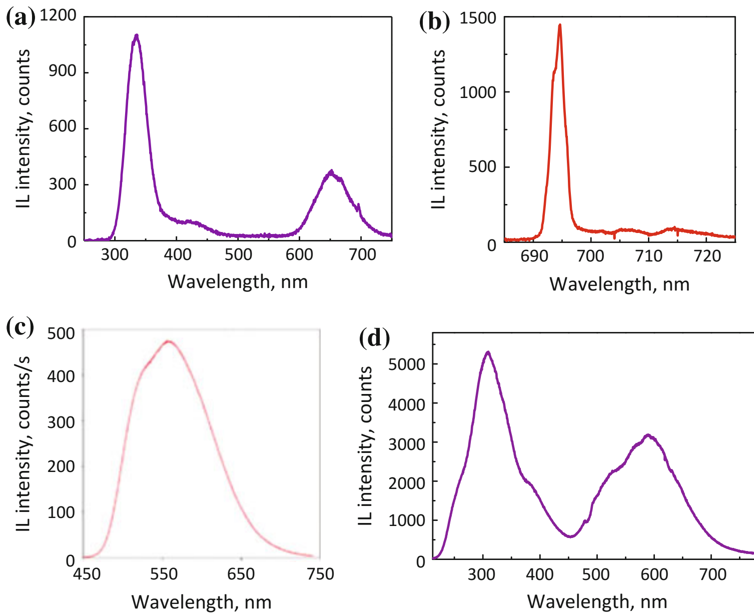

Fig. 14.9 IL spectra of various minerals: **a** sapphire [18], **b** ruby, **c** yttrium aluminum garnet (YAG:Ce) [11], **d** calcium fluorite

centers. At ion fluencies above 2×10^{16} ions/cm^2 the IL intensity started to decrease due to annihilation of emission centers by extended defect formation.

An IL spectrum from sapphire obtained in the HIM is shown in Fig. 14.9a [18]. As expected, the sapphire exhibits luminescence around 415 nm corresponding to the emission from F–centers [67]. An F–center in sapphire (α-Al_2O_3) consists of two electrons, which occupy one oxygen vacancy. However, the by far strongest peak is observed at 330 nm which corresponds to the emission of F^+–centers [66, 67]. Under irradiation an F–center can lose an electron and is converted into an F^+–center [67]. A conversion of F– to F^+–centers with increasing ion fluence was observed by Jardin et al. [66] as well. The authors traced the growth of the 330 nm peak at the expense of the 415 nm peak. A small sharp peak at ~695 nm in the sapphire spectrum in Fig. 14.9a originates from the impurity Cr^{3+} ions [66, 68]. The band at 660 nm is a superposition of the Cr^{3+} N–lines and sidebands (see Sect. 14.2.3.2) with the second–order peak of the 330 nm emission.

14.2.3.2 Ruby

Luminescence of ruby is activated by Cr^{3+} which substitute Al^{3+} ions in α-Al_2O_3 [68, 69]. It is those Cr^{3+} ions which cause the red color of ruby crystals. An IL spectrum from a synthetic ruby measured in the HIM is shown in Fig. 14.9b. Ruby samples

have demonstrated a strong, but degrading IL signal. The obtained spectrum is in good agreement with the literature [68, 69]. It consists of two dominant sharp peaks, so–called R–lines at 693.4 and 694.7 nm, and weak bands, so–called N–lines, centered around 706 and 714 nm. The measured positions of R–lines are 0.6 nm off from the expected values [69], which can be attributed to the error in the calibration of the system. R–lines originate from the transition of Cr^{3+} ions from the first excited state (^2E) into the ground state ($^4A_2$) [68]. The crystal field and spin–orbit coupling splits each of these states into two, leading to a doublet. The appearance of the N–lines is related to the generation of phonons along with the electronic transitions [68].

14.2.3.3 Garnet

Cerium activated yttrium aluminum garnet (YAG:Ce) is known to exhibit intense CL as a result of 5d–4f transitions in the Ce^{3+} ions [70]. A YAG:Ce bulk sample allowed to obtain a sufficiently large IL signal for a spectrum collection and IL imaging at low magnification [11]. The obtained IL spectrum agreed well with CL spectra of similar samples found in the literature [70]. The sample showed a broadband emission centered on a wavelength of 555 nm (Fig. 14.9c). An exposure test performed on the sample revealed an initial drop of the signal. The IL intensity leveled out [11] after reaching a fluence of 10^{13} ions/cm^2. However, a continuous decrease is normally expected with increasing fluence due to quenching of the luminescent centers. The authors also observed an anomalous slight rise of the IL signal with a subsequent decrease. This was attributed to instabilities caused by sample charging.

14.2.3.4 Fluorite

Fluorites (e.g. CaF_2) are well known to exhibit luminescence over a wide range of wavelengths. G. G. Stokes even named the phenomenon of fluorescence after this crystal in 1852 [71]. Light emission from fluorites originates from impurities and a variety of color–centers. Calcium fluorite with 99.99% purity has been shown to exhibit a strong IL signal under the conditions found in the HIM (see SE and IL images of the crystals in Fig. 14.10).

The SE image (left in Fig. 14.10) has a poor quality due to charging of the crystals and the fact that the SE signal is mostly blocked by the IL mirror. Although HIM provides a unique opportunity to image insulating samples using charge compensation (see Chaps. 1 and 6), utilization of flood gun is not possible during IL imaging since its glowing filament would dominate the optical signal. Conversely, the IL image (right in Fig. 14.10) demonstrates a rich contrast.

An IL spectrum obtained from the sample is presented in Fig. 14.9d. It consists of two wide bands, each of which is composed by several peaks. The band around 300 nm is in very good correlation with results obtained by Calvo del Castillo et al. [72], where IL from an ultra–pure synthetic fluorite sample was excited by a 1.8 MeV proton beam. This emission is attributed to the intrinsic crystal defects

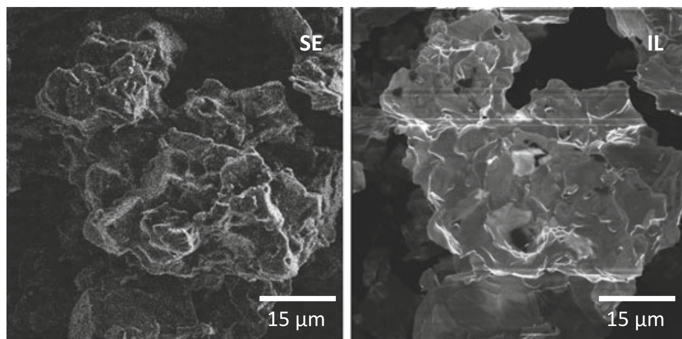

Fig. 14.10 SE (*left*) and IL (*right*) images of CaF_2 crystals. The poor quality of the SE image is caused by the charging of the crystals and the inability to use the charge compensation along with IL imaging. Also, the SE signal is partly blocked by the IL mirror

including recombination luminescence from STEs [73–75]. A V_k–center (F_2^- molecular ion aligned along a $\langle 1\,0\,0 \rangle$ axis) upon capturing an electron, becomes a STE. However, the STE in fluorite cannot be simply regarded as a pair of V_k–center and an electron with the same symmetry as the V_k–center [76]. Various configurations of STEs with different optical properties can be formed in CaF_2 depending on the distance between the components (F– and H–centers) [73].

A wide emission band from M–centers—sometimes called F_2–centers as they consist out of two adjacent F–centers—is centered at ∼580 nm and also contributes to the second band in Fig. 14.9d [77]. The other contributions into the band could be emission from impurities (see e.g. [46]) and complex crystal defects.

14.2.4 Immunofluorescence

Immunofluorescence (IF) is a technique for the visualization of specific proteins or antigens in cells or tissue sections (see e.g. [78]). Generally speaking, biomolecules consist out of four basic elements (H, C, O, N) and are practically impossible to differentiate using traditional light or electron microscopies. IF is based on targeting of specific antigens (molecules of interest) by antibodies that are chemically conjugated to fluorophores. Subsequently, the fluorophores are excited and emit light at a characteristic wavelength which is detected for imaging. Mainly two light microscopy techniques are used for IF: epifluorescence [79] and confocal microscopy [80].

The main advantage of IL imaging over conventional fluorescence imaging would be the absence of diffraction limits that restrict the spatial resolution (about 200 nm). There are several studies of application of a few MeV proton beams for IL imaging of biological samples [81–84]. Norarat et al. [84] have demonstrated a resolution of 150 nm.

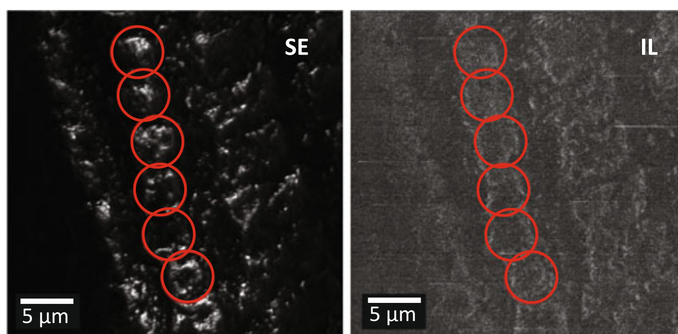

Fig. 14.11 SE and IL images of Alexa Fluor® 488 tagged mouse tooth showing rows of prisms (*prisms circled*) [4]

14.2.4.1 Organic Fluorophores

Fluorescein derivatives are probably the most widely used fluorophores in biological research [85]. A fluorophore has to be functionalized to be used for IF. In the case of fluorescein this is done by adding an isothiocyanate group, forming fluorescein isothiocyanate (FITC) which has an emission maximum at 521 nm in water. Alexa Fluor® 488 dye has almost identical spectral characteristics as FITC, but is known to be more photostable and has a higher quantum efficiency [85]. It is obtained through sulfonation of fluorescein. IL of both of these dyes was investigated by Franklin [4]. Alexa Fluor® 488 was found to be more susceptible to bleaching than FITC when considering the luminescence halving ion fluences. However, it has ∼60 times the quantum efficiency of FITC.

Thereafter, IL imaging of a biological sample—a cross–section of a mouse incisor was performed using Alexa Fluor® 488 for dying. During the process of tooth enamel formation ameloblast cells excrete a protein called amelogenin [86]. These proteins are grouped in structures called prisms, which interweave and eventually mineralize forming enamel [87]. Amelogenin was tagged by Alexa Fluor® 488 for the IL measurements. SE and IL images presented in Fig. 14.11 show the enamel matrix with rows of prisms which are 3 µm to 5 µm in diameter and are apparent in both imaging modes. An IL image of a single 4 µm prism could also be obtained. It revealed approximately 200 nm in diameter luminescent areas which were suggested to be protruding groups of amelogenin strands [4].

14.2.4.2 Rare–Earth Doped Nanoparticles

Inorganic fluorophores such as rare–earth doped nanoparticles were found to be more stable and exhibit a higher quantum yield under an electron beam compared to organic fluorophores [88]. Therefore, their suitability as fluorophores for IL imaging

was tested [4, 11]. Boden et al. investigated Eu and Ce/Tb doped $LaPO_4$ nanocrystals deposited on an aluminum substrate from aqueous solutions. The luminescence from rare–earth doped nanoparticles originates from transitions between f electron states in dopant ions and does not depend on their size.

The SE and IL images of Ce/Tb doped sample are shown in Fig. 6.8a–b and of the Eu doped sample in Fig. 14.12a–b. Luminescence from agglomerates of the nanocrystals is clearly visible in these images. The peaks in the IL spectrum from $LaPO_4$:Eu nanocrystals (Fig. 14.12c) correspond to the transitions of f electrons of the Eu^{3+} dopants from the excited $^5D_0$ state into the ^7F_J $(J = 1 - 4)$ states [11, 89]. Likewise the observed IL emission from $LaPO_4$:Ce/Tb nanocrystals (Fig. 6.8d) originates from the transitions in the Tb^{3+} dopant ions from the excited state $^5D_4$ into the ^7F_J $(J = 2 - 6)$ states [11, 90].

Similar to the previously discussed examples the IL from rare–earth doped nanoparticles also degrades under the exposure to the He^+ beam [11]. Based on the results of exposure tests the authors suggest that there are two mechanisms involved

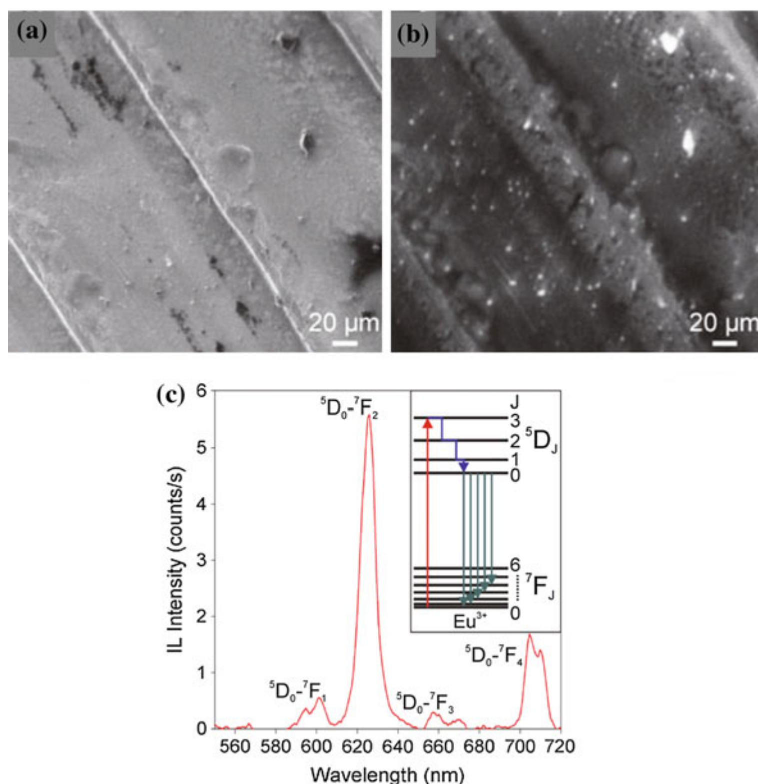

Fig. 14.12 **a** and **b** SE and IL images of $LaPO_4$:Eu nanocrystals respectively. **c** IL spectrum from $LaPO_4$:Eu nanocrystals with inset illustrating f electron transitions in the Eu^{3+} dopant ions

in the quenching of the luminescence. There can be two general mechanisms of IL excitation in rare–earth doped material: direct and indirect. In the case of direct, excitation energy is transferred from an He^+ ion to an f electron of a rare–earth ion. As the result, the electron is excited into one of the D states from where it non–radiatively decays into the lowest D state. Afterwards, it falls back into an F state emitting a photon (see the insets in Fig. 14.12e and f). Indirect excitation occurs via the transfer of energy to f electrons from electron–hole pairs (EHPs) generated in the host crystal by the incoming ion beam. Quenching of the indirect excitation by defect formation can be one of the explanations of the observed IL decay [11]. The defects generated in the crystal by the ion beam act as centers for non–radiative recombination of EHPs reducing the number available for excitation of the rare–earth dopants. As the number of defects increases the indirect excitation mechanism becomes less efficient resulting in the decrease of the IL.

14.2.4.3 Nanodiamonds

Nanodiamonds with nitrogen–vacancy (NV) color–centers appear to be promising biomarkers due to their photostability and cytocompatibility [91]. NV defects consist of a nearest–neighbor pair of a nitrogen atom substituting a carbon atom and a lattice vacancy. IL of nanodiamonds was investigated using nanodiamonds with diameters of 35 and 100 nm [4]. The study has demonstrated that nanodiamond samples are not photostable under ion beam exposure. The IL intensity was halved after a He^+ ion fluences of 2×10^{13} and 4×10^{13} ions/cm^2 for 35 and 100 nm nanodiamonds respectively. Defect generation in nanodiamonds under the ion irradiation eliminates NV color–centers leading to the bleaching of the IL. Despite the small size of the nanodiamonds, sputtering of the particles was found to be not an issue [4]. This is due to the strength of the covalent bonding.

14.3 IL Patterning

The local modification of material properties is an interesting topic since it gives an opportunity to tune the material parameters for one's needs and by doing so design various devices. The sub–nanometer He^+ ion beam available in HIM makes the technique a very attractive tool for such purposes. HIM has been successfully employed for surface patterning and nanofabrication (see part IV of this book for examples). However, HIM can be also applied for precise modification of material properties without creating a detectable change to the sample surface and morphology [15, 92]. As described above irradiation of alkali halides with the He^+ beam causes defect formation and subsequent crystal coloration (see Sect. 14.2.2). Such generation of color–centers with a narrow ion beam gives local control over the defect density and gives the possibility to create luminescent patterns.

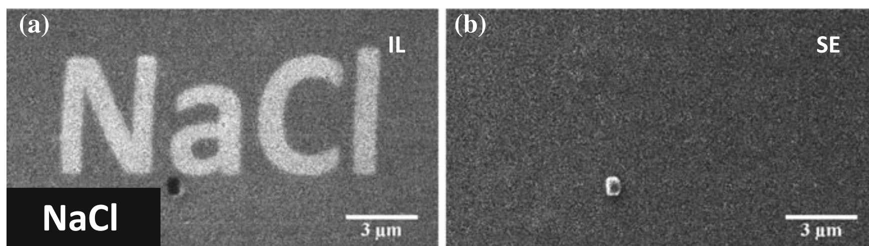

Fig. 14.13 **a** IL and **b** SE images of a pattern in a NaCl crystal. The He^+ beam energy was 35 keV. FOV is 18 μm × 10 μm. The inset in (**a**) demonstrates the desired pattern [15]

An example of such patterning has been published in [15]. A luminescent pattern on a NaCl crystal was created by implantation of only 16 helium ions per nm^2 and using the beam as a high resolution stylus to write the desired pattern. Later, the patterned area was imaged using a much smaller ion fluence. The panchromatic IL and the simultaneously recorded SE images of the patterned area are shown in Fig. 14.13a and 14.13b, respectively. The created pattern is clearly visible in the IL image (Fig. 14.13a). However, no surface damage is observed in the SE image presented in Fig. 14.13b.

Patterned structures created in such way luminesce not only under ion irradiation, but can be excited by any suitable radiation. An example of a pattern created using helium ions and imaged with cathodoluminescence is given in [15]. The CL image shows a better signal–to–noise ratio compare to IL, because higher beam currents could be used in SEM due to the lower destructiveness of the technique.

Some discrepancy in the designed and actual lateral size of the pattern was observed. For instance, the width of the letter *l* in the pattern presented in Fig. 14.13a is ∼1.16 μm, whereas, the desired width was only 1.0 μm. This is a result of the lateral range of the beam due to scattering. As a result the volume affected by the beam is much larger than the beam diameter.

An energetic ion beam preserves its shape in the surface vicinity (a couple of nanometers[1]), however, the beam profile broadens within the material due to nuclear collisions [93]. Additionally, the actual interaction volume relevant for IL is not identical with the size of the volume of the ion induced collision cascades. The generation of electrons by the moving atoms has to be taken into account too. In other words: the minimal possible lateral pattern size is limited by the beam interaction volume with a particular material. Moreover, in the present study, the ion beam itself is used as a probe. For the actual probe size similar considerations as above can be made. Therefore, the convolution of the probe size and the pattern being measured also contributes in the discrepancy in the anticipated and measured size of the pattern.

[1]This is responsible for the high lateral resolution in SE mode.

14.4 Interaction Volume Measurements Using IL

In contrast to SE images in HIM which provide a high surface sensitivity (see Chaps. 6, 9, and 10), the IL signal represents bulk information. Essentially, the IL images are projections of the concentration of light emitting centers on to the sample surface. This allows a direct visualization of the beam interaction volume diameter using IL imaging.

An example of the direct measurement of the lateral size of the interaction volume of the 35 keV He^+ beam with a NaCl crystal is presented in Fig. 14.14a [15]. An array of single pixel impacts was created applying different amounts of He^+ ions by varying the ion beam current and dwell time. Later the patterned areas were imaged using panchromatic IL imaging at a relatively low ion fluence. Each of the four bright spots in the IL image in Fig. 14.14a is a single pixel ion beam impact, but after different amounts of helium were implanted. These measurements allowed to extract the IL spots radial profiles and obtain a correlation between the spot radius and the ion dose (red squares in Fig. 14.14b).

The actual ion beam profile can be neglected due to its extremely small diameter (less than 0.5 nm) and the situation can be considered as a single point impact. The central part of the IL spot—in the vicinity to the ion beam impact point—has a very high defect concentration and is hard to predict and describe. The interaction of the defects and the unavoidable clustering in this area can affect the generation of the IL signal in a complicated way (see Sect. 14.2.2.2). However, the defect concentration in the outer part of the IL profile is low. For this rim area it is valid to assume that the

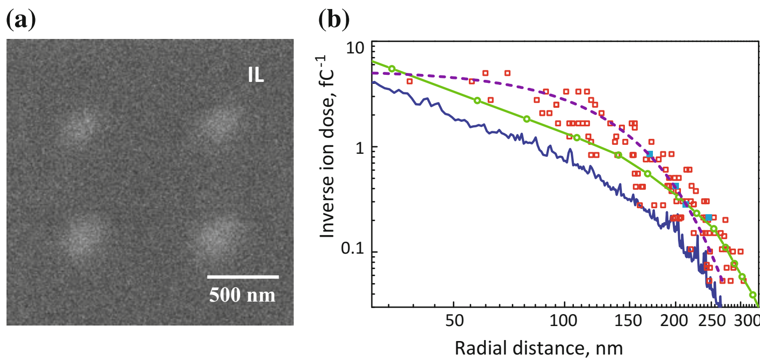

Fig. 14.14 **a** Panchromatic IL image of a NaCl crystal surface after patterning four pixels with a 35 keV focused He^+ beam. Beam current was 4.7 pA. Ion doses, moving by rows from top left corner to the bottom right corner are 7340, 14680, 22020, and 29360 ions per pixel. The imaging was done at ∼200 He^+ ions per pixel. **b** Comparison of the SRIM simulation (*green circles and line*), the fit obtained using (14.3) (*dashed purple line*) and the calculated point spread function (*solid blue line*) from [94] with the experimentally measured radius of the interaction volume (*red squares*). *Solid light blue squares* correspond to the data points from the measurement presented in (**a**) [15]

displacements can be treated as individual non–interacting defects. Therefore, the IL signal should have a linear response to the increase of the ion dose, and the edge of the IL spot profiles can be described by a Gaussian function with the center at the point of incidence and a common standard deviation. The following expression can be written:

$$\frac{\alpha I}{\sigma} \exp\left(-\frac{r^2}{2\sigma^2}\right) = S \tag{14.2}$$

where I is the amount of incident ions, r is the spot radius, σ is the standard deviation, α is a scaling constant, and S the threshold value to obtain a measurable IL signal. From this expression the following dependence of the spot radius on ion dose is derived:

$$r = \sigma\sqrt{2\ln I - B} \tag{14.3}$$

where $B = 2ln(\sigma S/\alpha)$.

The value of σ can then be extracted from the fit of the experimental data with (14.3). It represents the characteristic length scale of the radius of the volume containing the generated defects, or to be more precise, the active emission centers. From the obtained fit, which is shown in Fig. 14.14b as a purple dashed line, σ was found to be 88.3 ± 1.5 nm.

A commonly used tool for the simulation of ion interaction with matter and the associated defect generation is SRIM [95]. As discussed above (see Sect. 14.2.2.1) the dominant IL signal from NaCl is α-emission, which in the end is associated with cation vacancies. Therefore, to predict the dose dependence of the defect generation one needs to find the vacancy distribution. However, SRIM output is available only in the form of a pre–binned 3D vacancy distribution which contains projections of the vacancies on planes which are perpendicular to the surface, while a cross-section of the projection on the sample surface is needed in the current situation. In order to extract this cross-section the full collision data containing details about the generated recoils has to be processed. The vacancy profile obtained in this way shows an extremely high defect concentration at the point of incidence which rapidly decreases with radial distance. It differs from the experimental spot profile which tends to have a bell–shape. This is related to the above discussed unrealistic high defect density at the point of impacts. The vacancy distribution profiles derived from SRIM can be used to predict the spot radius dependence on the ion dose. The minimal defect concentration required for the generation of a measurable IL signal can be estimated from the fit of the obtained dependence to the experimental data. To do so, we computed the vacancy profiles for different ion doses, and then extracted from them the radial distances which correspond to a fixed predefined number of vacancies [15]. In this way a correlation between ion dose and spot radius was derived and is compared to the experimental data in Fig. 14.14b (green circles and line). The obtained curve shows a correct trend. The number of vacancies was optimized for minimal deviations between the fit and data. The best fit was obtained for 3 vac/nm^2, corresponding to about 17 vacancies per pixel. These vacancies are distributed in a direction perpendicular to the surface over the complete interaction volume. Please note that even

at low ion fluences for imaging this pattern the IL signal is collected from a volume which is bigger than the pixel size. Therefore, the experimentally obtained profile is a convolution of the actual defect distribution profile with the probe profile. The influence of the non-zero probe size is more significant at low ion doses, where the spot radii are small (and therefore similar to the probe size). Thus, the IL spot radius will be overestimated for these fluencies (see Fig. 14.14b).

Winston et al. [94] developed a software which combines SRIM and secondary electron generation using a Monte Carlo method for the calculation of the point–spread function (PSF) in the HIM. The PSF provides a spatial distribution of the energy dissipation for a single point impact [96, 97]. Thus, the calculation provides the amount of the dissipated energy per volume unit and ion as a function of the radial distance from the impact point. Since the IL signal has a bulk nature, the dissipation of the energy has to be calculated over a slab with a thickness equal or bigger than ion penetration depth to incorporate the complete collision cascade. The simulated PSF is compared to the experimental results in Fig. 14.14b (blue solid line). It is clear that the PSF underestimates the spot radius. The reason for this underestimation is that the PSF calculation does not take into account the generation of recoils. However, from the above presented SRIM calculations it becomes clear that nearly half of the generated vacancies are created by the recoiling target atoms. This changes the spatial distribution of the energy dissipation. Additionally, no significant difference in shape between the PSF and the curve derived from SRIM was observed at the used ion doses. This is due to the short electron mean free path which is only 1–2 nm in NaCl [98].

14.5 Summary

In this chapter we have shown that the IL signal could be detected from a variety of samples. It could further be used for imaging and spectrum acquisition. However, the IL signal is usually rapidly quenched due to the ion beam induced defect formation. Therefore, in the case of semiconductors a He^+ ion beam is not suitable for the characterization of their electronic structure (Sect. 14.2.1). Nevertheless, the IL technique can be applied for the characterization of the radiation damage. Additionally, it was demonstrated that the stability of the IL signal from the semiconductor samples depends not only on the sample composition, but on its dimensions as well. In general, the IL signal was shown to be more stable from nanostructures than from bulk materials because of the lower defect generation rate.

IL spectra were acquired from several minerals (Sect. 14.2.3). The IL findings are in good agreement with the information previously obtained by other luminescence techniques. However, the IL signal also vanishes with increasing ion fluence.

Several luminescent markers were tested for a possibility of IL imaging of biological samples: organic fluorophores, rare–earth doped nanoparticles, nanodiamonds (Sect. 14.2.4). Unfortunately, they all were found to be unstable under the He^+ ion

beam. Nevertheless, the amelogenin structures in a mouse incisor with diameter of ~200 nm were tagged with Alexa Fluor® 488 and visualized using IL.

The behavior of alkali halides under the ion irradiation is different compared to the above discussed materials: the crystal coloration is observed as the result of the creation of various color–centers (Sect. 14.2.2). The defect formation was studied in details on the example of NaCl in a fluence and rate dependent manner. The damage accumulation was found to depend on the beam scanning parameters since they influence the balance between different defects (Sect. 14.2.2.2). The generation of color–centers was successfully applied for writing luminescent patterns (Sect. 14.3). The minimal size of such patterns is limited by the size of the ion beam interaction volume with the material. Furthermore, the IL technique was used for the visualization of the interaction volume and the direct measurement of its lateral size for the case of NaCl crystal. Finally, the IL signal has a bulk nature which may restrict resolution capabilities of the IL imaging.

Acknowledgments Support from the Dutch Technology Foundation STW, which is part of the Netherlands Organization for Scientific Research (NWO), and which is partly funded by the Dutch Ministry of Economic Affairs is acknowledged.

References

1. A. Marfunin, in *Spectroscopy, Luminescence and Radiation Centers in Minerals* (Springer, Berlin, Heidelberg, 1979), chap. 5, pp. 141–222. doi:10.1007/978-3-642-67112-8_5
2. W. Baird, M. Zivitz, E. Thomas, Phys. Rev. A **12**(3), 876 (1975). doi:10.1103/PhysRevA.12.876. http://link.aps.org/doi/10.1103/PhysRevA.12.876
3. C. White, Nucl. Instrum. Methods **149**(1–3), 497 (1978). doi:10.1016/0029-554X(78)90916-3. http://linkinghub.elsevier.com/retrieve/pii/0029554X78909163
4. T. Franklin, Scanning Ionoluminescence Microscopy with a Helium Ion Microscope. Ph.D. thesis, University of Southampton (2012)
5. B. Valeur, M. Berberan-Santos, *Molecular Fluorescence: Principles and Applications*, 2nd edn. (Wiley-VCH Verlag GmbH & Co. KGaA, 2012). http://dx.doi.org/10.1002/9783527650002
6. U. Scherz, in *Lehrbuch der Experimentalphysik* (1992), pp. 1–107
7. R. Williams, K. Song, J. Phys. Chem. Solids **51**(7), 679 (1990). doi:10.1016/0022-3697(90)90144-5. http://linkinghub.elsevier.com/retrieve/pii/0022369790901445
8. B. Yacobi, D. Holt, J. Appl. Phys. **59**(4), R1 (1986). doi:10.1063/1.336491. http://scitation.aip.org/content/aip/journal/jap/59/4/10.1063/1.336491
9. M. Pagel, V. Barbin, P. Blanc, D. Ohnenstetter (eds.), *Cathodoluminescence in Geosciences.* (Springer-Verlag, Berlin Heidelberg, 2000). doi:10.1007/978-3-662-04086-7
10. P. Townsend, Nucl. Instrum. Meth. B **286**, 35 (2012). doi:10.1016/j.nimb.2011.10.070. http://linkinghub.elsevier.com/retrieve/pii/S0168583X11010305
11. S. Boden, T. Franklin, L. Scipioni, D. Bagnall, H. Rutt, Microsc. Microanal. **18**(6), 1253 (2012). doi:10.1017/S1431927612013463. http://www.ncbi.nlm.nih.gov/pubmed/23237545
12. S. Ogawa, T. Iijima, S. Awata, R. Sugie, N. Kawasaki, Y. Otsuka, Microsc. Microanal. **18**(S2), 814 (2012). doi:10.1017/S1431927612005922. http://www.journals.cambridge.org/abstract_S1431927612005922
13. J. Demarche, D. Barba, G. Ross, G. Terwagne, Nucl. Instrum. Methods B **272**, 141 (2012). doi:10.1016/j.nimb.2011.01.051. http://www.sciencedirect.com/science/article/pii/S0168583X1100070X

14. V. Veligura, G. Hlawacek, R. van Gastel, H. Zandvliet, B. Poelsema, J. Phys. Condens. Matter **26**(16), 165401 (2014). doi:10.1088/0953-8984/26/16/165401. http://stacks.iop.org/0953-8984/26/i=16/a=165401?key=crossref.aa13e4af4cd25fe281ac4640b30baa88. http://www.ncbi.nlm.nih.gov/pubmed/24691214
15. V. Veligura, G. Hlawacek, U. Jahn, R. van Gastel, H. Zandvliet, B. Poelsema, J. Appl. Phys. **115**(18), 183502 (2014). doi:10.1063/1.4875480. http://scitation.aip.org/content/aip/journal/jap/115/18/10.1063/1.4875480
16. V. Veligura, G. Hlawacek, R. van Gastel, H. Zandvliet, B. Poelsema, J. Lumin. **157**, 321 (2015). doi:10.1016/j.jlumin.2014.09.016. http://www.sciencedirect.com/science/article/pii/S0022231314005249
17. S. Pennycook, Scanning **30**(4), 287 (2008). doi:10.1002/sca.20114. http://dx.doi.org/10.1002/sca.20114
18. V. Veligura, Material characterization and modification using helium ion microscopy: various examples. Ph.D. thesis, University of Twente, Enschede (2014). http://doc.utwente.nl/90190/
19. M. Reshchikov, M. H. J. Appl. Phys. **97**(6), 061301 (2005). doi:10.1063/1.1868059. http://link.aip.org/link/JAPIAU/v97/i6/p061301/s1&Agg=doi
20. A. Cremades, J. Piqueras, C. Xavier, T. Monteiro, E. Pereira, B. Meyer, D. Hofmann, S. Fischer, Mater. Sci. Eng. B **42**(1–3), 230 (1996). doi:10.1016/S0921-5107(96)01712-6. http://linkinghub.elsevier.com/retrieve/pii/S0921510796017126
21. M. Herrera Zaldivar, P. Fernández, J. Piqueras, J. Appl. Phys. **83**(5), 2796 (1998). doi:10.1063/1.366634. http://link.aip.org/link/JAPIAU/v83/i5/p2796/s1&Agg=doi
22. M. Herrera, A. Cremades, J. Piqueras, M. Stutzmann, O. Ambacher, J. Appl. Phys. **95**(10), 5305 (2004). doi:10.1063/1.1690454. http://link.aip.org/link/?JAP/95/5305/1&Agg=doi
23. W. Lee, H. Lee, S. Park, K. Watanabe, K. Kumagai, T. Yao, J. Chang, T. Sekiguchi, J. Cryst. Growth **351**(1), 83 (2012). doi:10.1016/j.jcrysgro.2012.04.016. http://linkinghub.elsevier.com/retrieve/pii/S0022024812002825
24. A. Kakanakova-Georgieva, D. Nilsson, X. Trinh, U. Forsberg, N. Son, E. Janzén, Appl. Phys. Lett. **102**(13), 132113 (2013). doi:10.1063/1.4800978. http://link.aip.org/link/APPLAB/v102/i13/p132113/s1&Agg=doi
25. V. Vil'kotskii, V. Pivovarov, J. Appl. Spectrosc. **19**(6), 1604 (1973). doi:10.1007/BF00611068. http://link.springer.com/10.1007/BF00611068
26. T. Zhang, R. Elliman, G. Carter, Nucl. Instrum. Methods **209–210**, 761 (1983). doi:10.1016/0167-5087(83)90880-3. http://linkinghub.elsevier.com/retrieve/pii/0167508783908803
27. R. Livengood, S. Tan, Y. Greenzweig, J. Notte, S. McVey, J. Vac. Sci. Technol. B **27**(6), 3244 (2009). http://search.ebscohost.com/login.aspx?direct=true&db=inh&AN=11023193&site=ehost-live
28. L. Joulaud, J. Mangeney, N. Chimot, P. Crozat, G. Fishman, J. Bourgoin, J. Appl. Phys. **97**(6), 063515 (2005). doi:10.1063/1.1861966. http://link.aip.org/link/JAPIAU/v97/i6/p063515/s1&Agg=doi
29. H. Němec, L. Fekete, F. Kadlec, P. Kužel, M. Martin, J. Mangeney, J. Delagnes, P. Mounaix, Phys. Rev. B **78**(23), 235206 (2008). doi:10.1103/PhysRevB.78.235206. http://link.aps.org/doi/10.1103/PhysRevB.78.235206
30. A. Kamarou, W. Wesch, E. Wendler, A. Undisz, M. Rettenmayr, Phys. Rev. B **78**(5), 054111 (2008). doi:10.1103/PhysRevB.78.054111. http://link.aps.org/doi/10.1103/PhysRevB.78.054111
31. M. Verheijen, R. Algra, M. Borgström, G. Immink, E. Sourty, W. van Enckevort, E. Vlieg, E. Bakkers, Nano Lett. **7**(10), 3051 (2007). doi:10.1021/nl071541q. http://www.ncbi.nlm.nih.gov/pubmed/17887714
32. R. Algra, M. Hocevar, M. Verheijen, I. Zardo, G. Immink, W. van Enckevort, G. Abstreiter, L. Kouwenhoven, E. Vlieg, E. Bakkers, Nano Lett. **11**(4), 1690 (2011). doi:10.1021/nl200208q. http://www.ncbi.nlm.nih.gov/pubmed/21417242
33. V. Veligura, G. Hlawacek, R. Berkelaar, R. van Gastel, H. Zandvliet, B. Poelsema, Beilstein J. Nanotechnol. **4**, 453 (2013). doi:10.3762/bjnano.4.53. http://www.beilstein-journals.org/bjnano/content/4/1/53. http://www.pubmedcentral.nih.gov/articlerender.fcgi?artid=3740815&tool=pmcentrez&rendertype=abstract

34. H. Hersh, Phys. Rev. **148**(2), 928 (1966). doi:10.1103/PhysRev.148.928. http://link.aps.org/doi/10.1103/PhysRev.148.928
35. H. Pick, Il Nuovo Cimento **7**(S2), 498 (1958). doi:10.1007/BF02751492. http://www.springerlink.com/index/M6T258G807GH15Q8.pdflink.springer.com/10.1007/BF02751492
36. D. Pooley, Proc. Phys. Soc. **87**(1), 245 (1966). doi:10.1088/0370-1328/87/1/327. http://stacks.iop.org/0370-1328/87/i=1/a=327?key=crossref.5988e3ad3f8a3678dabafbc8a28098f1
37. A. Onaka, I. Fujita, A. Fukuda, J. Phys. Soc. Jpn **18**(Suppl. 2), 263 (1963)
38. C.R.A. Catlow, K.M. Diller, L.W. Hobbs, Philos. Mag. A **42**(2), 123 (1980). doi:10.1080/01418618009365806. http://www.tandfonline.com/doi/abs/10.1080/01418618009365806
39. V. Puchin, A. Shluger, N. Itoh, Phys. Rev. B **52**(9), 6254 (1995). doi:10.1103/PhysRevB.52.6254. http://link.aps.org/doi/10.1103/PhysRevB.52.6254
40. T. Castner, W. Känzig, J. Phys. Chem. Solids **3**(3–4), 178 (1957). doi:10.1016/0022-3697(57)90023-9. http://linkinghub.elsevier.com/retrieve/pii/0022369757900239
41. A. Shluger, K. Tanimura, Phys. Rev. B **61**(8), 5392 (2000). doi:10.1103/PhysRevB.61.5392. http://link.aps.org/doi/10.1103/PhysRevB.61.5392
42. T. Ukai, N. Matsunami, K. Morita, N. Itoh, Phys. Lett. A **56**(2), 127 (1976). doi:10.1016/0375-9601(76)90169-9. http://linkinghub.elsevier.com/retrieve/pii/0375960176901699
43. Y. Kawaguchi, M. Dawes, S. Langford, J. Dickinson, J. Appl. Phys. **89**(4), 2370 (2001). doi:10.1063/1.1340599. http://link.aip.org/link/JAPIAU/v89/i4/p2370/s1&Agg=doi
44. M. Aguilar, P. Chandler, P. Townsends, Radiat. Eff. **40**(1–2), 1 (1979). doi:10.1080/00337577908234484. http://www.tandfonline.com/doi/abs/10.1080/00337577908234484
45. M. Suchańska, A. Bazhin, E. Konopelko, Phys. Status Solidi B **182**(1), 231 (1994). doi:10.1002/pssb.2221820124. http://doi.wiley.com/10.1002/pssb.2221820124
46. B. Gorobets, A. Rogojine, *Luminescent spectra of minerals* (Ed. WIMS, 2002)
47. R. Webb, L. Jensen, S. Langford, J. Dickinson, J. Appl. Phys. **74**(4), 2338 (1993). doi:10.1063/1.354719. http://link.aip.org/link/JAPIAU/v74/i4/p2338/s1&Agg=doi
48. N. Nesmelov, Sov. Phys. J. **22**(12), 1306 (1979). doi:10.1007/BF01220819. http://dx.doi.org/10.1007/BF01220819
49. T. Timusk, J. Phys. Chem. Solids **26**(5), 849 (1965). doi:10.1016/0022-3697(65)90260-X. http://linkinghub.elsevier.com/retrieve/pii/002236976590260X
50. T. Timusk, W. Martienssen, Phys. Rev. **128**(4), 1656 (1962). doi:10.1103/PhysRev.128.1656. http://link.aps.org/doi/10.1103/PhysRev.128.1656
51. Z. Egemberdiev, A. Elango, S. Zazubovich, Phys. Status Solidi B **97**(2), 449 (1980). doi:10.1002/pssb.2220970208. http://doi.wiley.com/10.1002/pssb.2220970208
52. M. Panik, *Growth Curve Modeling* (John Wiley & Sons, Inc., 2014). doi:10.1002/9781118763971. http://dx.doi.org/10.1002/9781118763971
53. A. Lushchik, C. Lushchik, K. Schwartz, F. Savikhin, E. Shablonin, A. Shugai, E. Vasil'chenko, Nucl. Instrum. Methods B **277**, 40 (2012). doi:10.1016/j.nimb.2011.12.051. http://linkinghub.elsevier.com/retrieve/pii/S0168583X11011700
54. A. Quaranta, F. Gramegna, V. Kravchuk, C. Scian, Nucl. Instrum. Methods B **266**(12–13), 2723 (2008). doi:10.1016/j.nimb.2008.03.195. http://linkinghub.elsevier.com/retrieve/pii/S0168583X08003753
55. Y. Suzuki, H. Abe, M. Hirai, J. Phys. Soc. Jpn. **61**(8), 2964 (1992). doi:10.1143/JPSJ.61.2964. http://jpsj.ipap.jp/link?JPSJ/61/2964/
56. R. Williams, K. Song, W. Faust, C. Leung, Phys. Rev. B **33**(10), 7232 (1986). doi:10.1103/PhysRevB.33.7232. http://link.aps.org/doi/10.1103/PhysRevB.33.7232
57. E. Balanzat, S. Bouffard, A. Cassimi, E. Doorhyee, L. Protin, J. Grandin, J. Doualan, J. Margerie, Nucl. Instrum. Methods B **91**(1–4), 134 (1994). doi:10.1016/0168-583X(94)96203-0. http://linkinghub.elsevier.com/retrieve/pii/0168583X94962030
58. E. Sonder, J. Phys. **34**(C9), C9 (1973). doi:10.1051/jphyscol:1973979. http://www.edpsciences.org/10.1051/jphyscol:1973979
59. W. Soppe, J. Phys. Condens. Matter **5**(22), 3519 (1993). doi:10.1088/0953-8984/5/22/005. http://stacks.iop.org/0953-8984/5/i=22/a=005?key=crossref.7674ae0c6a8d8d31fbb406ac479d2ac0

60. A. Dauletbekova, A. Akilbekov, M. Zdorovets, A. Vassil'eva, D. Akilbekova, Nucl. Instrum. Methods B **268**(19), 3005 (2010). doi:10.1016/j.nimb.2010.05.028. http://linkinghub.elsevier.com/retrieve/pii/S0168583X10004465
61. K. Schwartz, M. Sorokin, A. Lushchik, C. Lushchik, E. Vasilchenko, R. Papaleo, D. de Souza, A. Volkov, K. Voss, R. Neumann, C. Trautmann, Nucl. Instrum. Methods B **266**(12–13), 2736 (2008). doi:10.1016/j.nimb.2008.03.107. http://linkinghub.elsevier.com/retrieve/pii/S0168583X08003777
62. W. Soppe, H. Donker, A. García, Celma. J. Prij J. Nucl. Mater. **217**(1–2), 1 (1994). doi:10.1016/0022-3115(94)90301-8. http://www.sciencedirect.com/science/article/pii/0022311594903018linkinghub.elsevier.com/retrieve/pii/0022311594903018
63. J. Smith, R. Stenstrom, J. Geol. **73**(4), pp. 627 (1965). http://www.jstor.org/stable/30069385
64. J. Long, S. Agrell, Mineral. Mag. **34**, 318 (1965)
65. R.F. Sippel, Rev. Sci. Instrum. **36**(11), 1556 (1965). doi:10.1063/1.1719391. http://scitation.aip.org/content/aip/journal/rsi/36/11/10.1063/1.1719391
66. C. Jardin, B. Canut, S. Ramos, J. Phys. D Appl. Phys. **29**(8), 2066 (1996). doi:10.1088/0022-3727/29/8/002. http://stacks.iop.org/0022-3727/29/i=8/a=002?key=crossref.f8e274fd953d7a65e4ba67e55da4d75e
67. K. Lee, J. Crawford, Phys. Rev. B **19**(6), 3217 (1979). doi:10.1103/PhysRevB.19.3217. http://link.aps.org/doi/10.1103/PhysRevB.19.3217
68. D. Nelson, M. Sturge, Phys. Rev. **137**(4A), A1117 (1965). doi:10.1103/PhysRev.137.A1117. http://link.aps.org/doi/10.1103/PhysRev.137.A1117
69. C. Guguschev, J. Gotze, M. Gobbels, Am. Mineral. **95**(4), 449 (2010). doi:10.2138/am.2010.3291. http://ammin.geoscienceworld.org/cgi/doi/10.2138/am.2010.3291
70. H. Jang, J. Kang, Y.H. Won, S. Lee, D. Jeon, Appl. Phys. Lett. **90**(7), 071908 (2007). doi:10.1063/1.2643064. http://scitation.aip.org/content/aip/journal/apl/90/7/10.1063/1.2643064
71. G. Stokes, Philoso. Trans. R. Soc. Lond. **142**, 463 (1852). doi:10.1098/rstl.1852.0022. http://rstl.royalsocietypublishing.org/content/142/463.short
72. H. Calvo del Castillo, A. Millán, P. Beneitez, J. Ruvalcaba-Sil, T. Calderón, Rev. Mex. Fis. **54**(2), 93 (2008). http://www.scielo.org.mx/scielo.php?pid=S0035-001X2008000200002&script=sci_arttext&tlng=pt
73. E. Chinkov, V. Shtanko, Phys. Solid State **40**(7), 1117 (1998). doi:10.1134/1.1130500. http://link.springer.com/10.1134/1.1130500
74. R. Williams, M. Kabler, W. Hayes, J. Stott, Phys. Rev. B **14**(2), 725 (1976). http://prb.aps.org/abstract/PRB/v14/i2/p725_1
75. C. Görling, U. Leinhos, K. Mann, Opt. Commun. **216**(4–6), 369 (2003). doi:10.1016/S0030-4018(02)02344-1. http://linkinghub.elsevier.com/retrieve/pii/S0030401802023441
76. M. Adair, C. Leung, K. Song, J. Phys. C Solid State Phys. **18**(28), L909 (1985). doi:10.1088/0022-3719/18/28/003. http://stacks.iop.org/0022-3719/18/i=28/a=003?key=crossref.3ea92f06ef2a8a68d3d7681637f4dccf
77. J. Beaumont, A. Harmer, W. Hayes, J. Phys. C Solid State Phys. **5**(12), 1475 (1972). doi:10.1088/0022-3719/5/12/023. http://stacks.iop.org/0022-3719/5/i=12/a=023?key=crossref.bc9dc7967b9183e662acf2bf6fb2b1db
78. J.M. Fritschy, W. Härtig, *Immunofluorescence* (John Wiley & Sons, Ltd, 2001). doi:10.1038/npg.els.0001174. http://dx.doi.org/10.1038/npg.els.0001174
79. D. Webb, C. Brown, in *Cell Imaging Techniques*, Methods Mol. Biol., vol. 931, ed. by D. Taatjes, J. Roth (Humana Press, 2013), pp. 29–59. doi:10.1007/978-1-62703-056-4_2. http://dx.doi.org/10.1007/978-1-62703-056-4_2
80. M. Müller, *Introduction to Confocal Fluorescence Microscopy*, 2nd edn. (SPIE, 2005). doi:10.1117/3.639736
81. J. Pallon, C. Yang, R. Utui, M. Elfman, K. Malmqvist, P. Kristiansson, K. Sjöland, Nucl. Instrum. Methods B **130**(1–4), 199 (1997). doi:10.1016/S0168-583X(97)00182-1. http://linkinghub.elsevier.com/retrieve/pii/S0168583X97001821
82. P. Rossi, C. Di Maggio, G. Egeni, A. Galligioni, G. Gennaro, L. Giacomelli, A. Lo Giudice, M. Pegoraro, L. Pescarini, V. Rudello, E. Vittone, Nucl. Instrum. Methods B

181(1-4), 437 (2001). doi:10.1016/S0168-583X(01)00465-7. http://linkinghub.elsevier.com/retrieve/pii/S0168583X01004657
83. F. Watt, A. Bettiol, J. van Kan, M. Ynsa, R. Minqin, R. Rajendran, C. Huifang, S. Fwu-Shen, A. Jenner, Nucl. Instrum. Methods B **267**(12–13), 2113 (2009). doi:10.1016/j.nimb.2009.03.069. http://linkinghub.elsevier.com/retrieve/pii/S0168583X09003541
84. R. Norarat, V. Marjomäki, X. Chen, M. Zhaohong, R. Minqin, C.B. Chen, A. Bettiol, H. Whitlow, F. Watt, Nucl. Instrum. Methods B **306**, 113 (2013). doi:10.1016/j.nimb.2012.12.052. http://linkinghub.elsevier.com/retrieve/pii/S0168583X13000281
85. I. Johnson, M. Spence (eds.), *The Molecular Probes Handbook: A Guide to Fluorescent Probes and Labeling Technologies*, 11th edn. (Life Technologies Corporation, 2010). https://books.google.com/books?id=djuacQAACAAJ
86. E. Beniash, J. Simmer, H. Margolis, J. Struct. Biol. **149**(2), 182 (2005). doi:10.1016/j.jsb.2004.11.001. http://www.sciencedirect.com/science/article/pii/S1047847704002138
87. T. Jin, Y. Ito, X. Luan, S. Dangaria, C. Walker, M. Allen, A. Kulkarni, C. Gibson, R. Braatz, X. Liao, T. Diekwisch, PLoS Biol. **7**(12), e1000262 (2009). doi:10.1371/journal.pbio.1000262. http://dx.doi.org/10.1371%2Fjournal.pbio.1000262
88. P. Fisher, W. Wessels, A. Dietz, F. Prendergast, Microsc. Today **18**, 8 (2010). doi:10.1017/S1551929510000805. http://journals.cambridge.org/article_S1551929510000805
89. K. Riwotzki, H. Meyssamy, A. Kornowski, M. Haase, J. Phys. Chem. B **104**(13), 2824 (2000). doi:10.1021/jp993581r. http://dx.doi.org/10.1021/jp993581r
90. K. Riwotzki, H. Meyssamy, H. Schnablegger, A. Kornowski, M. Haase, Angew. Chem. Int. Ed. **40**(3), 573 (2001). doi:10.1002/1521-3773(20010202)40:3<573:AID-ANIE573>3.0.CO;2-0. http://dx.doi.org/10.1002/1521-3773(20010202)40:3<573:AID-ANIE573>3.0.CO;2-0
91. A. Cuche, Y. Sonnefraud, O. Faklaris, D. Garrot, J.P. Boudou, T. Sauvage, J.F. Roch, F. Treussart, S. Huant, J. Lumin. **129**(12), 1475 (2009). doi:10.1016/j.jlumin.2009.04.089. http://www.sciencedirect.com/science/article/pii/S0022231309002786. Special Issue based on The 15th International Conference on Luminescence and Optical Spectroscopy of Condensed Matter (ICL'08)
92. F. Röder, G. Hlawacek, S. Wintz, R. Hübner, L. Bischoff, H. Lichte, J. Lindner, J. Fassbender, R. Bali, Sci. Rep. **accepted**, 1 (2015). doi:10.1038/srep16786
93. G. Hlawacek, V. Veligura, R. van Gastel, B. Poelsema, J. Vac. Sci. Technol. B **32**(2) (2014). doi:10.1116/1.4863676. http://scitation.aip.org/content/avs/journal/jvstb/32/2/10.1116/1.4863676
94. D. Winston, J. Ferrera, L. Battistella, A. Vladár, K. Berggren, Scanning **34**(2), 121 (2012). doi:10.1002/sca.20290
95. J. Ziegler, M. Ziegler, J. Biersack, Nucl. Instrum. Meth. B **268**(11), 1818 (2010). http://search.ebscohost.com/login.aspx?direct=true&db=inh&AN=11826951&site=ehost-live
96. T. Chang, J. Vac. Sci. Technol. **12**(6), 1271 (1975). doi:10.1116/1.568515. http://link.aip.org/link/?JVS/12/1271/1&Agg=doi
97. M. Parikh, J. Appl. Phys. **50**(6), 4371 (1979). doi:10.1063/1.326423. http://link.aip.org/link/JAPIAU/v50/i6/p4371/s1&Agg=doi
98. T. Boutboul, A. Akkerman, A. Breskin, R. Chechik, J. Appl. Phys. **79**(9), 6714 (1996). doi:10.1063/1.361491. http://link.aip.org/link/JAPIAU/v79/i9/p6714/s1&Agg=doi

Part IV
Modification

Chapter 15
Direct–Write Milling and Deposition with Noble Gases

Ivan Shorubalko, Lex Pillatsch and Ivo Utke

Abstract The performance of He-FIB milling and direct-write He-FIB induced deposition is compared to the performance achieved by other noble gas ions as well as the more conventionally used beams of electrons and Ga-ions. Experimental results, simulations, and in-depth discussions of mechanisms highlight the peculiarities of each ion species with respect to nanostructuring issues like lateral sputter resolution, sputter rate, damage, amorphization, implantation, high-aspect ratio nanostructuring, deposition rate, chemical composition of deposits, and nanostructure shape fidelity. He-FIB is peculiar with respect to its small primary interaction volume and high secondary electron yield leading to excellent small milling and deposition features. The other noble gas ions perform better than He with respect to unwanted ion implantation (leading to swelling), higher sputter yields, or deposition of purer material from organometallic precursors.

15.1 Nanostructuring with Focused Noble Gas Ion Beams

It was in 2006 when Ward et al. [1] published about the development of a scanning He-ion microscope as a new tool for nanoscale microscopy and metrology and 2012 when Hrincir et al. [2] published about a novel plasma FIB/SEM (focused ion beam/scanning electron microscope) for high speed failure analysis and real time imaging of large volume removal. Being commercially available since then these noble gas based scanning ion microscopes start to re-shape the landscape of

I. Shorubalko (✉)
Empa, Swiss Federal Laboratories for Materials Science and Technology,
Laboratory for Reliability Science and Technology, Ueberlandstrasse 129,
8600 Dübendorf, Switzerland
e-mail: ivan.shorubalko@empa.ch

L. Pillatsch · I. Utke
Empa, Swiss Federal Laboratories for Materials Science and Technology,
Laboratory for Mechanics of Materials and Nanostructures, Feuerwerkerstrasse 39,
3602 Thun, Switzerland

© Springer International Publishing Switzerland 2016

G. Hlawacek and A. Gölzhäuser (eds.), *Helium Ion Microscopy*,
NanoScience and Technology, DOI 10.1007/978-3-319-41990-9_15

nanostructuring and lithography processes after the about half a century lasting dominance of scanning gallium ion microscopes and scanning electron microscopes. Both noble gas source ion microscopes have been pushing the limits with respect to lateral resolution in direct-write nanostructuring (He-ions) as well as throughput for direct-erase nanostructuring by high milling rates (Xe-ions). The newest generation of gas-field ion microscopes can produce focused neon ion beams as well, providing new possibilities for high-resolution nano-fabrication.

Until then focused ion beam nanostructuring was dominated by the availability of bright metal ion sources and focusing ion optics, headed by Ga ion microscopes, for a review see [3], and followed by (comparatively broad beam) Au, Be, Si, Pd, B, P, As, Ni, Sb-ions mainly for implantation purposes [4].

In this chapter we will shortly review the state of the art fundamental understanding of noble gas FIB milling and gas assisted deposition and etching with respect to nanopatterning. Comparison of strengths and weaknesses to the analogous wide-spread nanopatterning techniques using Ga-ion and electron beams will be given. The reader is invited to consult further detailed literature comprising reviews about He-ion deposition [5], ion irradiation induced defects in nanostructured materials [6], and gas assisted nanofabrication with focused electron and ion beams [7] as well as a book with comprehensive details on theory and practice of focused ion beam and focused electron beam nanofabrication [8].

15.2 FIB Milling with Noble Gas Ions

15.2.1 Bulk Material

When an ion hits a solid surface, it loses kinetic energy through interactions with the sample atoms. The transfer of energy from the ion to the solid leads to a number of different processes, see Fig. 15.1:

(i) Sputtering of target atoms, resulting in the direct patterning of the sample.
(ii) Generation of excited surface atoms (ESAs) through the collision cascade having energy less than the surface binding energy of the bulk and can thus not be sputtered, see also Fig. 15.16b.
(iii) Emission of so called secondary electrons (SE) from the target, detection of these results in the main imaging mechanism of He ion microscopy, but also lead to adsorbate dissociation for deposition.
(iv) Local heating, which can thermally dissociate adsorbates and lead to local chemical vapor deposition.
(v) Target material damage and implantation of incident ions, resulting typically in limitations of the patterning technique.
(vi) Backscattering or reflection of incident ions (BSI), these can be detected with a special BSI detector and serve as additional imaging mode in He ion microscopy.

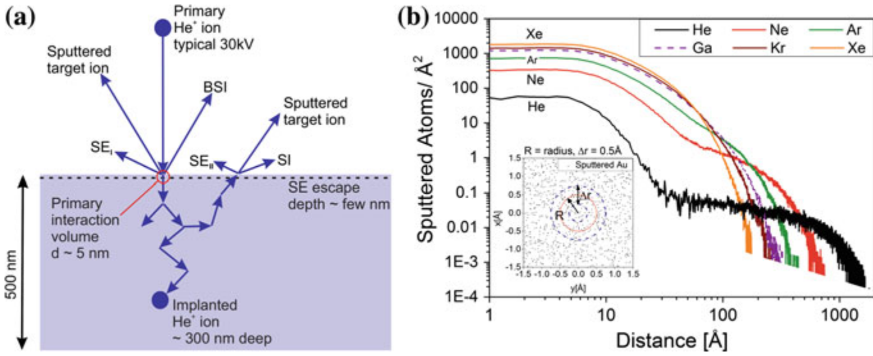

Fig. 15.1 **a** Focused He- ion beam sputtering: a primary and secondary interaction volume can be defined. The first collisions of the primary ion define the primary interaction volume where it generates secondary electrons (SE1), sputtered atoms, or is backscattered (BSI). Penetrating deeper it will be implanted or reflected back to the surface where it can generate secondary SEs and SIs within the surface range of the secondary interaction volume. **b** The radial sputter distribution of 30 keV noble gas ions impinging on gold (with zero diameter beam size) shows that for noble gas ions > Ar a distinction between primary and secondary sputter volume cannot be made anymore. The graph was simulated by SRIM [9] with a radial binning of 0.5 Å

(vii) Electromagnetic radiation which can be used for cathodoluminescence studies and X-ray elemental analysis.

Other effects, such as re-deposition of sputtered ions and material stress are important for understanding the full nanopatterning picture.

It is important to realize that incident ions transfer not only kinetic energy to the target atoms but also momentum obeying both: energy and momentum conservation laws. In such a way, interactions can be elastic and inelastic. During inelastic interactions energy is transferred to the electrons in the sample and results in the emission of secondary electrons and electromagnetic radiation. In elastic interactions, ion energy and momentum are transferred to the target atoms and can result in displacement of these atoms and sputtering from the surface. Sputtered atoms from the surface have momentum oriented in opposite direction to the incident ion. A single binary collision cannot lead to such a result. Thus, sputtering is possible only after a sequence (cascade) of independent binary collision events between neighboring target atoms and enough energy (at least displacement energy) transferred to the next atom during each of these collisions. Finally, if such a displacement collision occurs next to the surface, the recoil atom may be knocked out of the solid and lead to sputtering. For example, for He-ions impinging on gold the typical volume of a region with such collision sequences is approximately 4 nm diameter around the impact point [10]—noted as primary interaction volume in Fig. 15.1a and quantified in Fig. 15.1b. After the first collision the incident ions have enough energy to create more collision events and travel further into the sample (if not backscattered) ending on a certain average depth under the surface (called implantation depth). Some of them, after a sequence of collision events, may

end-up back at the surface and create a point of secondary events: emitting secondary electrons (SEII), sputtered target atoms, and original impact ions escape from the sample (SI), see Fig. 15.1. Excited surface atoms (ESAs) arise from the collision cascade and have energies smaller than the surface binding energy. They are thus not sputtered and remain in the solid but can transfer energy to surface adsorbates for nanofabrication direct-writing purposes. The yield of ESAs and sputtered atoms per primary ion for a specific target and ion energy can be quantified by SRIM calculations, see Fig. 15.16b.

The distance of these secondary event points from the impact point (secondary's distance) is a very important parameter. It makes helium ion beam interaction with solids special comparing to other ion species.

Figure 15.2 compares SRIM [9] simulated interaction volumes and implantation depths of the noble gas ions impinging with 30 keV normal on planar silicon. As can be seen, the mass (size) of the incident ions defines the implantation depth. The smaller the mass, the deeper and broader ions penetrate. Smaller collision cascade volumes mean that the implanted energy *density* by the primary ions becomes very high which in turn results in increased sputter yields as well as the increased yields of excited surface atoms for heavier ions, see Table 15.2.

Increasing sputter yields and decreasing interaction volumes are a result of the increasing nuclear stopping power from He to Xe, compare Fig. 15.3a. There is

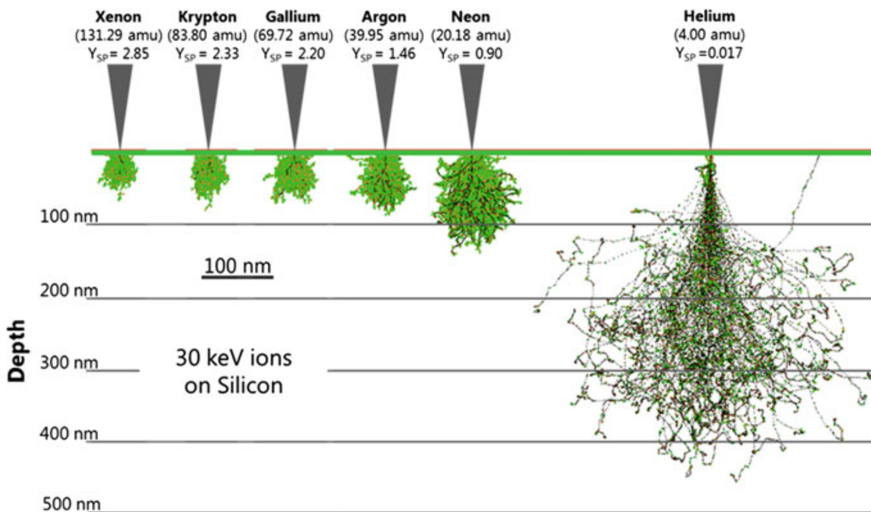

Fig. 15.2 Cascade simulations with SRIM [9] of noble gas ions impinging on bulk silicon with 30 keV energy in comparison to Ga ions. Sputter yields Y_{SP} are indicated. The simulated impinging beams had zero diameters. Trajectories of primary ions are *black* while the *green do*ts are collisions between recoiling target atoms. The *red dots* signify target atoms knocked from their lattice by the incident primary ion. Note that for He-ions the implantation depth is far below the substrate surface and that the collision cascade of the target atoms for noble gas ions > He is far more laterally extended at the surface around the impact point of the primary focused ion beam, yet with comparatively low intensity as quantified in Fig. 15.1b

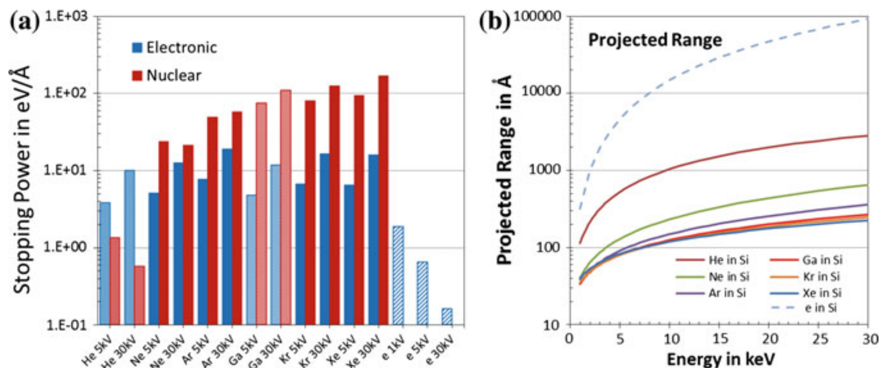

Fig. 15.3 Comparison of ion and electron interaction with a silicon substrate. **a** Stopping powers at 5 and 30 keV; note that the ratio of electronic to nuclear stopping power is >1 for the He-ions. **b** Comparison of the average projected ranges of noble gas ions versus electrons and Ga ions; 5 keV electrons have an interaction volume comparable to 30 keV He-ions, while 1 keV electrons have an interaction volume roughly comparable to 30 keV Ar, Ga, Kr, and Xe-ions

about an order of magnitude difference in the cascade dimensions of He ions and the remaining noble ions (including Ga ions) as can be seen in Fig. 15.3b. Consequently, the main peculiarity of helium ion interaction with solids is a large difference between the high interaction intensity within the primary interaction volume radius (few nm) and the low interaction intensity within the secondary interaction volume radius (about 100 nm), see Fig. 15.1b. For the heavier mass ion species Ne and Ar primary and secondary interaction volumes can still be defined while for Ga, Kr, and Xe the length-scales of primary and secondary interaction volumes overlap resulting in larger sputtering feature size than for Helium ions.

The majority of the primary ions is implanted at their final trajectory position and will be only able to change their position by solid state diffusion. For instance, out diffusion of implanted He from Si at practical rates was observed only above 650 °C [11]. Thus He-ion patterning at high doses can lead to He-blisters due to sub-surface implanted He [12] especially during initial stages of gas assisted pillar deposition [13]. The subsurface concentration of implanted ions below the sputter front depends on the sputter yield. Smaller implantation volumes (ion ranges) for the heavy ions imply that the implanted ions will be partly sputtered away during the milling process and may also out diffuse faster as the collision cascade allows for faster diffusion in the amorphized volume. In contrast to other ions, implanted noble gas ions do not electronically dope the material. The issue of secondary electron generation (or electron implantation if electrons were used as primary charged particles) is less important as they rapidly recombine with the related holes or into the electronic band structure of the material.

Properties of the target sample may strongly influence the FIB nano-pattern shape. The most important are listed below, see also [7] and references cited therein:

(i) The mass of the target atoms and its elemental composition. It can change substantially the interaction volume, sputtering yield, patterning resolution, and even sputtering selectivity with respect to the constituent compound elements. Some elements can be sputtered easier than others leading to non-stoichiometric compositions.
(ii) Crystallinity and crystal orientation. Different types of crystal lattice planes may have different sputtering properties. Crystal orientations aligned parallel to the ion beam result in the so-called channeling effect. Incident ions can penetrate much deeper into the sample and the sputtering yield decreases dramatically.
(iii) Surface morphology. Usually, sputtering yield is increasing when the incident ion beam angle to the sample surface is deviating from the normal incidence. Thus, original roughness of the target surface may evolve in even rougher and difficult to predict structured surface.
(iv) Electrical conductivity. Most of the FIB-milling studies in literature are reported for conductive samples, where no problem of charging is present. The non-conductive samples may give rise to a number of patterning problems. The major one is generation of strong local electric fields that effect ion trajectories and re-deposition mechanisms. Another practical problem is a strong deterioration of imaging quality. Even if nano-patterns are written by FIB, the direct SE-imaging has difficulties to reveal it. In such a way it becomes difficult to adjust patterning parameters.

Apart from material properties, the final shape of the nanopattern strongly depends on re-deposition of sputtered material on high aspect ratio structure side walls as present in groove, pit and hole geometries. Illustrative example of shape fidelity can be found in Rommel et al. [14], where spiral scans (inwards and outwards) and serpentine scans were compared to nanopattern a micropillar structure in Si with Ga-FIB. Simulation tools for sputter shapes were discussed for instance by Kim and Hobler [15] and the role of reflected primary ions with grazing incidence angle on steep slopes considered for Ar-ion milling in Si [16]. With respect to the disadvantages of deep He-implantation (sub surface damage) and low sputter yield during He-ion nanofabrication, Ne-ion sputtering is now more intensively investigated and modeled [17], see also Sect. 15.2.1.1.

15.2.1.1 Sputtering Resolution and Yield: He FIB

As already mentioned above, one of the main advantages of direct nano-structuring by He-FIB comparing to other ion-species-FIBs is its superior resolution. SRIM simulations on gold bulk material in Fig. 15.1a show that the main sputtering of target atoms occurs in a 4–5 nm diameter size area around the incident point (for a zero diameter beam) where the intensity of sputter atoms drops by about a factor of 100. This is the so called primary interaction volume. Experimental studies support the SRIM predicted resolution value. Figure 15.4 shows examples of

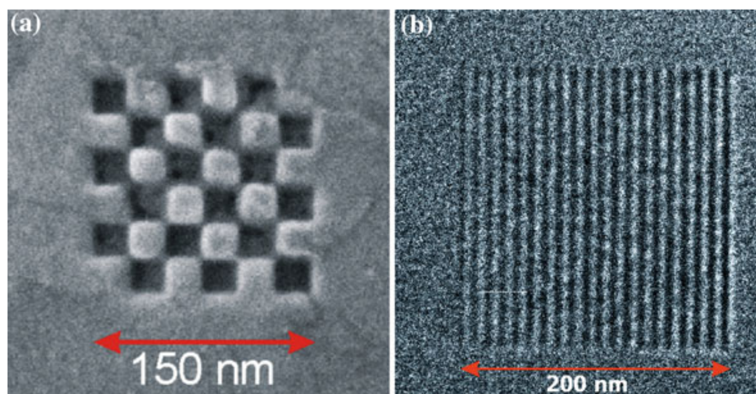

Fig. 15.4 He-FIB patterning resolution. **a**, **b** He-ion microscope images of high resolution nano-patterns created in gold by He-FIB. The period of the lines in (**b**) is 10 nm, the width of the trenches is ~5 nm. The depth varies between 0.5 and 10 nm with a step of 0.5 nm from the *left* trench to the *right*

high-resolution patterns in gold created by He-FIB. 25 × 25 nm squares were milled in a chessboard order in a 50-nm-thick gold layer on silicon, see Fig. 15.4a. The gold is almost fully removed in the milled areas. The darker spots correspond to the Si substrate. The milling inhomogeneity arises from the polycrystalline structure of the gold film. Thus, the image shows not only high resolution but also a potential to create well-defined 2:1 aspect ratio structures (25 × 25 nm wide and 50 nm deep). Figure 15.4b shows 20 trenches created in gold with a period of 10 nm. The most left trench has been written with one loop exposure and each next one has an addition of one extra loop with the same dose, ending with the most right trench having 20 loops of exposure. Knowing the exposure dose (beam current 0.8 pA, pixel spacing 0.5 nm, dwell time 200 µs per pixel, results in 4×10^5 ions per 200-nm-long line and loop) and sputtering yield of 30 keV He-ions in gold (=0.07), the estimated depths of the trenches range from 0.5 to 10 nm (left to right). As can be seen the trench widths are about 5 nm which agrees very well with the SRIM simulated value in Fig. 15.1b taking into account the finite (typically 0.5 nm wide) He-ion beam diameter. The different trench depths illustrate a possibility to create 3D structures with direct FIB sputtering. This is one of the important advantages of the technique compared to lithographic patterning and parallel etching via a mask. As a final remark for the patterning resolution we would like to note that, in some cases, the trench width can be reduced because of the redeposition effect. The hill between the trenches may become in principle a nanometer sharp, as has been demonstrated even by conventional Ga-FIB direct milling technique [18].

Another important parameter of any direct FIB writing technique is the sputter yield. In this respect He-FIB has the lowest sputter yield compared to other FIB ions. Figure 15.5 shows an experimental determination of the sputter yield of helium ions on gold. The experiment has been performed in the following way: Boxes with a side length of 100 × 100 nm were milled into a gold film by a

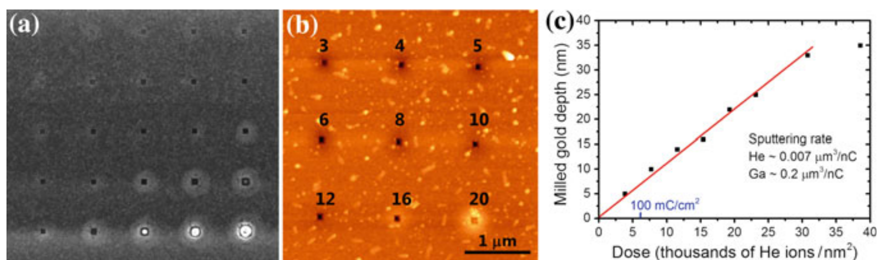

Fig. 15.5 He-FIB gold sputter yield determination. **a** HIM image of He-ion exposed array of 100 × 100 nm boxes with different doses. **b** 4 × 4 µm AFM image of upper right area of (**a**). Note the halo effects of substrate swelling for the dose factor of 20. **c** Experimental gold sputtering yield by 30 keV He ions. Note that the linear dependence saturates with dose; this is due to the swelling effect

30 kV, 1.2 pA He-ion beam with different doses. The reference dose (dose factor = 1) was defined by an exposure dwell time of 5 microseconds per pixel, a step size of 1 nm, and number of loops = 100 corresponding to a dose of 60 mC/cm^2 or 3750 He ions per nm^2. The entire exposed pattern was an array of 5 × 5 boxes, Fig. 15.7a. The dose factor was increased for each box by increasing the number of exposure loops: the top line boxes had dose factors from 1 to 5 from left to right which were multiplied by 2 on the vertical axes. In such a way doses with factors between 1 and 80 were covered with some boxes exposed twice with the same dose. Atomic force microscopy (AFM) was used to determine the depth of each milled box. Figure 15.5b shows an AFM image of the upper right part of the array with numbers corresponding to dose factors for each box. The depth of the milled gold structure versus the helium ion dose is plotted in Fig. 15.5c. The slope of the curve gives an experimental sputter rate of 0.007 µm^3/nC (for comparison, Ga sputters at about 0.2 µm^3/nC and is thus approximately 30 times larger). Taking into account the gold density we arrive at the sputter yield of ~0.07 gold atoms per 30 keV He ion. The low sputter yield and small beam current make He-FIB direct writing a slow technique. On the other hand this is by far compensated by offering the most precise FIB direct sputtering. Creating small nanostructures by He-ion FIB still takes affordable amount of exposure time for academia purposes.

15.2.1.2 Sputter Resolution and Yield: Xe and Ne FIB

The reverse scenario to He-FIB, namely high throughput sputtering (and thus high sputter yield) and moderate to low lateral resolution was realized by the scanning Ga-ion microscope and, more recently, the Xe-ion microscope. Ga-ions, delivering orders of magnitude higher sputter yields compared to He-ions while maintaining a 20 nm resolution in Au as was shown by [10]. If low lateral resolution of *micrometer size* is not an issue and rather large volumes are required to be milled, then Xe-FIBs are even more advantageous. At high ion currents the sputter rates of Xe-FIB sources with respect to Ga-FIB sources can be 30 to 50 times higher which

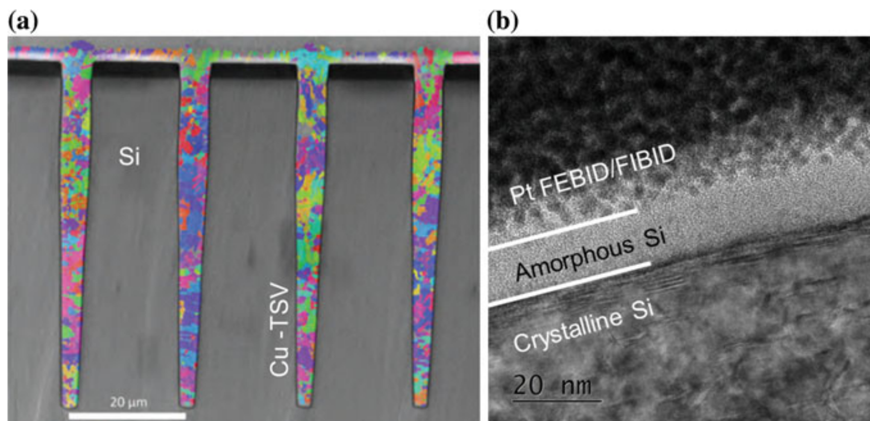

Fig. 15.6 **a** Xe Plasma FIB cross sectioning of through-silicon-vias (TSV) filled by copper and in-situ polished for backscattered electron diffraction (coloured overlay showing polycrystalline grain orientation). Modified from [19]. **b** TEM image of the amorphous damage of Si surface after polishing it tangentially by Xe ion beam at 30 keV beam energy and probe current 100 pA: A—Si lattice, B—the amorphous layer created by Xe ion beam milling, C—Pt FEBID and FIBID protection layers. The measured thickness of the damaged layer is 13 nm. Modified from [20]

makes them an ideal tool for cross sectioning. An example of a through-silicon-via cross section [19] is shown Fig. 15.6a. The considerable increase of the sputter rate of gallium versus xenon FIBs cannot be attributed to the increase in nuclear stopping power, see Fig. 15.3a, as this results only in an increase of about 1.2 in sputter rate in Si according to Fig. 15.2. The high sputter rate is rather related to the higher Xe ion current (up to 2 μA into a spot of about 1–2 μm size) compared to the Ga-ion current that is limited to about 100 nanoamperes at these spot sizes [2]. Besides, the Ga ion current is usually limited to around 60 nA maximum beam current in standard Ga FIB machines. On the low current side, the Xe-FIB can still be used to pattern (or polish) with a beam size of about 40 nm using sub-pico ampere currents [2].

Interestingly, damage during lamella preparation can be reduced when using 30 keV Xe-ions compared to 30 keV Ga-ions. Hrincir et al. [20] showed that TEM sample preparation by a Xe ion beam causes less amorphous damage and increased the quality of the lamella while doing the finish even at 30 keV, without the final cleaning step at the low beam energy, see Fig. 15.6b. A final polishing step by the Xe beam at beam at 3 keV energy further reduces the amorphous layer, but the difference against Ga beam is not as significant as at 30 keV.

The high current capability of 2 μA at 30 kV for plasma FIB sources of Xe and Ar from Orsay Physics also proved to be advantageous for deep depth profiling of FIB secondary ion mass spectrometry: a 250 μm × 250 μm crater in Si can be sputtered to 140 μm depth in 1 h while taking trace element profiles of Li, Na, K and implanted B. According to [21] this capability cannot be overstated as opens the door for SIMS profiles taken to 100 μm depth.

Neon focused ion beam nanopatterning is rather a new technique, recently commercially available by the Zeiss ORION NanoFab machine. The main historical reason for producing a Ne-FIB was actually the fact that already the He-FIB was capable of operating with Ne gas. Also the idea of having a sub-1-nm diameter Ne-ion beam (as for He-ions) capable to mill materials with sputter yields of at least an order of magnitude higher, see Fig. 15.2, was the main driving force in this development. The amount of work done by Ne-FIBs by now is still quite limited. Nevertheless, the main features of the Ne-FIB direct nanostructuring were already studied [22–24]. As expected, the sputtering yield is smaller than for Ga and larger than for He-FIBs. Concerning the resolution of direct nanopatterning it turned out to be substantially lower than He and comparable to Ga-FIB [22]. This can also be expected from the interaction profile of the Ne-beam with targets calculated in Figs. 15.1b and Fig. 15.2. As inert gas, Ne is not expected to dope substrates. Thus applications in circuit editing, failure analysis [24] and in other general non-doping nano-modification processes (for example in the field of plasmonics) can be foreseen for Ne-FIBs.

15.2.1.3 Limitations and Unwanted Artifacts

As explained above, one of the features for He-FIB at 30 keV is a large, about 100 nm radius distant, area of secondary effects around the He-ion impact point when sputtering gold atoms, see Fig. 15.1b. This is in contrast to Ga ions where primary and secondary sputtering distributions cannot be separated in intensity. While for He ions the primary sputter distribution is sharp (note the double logarithmic scale in Fig. 15.1b) it is very shallow for Ga-ions in comparison. This is the main reason why He-FIB milling has such high lateral resolution. The long range order sputtering for He-ions can also be observed experimentally when large doses are involved, see Fig. 15.7. The dark areas around the milled boxes indicate removed gold and their size is ~300 nm. Taking into account the size of the box (100 nm) it agrees well with the calculated values. The AFM profile indicates that the unwanted material removal around the area of interest can be even a couple of nm deep. For many nanopatterning applications this effect is probably tolerable but for some it may be really crucial; for example, when patterning nanoribbons in supported graphene one has to keep in mind that all graphene in a radius of ~100 nm around the patterning point will be damaged [25, 26]. This may dramatically deteriorate electrical properties of the final nano-devices.

Secondly, an important drawback of the He and Ne-FIB milling technique is the subsurface damage at sufficiently high irradiation doses [12, 24]. The critical dose for substrate swelling can be determined from Fig. 15.5b. For doses with the factor lower than 10 no swelling is observed in gold. At dose 12 no dark region around the box is observed and at dose 16 a clear swelling effect appears. The swelling then grows very quickly and at dose 20 basically it overtakes the sputtering effect. At higher doses, swelling and crack formation (dose 80, Fig. 15.5a right lower box) starts. The observed swelling behavior (with dose threshold) is easily

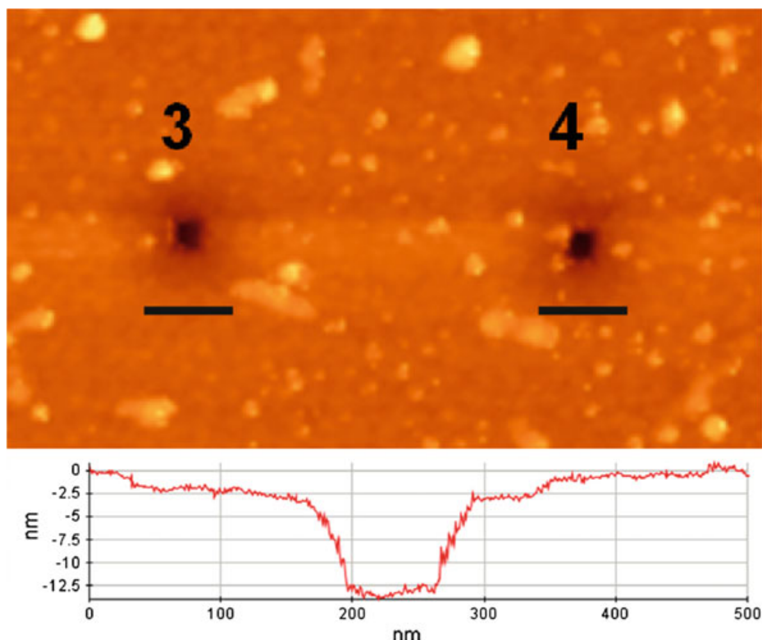

Fig. 15.7 Surface damage by the secondary interaction volume. AFM image of 100 × 100 nm He-FIB exposed boxes (see also Fig. 15.5) and AFM profile through the *left* box (dose 3). Dose factor 3 corresponds to 11250 He ions per nm^2 and dose factor 4 to 15000 He ions per nm^2. A 300 nm sized shallow pit of ~2 nm depth is visible around the 13 nm deep box. The 2 nm deep pit is an experimental evidence of gold sputtering due to the collision cascade effect. *Bars* on the image are 300 nm

distinguishable from contamination deposition effect. No dose threshold is observed as it is for contamination deposition under a charged particle beam. Part of the implanted helium (or neon) may diffuse out but largely stays at interstitial positions between the substrate atoms. In such a way, no swelling occurs until a critical dose of helium is accumulated and enough stress is built to break the substrate. Then, the so called bubble formation process starts and moves the substrate material up until it starts to crack and break [12]. Thus, the above mentioned critical dose depends on the ratio of incident ion beam dose rate to helium outgassing rate from the substrate. The helium diffusion coefficient in its turn depends on substrate material and temperature. An increase of the substrate temperature to 650–700 °C resulted in the avoidance of swelling, bubbling, and damage effects for Si and $SrTiO_3$ [11]. The critical accumulated stress depends also on substrate material and temperature, usually related to the ductility of the material. The interdependence of all of these parameters makes it difficult to precisely determine the critical He implantation dose for each individual case. For the case presented above, the dose factor 20 corresponds to a total of 7.5×10^8 He-ions implanted per 100 × 100 nm box. The visible swelling due to implanted helium atoms is broadened by another ~150 nm

to all sides. The implantation volume is estimated to be ~400 nm in diameter and ~300 nm in depth, resulting in ~4 $\times$ 10^7 nm^3. Thus, the estimated implantation dose is ~2 $\times$ 10^{22} ions/cm^3. This is as much as the density of atoms in liquid helium and almost as large as a typical density of atoms in a solid. The number serves as a good estimate of a maximal He-ion dose that can be applied for a useful nanopatterning.

15.2.1.4 Examples of Applications

Main applications of He-FIB direct nanopatterning are those aiming at high resolution, no electrical doping, and small volume sputtering. Presently, plasmonics is the field that exploits He-FIB nanopatterning the most. The main goal of plasmonics is controlling light on the sub-wavelength scale, in reality down to the one nm-scale. For this purpose very precise control over metallic nanostructures is needed. Even small changes of plasmonic geometries will change significantly its optical properties. Figure 15.8 shows an example of gold dipole plasmonic antennas fabricated with a focused He-ion beam. The main advantages of this fabrication method are its reliability and reproducibility compared to other fabrication techniques. The designed gap width is precisely created in gold at scales down to 5 nm [27]. Up to now this is the only technique that is capable of easy engineering approach for fabricating such nanostructures.

Plasmonic structures in materials different than gold were also successfully demonstrated by means of He-FIB milling. An example of a silver split-ball resonator is presented in [28]; optical properties of such plasmonic structures were carefully analyzed and a good agreement to the theoretically expected properties was found. Figure 15.9a shows a comparison of Ga- and He-FIB direct-write fabricated plasmonic nano-resonators in gold. Below each image an optical spectral response (a resonance curve) is indicated. Only the He-FIB manufactured resonators reached the theoretical quality factor for such structures [29]. One way to modify optical properties of dipole nano-antennas is loading it by a small resistor, i.e. creating a small electrically conductive bridge between the two main parts of a dipole antenna. Changing the geometry of this bridge will change its electrical conductivity and therefore the total plasmonic resonance. Figure 15.9b shows an example of progressively loaded (by a bridge) dipole plasmonic nanoantennas.

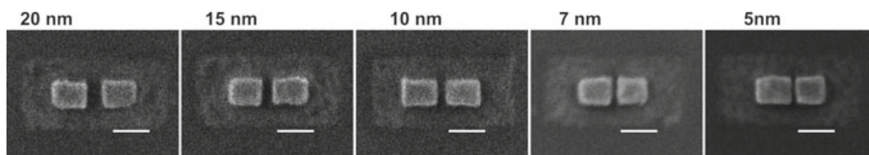

Fig. 15.8 Gap on demand. Helium ion microscope images of He-FIB fabricated gold plasmonic dipole-antennas with a gap width down to the 5-nm-scale. The gap distance is noted on top of the image. *Scale bars* are 50 nm

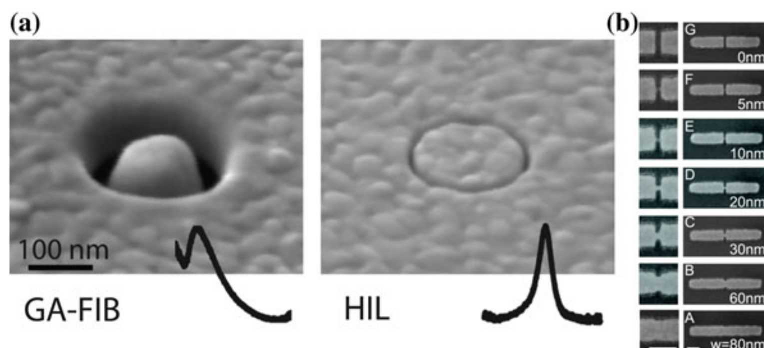

Fig. 15.9 Examples of plasmonic structures fabricated using He-FIB milling. **a** Coaxial plasmonic nanoresonators fabricated by Ga- and He-FIB milling in gold. The *black curves* represent optical response spectra, which show a sharp resonance peak for the He-FIB milled structure while broad double peak resonances were obtained from the Ga-FIB structure. Reprinted with permission from [29] Copyright 2013 American Chemical Society. **b** Progressively loaded plasmonic nanoantennae fabricated in gold, *scale bars* are 100 nm. Reprinted with permission from [31] Copyright 2013 American Chemical Society

Both, the connecting bridge width and height can be controlled by He-FIB milling. In such a way He-FIB direct-writing opened a path to study small and complex plasmonic geometries. The number of reported plasmonic structures created by He-FIB milling increased over the past years. An example of using such antennas for applications in nonlinear optics was reported in [30].

Narrow gaps in metals find their applications also in molecular electronics. Two metal areas separated by a few-nm-trench can serve as electrodes for electrical characterization of molecules trapped in the gap. Recently, it was demonstrated that such electrodes can be fabricated from individual carbon nanotubes by He-FIB: a gap as small as ~ 3 nm could be reproducibly milled into metallic carbon nanotubes [32].

Magnetic materials are known to be difficult for precise nanostructuring. Standard electron beam lithography has problems with such samples because of electron beam distortion by local magnetic fields. He-FIB suffers much less from these local magnetic fields because the mass of the He-ion is much higher than the electron mass. Thus, He-FIB is capable of structuring magnetic materials with a precision down to sub 10 nm scale as is shown for a FeCo-tip in Fig. 15.10. Interestingly, these structured magnetic materials still exhibit their magnetic properties indicating that the damage level is tolerated [33].

Another growing field for FIB applications is small-scale fracture mechanics. In typical fracture toughness experiments a micrometer-sized cantilever is prepared by a FIB. Then a sharp notch (a trench) is fabricated on the anchored side of the cantilever. The mechanical part of the experiment itself takes place in an SEM where displacement can be visualized. Pushing the unanchored side of the cantilever with a diamond probe will eventually result in a fracture of the cantilever at the notch position. By those experiments, local fracture toughness values can be extracted. Figure 15.11 shows images of three notches fabricated by Ga, Xe, and

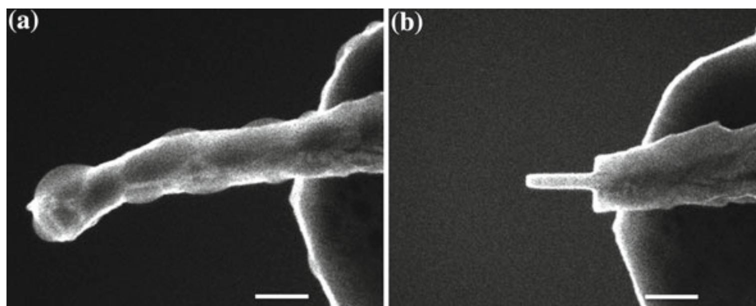

Fig. 15.10 Magnetic FeCo tip modification. **a** Image before, and **b** after nanostructuring by He-FIB. *Scale bar* is 200 nm

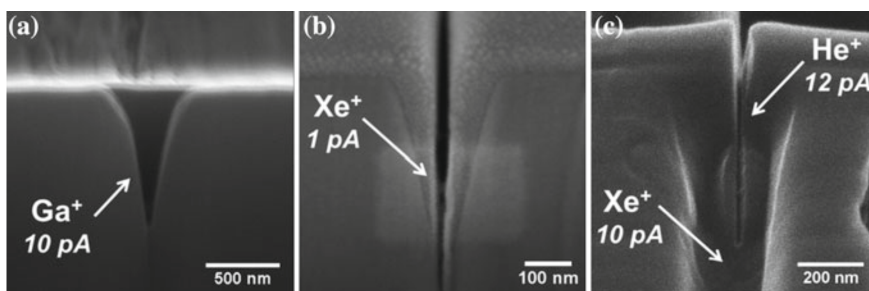

Fig. 15.11 Images of notches fabricated using different FIBs at 30 keV. SEM cross-section views of **a** 10 pA Ga-beam and **b** 1 pA Xe-beam. **c** He-ion microscope image of a 10 pA Xe notch with a thin, 12 pA He milled notch at the center to demonstrate the relative sputtering sizes. From [34]. Reprinted with permission from AAAS

He FIBs. The typical root radii of the notches are 15–25 nm for a 10 pA Ga-beam, 35–50 nm for a 1 pA Xe-beam, and <5 nm for a 12 pA He-beam. The depth of the notches can be well controlled for Ga and Xe beams. With the He-FIB, notches of only ~200 nm depth could be achieved. Attempts to create deeper notches by He-FIB resulted in He bubble formation due to high dose implantation. All three notches showed different values for the measured fracture toughness [34]. This highlights the influence of ion-material interactions not only with respect to implantation depth, see Fig. 15.2, but also in creating residual stress or embrittlement in the small volumes around the notch root. Further investigations are needed in order to understand the cause of the observed variance.

15.2.2 Membranes

An aspect of importance in FIB nano-structuring that rose recently is the thickness of the target sample. From Fig. 15.2 it becomes clear that two characteristic length

scales are involved in sputtering of bulk material: the ion implantation depth and the primary interaction radius. In the following we will describe two types of membranes: thin membranes which are thinner than the primary interaction radius (typically < about 4 nm for 30 keV He ions) and thick membranes which are thinner than the ion implantation depth (typically < about 300 nm for 30 keV He ions) but still thicker than the primary interaction radius.

15.2.2.1 Thick Membranes

When the target thickness is smaller than the implantation depth (about 300 nm for 30 keV He ions, see Fig. 15.2; except properly aligned monocrystals where the ion channeling effect is observed), then sputtering is expected to occur on both surfaces of the target sample, as illustrated by SRIM simulations, see Fig. 15.12. Interestingly, for He-ion sputtering the peak value of sputtered atoms from the back and bottom is not in the center but rather about 4 Å distant. Also, the top and bottom distribution resemble in shape and value having both a full width at half maximum (FWHM) of about 6 Å. However, the radial ion beam intensity profile needs to be convoluted to make a conclusive statement about the smallest ultimate pore diameter achievable. Furthermore, the pore diameter will finally depend on endpoint detection, i.e. on the exposure time, see Fig. 15.12d. The increase of pore diameter can be attributed to the beam tails, mechanical stability of the sample, or electronic noise on beam position. Comparing He, Ne, and Ga-ion simulations and the deduced FWHMs in Fig. 15.12, it is obvious, that He-ion beams have the highest potential for ultimate resolution in membrane patterning.

However, the actual pore formation mechanism is more complicated than predicted by the SRIM simulations, mainly because of re-deposition processes in high aspect ratio geometries [35]. By carefully tuning the process parameters for *redeposition* one can fabricate pores of a nanometer diameter. An important issue to mention is amorphization around the pore. TEM images of Si membranes clearly reveal amorphous silicon formation within all the He-beam/membrane interaction volume, see Chap. 19.

Another important issue to mention is that helium bubble formation in membrane samples is practically impossible. First of all a large fraction of He-ions are transmitted through the membrane. The small implanted fraction is located on a small distance from either of the surfaces which facilitates out diffusion of implanted He ions leaving amorphous sample material behind.

15.2.2.2 Thin Membranes

Emerging suspended two-dimensional (2D) materials such as graphene have thicknesses of only one atomic layer. This means that there is eventually no primary interaction volume in such cases and that there is no collision cascade created at all. Atoms of 2D membrane materials will be sputtered only to the direction of incident

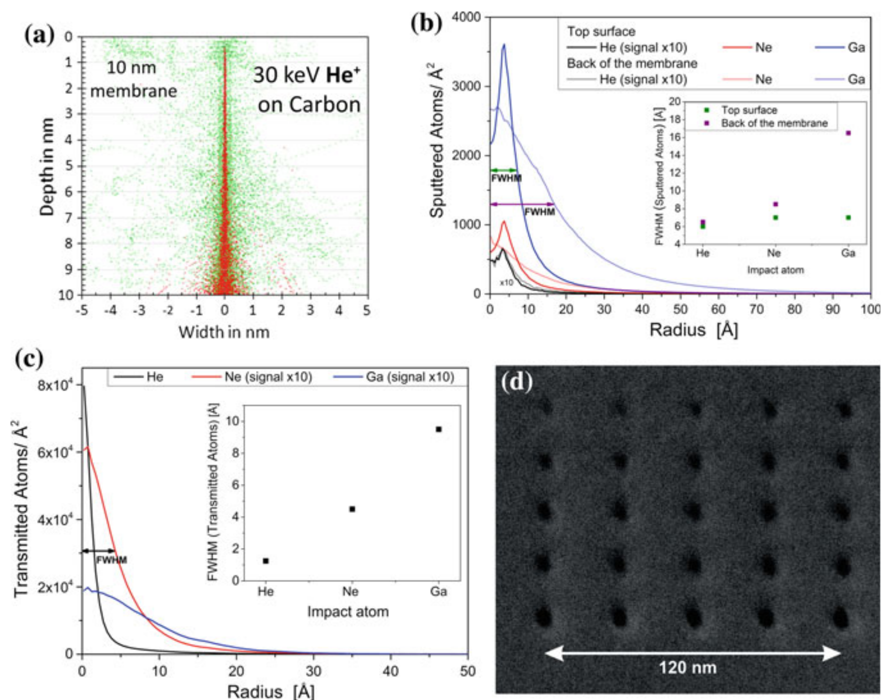

Fig. 15.12 SRIM [9] simulated zero diameter 30 keV He-, Ne-, and Ga-ion beam impinging on a 10 nm membrane of carbon. **a** Illustration of collision cascade for impinging 30 keV He atoms. Primary ion collisions are shown in *red* and the collision cascade is shown in *green*. Modified from [8]. **b** Radial distribution of sputtered atoms at the *top* surface and *bottom* of the membrane. Both the *top* and *bottom* surface distributions will determine the lateral resolution of the pore; the *inset* shows the full widths at half maximum FWHM. **c** Radial distribution of the transmitted incident ions with FWHM *inset*. **d** Example of 30 kV He-ion sputtered holes into a 15 nm thick freestanding amorphous carbon membrane. The ion dose per pore increases from *upper left corner* towards *right bottom corner* of the figure. The minimum observed pore diameter is about 4 nm

ion momentum, i.e. they leave the bottom surface. The incident ion either transfers enough energy to a membrane atom (or a number of atoms if the interaction cross section is large enough) and sputters it or transmits without sputtering. The patterning resolution is then set by the ion-beam intensity profile and not by the interaction volume [36]. The final pore shape or individual defects depend then very much on open bond passivation in such cases [37].

Essential understanding of graphene sputtering by FIBs can be done by rather simple binary collision theory [39, 40]. Experimental sputter yields were determined from controllable irradiation of free-standing graphene membranes (from 1 to 4 layers) by He+ or Ga+ ions to the state when the membrane was completely removed, see Fig. 15.13a, b. Graphene turns out to be semi-transparent for 10–30 keV energetic He-ions, 99–97% of He-ions pass graphene without creating lattice defects. In contrast, 80–50% of the large Ga-ions sputter carbon atoms from

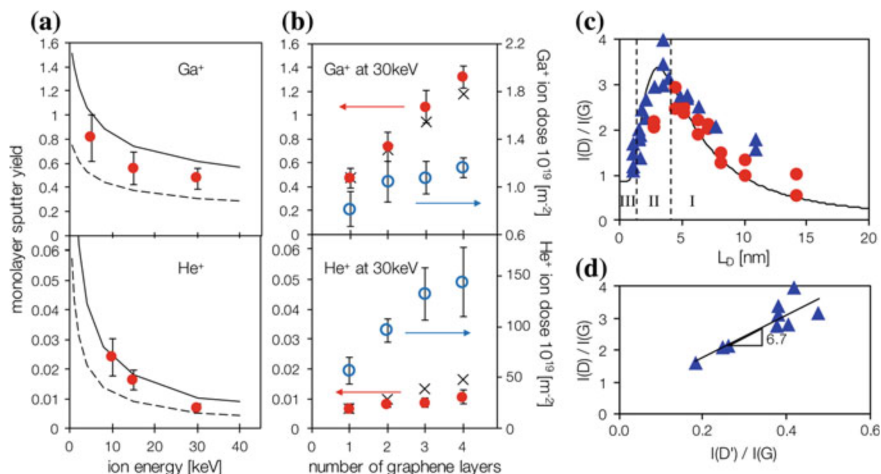

Fig. 15.13 **a** Monolayer graphene sputter yield as function of ion energy for Ga^+ and He^+ ions. *Solid* and *dashed line* show upper and lower bounds of theoretically calculated sputter yield using the binary collision model. *Dots* represent experimentally determined sputter yields. **b** Sputter yield and ion dose necessary to completely etch graphene as function of graphene layer number. *Circles* show experimentally determined data points. *Crosses* correspond to binary collision model sputter yield assuming a layer-number-independent probability of the carbon atom to sputter upon collision. **c**, **d** Raman spectroscopy of He^+ ion irradiated graphene. **c** Measured intensities ratio of D to G peak I(D)/I(G) versus average defect distance L_D, extracted from irradiation dose and experimental sputter yield. *Triangles* correspond to experiments with monolayer graphene and *circles* to double layer graphene. The *line* is calculated according to the empirical function from [38]. **d** I(D)/I(G) versus I(D′)/I(G) for monolayer graphene irradiated by He^+ ions with fitted linear proportionality. The figure is adopted from [39]—Published by The Royal Society of Chemistry

graphene depending on their kinetic energy ranging from 5 to 30 keV. The decrease of sputter yield for increased ion energy can intuitively be understood invoking the interaction time of the ions in the graphene membrane. Fast ions have shorter interaction time with graphene carbon atoms, thus transferring less energy while passing by. This finding is described well by binary collision theory. Interestingly, the experiment showed that the sputter yield increases roughly linear (at least up to 4 layers) with the number of graphene layers forming the membrane. This corresponds to simple addition of sputter probabilities of the carbon atoms in each layer; see Fig. 15.13b. Actually, the amount of transmitted He-ions can be quantitatively correlated to the thickness of the sample. Determining the geometry of glass nanocapillaries by scanning transmission He-ion microscopy has been recently demonstrated [41].

It was shown that Raman spectroscopy is a powerful method to study milling-caused damage in supported graphene exposed to a non-focused low energy argon ion source [38, 42, 43]. In these experiments no pores were formed but the lateral electronic damage extension of the structural defect (due to removal of individual atoms) into the adjacent periphery was studied by Raman spectroscopy and modeled from the D to G band ratio. Similar Raman spectroscopic analysis of

FIB damaged free-standing graphene reveals the defect formation mechanisms, Fig. 15.13c, d. He-ions create individual carbon vacancies at low exposure doses, see region I in Fig. 15.13c. Lattice disorder increases leading to an increase of the D to G peak ratio. At less than around 4 nm of average defect distance the D to G peak ratio starts to decrease (region II) corresponding to vanishing of the hexagonal periodic lattice. Region III corresponds to a saturation of D to G peaks ratio around unity. At these irradiation doses the graphene membrane is transferred to a loose network of sp^2-bonded carbon atoms. Further increase of irradiation dose removes carbon atoms without significant changes in bonding structure until nearly all atoms are removed. Individual monovacancies creation in the regime I is further supported by analysis of the I(D)/I(G) versus the I(D')/I(G) slope, which is about 7, see Fig. 15.13d. Reference [44] attributes the slope value of around 3.5 to many grain boundaries in graphene, around 13 in the case of sp^3 bond creation, and around 7 in the case of individual vacancy defects.

Understanding the physics of the sputtering process allows practical direct nanostructuring of free-standing graphene by FIBs. Pores of only a few nm in diameter, <3 nm for He-beam and <4 nm for Ga-beam can be fabricated, see Fig. 15.14. It is eventually limited by the focused ion beam diameter. Even if the sputtering yield for He ions is very low, it is still much higher than for electrons in a transmission electron microscope. Millions of nm-pore arrays can be fabricated showing narrow pore diameter distribution. This finds its application niche in perforating 2D materials on a large scale [40] for realization of the thinnest Goretex® like material. The ultimate pore diameters which can be milled in thin carbon membranes by focused He-ion beams are close to 1 nm [45] and necessitate an endpoint detection to stop beam exposure when breakthrough of the pore through the membrane is achieved, see Chap. 7. Another example of nano-patterned freestanding graphene membranes comprises a matter-wave beam splitter which gave experimental evidence that quantum coherence prevails even at the limit of atomically thin gratings [46].

15.3 Gas Assisted Deposition with Noble Gas Ions

Introducing volatile compounds, like organometallics, halides, or halogenides, in small quantities into the FIB chamber enables direct writing using the focused ion beam. The molecules physisorb on the surface and are dissociated locally in the close vicinity of the ion interaction range where the ion beam strikes the substrate. According to the nature of the injected volatile compound one can deposit three dimensional nanostructures (non-volatile fragments form the deposit), see Fig. 15.15, or one can also enhance the physical milling rate by adding compounds which locally decompose upon ion induced dissociation into etch molecules and attack the substrate.

The direct write and direct etch process is minimally invasive as the non-irradiated adsorbates will desorb after the gas flux is stopped at the end of the

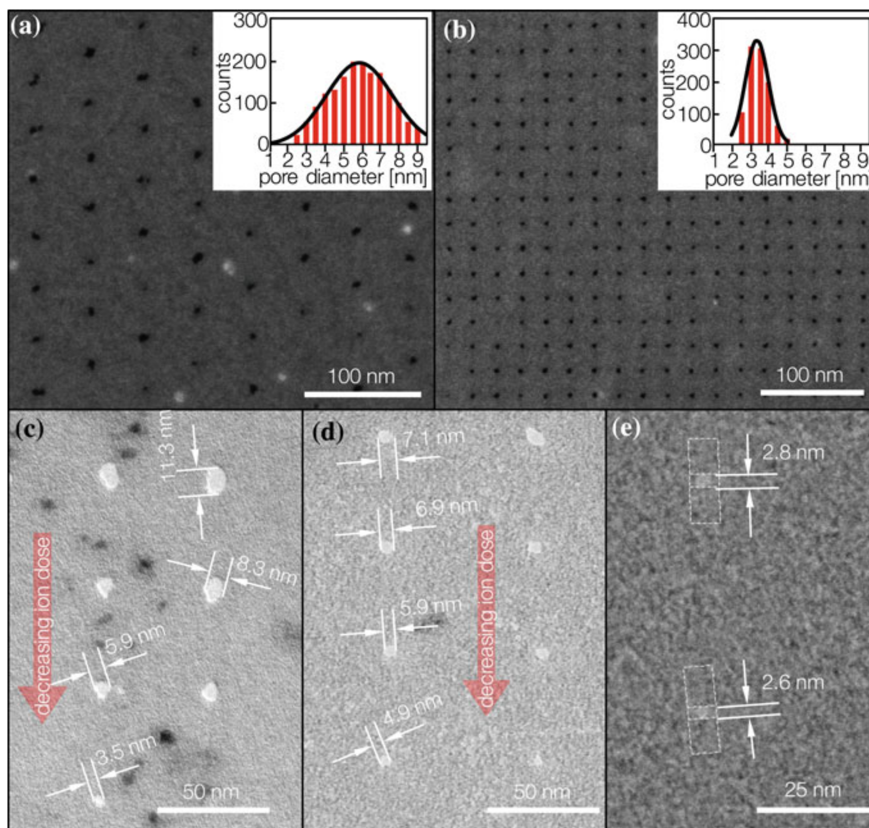

Fig. 15.14 An example of nanostructuring of free-standing graphene membranes by FIBs. **a** ~5-nm-diameter pores made by Ga-FIB, *scale bar* is 100 nm. **b** An array of ~3 nm pores fabricated by He-FIB, *scale bar* is 100 nm. *Insets* show corresponding diameter distributions. **c** STEM image of smallest pores in graphene fabricated by Ga-FIB, *scale bar* is 50 nm. **d**, **e** STEM images of smallest pores in graphene fabricated by He-FIB. The pores diameter dependence on the irradiation doses reflects the shapes of the ion beam profile. The figure is adopted from [39]—Published by The Royal Society of Chemistry

writing procedure. Table 15.1 gives an overview over several gas compounds used in combination with noble gas ion beams by now. Many more gas compounds were already reported for the more mature beam technologies of focused Ga-ions and electrons and can be found in [7, 8].

Although it may appear that direct writing with focused ion beams by introducing gases is a relatively straightforward technology to implement by adding a gas injection system to the chamber (for a review on gas injection systems see [59] we need to advert the reader that optimizing a gas-assisted FIB process (for deposition or etching) is a complex challenge which necessitates fundamental studies involving the precursor chemistry, the adsorption-desorption and surface

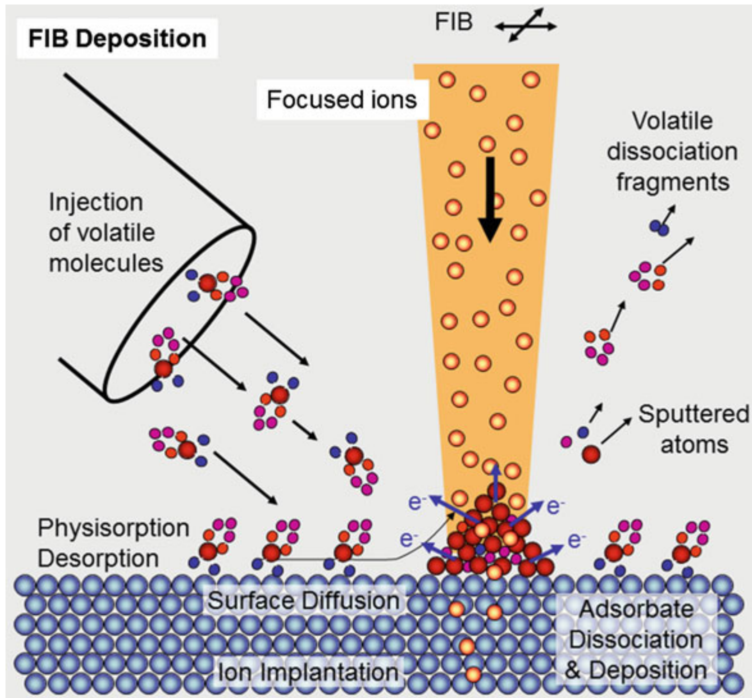

Fig. 15.15 Principle of FIB induced deposition using a gas injection system for local deposition of 3D nanostructures by dissociating the physisorbed molecules. Gas related processes include adsorption/desorption and surface diffusion to replenish the FIB dissociated adsorbates. Note that deposition only occurs when the sputter yield is smaller than the deposition yield

diffusion behavior of the precursor on the specific substrate material or the deposit itself, and the non-thermal dissociation of the precursor adsorbates by ions (and secondary electrons and excited surface atoms). Luckily, research of the past 60 decades already returned first insights and process protocol suggestions for a few materials which we want to summarize in the following sections.

15.3.1 Deposition Regimes: Reaction Limited Versus Mass-Transport Limited

Dissociation reactions of the adsorbates induced by the primary ions (PI) as well as the generated excited surface atoms (ESAs) and the exiting secondary electrons (SEs) can, at their extremes, proceed reaction limited or mass transport limited.

The reaction limited regime holds when there are more adsorbates than dissociation events, and, vice versa, the mass transport limited regime holds for less adsorbate available than dissociation events may happen by available ESAs, SEs,

Table 15.1 Summary of noble gas ion induced deposition and etching experiments from literature

Noble ion beam induced deposition				
Precursor	Ion	Deposit composition at.%	Total deposition yield deposited atoms/ion	References
$Al(CH_3)_3$	3.5–10 keV Ar	Al 53, C 8, O 37	3–8	[47]
$Ta(OC_3H_5)_5$	50 keV He, Ar, Ne, Xe	Ta 56, C 17, O 25	10–50	[48]
WF_6	50 keV He, Ar, Ne, Xe	W 75, O 25	10–50	[48]
WF_6	0.5 and 2 keV He, Ar	W 93, F 5, O 2	10–50	[49]
$Me_2Au(hfa)$	2–10 keV He, Ne, Ar, Kr, Xe	Au 55, C 45	4–17	[50]
$Co_2(CO)_8$	He	Pure Co		[51]
$MeCpPtMe_3$	30 keV He, Ne	Pt 16–17		[52]
$MeCpPtMe_3$	30 keV He	Pt 9–20	5	[53]
$MeCpPtMe_3$	Xe			[54]
(hfa) CuVTMS & atomic H	0.5 keV Ar	Cu 99		[55]
$W(CO)_6$	30 keV He	WC_{1-x} & $W_2(C,O)$ grains		[56]

Noble ion beam induced etching				
Precursor	Ion	Material	Etch enhancement to physical sputtering	References
XeF_2	50 keV Ar, Xe	SiO_2	100	[49]
XeF_2	50 keV Ar, Kr, Xe	SiNx	40, 80, 160	[57]
XeF_2	50 keV He, Ar, Ne, Kr, Xe	PMMA	1–5	[58]

Of note is that the total deposition yield and the etch enhancement are subject to the deposition regime as well as the composition, see text further below

and PIs, see Fig. 15.16. For the mass transport limited regime, the reaction zone becomes depleted from adsorbates and growth extends laterally to the less intense tails of the SE, ESA, and primary ion beam distributions. The number of available adsorbates in the irradiated region depends on four contributions which balance each other, see Fig. 15.15:

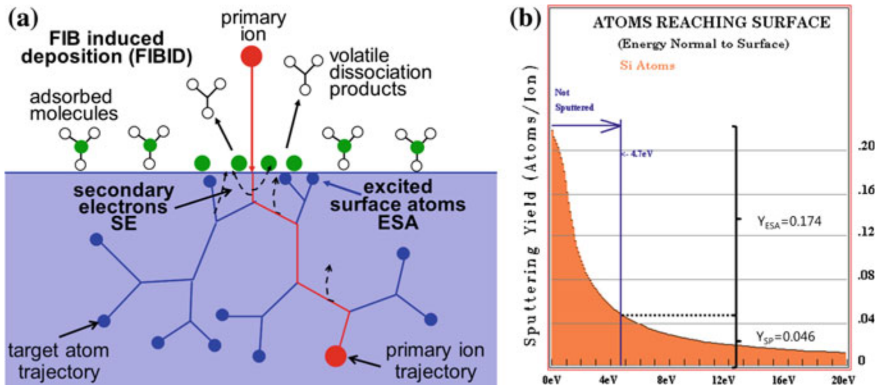

Fig. 15.16 **a** The (physisorbed) adsorbates will be dissociated into volatile and non-volatile fragments by excitation of primary ions, secondary electrons (SEs) and excited surface atoms (ESAs) produced by the impinging primary beam and the collision cascade. Modified from [7]. Local heat formation as possible thermal dissociation mechanism was omitted in the sketch. Note that the collision cascade in (**b**) does not distinguish between primary and secondary interaction volumes and thus sketches the situation of ions > Ar, in contrast to Fig. 15.1a. **b** The energy distribution normal to the surface of surface atoms as calculated by SRIM [9]. The excited surface atom yield (Y_{ESA}) and the sputter atom yield (Y_{SP}) for 30 keV He ions impinging on an silicon target is indicated as well as the surface binding energy of 4.7 eV of silicon

(i) The injected molecule flux impinging on the substrate and the reaction zone.
(ii) The desorption rate—depending on the residence time of the physisorbed adsorbates.
(iii) The surface diffusion rate—depending on the adsorbate mobility on the surface.
(iv) The dissociation rate of adsorbates—depending on their dissociation yields (sometimes reported as dissociation or deposition cross section).

If the number of available adsorbates is too small, milling will occur instead of deposition. Therefore, the pixel exposure time (dwell time) of the focused ion beam may need to be adjusted to small values as prolonged stationary irradiation will exponentially deplete with time the adsorbates at a much higher rate than they can be refreshed. On the other hand, also the ion current can be minimized, which is possible for He-ions down to a few femto amperes. Such small currents will also prevent depletion of adsorbates and unwanted milling during deposition. A continuum theory describing the deposition rate resulting from the balance of above adsorbate contributions and the resulting deposit shapes for stationary and pulsed focused ion beam deposition with radial distributions assumed to be Gaussian or exponential deposits can be found in a review of Utke et al. [7] and a book chapter [60]. The theory was recently comprehensively reviewed by Toth et al. [61] for focused electron beam induced deposition and etching and source codes released. For making the theory fit for focused ion beam induced deposition a sputter term needs to be added, see for example [60].

15.3.1.1 Beam Scan Parameters and Scan Strategies

Closely related to the deposition regimes is the scan strategy to be chosen to deposit certain nanostructure geometry with a certain composition. Generally, for deposits other than dot deposits the movement of the beam is digitized and can follow various sequences as shown in Fig. 15.17.

The influence of the parameters of pixel dwell (exposure) time and pixel refresh time on growth rate were already studied in the ninetieth [62] for Ga-ion beams and were extended to comprise composition effects [63], for a review see for instance in [7]. Basically, during the pixel dwell time the physisorbed adsorbate gets depleted (as it is deposited) and during the refresh time it gets replenished. Therefore, depleting the adsorbate with a long dwell time will not increase the deposition rate (but rather eventually lead to sputtering) neither a short refresh time will increase the deposition as the adsorbate is not refreshed to its initial coverage. The time ranges of practical dwell and refresh are nano/microseconds and milliseconds respectively, thus about 3 orders of magnitude different as visible in Fig. 15.18a, b, comprising experimental values for electrons and Ga-ions from [64].

More recently, proximity effects were studied in more detail by using a novel interlace pattern strategy in contrast to the conventionally machine-integrated raster, serpentine, or spiral scan strategies, see Fig. 15.19. The dependence of growth rate on interlace pitch for an interlace pattern strategy was studied for He-ions [5] and for electrons [65], see Fig. 15.18c: Plank et al. used an interlace pitch of 13 nm to deposit PtC_x boxes with smooth surfaces. However, an 80% higher growth rate was obtained increasing the pitch to 100 nm which avoided adsorbate depletion due to proximity effects (see Fig. 15.17). Alkemade et al. performed a similar experiment

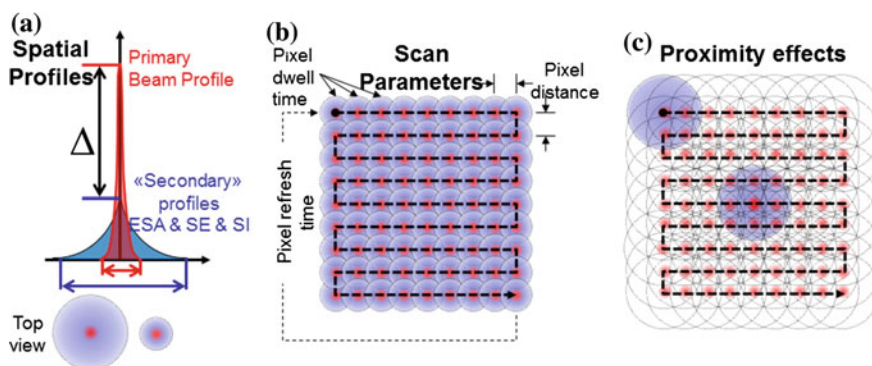

Fig. 15.17 Illustration of proximity effects in digitized scans. **a** Illustration of primary ion beam profile and secondary ESA, SE, and SI profiles. The *top view* presents a large and low proximity profile. Note that the proximity effect not only depends on the lateral extension but also on the peak ratio Δ. **b** The scan parameters are generally: pixel dwell time, pixel distance or overlap (mostly defined in percentage of primary beam size), and pixel refresh time. **c** Illustration of possible proximity effects caused by the secondary distributions. In this example, the secondary ESA or SE profile (or even local heating profile) affects the eight nearest neighbor pixels

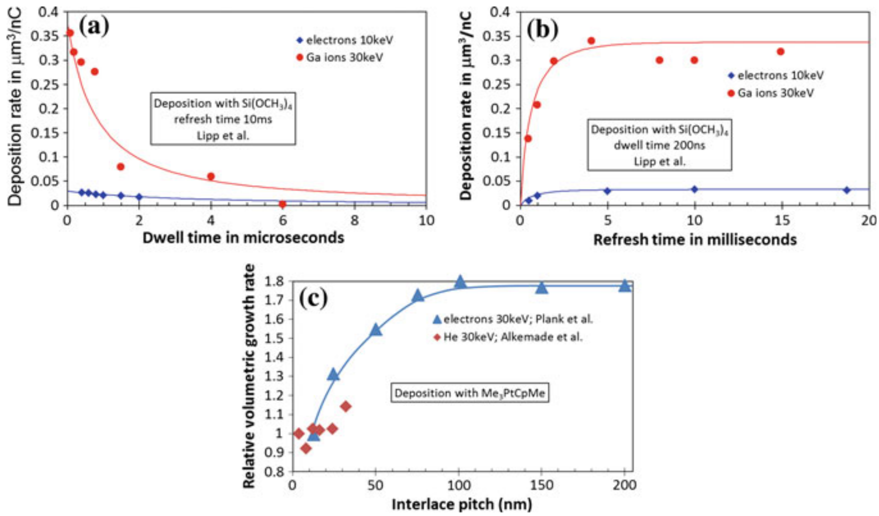

Fig. 15.18 Deposition rate versus pixel dwell time, refresh time, and interlace pitch for a parallelepiped shaped deposit. **a** Deposition rate versus pixel dwell time compared for Ga-ions and electrons. **b** Deposition rate versus refresh time for constant pixel dwell time compared for Ga-ions and electrons. **c** Deposition rate versus interlace pitch for electrons and He-ions. The interlace distance of 100 nm resulted in a kind of saturated growth rate for electrons [65]. Small interlace pitches for He-ions resulted in an almost constant growth rate [5]

with He-ions focused to 1 nm beam size which is also reported in Fig. 15.18c. They concluded that the growth rate at 32 nm interlace pitch was barely 10% higher than at the smallest pitch of 4 nm, and thus in He-IBID, the depletion zone is more than an order of magnitude smaller than in EBID. Although more data points would be desirable to back this statement more rigidly, it is known that halos—i.e. growth of a thin deposit in a wide area around the actual deposit—is much more prominent for electron beams than for He-ion beams.

15.3.2 Adsorbate Dissociation: ESA, SE, and Thermal Spikes

For local deposition with ions four trigger mechanisms can contribute to dissociation of physisorbed adsorbates:

(i) excited surface atoms
(ii) thermal spikes
(iii) secondary electrons
(iv) primary ions.

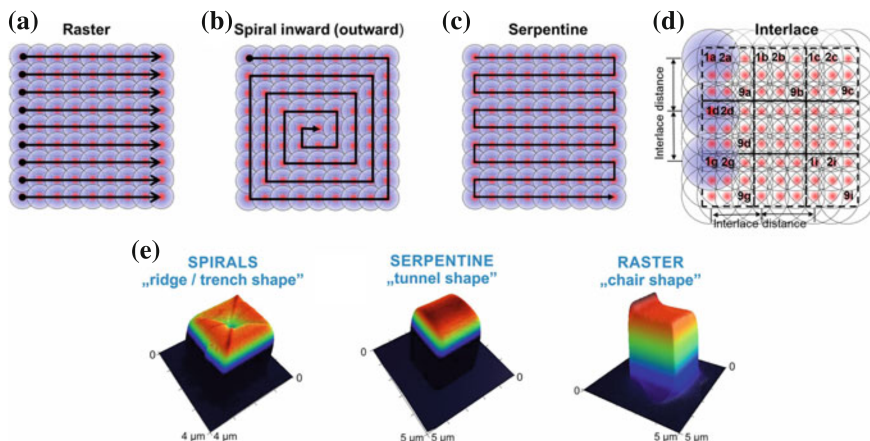

Fig. 15.19 **a**–**d** Various scan strategies to obtain the same parallelepiped (*box*) shaped deposit with an intended flat top surface. Each pixel will be irradiated with the same dose. Note that slow and fast scan axes (or areas) exist in raster, spiral, and serpentine scans which will show distinct deviations in deposition rates for mass-limited regimes. This is not the case for interlace scans where the deposit area is subdivided into sub-areas of the size of the proximity range. The beam is toggled between them and has the writing sequence: Xa to Xi with X looping from 1 to 9. **e** True deposit shapes obtained from FEBID with $MeCpPtMe_3$ using three different scan strategies in the mass limited regime. Reprinted with permission from [66] Copyright 2015 American Chemical Society

The ESA and SE mechanisms are shown in Fig. 15.16b. ESAs and thermal spikes were proposed by Dubner et al. [50] already in the nineties. The ESAs are a product of the collision cascade and thus proportional to the nuclear stopping power of the ion in the substrate material. ESAs have energy smaller than the surface binding energy, can thus not leave the surface but can transfer their energy to the surface adsorbates which in turn dissociate. In the thermal spike mechanism the energy of the implanted ions transforms into a heat spike at the surface where the beam impinges. When the temperature at the surface becomes higher than the temperature of thermal decomposition of the adsorbate molecule a thermal dissociation of the adsorbate can occur—very much like in a thin film chemical vapor deposition process (with deposition temperature windows of roughly 100–500 °C depending on the molecule) but very locally confined around the impinging focused ion beam. Wu et al. [52] were applying the thermal point spike model of Dubner et al. [50] to He and Ne-ion induced deposition and estimated temperature rises at 1 and 5 ps for He ions to 1450 and 130 K, respectively, while for Ne ions 3860 and 350 K were obtained. These values certainly suffer from the simplifications (especially the point source of heat assumption of the model) and are overestimated but highlight the complexity of the situation calling for more precise modelling.

For the light ion He-ion beam induced deposition with $Me_3PtCpMe$ by Alkemade [5] the thermal spike mechanism was ruled unlikely, due to similar deposition yields of flat deposits and pillars (the latter dissipating the heat badly compared to the planar substrate). However, for heavier ions the thermal spike mechanism

cannot be ruled out as the nuclear stopping power becomes large compared to the electronic stopping power, see Fig. 15.3, and thus the energy absorption. Experimental agreement with the thermal spike model was found for ion irradiation of polymer material and an interlacing scan strategy was proposed to avoid heat accumulation during sputtering [67].

Even for the very light electrons, heating effects and related local chemical vapor deposition was experimentally proven for focused electron beam induced deposition with heat sensitive molecules, like $Co_2(CO)_8$ [68, 69] and (hfac) CuVTMS [70] decomposing below 100 °C. They resulted in increased metal contents or even pure metal deposits. Keeping in mind that the nuclear stopping power at a given energy of ions in materials is always larger than for electrons (and considerably higher for heavy ions) the generated heat at the point of impact will be accordingly higher.

The SE mechanism can lead to dissociation of the adsorbates through dissociative ionization (well-known from mass spectrometry), dissociative electron attachment, or dissociation into neutrals, the efficiencies of each dissociation channel depending on the energy of the electron upon collision with the adsorbate [71, 72]. Which of the dissociation mechanisms dominates depends on the ion and the material involved in deposition.

The noble gas deposition data of Dubner et al. [50] was replotted in Fig. 15.20a to elucidate the dissociation mechanisms: they measured the deposition yield of gold-carbon nanocomposite deposits obtained from dimethyl-gold-hexafluoroacetylacetonateMe_2Au (hfa) by depositing planar structures in the reaction-limited regime using noble gas ions at various energies. Their data shows a linear dependence of the deposition yields versus the ESA yields (ESA yields being proportional to the stopping power); a deposition yield of 0.5 gold atoms per gold ESA was obtained. Figure 15.20b shows a replot of Dubner's data against the secondary electron yields obtained from experimental measurements from Alonso et al. [73] and Baragiola [74]; the plot is versus the aluminum SE yield as experimental values for SE yields of gold cannot be found. The SE yield for Au (which is the main deposit material besides carbon from Me_2Au(hfa) would proportionally differ due to the Z dependence, however, probably not to such an extent that a linear dependence could be re-established between the deposition yield and the SE yield. As the deposit material was close to AuC, see Table 15.1, both the deposition yield of 0.5 Au atoms per ESA deduced from Fig. 15.20a as well as the SE yields also contain a certain systematic error which is difficult to quantify but unlikely to shift the SE-data to a straight curve. As a final note we would like to point out that experiments for establishing graphs as shown in Fig. 15.20 need to be performed in the reaction-limited regime; in mass transport limited regime conditions no firm conclusion about the dominance of a certain deposition mechanism can be obtained from yield experiments as it would only reflect the efficiency of precursor supply.

Although Fig. 15.20 would imply an ESA mechanism for He-ion deposition a closer look to the ESA and SE generation for He-ions reveals a more subtle picture. In Table 15.2 we compare the TRIM calculated yields of excited surface atoms together with secondary electron yields for an aluminum target and various noble

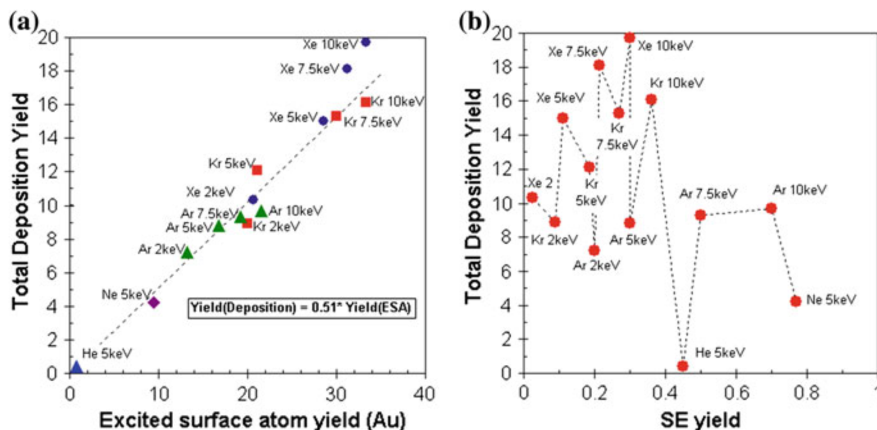

Fig. 15.20 Total deposition yield of Au-C deposits for reaction-limited FIBID with $Me_2Au(hfa)$. **a** Deposition yield versus ESAs. The ESA yield was calculated by TRIM for Au. Modified from [50]. **b** Deposition yield versus secondary electron yield. As experimental SE data on gold are missing the SE yields from Al were taken from [73, 74]. Note that these graphs relate to large planar deposits—for deposit sizes comparable to the surface cascade range the ESA and SE distributions cannot be assumed radially constant and yields may change

gas ions where experimental data were accessible. The SE to ESA ratio of He is considerably higher than for the rest of the noble gas ions which is in agreement with the ratio of electronic to nuclear stopping powers for He-ions. Weighing this ratio with the corresponding dissociation efficiencies of adsorbates—about 0.5 deposited atoms per ESA and about 0.05 deposited atoms per SE (deduced from FEBID experiments from [75, 76], respectively)—we can conclude that both mechanisms become comparable for He FIBID. Referring to Fig. 15.3, we could conclude that the ESA mechanism probably dominates for the remaining noble gas species as the nuclear stopping power is always larger than the electronic stopping power. Naturally, the latter statement needs to be reconsidered for any other substrate, deposited material, and ion other than presented in Table 15.1 and Fig. 15.3.

Table 15.2 Comparison of yields for noble gas ions landing on planar bulk aluminum with an energy of 30 keV

Yield/ion	He	Ne	Ar	Kr	Xe	Ga	e^-
SE	1.1	1.4	1.5	0.9	0.8	–	0.08
ESA	0.08	2.9	3.6	6.0	6.6	5.2	–
SE: ESA	13.75	0.48	0.42	0.15	0.12	–	–

Excited surface atom yields (ESA) were TRIM—simulated [9]. Secondary electron yields were taken from [73, 74]. For comparison, values for 30 keV Ga ions and 30 keV electrons [77] were added

15.3.3 Lateral Resolution

It is the *radial* distribution of ESAs and SEs (and the primary ion beam profile) at the growing surface as well as their intensity which will determine the *ultimate* lateral resolution of the deposits. The term "ultimate" implies that the deposition regime must be reaction-limited as any deviation from this situation will broaden the deposit laterally as we will outline in the following. Consider that generally the radial distribution of the primary ion beam has a profile of a peak function (which, to a very good extent, can be described by a Gaussian). Also the radial distributions of ESAs and SEs have peak functions on the surface around the incident primaries. For the case of planar surfaces the situation is depicted in Fig. 15.21.

The direct consequence is that reaction-limited conditions necessarily hold for the low intensity tails of such distributions but they do not necessarily hold for the high intensity center part of the distributions where often the adsorbates are depleted and deposition thus proceeds at a lower, mass-transport-limited, rate than at the tails. The steady state balance of depletion and refreshment of adsorbates depends on precursor adsorption (balance of supply and desorption), adsorbate mobility (surface diffusion) on the one hand and on adsorbate dissociation (depletion) by the ions on the other hand. The pixel exposure time, or dwell time, of the focused ion beam will then determine if the steady state adsorbate depletion will be reached or if a programed refresh time period during which the beam is blanked

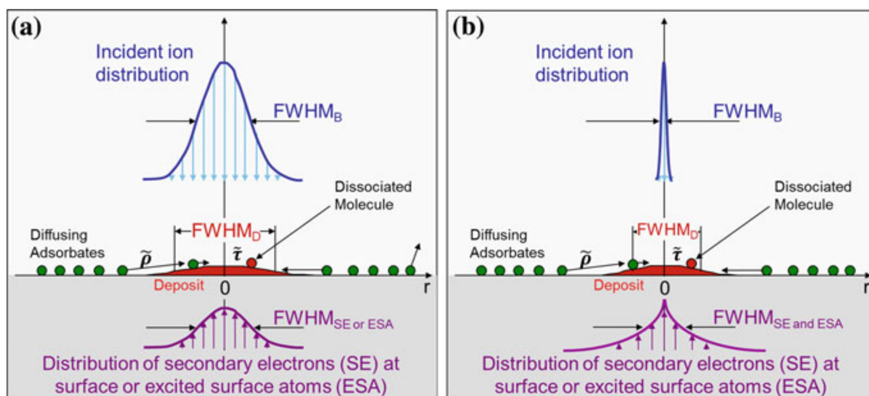

Fig. 15.21 Overview of size profiles involved in lateral resolution during focused ion beam induced deposition. Sizes of distributions of incident ions, generated secondary electrons (SE), excited surface atoms (ESA), and of the deposit shape are given in terms of full width half maximum. The parameters $\tilde{\tau}$ and $\tilde{\rho}$ refer to 15.1 in the text. **a** The ESA and SE profile with size $FWHM_{ESA\ or\ SE}$ is a result of convolution with the beam profile having a large size. **b** Beam profiles with smaller 1 nm size may generate SE and ESA profiles much larger in extent and different in radial dependency. In both cases the lateral resolution ($FWHM_D$) of the deposit will depend on the regime in which deposition occurs. Adsorbate depletion in the centre will lead to larger sizes than the SE, ESA, and PI involved. For large primary beam profiles the SE or ESA profile needs to be convolved

would allow the adsorbate to be replenished. Both, pixel dwell and refresh time crucially determine the lateral resolution of dot or line deposits. This statement is in addition to the growth rate considerations elaborated in Sect. 15.3.1.

15.3.3.1 Low Aspect Ratio Structures

An analytical universal scaling law for lateral resolution taking into account all above contributions was recently established for focused electron beam induced deposition by Szkudlarek et al. [78] assuming a Gaussian incident beam profile:

$$FWHM_{Deposit} \cong \left(\log_2\left(2 + \frac{\tilde{\tau} - 1}{1 + \bar{t}_D^{-1} + \tilde{\rho}_{out}^2}\right)\right)^{0.5} \cdot FWHM_{Beam} \tag{15.1}$$

where FWHM is the lateral extension of the deposit and beam measured at full width half maximum, while $\tilde{\tau}$, $\tilde{\rho}_{out}$, and $\bar{t}_D$ are normalized parameters describing the irradiative depletion, the surface diffusion, and beam exposure time on a pixel, respectively. Without going into detail, 15.1 states that the reaction-limited regime (and thus the highest lateral resolution) can be reached by all the three parameters individually: when the irradiative depletion $\tilde{\tau}$ is close to 1 (employing very low ion beam current), when the surface diffusion replenishment $\tilde{\rho}_{out}$ is large enough to overcome irradiative depletion (this depends on the strength of physisorption of adsorbate to the surface), or with a very short beam exposure dwell time $\bar{t}_D$ per pixel. If any of the parameters fulfils those conditions the fraction term becomes smaller than unity [78]

$$\frac{\tilde{\tau} - 1}{1 + \bar{t}_D^{-1} + \tilde{\rho}_{out}^2} \ll 1 \tag{15.2}$$

which is basically required for obtaining the conditions for reaction limited regime during deposition introduced in Sect. 15.3.2. The condition established in 15.2 also holds for focused ion beam induced deposition while the lateral resolution given by 15.1 would be modified due to the sputter term which needs to be involved in the derivation. An interesting consequence of the sputter term is that self-limiting hole diameters in membranes can be achieved by simultaneously supplying precursor molecules to the milling spot [79] which can theoretically be smaller than the beam size [60]. As a last note on lateral resolution, when the incident beam profile becomes very small the generated ESA or SE distributions on the surface retake their own radial profile (which is now not governed in shape anymore by the convolution with an incident primary ion Gaussian profile), see Fig. 15.21b. Equation 15.1 would change accordingly; for instance, for a simple exponential radial decay the power exponent in 15.1 changes to unity [60, 80].

15.3.3.2 High Aspect Ratio Structures

For a fundamental understanding of the resulting deposit shapes in high aspect ratio deposition structures like pillars, the spatial distributions of ESAs, SEs, as well as of the impinging and out scattered primary ions on the growing deposit's surface geometry needs to be followed as well as the spatial concentration distribution of adsorbates. A model taking into account recoil cascades in deposition was published by Ebm et al. [81] and applied to deposition with Ga ions and pentamethylcyclopentasiloxane ($C_5H_{20}O_5Si_5$); the main conclusion was that pillar broadening was due to primaries exiting the pillar side walls and that the scan overlap, see Fig. 15.17, determines the angle of deposited freestanding roof geometries. For SE-generation induced by He and Ne ions, recently the Monte-Carlo based code IONiSE was developed in Joy's group [82] with roots to the original TRIM/SRIM ion beam simulation codes [9], see also Chap. 4. The IONiSE code was combined with the EnvisION code from Rack's group which allows for the adsorbate and dissociation kinetics on the growing surface to be included [83] and applied to simulate He-ion deposition with the precursor WF_6. Figure 15.22a illustrates the different adsorbate dissociation events the authors considered; obviously the ESA mechanism was omitted due to the fact that the electronic stopping power (SE generation) dominates over the nuclear stopping power (collision cascade and ESA generation) for He ions. One should keep in mind that the reverse holds already true for the remaining noble ions Ne, Ar, Kr, Xe as well as Ga on Si, see Fig. 15.3a. Nonetheless, important insight about the distribution of adsorbate dissociation mechanisms and related 3D resolution of pillars can be gained: Reaction rate limited growth leads to fast vertical growth from incident primary ions and minimal lateral broadening, whereas mass transport limited growth has lower vertical growth velocity and exhibits broadening due to scattered ions and secondary electrons [83], compare with Fig. 15.22c, d.

Chen et al. [76] applied the EnvisION code to compare simulations and experiments of He-ion deposition of pillars with $MeCpPtMe_3$. Figure 15.23 reveals the simulated contributions of primary ions, forward scattered ion, SE1, and SE2 to deposition and final shape of the pillar grown by a finely focused He-ion beam with a diameter of 1 nm. Obviously, although using a small beam diameter for the exposure, a larger cylinder diameter as well as a larger top cone diameter develops. The present understanding of this shape is as follows: the vertical growth rate is constant (the cone shape does not vary while the pillar grows) while the lateral growth rate varies according to the position on the pillar. It becomes zero for the base part of the pillar as all incident He-ions were scattered out of the pillar within the cone volume. Surface distributions of SE1s, SE2s, PIs, and forward scattered ions together with the surface density distribution of adsorbates form the final specific geometry of the cone region. Alkemade et al. [84] concluded that both the ratio between SE1 and SE2 emission and the ratio between the precursor adsorbate coverage at the apex and at the flanges determine the ratio of vertical and lateral growth speeds and thus the final width of the pillar.

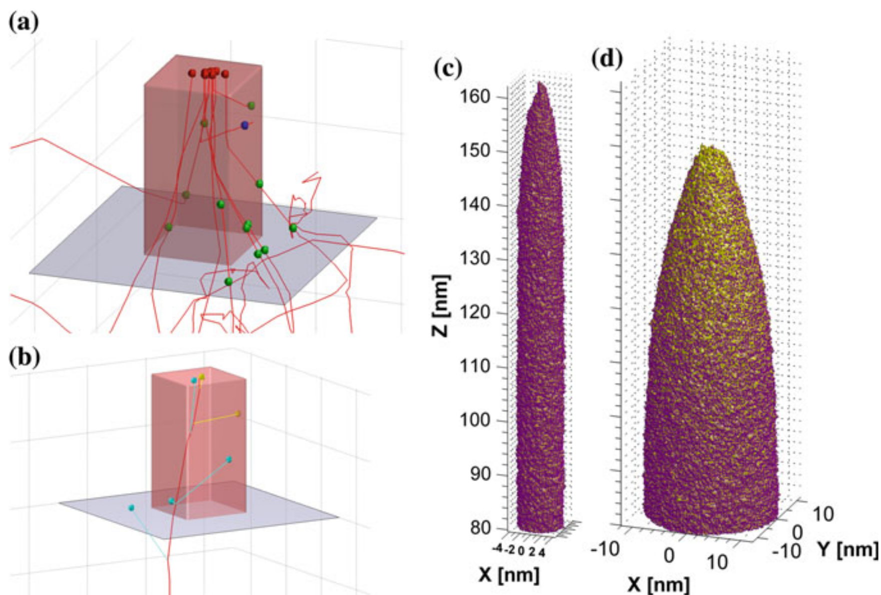

Fig. 15.22 **a**, **b** The differing adsorbate dissociation (deposition) mechanism events considered in the Monte Carlo based IONise/EnvisION simulation and their distribution on a 10 nm × 10 nm 20 nm tungsten nanostructure on a tungsten substrate permission. Taken from Smith et al. [83]; © IOP Publishing. Reproduced with permission. All rights reserved. The color code of deposition events is, *red* by primary ions (25 keV He^{+}), *blue* by backscattered ions, *green* by forward scattered ions, *yellow*—by SE1 electrons, and *cyan*—by SE2 electrons. **a** Only the primary ion trajectories and ion-induced dissociation events are shown. **b** Only the primary ion trajectories and secondary electron trajectories with their related dissociation events are shown. **c**, **d** Pillar shapes including adsorbate kinetics on the surface. The color signifies the adsorbate coverage distribution on the pillar surface: *purple color* signifies 100% adsorbate coverage while the *yellow color* stands for 10% coverage. **c** A slim pillar with a sharp cone is obtained in the reaction limited regime (note that 100% coverage is maintained over the whole pillar surface). **d** A broad pillar is obtained in the mass limited regime—note the low adsorbate coverage at the pillar apex and the cone flanges. Consequently the vertical growth rate decreases and the lateral growth can proceed for longer time

Actually, the approach and terminology for understanding shape development in He-ion beam induced deposition is analogous to models developed for electron beam induced deposition previously. Similar simulations were performed for FEBID pillars by Fowlkes et al. [85] who showed that the fundamental arguments involved in obtaining the analytical expressions for lateral resolution in 15.1 and 15.2 for low aspect ratio structures can be also applied for high-aspect ratio ones. Indeed, Alkemade and Miro [5] pointed out that cone apex shapes of cylinder deposits obtained by electrons and He-ions have comparable sharpness which they attributed to similar beam broadening of 30 keV trajectories of electrons and He-ions. Nevertheless they also pointed out a few differences: (i) the SE yield for 30 keV He ion is typically larger than for 30 keV primary electron beams, see Table 15.2. Thus the growth rates in He-FIBID are larger than for FEBID.

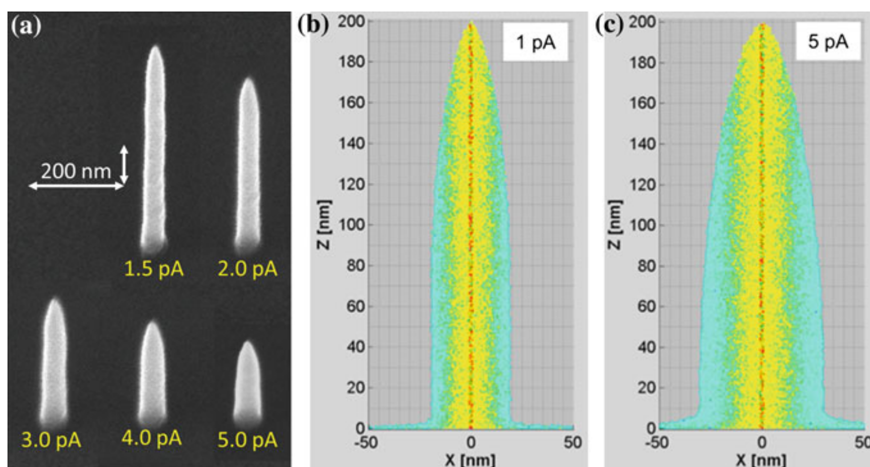

Fig. 15.23 **a** Tilt view of pillars grown with stationary 25 keV He-ion beams and Me3PtCpMe at various beam currents. The differing shapes are due to the balance of vertical to lateral growth. Taken from Chen et al. from [76]; © IOP Publishing. Reproduced with permission. All rights reserved. **b** Cross section of simulated pillar growth with Me3PtCpMe and 25 keV He stationary ion beam. Near the apex adsorbates are dominantly deposited by primary ions (*red*) and SE1 (*yellow*) and thus governing vertical growth. Lateral growth proceeds by SE1 (*yellow*), forward scattered ions (*green*), and finally by SE2 (*cyan*). The primary ion beam diameter was 1 nm. Increasing the beam current drives the deposition into the mass-limited growth as the adsorbates are depleted in the apex region and vertical growth is thus slowed down

(ii) The SE energy spectrum generated by a He-ion beam is mostly confined within 10 eV while electron irradiation generates a non-negligible fraction of higher-energy SEs. SEs with energies higher than 100 eV have a longer range than 10–50 eV electrons and lead thus to extended lateral growth. Consequently, high aspect cylinders grown by FEBID tend to be broader than He-FIBID cylinder diameters. Nonetheless, the world record for lateral resolution of dot patterns is hold by FEBID within a transmission electron microscope, where $W(CO)_6$ was used deposit a dot pattern on a silicon nitride membrane with sub-1-nm full width at half maximum [86]. State of the art lateral resolutions for lines and free standing structures can be found in the book chapter of Utke et al. [87].

Because gas-assisted focused noble gas ion beam nanofabrication is a relatively young research field, we would like to point out for reasons of inspiration some advances from the FEBID field which comprise mainly precursor issues, e.g. multiple adsorbate species [63, 88–91] as well as chemical aspects (physisorption versus chemisorption) of adsorption [61, 92]. Furthermore, there were a lot of post-growth purification activities published recently and achieving pure metal structures in FEBID [93–96]. It may be interesting to test these concepts also in noble gas FIBID.

15.3.4 Deposit Composition and Internal Structure

Focused He-ion and electron beam deposits result in comparable metal contents in deposits for the volatile precursor compounds $Me_3PtCpMe$, WF_6, and $Co_2(CO)_8$, see Table 15.1. He-ion deposit composition values compare to FEBID deposit compositions as (He FIBID vs. FEBID): 16–20 at.% [52, 53] versus 13–21 at.% Pt [97–99], pure Co [51] versus pure Co [100], and 75–93 at.% [48, 49] versus 85 at.% W [101]. The similarity in composition can be attributed to the dominating role of secondary electrons for precursor adsorbate dissociation for both He-ion and electron beams. The use of heavier ions, like gallium, for deposition always gave a higher metal content in the deposit for identical precursors; see a summary of compositions in [7]. This can be correlated to the ESA mechanism dominating over the SE-mechanism (we do not consider any heat spike mechanism as it is difficult to quantify) as well as to additional sputter effects in the deposits (although this would imply a preferential sputtering of carbon—the main ligand element of the precursor compound).

With respect to deposit microstructure, again, the He-ion and the electron beam deposits from $Me_3PtCpMe$ resemble each other [5]: the Pt grains embedded in the carbonaceous matrix of deposits obtained from He-ions have approximately the same size as for FEBID deposits. In contrast, Ne-ion beam induced deposition resulted in slightly larger grain sizes, around 4–5 nm. However, we would like to point out that the metal grain size will heavily depend on the overall metal concentration in the deposit; this in turn depends on the mass- or reaction-limited regime type established by the scan and exposure parameters during deposition.

15.4 Gas Enhanced Etching with Noble Gas Ions

While gas enhanced FIB induced etching with Ga-ions is a mature well-researched field, etching with noble gas ions is still in its infancy. Except for the examples mentioned in Table 15.1 no other studies were performed so far to our knowledge. This may be due to the considerable complexity described in Sect. 15.2 when involving gases and opting for optimization of the process. Nevertheless, there may be several advantages which would compensate for this effort: (i) The gas enhanced etch rates which can be a few ten times higher than the physical milling rate would reduce the total exposure time to the noble gas ion beam and thus the undesired implantation. (ii) Some material compounds tend to mill incongruently with respect to the elements for thermodynamical reasons. This changes the composition around the milling spot. (iii) When opting for milling high aspect ratio pores (holes) with straight sidewalls, proper gas assistance can be advantageous as re-deposition of sputtered material limits high-aspect ratios, for instance to 4–6 for InP—using iodine gas assistance during Ga-FIB milling increased the aspect ratio to 11 [102].

Many lessons can be learned from literature of Ga FIB induced etching and focused electron beam induced etching. Ebm et al. [103] were etching SiO_2 with XeF_2 and Ga FIB and were simulating the influence of the surface diffusion

coefficient of XeF_2 on the resulting bottom face shape (concave, planar, convex) of the pore (hole). Randolph et al. [104] were modelling the gas supply into high aspect ratio pores (holes) showing that precursor supply in high aspect ratio nanostructures can be the rate limiting contribution for the etch rate and verified it by FEB induced etching experiments on SiO_2.

15.5 Summary

Direct nanostructuring by milling with focused noble gas ion sources is a rather novel field but is already well established because of its unique opportunities. The number of noble-gas-FIB applications for nanopatterning grows continuously. He-FIB took its niche of the highest resolution in the field. Xe-FIB has the fastest material removal rate while still delivering nanoscale resolution. Ne-FIB has much higher sputtering yield than He-FIB and leaves no doping either but the lateral resolution for nanopatterning remains rather comparable to Ga-FIB. The basics of ion beam interaction with target material are well understood and main limitations are identified. Still, a number of issues remain open. To mention a few, active research is done in the fields of the damage done by the FIBs to the nanostructures and to the substrate, induced local (thermal) stress, intermixing in thin multilayer samples (welding), and modification of 2D materials.

So far gas assisted deposition and etching by focused noble gas ion beams was only sparsely reported in literature compared to the vast published results using focused beams of gallium ions and electrons. He-ion FIB deposition reproduces chemical compositions of deposits known from focused electron beam induced deposition, however at a higher deposition rate and with less proximity effects. The future use of $>$ He noble gas ions bears the potential of getting higher metal contents in deposits as well as a reduction in noble gas implantation and related bubble formation effects. Gas assistance during milling with focused noble gas ion beams could potentially decrease the implantation effects due to a chemically much enhanced milling rate. The vast precursor chemistries known for gas assisted Ga FIB and e-beam direct 3D write nanopatterning still await their use in noble gas ion microscopes!

Acknowledgements Support from the Swiss State Secretariat for Education, Research and Innovation SERI through project C14.0087 is acknowledged.

References

1. B.W. Ward, J.A. Notte, N.P. Economou, Helium ion microscope: a new tool for nanoscale microscopy and metrology. J. Vacuum Sci. Technol. B: Microelectr. Nanometer Struct. **24** (6), 2871–2874 (2006)
2. T. Hrncir et al., Novel plasma FIB/SEM for high speed failure analysis and real time imaging of large volume removal, in *Conference Proceedings of the 38th International Symposium for Testing and Failure Analysis*, 2012, pp. 26–29

3. J. Gierak, Focused ion beam technology and ultimate applications. Semicond. Sci. Technol. **24**(4), 043001 (2009)
4. J. Melngailis, Focused ion-beam technology and applications. J. Vac. Sci. Technol. B **5**(2), 469–495 (1987)
5. P.F.A. Alkemade, H. Miro, Focused helium-ion-beam-induced deposition. Appl. Phys. A-Mater. Sci. Process. **117**(4), 1727–1747 (2014)
6. A.V. Krasheninnikov, K. Nordlund, Ion and electron irradiation-induced effects in nanostructured materials. J. Appl. Phys. **107**(7), 071301 (2010)
7. I. Utke, P. Hoffmann, J. Melngailis, Review: gas-assisted focused electron beam and ion beam processing and fabrication. J. Vac. Sci. Technol. B **26**(4), 1197–1276 (2008)
8. J. Melngailis, S. Moshkalev, I. Utke, Focused beam processing: new beam technologies: new challenges in process development and nanofabrication, in *Nanofabrication Using Focused Ion and Electron Beams. Principles and Applications*, ed. by I. Utke, S. Moshkalev, P. Russell (Oxford University Press, Oxford, 2012), pp. 755–782
9. J.F. Ziegler, M.D. Ziegler, J.P. Biersack, SRIM: the stopping and range of ions in matter. Nucl. Instrum. Methods Phys. Res. Sect. B-Beam Interact. Mater. Atoms **268**(11–12), 1818–1823 (2010)
10. M. Ananth et al., Creating nanohole arrays with the helium ion microscope, in *Proceedings of SPIE—The International Society for Optical Engineering*, vol. 8036, 2011, p. 80360M
11. M. Rudneva et al., Novel nanosample preparation with a helium ion microscope. J. Mater. Res. **28**(8), 1013–1020 (2013)
12. R. Livengood et al., Subsurface damage from helium ions as a function of dose, beam energy, and dose rate. J. Vac. Sci. Technol. B **27**(6), 3244–3249 (2009)
13. Y. Drezner et al., Structural characterization of He ion microscope platinum deposition and sub-surface silicon damage. J. Vac. Sci. Technol. B **30**(4), 041210 (2012)
14. M. Rommel et al., Influence of FIB patterning strategies on the shape of 3D structures: comparison of experiments with simulations. Microelectron. Eng. **87**(5–8), 1566–1568 (2010)
15. H.-B. Kim, G. Hobler, Simulation of focused ion beam milling, in *Nanofabrication Using Focused Ion and Electron Beams. Principles and Applications*, ed. by I. Utke, S. Moshkalev, P. Russell (Oxford University Press, Oxford, 2012), pp. 755–782
16. C. Ebm, G. Hobler, Assessment of approximations for efficient topography simulation of ion beam processes: 10 keV Ar on Si. Nucl. Instrum. Methods Phys. Res. Sect. B **267**(18), 2987–2990 (2009)
17. H. Plank, Focused particle beam nano-machining: the next evolution step towards simulation aided process prediction. Nanotechnology **26**(5), 050501 (2015)
18. M.J. Vasile et al., Scanning probe tips formed by focused ion beams. Rev. Sci. Instrum. **62**(9), 2167–2171 (1991)
19. T. Hrncir et al., Advances in FIB-SEM analysis of TSV and solder bumps-approaching higher precision, throughput and comprehensiveness, in *Conference Proceedings of the 40th International Symposium for Testing and Failure Analysis*, 2014, pp. 136–42
20. T. Hrnčíř et al., How Xe and Ga FIB differ in inducing lateral damage on TEM samples, in *Conference Proceedings of the 41st International Symposium for Testing and Failure Analysis*, 2015, p. 60
21. F.A. Stevie et al., FIB-SIMS quantification using TOF-SIMS with Ar and Xe plasma sources. Surf. Interf. Anal. **46**(S1), 285–287 (2014)
22. F.H.M. Rahman et al., The prospects of a subnanometer focused neon ion beam. Scanning **34**(2), 129–134 (2012)
23. R. Timilsina et al., Monte Carlo simulations of nanoscale focused neon ion beam sputtering of copper: elucidating resolution limits and sub-surface damage. Nanotechnology **25**(48), 485704 (2014)
24. S. Tan et al., Nanomachining with a focused neon beam: a preliminary investigation for semiconductor circuit editing and failure analysis. J. Vac. Sci. Technol. B **29**(6), 06F604 (2011)

25. M.C. Lemme et al., Etching of graphene devices with a helium ion beam. ACS Nano **3**(9), 2674–2676 (2009)
26. S. Hang, Z. Moktadir, H. Mizuta, Raman study of damage extent in graphene nanostructures carved by high energy helium ion beam. Carbon **72**, 233–241 (2014)
27. O. Scholder et al., Helium focused ion beam fabricated plasmonic antennas with sub-5 nm gaps. Nanotechnology **24**(39), 395301 (2013)
28. A.I. Kuznetsov et al., Split-ball resonator as a three-dimensional analogue of planar split-rings. Nat. Commun. **5**, 3104 (2014)
29. M. Melli et al., Reaching the theoretical resonance quality factor limit in coaxial plasmonic nanoresonators fabricated by helium ion lithography. Nano Lett. **13**(6), 2687–2691 (2013)
30. H. Kollmann et al., Toward plasmonics with nanometer precision: nonlinear optics of helium-ion milled gold nanoantennas. Nano Lett. **14**(8), 4778–4784 (2014)
31. Y. Wang et al., Ultrafast nonlinear control of progressively loaded, single plasmonic nanoantennas fabricated using helium ion milling. Nano Lett. **13**(11), 5647–5653 (2013)
32. C. Thiele et al., Fabrication of carbon nanotube nanogap electrodes by helium ion sputtering for molecular contacts. Appl. Phys. Lett. **104**(10), 103102 (2014)
33. Y. Wang et al., Helium ion beam milling to create a nano-structured domain wall magnetoresistance spin valve. Nanotechnology **23**(39), 395302 (2012)
34. J.P. Best et al., A comparison of three different notching ions for small-scale fracture toughness measurement. Scripta Mater. **112**, 71–74 (2015)
35. S. Tan et al., Mechanism and applications of helium transmission milling in thin membranes. J. Vacuum Sci. Technol. B: Nanotechnol. Microelectr. **32**(6), 06FA01 (2014)
36. D.S. Fox et al., Nanopatterning and electrical tuning of MoS<inf>2</inf> layers with a subnanometer helium ion beam. Nano Lett. **15**(8), 5307–5313 (2015)
37. J. Lee et al., Stabilization of graphene nanopore. Proc. Natl. Acad. Sci. USA **111**(21), 7522–7526 (2014)
38. M.M. Lucchese et al., Quantifying ion-induced defects and Raman relaxation length in graphene. Carbon **48**(5), 1592–1597 (2010)
39. J. Buchheim et al., Understanding the interaction between energetic ions and freestanding graphene towards practical 2D perforation. Nanoscale (2016). doi:10.1039/C6NR00154H
40. K. Celebi et al., Ultimate permeation across atomically thin porous graphene. Science **344**(6181), 289–292 (2014)
41. L.P. Zweifel, I. Shorubalko, R.Y.H. Lim, Helium scanning transmission ion microscopy and electrical characterization of glass nanocapillaries with reproducible tip geometries. ACS Nano **10**(2), 1918–1925 (2016)
42. L.G. Cançado et al., Quantifying defects in graphene via Raman spectroscopy at different excitation energies. Nano Lett. **11**(8), 3190–3196 (2011)
43. R. Beams, L. Gustavo Cançado, L. Novotny, Raman characterization of defects and dopants in graphene. J. Phys.: Condens. Matter **27**(8), 083002 (2015)
44. A. Eckmann et al., Probing the nature of defects in graphene by Raman spectroscopy. Nano Lett. **12**(8), 3925–3930 (2012)
45. D. Emmrich et al., Nanopore fabrication and characterization by helium ion microscopy. Appl. Phys. Lett. **108**(16), 163103 (2016)
46. C. Brand et al., An atomically thin matter-wave beamsplitter. Nat. Nanotechnol. **10**(10), 845–848 (2015)
47. F.G. Rudenauer, W. Steiger, D. Schrottmayer, Localized ion-beam induced deposition of Al containing layers. J. Vac. Sci. Technol. B **6**(5), 1542–1547 (1988)
48. K. Gamo et al., Maskless ion beam assisted deposition of W and Ta films. Microelectron. Eng. **5**(1–4), 163–170 (1986)
49. K. Gamo, S. Namba, Microfabrication using focused ion beams. Microelectron. Eng. **11**(1–4), 403–408 (1990)
50. A.D. Dubner et al., The role of the ion-solid interaction in ion-beam-induced deposition of gold. J. Appl. Phys. **70**(2), 665–673 (1991)

51. H. Wu et al., Focused helium ion beam deposited low resistivity cobalt metal lines with 10 nm resolution: Implications for advanced circuit editing. J. Mater. Sci.: Mater. Electron. **25**(2), 587–595 (2014)
52. H.M. Wu et al., Synthesis of nanowires via helium and neon focused ion beam induced deposition with the gas field ion microscope. Nanotechnology **24**(17), 175302 (2013)
53. C.A. Sanford et al., Beam induced deposition of platinum using a helium ion microscope. J. Vacuum Sci. Technol. B: Microelectr. Nanometer Struct. **27**(6), 2660–2667 (2009)
54. C. Rue, B. Carrigan, A.S.M. Int, Dielectric and metal depositions using Xe+ focused ion beams, in *Istfa 2012: Conference Proceedings from the 38th International Symposium for Testing and Failure Analysis*, 2012, pp. 447–454
55. T.P. Chiang, H.H. Sawin, C.V. Thompson, Ion-induced chemical vapor deposition of high purity Cu films at room temperature using a microwave discharge H atom beam source. J. Vacuum Sci. Technol. A-Vacuum Surf. Films **15**(5), 2677–2686 (1997)
56. K. Kohama et al., Tungsten-based pillar deposition by helium ion microscope and beam-induced substrate damage. J. Vacuum Sci. Technol. B: Nanotechnol. Microelectr. **31**(3), 031802 (2013)
57. Z. Xu et al., In situ patterning of Si3N4 by an ion-beam-induced gas surface reaction. Nucl. Inst. Methods Phys. Res. B **39**(1–4), 750–753 (1989)
58. K. Gamo et al., Insitu development of ion bombarded Poly(Methylmethacrylate) resist in a reactive gas ambient. J. Vac. Sci. Technol. B **6**(3), 989–992 (1988)
59. V. Friedli, H.D. Wanzenboeck, I. Utke, Gas injection systems for FEB and FIB Processing: Theory and Experiment, in Nanofabrication Using Focused Ion and Electron Beams. Principles and Applications, ed. by I. Utke, S. Moshkalev, P. Russell (Oxford University Press, Oxford, 2012), pp. 248–285
60. I. Utke, FEB and FIB continuum models for one-adsorbate species, in Nanofabrication Using Focused Ion and Electron Beams. Principles and Applications, de. by I. Utke, S. Moshkalev, P. Russell (Oxford University Press, Oxford, 2012), pp. 248–285
61. M. Toth et al., Continuum models of focused electron beam induced processing. Beilstein J. Nanotechnol. **6**, 1518–1540 (2015)
62. L.R. Harriott, Digital scan model for focused ion-beam-induced gas etching. J. Vac. Sci. Technol. B **11**(6), 2012–2015 (1993)
63. L. Bernau et al., Tunable nanosynthesis of composite materials by electron-impact reaction. Angewandte Chemie - International Edition **49**(47), 8880–8884 (2010)
64. S. Lipp et al., Tetramethoxysilane as a precursor for focused ion beam and electron beam assisted insulator (SiOx) deposition. J. Vac. Sci. Technol. B **14**(6), 3920–3923 (1996)
65. H. Plank et al., Fundamental proximity effects in focused electron beam induced deposition. ACS Nano **6**(1), 286–294 (2012)
66. R. Winkler et al., Toward ultraflat surface morphologies during focused electron beam induced nanosynthesis: disruption origins and compensation. ACS Appl. Mater. Interf. **7**(5), 3289–3297 (2015)
67. R. Schmied et al., A combined approach to predict spatial temperature evolution and its consequences during FIB processing of soft matter. Phys. Chem. Chem. Phys. **16**(13), 6153–6158 (2014)
68. I. Utke et al., Cross section investigations of compositions and sub-structures of tips obtained by focused electron beam induced deposition. Adv. Eng. Mater. **7**(5), 323–331 (2005)
69. I. Utke et al., Thermal effects during focused electron beam induced deposition of nanocomposite magnetic-cobalt-containing tips. Microelectron. Eng. **73–74**, 553–558 (2004)
70. I. Utke et al., Focused-electron-beam-induced deposition of freestanding three-dimensional nanostructures of pure coalesced copper crystals. Appl. Phys. Lett. **81**(17), 3245–3247 (2002)
71. J.D. Wnuk et al., Electron beam deposition for nanofabrication: insights from surface science. Surf. Sci. **605**(3–4), 257–266 (2011)

72. S. Engmann et al., The role of dissociative electron attachment in focused electron beam induced processing: a case study on cobalt tricarbonyl nitrosyl. Angewandte Chemie - International Edition **50**(40), 9475–9477 (2011)
73. E.V. Alonso et al., Z1 dependence of ion-induced electron emission from aluminum. Phys. Rev. B **22**(1), 80–87 (1980)
74. R.A. Baragiola, E.V. Alonso, A.O. Florio, Electron emission from clean metal surfaces induced by low-energy light ions. Phys. Rev. B **19**(1), 121–129 (1979)
75. H. Plank et al., The influence of beam defocus on volume growth rates for electron beam induced platinum deposition. Nanotechnology **19**(48), 485302 (2008)
76. P. Chen et al., Nanopillar growth by focused helium ion-beam-induced deposition. Nanotechnology **21**(45), 455302 (2010)
77. D.C. Joy, A data base on electron-solid interactions. A data base on electron-solid interactions, http://web.utk.edu/~srcutk/database.doc (2008)
78. A. Szkudlarek et al., Lateral resolution in focused electron beam-induced deposition: scaling laws for pulsed and static exposure. Appl. Phys. A-Mater. Sci. Process. **117**(4), 1715–1726 (2014)
79. P. Chen et al., Fast single-step fabrication of nanopores. Nanotechnology **20**(1), 015302 (2009)
80. I. Utke et al., Resolution in focused electron and ion beam induced processing. J. Vac. Sci. Technol. B **25**(6), 2219–2223 (2007)
81. C. Ebm et al., Quantitative simulation of ion-beam induced deposition of nanostructures. J. Vac. Sci. Technol. B: Nanotechnol. Microelectr. **29**(1), 0110311–0110315 (2011)
82. R. Ramachandra, B. Griffin, D. Joy, A model of secondary electron imaging in the helium ion scanning microscope. Ultramicroscopy **109**(6), 748–757 (2009)
83. D.A. Smith, D.C. Joy, P.D. Rack, Monte Carlo simulation of focused helium ion beam induced deposition. Nanotechnology **21**(17), 175302 (2010)
84. P.F.A. Alkemade et al., Model for nanopillar growth by focused helium ion-beam-induced deposition. J. Vac. Sci. Technol. B: Nanotechnol. Microelectr. **28**(6), C6F22–C6F25 (2010)
85. J.D. Fowlkes, P.D. Rack, Fundamental electron-precursor-solid interactions derived from time-dependent electron-beam-induced deposition simulations and experiments. ACS Nano **4**(3), 1619–1629 (2010)
86. W.F. Van Dorp et al., Approaching the resolution limit of nanometer-scale electron beam-induced deposition. Nano Lett. **5**(7), 1303–1307 (2005)
87. I. Utke, H.W.P. Koops, The historical development of electron induced deposition and etching: from carbonaceous to functional materials, in *Nanofabrication Using Focused Ion and Electron Beams. Principles and Applications*, ed. by I. Utke, S. Moshkalev, P. Russell (Oxford University Press, Oxford, 2012), pp. 248–285
88. C.J. Lobo et al., High resolution radially symmetric nanostructures from simultaneous electron beam induced etching and deposition. Nanotechnology **19**(2), 025303 (2008)
89. F. Porrati et al., Room temperature L1 0 phase transformation in binary CoPt nanostructures prepared by focused-electron-beam-induced deposition. Nanotechnology **23**(18), 185702 (2012)
90. F. Porrati et al., Fabrication and electrical transport properties of binary Co-Si nanostructures prepared by focused electron beam-induced deposition. J. Appl. Phys. **113**(5), 053707 (2013)
91. M. Winhold et al., Binary Pt-Si nanostructures prepared by focused electron-beam-induced deposition. ACS Nano **5**(12), 9675–9681 (2011)
92. J. Bishop et al., Role of activated chemisorption in gas-mediated electron beam induced deposition. Phys. Rev. Lett. **109**(14), 146103 (2012)
93. J.D. Fowlkes et al., Electron nanoprobe induced oxidation: a simulation of direct-write purification. Phys. Chem. Chem. Phys. **17**(28), 18294–18304 (2015)
94. B. Geier et al., Rapid and highly compact purification for focused electron beam induced deposits: a low temperature approach using electron stimulated H2O reactions. J. Phys. Chem. C **118**(25), 14009–14016 (2014)

95. B.B. Lewis et al., Electron-stimulated purification of platinum nanostructures grown via focused electron beam induced deposition. Beilstein J. Nanotechnol. **6**(1), 907–918 (2015)
96. R. Sachser et al., Catalytic purification of directly written nanostructured Pt microelectrodes. ACS Appl. Mater. Interf. **6**(18), 15868–15874 (2014)
97. O. Yavas et al., Field emitter array fabricated using focused ion and electron beam induced reaction. J. Vac. Sci. Technol. B (Microelectronics and Nanometer Structures) **18**(2), 976–979 (2000)
98. L. Rotkina, J.F. Lin, J.P. Bird, Nonlinear current-voltage characteristics of Pt nanowires and nanowire transistors fabricated by electron-beam deposition. Appl. Phys. Lett. **83**(21), 4426–4428 (2003)
99. M. Weber et al., New compound quantum-dot materials produced by electron-beam-induced deposition. J. Vac. Sci. Technol. B **13**(3), 1364–1368 (1995)
100. A. Fernandez-Pacheco et al., Magnetotransport properties of high-quality cobalt nanowires grown by focused-electron-beam-induced deposition. J. Phys. D Appl. Phys. **42**(5), 055005 (2009)
101. S. Matsui, T. Ichihashi, M. Mito, Electron beam induced selective etching and deposition technology. J. Vac. Sci. Technol. B (Microelectronics Processing and Phenomena) **7**(5), 1182–1190 (1989)
102. V. Callegari, U. Sennhauser, H. Jaeckel, FIB etching of InP for rapid prototyping of photonic crystals, in *Nanofabrication Using Focused Ion and Electron Beams. Principles and Applications*, ed. by I. Utke, S. Moshkalev, P. Russell (Oxford University Press, Oxford, 2012), pp. 248–285
103. C. Ebm et al., Modeling of precursor coverage in ion-beam induced etching and verification with experiments using XeF2 on SiO2. J. Vac. Sci. Technol. B: Nanotechnol. Microelectr. **28**(5), 946–951 (2010)
104. S. Randolph et al., Kinetics of gas mediated electron beam induced etching. Appl. Phys. Lett. **99**(21), 213103 (2011)

Chapter 16
Resist Assisted Patterning

Nima Kalhor and Paul F.A. Alkemade

Abstract Helium ion beam lithography (HIL) has been demonstrated as a promising alternative to electron beam lithography (EBL) for R&D purposes, offering high-resolution lithography at high pattern densities. This chapter reviews focused He ion beam lithography, providing a detailed discussion on the ion beam-resist interaction mechanisms and latest experimental results in this field. In addition, impact of ion shot noise is examined, a comparison to He-ion beam milling is made, and future directions are mentioned.

16.1 Introduction to Lithography

Currently deep-ultraviolet photolithography is used for wafer-scale mass production of nanoelectronic devices. However, due to the high costs of equipment and masks, alternative lithography methods are required for device prototyping and R&D purposes. Electron beam lithography (EBL) is probably the most established techniques for top-down fabrication of prototype nanoelectronic devices. It was also employed by IBM in the 1980s as a supplement to photolithography to respond to time-sensitive orders [1]. EBL uses a focused beam of electrons to modify chemical properties of a thin layer of material (‘resist’) coated on a substrate into which nanoscale structures are to be created. Electron beam exposure alters the solubility of the exposed resist with respect to the surrounding resist material so that, through a subsequent development step with a chemical solvent, a topographical pattern can be formed in the resist. The pattern can then be transferred into the underlying substrate using a wet or dry etching process, whereby the remaining resist protects or ‘masks’ the substrate material directly underneath. Alternatively, a material can

N. Kalhor (✉) · P.F.A. Alkemade
Kavli Institute of Nanoscience, Delft University of Technology, Lorentzweg 1, 2628, Delft, The Netherlands
e-mail: n.kalhor@tudelft.nl

P.F.A. Alkemade
e-mail: p.f.a.alkemade@tudelft.nl

© Springer International Publishing Switzerland 2016

G. Hlawacek and A. Gölzhäuser (eds.), *Helium Ion Microscopy*, NanoScience and Technology, DOI 10.1007/978-3-319-41990-9_16

be deposited onto the patterned resist. After a subsequent lift-off process, the deposited material is present only in the regions of the substrate that were not covered by the resist. The chemical modification of resist in EBL is achieved primarily through the generation of low-energy secondary electrons (SEs). Focused ion beams (FIB) are also capable of generating SEs and therefore focused ion beam lithography (FIBL) emerged as a possible alternative to EBL. Focused ion beam lithography, mostly with Ga ions, being the standard ion source in most FIB systems, was investigated extensively in the late 1980s and early 1990s [2–6]. The studies found that FIBL with Ga-ions offers a higher sensitivity, due to a higher secondary electron (SE) yield, and a lower proximity effect, due to the short range of primary particles, compared to EBL. However, state-of-the-art gallium ion beam columns are only capable of achieving a spot size down to 4 nm [7] (almost half order of magnitude larger than the spot size achievable with EBL), limiting the ultimate resolution of this technology. Furthermore, heavy gallium ions can cause substantial damage in the underlying substrate due to ion collision cascades and sputtering. And the implanted Ga ions can become electrically-active contaminants, thus affecting the electrical properties of the substrate.

Proton beam lithography with high-energy (MeV) protons is another interesting option. Protons (1800 times more massive than electrons) have a very high penetration depth with a minimal lateral spread in materials, allowing fabrication of high aspect ratio three-dimensional structures with vertical sidewalls and low line-width roughness [8, 9]. Sub-100 nm features can be readily achieved in thick resist layers with this method [8]. Furthermore, because of the low mass of protons, proton beam lithography even at MeV energies is not expected to cause notable physical damage to the underlying substrate. This offers a great advantage in comparison to medium or heavy ion beam lithography for which substrate damage is always an issue. However, protons traveling into a substrate can create vacancies and cause damage at the end of their range [8].

The development of the gas-field-ion source (GFIS) [10] enables a focused positive ion beam with a spot-size in the sub-nanometer range, which is comparable or better than that which can be achieved with electron beams. Helium ion microscopy is a new surface imaging technique that involves scanning a focused beam of helium ions from a GFIS across a surface to generate an image from the resulting secondary electron (SE) emission [11]. This tool was primarily developed and introduced as an ultra-high resolution imaging instrument with unique contrast capabilities, see Chap. 1. However, as it produces an intense highly focused beam of He-ions, it can also be employed as a high resolution patterning tool, e.g. via milling or lithography [12]. Moreover, the light helium ions cause less damage than gallium ions near the surface of the exposed substrate, although high doses of He ions could induce damage by forming nano-bubbles at the end of range in the substrate [13].

Remarkable similarities in the activation response of resists to He-ions and to extreme-ultraviolet (EUV) photons in EUV lithography (EUVL) are expected [14]. Since EUVL is widely considered as the next platform for future mass production of nano devices with sub-20 nm resolution, it is indeed intriguing to employ helium

ion lithography (HIL) to investigate resolution-limiting factors in resist-assisted patterning. Unlike EUVL, HIL offers rapid device prototyping without the use of photo-masks or expensive equipment.

In this chapter, HIL is discussed as an alternative to electron beam lithography for device prototyping and R&D purposes. The chapter also reviews focused (helium) ion beam lithography by providing a detailed discussion on ion beam-resist interaction mechanisms and on HIL modelling and by summarising experimental results. In addition, possible future applications for HIL are discussed and a comparison to He-ion beam milling is made.

16.2 Helium Ion Beam-Resist Interaction

The achievable minimum lithographic feature size depends on resist properties, the interaction of the charged-particle beam with the resist, and post-exposure processes. In general, resist performance is evaluated in terms of resolution (*R*), line-width roughness (LWR), and sensitivity (*S*). Despite numerous efforts, it appears to be impossible to obtain high sensitivity, high resolution, and low line-width roughness simultaneously [15], presumably because these parameters are highly interdependent. Resists that offer the highest resolution often tend to be the least sensitive resists. Furthermore, pattern collapse becomes a significant problem with decreasing feature size. The use of thinner resists can prevent pattern collapse but could lead to an increase in LWR. These challenges are commonly referred to as the RLS-tradeoff or, rather melodramatically, 'the triangle of death' [15, 16]. The RLS-tradeoff is often quantified by the figure-of-merit for resist performance, the so-called '*Z*-factor', defined as [17]:

$$Z \equiv R^3 \times LWR^2 \times S \tag{16.1}$$

The dose-response curve is a plot of the normalised resist thickness after development as a function of lithography dose. It is obtained from large area exposures (in general micrometer-size square-shape patterns) with different doses. The resist thickness is measured using a profilometer or an atomic force microscope (AFM) after post-exposure resist processing and normalised to the thickness of the non-exposed parts. The sensitivity of a positive-tone resist is taken as the dose above which the resist dissolves in the development step, see Fig. 16.1. For negative-tone resists, the sensitivity is the dose above which the resist remains unaffected in the development step. However, the step in experimental dose-response curves has a finite width. The resist contrast value γ reflects the steepness of the step; it is defined as:

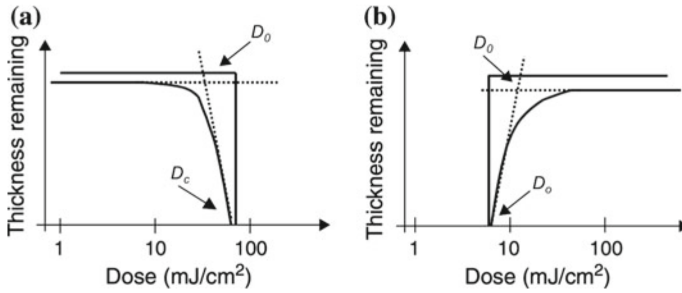

Fig. 16.1 Illustration of dose-response curves for **a** positive and **b** negative tone resists. D_c and D_o are the dose-to-clear and the onset dose for positive-tone and negative-tone resists, respectively. D_0 is the extrapolated dose at the kink of both contrast curves. Figure modified from [18]

$$\gamma \equiv [\log_{10}(D_{c/o}/D_0)]^{-1} \tag{16.2}$$

Here, D_c is the dose-to-clear for a positive resist, D_o is the onset dose for a negative resist, and D_0 is the (extrapolated) kink dose, see Fig. 16.1. Resist contrast is one contributing factor for the final lithography resolution. High contrast resists exhibit a quick transition between $D_{c/o}$ and D_0, resulting in lithographic features with steeper sidewalls as well as wider exposure latitudes. Note that the exposure latitude is the exposure dose range (expressed as percent variation from the dose-to-size) that keeps lithographic feature size within the desired critical dimension (i.e. the hole diameter for contact-hole patterns) or linewidth (for line-and-space patterns); the dose-to-size is the dose required to achieve a desired lithographic feature size.

In general, beam-resist interactions have a dominating influence on the patterning resolution. In this regard, HIL holds advantage over EBL and conventional FIBL because of its sub-nanometer probe size. However, in resist-assisted patterning, the ultimate resolution of lithographic features is predominantly determined by the spatial extent of the energy dissipation in the resist. Primary particles dissipate their kinetic energy gradually through atomic collisions. In this process, primary particles generate recoiled atoms, secondary electrons (SEs), phonons, and surface or volume plasmons [19], all of them can distribute the initial energy of the primary particles further in the resist.

Figure 16.2 demonstrates general interaction mechanisms involved in a particle beam exposure. Note that since the contribution of generated phonons and surface or volume plasmons is small [19], they are not treated further in the following discussions. A beam broadens as it enters a material due to forward scattering of the primary particles. Meanwhile, the beam-material interaction results in SE generation. The SEs can travel away from the location of generation, their average range depending on the SE energy. These two spreading mechanisms–ion deflection by forward scattering and SE travel–broaden the beam-resist interaction volume. It is

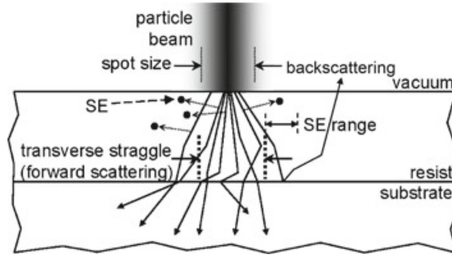

Fig. 16.2 Beam-sample interaction mechanisms involved in a lithography exposure. Forward scattering, secondary electron (SE) generation, and backscattering of primary particles are the main physical mechanisms that degrade the resolution of a lithography process. Figure modified from [20]

also possible that some primary particles backscatter in the substrate and find their way back to the resist.

Beam deflection, SE generation, and backscattering might have a lithographic effect at sites nearby the original beam incidence site, thus degrading the ultimate pattern resolution. This resolution degradation is called the proximity effect. In addition, statistical fluctuations in the delivered dose (i.e. shot noise), post-exposure processes (e.g. post-exposure bake and post-exposure resist pattern development), and pattern collapse can act upon the resolution and fidelity of the final patterns.

Proximity effects can be quantified by a point-spread function (PSF), which is the spatial distribution of lithographic activation in a resist as a function of the radial distance (r) from the primary beam incidence site. The PSF is a complex function which contains most, though not all, physical (primary particle penetration, recoil atom, and SE generation, etc.) and chemical (e.g. post-exposure development) phenomena involved during the exposure and the post-exposure processes [19]. For instance, if one only takes forward scattering and backscattering of the primary particles into account, the general mathematical expression of the PSF can be written as a sum of two Gaussian terms:

$$PSF(r) = A\left[\frac{1}{\alpha^2}\exp\left(-\frac{r^2}{\alpha^2}\right) + \frac{\eta}{\beta^2}\exp\left(-\frac{r^2}{\beta^2}\right)\right] \tag{16.3}$$

Here, A is a normalisation constant. The terms of this equation include a forward scattering range (with a typical distance α) and a backscattering range (with a typical distance β); η is the relative intensity ratio of backscattering to forward scattering. In general, detail study of the PSF is of great importance to understand and, hence, to improve the resolution of lithography techniques. Furthermore, accurate estimation of the PSF is crucial for pattern prediction and proximity-effect corrections in EBL [21]. The PSF can be measured by plotting the size of lithographic features (e.g. dots [22], single-pixel lines [23], and doughnut-shape features [24]) as a function of the reciprocal dose. The full width at half maximum (FWHM)

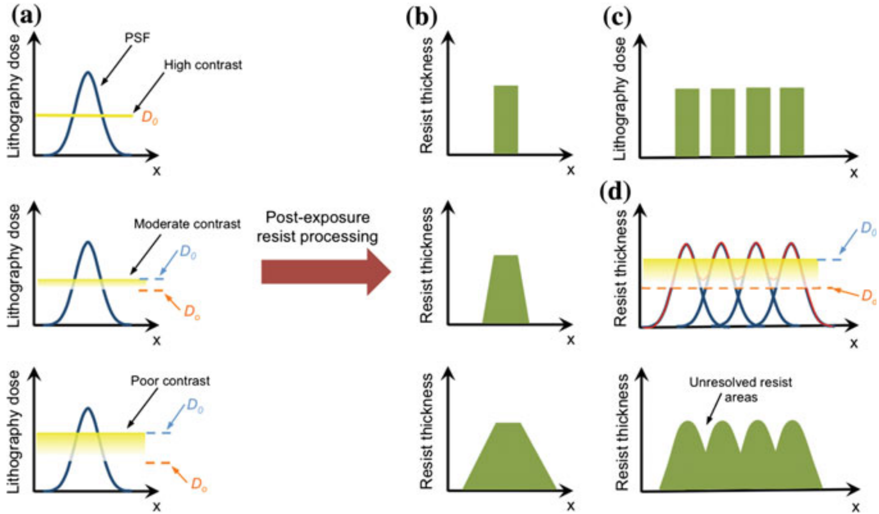

Fig. 16.3 Resist contrast impact in negative-tone lithography. **a** Lithography dose window for high (*top*), moderate (*centre*), and poor (*bottom*) resist contrast; the yellow band depicts the resist transition range from D_o to D_0. **b** Resist profiles for the corresponding resist contrasts; for high contrast (*top*), the sidewalls of the lithographic pattern are steep, but they degrade for lower contrasts (*centre and bottom*). **c** Lithography process outcome with a high contrast resist for a line-and-space pattern. **d** (*Top*) The resolution of lithographic features depends on the PSF and on the resist contrast (*yellow band*). (*Bottom*) Despite a narrow PSF, the poor contrast leads to unresolved areas between lithographic features

of the PSF is a commonly used measure for the resolution of a lithography process for isolated features [25].

An important point that must be highlighted is the fact that the ultimate resolution of lithographic features depends both on the PSF and the resist contrast. Poor resist contrast (Fig. 16.3a) results in merging of adjacent features if the sum of PSF in the centre between the exposed features exceeds the threshold dose (Fig. 16.3c). Poor contrast constrains faithful pattern transfer, thus degrading the ultimate resolution.

In the following sections we compare in detail the resolution-contributing factors of HIL and EBL.

16.2.1 Primary Beam Scattering (Forward Scattering)

The more directional profile of He^+ ion beams compared to electron beams is due to the different scattering behaviours of their primary particles as they move through a material. When helium ions enter a material they initially interact mainly with the material's electrons, scattering inelastically (known as electronic collisions),

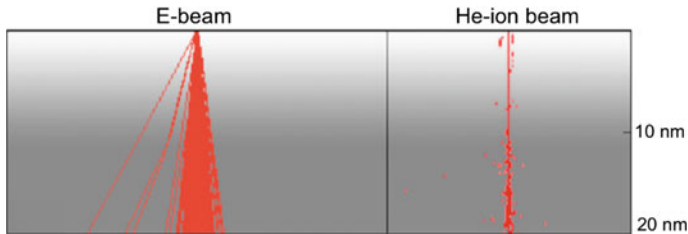

Fig. 16.4 Monte Carlo simulations of 30 keV electron and helium ion trajectories in a 20 nm thick slab of silicon. Figure from [34]

generating SEs, and losing a fraction of their kinetic energy. These processes are very similar to those of electrons at the same energy. However, since the mass of helium ions is approximately 7000 times larger than the electron mass, the ions maintain their initial trajectory much better and, hence, the beam profile remains confined within a narrow volume, see Fig. 16.4. Eventually, as the ions slow down, collisions with the material's nuclei begin to dominate and the ions undergo numerous elastic nuclear scatterings, which alter the trajectories and result in a strong broadening of the final beam profile [26]. The highly directional forward scattering of He ions in materials and the moderate energy loss lead to a narrow but long interaction volume and, hence, enables patterning of sub-10 nm features in thin layers of resist [20, 27–29]. Proton beams exhibit the same behaviour, but even more pronounced: the deflection and the energy loss are even less. In contrast, electrons, because of their low mass, collide elastically with target atoms and scatter far easier than helium ions or protons, resulting in a rapid broadening of the beam profile close to the surface of the resist and, thus, in a broader interaction volume. This different behaviour has been illustrated by Postek et al. using Monte Carlo simulation of trajectories of helium ions (modelled by SRIM 2008.04 [30]) and electrons (modelled by CASINO 2.42 [31–33]) in silicon, with both beams operating at 30 keV [34]. Figure 16.4 shows some simulated paths of the charged particles within the top 20 nm of the substrate, revealing beam broadening of 5 nm and 1 nm for the electron beam and the He^{+} beam, respectively. The simulation illustrates the smaller and more directional interaction volume of the latter beam.

It is worth mentioning that heavy ions, e.g. Ga-ions, predominantly undergo elastic nuclear scattering, resulting in broader beam profiles and, thus, poorer lithography resolution.

16.2.2 Secondary Electron (SE) Generation

The SEs generated by the primary beam are responsible for the chemical alteration of resists. Therefore, the lithography resolution is highly dependent on the behaviour of the SEs. The SEs form an expanding cloud around the primary beam,

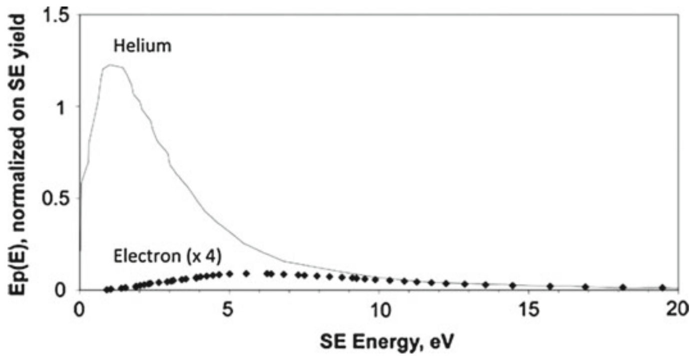

Fig. 16.5 Comparison of SE spectra generated in a SEM and in a HIM, both operating at 30 keV. The spectra are normalised according to the SE yield of the respective beam. Figure from [29]

resulting in a further broadening of the beam-resist interaction volume [35, 36]. The mean free path of the low-energy SEs is inversely proportional to their energy. However, SEs with energies below 4 eV are not expected to contribute to resist exposure. Note that the 4 eV refers to the energy of the SEs in vacuum [37], they have higher energies in the resist; the difference is the work function.

Classically, a He-ion at 30 keV (= E_0) can transfer a maximum energy ($T_{\max}$) of 16 eV to an electron that is initially at rest: $T_{\max} = 4(m_e/M) \times E_0$, where m_e and M are the electron and the ion mass, respectively. Plots of SE spectra generated by 30 keV electron and He-ion beams are shown in Fig. 16.5. One sees that for the He-ion beam the energy distribution of the SEs peaks at around 2 eV, as opposed to 6 eV for the electron beam [4, 29, 37–40]. Furthermore, the SE distribution generated by He-ions drops to zero above 20 eV, but remains finite for an electron beam. The narrow energy distribution, peaking just above zero energy, of the SEs generated by He-ions compared to electrons of the same energy [37, 40, 41] implies a lower lithographic sensitivity due to the insufficiency in energy to induce bond scission. For instance, the binding energy of the C–C bond in *poly methyl methacrylate* (PMMA) resist is 4.9 eV [35].

Perhaps the most striking difference between the SE energy distributions from He ion and electron beams in Fig. 16.5 is the much larger SE yield for the ion beam, resulting in a higher sensitivity of resist to He ions as compared to electrons. Although this offers benefits in terms of faster pattern writing, the consequently lower number of primary particles (N) required per pixel of the exposure pattern can diminish the exposure uniformity due to inherent shot noise effects. These effects scale with $1/\sqrt{N}$ and are in particular prominent for sensitive resists [29], and so impairing pattern fidelity. If only a handful of ions is required to expose a resist locally, primary ion distributions are sparse, resulting in significant statistical fluctuations in the deposited energy density. This issue manifests itself primarily at pattern edges where bunching or anti-bunching of a few particles may cause the effective dose (i.e. the deposited energy) to shift above or below the threshold dose,

thus impairing faithful patterning. Clearly this effect becomes a considerable issue with decreasing feature size, potentially resulting in local over- or under-exposure of a lithographic feature. Shot noise is regarded as a major factor in the RLS-tradeoff or 'triangle of death'. Recently, Kalhor et al. proposed pixel-dose optimized HIL to improve pattern fidelity [23]. This method is presented in detail in Sect. 16.5 of this chapter. For instance, single-pixel HIL of a 40-nm-full-pitch line-and-space pattern with a LWR of 4 nm on a sensitive chemically amplified resist (CAR), with a dose-to-clear (D_c) of 0.085 He-ions/nm^2, was demonstrated experimentally [14].

16.2.3 Backscattering of the Primary Beam

Secondary electrons created by the backscattered primary ions can also contribute to resist exposure and therefore the interaction volume and pattern resolution, see Fig. 16.2. Backscattered primary particles can travel from the substrate back to the resist and generate additional SEs, resulting in resist exposure far from the incident primary beam. This long-range proximity effect is described by the β-term in (16.3). Ramachandra et al. showed that the ratio between the number of SEs generated by the backscattered particles (the so-called SE2's) and those generated by the primary particles (the SE1's) is significantly less in He ion beam exposure than in electron beam exposure [40]. Backscattered ions have less energy than primary ions, lose less energy, and generate fewer SEs. These attributes imply that HIL exhibits a small contribution of backscattering to resist exposure, leading to a weak long-range proximity effect [27, 29, 42], i.e. η in (16.3) is small. This allows fabrication of high resolution features without resorting to complex exposure compensation strategies which are common in EBL. Note that with increasing beam energy the number of backscattered ions drops; moreover most SEs are then produced too deep beneath the surface to reach the resist. Thus, the impact of backscattering in HIL diminishes with beam energy.

16.3 HIL Experimental Results on EBL Resists

The above discussions highlight the potential of HIL as a promising alterative to EBL. This potential has inspired several groups to investigate experimentally the reaction of resists exposed to a focused beam of helium ions in a helium ion microscope. These studies have confirmed the expectations about sensitivity and resolution of the technique [22, 27, 42]. In this section, we discuss HIL experimental results on EBL resists, i.e. PMMA and hydrogen silsesquioxane (HSQ), and compare them with EBL results. It is worth mentioning that all following experiments were performed with a He-ion beam operating at 30 keV.

16.3.1 Contrast and Sensitivity

Resist contrast and resist sensitivity are extracted from dose-response curves. Figure 16.6 compares the dose-response curves for HIL and EBL on PMMA 950 K and HSQ resists. The experimentally obtained HIL dose-response curve of PMMA resist (Fig. 16.6a) demonstrates a resist tone change from positive at low dose to negative at high dose [29]; this double-tone behaviour was also reported for EBL [43]. The value for D_{50} (the dose at which the resist remaining after post-exposure processing was 50% of the unexposed resist thickness) was 2.0 μC/cm^2 (positive-tone) and 68 μC/cm^2 (negative-tone). Accordingly, PMMA shows in positive-tone a 69 times and in negative-tone a 116 times higher sensitivity for HIL than for EBL, both at a beam energy of 30 keV [29]. Thanks to the strong SE generation by He-ions, the required doses for these resists are one to two orders of magnitude lower than for electron beam lithography [44]. Note that the positive-tone is based on chemical chain scission of resist molecules into lower molecular weight fission products that dissolve faster in the development process. In contrast, the negative-tone of PMMA is caused by crosslinking or polymerizing of resist molecules that makes the resist more difficult to dissolve. Then, the exposed resist regions remain and the unexposed regions dissolve in the resist developer. The dose-response curve for HIL with HSQ has a similar shape as that for EBL (see Fig. 16.6b), both showing only negative-tone behaviour. HSQ resist is 55 times more sensitive for He-ions than for electrons at the same beam energy, whilst the contrast values are not very different (γ = 2.0 and 2.3 for EBL and HIL, respectively) [29].

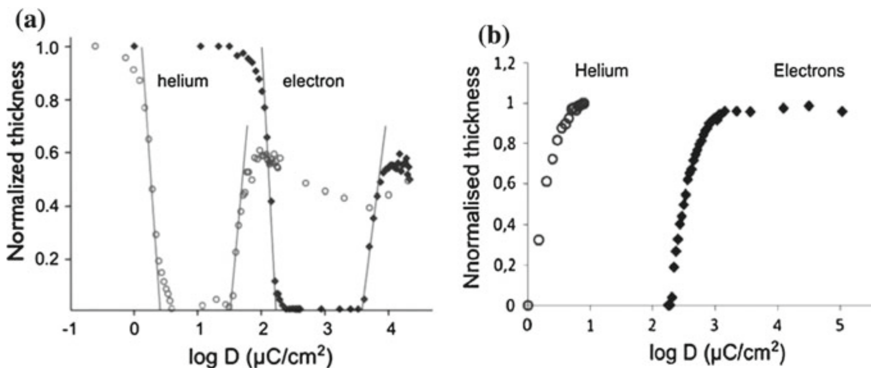

Fig. 16.6 Dose-response curves of **a** PMMA 950 K and **b** HSQ resist, for He-ions at 30 keV and electrons at 100 keV energy. The electron dose has been scaled down by a factor of 100/30 for comparison at the same beam energy. Figure from [29]

16.3.2 Resolution

High resolution patterning using HIL has been demonstrated in both PMMA and HSQ resists. Sidorkin achieved 15 nm wide lines in 20 nm thick PMMA on silicon in both positive and negative tone [45]. Similarly, Winston et al. demonstrated well-defined 10 nm wide lines at 20 nm pitch on a 25 nm thick HSQ resist [20]. However, self-terminating resist development and collapse of high-aspect-ratio (height vs. width) features because of capillary action during drying can impair the resolution [20]. The use of a 5 nm thick HSQ resist layer enabled Sidorkin et al. to fabricate high-density dot arrays with feature sizes down to 6 nm (Fig. 16.7) [27]. The authors observed little variation in dot size as a function of pitch, indicating an unobservable weak proximity effect for He-ion beam lithography. They linked the resolution limit of 6 nm to weak adhesion of small resist features to the substrate and the low number of cross-linked resist monomers at small features size [27]. A resolution of 4 nm half-pitch for a line-and-space pattern was obtained by Li et al. [46] for He-ion lithography on HSQ. These values are comparable to state-of-the-art EBL with a beam operating at 100 keV [47, 48]. Thus, HIL can offer minimum feature sizes comparable to EBL. In conclusion: despite the high yield and short range of low energy SEs and the weak deflection of He-ions, HIL has not yet proven superiority over EBL in terms of resolution.

Using the 5 nm HSQ resist, Van der Drift et al. demonstrated almost no influence of the pitch on the shape of 5 nm wide lines, indicating again the absence of a measurable proximity effect [29]. Furthermore, Shi et al. demonstrated 8.5 nm wide lines at 17 nm pitch on a negative-tone fullerene-based molecular resist [49].

It is worth mentioning that HIL on metal-oxide resists has also been reported [29]. Metal oxides (e.g. Al_xO_y) are considered as ultrahigh-resolution inorganic

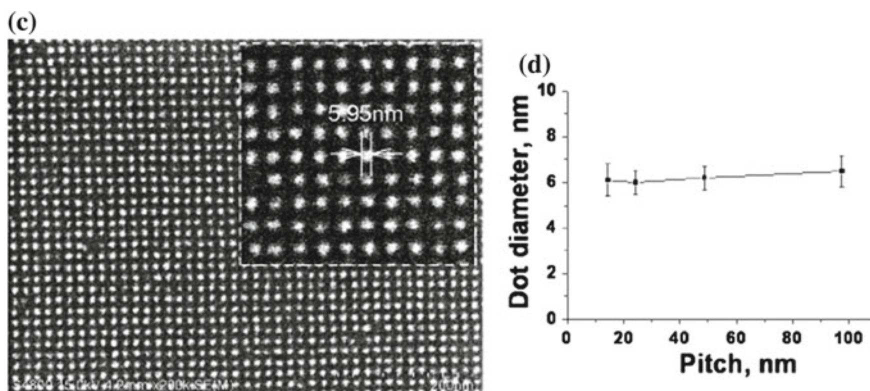

Fig. 16.7 SEM image of arrays of dots written in a 5 nm thick layer of HSQ resist by He-ion lithography at 14 nm pitch with remarkable minimum features of 6 nm (*left*). Little variation in the dots size as a function of pitch indicates a negligibly weak proximity effect for He-ion beam lithography (*right*). Figures from [27]

resists for EBL and EUVL. An Al_2O_3 layer can be spin-coated, sputtered, or grown by atomic layer deposition (ALD). Successful fabrication of 5 nm lines with a He-dose of 14 mC/cm^2 on a 5 nm thick layer of ALD grown Al_2O_3 has been reported [29], which is comparable to EBL [50, 51].

16.3.3 Point-Spread Function (PSF)

Proximity effects can be quantified by the PSF, the spatial distribution of the energy deposition in a resist as a function of the radial distance from the primary beam incidence point. Experimentally, the PSF is often plotted as the inverse dose versus the half-width of a lithographic feature.

In an initial study Winston et al. [17] found that the PSF of HIL resembled well the double-Gaussian profile of (16.3), comparable to EBL but wider than expected, considering the sub-nm beam spot size and the negligibly weak proximity effect. However, a more detailed follow-up study revealed a PSF–shown in Fig. 16.8—that exhibits exponential and power-law-like dependencies, particularly in its mid-range parts [22].

Furthermore, the authors calculated theoretically [22] the PSF for HIL on a 12 nm thick HSQ resist layer on a silicon substrate by combining ion trajectory simulation (by SRIM) with SE simulation (using the IONiSE simulator [40]). Interestingly, the calculated PSF was found in good agreement with the experiment in the mid-range of the experimental curve (see Fig. 16.8). However, further investigation is required to understand quantitatively the physical factors of the PSF, particularly in the mid-range region.

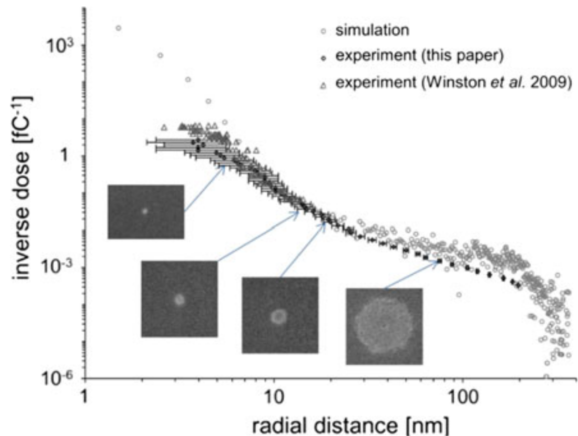

Fig. 16.8 Comparison between PSF profiles for HIL by simulation and experiment. The 200 nm wide SEM images of point-exposed features illustrate the experimental method to construct the plot. Figure from [22]

16.4 HIL Applications

As discussed, HIL offers high patterning resolution and, compared to EBL, weaker proximity effects, thanks to the weak deflections and the low fraction of backscattered primary particles. These characteristics have promoted HIL for device prototyping and R&D purposes. In this section we discuss recent applications of HIL.

16.4.1 Pre-screening of EUV Resists

As it was mentioned earlier in this chapter, EUV lithography (EUVL) is considered as the next industrial platform for future sub-20 nm lithography. However, one of the main challenges to establish EUVL reliably is the need for high performance resists that can meet industry requirements for resolution, sensitivity and line width roughness.

Remarkably, unique similarities in the activation response of resists to He-ions and extreme-ultraviolet (EUV) photons are anticipated [14, 23]. Both primary beams produce low-energy secondary electrons (SEs) and exhibit negligible proximity effects. However, unlike an EUV photon, which only interacts with one resist molecule and so generating only one medium-energy electron, a He-ion experiences a chain of collisions with resist molecules, producing multiple low-energy SEs along its way. Recently Maas et al. compared HIL and EUVL on a chemically amplified resist (CAR) [14]. Thanks to the higher efficiency of a He-ion in generating SEs and the high sensitivity of the resist, the dose-to-clear D_c was low, only 0.085 He-ions/nm^2 (1.4 μC/cm^2).

In particular, 150 times less ions than EUV photons were required to achieve similar resist activation. Detailed analysis of pattern fidelity for both exposure methods revealed better LWR, but worse local critical dimension uniformity (LCDU) for HIL [14]. Figure 16.9 shows SEM images of HIL and EUVL on CAR results for contact hole (CH) and lines patterns. The poorer LCDU was attributed, at least partially, to an instability of the ion source [23].

Despite the high sensitivity of CAR to He-ions, ion shot noise was not found to limit pattern fidelity [14, 23]. Optimization of the experimental conditions (e.g. more stable ion source emission and post-exposure resist pattern development) is expected to improve the results. Therefore, HIL seems a promising cost-effective method for pre-screening chemically amplified resists prior to their final performance evaluation in an EUV scanner.

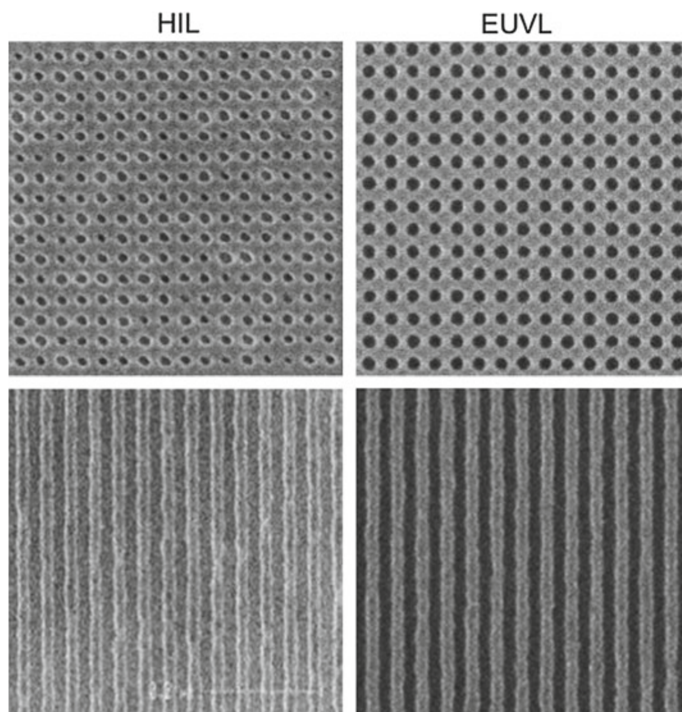

Fig. 16.9 SEM images (taken at 500 eV) of HIL and EUVL on CAR. (*Top row*, *left to right*) 40 nm full-pitch contact hole (CH) pattern exposed to a He-dose of 150 ions/CH and an EUV-dose of 20000 photons/CH, respectively. *Bottom row* 40 nm full-pitch line-and-space pattern for (*left*) a He-line dose of 4.3 ions/nm and (*right*) a EUVL dose of 40 mJ/cm^2. Figure from [14]

16.4.2 Fabrication of Nanoimprint Templates

Another exciting application of HIL is the fabrication of nanoimprint templates. Nanoimprint lithography (NIL) is a low-cost lithography method that offers high throughput with molecular-scale resolution. In this method, a template with features down to several nanometers is brought into contact with a resist material. Next, the desired pattern is transferred via mechanical deformation of the resist, followed by a thermal or a UV hardening step. Using HIL, Li et al. [46] fabricated NIL templates in thin HSQ layers, see Fig. 16.10a. With these templates, the authors successfully demonstrated NIL of a 4 nm half-pitch line pattern into a layer of UV resist (see Fig. 16.10b), achieving a better resolution than previously reported for NIL with conventionally designed templates [52].

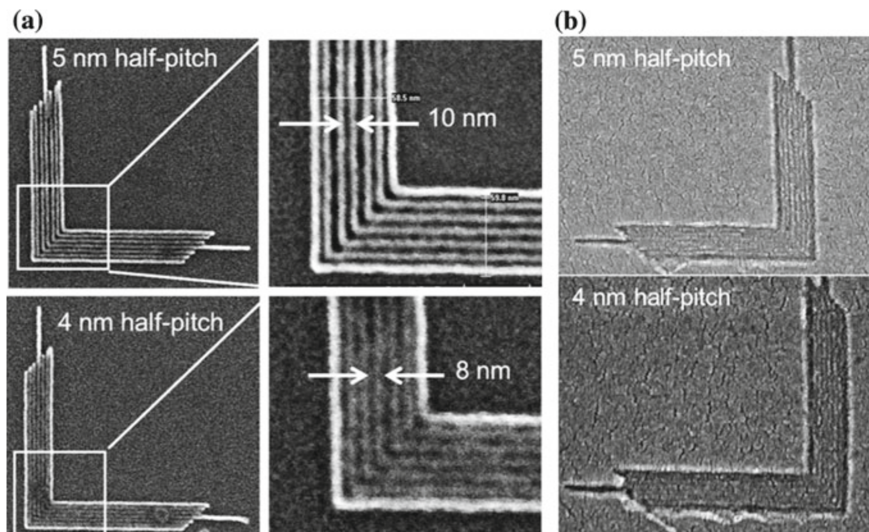

Fig. 16.10 SEM images. **a** 5 nm half-pitch (*top*) and 4 nm half-pitch (*bottom*) nested L's on a 12 nm thick HSQ layer using HIL. **b** Nanoimprint lithography on a UV resist using the HSQ templates of (**a**). The 'grainy' appearance of the NIL patterns is attributed to a thin Pt coating, applied to minimize sample charging during SEM imaging. Figures from [46]

16.5 HIL Dose Optimization Modelling

Ongoing efforts in electronic device downscaling stimulate process modelling and fundamental studies of beam-resist interactions. So far, there appeared two HIL modelling studies [23, 53]. Roy et al. investigated shot noise impact in HIL, using proximity lithography with a 10 keV He-ion beam exposing a PMMA resist through a mask at a proximity gap, i.e. mask-resist distance, of 110 μm [50]. They modelled the experiments using Monte Carlo calculations, accounting for the penumbral image blur, ion shot noise, and statistical variations in ion trajectories in the resist. However, due to the large proximity gap, the penumbral blur dominated the shape of patterned features.

Kalhor et al. modelled single-pixel HIL experiments on CAR using a PSF to account for the physical and chemical factors that contribute to resist activation [23]. A resist activation map was obtained by convolving the ion dose map with the PSF. Poisson statistics were employed to include the ion shot noise. The modelling results were in good agreement with the experiments. In addition, the authors proposed pixel-dose optimization to improve pattern fidelity and exposure latitude for HIL. The model constructs a dose profile for the best possible obtainable lithographic features in accordance with the characteristics of the exposure tool (e.g. resolution, beam step size, etc.), resist properties (i.e. dose-response curve), and ion shot noise. This exposure method offers two advantages over single-pixel HIL. First, lithographic feature edges are exposed at the steepest part of the PSF,

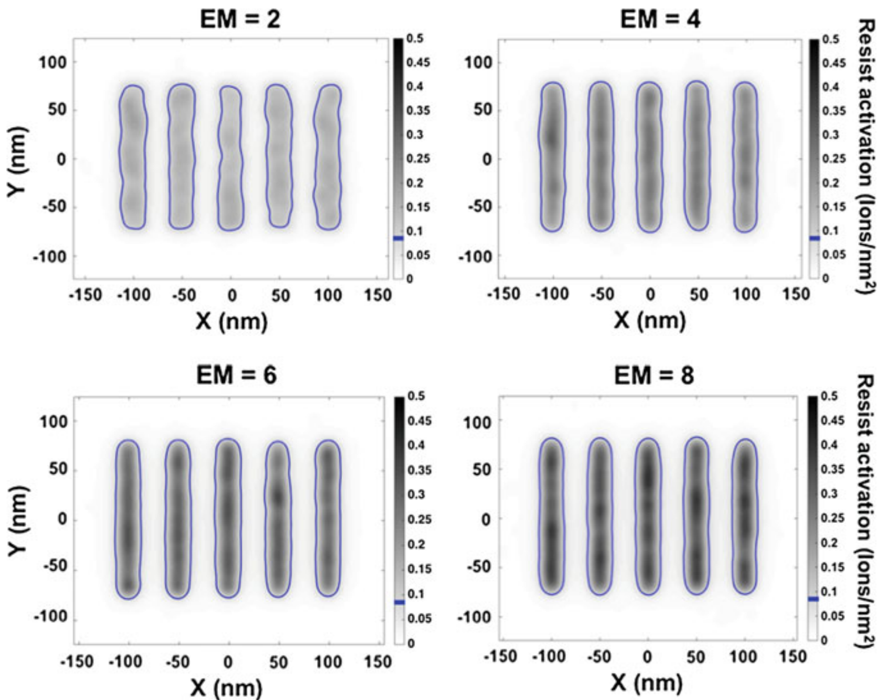

Fig. 16.11 Modelled resist activation maps using pixel-dose optimization for a 50 nm full-pitch line-and-space pattern for different exposure margins (EM). The blue stripes on the scale bar and the blue contour around the line-and-space patterns indicate the dose-to-clear. Figure from [23]

resulting in a higher pattern contrast around the dose-to-clear. Second, the central area of a pattern can be realized with a significantly lower dose, thus avoiding pattern ablation as well as reducing the exposure time [23]. However, it was shown that this method is advantageous only if the minimal feature size is at least twice the FWHM of the PSF. Using this approach the authors calculated a LWR of 1.6 nm (3-sigma) for a 50 nm full-pitch line-and-space pattern with a concurrent 15% dose reduction as compared to single-pixel HIL experiments. Figure 16.11 shows an example of an optimized resist activation map for 50 nm full-pitch line-and-space patterns at different exposure margins (EM). Note that EM is the ratio of the dose-to-size to the dose-to-clear.

16.6 HIL Versus Milling

Helium ion beam milling, i.e. the direct removal of material by He-ion collisions, is capable of offering higher resolution patterning than HIL, see also Chap. 15. Milled features below 5 nm have been reported [54], even down to 1 nm [55]. In contrast,

the best resolution of HIL is 4 nm [46], presumably mainly limited by resist performance and post-exposure processes. Both helium ion beam nanofabrication techniques are very different. Consequently, there are considerable advantages to each of them, depending on the application. For instance, He ions are light and penetrate deep into materials, which might thwart both milling and lithography applications. Moreover, HIL requires many more processing steps than He ion beam milling, making the latter technique more useful for prototyping purposes. Due to low mass of the He-ions, milling is slow and only suited for patterning thin layers or membranes (e.g. graphene [12]). However, deep damage during HIL could be irrelevant if features in a resist layer, patterned with a He-ion beam, are transferred deeper into the substrate by subsequent etching, though probably at the expense of resolution. Moreover, because of the high sensitivity of resists to He-ions, lower He-doses are required for resist patterning than for He-ion milling. This minimizes both damage to the underlying substrate [12, 13, 56] as exposure times [12]. Although shot noise at low doses could impair pattern fidelity in HIL, no sign of ion shot noise has been reported so far [14, 23]. At the moment, helium ion beam milling has proven to be more practical than helium ion lithography.

16.7 Conclusions and Outlook

The emergence of the helium ion microscopy with the sub-nanometer probe beam sparked renewed interest in ion beam lithography. First studies of helium ion lithography (HIL) showed unequivocally excellent results, in terms of sensitivity and resolution. In particular, HIL is more effective than electron beam lithography (EBL), exhibits comparable resolution, and does not suffer noticeably from proximity effects. These characteristics would make HIL a preferred nanofabrication technique above EBL. However, decades of practical experience with EBL resulted in optimized instruments, extended operating software, and well-established processing procedures and materials. Although dedicated applications have arisen and will continue to arise for which HIL is superior, at the moment we do not foresee realistically a replacement of EBL by HIL. Apart from the backlog in equipment, materials, and procedures, an important shortcoming of HIL will remain damage caused by the implanted helium ions to the substrate material.

Nevertheless, studies showed that at present HIL might already be superior for fabrication of resist patterns at high resolution and high pattern density. Another promising application is the fabrication of nanoimprint templates. A completely different application of HIL is the use of He ions to screen resists potentially useful for EUV lithography. Furthermore, investigation of lithography with other light ions (e.g. H, Li, Ne, or N) is alluring for expanding our knowledge of particle-resist interactions and possibly for special applications. The current developments in novel ion sources for high-resolution imaging and nanofabrication will open, we expect, new possibilities in this area.

Acknowledgments Support from the Dutch Technology Foundation STW, which is part of the Netherlands Organization for Scientific Research (NWO), and which is partly funded by the Dutch Ministry of Economic Affairs is acknowledged.

References

1. W.E. Harding, Semiconductor manufacturing in IBM, 1957 to the present: a perspective. IBM J. Res, Dev. **25**, 647–658 (1981)
2. R.L. Kubena, Dot lithography for zero-dimensional quantum wells using focused ion beams. J. Vac. Sci. Technol., B **6**, 353 (1988). doi:10.1116/1.583997
3. R.L. Kubena, A low magnification focused ion beam system with 8 nm spot size. J. Vac. Sci. Technol., B **9**, 3079 (1991). doi:10.1116/1.585373
4. S. Matsui, Y. Kojima, Y. Ochiai, High-resolution focused ion beam lithography. Appl. Phys. Lett. **53**, 868 (1988). doi:10.1063/1.100098
5. J. Melngailis, Focused ion beam lithography. Nucl. Instrum. Methods B **80–81**, 1271–1280 (1993)
6. K. Gamo, Focused ion beam lithography. Nucl. Instrum. Methods B **65**, 40–49 (1992)
7. S. Tan, K. Klein, D. Shima et al. Mechanism and applications of helium transmission milling in thin membranes. J. Vac. Sci. Technol. B **32**:06FA01 (2014). doi:10.1116/1.4900728
8. F. Watt, M.B.H. Breese, A.A. Bettiol, J.A. van Kan, Proton beam writing. Mater. Today **10**, 20–29 (2007). doi:10.1016/S1369-7021(07)70129-3
9. J.A. van Kan, F. Zhang, C. Zhang et al., Exposure parameters in proton beam writing for hydrogen silsesquioxane. Nucl. Instrum. Methods B **266**, 1676–1679 (2008). doi:10.1016/j.nimb.2007.12.081
10. A.J. Melmed, Recollections of Erwin Müller's laboratory: the development of FIM (1951–1956). Appl. Surf. Sci. **94–95**, 17–25 (1996). doi:10.1016/0169-4332(95)00351-7
11. B.W. Ward, J.A. Notte, N.P. Economou, Helium ion microscope: A new tool for nanoscale microscopy and metrology. J. Vac. Sci. Technol., B **24**, 2871 (2006). doi:10.1116/1.2357967
12. N. Kalhor, S.A. Boden, H. Mizuta, Sub-10 nm patterning by focused He-ion beam milling for fabrication of downscaled graphene nano devices. Microelectron. Eng. **114**, 70–77 (2014). doi:10.1016/j.mee.2013.09.018
13. R. Livengood, S. Tan, Y. Greenzweig et al., Subsurface damage from helium ions as a function of dose, beam energy, and dose rate. J. Vac. Sci. Technol. B **27**, 3244 (2009). doi:10.1116/1.3237101
14. D. Maas, E. van Veldhoven, A. van Langen–Suurling et al. Evaluation of EUV resist performance below 20 nm CD using helium ion lithography, eds. by O.R. Wood, E.M. Panning, SPIE Adv Lithogr International Society for Optics and Photonics (2014). p. 90482Z
15. J.A. Liddle, G.M. Gallatin, Lithography, metrology and nanomanufacturing. Nanoscale **3**, 2679 (2011). doi:10.1039/c1nr10046g
16. G.M. Gallatin, Resist blur and line edge roughness, in *Smith BW*, ed. by S.P.I.E. Adv (Lithogr International Society for Optics and, Photonics, 2005), pp. 38–52
17. T. Wallow, C. Higgins, R. Brainard et al., Evaluation of EUV resist materials for use at the 32 nm half-pitch node, in *Schellenberg FM*, ed. by S.P.I.E. Adv (Lithogr International Society for Optics and, Photonics, 2008), pp. 6921–69211F
18. S. Franssila, Introduction to Microfabrication, 1st edn. (John Wiley & Sons, Ltd. 2004)
19. V.R. Manfrinato, J. Wen, L. Zhang et al., Determining the resolution limits of electron-beam lithography: direct measurement of the point-spread function. Nano Lett. **14**, 4406–4412 (2014). doi:10.1021/nl5013773
20. D. Winston, B.M. Cord, B. Ming et al., Scanning-helium-ion-beam lithography with hydrogen silsesquioxane resist. J. Vac. Sci. Technol., B **27**, 2702 (2009). doi:10.1116/1.3250204

21. C.-H. Liu, P.C.W. Ng, Y.-T. Shen et al., Impacts of point spread function accuracy on patterning prediction and proximity effect correction in low-voltage electron-beam–direct-write lithography. J. Vac. Sci. Technol., B **31**, 021605 (2013). doi:10.1116/1.4790655
22. D. Winston, J. Ferrera, L. Battistella et al., Modeling the point-spread function in helium-ion lithography. Scanning **34**, 121–128 (2009)
23. N. Kalhor, W. Mulckhuyse, P. Alkemade, D. Maas, Impact of pixel-dose optimization on pattern fidelity for helium ion beam lithography on EUV resist, eds. by T.I. Wallow, C.K. Hohle, SPIE Adv Lithogr International Society for Optics and Photonics (2015) p. 942513
24. E. Boere, E. van der Drift, J. Romijn, B. Rousseeuw, Experimental study on proximity effects in high voltage e-beam lithography. Microelectron. Eng. **11**, 351–354 (1990). doi:10.1016/0167-9317(90)90128-G
25. S. Cabrini, S. Kawata Nanofabrication Handbook (CRC press, 2012)
26. D. Cohen-Tanugi, N. Yao, Superior imaging resolution in scanning helium-ion microscopy: A look at beam-sample interactions. J. Appl. Phys. **104**, 063504 (2008). doi:10.1063/1.2976299
27. V. Sidorkin, E. van Veldhoven, E. van der Drift et al., Sub-10-nm nanolithography with a scanning helium beam. J. Vac. Sci. Technol. B **27**, L18 (2009). doi:10.1116/1.3182742
28. D. Maas, E. van Veldhoven, P. Chen et al., Nanofabrication with a Helium Ion Microscope. Proc. SPIE **7638**, 763814 (2010). doi:10.1117/12.862438
29. E. van der Drift, D.J. Maas, Helium ion Lithography, in *Nanofabrication Tech*, ed. by M. Stepanova, S. Dew (Princ, Springer Wien NewYork, 2012), pp. 93–116
30. J.F. Ziegler, J.P. Biersack, M.D. Ziegler, SRIM–The Stopping and Range of Ions in Matter. SRIM Co (2008). www.srim.org
31. P. Hovington, D. Drouin, R. Gauvin, CASINO: a new monte carlo code in C language for electron beam interaction–part I: description of the program. Scanning **19**, 1–14 (2006). doi:10.1002/sca.4950190101
32. D. Drouin, P. Hovington, R. Gauvin, CASINO: a new monte carlo code in C language for electron beam interactions–part II: tabulated values of the mott cross section. Scanning **19**, 20–28 (2006). doi:10.1002/sca.4950190103
33. D. Drouin, A.R. Couture, D. Joly, et al. CASINO V2.42: a fast and easy-to-use modeling tool for scanning electron microscopy and microanalysis users. Scanning **29**:92–101. doi:10.1002/sca.20000
34. M.T. Postek, A. Vladár, C. Archie, B. Ming, Review of current progress in nanometrology with the helium ion microscope. Meas. Sci. Technol. **22**, 024004 (2011). doi:10.1088/0957-0233/22/2/024004
35. B. Wu, A.R. Neureuther, Energy deposition and transfer in electron-beam lithography. J. Vac. Sci. Technol., B **19**, 2508 (2001). doi:10.1116/1.1421548
36. K.W. Lee, S.M. Yoon, S.C. Lee et al., Secondary electron generation in electron-beam-irradiated solids:resolution limits to nanolithography. J. Korean Phys. Soc. **55**, 1720 (2009). doi:10.3938/jkps.55.1720
37. Y. Petrov, O. Vyvenko Secondary electron emission spectra and energy selective imaging in helium ion microscope. Proc. SPIE. (2011), p 80360O–80360O–10
38. J. Morgan, J. Notte, R. Hill, B. Ward, An Introduction to the Helium Ion Microscope. Micros Today **14**, 24 (2006)
39. W.-Q. Cheng, M. Rudd, Y.-Y. Hsu, Angular and energy distributions of electrons from 7.5–150 keV proton collisions with oxygen and carbon dioxide. Phys. Rev. A **40**, 3599–3604 (1989). doi:10.1103/PhysRevA.40.3599
40. R. Ramachandra, B. Griffin, D. Joy, A model of secondary electron imaging in the helium ion scanning microscope. Ultramicroscopy **109**, 748–757 (2009)
41. I. Adesida, Ion beam lithography at nanometer dimensions. J. Vac. Sci. Technol. B **3**, 45 (1985). doi:10.1116/1.583288
42. P.F.A. Alkemade, E.M. Koster, E. van Veldhoven, D.J. Maas, Imaging and nanofabrication with the helium ion microscope of the Van Leeuwenhoek Laboratory in Delft. Scanning **34**, 90–100 (2012). doi:10.1002/sca.21009

43. A.N. Broers, J.M.E. Harper, W.W. Molzen, 250-Å linewidths with PMMA electron resist. Appl. Phys. Lett. **33**, 392 (1978). doi:10.1063/1.90387
44. A.E. Grigorescu, M.C. van der Krogt, C.W. Hagen, P. Kruit, Influence of the development process on ultimate resolution electron beam lithography, using ultrathin hydrogen silsesquioxane resist layers. J. Vac. Sci. Technol. B **25**, 1998 (2007). doi:10.1116/1.2794316
45. V.A. Sidorkin, Resist and Exposure Processes for Sub-10-nm Electron and Ion Beam Lithography. PhD thesis, Delft University of Technology, Delft (2010)
46. W.-D. Li, W. Wu, R. Stanley Williams, Combined helium ion beam and nanoimprint lithography attains 4 nm half-pitch dense patterns. J. Vac. Sci. Technol. B **30**, 06F304 (2012). doi:10.1116/1.4758768
47. M.C. van der Krogt, Limiting factors for electron beam lithography when using ultra-thin hydrogen silsesquioxane layers. J. Micro/Nanolithography, MEMS, MOEMS **6**, 043006 (2007). doi:10.1117/1.2816459
48. J.K.W. Yang, K.K. Berggren, Using high-contrast salty development of hydrogen silsesquioxane for sub-10-nm half-pitch lithography. J. Vac. Sci. Technol. B **25**, 2025 (2007). doi:10.1116/1.2801881
49. X. Shi, P. Prewett, E. Huq et al., Helium Ion Beam Lithography on Fullerene Molecular Resists for Sub-10 nm Patterning. Microelectron. Eng. (2016). doi:10.1016/j.mee.2016.02.045
50. A.E. Grigorescu, C.W. Hagen, Resists for sub-20 nm electron beam lithography with a focus on HSQ: state of the art. Nanotechnology **20**, 292001 (2009). doi:10.1088/0957-4484/20/29/292001
51. M.S.M. Saifullah, K. Kurihara, C.J. Humphreys, Comparative study of sputtered and spin-coatable aluminum oxide electron beam resists. J. Vac. Sci. Technol. B **18**, 2737 (2000). doi:10.1116/1.1323970
52. W. Wu, W.M. Tong, J. Bartman et al., Sub-10 nm nanoimprint lithography by wafer bowing. Nano Lett. **8**, 3865–3869 (2008). doi:10.1021/nl802295n
53. A. Roy, B. Craver, L.E. Ocola, J.C. Wolfe, Image noise in helium lithography. J. Vac. Sci. Technol. B **29**, 041005 (2011). doi:10.1116/1.3597835
54. M. Melli, A. Polyakov, D. Gargas et al., Reaching the theoretical resonance quality factor limit in coaxial plasmonic nanoresonators fabricated by helium ion lithography. Nano Lett. **13**, 2687–2691 (2013)
55. Y. Wang, M. Abb, S.A. Boden et al., Ultrafast nonlinear control of progressively loaded, single plasmonic nanoantennas fabricated using helium ion milling. Nano Lett. **13**, 5647–5653 (2013)
56. D.C. Bell, M.C. Lemme, L.A. Stern et al., Precision cutting and patterning of graphene with helium ions. Nanotechnology **20**, 455301 (2009). doi:10.1088/0957-4484/20/45/455301

Chapter 17
Focused Helium and Neon Ion Beam Modification of High-T_C Superconductors and Magnetic Materials

Shane A. Cybart, Rantej Bali, Gregor Hlawacek, Falk Röder and Jürgen Fassbender

Abstract The ability of gas field ion sources (GFIS) to produce controllable inert gas ion beams with atomic level precision opens up new applications in nanoscale direct-write material modification. Two areas where this has recently been demonstrated is focused helium ion beam production of high-transition temperature (high-T_C) superconductor electronics and magnetic spin transport devices. The enabling advance in the case of superconducting electronics is the ability to use the GFIS to make features on the small length-scale of quantum mechanical tunnel barriers. Because the tunneling probability depends exponentially on distance, tunnel barriers must be less than a few nanometers wide, which is beyond the limits of other nanofabrication techniques such as electron beam lithography. In magnetism, the GFIS has recently been used to generate chemical disordering and modify magnetic properties at the nanoscale. The strongest effect is observed in materials where ion-induced chemical disordering leads to increased saturation magnetization, enabling positive magnetic patterning. In this chapter, we review the latest results and progress in GFIS ion beam modification of (high-T_C) superconductors and magnetic materials.

S.A. Cybart (✉)
Oxide Nano Electronics Laboratory, University of California Riverside,
Riverside, CA, USA
e-mail: cybart@ucr.edu

R. Bali · G. Hlawacek · F. Röder · J. Fassbender
Helmholtz-Zentrum Dresden-Rossendorf,
Institute of Ion Beam Physics and Materials Research, Dresden, Germany
e-mail: r.bali@hzdr.de

F. Röder · J. Fassbender
Technische Universität Dresden, Dresden, Germany

© Springer International Publishing Switzerland 2016

G. Hlawacek and A. Gölzhäuser (eds.), *Helium Ion Microscopy*,
NanoScience and Technology, DOI 10.1007/978-3-319-41990-9_17

17.1 Introduction

Devices employing phenomena such as superconductivity and magnetism are of vital technological importance. Josephson junctions composed of superconducting layers are used for extremely sensitive sensing of magnetic fields. Nanoscale magnets are useful as data storage bits. Spin-valve devices consisting of magnetic layers are used for sensing magnetic fields, including as read heads for data bits. Continued progress in these fields typically requires not only scaling down the devices, but to tailor magnetic and superconducting characteristics at the nanoscale.

Irradiation with accelerated ions can modify the crystal structure, and sensitively vary a variety of material properties. The advent of Gas Field Ion Sources (GFIS) makes it possible to achieve highly focused He^+ and Ne^+ ion beams of $\sim$1 nm diameters. Available GFIS instruments accelerate the ions at up to 30 keV energies, which is sufficient to penetrate the thin film materials used in present day devices. The above instrument characteristics make the GFIS immediately relevant to nanoscale modifications of crystal structure and consequent patterning of superconducting and magnetic properties.

Research in GFIS-assisted modifications of superconductivity and magnetism is still in its early stages. This chapter aims to highlight some of the most promising lines that have emerged until now. In Superconductivity, GFIS direct write modification of superconductors for the patterning of Josephson junctions and nanowires is described. We discuss the physics of ion irradiated superconductors and highlight the differences in GFIS fabricated junctions with prior masked implanted devices. In particular GFIS defined devices are an order of magnitude smaller which leads to new and improved properties.

In Magnetism, we focus on the GFIS-assisted modification of the saturation magnetization, M_s. In particular we focus on alloy thin films which are non-ferromagnetic or possess a weak M_s, and transform to a high M_s state by ion-induced modifications of the crystal structure. The possibility to induce a large increase in M_s via highly focused ion-beams makes it possible to embed nanomagnets in the initially non-ferromagnetic precursor at desired locations. The resolution of the magnetic objects is limited only by the effects of lateral ion-scattering, which will be discussed in this chapter. The focused ion-beam effectively acts a magnetic stylus for rapid patterning of 2-dimensional nanomagnets. This ability may prove valuable in prototyping devices that employ complex magnet geometries.

Section 17.1 describes the basic concepts of Superconductivity necessary to understand Josephson's junctions. Section 17.2 describes the GFIS-assisted patterning of Josephson's junctions and their characteristics. Section 17.3 discusses GFIS-assisted magnetic writing.

17.2 Introduction to Ion Beam Modification of Superconductors

In 1987, the discovery of high transition temperature (high-T_C) superconductivity in ceramic materials at temperatures around 90 K [1] set off a frenzy of research in the development of high-T_C electronics, motivated by the prospects of electronics operating in low cost liquid nitrogen at 77 K opposed to 4 K liquid helium. Unfortunately, researchers soon discovered that these new materials were much more difficult to process into devices than conventional metal low transition temperature (low-T_C) superconductors. High-T_C materials are very anisotropic [2] and the superconducting properties vary along the different crystallographic directions which severely complicates manufacturing of the basic building blocks of superconducting electronics: Josephson junctions. Furthermore, the length scale of superconductivity in high-T_C ceramics is very short ($\xi_{htc} < 2$ nm) [3] compared to low-T_C metals ($\xi_{ltc} > 50$ nm). Despite this and other challenges many high-T_C Josephson junction manufacturing techniques have emerged over the last three decades but none of these techniques is able to generate large numbers of junctions with predictable characteristics necessary for large scale circuits.

Prior manufacturing techniques rely on small centimeter sized substrates that must be processed one-at-a-time and rigorously tested one-by-one to find the few devices with suitable characteristics. The low yields and low throughput has kept the costs too high for high-T_C superconductor electronic applications. GFIS based scalable nanomanufacturing of high-T_C electronics [4] has the potential to provide a much needed break-through in this field and deliver large numbers of high-quality circuits while at the same time reducing the costs by orders of magnitude.

In order to understand and interpret the results of ion beam modification of superconducting materials for electronic devices, it is necessary to have some familiarity with the properties and physics of superconducting electronics and the physical mechanism of ion beam induced disorder in superconductors. The discussion in this section will only introduce the most basic concepts. A more detailed description of superconducting electronics can be found here [5].

17.2.1 Josephson Junctions

The basic building block of superconducting electronics is the Josephson junction. It is analogous to superconductors as a transistor is to semiconductors. A junction consists of two superconducting electrodes coupled through a weak barrier such as an insulator or normal metal.

Josephson Equations

In a Josephson junction (Fig. 17.1) a "supercurrent" will flow in the absence of a potential difference (voltage) if there is a phase difference between the order parameters of the two superconductors. The difference between the phases of the

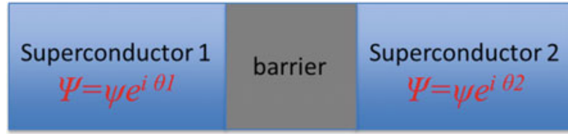

Fig. 17.1 Josephson junction

two superconductors is defined as the Josephson phase, $\varphi \equiv (\theta_1 - \theta_2)$. The supercurrent in the simplest case is described by the first Josephson equation [6]:

$$I_S = I_C \sin\varphi, \tag{17.1}$$

where the critical current, I_C is the maximum supercurrent that the junction will sustain and is determined by junction geometry, temperature, and the materials of the weak link and electrodes, amongst other factors. Furthermore, if there is a potential difference V, between the two superconductors the phase difference changes with time and is described by the second Josephson equation [6],

$$\partial\varphi/\partial t = 2eV/\hbar, \tag{17.2}$$

where e is the charge of an electron and $\hbar$ is the reduced Planck's constant. The second Josephson equation is exact and only depends on fundamental constants. If a dc voltage is applied across a junction the phase evolves with time at a frequency, $f = 2\ eV/h$. This results in an ac supercurrent oscillating between the two superconductors at frequency f. The proportionality factor between voltage and frequency is referred to as the Josephson constant, $K_J = 2e/h = 483.597879$ THz/V. This forms the basis for the definition of the volt and the Josephson voltage standard [7].

Resistive, Capacitive, Shunted Josephson Junction Circuit Model (*RCSJ*)
An equivalent circuit model of a Josephson junction was put forth independently by Stewart [8] and McCumber [9]. They modeled junctions as a resistor, capacitor, and a current source connected in parallel as shown in Fig. 17.2. This is called the resistive and capacitive shunted Junction model (*RCSJ*).

In practice Josephson junctions are typically current biased and equating the bias current to the currents through the three parallel elements yields:

$$I = I_C \sin\varphi + V/R_N + C\,\partial V/\partial t \tag{17.3}$$

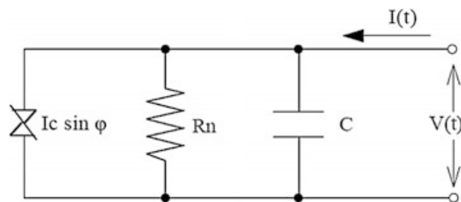

Fig. 17.2 Schematic representation of the *RSCJ* Josephson junction equivalent circuit model

The sinusoidal term represents the supercurrent from the first Josephson equation 17.1. The second term is the normal non-superconducting current in the finite voltage regime that obeys Ohms law. The final term represents the capacitance between the electrodes. Using the second Josephson equation 17.2, the voltage in the resistive and capacitive terms can be rewritten in terms of the Josephson phase:

$$I = I_C sin\,\varphi + \partial\varphi/\partial t(\hbar/2eR_N) + C(\hbar/2e)\partial^2\varphi/\partial t^2 \tag{17.4}$$

In the case of junctions, with metallic barriers or small electrodes the capacitive term may be omitted. In this limit, the model becomes the resistive shunted junction model (RSJ) and (17.4) reduces to a first order differential equation with the following time average dc voltage solution:

$$V = 0, \text{ for } I < I_C$$
$$V = I_C R_N \left[(I/I_C)^2 - 1\right]^{1/2}, \text{ for } I > I_C$$

This results in a parabolic current-voltage characteristic at biases near I_C, that approaches Ohms law at higher voltages (Fig. 17.3). The critical voltage or product $I_C R_N$ is an important figure of merit for Josephson junctions and is a measure of the Josephson binding energy of the two superconducting electrodes. For applications it is generally desirable to maximize $I_C R_N$ with the ability to control the ratio I_C/R_N.

17.2.2 Ion Irradiation in High-T_C Superconductors

The second topic we introduce in this chapter is a discussion of the effects and mechanisms of ion irradiation in high-T_C superconductors. These materials are complex transition-metal oxides that are very sensitive to point defects in the crystal lattice caused by ion irradiation. To illustrate this we present in Fig. 17.4, data adapted from White et al. [10] that shows the resistivity as a function of temperature

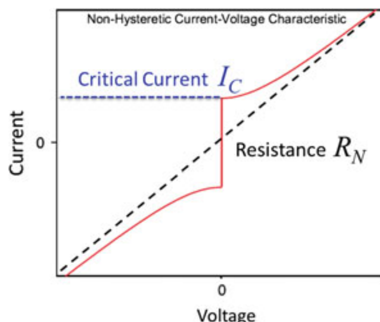

Fig. 17.3 Current-voltage characteristic of a resistive shunted Josephson junction

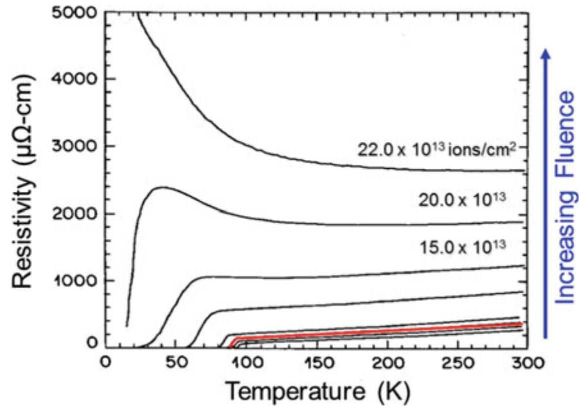

Fig. 17.4 Ion irradiation of a YBCO film. Resistivity as a function of temperature for ion irradiated films of YBCO adapted from White et al. [10]

for $YBa_2Cu_3O_{7\text{-}\delta}$ (YBCO) thin films irradiated with several different doses of 1 meV neon ions. Increasing irradiation levels has the effects of increasing resistivity and reducing the superconducting transition temperature T_C. At moderate irradiation doses of 2.2×10^{14} ions/cm^2 the material no longer superconductors and becomes insulating. The irradiation induced metal to insulator transition in the normal state comes about because the electron mean free path is very sensitive to disorder of the oxygen lattice. Disorder shortens the mean free path and increases resistivity [11].

Altering the superconducting properties with disorder is understood as a phase transformation, where disorder disrupts the macroscopic superconducting electron condensate wave function, $\Psi = \delta^{i\theta}$, where δ is the superconducting pair amplitude and θ is the phase. There are two mechanisms for destroying the superconducting state: phase decoherence and amplitude suppression. A model system to study these two mechanisms is quench condensed thin films of conventional superconductors [12–14]. Quench condensation involves thermally evaporating a superconducting material such as lead onto a substrate at cryogenic temperatures. In the case of lead evaporated on glass substrates, the lead forms a network of disconnected grains (Fig. 17.5) [14]. Each grain is superconducting at the bulk T_C of lead (7.2 K) with its own unique phase. Electrically the superconducting transition of the film of grains is very broad with respect to temperature. The onset of superconductivity is seen near 7.2 K when each individual grain superconductors. However the end of the transition occurs at much lower temperatures when the phases Josephson couple together.

Suppression of the wave function amplitude can also be studied in quench condensation by reducing the size of the grains to be less than the coherence length. This has been done experimentally in quench condensation by depositing multilayers of lead interleaved with thin layers of germanium or antimony which prevents grain formation and results in fully amorphous films. Figure 17.6 is example data for multilayers of Pb-Sb from Xiong et al. [13]. In this work the

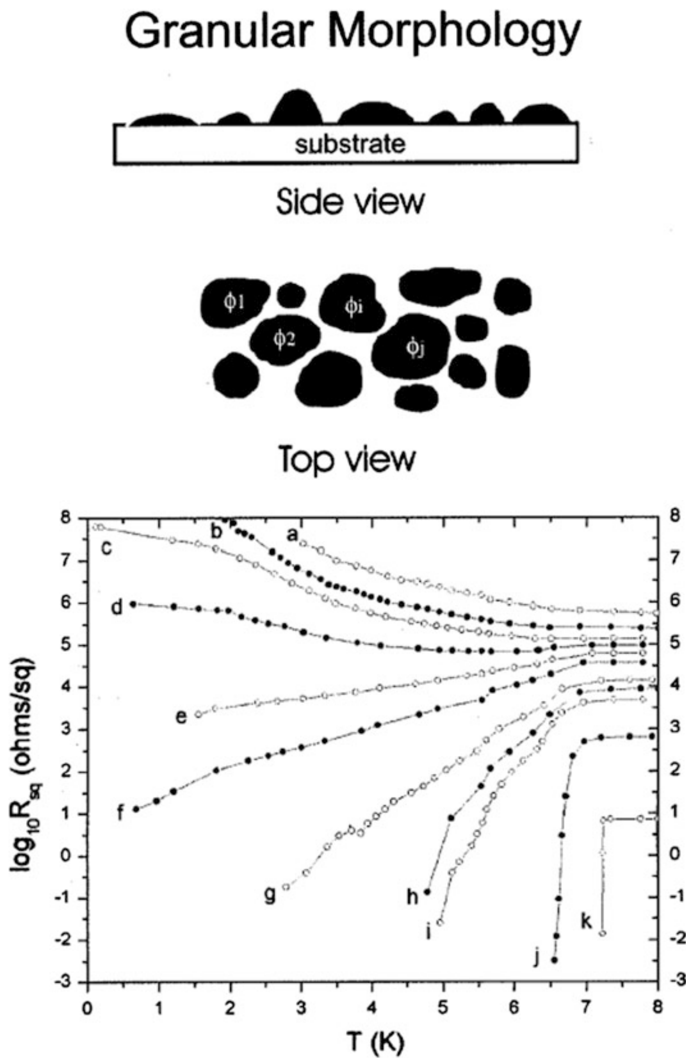

Fig. 17.5 Quench condensation of granular lead films. This model system is used to study phase decoherence in superconductors. The individual grains superconduct at 7.2 K but phase coherence doesn't occur until much lower temperatures creating a broad transition. Adapted from Merchant et al. [14]

superconducting transition remains very sharp but the onset of superconductivity increases with the numbers of layers in the structure because the pair amplitude is getting larger.

In the case of ion irradiation of oxide superconductors, both mechanisms are observed. Figure 17.7 shows data taken from transition temperature measurements of YBCO samples irradiated with both helium and neon ions [11]. In Fig. 17.7a the

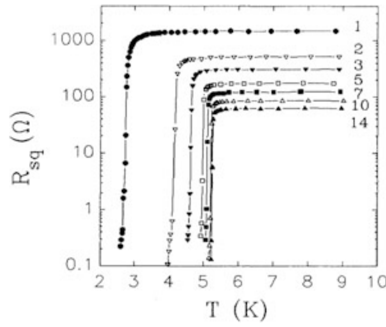

Fig. 17.6 Quench condensation of amorphous lead films. This model system is used to study amplitude suppression in superconductors. The sheet resistance as a function of temperature for Pb-Sb multi layers showing that the superconducting transition temperature remains sharp but increases with the total number of layers. Reproduced from Xiong et al. [13]

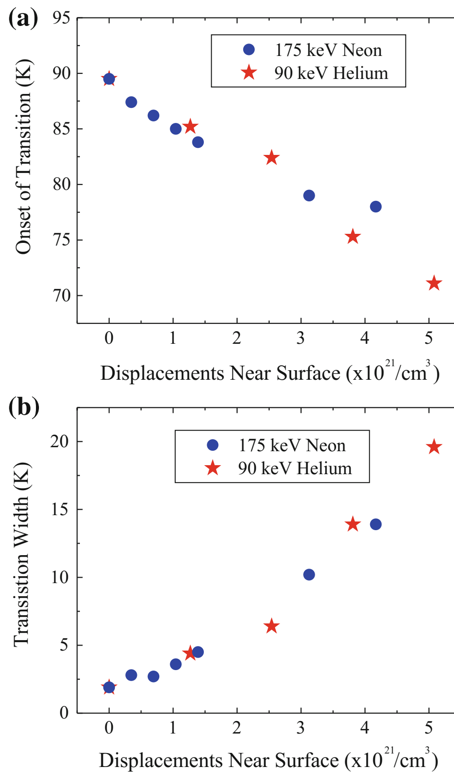

Fig. 17.7 Reduction of the superconducting onset temperature **a** and broadening of the transition width **b** in thin films irradiate with helium and neon indicating both amplitude and phase disruption of superconductivity. Reproduced from Cybart et al. [11]

onset of the transition temperature decreases linearly with the number of ion induced displacements which suggests amplitude destruction of the superconducting order parameter. Whereas in Fig. 17.7b the transition width increases from 2 to 20 K indicating a large degree of phase decoherence.

17.3 Ion Irradiated Josephson Junctions

17.3.1 Masked Ion Irradiated Josephson Junctions

The ability to precisely tune oxide superconductors on a small scale with ion irradiation provides for a mechanism to fabricate in plane Josephson junctions. In this method the irradiation damage reduces the T_C in a narrow region of a superconducting bridge that can serve as a Josephson junction at temperatures above the narrow region reduced T_C and below the undamaged electrodes T_C. The defects and disorder generated in this manner is very reliable and has been shown to be stable for several years [15]. Historically, Josephson junction fabrication in this manner has involved ion implantation of a high-T_C film with an ion implanter through a nano-patterned thick resist mask [16–19] to protect the superconducting electrodes while damaging unmasked regions with ion irradiation (Fig. 17.8).

The typical width of the trenches used in the high-aspect-ratio masks used for defining these barriers is process limited and typically of the order or larger than 25 nm [20], however lateral straggle of defects from the implantation process broadens out the barrier so that the actual width of the irradiated region can approach 100 nm [21]. Josephson super currents can only propogate through such large regions by a mechanism called the superconducting proximity effect [22], which is a phenomenon where non-superconducting materials in close electrical proximity with a superconductor become superconducting themselves. In the case of ion irradiated weak links the coupled materials are the same, but the irradiated region has a reduced transition temperature T'_C. If the irradiated region is narrow (<100 nm) it will sustain a Josephson current above T'_C but the pair amplitude is

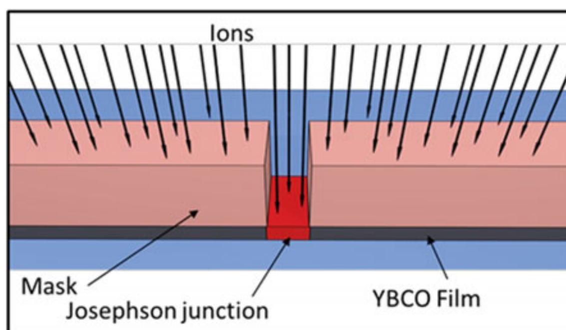

Fig. 17.8 Masked Ion damage Josephson junction

significantly reduced from that of the electrodes which results in much smaller values of $I_C R_N$, typically an order of magnitude smaller [23] than other technologies [24–26].

Another drawback related to the barrier length of masked ion irradiated Josephson junctions is the presence of a large non-Josephson excess current at zero voltage that does not exhibit either the DC or AC Josephson effects. The physical origin of the excess current is understood in the framework of the Blonder, Tinkham, and Klapwijk model [27] (BTK) for microscopic electrical transport at an interface between a superconductor and a normal material. The BTK model describes current-voltage characteristics for barriers ranging from a strong barrier, such as an insulator in a tunnel junction, to a weak barrier like a normal metal, using a single parameter related to barrier strength. In the case of a strong barrier (insulator) the only transport mechanism for supercurrent is direct Josephson tunneling whereas with weaker (metallic) barriers both pair tunneling and Andreev reflection occur. Therefore to maximize the Josephson current and reduce excess current a strong barrier is required but it must also be confined to less than a few nanometers wide in order for tunneling to occur as the tunneling probability depends exponentially on the insulator thickness.

17.3.2 GFIS Direct-Write Josephson Junctions

The sub-ten nanometer requirement for high-aspect ratio mask fabrication is very challenging which has motivated studies for direct-write implantation using focused ion beams of gallium [28, 29] and silicon [30]. Unfortunately, the large diameters of liquid metal ion beam sources is still too large. Furthermore, gallium reacts chemically with the superconductor and adversely affects the electrical properties. The recent advances and commercial availability of ultra-small diameter (0.5 nm) inert gas field ion sources [31–34] has solved many of the problems in the production of ion damaged Josephson junctions. Figure 17.9 shows a scale model of using a helium GFIS focused down to 0.5 nm to shoot through a thin YBCO film to disorder the lattice and fabricate an in plane Josephson junction. The very small size of the beam is of the order of the YBCO unit cell 0.38 nm. In Fig. 17.10, we compare ion implantation simulations using the binary collision approximation (BCA) in Silvaco Athena™ of a typical 200 keV neon masked ion irradiated junction with that of a 30 keV helium GFIS direct write junction. The difference in size is over an order of magnitude, and has a very important effect on the electrical properties that will be discussed in detail in the proceeding sections.

GFIS Direct Write Junction Fabrication

To create Josephson junctions using a helium GFIS [35], large circuit features for electrical contacts, and 4-μm wide strips of YBCO were patterned with conventional photolithography into a YBCO thin film that had an in situ deposited Au contact layer on top (Fig. 17.11). The starting YBCO film thickness was 150 nm,

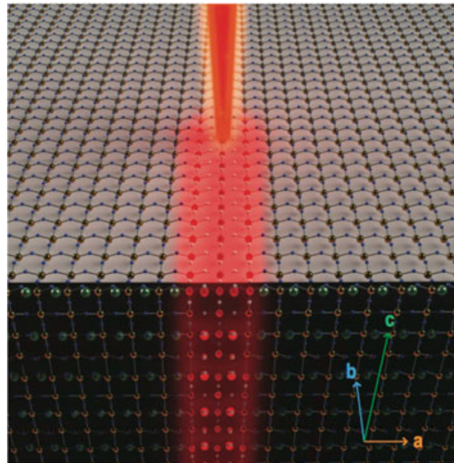

Fig. 17.9 Direct write helium ion implantation. Adapted from Cybart et al. [35]

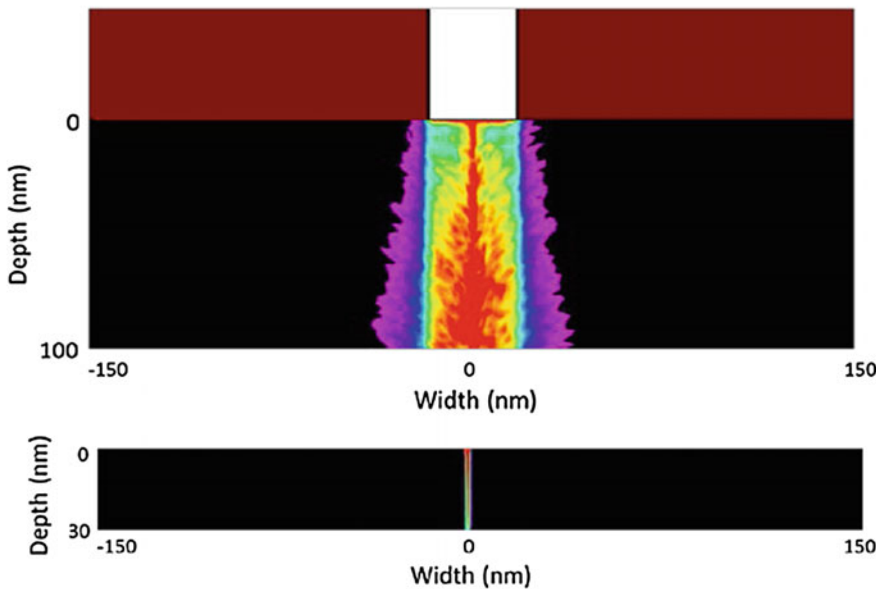

Fig. 17.10 Comparison of a masked versus GFIS direct-write ion irradiated Josephson junction. The *red area* represents the highest defect densities whereas the *purple* is the lowest

but the Au was removed and the YBCO was etched to a thickness of ~30 nm in the junction area (Fig. 17.11 inset). This was to ensure that the helium ions fully penetrated the YBCO with very little lateral straggle. Several test samples were made and the GFIS of a Zeiss Orion Plus at 30 kV was scanned across the 4-μm

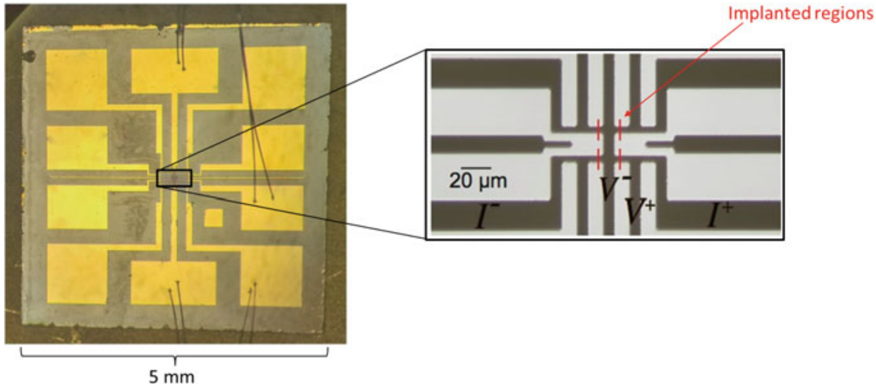

Fig. 17.11 GFIS direct write Josephson junction test sample. Adapted from Cybart et al. [35]

wide strips with ion doses ranging between 10^{14} and 10^{18} He^+/cm^2. At the lower values very little Josephson current was observed and Andreev reflections dominated transport. In contrast, at the highest doses the devices exhibited insulating behavior. In between these two extremes we found doses that could create very high-quality Josephson junctions and continuously transition, as predicted by BTK, from SNS junctions, well-described by the resistively shunted Josephson model (RSJ), to Superconductor-Insulator-Superconductor (SIS) Josephson tunnel junctions.

GFIS Direct Write Junction Electrical Properties

The current-voltage characteristics (*I-V*) are shown in Fig. 17.12a for a typical SNS Josephson junction measured at several temperatures. The resistance ~1 Ω is 10 times larger than masked ion irradiated junctions with the same dimensions [36]. The Fraunhofer diffraction pattern of the supercurrent in applied magnetic field (Fig. 17.12a inset) demonstrates the dc Josephson effect, however the pattern is skewed due to self-field effects from the very high current density of 100 kA/cm^2.

The temperature dependence of I_C, R_N and their product is shown in Fig. 17.12b inset. The decrease in resistance as temperature is lowered indicates the barrier is a conductor. The temperature range for RSJ characteristics (~30 K) is much larger than that for masked ion irradiated junctions [36] (~3 K) suggesting that the strength of the barrier is much higher and more efficient at suppressing the Andreev reflection (excess current) transport mechanism. In stark contrast to the SNS junction, Fig. 17.12c shows *I-V* for several temperatures of a YBCO, SIS junction fabricated by irradiation with a higher dose (6×10^{16} He^+/cm^2). These junctions do not exhibit hysteresis in the *I-V* characteristic like typical SIS junctions because the capacitance is very small. This comes about because of the small area of the planar electrodes normal to the transport direction. The Fraunhofer diffraction pattern for this junction is shown in Fig. 17.12c inset. The amplitudes of the side lobes fall off much slower than the patterns from ideal sandwich junctions because the current is concentrated closer to the edges. Unlike the junction shown in

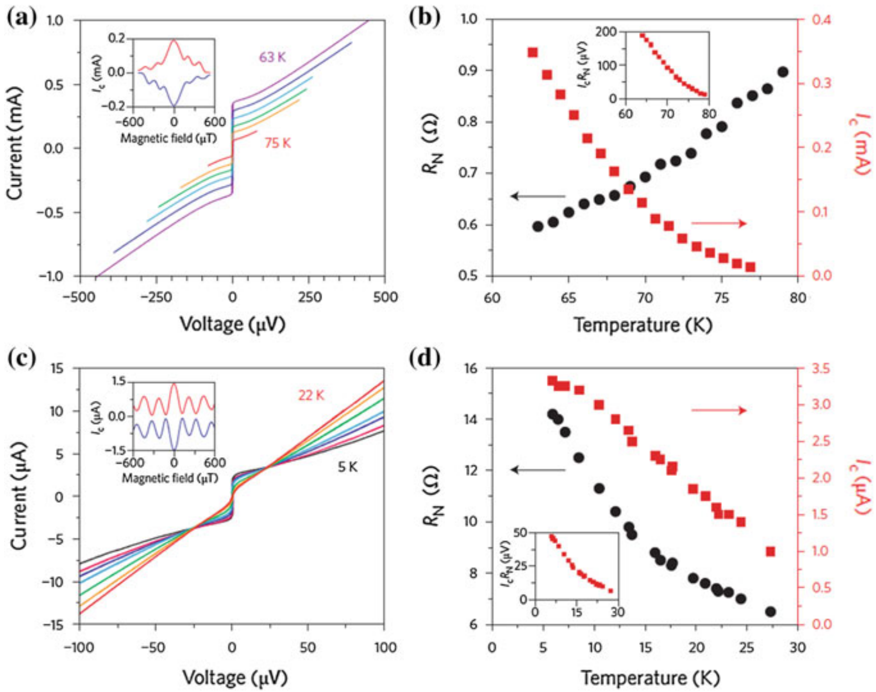

Fig. 17.12 Electrical measurements for GFIS direct write Josephson junctions. A SNS Josephson junction fabricated using a dose of 2×10^{16} He^{+}/cm^{2}. **a** *I-V* characteristics measured for temperatures 63, 65, 67, 69, 71, and 75 K (*inset*). The Fraunhofer diffraction pattern for the critical current in magnetic field. **b** The temperature dependence of the I_C, R_N and their product. Electrical measurements for a SIS Josephson junction fabricated using a dose of 6×10^{16} He^{+}/cm^{2}. **c** *I-V* characteristics measured at 5, 10, 12, 14, 16, 18, and 22 K (*inset*). The Fraunhofer diffraction pattern for the critical current in magnetic field at 6 K. **d** The temperature dependence of I_C and R_N and their product. Reproduced from Cybart et al. [35]

Fig. 17.12a, the resistance of this junction increases as temperature is decreased indicating that the barrier is an insulator Fig. 17.12d. Furthermore, unlike the SNS junction, the critical current more weakly depends on temperature and is asymptotic at low temperatures as expected for an insulating barrier junction Fig. 17.12d. The values of $I_C R_N$ range between 50 and 200 μV and are approximately an order of magnitude higher than masked ion irradiated junctions and comparable with other high-T_C Josephson junctions. Transport data for the same junction from Fig. 17.12c is shown measured at higher current bias in Fig. 17.13. The SIS nature of *I-V* (Fig. 17.13b) is more apparent and conductance peaks are visible at in the derivative (Fig. 17.13c) around V = ±32 mV, which we contribute to the gap edge of the superconductor from quasi particle tunneling. This is rarely seen in high-T_C junctions because it requires a very narrow <3 nm insulating barrier. This observance is a testament to the quality and potential of helium GFIS direct-write lithography to pattern sub-10 nm features.

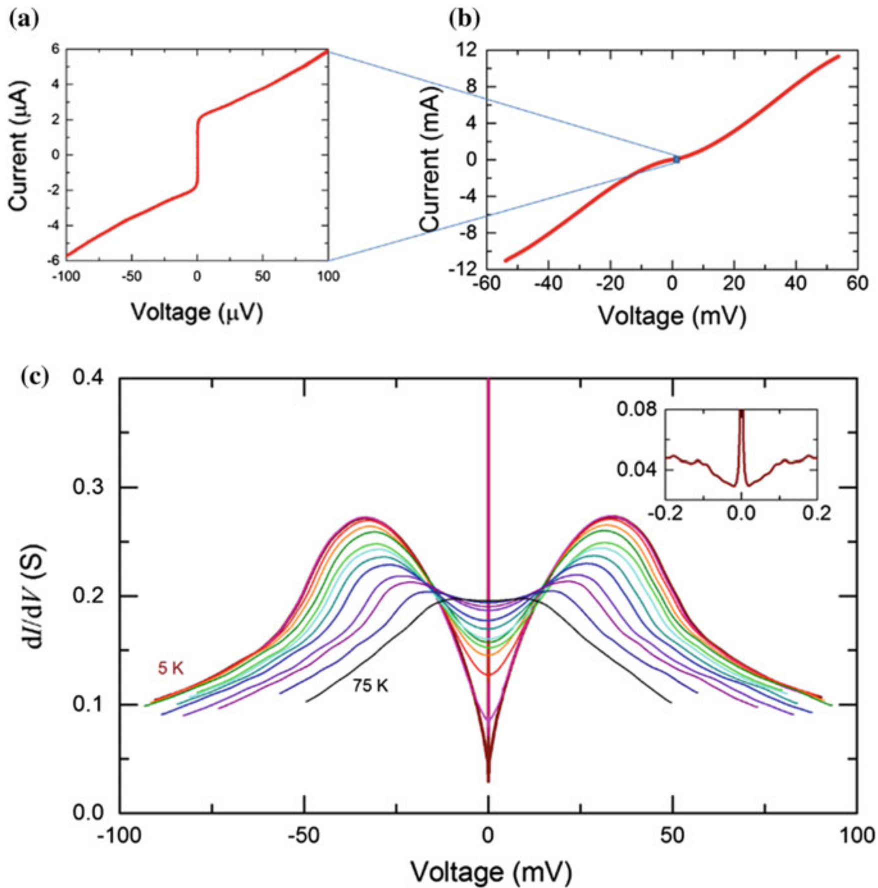

Fig. 17.13 The energy gap of YBCO. *I-V* characteristic of an insulating barrier Josephson junction. The small voltage range **a** shows the Josephson super current at zero voltage whereas the higher range **b** data shows the non-linearity associated with the insulating barrier. **c** Differential conductance (d*I*/d*V*) versus voltage for different temperatures for the same insulating Josephson junction showing the quasiparticle tunneling and the energy gap of YBCO ranging from 70 to 5 K in 5 K increments. Adapted from Cybart et al. [35]

To further test the uniformity of GFIS helium ion beam junctions, we also constructed arrays of closely spaced junctions connected in series, by scribing multiple lines across the bridge. Figure 17.14 shows *I-V* for several temperatures of a 20 junction SNS series array with inter-junction spacing of 500 nm. The arrays show much less rounding near the critical current then previously reported masked ion irradiated Josephson arrays [23, 36–38] suggesting very good uniformity of $I_C R_N$. This high level of uniformity is also apparent when characterizing the array

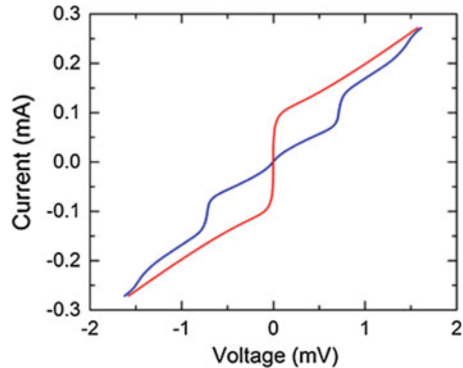

Fig. 17.14 *I*-*V* of YBCO, Josephson junction arrays containing 20 junctions. With (*blue*) and without (*red*) applied 17.6 GHz microwave radiation. A giant Shapiro step is observed at $20f/K_J = 0.727$ mV

using the AC Josephson effect. Figure 17.14 shows a 20 junction array irradiated with rf from an open circuited coax cable at $f = 17.6$ GHz. A large pronounced flat giant Shapiro step is observed at $20 \times f/K_J = 0.727$ mV, implying that the fundamental voltage step for each junction within the array is occurring at the same bias current. This situation will only occur if the resistances are nearly the same.

17.3.3 GFIS Direct Write Superconducting Quantum Interference Devices

One of the simplest Josephson junction circuits is a highly sensitive magnetic flux detector called a superconducting quantum interference device (SQUID) [3, 5]. It consists of two Josephson junctions connected in parallel within a superconducting loop. In practice the SQUID is typically current biased above the critical current and the voltage oscillates as a function of the magnetic flux contained within the loop having the period of the magnetic flux quantum Φ_0. Using GFIS direct-write junctions we have fabricated and tested both SNS and SIS DC-SQUIDs in a typical washer configuration (Fig. 17.15a) [39]. A 1×1 mm^2 flux focusing washer was fabricated with a 12×4 μm^2 slit in the center (Fig. 17.15a inset). A Josephson junction was written into each arm of the SQUID with the Zeiss Orion Plus. The SNS SQUID (Fig. 17.15b) has a resistance of about 1 Ω and exhibits a very uniform Fraunhofer diffraction pattern (Fig. 17.15c) with a large 20 μV SQUID interference modulation (Fig. 17.15c inset). This SQUID exhibited a very low flux noise for high-T_C SQUIDs (Fig. 17.15d) and with proper optimization of the manufacturing process it has potential to serve as a very sensitive biomagnetic magnetometer.

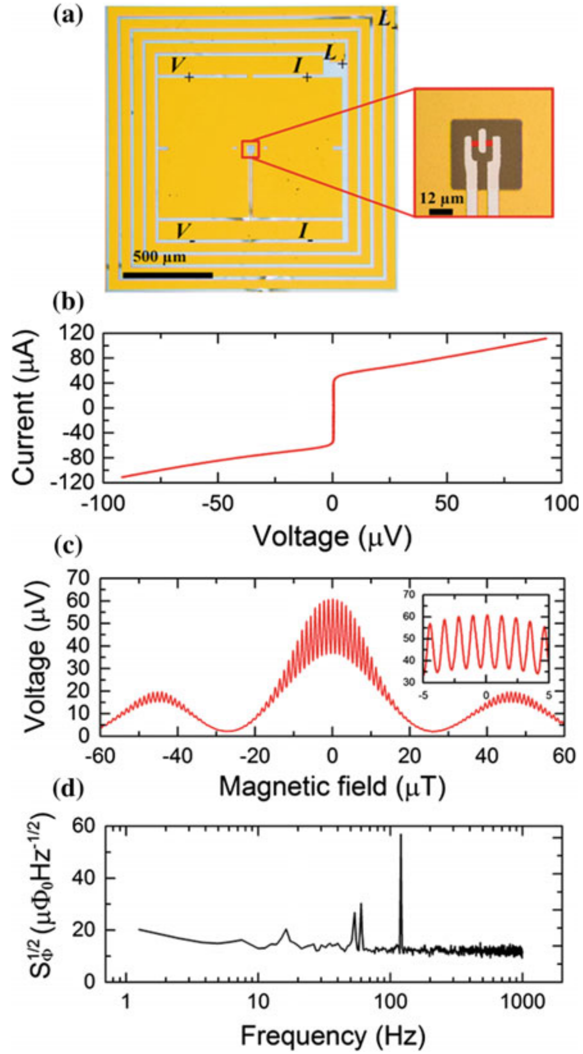

Fig. 17.15 Properties of a high quality prototype **a** DC washer SQUID illustrating the potential for large scale production. **b** *I*-*V* exhibits near ideal Josephson behavior and the magnetic diffraction **c** and interference patterns (**c** *inset*) illustrate that the junctions are well defined. The flux noise (**d**) is very low compared to other technologies especially in the 1/*f* region. Adapted from Cho et al. [39]

17.3.4 Nanowire Josephson Junctions

Typical values of junction width are limited by feature etching with isotropic Ar^+ milling. Overheating of the material causes deoxygenation which in most cases transforms the superconductor into an insulator. Therefore, the critical dimension for dry etching is limited to a few microns. However recently we have shown that the width can be aggressively scaled to smaller dimensions by using the same helium GFIS technology that we use to make the barrier. Nano wire test samples were made by irradiating insulating barriers to constrict the current path in

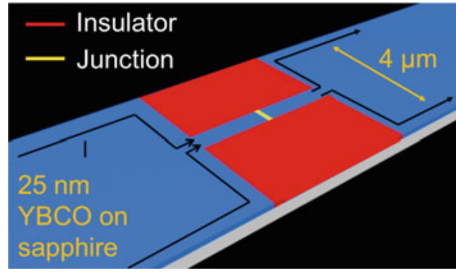

Fig. 17.16 Nanowire Josephson junction circuit. The width is narrowed down by using helium ion irradiation as opposed to ion milling. This allows for nanoscale features

photolithographically patterned 4 µm wires as shown in Fig. 17.16. We used a dose of 6 × 10^{16} He^+/cm^2 to write a Josephson junction in the circuit, and a higher dose of 2 × 10^{17} He^+/cm^2 to create the insulating barriers that define the nano wire width. Measurement of the junction I_C and R_N, provides an accurate way to determine the wire width restricted by ion beam patterning. Four test samples were made with wire widths of 50, 250 and 500 nm, and a 4 µm control sample without narrowing the wire.

I-V were measured and are shown in Fig. 17.17 for the devices. All of the junctions have an $I_C R_N$ product approximately equal to 400 µV. This implies that material quality in the wire remained the same and that there was no thermal damage from the focused helium ion beam process. Furthermore, R_N of the widths 50, 250, 500 nm and 4 µm are 210, 70, 38 and 5.6 Ω, respectively. These values scale inversely proportionally with the width $1/R_N \propto/w$. Similarly I_C for the junctions are 2, 5.6, 10.3 and 70 µA, respectively, and scale proportionally with the width $I_C \propto w$ as expected. These results strongly indicate that the current only flows through the restricted channel by the insulator as designed. The remarkable thing about this demonstration and technique is it provides a mechanism to fabricate high

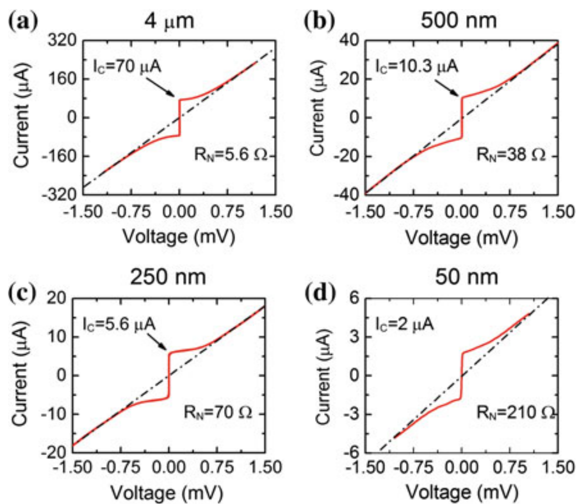

Fig. 17.17 Current-voltage characteristics of YBCO nanowire Josephson junctions. with **a** 4 µm, **b** 500 nm, **c** 250 nm and **d** 50 nm. The *red lines* are measured data and R_N was extracted following the *black dashed line* passing through the origin. I_C of The parameters scale with the dimensions

impedance Josephson circuits. Most conventional junctions have resistances of a few ohms and require matching transformers to eliminate the large mismatch between the junction and semiconductor amplifiers. High impedance nanowires can eliminate this requirement and substantially increase bandwidth which is hampered by the inductance of the transformer.

17.3.5 Concluding Remarks on GFIS Fabricated High-T_C Josephson Junctions

These initial studies demonstrated a new level of control that can be achieved in high-T_C junction fabrication. These devices are the first insulating barriers created in all YBCO junctions in a reproducible manner. While the barriers do exhibit some hopping conduction and are not as strong as those in conventional metal niobium circuits, they are nonetheless an order of magnitude better than prior ion irradiated devices. The ease of the process and the relatively few numbers of processing steps opens up a promising pathway to a new large scale inexpensive manufacturing process that can deliver high-T_C circuits for a myriad of applications.

The new advances in fabrication of high-T_C Josephson junctions using GFIS technology has a great deal of promise in future applications which were previously not possible or feasible using other methods. Affordable low noise SQUID bio-magnetometers could spur breakthroughs in medicine by providing highly sensitive brain and heart imaging tools. They could also play a big role in the next generation of high performance computing. We have only scratched the surface of the potential in this area and there are likely many more surprises on the horizon as GFIS technology continues to grow and improve.

17.4 Nanoscale Manipulation of Magnetization Using GFIS

Ion beams can be effectively used to modify the magnetic behavior of alloys [40, 41]. Magnetic patterning can be achieved by the localized re-arrangement of the crystal structure. Binary alloys of the formula $M_{100-x}N_x$, where M is a magnetic species and N is non-magnetic are well-suited for ion-induced modifications since the magnetism of these alloys tends to be extremely sensitive to their atomic arrangement [42–44]. Magnetism in metals is the manifestation of exchange coupling via itinerant electrons; variation in the number of M-M interactions can modify the electron exchange and consequently the magnetic behavior. Only a few exchanges of M and N site occupancies, forming anti-site defects, may cause drastic changes to the extrinsic as well as intrinsic magnetic properties.

Examples of such site-occupancy linked modifications are abundant in literature. In the last 20 years, researchers have frequently applied ion-irradiation to modify

extrinsic magnetic properties of M_xN_{1-x} alloys, particularly in alloys of the $L1_0$ and $L1_2$ structures. For instance, properties such as the coercive field and associated quasi-static magnetization reversal behaviour, and similarly, magnetic damping and dynamic response to AC fields can all be manipulated in FePt [45, 46], FePd [47], or $CrPt_3$ [48]. Typically, ion-induced chemical disorder causes modifications of properties such as the magnetic anisotropy axes [46], switching fields [49], magnetic damping [50, 51], and interlayer exchange coupling [52–54].

The usefulness of modulating the above extrinsic magnetic parameters is limited. What is needed are magnetic materials where desired magnetic properties can be activated by localized ion-irradiation. Materials in which large variation of intrinsic properties such as the saturation magnetization (M_s) is possible may be of technological significance, as magnets could then be written onto a non-magnetic template at desired locations. We refer to this process where M_s is induced via ion-induced disorder as positive magnetic patterning.

In certain B2-structured alloys such as $Co_{50}Ga_{50}$ [55], $Co_{50}Al_{50}$ [56], $Fe_{50}V_{50}$ [57], $Fe_{60}Al_{40}$ [58], and $Fe_{50}Rh_{50}$ [59], a large variation of M_s is achieved via chemical disordering. These B2 alloys consist of atomic planes of exclusively M atoms separated by planes of N atoms (when $x = 50$) or majority M atoms (when $x < 50$). The B2 arrangement in these alloys tends to possess reduced ferromagnetic (FM) moment. In the case of $Fe_{60}Al_{40}$ and $Fe_{50}Rh_{50}$, the ordered alloys are paramagnetic (PM) and antiferromagnetic (AFM) respectively. Localized GFIS-assisted chemical disordering of the above B2 alloys can lead to positive magnetic patterning.

The field of magnetism and magnetic devices has been moving towards the use of smaller magnets, well below the 100 nm scale. Such magnets tend to be in the form of regular arrays of nanomagnets of simple geometries. In certain types of devices, particularly Magnonic devices [60, 61], it may be necessary to produce magnets at these scales with a variety of shapes, both in the form of arrays of magnetic objects as well as non-repeating magnetic shapes. The process of GFIS-assisted positive magnetic patterning is depicted schematically in Fig. 17.18.

With its unprecedented sharpness of the ion-beam, the GFIS may prove useful for producing prototype magnetic devices, as it enables the fabrication of

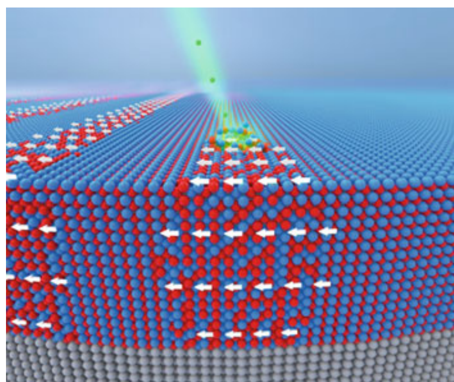

Fig. 17.18 Direct magnetic writing using a nano-focussed ion-beam. A ~2 nm diameter Ne^+ beam of a GFIS can be used to generate confined atomic rearrangements at desired locations to induce magnetized regions (Reprinted with permission from F. Röder et al., *Scientific Reports* 5 16786 (2015))

nanomagnets of any desired geometry. Nanomagnets are of vital importance for devices such as patterned data storage media and magnetic random access memories. Continued increase of data storage capacity may depend on the ability to fabricate magnetic nano-elements on large wafers using commercially viable processes. A key advantage of GFIS assisted magnetic patterning lies in device prototyping, whereby desired magnetic patterns can be imprinted onto B2-ordered templates in a 1-step direct writing process.

From the view point of positive magnetic patterning of the M_s, B2-$Fe_{60}Al_{40}$ is a model system. In the remaining part of the chapter we describe the phenomenon of ion-induced ferromagnetism in this model B2-alloy, and the use of GFIS for positive magnetic patterning. This alloy has been investigated by physicists for several decades [62–69], however the study of its ion-induced variations of magnetic properties has only been approached recently [62, 70, 71]. In this section we confine ourselves to the modification of M_s using GFIS and consider the example of B2-$Fe_{60}Al_{40}$, for the patterning of magnets of sub-50 nm resolution. Magnetic modifications using GFIS is a very recent area of research, and several possible materials have yet to be exploited for the purpose.

17.4.1 The Effect of Ion-Irradiation on Certain B2 Alloy Thin Film

The order-disorder phase transition in $Fe_{60}Al_{40}$ is schematically illustrated in Fig. 17.19, showing a $Fe_{60}Al_{40}$ alloy with the B2 structure, where planes of pure-Fe are separated by Al-rich planes. In the B2 structure, $Fe_{60}Al_{40}$ *thin films* have been observed to be very weakly ferromagnetic with the Fe atoms possessing a moment of 0.04 μB per atom. Irradiation with light noble gas ions such as He^+ or Ne^+ is sufficient to knock atoms from their ordered sites thereby generating vacancies. The

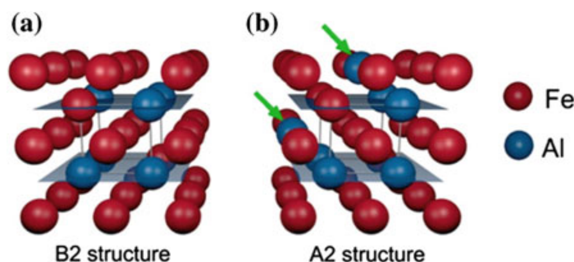

Fig. 17.19 B2 to A2 phase transition in $Fe_{60}Al_{40}$. **a** Schematic structure of chemically ordered (B2) Fe-Al, where pure-Fe planes separate Al-rich planes. **b** The disordered (A2) structure showing the occurrence of Al sites in the initially pure-Fe planes, indicated by the *arrows* (Reprinted with permission from R. Bali et al., Nano Letters 14 435 (2014). Copyright 2013 American Chemical Society)

vacancies recombine randomly with diffusing atoms at room temperature, resulting in a large fraction of the ordered sites being replaced by antisite defects. Antisite defects are essentially the replacement of say an Fe atom with an Al atom, and transform the B2-structure to the A2, which is bcc (Fig. 17.19b).

The transformation of B2 to the A2 structure leads to a vast change in the local environment of the Fe atom, namely in the Fe-Fe nearest-neighbours (n-ns). The moment per Fe-atom increases rapidly to 1.67 μB [70]. In the B2-structure, each Fe-atom has an average of 2.67 Fe-Fe n-ns. The Fe-Fe n-ns increase to 4.8 for the disordered structure where the Fe and Al atoms are randomly arranged. This increase in Fe-Fe n-ns due to disordering is crucial for setting up exchange coupling and inducing ferromagnetism [64, 67].

The magnetic phase transition can be observed experimentally by broad-beam irradiation of B2-$Fe_{60}Al_{40}$ thin films. As shown in Fig. 17.20, a 40 nm thick B2-$Fe_{60}Al_{40}$ film shows an M_s of 20 kA m^{-1}. Such a film can be prepared by magnetron sputtering from a stoichiometric target directly onto a SiO_2/Si(100) substrate, and subsequently annealing at 773 K for 1 h in vacuum to achieve B2-ordering. Irradiation of the B2-$Fe_{60}Al_{40}$ film with 6×10^{14} ions cm^{-2} of Ne^+-ions 25 keV leads to an increase of the M_s to ≈700 kA m^{-1} [70]. Annealing the film to 773 K in vacuum restores the B2 structure, fully erasing the induced magnetization.

In general, the interaction of a penetrating ions with the host atoms is spatially inhomogeneous, and can translate into inhomogeneity of the induced magnetization. This can be illustrated by calculating the average displacements undergone by Fe and Al atoms in the collision cascades formed by the Ne^+ ions. The displacements per atom, *dpa*, caused by penetrating ions of a given energy can be estimated by applying the binary collision approximation using software packages such as SRIM [71] and TRIDYN [72]. Figure 17.21 shows the *dpa*-distribution for 25 keV Ne^+ ions for a fluence of 6 ions nm^{-2}; conditions that are similar to those in the experiment. The 25 keV Ne^+ energy is well within the energy range of GFIS

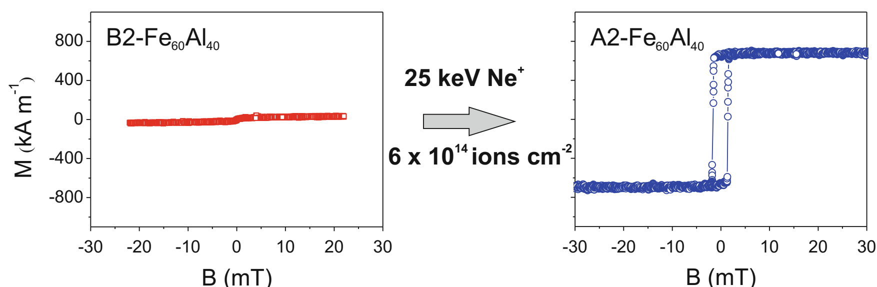

Fig. 17.20 Effect of ion-irradiation on the magnetic properties of $Fe_{60}Al_{40}$ films. Irradiation with Ne^+ ions at 25 keV causes the initially B2-ordered 40 nm thick $Fe_{60}Al_{40}$ films to transition to the A2-phase, resulting in an increase of the saturation magnetization (Adapted with permission from R. Bali et al., Nano Letters 14 435 (2014). Copyright 2013 American Chemical Society)

instruments. The simulation considers a case where an ideal ion beam of infinitely small diameter is scanned along the surface of the $Fe_{60}Al_{40}$ film. The scan ends at the lateral position designated 0 on the *x*-axis, forming an edge between the irradiated and unirradiated regions. The *dpa*-distribution in a region covering −25 to +25 nm positions has been shown. In regions lying well within the irradiated region, at say the −25 nm position, the lateral variation of *dpa* is negligible. However, there is significant depth variation, from a peak of 0.9 *dpa* at ≈15 nm to 0.2 *dpa* at the film/substrate interface. Nevertheless, it has been shown experimentally that further increase in ion-energy or fluence does not significantly increase the induced magnetization. This implies that a *dpa* of 0.2 is sufficient to induce maximum M_s, which we may treat as a rule-of-thumb threshold value for reaching saturation. Homogeneously magnetized films can be achieved by ensuring that the *dpa* is above this threshold.

Whereas it is trivial to obtain magnetically depth homogeneous thin films, lateral scattering of ions makes it a challenge to achieve homogeneity at the edges of magnetic nanostructures. Lateral scattering can be clearly seen in the *dpa* variation of Fig. 17.21 where all *dpa* values in the region $x > 0$ are due to lateral ion-scattering. The *dpa* for $x > 0$ shows a gradual lateral variation extending over 10 nm beyond the edge of the ion-irradiated region, falling below the threshold of 0.2. Under these conditions, lateral variations of the induced magnetization are bound to occur over a large lateral distance thus reducing the resolution of GFIS-assisted magnetic patterning. A model linking the induced magnetization, to the atomic displacements can be applied to the *dpa*-distribution to visualize the spatial variation of the ion-induced magnetization, and help estimate the extent of magnetic inhomogeneity.

An empirical model for the B2 → A2 phase transition, where the B2 and A2 phases co-exist, can be written as [70]:

$$m = \left(\frac{dpa}{dpa_0}\right)^p \left[1 + \left(\frac{dpa}{dpa_0}\right)^p\right]^{-1} \tag{17.5}$$

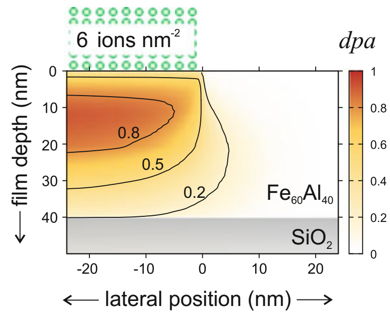

Fig. 17.21 Lateral ion-scattering. Distribution of the displacements per atom (*dpa*) at the edge of a surface scanned by a 25 keV Ne^+ beam

where m varies between 0 and 1 and is the ion-induced magnetization normalized to the maximum M_s. The parameter dpa_0 is the dpa at which m equals 0.5 whereas parameter p is related to the slope at the centre of the sigmoid. The values of dpa_0 and p can be obtained by correlating the simulated dpa spatial distribution to the experimentally observed m measured after uniformly irradiating continuous films of B2-$Fe_{60}Al_{40}$ films with known Ne^+-ion energies and fluences [70]. The values have been estimated to be $dpa_0 = 0.06$ and $p = 2.3$ [70]. Simulating collision cascades of a crystalline material is non-trivial, and impractical for routine irradiation calculations—SRIM assumes an amorphous material composed of Fe and Al atoms of fixed density and composition. Effects such as channeling of ions through crystallographic planes are therefore neglected.

Applying (17.5) to the dpa-distributions calculated by the binary collision approximation software helps visualize the spatial distribution of m. Figure 17.22 shows the m-spatial distributions for Ne^+ ions incident on 40 nm thick B2-$Fe_{60}Al_{40}$ at 25 keV and fluences of 1, 6 and 600 ions nm^{-2} respectively. Cross-sectional views of the m-distribution for the case of the single line scan are shown in Fig. 17.22a–c and for the surface scanning in d–f.

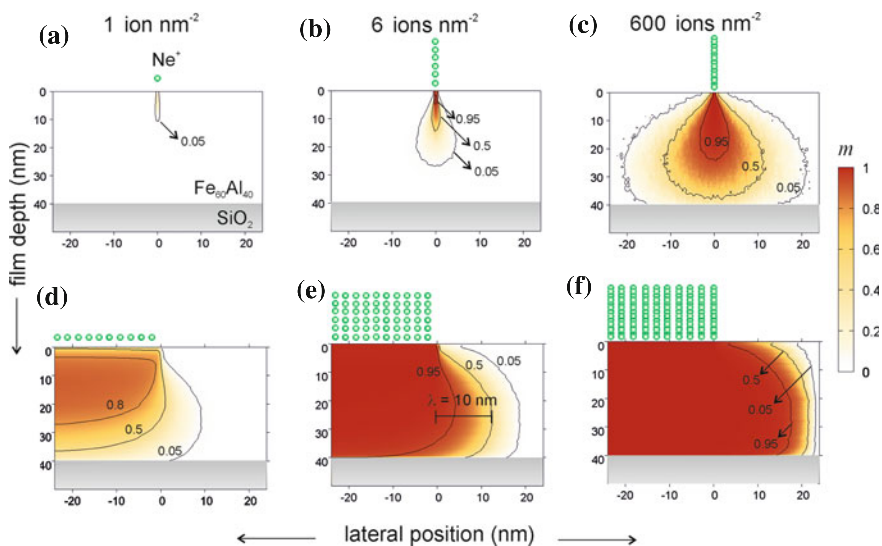

Fig. 17.22 Simulations of magnetization induced by a nano-focussed ion-beam incident on a B2-$Fe_{60}Al_{40}$ film. Cross-sectional views of the distribution of the induced magnetization, m, are shown when **a**–**c** the 25 keV Ne^+ beam irradiates the sample along a line on the film surface and **d**–**f** the ion-beam scanned over a surface region defined by negative lateral position. The m-distribution around the lateral position = 0 is considered. The Ne^+ fluences considered in the simulations are **a** 1 **b** 6 and **c** 600 ions nm^{-2} for irradiation along a line and similarly for the rastered irradiation the fluences are **d** 1 **e** 6 and 600 ions nm^{-2}. The lateral spread of induced m at the edge of the rastered region is indicated by the distance, λ, from the edge where $m = 0.5$

As seen in Fig. 17.22a, for the line scan at the lowest fluence of 1 ion nm^{-2}, the *m*-distribution is narrow, however magnetization is not induced within the full film depth. This fluence is not sufficient to induce the maximum *m* (=1) when the ion-beam is scanned along a line. Increasing the fluence to 6 ions nm^{-2} (Fig. 17.22b) helps achieve an m ≈ 1, however with an increased lateral spread of *m*. Further increase in the fluence say to 600 ions nm^{-2}, causes increased depth as well as lateral penetration of *m*. The lateral spread of *m* limits the magnetic patterning resolution.

Next we consider the case of surface rastering, shown in Fig. 17.22d–f. The region of interest is at the edge of the surface scan, where an interface between the magnetized and non-magnetized regions is formed. The cumulative effect of rastering induces the maximum *m* throughout the film depth even for fluences of 1 ion nm^{-2} (Fig. 17.22d). The effect of lateral ion-scattering causes significant inhomogeneities at the nominal edge of the rastered region. The lateral spread of *m* can be described by a term λ, which is the maximum distance from the edge of the rastered region, reached by the $m = 0.5$ contour line. A contour line for $m = 0.5$ extends up to 5 nm laterally into the unirradiated region. Increasing the ion-fluence to 6 ions nm^{-2} causes a λ of 10 nm from the nominal edge (Fig. 17.22e). Further increase in the Ne^+-fluence to 600 ions nm^{-2} achieves an $m = 0.5$ at a distance of 20 nm from the raster edge (Fig. 17.22f). Knowledge of the lateral spread of *m* can be useful in estimating the magnetic patterning resolution for given ion-energies and fluences. Furthermore, it may be possible to compensate for the lateral spread and adjusting spacing between magnetic objects accordingly, allowing further reduction of widths of the non-ferromagnetic features.

17.4.2 Application of Nanofocussed Ne^+ Beam to B2 Alloy Thin Films

To experimentally demonstrate direct GFIS-assisted magnetic writing, a nano-focussed Ne^+ beam was used to generate a magnetic stripe-pattern on a 10 μm wide and 40 nm thick B2-$Fe_{60}Al_{40}$ template [73]. The sample was irradiated using a GFIS with a ~2 nm diameter Ne^+ beam at 25 keV and a fluence of 6 ions nm^{-2}, corresponding to the simulations shown in Fig. 17.22e. A 10 μm beam limiting aperture and very short dwell time of 0.1 μs were used to write the pattern at a current of 0.8 pA. To achieve the desired fluence while reducing inhomogeneities related to the low beam current, each pattern was scanned several times.

The 2-dimensional stripe pattern consisted of 500 nm wide irradiated regions, separated by 100 nm wide unirradiated spacings. The existence of the magnetic stripe pattern was confirmed by observing magnetic contrast using the Kerr effect with polarized light in an optical microscope (Fig. 17.23a), where the magnetized regions show dark contrast. The resolution achievable in the optical microscope is insufficient to resolve the 100 nm wide separations between the magnetized stripes.

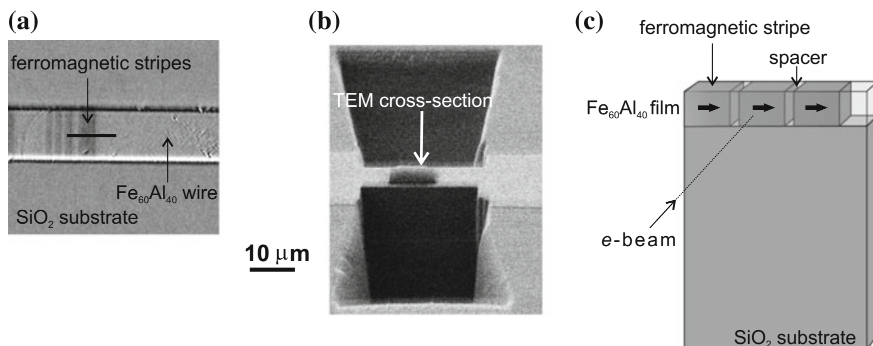

Fig. 17.23 Magnetic stripe pattern generated using GFIS. A Ne^+ beam was used to irradiate a B2-$Fe_{60}Al_{40}$ template of 10 μm width and 40 nm thickness. The irradiated regions were in the form of stripes of 500 nm widths separated by 100 nm unirradiated regions. **a** Magnetic contrast image obtained using Kerr effect of the B2-$Fe_{60}Al_{40}$ wire after magnetic patterning. The magnetized regions show dark contrast, and consist of bunches of 5 stripes each separated by the 100 nm wide non-ferromagnetic spacings. A region containing 500 nm wide stripes was selected for cross-sectioning, indicated by the *solid black line*. **b** Scanning Electron Microscopy image of the cross-section prior to lift-out. **c** Schematic of the extracted cross-section. The *block arrows* indicate the direction of magnetization prior to holographic imaging (Reprinted with permission from F. Röder et al. *Scientific Reports* 5 16786 (2015))

Figure 17.23a shows that magnetization has been induced in a region covering several 500 nm wide stripes. Imaging at much higher resolution was necessary to confirm the existence of the non-ferromagnetic gaps between the magnetized stripes.

High resolution magnetic imaging can be performed using Electron Holography, which is a Transmission Electron Microscopy (TEM) based phase-retrieval method requiring samples with thin cross-sections. A cross-section was carved using a beam of Ga^+ ions (Fig. 17.23b). The cross-section, containing a few patterned stripes was lifted out and fine polished. A schematic of the cross-section is shown in Fig. 17.23c. Prior to imaging a saturating magnetic field was applied such that the magnetization within the stripes was aligned along the 500 nm wide stripe edges, as depicted by the block arrows in Fig. 17.23c.

The structure of the patterned cross-section is seen in the bright-field amplitude image shown in Fig. 17.24a. The cross-section of the film shows a polycrystalline 40 nm thick $Fe_{60}Al_{40}$ film—any damage due to ion-irradiation is negligible. The contrast in the holographic phase image (Fig. 17.24b) depends on the local magnetic flux density, and reveals two ferromagnetic stripes in the identical region—a full-stripe at the centre and a half-stripe on the left separated by a sub-100 nm wide non-ferromagnetic spacer. The right hand side of the observed region was not irradiated by the GFIS beam.

Ferromagnetic regions can be identified by the coherent flux lines observed within the film volume. Analysis of the flux density in the magnetized regions consisting of coherent flux lines shows a flux density of ≈1 T, matching well with the expected $\mu_0 M_s$ ($M_s \approx 700$ kA m^{-1}) observed on uniformly irradiated

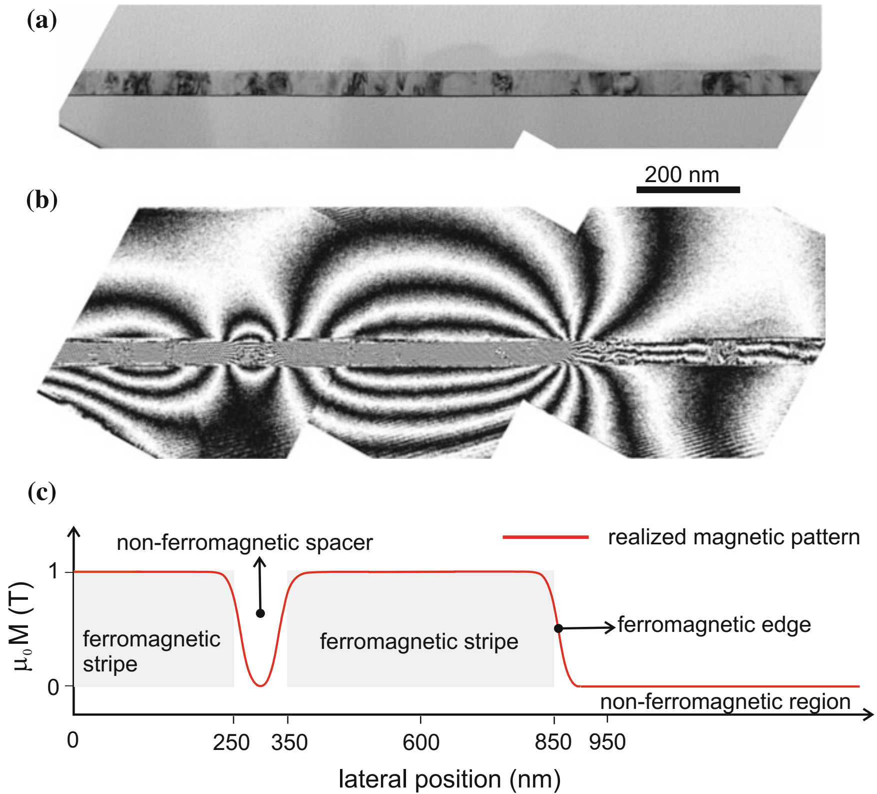

Fig. 17.24 GFIS-assisted patterning of ferromagnetic stripes. **a** Holographic amplitude image of the thin film. **b** Holographic phase image of the flux lines of the patterned magnetic stripes. **c** Schematic of the experimentally realized ferromagnetic stripe pattern, showing the blurring of ferromagnetic edges due to lateral-ion scattering (Adapted with permission from F. Röder et al., *Scientific Reports* 5 16786 (2015))

B2-$Fe_{60}Al_{40}$ films under conditions similar to the GFIS irradiation [71, 73]. These magnetic regions are embedded within the continuous film seen in Fig. 17.24a. A schematic of the observed ferromagnetic-stripe/spacer/ferromagnetic-stripe/non-ferromagnetic region is shown in Fig. 17.24c.

Stray flux lines emerge from the ends of the well-formed ferromagnetic stripes due to magneto-static coupling between the magnetic poles of the ferromagnetic stripes, traversing from the north pole of the central ferromagnetic stripe to its south. Flux lines also connect the two neighbouring ferromagnetic stripes largely by passing through the non-ferromagnetic spacer. However, while the spacer region shows high flux density, the flux lines are observed to be incoherent, indicating the much lower local M_s in this region. At the region where the magnetized stripe interfaces with the unirradiated region, stray flux lines emerge from the corners of the ferromagnetic stripe and traverse towards the opposite end, similar to the flux

lines observed on a macroscopic bar magnet. Flux lines also leak at defect sites within the well-formed ferromagnetic stripes. These defects can occur for instance due to missed scan lines and highlight the sensitivity of the *m* on the ion-irradiation—if the GFIS beam is finely controlled it may be possible to achieve magnetic modulations of <50 nm lateral dimensions. These results show that GFIS-assisted magnetic writing is an effective method to produce nanomagnets.

A detailed analysis of the flux density within the spacer region between the two ferromagnetic stripes can be found in [73] and is beyond the scope of this chapter. As depicted by the red line in the schematic of Fig. 17.24c, the ferromagnetic/non-ferromagnetic interfaces are expected to be blurred as a consequence of lateral scattering of ions. An *m*-distribution at the ferromagnetic edge region can be modelled so as to fit the observed flux density distribution. The lateral spread of the *m*-distribution estimated from the holography showed that *m* reaches a value of 0.5 at a distance of approximately 20 nm from the nominal edge of the ferromagnetic stripe which is larger than the λ term of 10 nm expected from the semi-empirical model. The difference may have been caused by the lamella preparation process, or point to necessary refinements of the semi-empirical model. Both the model as well as the holographic imaging show that applying a corrective increase of the ion-fluence in the vicinity of the ferromagnetic/non-ferromagnetic interfaces can improve the resolution of the patterned nanomagnets.

17.4.3 Future Scope of GFIS-Assisted Magnetic Writing

Magnetic writing using GFIS opens fascinating prospects in the field of nanomagnetism, whereby it is possible to write nanomagnets of desired shapes onto materials that exhibit ion-induced ferromagnetism. The flexibility with which the magnetic nanostructures can be written makes ion-induced ferromagnetism an ideal pathway for rapidly producing prototypes of novel magnetization configurations for use in future magnetic devices. Until now B2-$F_{60}Al_{40}$ has been used as a model system, however, a variety of alloys such as B2-$Fe_{50}Rh_{50}$, -$Fe_{50}V_{50}$ and -$Co_{50}Ga_{50}$ are candidate materials for GFIS-assisted magnetic writing. The application of GFIS to magnetic patterning opens vast opportunities not only in the field of nanomagnetism and devices, but also in the study of ion-induced magnetic phase transitions at the nanoscale in a variety of different alloys.

17.5 Conclusions

The above demonstrations reveal a markedly different approach to nanopatterning that is a clear departure from the removal of material through masked etching or ion beam milling. Directly modifying the material properties not only reduces the number of process steps but in some cases such as the Josephson junctions allows

for smaller feature sizes. In case of magnetic writing, the nanomagnets are directly embedded within a conducting material which is difficult to achieve using conventional lithography.

The direct writing of superconductor and magnetic devices are just two examples of how GFIS can be used for material modification. We envision more direct-write applications in semiconductors, 2D materials (e.g. Graphene) and any other material systems that have functionalities which are sensitive to disorder. Furthermore, as the technology matures and the capabilities of the machines increase we expect even more advances. GFIS machines equipped with lithography stages and software for handling large area samples will stimulate commercial applications, whereas higher beam energies will allow implantation through thicker or denser materials—the possibilities of applying GFIS technology are immense.

References

1. M.K. Wu, J.R. Ashburn, C.J. Torng, P.H. Hor, R.L. Meng, L. Gao, Z.J. Huang, Y.Q. Wang, C. W. Chu, Superconductivity at 93-K in a new mixed-phase Y-Ba-Cu-O compound system at ambient pressure. Phys. Rev. Lett. **58**, 908–910 (1987). doi:10.1103/PhysRevLett.58.908
2. J.T. Kim, J. Giapintzakis, D.M. Ginsberg, Anisotropy of the resistivity in the a-b plane of a superconducting YBa2Cu3O7-delta single crystal. J. Supercond. **9**, 481–484 (1996). doi:10.1007/Bf00723518
3. D. Koelle, R. Kleiner, F. Ludwig, E. Dantsker, J. Clarke, High-transition-temperature superconducting quantum interference devices. Rev. Mod. Phys. **71**, 631–686 (1999) doi:10.1103/RevModPhys.71.631
4. S.A. Cybart, E.Y. Cho, T.J. Wong, B.H. Wehlin, M.K. Ma, C. Huynh, R.C. Dynes, Nano Josephson superconducting tunnel junctions in YBa2Cu3O7-delta directly patterned with a focused helium ion beam. Nat. Nanotechnol. **10**, 598–602 (2015). doi:10.1038/Nnano.2015.76
5. J. Clarke, A.I. Braginski, *The SQUID handbook* (Wiley-VCH, Weinheim, 2004)
6. B.D. Josephson, Possible new effects in superconductive tunnelling. Phys. Lett. **1**, 251–253 (1962). doi:10.1016/0031-9163(62)91369-0
7. S.P. Benz, C.A. Hamilton, C.J. Burroughs, L.A. Christian, Josephson standards for AC voltage metrology, in *Success in the 21st Century Depends on Modern Metrology*, vols. 1–2, 1997, pp. 355–363
8. W.C. Stewart, Current-voltage characteristics of Josephson junctions. Appl. Phys. Lett. **12**, 277 (1968). doi:10.1063/1.1651991
9. D.E. Mccumber, Effect of ac impedance on dc voltage-current characteristics of superconductor weak-link junctions. B Am. Phys. Soc. **13**, 476 (1968)
10. A.E. White, K.T. Short, R.C. Dynes, A.F. J. Levi, M. Anzlowar, K.W. Baldwin, P.A. Polakos, T.A. Fulton, L.N. Dunkleberger, Controllable reduction of critical currents in Yba2cu3o7-delta films. Appl. Phys. Lett. **53**, 1010–1012 (1988). doi:10.1063/1.100652
11. S.A. Cybart, P.X. T. Yen, E.Y. Cho, J.U. Huh, V.N. Glyantsev, C.S. Yung, B. Moeckly, J.W. Beeman, R.C. Dynes, Comparison of Y-Ba-Cu-O films irradiated with helium and neon ions for the fabrication of Josephson devices. IEEE T Appl. Supercon. **24**, 1100105 (2014). doi:10.1109/Tasc.2014.2311400
12. S.K. Bahl, N. Bluzer, R.E. Glover, In-situ optical properties of amorphous Ge films deposited at 4.2 k. B Am. Phys. Soc. **18**, 132–132 (1973)
13. P. Xiong, A.V. Herzog, R.C. Dynes, Superconductivity in ultrathin quench-condensed Pb/Sb and Pb/Ge multilayers. Phys. Rev. B **52**, 3795–3801 (1995). doi:10.1103/PhysRevB.52.3795

14. L. Merchant, J. Ostrick, R.P. Barber, R.C. Dynes, Crossover from phase fluctuation to amplitude-dominated superconductivity: a model system. Phys. Rev. B **63**, (2001). (Artn 134508, doi:10.1103/Physrevb.63.134508)
15. S.A. Cybart, P. Roediger, K. Chen, J.M. Parker, E.Y. Cho, T.J. Wong, R.C. Dynes, Temporal stability of Y-Ba-Cu-O nano Josephson junctions from ion irradiation. IEEE T Appl. Supercon. **23**, (2013). (Artn 1100103, doi:10.1109/Tasc.2012.2227646)
16. K. Chen, S.A. Cybart, R.C. Dynes, Planar thin film YBa2Cu3O7-delta Josephson junction pairs and arrays via nanolithography and ion damage. Appl. Phys. Lett. **85**, 2863–2865 (2004). doi:10.1063/1.1803620
17. J. Hollkott, S. Hu, C. Becker, J. Auge, B. Spangenberg, H. Kurz, Combined method of electron-beam lithography and ion implantation techniques for the fabrication of high-temperature superconductor Josephson junctions. J. Vac. Sci. Technol. B **14**, 4100–4104 (1996. doi:10.1116/1.588599
18. N. Bergeal, X. Grison, J. Lesueur, G. Faini, M. Aprili, J.P. Contour, High-quality planar high-T-c Josephson junctions. Appl. Phys. Lett. **87**, (2005). (Artn 102502, doi:10.1063/1.2037206)
19. D.J. Kang, N.H. Peng, R. Webb, C. Jeynes, G. Burnell, J.H. Yun, S.H. Moon, B. Oh, E. J. Tarte, D.F. Moore, M. Kelly, M.G. Blamire, Irradiation damage technology for manufacturable Josephson junctions. Nucl. Instrum. Meth. B **188**, 183–188 (2002). (Pii S0168-583x(01)01079-5, doi:10.1016/S0168-583x(01)01079-5)
20. S.A. Cybart, S.M. Wu, S.M. Anton, I. Siddiqi, J. Clarke, R.C. Dynes, Series array of incommensurate superconducting quantum interference devices from YBa2Cu3O7-delta ion damage Josephson junctions. Appl. Phys. Lett. **93**, (2008). (Artn 182502, doi:10.1063/1.3013579)
21. K. Chen, S.A. Cybart, R.C. Dynes, Study of closely spaced YBa2Cu3O7-delta Josephson junction pairs. IEEE T Appl. Supercon. **15**, 149–152 (2005). doi:10.1109/Tasc.2005.849722
22. K.K. Likharev, Superconducting weak links. Rev. Mod. Phys. **51**, 101–159 (1979). doi:10.1103/RevModPhys.51.101
23. S.A. Cybart, K. Chen, R.C. Dynes, Planar YBa2Cu3O7-delta ion damage Josephson junctions and arrays. IEEE T Appl. Supercon. **15**, 241–244 (2005). doi:10.1109/Tasc.2005.849768
24. K. Nakayama, Y. Ishimaru, H. Wakana, S. Adachi, Y. Tarutani, K. Tanabe, Fabrication of high-quality multilayer structure for HTS-SFQ circuits using surface treatments. IEEE T Appl. Supercon. **15**, 157–160 (2005). doi:10.1109/Tasc.2005.849729
25. C.P. Foley, E.E. Mitchell, S.K.H. Lam, B. Sankrithyan, Y.M. Wilson, D.L. Tilbrook, S. J. Morris, Fabrication and characterisation of YBCO single grain boundary step edge junctions. IEEE T Appl. Supercon. **9**, 4281–4284 (1999). doi:10.1109/77.783971
26. B.H. Moeckly, K. Char, Properties of interface-engineered high T-c Josephson junctions. Appl. Phys. Lett. **71**, 2526–2528 (1997). doi:10.1063/1.120107
27. G.E. Blonder, M. Tinkham, T.M. Klapwijk, Transition from metallic to tunneling regimes in superconducting micro-constrictions: excess current, charge imbalance, and super-current conversion. Phys. Rev. B **25**, 4515–4532 (1982). doi:10.1103/PhysRevB.25.4515
28. G. Burnell, E.J. Tarte, D.J. Kang, R.H. Hadfield, M.G. Blamire, Asymmetry modulated SQUIDs made by direct focused ion beam milling. Physica C **368**, 241–245 (2002). (Pii S0921-4534(01)01174-1, doi:10.1016/S0921-4534(01)01174-1)
29. G. Burnell, R.H. Hadfield, C. Bell, D.J. Kang, M.G. Blamire, Nanoscale superconductor-normal metal-superconductor junctions fabricated by focused ion beam. Physica C **372**, 14–17 (2002). (Pii S0921-4534(02)00691-3, doi:10.1016/S0921-4534(02)00691-3)
30. R.W. Simon, J.B. Bulman, J.F. Burch, S.B. Coons, K.P. Daly, W.D. Dozier, R. Hu, A.E. Lee, J.A. Luine, C.E. Platt, S.M. Schwarzbek, M.S. Wire, M.J. Zani, Engineered Hts microbridges. IEEE T Magn. **27**, 3209–3214 (1991). doi:10.1109/20.133894
31. B.W. Ward, J.A. Notte, N.P. Economou, Helium ion microscope: a new tool for nanoscale microscopy and metrology. J. Vac. Sci. Technol. B **24**, 2871–2874 (2006). doi:10.1116/1.2357967

32. J. Notte, N. Economou, B. Ward, New microscope technology emerges from research labs. R&D Mag. **49**, 38–39 (2007)
33. B. Ward, J.A. Notte, N.P. Economou, Helium-ion microscopy. Photonic Spectra **41**, 68–70 (2007)
34. R. Hill, J. Notte, B. Ward, The ALIS He ion source and its application to high resolution microscopy, in *Proceedings of the Seventh International Conference on Charged Particle Optics (Cpo-7)*, vol. 1, 2008, pp. 135–141. doi:10.1016/j.phpro.2008.07.088
35. S.A. Cybart, E.Y. Cho, T.J. Wong, B.H. Wehlin, M.K. Ma, C. Huynh, R.C. Dynes, Nano Josephson superconducting tunnel junctions in YBa2Cu3O7-delta directly patterned with a focused helium ion beam. Nat. Nanotechnol. **10**, 598–602 (2015). doi:10.1038/nnano.2015.76
36. S.A. Cybart, S.M. Anton, S.M. Wu, J. Clarke, R.C. Dynes, Very large scale integration of nanopatterned YBa2Cu3O7-delta Josephson junctions in a two-dimensional array. Nano Lett. **9**, 3581–3585 (2009). doi:10.1021/Nl901785j)
37. S.A. Cybart, T.N. Dalichaouch, S.M. Wu, S.M. Anton, J.A. Drisko, J.M. Parker, B.D. Harteneck, R.C. Dynes, Comparison of measurements and simulations of series-parallel incommensurate area superconducting quantum interference device arrays fabricated from YBa2Cu3O7-delta ion damage Josephson junctions. J Appl. Phys. **112** (2012) (Artn 063911, doi:10.1063/1.4754422)
38. S.A. Cybart, E.Y. Cho, T.J. Wong, V.N. Glyantsev, J.U. Huh, C.S. Yung, B.H. Moeckly, J.W. Beeman, E. Ulin-Avila, S.M. Wu, R.C. Dynes, Large voltage modulation in magnetic field sensors from two-dimensional arrays of Y-Ba-Cu-O nano Josephson junctions. Appl. Phys. Lett. **104** (2014) (Artn 062601, doi:10.1063/1.4865216)
39. E.Y. Cho, M.K. Ma, C. Huynh, K. Pratt, D.N. Paulson, V.N. Glyantsev, R.C. Dynes, S.A. Cybart, YBa2Cu3O7-delta superconducting quantum interference devices with metallic to insulating barriers written with a focused helium ion beam. Appl. Phys. Lett. **106** (2015) (Artn 252601, doi:10.1063/1.4922640)
40. J. Fassbender, J. McCord, J. Magn. Magn. Mater. **320**, 579 (2008)
41. J. Fassbender, D. Ravelosona, Y. Samson, J. Phys. D **37**, R179 (2004)
42. A. Taylor, R.M. Jones, J. Phys. Chem. Solids **6**, 16 (1958)
43. A. Parthasarathi, P.A. Beck, Solid State Commun. **18**, 211 (1976)
44. G.F. Zhou, H. Bakker, Mater. Trans. **36**, 329 (1995)
45. C. Antoniak, J. Lindner, K. Fauth, J.-U. Thiele, J. Minár, S. Mankovsky, H. Ebert, H. Wende, M. Farle, Phys. Rev. B **82**, 064403 (2010)
46. C. Chappert, H. Bernas, J. Ferré, V. Kottler, J.-P. Jamet, Y. Chen, E. Cambril, T. Devolder, F. Rousseaux, V. Mathet, H. Launois, Science **280**, 1919 (1998)
47. H. Bernas, J-Ph Attané, K.-H. Heinig, D. Halley, D. Ravelosona, A. Marty, P. Auric, C. Chappert, Y. Samson, Phys. Rev. Lett. **91**, 077203 (2003)
48. O. Hellwig, D. Weller, A.J. Kellock, J.E.E. Baglin, E.E. Fullerton, Appl. Phys. Lett. **79**, 1151 (2001)
49. J. McCord, T. Gemming, L. Schultz, J. Fassbender, M.O. Liedke, M. Frommgerger, E. Quandt, Appl. Phys. Lett. **86**, 162502 (2005)
50. J. Fassbender, J. McCord, Appl. Phys. Lett. **88**, 252501 (2006)
51. I. Barsukov, F.M. Römer, R. Meckenstock, K. Lenz, J. Lindner, S. Hemken to Krax, A. Banholzer, M. Körner, J. Grebing, J. Fassbender, M. Farle, Phys. Rev. B **84**, 140410(R) (2011)
52. B. Obry, P. Pirro, T. Brächer, A.V. Chumak, J. Osten, F. Ciubotaru, A.A. Serga, J. Fassbender, B. Hillebrands, Appl. Phys. Lett. **102**, 202403 (2013)
53. S.O. Demokritov, C. Bayer, S. Poppe, M. Rickart, J. Fassbender, B. Hillebrands, D.I. Kholin, N.M. Kreines, M.O. Liedke, Phys. Rev. Lett. **90**, 097201 (2003)
54. S. Wintz, C. Bunce, A. Banholzer, M. Körner, T. Strache, R. Mattheis, J. McCord, J. Raabe, C. Quitmann, A. Erbe, J. Fassbender, Phys. Rev. B **85**, 134417 (2012)
55. L.M. Di, H. Bakker, Y. Tamminga, F.R. de Boer, Phys. Rev. B **44**, 2444 (1991)
56. R. Butler, J.E. Hanlon, R.J. Wasilewski, J. Phys. Chem. Solids **30**, 1929 (1969)
57. J.C. Krauze, J. Schaf, M.I. da Costa Jr, C. Paduani, Phys. Rev. B **61**, 6196 (2000)

58. A. Arrott, H. Sato, Phys. Rev. **114**(6), 1420 (1959)
59. M. Fukuzumi, Y. Chimi, N. Ishikawa, F. Ono, S. Komatsu, A. Iwase, Nucl. Instrum. Methods Phys. Res. Sect. B Beam Interact. Mater. Atoms **230**(1–4), 269 (2005)
60. M. Krawczyk, D. Grundler, J. Phys.: Condens. Matter **26**, 123202 (2014)
61. S.O. Demokritov, A.N. Slavin (eds.), *Magnonics: From Fundamentals to Applications* (Springer, Berlin, 2013)
62. J. Fassbender, M.O. Liedke, T. Strache, W. Möller, E. Menéndez, J. Sort, K.V. Rao, S.C. Deevi, J. Nogués, Phys. Rev. B **77**, 174430 (2008)
63. G.P. Huffman, R.M. Fisher, J. Appl. Phys. **38**, 735 (1967)
64. E. Menéndez, J. Sort, M.O. Liedke, J. Fassbender, S. Suriñach, M.D. Baró, J. Nogués, New J. Phys. **10**, 103030 (2008)
65. A. Hernando, X. Amils, J. Nogués, S. Suriñach, M.D. Baró, M.R. Ibarra, Phys. Rev. B **58**, R11864 (1998)
66. J. Nogués, E. Apiñaniz, J. Sort, M. Amboage, M. d'Astuto, O. Mathon, R. Puzniak, I. Fita, J.S. Garitaonandia, S. Suriñach, J.S. Muñoz, M.D. Baró, F. Plazaola, F. Baudelet, Phys. Rev. B **74**, 024407 (2006)
67. L.E. Zamora, G.A. Pérez Alcázar, G.Y. Vélez, J.D. Betancur, J.F. Marco, J.J. Romero, A. Martínez, F.J. Palomares, J.M. González, Phys. Rev. B **79**, 094418 (2009)
68. D. Wu, I. Baker, Mater. Sci. Eng. **A329–331**, 334 (2002)
69. Q. Zeng, I. Baker, Intermetallics **14**, 396 (2006)
70. R. Bali, S. Wintz, F. Meutzner, R. Hübner, R. Boucher, A.A. Ünal, S. Valencia, A. Neudert, K. Potzger, J. Bauch, F. Kronast, S. Facsko, J. Lindner, J. Fassbender, Nano Lett. **14**(2), 435 (2014)
71. J.F. Ziegler, M.D. Ziegler, J.P. Biersack, Nucl. Instrum. Methods Phys. Res. Sect. B: Beam Interact. Mater. Atoms **268**(11–12), 1818 (2010)
72. W. Möller, W. Eckstein, Nucl. Instrum. Methods Phys. Res. Sect. B: Beam Interact. Mater. Atoms **2**, 814 (1984)
73. F. Röder, G. Hlawacek, S. Wintz, R. Hübner, L. Bischoff, H. Lichte, K. Potzger, J. Lindner, J. Fassbender, R. Bali, Scientific Reports **5**, 16786 (2015)

Chapter 18
Helium Ion Microscope Fabrication of Solid-State Nanopore Devices for Biomolecule Analysis

Osama K. Zahid and Adam R. Hall

Abstract Solid-state nanopores are an emerging technology for the detection and analysis of biomolecules at the single-molecule level. Consisting of one or more nanometer-scale apertures in a thin, solid-state membrane, a number of methods have been utilized to make these devices. However, conventional approaches are either non-trivial to scale up or lack sufficient precision for many applications. In this chapter, we describe the use of the helium ion microscope to produce nanopores. We demonstrate control over diverse aspects of the device and discuss a range of applications that have been enabled by their implementation.

18.1 Introduction

In the 1940s, Wallace H. Coulter developed a method of quantifying blood cells [1] that was initially criticized for being unsophisticated. The apparatus was built by producing a hole of ~10 μM in a cellophane cigarette wrapper and placing it in between two isolated chambers containing electrolyte solution, thus ensuring the opening as the only passage through which the chambers could interact. The application of an electrical bias between the two chambers generated a measurable ionic current that corresponded linearly to the applied voltage and when cells in solution were forced through the pore by pressure, their brief presence resulted in a transient decrease in the ionic current. The number of spikes, or resistive pulses, could be used to enumerate the cells while their individual amplitudes were shown to correspond to cell type (red or white blood cell), since these differ in volume and

O.K. Zahid · A.R. Hall (✉)
Virginia Tech-Wake Forest School of Biomedical Engineering and Sciences,
Wake Forest University School of Medicine, Winston Salem, NC 27101, USA
e-mail: arhall@wakehealth.edu

O.K. Zahid
e-mail: ozahid@wakehealth.edu

© Springer International Publishing Switzerland 2016

G. Hlawacek and A. Gölzhäuser (eds.), *Helium Ion Microscopy*,
NanoScience and Technology, DOI 10.1007/978-3-319-41990-9_18

displace ions proportionally. This simple detection principle is at the core of the Coulter Counter technology that has revolutionized the field of hematology and is still widely employed in the clinic [2].

Several decades later, another revolution is underway that is based on the same principle, but instead occurs at the nanoscale and probes individual molecules. This is being realized by the emerging technology of solid-state (SS-) nanopores [3, 4], wherein a nanometer size aperture is generated in an insulating membrane, most commonly through the use of charged particle beam fabrication techniques. As in the Coulter device, the chip containing a nanopore is positioned in a flow cell and electrolyte solution is introduced to the chambers, enabling a voltage-induced ionic current that can be measured in real-time using a patch-clamp amplifier. Using this system, molecules like DNA [5, 6], RNA [7], proteins [8, 9], and nanoparticles [10, 11] can be electrically threaded from one side (*cis* chamber) to the other (*trans* chamber) while being individually probed (Fig. 18.1).

Investigation at the molecular scale using SS-nanopores was first demonstrated [12] by the Golovchenko group in 2001 and has since been developed into a remarkably expansive technology, extending far beyond simple counting. For example, the system has been used to probe DNA-protein interactions [13–16], DNA epigenetics [17–19], and nucleic acid biomarkers [20, 21], and used to

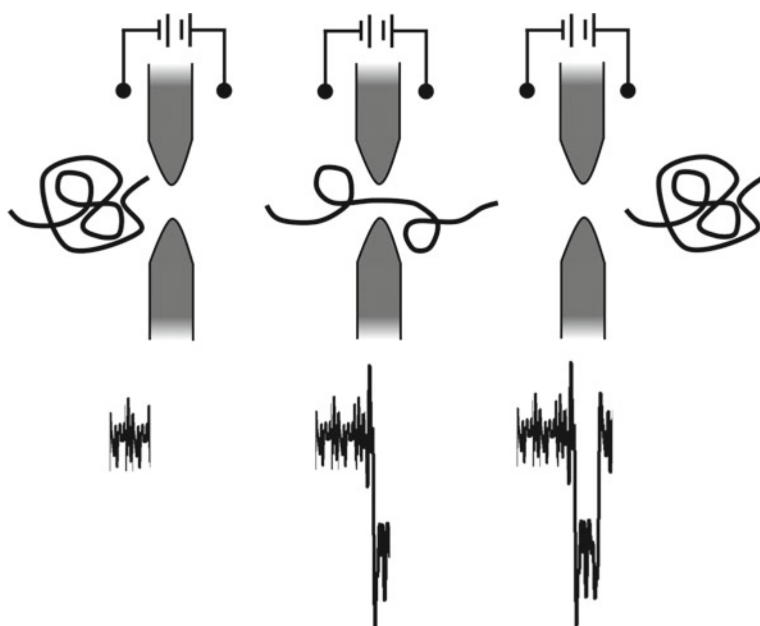

Fig. 18.1 SS-Nanopore detection scheme. Depiction of a biomolecule translocation with corresponding ionic current signal below: **a** baseline open-pore current; **b** threading of the molecule decreases ionic current; **c** current returns to baseline upon molecular passage. The total electrical signal is referred to as an event

generate devices that mimic nanopores found in nature, like the nuclear pore complex [22] and porins [23]. Simultaneously, significant advancements have been made towards understanding the fundamental physics of nanoscale confinement, such as ionic screening [24], electrical forces [25–27], translocation dynamics [6, 28], and the effects of solvent conditions [29–34]. Understanding these mechanisms is important both for improving devices and for developing novel measurement techniques.

Critical to all of these areas has been the realization of the SS-nanopore devices themselves, towards which several fabrication methods have been developed. The first demonstrated approach was ion beam sculpting[12], in which a defocused ion beam is used to controllably reduce the size of a pre-fabricated micropore. By monitoring ionic flux during the closing, a single nanopore can be produced with sub-nanometer precision. Soon after, devices were also demonstrated using transmission electron microscope (TEM) ablation of a thin membrane [35]. Similar precision is achievable with this method, and by virtue of the relative availability of TEM systems, it has become widely embraced by the field. Later, Ga+ focused ion beam (FIB) milling was also shown to be able to produce nanopores [36]. However, each of these charged particle beam approaches has significant challenges. For instance, both ion beam sculpting and TEM are low-throughput techniques, able to accommodate only a single device at a time, and can require many minutes to hours to produce a single pore. Ga+ FIB overcomes throughput, but at the expense of precision and resolution; it can typically produce pores only as small as about 15 nm and with low reproducibility. More recent innovations like the dielectric breakdown technique [37] offer tremendous advantages in fabrication cost, but may still have limitations in aspects of fabrication like throughput or array formation.

One candidate technology that can address many of these challenges is the scanning helium ion microscope (HIM). In this chapter, we review HIM nanofabrication as it relates to SS-nanopores, showing not only rapid and precise pore definition, but also the ability to manipulate other device properties as well. Finally, we describe a wide range of biosensing applications that have been and are currently being addressed using HIM SS-nanopores.

18.2 HIM Milling of SS-Nanopores

Milling by FIB is a well-characterized process that occurs by sputtering[38] when ions impinge on a surface with sufficient acceleration to knock out substrate atoms through nuclear-nuclear interactions (Fig. 18.2 scheme). The minimum feature resolution achievable through sputtering depends principally on two factors: the amount of momentum transfer and the size of the focal spot (i.e. exposure area). For example, conventional FIB uses large Ga+ ions (70 amu) with a typical acceleration voltage of 5–30 kV and can achieve a focal spot [39] of only ~10 nm. Consequently, the smallest nanopores that can be realized by the approach are ~10–20 nm, with low reproducibility [36, 40]. By virtue of using much smaller He+ ions (4 amu),

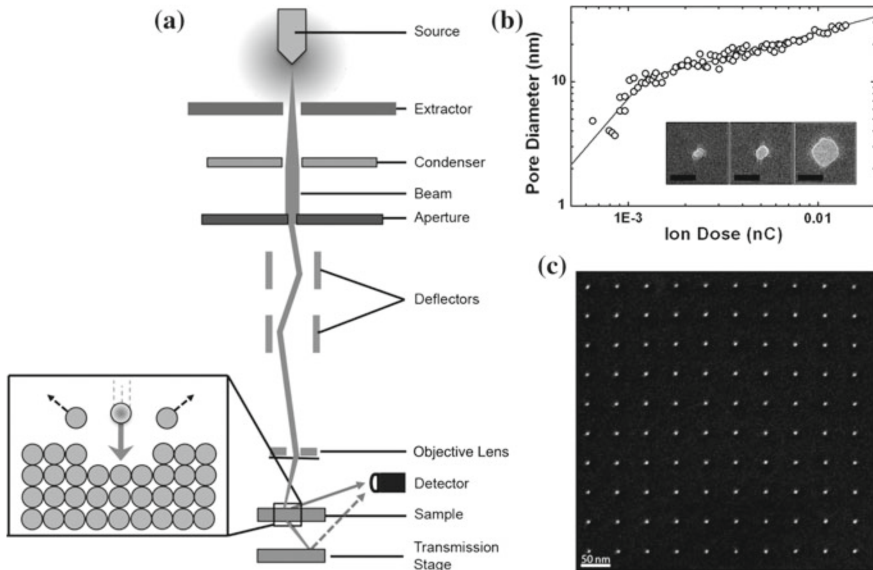

Fig. 18.2 HIM Nanopore fabrication. **a** Cross-sectional illustration of HIM components. *Inset* schematic of nuclear interactions of the impinging ionic beam with sample. **b** Log–log plot of He+ dose versus resultant nanopore diameter showing a fast rate below ~10 nm and a slower one above. *Solid lines* are power law fits to the respective regions. *Inset* TEM images of individual HIM nanopores with diameters (L-R) of 5, 10 and 20 nm. Scale bars are 20 nm. **c** STIM micrograph of a 10 × 10 array of 5 nm diameter nanopores

an atomically sharp source, and advanced focusing optics to achieve a focal spot [41] of ~0.34 nm, HIM improves significantly on these resolution limitations. As a result, it is a superior technology for the fabrication of SS-nanopores.

18.2.1 Nanopore Formation

Nanopores were fabricated in a thin, free-standing silicon nitride (SiN) membrane supported by a Si chip. For the measurements presented here, we used 30 nm thick SiN membranes that span an area of ~250 μm^2 in a 4.4 mm Si support frame with a thickness of 200 μm. Considering this particular size and the 50 mm X-Y travel range of the HIM sample stage, up to a 100 individual devices could be processed in a single sample exchange load cycle. However, the process is amenable to a wide range of device dimensions that could enable even more. Before mounting, chips are rinsed with acetone and ethanol, dried under nitrogen gas flow, and subsequently placed in a custom-built HIM sample holder. The holder containing the samples was treated under oxygen plasma (150 W) for 2–5 min to ensure removal of organic contaminants and was then immediately placed in the HIM sample

exchange chamber, where it underwent a further 3 min of air plasma treatment (10 W) before being transferred into the main chamber. This ensured elimination of minor contamination acquired in transit.

Once the sample stage was transferred into main imaging chamber, HIM beam current was adjusted through selection of appropriate condenser lens setting and aperture size and adjustment of He supply pressure. We typically utilized currents of at least 5 pA for SS-nanopore fabrication, but have achieved good results with at <1 pA as well. Low magnification imaging of the Si chip was used to determine the exact position of the SiN window and the beam was positioned on the Si substrate immediately adjacent to it. To ensure that the beam focus and stigmation was fine-tuned prior to fabrication, a brief (5–10 s) single spot exposure of the beam was used to produce a feature in the substrate that was subsequently used to optimize the beam conditions in conventional imaging mode. Immediately following this, the beam was blanked and the SiN window was moved into the beam path. Lithographic control elements were then used to perform beam exposure for a set time, progressively sputtering material and generating a single nanopore. Using measurements from low-energy (<150 kV) TEM images, we have found that SS-nanopore size varies with total incident ion dose (Fig. 18.2b). For a given dose, we observed only minor variation (±2–3 nm) in pore diameter, indicating high reproducibility. Post-fabrication analysis of the pore can also be acquired through transmission imaging, but resolution is limited and the imaging beam may affect pore dimensions.

The ionic resistance of each pore can also be used to confirm the fabricated dimensions using a simplified conductance model. Toward this end, a chip containing a single SS-nanopore was rinsed with clean deionized water (DiH_2O) and pure ethanol and then dried under air flow. Following an air (or oxygen) plasma treatment (15 W) for 2–5 min per side, the chip was positioned in a custom flow cell and high ionic strength electrolyte solution (1 M KCl) was introduced to both sides of the device. Ionic current was measured with a commercial patch-clamp amplifier (Axopatch 200B, Molecular Devices) by way of a pair of Ag/AgCl electrodes. All devices exhibited linear *I-V* curve characteristics and steady, low noise baseline current. Indeed, comparison of identical devices fabricated by TEM and HIM showed no significant difference in noise characteristics [42]. The diameter, d, of a SS-nanopore can be determined from its measured conductance, G, through the equation [29]

$$G = \frac{\pi d^2}{4L_{eff}}\left((\mu_K + \mu_{Cl})n_K e + \frac{4\sigma\mu_K}{d}\right),$$

where L_{eff} is the effective thickness of the membrane near the nanopore, μ_K and μ_{Cl} are the electrophoretic mobilities of potassium and chloride (7.616 and 7.909×10^{-8} m^2 V^{-1} s^{-1}, respectively), n_{K} is the number density of counterions, e is the elementary charge and σ is the surface charge density of the membrane

material. This model provides an independent verification of device dimensions, which we find to be in good agreement with direct TEM analysis [42].

In general, ion milling can be described by the relation [43]:

$$\log(d) = a + b\log(D),$$

where d is feature dimension (SS-nanopore diameter), a and b are correlation constants, and D is the total ion dose. As a result, HIM pore formation would be expected to manifest as a linear relationship on a log-log scale. However, we clearly observe two separate linear regimes: a fast pore growth rate regime below for small diameters, which then transitions to a slower increase for larger diameters [42]. This transition occurs consistently at a diameter of ~10 nm across a range of initial conditions [44]. We interpret this observation to be the result of nanopore shape. The intense center of the Gaussian beam is able to sputter the initial SiN membrane efficiently, resulting in a high growth rate. However, beyond the Full Width Half Maximum (FWHM), sputtering is induced only by the less intense edges of the beam, resulting in a significantly lower yield. Thus the transition between these two regimes is related to beam characteristics and is intrinsic to the approach.

18.2.2 DNA Translocation

Having established the ability to produce SS-nanopores with HIM milling, we next turn to the central aspect of their utility in single-molecule detection. While ionic current measurements were demonstrated, a number of factors could be important to supporting molecular translocation, including implanted charge, surface roughness, and microscopic pore shape. Therefore, direct confirmation of device viability is critical.

We used translocation of the well-characterized λ bacteriophage double-stranded (ds-) DNA genome (48 kbp) as a model because it is the most widely studied material in the field and is therefore an ideal benchmark. Figure 18.3a shows a typical conductance trace with characteristic discrete event amplitudes at integer multiples of the first non-baseline conductance level. The spacing of these event profiles (Fig. 18.3b) are indicative of the conformation of DNA molecules as they pass through the pore: a molecule translocating linearly reduces the conductance by a standard amount; a singly-folded molecule reduces it twice as much, and so on (Fig. 18.3c). These data are in agreement with numerous previous reports [5, 6] and confirm that translocations dynamics through HIM nanopores are essentially indistinguishable from those made by other fabrication methods.

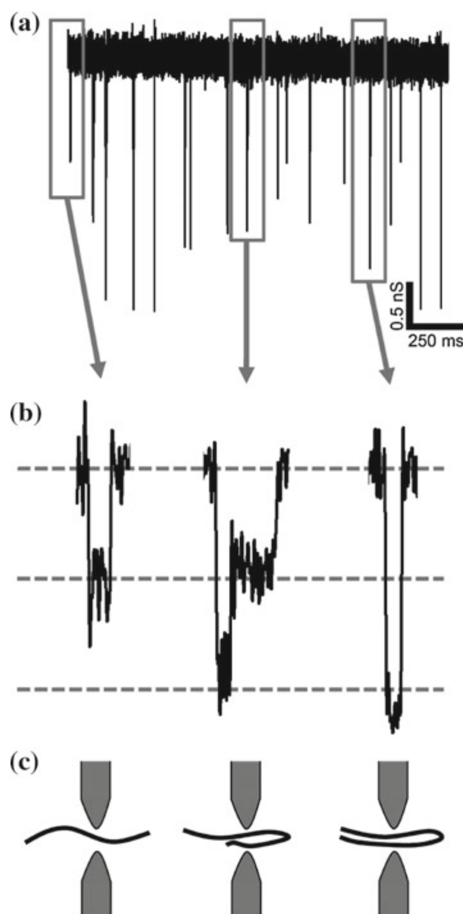

Fig. 18.3 DNA translocation through HIM Nanopores. **a** A typical measured conductance trace (150 mV applied voltage, low pass filtered at 5 kHz) showing downward spikes indicative of 48.8 kbp dsDNA translocations. **b** Examples of individual events from the conductance trace in (**a**), indicating the translocation of unfolded (*left*), partially folded (*center*) and folded (*right*) dsDNA. *Dashed lines* represent baseline and discrete conductance blockade levels. **c** Diagrammatic illustration of dsDNA conformation corresponding to each event in (**b**)

18.2.3 Nanopore Arrays

SS-nanopore arrays will enable parallel sensing platforms that have high throughput and thus potential for wide-ranging applications. While several studies have utilized nanopore arrays, the methods used to achieve them have suffered from either prolonged, manual fabrication time [22] or have required sophisticated post-fabrication treatments such as atomic layer deposition (ALD) to reduce pore sizes to optimal dimensions [45]. Each of these factors affects throughput and overall cost of production.

With HIM milling, arrays of arbitrary dimension and consisting of individual pores as small as 2–3 nm can be achieved. Using the integrated HIM lithographic system, the position and exposure time of each pixel in a pattern file can be controlled with no loss in resolution and no further alignment necessary. For example, Fig. 18.2c shows an array of 100 individual SS-nanopores in a single

device, each with a diameter of 5 nm. The total fabrication time for this array was about a minute. While the total number of pores can in principle be expanded without restraint, there are practical limits imposed by factors like sample linearity (substrate position relative to focal plane) and dynamic instrumental drift (stage, stigmators), which can alter beam conditions over time. Nonetheless, we have produced arrays of up to 10^4 pores and observed good reproducibility between the first and last pore formed.

18.2.4 Applications of HIM Drilled Nanopores

SS-Nanopores offer the distinct advantage of single-molecule analysis of biomolecules and offers insight into their functions and interactions. Of the many potential and realized [46] applications of the platform, we describe here three research areas that have been impacted directly by HIM nanopores: induced DNA damage; nucleoprotein interactions; and selective quantification of DNA with single-base modifications.

DNA damage by depurination is a common process that occurs spontaneously under physiological conditions [47]. Here, the loss of adenine and guanine nucleotides occurs due to hydrolysis of the N-glycosyl linkages to the deoxyribose backbone resulting in an apurinic (AP) site. Under normal conditions, these lesions are repaired by the base excision pathway (BER) and therefore occur at a low frequency. However evidence suggests in disease states such as cancers [48] and anemia [49] where homeostatic conditions are compromised, AP site damage is enhanced. Therefore, a rapid and direct determination of DNA damage would allow disease initiation and progression to be monitored. HIM nanopores have been employed to detect depurination using short (61 bp) dsDNA molecules as a demonstration vehicle [50]. DNA depurination was induced by incubating molecules at various pH (ranging from 2 to 10) and subsequently performing SS-nanopore analysis. Under all investigated pH conditions, translocation event depth (amplitude) was found to be consistent, indicating conformational integrity. However, under increasingly acidic conditions, event durations transitioned from a single, defined population to a biomodal distribution (Fig. 18.4a). The first, unyielding population was attributed to translocation of unmodified dsDNA, while the second population emerged due to increased DNA damage. The generation of AP sites resulted in strand separations and unstructured regions that caused increased interaction with the pore walls. Excessively damaged DNA was shown to exhibit mean translocation durations more than an order of magnitude greater than the unmodified duration. Thus, the results clearly demonstrated label-free SS-nanopore detection and rough estimation of DNA depurination.

HIM nanopores have also been to used to analyze nucleoprotein structure. To this end, the selective interaction of single-stranded DNA binding protein (SSB) with single-strand (ss-) DNA to form nucleoprotein complexes was investigated [51]. Saturated nucleoprotein complexes were discriminated from free SSB, ssDNA

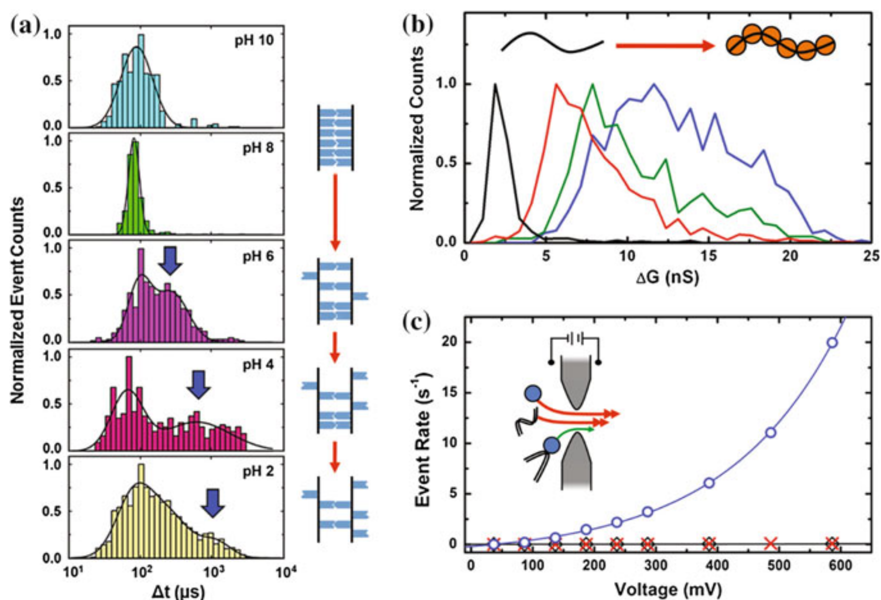

Fig. 18.4 Applications of HIM Nanopores. **a** Detecting DNA depurination [50]. Event duration histograms for 61 bp DNA translocation events from pH 10 (*top*) to pH 2 (*bottom*). Total numbers of events considered are n = 714 (pH 10), 662 (pH 8), 552 (pH 6), 423 (pH 4) and 1852 (pH 2). The *black lines* represent Gaussian fits to the data (pH 10 and 8: single peak; pH 6 and 4: two peaks; pH 2: three peaks). The prolonged translocation dwell times (*blue arrows*) indicate progressive DNA damage represented by the cartoon schematic next to the histograms. From [50]. **b** Nucleoprotein complex analysis [51]. Mean conductance blockade (ΔG) histograms for ssDNA incubated with SSB in ratios of 1:0 (ssDNA alone, n = 551, *black*), 1:114 (n = 1048, *red*), 1:199 (n = 682, *green*), and 1:284 (n = 517, *blue*). The illustration (*top*) represents progressive complex formation as SSB concentration is increased. **c** Selective detection of modified dsDNA [52]. Event rate versus applied voltage for 150 bp dsDNA containing a single biotin (*red crosses*), MS (*black diamonds*) and dsDNA:MS (*blue circles*). DNA and complex concentrations were 1 μM and MS concentration was 2 μM. *Solid lines* are exponential fits to the data. *Inset* Illustration of differentiation of dsDNA:MS complex (*green arrow*) from either constituent molecule

and dsDNA individually by virtue of their characteristic translocation event depth (ΔG). Binding dynamics were also studied by titrating SSB against ssDNA. Figure 18.4b depicts ΔG histograms for SS-nanopore measurements as protein concentration was increased, showing that mean event depth shifts progressively due to complex formation. Additionally, nucleoprotein structure was probed by comparing linearized and circular ssDNA constructs, yielding a new model of filament formation.

As a final example, HIM SS-nanopores have been used to achieve selective detection and quantification of dsDNA featuring a single base modification [52]. For very small and/or highly charged biomolecules, the speed of electrical translocation is sufficiently high to render their threading undetectable by conventional electronics [9]. In this approach, specific binding was used to make two

types of undetectable molecule resolvable. In the initial demonstration, these components were a monovalent streptavidin (MS) [53, 54] protein variant that is compact and highly charged, and a short, dsDNA featuring a biotin tag (i.e. the high-affinity recognition molecule of streptavidin). Neither constituent produced significant events, but when they were bound together to form a MS-dsDNA complex, a remarkable increase in the rate of translocation events was observed (Fig. 18.4c), likely a consequence of increased interactions of the bulkier complex with the pore walls slowing threading speed stochastically. Since events were due exclusively to the bound population, event rate could be used to discriminate MS-dsDNA, even among a background. Indeed, biotinylated dsDNA was detected and quantified within a mixture of unlabeled molecules [52]. This powerful approach holds great potential to probe a wide range of biomolecules with intrinsic selectivity and sensitivity.

18.3 Manipulation of Device Thickness

The detection of small molecules or features along the length of large molecules is a specific challenge for SS-nanopore detection, driven largely by limitations in the signal-to-noise ratio (SNR) of the electrical measurement. One approach to addressing this challenge has been the use of nanopore devices fabricated in ultrathin membranes [20]. Toward this end, 2D materials such as graphene [56, 57], MoS_2 [57], and boron nitride [58] are being pursued as alternate membrane materials. However, integrating these materials is considerably more difficult than with Si-based materials, and they often bring with them additional challenges like substantial interaction with target biomolecules that can frustrate nanopore analysis [55]. An alternative approach instead aims to manipulate the thickness of conventional membranes through top-down processing. For instance, lithographically-defined reactive ion etching has been used to reduce the thickness of SiN membranes prior to SS-nanopore definition, thereby enabling analysis of short nucleic acids [20, 59] and protein structure [60]. However, this approach still requires considerable processing in addition to pore formation. HIM offers an ideal solution as a single method that is capable of both local manipulation of membrane thickness and nanopore milling.

18.3.1 Membrane Thinning

Just as sufficient HIM beam dose at a single point can result in complete sputtering of SiN atoms to form nanopores, exposure to a reduced dose across a localized region can induce more limited damage that can be used to control substrate thickness. In the case of a thin membrane, there are two types of sputtering interactions to consider: direct sputtering, which occurs by removal of atoms by direct

interaction at the point of incidence, and transmission sputtering, which occurs by both direct and indirect removal of atoms at the opposite (exiting) surface (Fig. 18.5a). Both of these contribute to membrane manipulation and must be characterized to achieve a desired thickness.

Early investigation [61] of this process focused on direct topographic analysis by atomic force microscopy (AFM). To accomplish this, two Si chips containing SiN

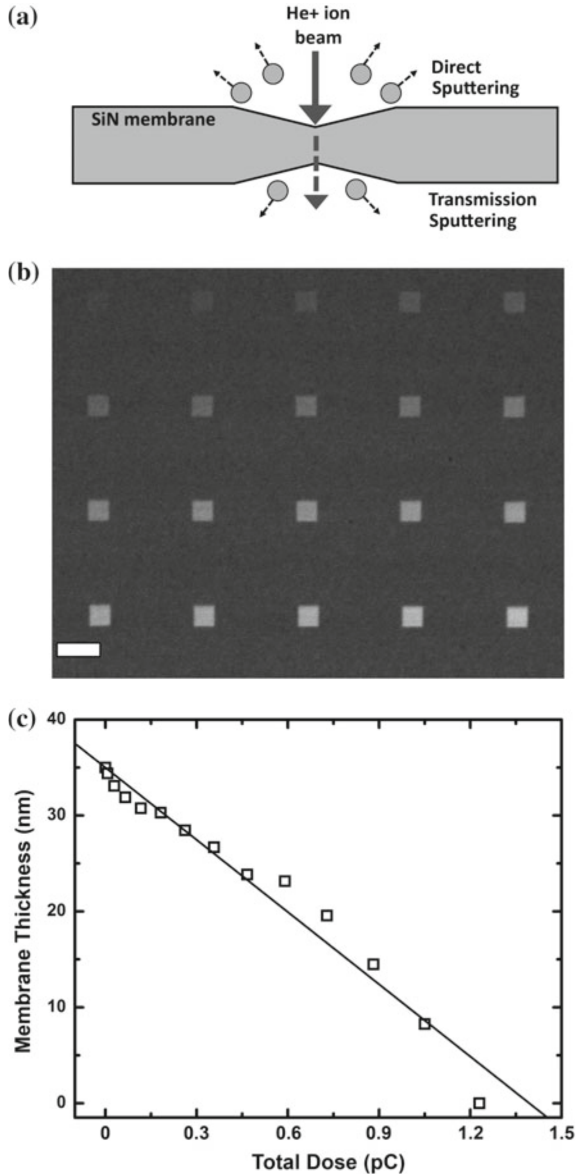

Fig. 18.5 Manipulation of device thickness. **a** Schematic representation of direct and transmission milling. *Arrow* indicates incident He+ ion beam and milling direction. **b** STIM micrograph of an array of 100 nm squares milled in a SiN membrane. Scale bar is 200 nm. **c** Relationship between total He+ ion dose and remaining thickness of a SiN membrane (initial thickness 35 nm), determined in situ by measuring relative STIM brightness of patterned regions compared to native membrane

membranes were introduced to the HIM chamber, one with its flat (unetched) surface facing up and one facing down, and the beam condition was adjusted as described in Sect. 18.2. Here, an initial membrane thickness of 105 nm was used for easier characterization. HIM lithographic patterning was then used to produce an identical series of 500 nm square patterns on each chip with increasing total doses. Importantly, each pattern was exposed by repeatedly rastering over the pattern to reduce redeposition of ablated material [62] or sample charging. Following processing, the flat surface of each chip was analyzed by AFM for a complete quantitative description. From these measurements, direct milling depth was found to vary linearly with total incident ion dose while transmission milling depth varied with the square of the dose. While transmission milling was considerably less efficient than direct milling, as expected qualitatively from its mechanistic nature, it was found to contribute significantly to overall membrane thickness. Thus, the combination of these two milling rates could enable arbitrary membrane thickness to be achieved.

While robust, the AFM approach adds additional analytical burden to the membrane thinning process. A more powerful technique was realized when scanning transmission ion microscopy (STIM) was shown to allow quantitative, *in situ* assessment of membrane thickness [63]. In STIM, an image is formed using secondary electrons produced at a metal surface below the SiN membrane. In this case, image brightness is reduced by scattering losses in the beam, and so thinned regions will appear progressively brighter than the surrounding membrane (Fig. 18.5b). Crucially, pixel brightness was demonstrated to scale directly with membrane thickness, such that a single calibration of image brightness to actual membrane dimension (Fig. 18.5c) enables thickness determination from a single STIM image. As a result, membrane manipulation and characterization could be achieved in a single step.

18.3.2 HIM Control of SS-Nanopore Device Dimensions

Subsequent to membrane thinning, SS-nanopores can be fabricated in the same processing step (Fig. 18.6a). However, the dose-diameter relationship of HIM pore formation (see Sect. 18.2.1) depends acutely on membrane characteristics. As a result, a quantitative understanding how pore formation varies with membrane thickness is critical.

An assessment of this interplay was carried out by measuring SS-nanopore diameter dependence on exposure dose as a function of membrane thickness [44]. Because thinner membranes require less sputtering to produce a pore of a given size, the trend is observed to shift to lower dose with a monoexponential dependence as membrane thickness is reduced (Fig. 18.6b). This analysis enables comprehensive control over SS-nanopore device dimensions in a single step. Using these findings, pores as small as 2 nm can be produced in a membrane only 1.4 nm thick (Fig. 18.6b inset). It is also important to note that regardless of the membrane

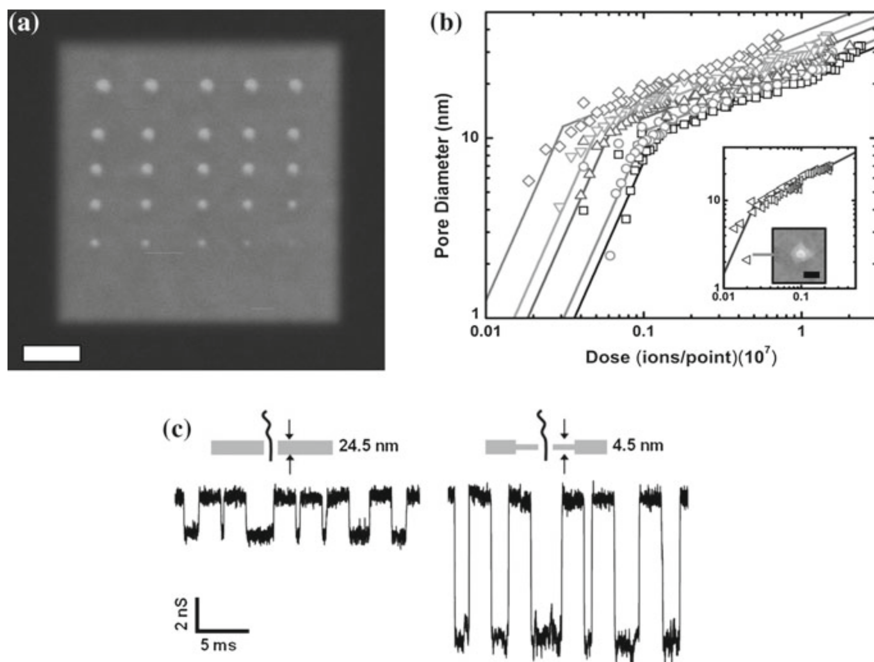

Fig. 18.6 Fabrication of ultrathin nanopore devices. **a** STIM micrograph of a nanopore array fabricated in a 500 nm^2 thinned region of the SiN membrane. Scale bar is 100 nm. **b** Log-log plot of ion dose versus resulting pore diameter over a range of membrane thicknesses: (L-R) 4.5 nm (*diamonds*), 7.9 nm (*downward facing triangles*), 11.3 nm (*upward facing triangles*), 14.8 nm (*circles*), and 18.2 nm (*squares*). Each data set indicates a fast regime (*left*) and a slow regime (*right*) of pore growth with a transition in slope at a diameter of ~10 nm. *Solid lines* are power law fits to relevant sections of the data. Inset shows data for a 1.2 nm thick membrane, shown separately for clarity. Indicated data point is the smallest pore realized in that membrane (~2 nm diameter). **c** Concatenated event traces of dsDNA translocation measurements with two SS-nanopore devices: one 3.1 nm in diameter in a 24.5 ± 0.8 nm thick membrane (*left*) and one 3.2 nm in diameter in a 4.5 ± 0.6 nm thick membrane (*right*). All traces were low-pass filtered at 10 kHz. See [44]

thickness, pore formation follows the same two-regime growth that was observed in native membranes [42], with the transition from fast to slow growth appearing consistently at a ~10 nm diameter.

To confirm the viability of HIM-thinned devices and their utility in enhancing SNR, a comparative analysis of dsDNA translocations through SS-nanopores with identical diameters (~3.2 nm) fabricated in membranes with disparate thickness (4.5 ± 0.6 nm and 24.5 ± 0.8 nm, respectively) was conducted. Ionic current was used to confirm the device dimensions before measurement, showing that actual pore diameter matched well with the target size. Measurement of 3 kbp dsDNA translocation events showed conclusively [44] that use of the thinned device improved SNR by about a factor of 2 (Fig. 18.6c).

18.3.3 Applications of HIM-Thinned SS-Nanopores

While the operating principle of resistive pulse sensing is straightforward, the resulting electrical signals can be surprisingly complex and thus challenging to interpret. One source of this behavior is the interaction of biomolecules with the access regions [64], a sensing volume that extends from both openings of the nanopore and into the measurement solution. Several studies have suggested that complicated conductance blockade levels can arise for dsDNA due to stochastic interactions with the access regions or occur prior to threading of dsDNA into the pore [7, 65–68]. However, a definitive explanation has not been presented, in part due to SNR limitations in conventional devices. SS-nanopores formed in HIM-thinned SiN membranes have enabled new investigations into the origin of these heretofore unexplained aspects of translocation events [69]. Figure 18.7 shows an example of signal complexity, depicting event depth (ΔG) histograms with Gaussian fits (grey lines) for 3 kbp dsDNA translocations through a 3.4 nm diameter pore fabricated in a 4.5 nm thick membrane. Crucially, across all

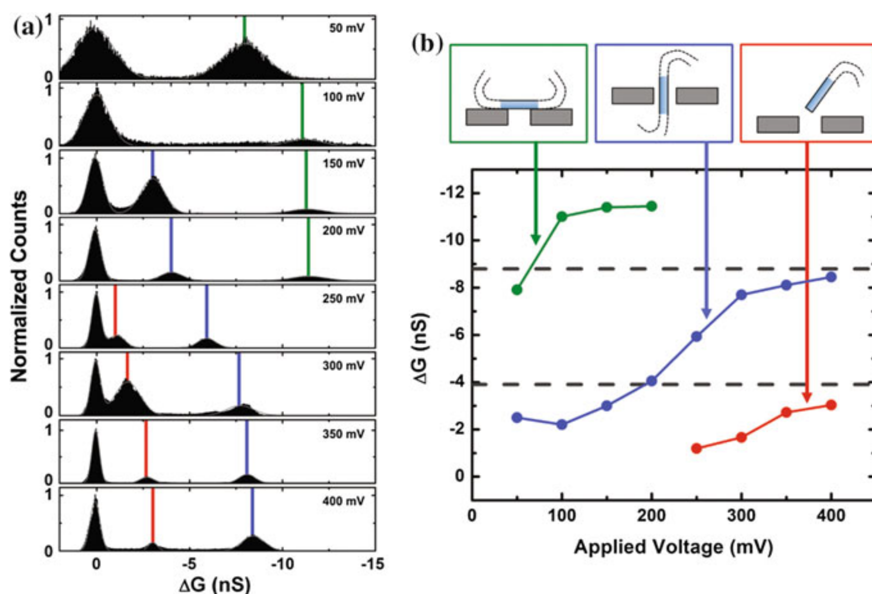

Fig. 18.7 Application of HIM fabricated ultrathin nanopore devices. **a** All-points histograms of (concatenated) conductance blockades from 50 to 400 mV (low-pass filtered at 10 kHz) for 3 kbp dsDNA using a 4.5 nm thick, 3.4 nm diameter SS-nanopore. In each panel, the left-most peak corresponds to the baseline (open-pore) conductance. *Vertical lines* indicate the center of the Gaussian fit (*gray line*) and indicate the evolution of individual conductance populations designated by color. **b** Average conductance change versus applied voltage. The *dashed lines* represent the calculated ΔG from geometric models [69] for the *blue* and *red* populations, respectively. Schematics (*top*) represent the DNA configuration proposed for each population. Colors match those in (**a**). See [69]

investigated voltages (50–400 mV), distinct populations emerged, the mean ΔG of which evolve with applied voltage (Fig. 18.7a). Each conductance population was attributable to a distinct type of interaction: the deepest events (green) were caused by non-translocative perpendicular blockages of the pore by the dsDNA; the intermediate level events (blue) were linear translocation through the pore; and shallow events (red) were transient interactions with only the access region (Fig. 18.7b). Each of these could be described by a simple geometric model. A detailed understanding of translocation dynamics and elucidation of translocation signals is important towards accurate data assessment and analysis in all SS-nanopore measurements, but especially in studies using thin nanopore devices [19, 70] where these effects are pronounced.

18.4 Manipulating Intrinsic Membrane Fluorescence

The conventional measurement of conductance through SS-nanopores has been a powerful tool for biomolecule characterization, but has limitations. Critically, electrical measurements on multiple nanopores simultaneously is challenging, requiring sophisticated electronics and separated measurement chambers. As a result, massively parallel detection schemes are difficult to execute, in spite of the potential benefit to detection throughput and costs. An alternate approach that could address this obstacle is the employment of single-molecule fluorescence as the detection mechanism. Here, the use of fluorescent molecules or buffer components [71–73] allows translocations to be monitored through direct, high-speed optical recording during the application of voltage. The technique offers several potential advantages. First, direct observation can be conducted in wide-field, enabling simultaneous detection on arbitrary numbers of pores, limited only by field of view and diffraction. Furthermore, the use of multispectral imaging and the integration of powerful techniques like total internal reflection microscopy (TIRF) [74] and Förster resonance energy transfer (FRET) [75] could facilitate additional flexibility, sensitivity, and selectivity.

A critical factor in optical detection is the photoluminescence (PL) of the solid-state membrane. Intrinsic PL increases the fluorescence noise floor, and so should be minimized in an ideal device to maximize resolution and to enable a wide-array of flourophores. Importantly, most common membrane materials exhibit considerable PL, including SiN, which emits in the important wavelength range of 400–800 nm. However, few studies have addressed PL in optical SS-nanopore detection. Recently, dela Torre et al. demonstrated [45] that atomic layer deposition of TiO_2 could be used on nanopores fabricated in SiN by FIB to both control pore diameter and reduce membrane PL. Additionally, Schmidt et al. [76] used electrochemical etching to fabricate nanopore arrays in a silicon membrane, chosen in part for its low inherent PL. However, these methodologies required additional

fabrication steps or produced thick devices with low yield, respectively. Therefore, there is a need for integrated fabrication techniques that can rapidly address membrane PL and produce SS-nanopores concomitantly.

18.4.1 HIM Photoluminescence Reduction

SiN PL is thought to arise from the presence of nanocrystalline domains within the matrix that act as radiative centers [77, 78]. Therefore, amorphization of those domains is a direct route to controllable reduction of membrane PL. With HIM, it has been demonstrated [79] that the beam penetrates substrate material efficiently, resulting in atom-atom interactions and implantations that can affect the internal structure. Therefore, by utilizing beam doses lower than the SiN surface binding energies (i.e. doses that do not sputter significant material), internal amorphization could be achieved with minimal change to membrane thickness or roughness (Fig. 18.8a).

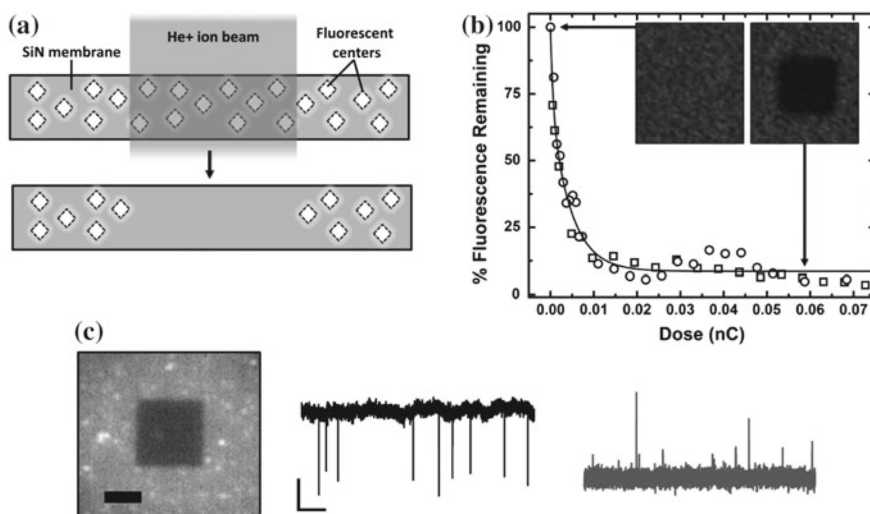

Fig. 18.8 SiN membrane PL reduction by HIM. **a** Schematic illustration of a native SiN membrane containing photoluminescent defects. Exposure to a low intensity He+ ion beam amorphizes these defects and thus reduces membrane PL. **b** Analysis of membrane fluorescence intensity in 500 nm^2 square patterns with varying He+ ion dose. *Circles* and *squares* are data from two separate chips and the *solid line* is an exponential fit to the data. *Inset* fluorescence image of a native membrane (*left*) and nearly total PL suppression (*right*). *Arrows* indicate respective data points. **c** Optical image (*left*) of a He+ ion-bleached square containing a single SS-nanopore with diameter of 5 nm. Scale bar is 2 μm. Typical raw traces taken with the device, showing Cy3-labeled DNA translocation events using both conventional ionic conductance (*center*) and fluorescence intensity (*right*). Scale bar applies to both traces, with a horizontal scale of 2.5 s and a vertical scale of 0.5 nS (electrical) and 12.5 a.u. of gray scale (optical). See [79]

To investigate this, a 30 nm thick SiN membrane was patterned with varying He+ ion doses, similar in methodology to membrane thinning described above (Sect. 18.3.1), and then imaged using TIRF microscopy. This treatment resulted in a clear reduction of membrane PL (Fig. 18.8b) that decreased exponentially with ion exposure. For example, greater than 90% of membrane PL was removed with a dose of 300–400 ions/nm^2; an exposure that would result in a mean decrease in membrane thickness of less than 1 nm. As a result, removal of essentially all PL does not significantly alter overall membrane morphology.

Following PL suppression, the HIM beam can subsequently be used to fabricate SS-nanopores within the patterned region using the dose-diameter relationship of the native membrane. The device can then be used to detect fluorescently-labeled biomolecules with minimal interference. As a demonstration, a 4 µm square region was exposed with a dose of 400 ions/nm^2 to remove PL and a single 5 nm pore was subsequently fabricated at its center. After mounting the device in a custom holder, a 2.8 kbp dsDNA with a fluorophore label (Cy3) was introduced and subjected to electrokinetic translocation. Figure 18.8c shows typical traces obtained from the device, first in the form of conventional ionic current measurement and then as dynamic nanopore fluorescence derived from high-speed video (500 Hz) of TIRF observation during the applied voltage. While these measurements could not be conducted simultaneously, analysis of both traces yielded event rates 0.45 Hz, demonstrating correlative results.

18.4.2 Application of HIM Photoluminescence Reduction

Optical detection can enable massively parallel detection schemes by allowing analysis of dynamic fluorescence across many SS-nanopores simultaneous. An important design aspect to consider for this purpose is the ability to accurately localize each individual pore. The HIM fabrication process addresses this issue inherently. Since the total He+ ion beam diameter (i.e. the full width of its Guassian intensity profile) is larger than the nanopore that results from a single point exposure, the region around the pore edges is subjected a significant ion dose that decreases radially in intensity. The local PL is thus suppressed during normal pore formation, manifesting as a non-emitting region around the pore that can typically extend 100–300 nm past the edge of the SS-nanopore [79].

In following, the PL of a 5 µm square region in a SiN membrane was reduced by ~80%, and an array of 400 individual SS-nanopores (diameter ~5 nm) was fabricated in its confines. Each individual pore is resolvable as a dark spot in a wide-field TIRF micrograph (Fig. 18.9a). DNA translocations were then performed under application of 1 V bias and while collecting TIRF microscopy images at a rate of 675 Hz. To avoid issues with pore-fouling, short (55 nt) ssDNA homopolymers were investigated, each containing 3 Cy3 fluorophores. Stochastic increases in fluorescence intensity could be observed at the site of individual SS-nanopores

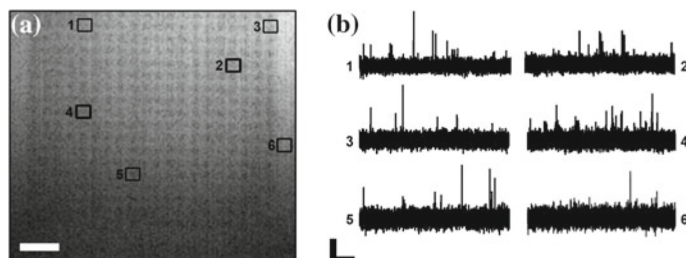

Fig. 18.9 High-throughput optical detection of ssDNA translocations. Fluorescence image of a 20 × 20 array of ~5 nm diameter SS-nanopores formed in a SiN membrane with locally-quenched background fluorescence. Image is an average of 100 video frames and contrast has been adjusted for clarity. Scale bar is 2.5 μm. **b** Raw fluorescence intensity traces measured simultaneously from video of Cy3-labeled ssDNA translocations through five typical nanopores within the array, each outlined with a square and numbered. Trace 6 is measured on a proximal region of the membrane with reduced-fluorescence but no pore. Scale bar is 0.5 s (*horizontal*) and 30 a.u. (*vertical*). See [79]

(Fig. 18.9b), indicative of molecular translocations; importantly, such analysis could be performed simultaneously across the array with a single video.

Transient diffusion of labeled molecules into the sensing volume could contribute to the optical translocation events observed in these traces. To explore this issue, dynamic fluorescence intensity was also analyzed in regions adjacent to the array, but not at the location of a pore, where diffusion can still deliver molecules but there is no electrical driving force. The rate of events in these regions was found to be 0.03 Hz; about an order of magnitude lower than the 0.27 Hz rate observed at the location of SS-nanopores. Therefore, at least 90% of the optical events collected throughout the nanopore array are attributable to electrokinetic translocation.

18.5 Conclusions and Outlook

In conclusion, HIM milling is a versatile and rapid technique for fabricating SS-nanopores devices, offering tremendous control over device dimensions and properties. The capabilities of this approach are best captured as a function of He+ ion dose (Fig. 18.10). At high doses (>~10^6 ions/nm^2), the HIM beam can rapidly sputter membrane material to form SS-nanopores. Through control of beam current and exposure time, pore diameters can be produced with high precision (±2–3 nm) and resolution (down to ~2.5 nm). Crucially, HIM features like a large range of stage motion and lithographic beam control enable high throughput processing and array formation as well. At intermediate doses (~10^3–10^5 ions/nm^2), the HIM beam is able to sputter some but not all membrane material, resulting in controllable reduction in thickness. This process is patternable and can be used to realize membrane regions as thin as 1–2 nm, which can subsequently be targeted for

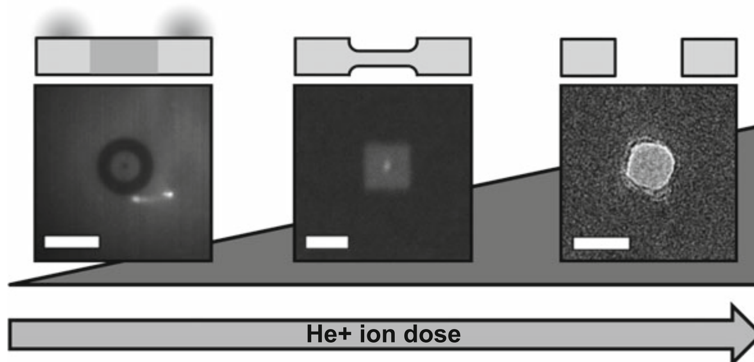

Fig. 18.10 Manipulation of SS-nanopore device properties with He+ ions. Varying He+ ion dose can be used to control a range of device properties. *Images show* TIRF micrograph of a ring pattern (*left*) exposed to low He+ ion dose around a single pore, demonstrating PL reduction; STIM micrograph (*center*) of a nanopore (*bright spot*) fabricated in a square region of reduced thickness, demonstrating the effect of intermediate ion dose on membrane thickness; TEM image (*right*) of a ~20 nm diameter nanopore, demonstrating complete ablation of membrane material to form a pore. Scale bars are 4 μm, 100 nm, and 20 nm, respectively. Schematic above each image illustrates the affect of incident He+ ion dosage on membrane properties and dimensions

SS-nanopore formation to achieve high measurement sensitivity. Finally, at low doses ($<\sim 10^3$ ions/nm^2), the HIM beam can be used to control intrinsic membrane PL by causing internal structural deformation (e.g. amorphization of radiative centers) without inducing significant sputtering. As a result, membrane fluorescence can be reduced or removed while maintaining its initial dimensions. Subsequently, PL reduction was achieved using TEM as well [80], however that instrument is difficult to incorporate into high-throughput fabrication.

We have described here several applications of HIM SS-nanopore devices that take advantage of the various aspects enabled by the fabrication method. From elucidating electrokinetic translocation dynamics to massively parallel sensing, these efforts establish the utility of both the platform in general and devices produced by HIM in particular. In continuing work, these measurements will be expanded and improved. For example, the selective modification detection assay developed with HIM nanopores is currently the focus of extensive research as a possible route toward nucleic acid biomarker identification. Such a capability could be a valuable asset for the rapid diagnosis of diseases like cancer [81] and Alzheimer's disease [82]. Additionally, the potential for massively-parallel analysis could be an important capability for a future high-throughput genetic sequencing device [83].

SS-nanopores hold remarkable potential as the basis of a wide range of cost-effective and highly sensitive detection devices. As a consequence, they could revolutionize the future of medical diagnostics, just like the Coulter Counter did decades ago. However, one of the most daunting obstacles to their development and integration is simple availability. Since the introduction of platform, several

fabrication strategies have been effectively employed, but each has brought with it significant limitations in speed, resolution, or throughput. As we have discussed here, HIM addresses each of these challenges while also offering tremendous flexibility in controlling a range of additional device characteristics that will result in a more versatile system. Accordingly, the capabilities afforded by helium ion microscopy will play a critical role in the future of SS-nanopore technologies.

References

1. W.H. Coulter, Means for counting particles suspended in a fluid. US2656508 A, 20 Oct 1953
2. M.D. Graham, The coulter principle: foundation of an industry. J. Assoc. Lab. Autom. **8**(6), 72–81 (2003)
3. C. Dekker, Solid-state nanopores. Nat. Nanotechnol. **2**(4), 209–215 (2007)
4. M. Wanunu, Nanopores: a journey towards DNA sequencing. Phys. Life Rev. **9**(2), 125–158 (2012)
5. J. Li, M. Gershow, D. Stein, E. Brandin, J.A. Golovchenko, DNA molecules and configurations in a solid-state nanopore microscope. Nat. Mater. **2**(9), 611–615 (2003)
6. A.J. Storm, C. Storm, J. Chen, H. Zandbergen, J.-F. Joanny, C. Dekker, Fast DNA translocation through a solid-state nanopore. Nano Lett. **5**(7), 1193–1197 (2005)
7. G.M. Skinner, M. van den Hout, O. Broekmans, C. Dekker, N.H. Dekker, Distinguishing single- and double-stranded nucleic acid molecules using solid-state nanopores. Nano Lett. **9** (8), 2953–2960 (2009)
8. D. Fologea, B. Ledden, D.S. McNabb, J. Li, Electrical characterization of protein molecules by a solid-state nanopore. Appl. Phys. Lett. **91**(5), 053901 (2007)
9. C. Plesa, S.W. Kowalczyk, R. Zinsmeester, A.Y. Grosberg, Y. Rabin, C. Dekker, Fast translocation of proteins through solid state nanopores. Nano Lett. **13**(2), 658–663 (2013)
10. A.R. Hall, J.M. Keegstra, M.C. Duch, M.C. Hersam, C. Dekker, Translocation of single-wall carbon nanotubes through solid-state nanopores. Nano Lett. **11**(6), 2446–2450 (2011)
11. K.E. Venta, M.B. Zanjani, X. Ye, G. Danda, C.B. Murray, J.R. Lukes, M. Drndić, Gold nanorod translocations and charge measurement through solid-state nanopores. Nano Lett. **14** (9), 5358–5364 (2014)
12. J. Li, D. Stein, C. McMullan, D. Branton, M.J. Aziz, J.A. Golovchenko, Ion-beam sculpting at nanometre length scales. Nature **412**(6843), 166–169 (2001)
13. G.V. Soni, C. Dekker, Detection of nucleosomal substructures using solid-state nanopores. Nano Lett. **12**(6), 3180–3186 (2012)
14. D. Japrung, A. Bahrami, A. Nadzeyka, L. Peto, S. Bauerdick, J.B. Edel, T. Albrecht, SSB binding to single-stranded DNA probed using solid-state nanopore sensors. J. Phys. Chem. B **118**(40), 11605–11612 (2014)
15. R.M.M. Smeets, S.W. Kowalczyk, A.R. Hall, N.H. Dekker, C. Dekker, Translocation of RecA-coated double-stranded DNA through solid-state nanopores. Nano Lett. **9**(9), 3089–3095 (2009)
16. S.W. Kowalczyk, A.R. Hall, C. Dekker, Detection of local protein structures along DNA using solid-state nanopores. Nano Lett. **10**(1), 324–328 (2010)
17. M. Wanunu, D. Cohen-Karni, R.R. Johnson, L. Fields, J. Benner, N. Peterman, Y. Zheng, M. L. Klein, M. Drndic, Discrimination of methylcytosine from hydroxymethylcytosine in DNA molecules. J. Am. Chem. Soc. **133**(3), 486–492 (2011)
18. J. Shim, G.I. Humphreys, B.M. Venkatesan, J.M. Munz, X. Zou, C. Sathe, K. Schulten, F. Kosari, A.M. Nardulli, G. Vasmatzis, R. Bashir, Detection and quantification of methylation in DNA using solid-state nanopores. Sci. Rep. **3** (2013)

19. J. Shim, Y. Kim, G.I. Humphreys, A.M. Nardulli, F. Kosari, G. Vasmatzis, W.R. Taylor, D.A. Ahlquist, S. Myong, R. Bashir, Nanopore-based assay for detection of methylation in double-stranded DNA fragments. ACS Nano **9**(1), 290–300 (2015)
20. M. Wanunu, T. Dadosh, V. Ray, J. Jin, L. McReynolds, M. Drndić, Rapid electronic detection of probe-specific microRNAs using thin nanopore sensors. Nat. Nanotechnol. **5**(11), 807–814 (2010)
21. A. Singer, S. Rapireddy, D.H. Ly, A. Meller, Electronic barcoding of a viral gene at the single-molecule level. Nano Lett. **12**(3), 1722–1728 (2012)
22. S.W. Kowalczyk, L. Kapinos, T.R. Blosser, T. Magalhães, P. van Nies, R.Y.H. Lim, C. Dekker, Single-molecule transport across an individual biomimetic nuclear pore complex. Nat. Nanotechnol. **6**(7), 433–438 (2011)
23. A.R. Hall, A. Scott, D. Rotem, K.K. Mehta, H. Bayley, C. Dekker, Hybrid pore formation by directed insertion of α-haemolysin into solid-state nanopores. Nat. Nanotechnol. **5**(12), 874–877 (2010)
24. M. Firnkes, D. Pedone, J. Knezevic, M. Döblinger, U. Rant, Electrically facilitated translocations of proteins through silicon nitride nanopores: conjoint and competitive action of diffusion, electrophoresis, and electroosmosis. Nano Lett. **10**(6), 2162–2167 (2010)
25. U.F. Keyser, B.N. Koeleman, S. van Dorp, D. Krapf, R.M.M. Smeets, S.G. Lemay, N.H. Dekker, C. Dekker, Direct force measurements on DNA in a solid-state nanopore. Nat. Phys. **2** (7), 473–477 (2006)
26. S. van Dorp, U.F. Keyser, N.H. Dekker, C. Dekker, S.G. Lemay, Origin of the electrophoretic force on DNA in solid-state nanopores. Nat. Phys. **5**(5), 347–351 (2009)
27. A.R. Hall, S. van Dorp, S.G. Lemay, C. Dekker, Electrophoretic force on a protein-coated DNA molecule in a solid-state nanopore. Nano Lett. **9**(12), 4441–4445 (2009)
28. C. Plesa, N. van Loo, P. Ketterer, H. Dietz, C. Dekker, Velocity of DNA during translocation through a solid-state nanopore. Nano Lett. **15**(1), 732–737 (2015)
29. R.M.M. Smeets, U.F. Keyser, D. Krapf, M.-Y. Wu, N.H. Dekker, C. Dekker, Salt dependence of ion transport and DNA translocation through solid-state nanopores. Nano Lett. **6**(1), 89–95 (2006)
30. D. Fologea, J. Uplinger, B. Thomas, D.S. McNabb, J. Li, Slowing DNA translocation in a solid-state nanopore. Nano Lett. **5**(9), 1734–1737 (2005)
31. D.V. Verschueren, M.P. Jonsson, C. Dekker, Temperature dependence of DNA translocations through solid-state nanopores. Nanotechnology **26**(23), 234004 (2015)
32. M. Wanunu, W. Morrison, Y. Rabin, A.Y. Grosberg, A. Meller, Electrostatic focusing of unlabelled DNA into nanoscale pores using a salt gradient. Nat. Nanotechnol. **5**(2), 160–165 (2010)
33. C. Plesa, N. van Loo, C. Dekker, DNA nanopore translocation in glutamate solutions. Nanoscale **7**(32), 13605–13609 (2015)
34. S.W. Kowalczyk, D.B. Wells, A. Aksimentiev, C. Dekker, Slowing down DNA translocation through a nanopore in Lithium Chloride. Nano Lett. **12**(2), 1038–1044 (2012)
35. A.J. Storm, J.H. Chen, X.S. Ling, H.W. Zandbergen, C. Dekker, Fabrication of solid-state nanopores with single-nanometre precision. Nat. Mater. **2**(8), 537–540 (2003)
36. B. Schiedt, L. Auvray, L. Bacri, G. Oukhaled, A. Madouri, E. Bourhis, G. Patriarche, J. Pelta, R. Jede, J. Gierak, Direct FIB fabrication and integration of 'single nanopore devices' for the manipulation of macromolecules. Microelectron. Eng. **87**(5–8), 1300–1303 (2010)
37. H. Kwok, K. Briggs, V. Tabard-Cossa, Nanopore fabrication by controlled dielectric breakdown. PLoS ONE **9**(3), e92880 (2014)
38. P. Sigmund, Mechanisms and theory of physical sputtering by particle impact. Nucl. Instrum. Methods Phys. Res. Sect. B-Beam Interact. Mater. At. **27**(1), 1–20 (1987)
39. J. Orloff, High-resolution focused ion-beams. Rev. Sci. Instrum. **64**(5), 1105–1130 (1993)
40. C.J. Lo, T. Aref, A. Bezryadin, Fabrication of symmetric sub-5 nm nanopores using focused ion and electron beams. Nanotechnology **17**(13), 3264–3267 (2006)
41. B.W. Ward, J.A. Notte, N.P. Economou, Helium ion microscope: a new tool for nanoscale microscopy and metrology. J. Vac. Sci. Technol., B **24**(6), 2871–2874 (2006)

42. J. Yang, D.C. Ferranti, L.A. Stern, C.A. Sanford, J. Huang, Z. Ren, L.-C. Qin, A.R. Hall, Rapid and precise scanning helium ion microscope milling of solid-state nanopores for biomolecule detection. Nanotechnology **22**(28), 285310 (2011)
43. A.A. Tseng, Recent developments in nanofabrication using focused ion beams. Small **1**(10), 924–939 (2005)
44. F. Sawafta, A.T. Carlsen, A.R. Hall, Membrane thickness dependence of nanopore formation with a focused helium ion beam. Sensors **14**(5), 8150–8161 (2014)
45. R. dela Torre, J. Larkin, A. Singer, A. Meller, Fabrication and characterization of solid-state nanopore arrays for high-throughput DNA sequencing. Nanotechnology **23**(38), 385308 (2012)
46. L. Galla, A. Meyer, A. Spiering, A. Sischka, M. Mayer, A.R. Hall, P. Reimann, D. Anselmetti, Hydrodynamic slip on DNA observed by optical tweezers-controlled translocation experiments with solid-state and lipid-coated nanopores. Nano Lett. (2014) doi:10.1021/nl501909t
47. T. Lindahl, Instability and decay of the primary structure of DNA. Nature **362**(6422), 709–715 (1993)
48. E. Cavalieri, M. Saeed, M. Zahid, D. Cassada, D. Snow, M. Miljkovic, E. Rogan, Mechanism of DNA depurination by carcinogens in relation to cancer initiation. IUBMB Life **64**(2), 169–179 (2012)
49. J.R. Alvarez-Dominguez, O. Amosova, J.R. Fresco, Self-catalytic DNA depurination underlies human β-Globin gene mutations at Codon 6 that cause Anemias and Thalassemias. J. Biol. Chem. **288**(16), 11581–11589 (2013)
50. M.M. Marshall, J.A. Ruzicka, E.W. Taylor, A.R. Hall, Detecting DNA depurination with solid-state nanopores. PLoS ONE **9**(7), e101632 (2014)
51. M.M. Marshall, J. Ruzicka, O.K. Zahid, V.C. Henrich, E.W. Taylor, A.R. Hall, Nanopore analysis of single-stranded binding protein interactions with DNA. Langmuir **31**(15), 4582–4588 (2015)
52. A.T. Carlsen, O.K. Zahid, J.A. Ruzicka, E.W. Taylor, A.R. Hall, Selective detection and quantification of modified DNA with solid-state nanopores. Nano Lett. **14**(10), 5488–5492 (2014)
53. M. Howarth, D.J.F. Chinnapen, K. Gerrow, P.C. Dorrestein, M.R. Grandy, N.L. Kelleher, A. El-Husseini, A.Y. Ting, A monovalent streptavidin with a single femtomolar biotin binding site. Nat. Methods **3**(4), 267–273 (2006)
54. M. Fairhead, D. Krndija, E.D. Lowe, M. Howarth, Plug-and-play pairing via defined divalent streptavidins. J. Mol. Biol. **426**(1), 199–214 (2014)
55. C.A. Merchant, K. Healy, M. Wanunu, V. Ray, N. Peterman, J. Bartel, M.D. Fischbein, K. Venta, Z. Luo, A.T.C. Johnson, M. Drndic, DNA translocation through graphene nanopores. Nano Lett. **10**(8), 2915–2921 (2010)
56. G.F. Schneider, S.W. Kowalczyk, V.E. Calado, G. Pandraud, H.W. Zandbergen, L.M.K. Vandersypen, C. Dekker, DNA translocation through graphene nanopores. Nano Lett. **10**(8), 3163–3167 (2010)
57. K. Liu, J. Feng, A. Kis, A. Radenovic, Atomically thin molybdenum disulfide nanopores with high sensitivity for DNA translocation. ACS Nano **8**(3), 2504–2511 (2014)
58. S. Liu, B. Lu, Q. Zhao, J. Li, T. Gao, Y. Chen, Y. Zhang, Z. Liu, Z. Fan, F. Yang, L. You, D. Yu, Boron nitride nanopores: highly sensitive DNA single-molecule detectors. Adv. Mater. **25**(33), 4549–4554 (2013)
59. K. Venta, G. Shemer, M. Puster, J.A. Rodriguez-Manzo, A. Balan, J.K. Rosenstein, K. Shepard, M. Drndic, Differentiation of short, single-stranded DNA homopolymers in solid-state nanopores. ACS Nano **7**(5), 4629–4636 (2013)
60. D.J. Niedzwiecki, C.J. Lanci, G. Shemer, P.S. Cheng, J.G. Saven, M. Drndić, Observing changes in the structure and oligomerization state of a helical protein dimer using solid-state nanopores. ACS Nano (2015)
61. M.M. Marshall, J. Yang, A.R. Hall, Direct and transmission milling of suspended Silicon Nitride membranes with a focused Helium Ion beam. Scanning **34**(2), 101–106 (2012)

62. D. Santamore, K. Edinger, J. Orloff, J. Melngailis, Focused ion beam sputter yield change as a function of scan speed. J. Vac. Sci. Technol. B **15**(6), 2346–2349 (1997)
63. A.R. Hall, In situ thickness assessment during ion milling of a free-standing membrane using transmission helium ion microscopy. Microsc. Microanal. **19**(3), 740–744 (2013)
64. J.E. Hall, Access resistance of a small circular pore. J. Gen. Physiol. **66**(4), 531–532 (1975)
65. M. Wanunu, J. Sutin, B. McNally, A. Chow, A. Meller, DNA translocation governed by interactions with solid-state nanopores. Biophys. J. **95**(10), 4716–4725 (2008)
66. M. van den Hout, V. Krudde, X.J.A. Janssen, N.H. Dekker, Distinguishable populations report on the interactions of single DNA molecules with solid-state nanopores. Biophys. J. **99**(11), 3840–3848 (2010)
67. S.W. Kowalczyk, C. Dekker, Salt and voltage dependence of the conductance blockade induced by translocation of DNA and RecA filaments through solid-state nanopores, in *Salt and Voltage Dependence of the Conductance Blockade Induced by Translocation of DNA and RecA Filaments Through Solid-state Nanopores* (2012)
68. S.W. Kowalczyk, C. Dekker, Measurement of the docking time of a DNA molecule onto a solid-state nanopore. Nano Lett. **12**(8), 4159–4163 (2012)
69. A.T. Carlsen, O.K. Zahid, J. Ruzicka, E.W. Taylor, A.R. Hall, Interpreting the conductance blockades of DNA translocations through solid-state nanopores. ACS Nano **8**(5), 4754–4760 (2014)
70. J. Ma, Y. Qiu, Z. Yuan, Y. Zhang, J. Sha, L. Liu, L. Sun, Z. Ni, H. Yi, D. Li, Y. Chen, Detection of short single-strand DNA homopolymers with ultrathin Si_3N_4 nanopores. Phys. Rev. E **92**(2), 022719 (2015)
71. A.J. Heron, J.R. Thompson, B. Cronin, H. Bayley, M.I. Wallace, Simultaneous measurement of ionic current and fluorescence from single protein pores. J. Am. Chem. Soc. **131**(5), 1652–1653 (2009)
72. A. Ivankin, R.Y. Henley, J. Larkin, S. Carson, M.L. Toscano, M. Wanunu, Label-free optical detection of biomolecular translocation through nanopore arrays. ACS Nano **8**(10), 10774–10781 (2014)
73. B.N. Anderson, O.N. Assad, T. Gilboa, A.H. Squires, D. Bar, A. Meller, Probing solid-state nanopores with light for the detection of unlabeled analytes. ACS Nano **8**(11), 11836–11845 (2014)
74. K.N. Fish, Total internal reflection fluorescence (TIRF) microscopy, in *Current Protocols in Cytometry* ed. by *Editorial Board J. Paul Robinson Managing Editor*, vol. Chapter 12, p. Unit 12.18, Oct 2009
75. R. Roy, S. Hohng, T. Ha, A practical guide to single-molecule FRET. Nat. Methods **5**(6), 507–516 (2008)
76. T. Schmidt, M. Zhang, I. Sychugov, N. Roxhed, J. Linnros, Nanopore arrays in a silicon membrane for parallel single-molecule detection: fabrication. Nanotechnology **26**(31), 314001 (2015)
77. S.V. Deshpande, E. Gulari, S.W. Brown, S.C. Rand, Optical properties of silicon nitride films deposited by hot filament chemical vapor deposition. J. Appl. Phys. **77**(12), 6534–6541 (1995)
78. B.-H. Kim, C.-H. Cho, T.-W. Kim, N.-M. Park, G.Y. Sung, S.-J. Park, Photoluminescence of silicon quantum dots in silicon nitride grown by NH3 and SiH4. Appl. Phys. Lett. **86**(9), 091908 (2005)
79. F. Sawafta, B. Clancy, A.T. Carlsen, M. Huber, A.R. Hall, Solid-state nanopores and nanopore arrays optimized for optical detection. Nanoscale **6**(12), 6991–6996 (2014)
80. O.N. Assad, N. Di Fiori, A.H. Squires, A. Meller, Two color DNA barcode detection in photoluminescence suppressed silicon nitride nanopores. Nano Lett. **15**(1), 745–752 (2015)
81. P.R. Srinivas, B.S. Kramer, S. Srivastava, Trends in biomarker research for cancer detection. Lancet Oncol. **2**(11), 698–704 (2001)
82. N. Coppieters, B.V. Dieriks, C. Lill, R.L.M. Faull, M.A. Curtis, M. Dragunow, Global changes in DNA methylation and hydroxymethylation in Alzheimer's disease human brain. Neurobiol. Aging **35**(6), 1334–1344 (2014)

83. D. Branton, D.W. Deamer, A. Marziali, H. Bayley, S.A. Benner, T. Butler, M. Di Ventra, S. Garaj, A. Hibbs, X. Huang, S.B. Jovanovich, P.S. Krstic, S. Lindsay, X.S. Ling, C.H. Mastrangelo, A. Meller, J.S. Oliver, Y.V. Pershin, J.M. Ramsey, R. Riehn, G.V. Soni, V. Tabard-Cossa, M. Wanunu, M. Wiggin, J.A. Schloss, The potential and challenges of nanopore sequencing. Nat. Biotechnol. **26**(10), 1146–1153 (2008)

Chapter 19
Applications of GFIS in Semiconductors

Shida Tan and Rick Livengood

Abstract Electron beam and ion beam based techniques such as SEM, TEM, and FIB are used extensively by the semiconductor industry to provide analytical, metrology, and debug capabilities for process development, manufacturing yield monitoring, and new product ramp. The unique imaging and nanomachining attributes of the helium and neon Gas Field Ionization Source (GFIS) technology may extend beyond what electron and gallium beams can achieve alone. In this chapter, emerging semiconductor applications for helium and neon GFIS are reviewed and the key imaging and nanomachining limitations and attributes of both are discussed.

19.1 Introduction

Semiconductor process technology advancement has been fueling the steady increase in computing power and energy efficiency for the past 50 years. The second generation 3D tri-gate transistors were introduced to the broad market in early 2015 supporting a wide range of products from mobile devices to servers, delivering high performance, power, density, and cost per transistor. Moore's Law is accomplished through a combination of reducing feature and cell sizes, implementing novel device architectures, and introducing new materials in the process technology (Fig. 19.1). However, to enable timely introduction of new products to the market, not only the development in novel designs and process technologies are critical, analytical techniques scaling is also essential. One of the important tools in the analytical and silicon debug space is the focused ion beam (FIB), which has been widely applied for over 20 years in the semiconductor industry for failure analysis (FA), fault isolation (FI), transmission electron microscope (TEM) sample preparation, mask repair, and backside circuit edit (CE) [1–3].

S. Tan (✉) · R. Livengood
Intel Corporation, 2200 Mission College Blvd., Santa Clara, CA 95054, USA
e-mail: shida.tan@intel.com

© Springer International Publishing Switzerland 2016

G. Hlawacek and A. Gölzhäuser (eds.), *Helium Ion Microscopy*,
NanoScience and Technology, DOI 10.1007/978-3-319-41990-9_19

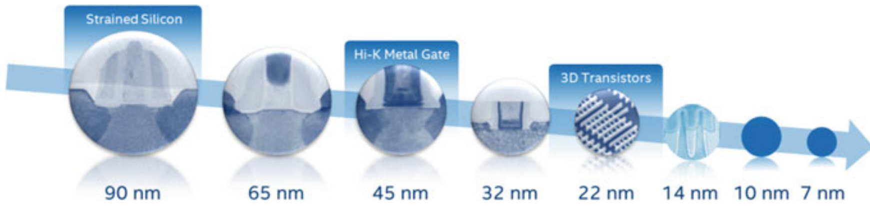

Fig. 19.1 Moore's Law—Process technology scaling through device architecture, lithography, and material innovations (2002–2015), diagram courtesy of Intel Corporation [4]

The transistor fin, gate, and interconnect pitch scaled by ~0.7x from the 22 nm 1st generation to the 14 nm 2nd generation 3D tri-gate transistors [4]. The areal scaling and volumetric scaling factors of the device are 0.5x and 0.35x, respectively. To meet these process scaling challenges, FIB technology needs to scale not only for imaging resolution and X-Y nanomachining precision, but also in material removal controllability, material selectivity, ion beam induced damage minimization, and improved signal to noise ratio (SNR) in high aspect ratio milling structures.

Although the traditional gallium liquid metal ion source (LMIS)[5, 6] continues to scale in probe size, there are fundamental limits associated with it, i.e. sputter yield, secondary electron (SE) yield, gallium contamination, etc. Looking beyond gallium, several novel ion beam technologies have emerged in the past decade: helium and neon gas field ionization sources (GFIS), [7, 8] lithium magneto-optical ionization sources (MOTIS), [9] cesium low temperature ion source (LoTIS), [10] multicusp plasma ion source, [11] and alloy liquid metal ion sources, [12] providing a broad range of ion species as alternative candidates. Among these, helium and neon GFIS appears to be one of the most promising alternatives to gallium LMIS due to the unique combination of desirable attributes of high resolution, low energy spread, high secondary electron yield, and low sputter yield [13–17]. However, significant challenges associated with applying light element ion species to semiconductor devices was reported as well [18, 19].

This chapter discusses the tradeoffs of various ion beams and their operating parameters in different semiconductor application scenarios, i.e., interaction volume, sputter yield, beam profile, and machining mechanism for bulk and membrane substrates. The combination of these parameters determines the ultimate profile and precision of FIB nanomachining. Preliminary results, advantages, and challenges in applying GFIS technology in semiconductor devices will be discussed as well.

19.2 GFIS Nanomachining Characteristics

19.2.1 Charged Particle Interaction with Materials

Ion beam imaging and patterning introduce substrate damages in the form of dislocated substrate atoms from their original lattice positions, implantation of the

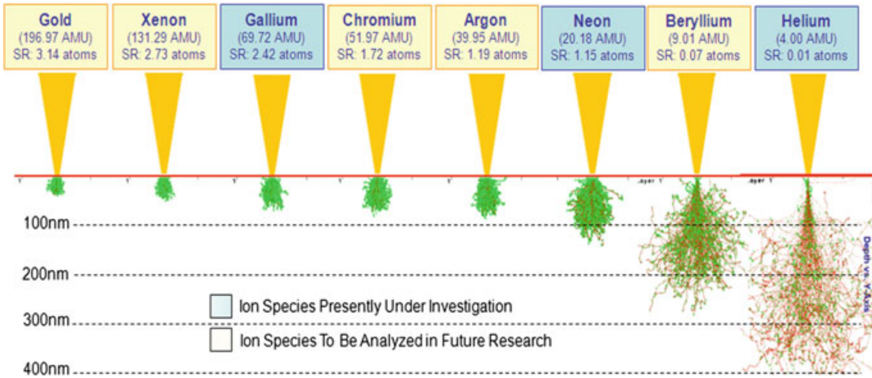

Fig. 19.2 Simulated sputter yield, interaction volume, and implant depth of He^+, Be^+, Ne^+, Ar^+, Cr^+, Ga^+, Xe^+, and Au^+ at 30 keV beam energies in a silicon substrate

incident ion beam, and sputtering of the sample. The ion mass, beam energy, and material properties determine the ion material interaction volume, damage density, and the material sputter yields [19]. TRIM[20] simulation results on several established ion source technologies are shown in Fig. 19.2. Results from ion species from atomic weight of 4–197 AMU irradiating a silicon substrate at normal incidence at an incident energy of 30 keV are compared [21]. The TRIM results illustrate the ion implant range and interaction volume decrease with the increase of the atomic weight of the ion; hence the potential impact of interaction volume and ion beam induced damage on transistors and other materials need to be considered especially for light element ions such as He^+.

Another consideration for FIB imaging and beam induced nanomachining is sputter yields. Simulated sputter yield for He^+, Be^+, Ne^+, Ar^+, Cr^+, Ga^+, Xe^+, and Au^+ in silicon and copper between beam energies of 1 and 50 keV are plotted in Fig. 19.3 [21]. With increasing beam energy, Low mass ions (e.g. He^+, Be^+)

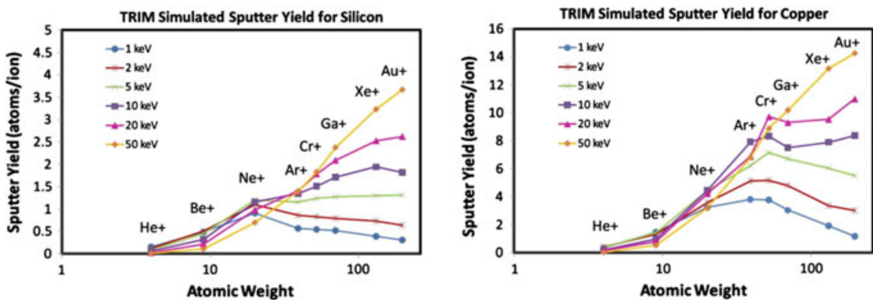

Fig. 19.3 Simulated sputter yield of He^+, Be^+, Ne^+, Ar^+, Cr^+, Ga^+, Xe^+, and Au^+ at 1, 2, 5, 10, 20, and 50 keV energy at normal incidence to silicon and copper. The sputter yield is plotted against atomic weight of the incident ion species

penetrate deeper into the sample producing relatively low sputter yield, while the high mass ions (e.g. Xe^+, Au^+) have an opposite trend. The reversal of this beam energy dependency occurs for ion species with atomic weight between 20 and 40 AMU. It is relevant to note that many common nanomachining applications use heavier ions with an energy between 30 and 50 keV.

The understanding of the tradeoffs in applying various beam parameters is critical to successful FIB implementations in different applications. Using circuit edit as an example, lower beam acceleration energy and heavier ions are desired in order to minimize the number of ions needed and ion beam induced damage range to the transistor channel/gate and the circuitry timing. However, the beam attributes associated with high beam acceleration energy and lighter ions are preferred in order to achieve high resolution, high signal to noise, and a high degree of controllability while machining through mixed material.

19.2.2 Charged Particle Interaction in Bulk Versus Membrane Substrates

Besides the beam characteristics, substrate geometry and material crystallinity are important factors influencing the ion beam nanomachining characteristics. While great successes have been demonstrated on fabricating structures in thin membrane samples using helium, such as 10 nm critical dimension plasmonic devices, [22] 4 nm SiN_x nanopores, [23] and 10 nm graphene-based devices; [17, 24, 25] drastically different results were reported for bulk materials [18, 19]. High levels of damage and surface deformation in various crystalline bulk substrates such as Si, Cu, and Au are caused by the high ion implantation range, low sputter yield, and low diffusivity of the helium ions. However, controlled defect injection is utilized for device bandgap alteration [26] and nano superconducting tunnel junction fabrication [27]. In majority of the semiconductor applications, defect creation and material removal mechanism need to be understood and carefully minimized.

A close analysis of the different interaction and sputter mechanism of the helium beam in single crystal silicon in bulk versus membrane geometry was reported in a joint Intel—NIST study [28]. Clear sputter mechanism differences in the membrane versus the bulk sample were observed when the thickness of the membrane sample is less than the nuclear stopping range of the primary ions in the material.

The evolution of the formation of the dislocations, the amorphization region, and the material removal in a single crystalline membrane and a bulk silicon substrate are captured via TEM imaging as shown in Figs. 19.4 and 19.5, respectively [28]. In both the membrane and the bulk samples, no noticeable beam induced subsurface damage is revealed in the TEM micrographs below a dose of 6.4×10^3 ions nm^{-1}. With increasing dose, some dislocations become visible at the entry location of the beam (Figs. 19.4a and 19.5a). Initially, noticeable crystalline lattice disruptions at the center region of the ion beam entry point are detected (where the beam current

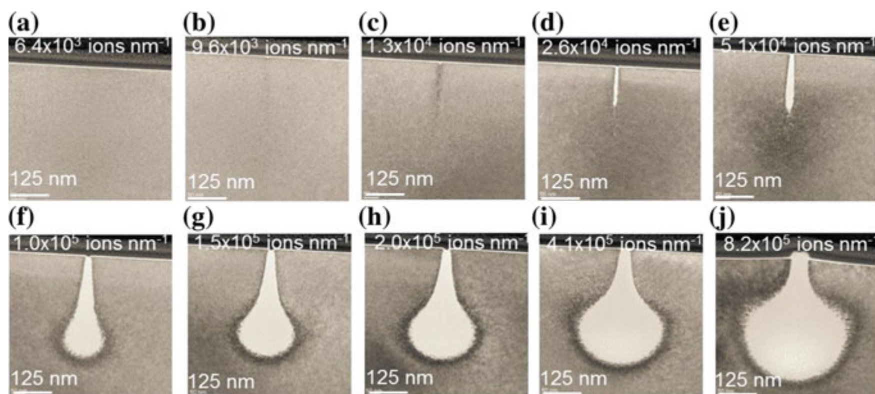

Fig. 19.4 High resolution TEM micrographs of the He^+ milling progression a bulk Si samples at doses ranging from **a** 6.4×10^3 to **j** 8.2×10^5 ions nm^{-1}

density is highest). Once the damage density exceeds a certain threshold, the substrate becomes amorphized and appears as bright regions in the TEM micrographs (Figs. 19.4d and 19.5c). At even higher doses, the amorphous regions close to the surface of the sample grow both laterally and through the depth of the sample as the damage density created by the outer part of the probe current exceed the damage threshold.

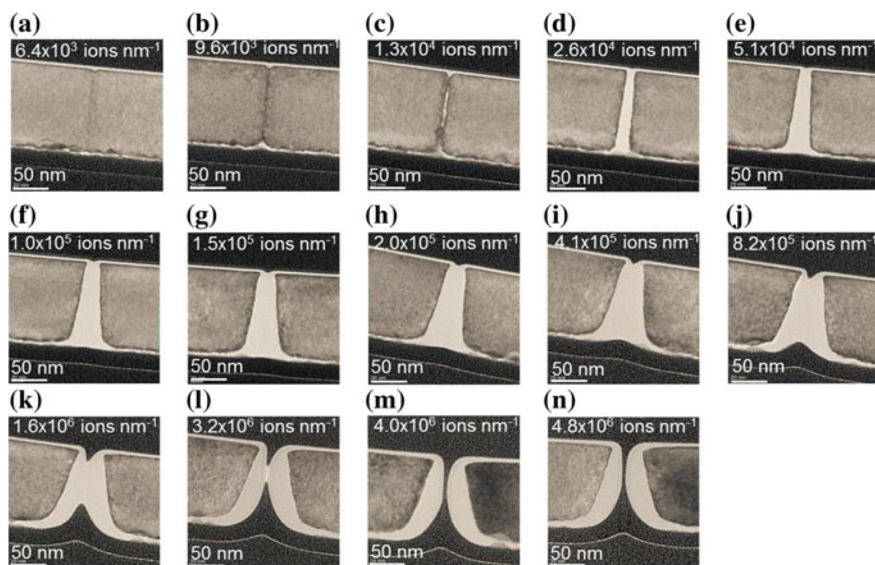

Fig. 19.5 High resolution TEM micrographs of the He^+ milling progression in membrane Si samples at doses ranging from **a** 6.4×10^3 to **n** 4.8×10^6 ions nm^{-1}

The crystalline to amorphous interface follows the contour that corresponds to the critical threshold of the ion beam induced damage density. Therefore, the ion trajectory and the interaction volume in a crystalline substrate can be tracked with high sensitivity and be used for quantitative empirical measurements of the ion beam current density [29].

In the bulk substrate (Fig. 19.4), the expansion of the amorphization zone below the surface tracks the damage density distribution predicted by TRIM [20] simulation at the lowest doses. As the amorphization zone enlarges with increasing ion doses, the material density in the ion beam interaction region continues to decrease. The initial density reduction is caused by the single crystalline silicon turning amorphous from the ion beam induced knock-on events, introducing a 1.8% gradual decrease in density [30]. This is followed by a second density reduction stage as a result of the subsurface implantation of helium that coalesces into nano-bubbles [19]. The nano-bubbles are not clearly visible in the micrographs included here due to the magnification of the images. Along with material density reduction, the interaction volume continues to expand beyond what is estimated by the TRIM with doses beyond 4.1×10^5 ions nm^{-1}. This is most evident by comparing the depths of the amorphization zones in Fig. 19.4i, j. This phenomenon could be explained by the reduced substrate density and its resulting increase of the ion beam propagation length in the substrate.

At milling doses between 2.6×10^4 and 2.0×10^5 ions nm^{-1} (Fig. 19.4d–h), the net material removal from the sample surface resulted in a shallow via at the beam entry point on the surface, since at these doses the net material volume removal rate is greater than the net volume expansion from the substrate density changes. However, at dose of 4.1×10^5 ions nm^{-1} (Fig. 19.4i), the density induced volume expansion exceeds the net material removal rate, causing the initial via sputtered by the beam to all but disappear. With doses higher than 4.1×10^5 ions nm^{-1}, surface distortion caused by increased implantation of helium becomes evident. This series of TEM micrographs reveals the typical bulk sample distortion results reported for crystalline samples [19].

Similar to the bulk sample, initially, a very small surface via is formed at a dose of 2.6×10^4 ions nm^{-1} in the Si membrane sample (Fig. 19.5d). At a dose of 5.1×10^4 ions nm^{-1}, evidence of forward sputtering can be seen at the exit surface of the membrane, i.e. the substrate atoms are ejected from the beam exiting surface of the membrane sample instead of being back sputtered. At a dose of 4.1×10^5 ions nm^{-1}, the bulk sample starts to show surface distortions (Fig. 19.4i), the membrane sample continues to be back sputtered from the beam incident surface while the vias form and grow from the top and the bottom surfaces simultaneously (Fig. 19.5i). The nuclear stopping range of the helium ions at 35 keV is 318 nm, [20] which is greater than the thickness of the membrane (140 nm). Unlike in the case of the bulk substrate sample where no net volume removal is observed; backward sputtering in the membrane sample continues with net volume reduction even at the higher doses. This net sum reduction in material is caused by the fact that there is very little subsurface helium implantation induced volume expansion to counteract the bulk material removal of the substrate.

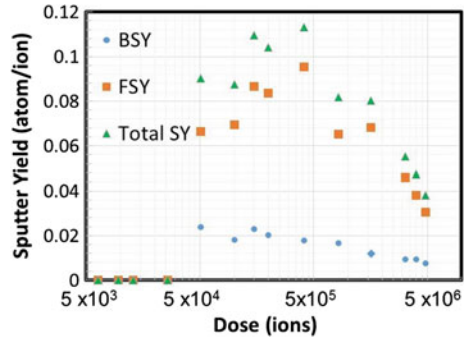

Fig. 19.6 Experimental back sputtered yield, forward sputtered yield, and total sputter yield with increasing helium doses in the Si membrane sample

In the membrane sample, forward sputtering is determined as the dominant contributor to the material milling [28]. Relative forward sputter yield (FSY) to backward sputter yield (BSY) ratio ranges from 3 to 5 in the membrane milling process (Fig. 19.6). BSY roughly follows the bulk material sputter yield while the FSY is heavily dependent on the membrane thickness to ion range ratio and the progression of the milling process.

Membrane material properties, membrane thicknesses, ion beam species, and beam energy all play into the end results. As the forward sputtered via starts to develop, the helium exit points retract to be above the bottom surface of the membrane and have an increasing probability to re-enter the sample at a glancing angle with reduced beam energy. This unique process of lower energy particles re-entering the substrate at a glancing angle causes the forward sputtered via to enlarge rapidly and FSY to significantly increase initially during the membrane sputter process. As both the forward and the backward sputtered vias continue to develop, the thickness of the membrane in the beam path reduces. The lateral distribution of the helium atoms exiting the sample becomes narrower and the beam energy loss reduces. These changes cause a lower sputter yield and reduced probability of the exit beam re-entering the substrate. Eventually the initial acceleration of the forward sputtering process was reversed.

19.2.3 Ion Beam Probe Current Distribution

In addition to considering the influences from the ion material interaction and substrate types on the nanomachining characteristics, a clear understanding of the ion probe current distribution is critical in achieving desired precision in the nanofabrication processes as well. A quantitative characterization methodology for understanding the ion probe current distribution was discussed by Tan et al. [29]. A gallium beam based straight sputtered versus gas assisted etched (GAE) via

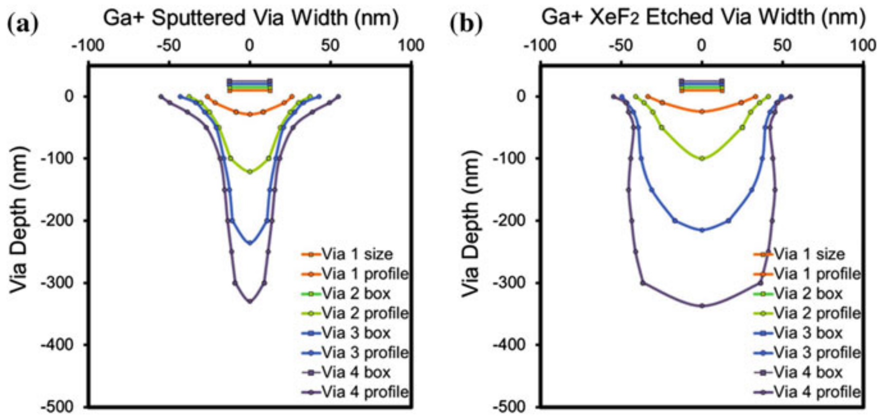

Fig. 19.7 Digitized via width versus depth profiles for **a** sputtered and **b** XeF_2 etched vias. All vias were patterned at 25 nm width. Patterns 1–4 received ion doses of 0.23, 0.90, 1.8, and 3.6 nC μm^{-2}, respectively, for series (**a**) and 0.028, 0.11, 0.22, and 0.43 nC μm^{-2}, respectively, for series (**b**)

profile comparison illustrated the influences of the ion beam probe tail on the ultimate ion beam nanomachining precision [31]. In the sputtered via example, the via profile is proportionally influenced by the current density in the ion beam's center Gaussian, Gaussian tail, and the beam material interaction. The sputtered via width close to the surface has lateral over-etch, while the width at via full width at half maximum (FWHM) is roughly equivalent to the patterned dimension (Fig. 19.7a). Conversely, the GAE via profile has high isotropy (Fig. 19.7b), with lateral of 30–50 nm of sidewall overetch throughout the depth of the via. The Ga^+ etched via dimension using enhancing gas chemistry is predominantly influenced by the beam tail, which is quite prevalent in Ga^+ LMIS beams due to chromatic aberrations.

By comparison, Fig. 19.8 shows a He^+ GFIS beam etched via with XeF_2 GAE at a beam energy of 34.5 keV and a dose of 1×10^{19} ions cm^{-2}. The bottom of this via is measured almost exactly 100 nm - same as the pattern dimension. The top of the via is measured to be 124.5 nm, with the maximum lateral over-etch of 12.3 nm. The lateral over-etch from the He^+ XeF_2 etched via is much smaller compared to those of the Ga^+ sputtered or XeF_2 GAE vias (Fig. 19.7) at $\pm$ 10 to 50 nm and $\pm$ 30 to 50 nm, respectively. This is in line with the nanomachining performance we would expect from He^+, a close to ideal Gaussian beam. It also shows the criticality in minimizing the beam tail in the ion beam probe profile in order to achieve sub-20 nm nanomachining capabilities necessary for the 10 nm process node and beyond.

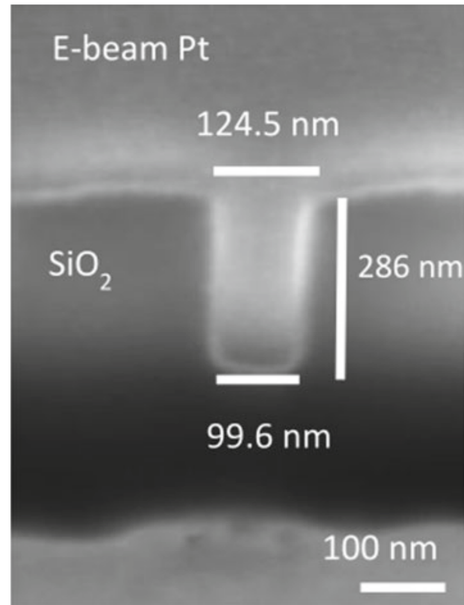

Fig. 19.8 Cross-section image of a He^+ XeF_2 GAE via patterned with 100 nm width

19.3 Applications of GFIS in Semiconductors

GFIS technology has been explored in the semiconductor space for a number of applications, including high resolution microscopy, failure analysis, fault isolation, mask repair, circuit edit, and TEM sample preparation. Although the unique attributes of a Helium GFIS ion beam have been widely studied, neon GFIS applications are not nearly as well explored and documented since it only became commercially available in 2014. The use of GFIS beams for semiconductor industry applications is still in its infancy, but it is anticipated to evolve extensively over the next few years, particularly as academia and industry tackle the challenges of performing analysis on devices fabricated on sub-10 nm process nodes. In this section, we will dive into the emerging applications of GFIS in the semiconductor industry.

A relative comparison of key attributes for gallium LMIS, neon GFIS, and helium GFIS are shown in Table 19.1. The absolute values for sputter rate and secondary electron yield vary depending on the substrate material, beam energy, and other patterning variables [32]. The GFIS performance attribute values shown in Table 19.1 are normalized to those of the Ga^+ for comparison purposes. Helium has approximately only 1% of the sputter yield compared to Ga^+ in the 10–40 keV beam energy range, which is typically used in Ga^+ ion beam nanomachining applications. This limits the applicability of He^+ for machining purposes. Neon, however, has a sputter yield of approximately half that of Ga^+, which makes it much more suitable candidate for nanomachining. The relatively high secondary

Table 19.1 Comparison of key attributes of the He^+ and the Ne^+ GFIS beams relative to the Ga^+ LMIS beam

	Beam energy (keV)	Resolution (1pA) (nm)	SE yield (relative)	Sputter yield (relative)	SE yield per sputtered atom	Current range
Ga^+ LMIS	10–40	3	1x	1x	1x	0.7 pA–100 nA
He^+ GFIS	10–35	0.5	3–8x	0.01x	300–800x	<50 pA
Ne^+ GFIS	10–30	1.5–2	2–3x	0.3–0.5x	4–9x	<10 pA

electron yields and lower sputter yields of helium and neon GFIS beams make them highly desirable for imaging applications where the ion induced damage minimization is required. A new figure of merit—*SE yield per sputtered atom* is defined as an ion beam's ability to precisely control the removal rate and removal depth of the substrate. As shown in the table, both the He^+ and the Ne^+ have high figure of merit, indicating great spatial and temporal precision scaling relative to the Ga^+ FIB.

19.3.1 Helium Applications

Helium GFIS has been explored for its high imaging resolution, unique contrast mechanism, surface sensitivity, and high sensitivity voltage contrast attributes [13, 14, 16, 33, 34]. Helium has also been successfully used for nano-patterning and nanomachining in thin films for applications such as plasmonic device fabrication, graphene device fabrication, and other direct-write nanomachining applications [22, 24, 25, 35–37]. More recently, other light element GFIS beams have also been explored for potential mask repair applications [38–40]. In spite of these successes in imaging and thin film patterning, helium GFIS has had limited use for semiconductor nanomachining, microscopy, and material analysis applications due to the risks of beam induced subsurface damage and implantation causing variation in the transistor performance [19].

19.3.1.1 Helium Ion Microscopy

One of the major challenges of imaging semiconductor materials is imaging insulators and materials with floating substrates. This is due to the surface charge accumulation from the primary beam implantation and the loss of electrons through the secondary electron emission. As the surface charge accumulates, not only the corresponding electric fields cause the SE emission to reduce, resulting in poorer image SNR; the electric fields from the surface charge accumulation also cause the beam to shift from targeted landing area resulting in degradation of the resolution.

Such influence to the beam is particularly significant at lower acceleration voltages, i.e. 500–1000 V which is typically used for critical dimension (CD) metrology. Certain mitigation techniques can be used for SEM to compensate the charging effects; however, it cannot be completely eliminated. One advantage that positive ion FIB imaging has over SEM is the ability to neutralize the surface charge through in situ irradiation of the sample surface with low energy electrons [41, 42]. With the flood gun applied during imaging, the electrons are drawn to the positively charged area and thus self-regulate to achieve charge compensation. Charge neutralization, high resolution, and low sputter yield characteristics of the He^+ makes the helium ion microscope (HIM) an excellent option for imaging these types of substrates.

A good example of charge neutralization is in imaging a chromium photomask. The images shown in Fig. 19.8 were imaged with He^+ at 17 keV beam energy with 1 pA beam current [42]. With flood gun applied to the sample surface between He^+ line scans, the image SNR improved dramatically. In the charge neutralized image (Fig. 19.9b), the transition from the chromium edge to the quartz can be clearly seen and the particle defect located in the center of the chromium line can be much better delineated compared to when the flood gun was off (Fig. 19.9a).

Figure 19.10 shows images of an advanced photo-mask patterned with resist taken at 2 μm field of view (FOV) with 20 keV He^+ beam at 200 fA beam current [19]. Not only do the images have great SNR and no lateral smearing from charge induced drift, but the He^+ beam's high depth of focus and surface sensitivity reveals rich information related to the resist surface and the sidewall, which is not possible to achieve with a SEM.

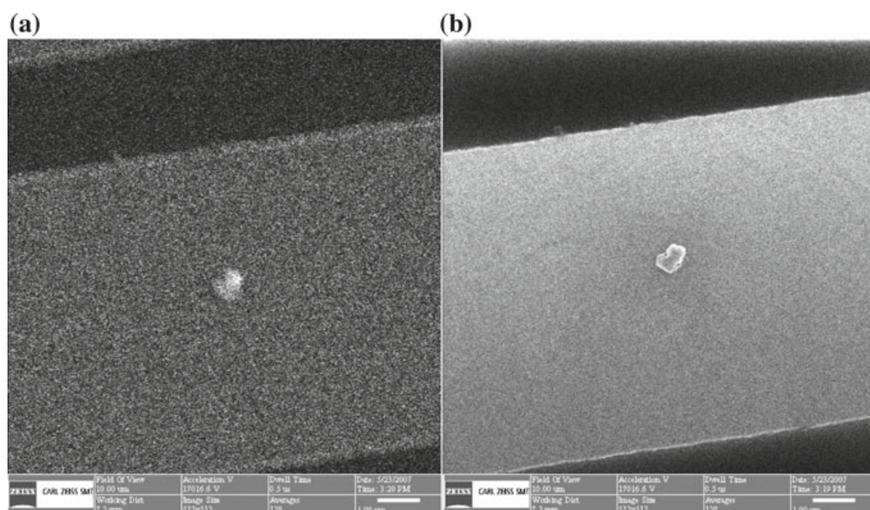

Fig. 19.9 Patterned chromium on quartz photomask imaged with a HIM. **a** Effects of beam induced surface charge degrade image SNR and resolution. **b** Charge neutralization significantly improved the SNR and resolution

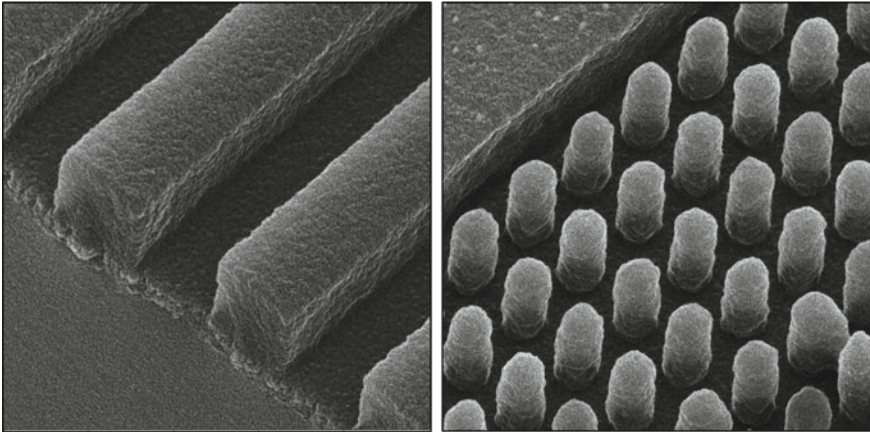

Fig. 19.10 High resolution and depth of field helium images of photoresist on a mask sample

19.3.1.2 Voltage Contrast Imaging

One of the promising areas for He^+ FIB microscope is for beam induced voltage contrast applications. The voltage contrast (VC) effect can be the manifestation of either a capacitive effect (induced voltage equivalent to deposited charge divided by device capacitance) or a resistive effect (induced voltage equivalent to charging rate times device resistance). In either case, the induced voltage enhances or retards the detector's ability to collect and hence modulates the signal strength. Passive voltage contrast (PVC) localization uses the brightness differences in the FIB or the SEM images of conducting structures in the semiconductor circuits to isolate failures like opens or shorts. Active voltage contrast method where an external bias is applied to certain structures can offers even more localization possibilities for the resistive failures [43, 44]. If the electrical feature of interest is below the surface, static capacitive contrast (SCC) is responsible for creating the contrast [45]. In this phenomenon, conducting features buried beneath an insulating layer are imaged brighter according to their capacitance, which reduces the surface field buildup thus allowing secondary electrons to escape more readily.

Failure localization with PVC is based on the fact that floating structures are charging up under the influence of the primary beam in the FIB or the SEM. In the FIB, this charging is always positive and greatly depends on the primary beam current. In the SEM, the charging can be positive or negative depending on the primary beam's energy and current. The FIB in general has stronger charge effects than the SEM since the incoming primary electrons and the exiting secondary electrons are partially compensating each other in the SEM. Ga^+ FIB induced charge contrast was quite commonly used for this purpose until about 2005. After the semiconductor minimum feature size dropped to below 100 nm, the high sputter rates and the p-type doping influence from the Ga^+ beam became too invasive to the transistors. This invasiveness combined with the resolution limitations of the

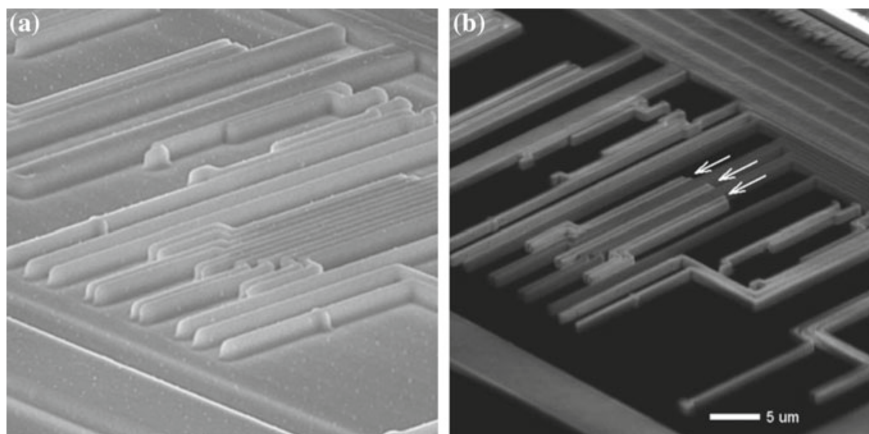

Fig. 19.11 **a** SEM. **b** HIM images of a fully process DRAM sample with leaky connections

Ga^+ FIB resulted in this technique being replaced with other more cumbersome, but less invasive techniques such as Atomic Force Probing (AFP) [46]. The combination of the superior resolution, the high SE yield, and the relatively low sputter rates of the light element ions provides a great opportunity for HIM to be used for charge contrast analysis.

Figure 19.11 shows an example of electrical inspection on a fully processed DRAM sample that has been passivated with silicon nitride (Si_3N_4) [33]. The SEM image did not reveal any noticeable contrast variation, but the HIM imaging, provided very strong contrast for this application showing three pairs of lines near the center of the image, which are much brighter relative to adjacent lines, indicating a good continuity to ground. The interlayer dielectric layer beneath and adjacent to the lines also had strong contrast, appearing almost black. This difference in the SEM and the HIM image contrast is theorized to be caused by the lower mean energies of the ion beam induced secondary electrons comparing to the SEs generated by the electron beam, making them more sensitive to the influence of subsurface fields [33].

Another example of beam induced voltage contrast application is shown in Fig. 19.12. In this example, the top interconnect layers of a DRAM sample were removed via polishing, exposing the substrate contact level. The upper left contact is connected to a p-type diffusion area and the lower right contact is connected to a n-type diffusion area. He^+ creates positive charging in the sample, resulting in a forward bias in the p-type connection. Since charge can be replenished from the substrate, the forward biased contact appears brighter than the contact with connection to the n-type diffusion. The contrast variation between the two contacts can be increased from 30 to 235% through lowering the beam landing energy, as seen in Fig. 19.12 [47]. Knowledge of all factors influencing the VC generation such as capacitance, leakage, doping, bias, and circuitry is very important for successful failure localization with charged particle beam technology.

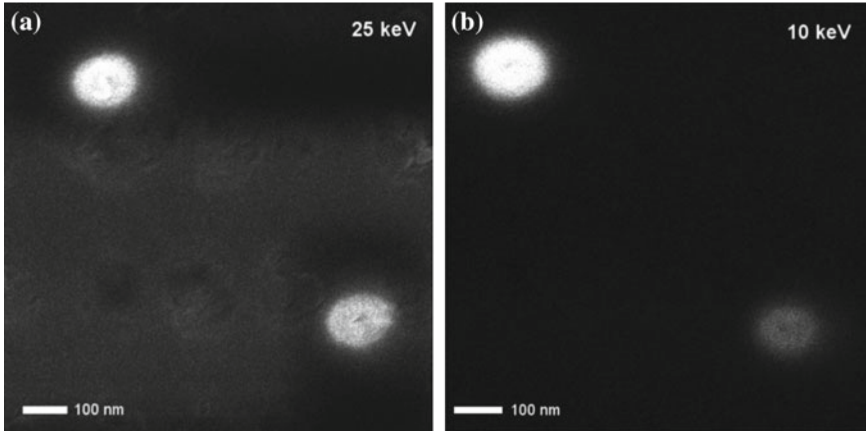

Fig. 19.12 **a** 25 keV. **b** 10 keV HIM images of a deprocessed DRAM sample with the upper left contact connected to a p-type diffusion area and lower right contact connected to a n-type diffusion area

19.3.1.3 Doping Contrast Imaging

There is an increasing need for characterizing the nanoscale dopant distributions due to the miniaturization of the semiconductor devices. HIM imaging has been reported to have improved spatial resolution and less lateral spread of SEs with respect to SEM [16]. It could potentially be developed into a major contender for dopant mapping of future nanoscale semiconductor devices.

19.3.1.4 Mask Repair

Most defects on high-end photo masks used in current semiconductor processes are repaired with electron beam (EB) based systems. Extreme-UV lithography (EUVL) is a next generation lithographic technique expected to continue the trend of miniaturization in the nanoelectronics industry towards the 10 nm node. A next generation mask repair beam for both the optical and the EUV masks will require improvements in every major repair attributes, i.e. higher repair precision; minimal absorber side etching; limited material layer intermixing; low reflectivity loss; and high etch selectivity, etc. The minimum repairable dimension of the current state-of-the-art repair EB systems is about 20–30 nm and the selectivity between the MoSi and quartz substrate in phase shift masks (PSM) to avoid over etching is not sufficient.

F. Aramaki et al. conducted detailed analysis in applicability of H^+, H_2^+, N_2^+ and He^+ GFIS for phase shift mask and EUV mask repair [38, 39, 48]. In their publications, a minimum repairable dimension by H_2^+ was reported to be 11 nm, half of that with EB [39]. The etching rates was reported to be 0.0762 nm^3 per

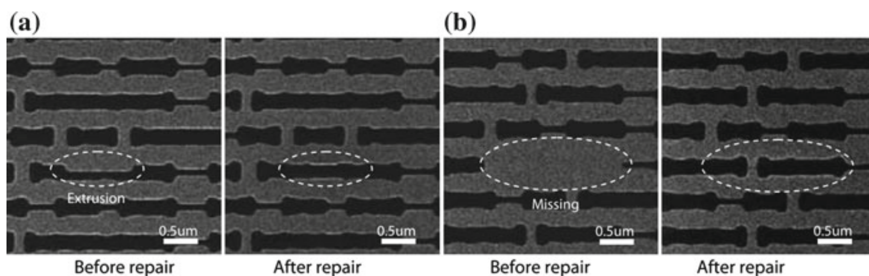

Fig. 19.13 Scanning ion images of holes on MoSi (HOYA A6L2) mask before and after repair for **a** extrusion defect and **b** missing defect

incident ion for MoSi and 0.0124 nm^3 per incident ion for quartz, resulting in an etch selectivity of 6.1:1 [39]. EUV reflectivity is altered by 30 keV He^+ at a small dose of 2×10^{15} ions cm^{-2}, but H_2^+ at 15 keV with a dose up to 1×10^{16} ions cm^{-2} showed no reflectivity change [38]. This improvement was attributed to the significantly fewer substrate atom recoil events induced by H_2^+ compared to He^+. These results suggest that the H_2^+ GFIS technology could be a promising candidate for repairing the advanced masks.

Figure 19.13 shows examples of before and after images of an extrusion defect and a missing pattern defect on a MoSi (HOYA A6L2) mask repaired with a H_2^+ beam at 25 keV. AFM images of the edited regions before and after repair showed no significant difference between the repaired section and the defect free regions of the mask (Fig. 19.14).

Other mask repair studies by Rack et al. investigated both helium and neon as candidate techniques for EUVL mask editing [40]. Although He^+ etches certain EUV absorber (TaN) well, He^+ beams did not effectively remove nickel absorber layer at 16 or 30 keV with the dose parameters tested. In addition, unwanted

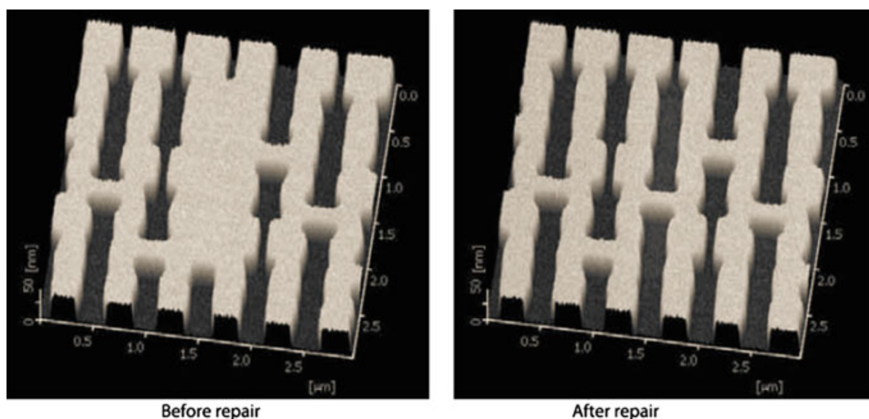

Fig. 19.14 AFM images of defects on MoSi (HOYA A6L2) mask before and after repair

intermixing of the underlying Mo/Si EUV reflector layers were created. At doses below 1×10^{17} ions cm^{-2}, a progressive contraction caused by molybdenum silicide formation is observed. With peak implant concentrations in excess of 1×10^{21} ions cm^{-2}, nanobubble formation occurs and causes substrate swelling. Neon at 30 keV removed the nickel absorber layer effectively at ~1.5 nickel atoms per neon ion; however, the TEM images revealed presence of nanobubbles at concentrations exceeding 10^{21} neon cm^{-3} and an extended region of apparent Mo Si intermixing.

Much further exploration and advanced gas chemistry developments are needed to enable GFIS in the mask repair applications.

19.3.2 Neon Applications

Gallium FIB nanomachining in failure analysis, fault isolation and circuit edit [3, 49] has been well studied and applied for over 20 years in the semiconductor industry. Some of these applications could potentially be improved and extended with neon's unique attributes discussed in the earlier part of this section.

19.3.2.1 Circuit Edit

FIB circuit edit, used for rewiring integrated circuits to validate design changes, isolating process faults, and generating engineering samples, provides physical validation of engineering changes in hours as opposed to weeks typically required for mask stepping changes [49]. This quick turn-around enables very rapid prototyping of design changes, which in turn allows the circuit designer to continue to validate the overall functionality of circuits in a device. Additionally, the engineering samples generated allow platform designers to start development early and eventually shorten the product time to market.

Neon GFIS has demonstrated very good nanomachining performance, with 2–3x lower sputter yield and 3x higher SE yield relative to Ga^+ [50], providing a high level of SNR and nanomachining controllability that is not attainable using a traditional Ga^+ LMIS based FIB systems. However, the invasiveness of the neon ion beam in terms of material property alteration, un-intended lateral sputtering, and transistor device timing impact needs to be considered in order to determine the limitation of neon for CE applications. As an example, Ne^+ has a 3x higher ion material interaction volume than Ga^+ at the equivalent beam energy. At 30 keV, an energy typical used for CE, Ga^+ and Ne^+ have an interaction depth of ~ 30 nm and ~ 100 nm in silicon, respectively. The larger interactive volume of neon limits the proximity for many of the nanomachining and ion beam induced deposition (IBID) applications to a distance greater than 100 nm from the critical circuits and interconnects. Additionally, implanted neon tends to cause substrate deformation in the forms of nanobubbles once the implanted dose exceed neon's solubility in the

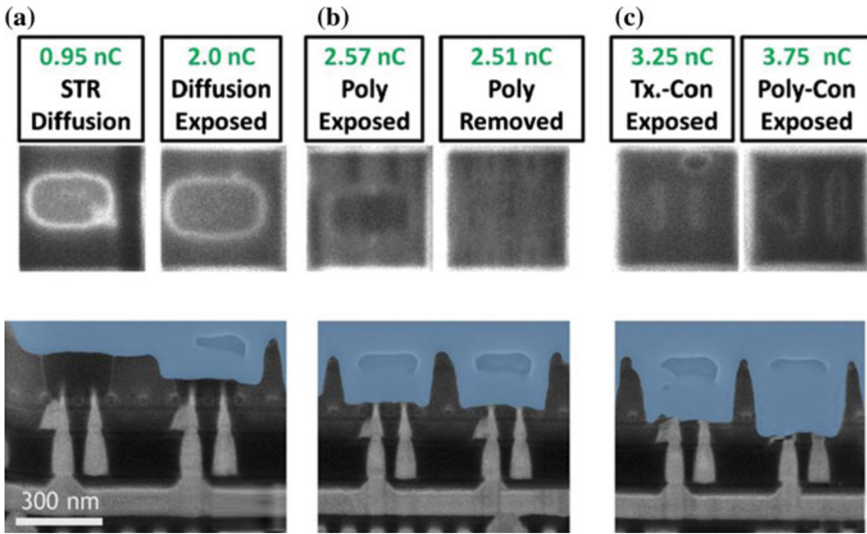

Fig. 19.15 Via milling and end-pointing on various process layers on a 32 nm test device using 10 keV neon beam with 1 pA current. Visual endpoint on metal 1; via 0; poly connect layer; transistor connect layer; poly layer, and diffusion layer **a**–**c** and their cross-sectional images are shown

substrate material [51]. To circumvent this, most of the early work published on neon was conducted at 10 keV beam energy, which limits the Ne^+ interaction depth to roughly equivalent to that of Ga^+ at 30 keV. Operating at a lower energy degrades the Ne^+ beam probe size and resolution, however, this was considered a necessary tradeoff to enable neon's use in CE applications [52]. Despite the degradation of the neon beam spot size at reduced beam energy, the resulting beam profile was still better than that of the state of the art Ga^+ FIB's.

The first proof of concept neon circuit edit was reported in 2011. Neon's nanomachining uniformity and endpointing capabilities on semiconductor mixed material substrates was studied using a 32 nm test device [53]. This early study demonstrated that a 10 keV Ne^+ beam could be used to machine through the silicon substrate and effectively stop on the transistor diffusion, poly gate, and various metal interconnect layers, as shown in Fig. 19.15a–c.

Additional neon circuit edit results are shown in Fig. 19.16. These edits were performed on a 22 nm Fin-FET device using a 10 keV neon beam. The target interconnect layers was exposed, IBID dielectric layer was deposited, and a narrow via was milled through the IBID dielectric layer to the specific interconnect signal line of interest to mimic the standard processes used in CE [54]. In Fig. 19.16a, the cross-section image shows the final result of a Ne^+ beam machined 250 nm mill box through the diffusion-poly-metal interconnect stack. The sample was exposed to the M1 layer, then followed by Ga^+ IBID insulation, and a connection point to the signal of interest with a 50 nm (FWHM) via. A more interesting and challenging

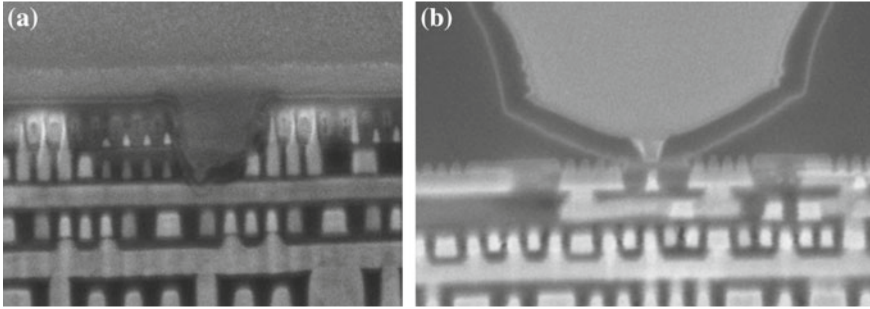

Fig. 19.16 Ne^+ beam induced via-nanomachining on 22 nm Fin-FET devices. **a** A Ne^+ beam machined via through transistor region endpointing on M1 signal routing layer. **b** A Ne^+ beam machined via through the silicon substrate endpointing on poly (metal-gate) line

application is shown in Fig. 19.16b where Ne^+ beam was used to edit between the p-device and n-device transistor fins. After successful endpointing on the very narrow contact layer and Ga^+ IBID dielectric step were completed, the contact layer was re-exposed by a Ne^+ beam with a 40 nm (FWHM) Via. This example is particularly intriguing because it demonstrates neon's ability to access a signal at the poly-gate, source, and drain levels without damaging the device. Currently, most edits performed on sub-22 nm process nodes by Ga^+ are done destructively, i.e. an active or passive device is removed to allow access to the signal in the signal routing layers below. The prospect of performing edits within the device cell of interest noninvasively could enable much more complex edits to be defined, which should allow more accurate representation of the design changes to be implemented at the mask level. It needs be noted that a Ga^+ FIB was used to perform the dielectric deposition steps between the line exposure and the via mill steps due to the limitations of the IBID capabilities at the time of these experiments. Subsequently, IBID dielectric deposition has been demonstrated using Ne^+ beam with PMCPS precursor; however those results are not shown in this chapter [55, 56].

19.3.2.2 Circuit Timing Invasiveness

The results discussed in the previous section demonstrated neon's ability to nanomachine down to key features in the semiconductor device stacks; however neon's invasiveness to the adjacent devices has not been quantified. To answer this question, a Ne^+ timing invasiveness analysis was conducted by the same group from Intel to benchmark Ne^+ beam's invasiveness with that of a 40 keV Ga^+ beam [57]. In this study, a group of discrete seven stage ring oscillator locations were used to study the proximity effects of ion beam machining to the adjacent active devices. Since the frequency of free running ring oscillators can differ by several percent from the variations in the test set up, the environmental conditions, and the sample preparation artifacts, the ring oscillator locations were selected to serve as the

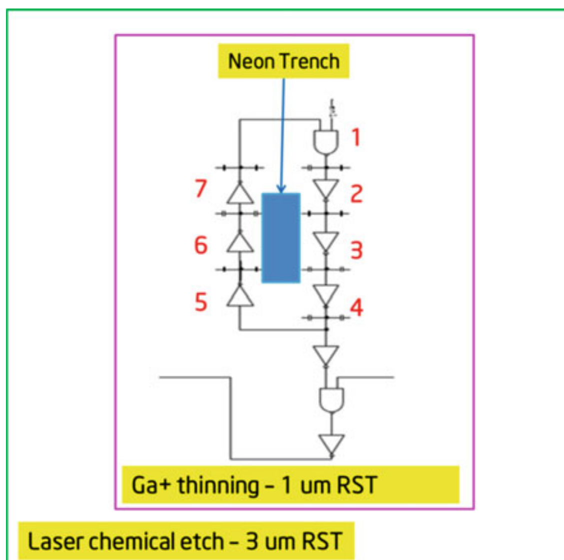

Fig. 19.17 Graphical illustrations of the test area ring oscillator circuit and deprocessing steps used for the neon nanomachining timing invasiveness study

frequency reference for both the oscillators within the region irradiated by the ion beam and outside the experiment region. All the timing invasiveness was characterized as a relative change to the lager population of reference ring oscillators.

A schematic of the ring oscillator circuit and the sample deprocessing steps are shown in Fig. 19.17. Prior to performing the neon nanomachining test, the silicon substrate was thinned to 1 μm using a combination of laser chemical etching (LCE) and Ga^+ FIB milling. In each test locations, the ion beam was used to open up a 350 nm × 700 nm area through the remaining silicon between the diffusion fin areas of several inverter structures in the ring oscillator. The oscillator timing degraded by 0.5% in the case of exposure from a 10 keV neon beam. The timing degradation of the oscillators from both 15 keV neon beam and 40 keV gallium beam exposure were at 1.5%. These results indicate that the neon beam can be safely used up to 15 keV without imposing worse timing invasiveness comparing to the current gallium techniques. This result has good agreement with the TRIM ion range simulation discussed in the previous session in this chapter.

19.3.2.3 Fault Isolation

With the increased complexity in the fab process and the reduced process geometry, isolating process faults and root causing them has become more and more difficult. Gallium FIB is widely applied in the area of fault isolation, but separating suspected defective areas less than 100 nm apart without introducing additional defects has become increasingly critical and challenging. This is another aspect where neon could potentially be very advantageous due to its nanomachining precision and the non-metallic doping.

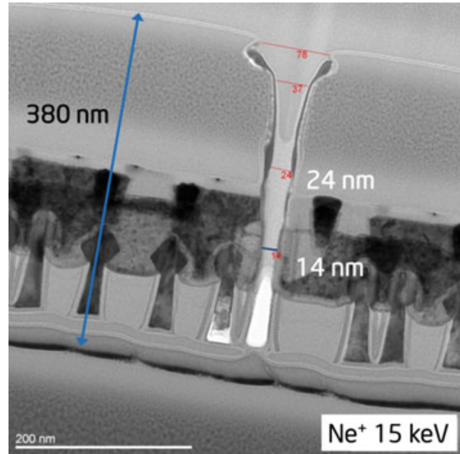

Fig. 19.18 An example fault isolation cut in a TEM lamella using a 15 keV neon beam

A TEM micrograph from a neon isolation cut is shown in Fig. 19.18 [58]. In this example, a 15 keV neon beam is used to create a narrow separation between adjacent contacts in a TEM lamella extracted from a 14 nm process wafer. The total sample height is 380 nm, consisting of 180 nm of the original lamella plus a 200 nm thick HMCTS oxide protection layer. In order to inspect the suspected areas thoroughly to accurately isolate the defects, a cross-sectional TEM lamella was lifted out from the original process lamella. Encouraging results are demonstrated in this example, with a 14 nm wide cut achieved at the narrowest point of the separation and a 27 to 1 aspect ratio through the 380 nm thick membrane. Closer inspection reveals that the neon cut through the lamella is quite anisotropic with very little lateral damage to the adjacent process fins. Similar attempts to perform isolation cuts with Ga^+ FIB showed that the Ga^+ milling precision was ~ 2x greater in width; had a higher lateral defect density; and caused undesired metallic implantation to the test area, which could potentially convolute the result interpretation.

19.3.2.4 TEM Lamella Preparation

TEM Lamella sample preparation using in situ or ex situ lift out techniques on Ga^+ based FIB systems are very essential process in the semiconductor industry [59]. TEM samples are sensitive to structural damages and chemical contamination from Ga^+. Low energy Ga^+ or Ar^+ beam final polish steps are typically applied to reduce these undesired side effects from the Ga^+ lamella preparation steps [60].

Preliminary study in Ne^+ beam polish in TEM lamella was reported recently [61]. The lamella was first thinned, lifted out, and welded onto an Omni grid using Ga^+ due to the limited beam current range from the Ne^+ GFIS. Once the lamella thickness was reduced to about 600 nm, a 25 keV Ne^+ beam was used to further polish the area of interest to create a 50 nm thick window on the lamella

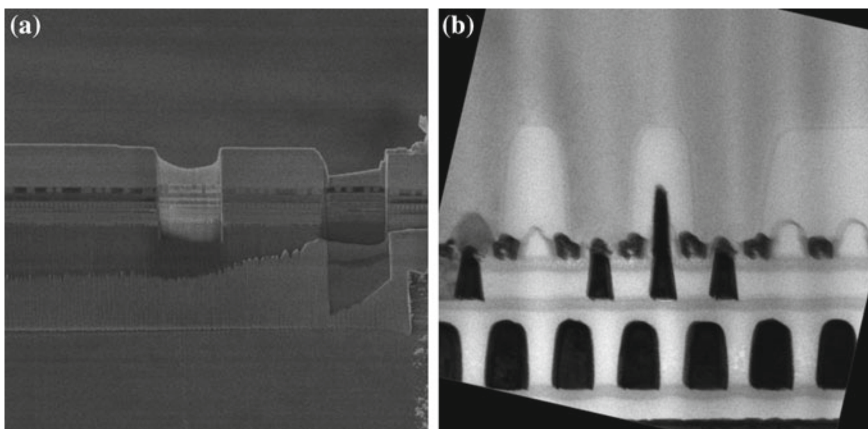

Fig. 19.19 Ne^+ beam was used to polish a Ga^+ thinned TEM lamella **a** a global view of the lamella with the Ne^+ thinned window. **b** TEM image through the neon polished window

(Fig. 19.19a). A bright field TEM image taken from the thin window area is shown in Fig. 19.19b. These are the earliest result published to date, it will be interesting to see the follow up investigation on the impact of the Ne^+ beam energy and the incident angle on the quality of TEM sample and determine if there are any scaling benefits in using Ne^+ versus Ga^+ beam for the TEM sample preparation.

19.4 GFIS Damage Mitigation

While low energy neon beam has demonstrated promising results for various nanomachining applications discussed in this chapter. The subsurface nanobubble to microbubble formation and the high damage distribution range of the helium beam and the neon beam above 15 keV impose a very narrow operating window. The smaller probe size, the higher SE yield, and the greater nanomachining precision at the high beam energy, could be utilized if techniques to prevent the gas bubbles to accumulate subsurface and to eliminate the damage formation can be applied.

Since the helium diffusion rate is exponentially dependent on the substrate temperature [62], raising the temperature of the sample substrate is a potential solution to mitigate this phenomenon. This enhanced helium diffusion through the sample substrate heating has been published in 2013 [51]. In this report, Si and $SrTiO_3$ samples were placed on a MEMS heater during milling. At 700 °C, the diffusion of the helium was sufficiently large to enable clean helium cuts on a 300 nm thick Si lamellae without any visible damage. This setup is a great demonstration of the concept, but the extended heating at 700 °C imposes several limitations including thermo-induced drift, restriction on sample geometry, and

applicability to temperature sensitive materials. For semiconductor devices, this is not a viable solution.

In situ pulsed-laser-assisted process has been used extensively in the last several years in the areas of process enhancement for e-beam induced processes [63, 64]. An approach utilizing a synchronized in situ infrared pulsed laser for helium and neon ion beam induced damage mitigation was recently reported [65]. The mitigation of subsurface damage induced by He^+ and Ne^+ ion exposures in silicon was demonstrated. The pulsed laser assist provides highly localized in situ photo-thermal energy which reduces the implantation and defect concentration by greater than 90%. The laser-assisted exposure process is also shown to reduce peripheral defects in He^+ patterned graphene, which makes this process an attractive candidate for application in direct-write nanoscale material processing via FIBs.

Figure 19.20 is a schematic illustrating the pulsed laser delivery system which is mounted onto the GFIS microscope. The schematic cross-section in Fig. 19.20a demonstrates the simulated room temperature helium, vacancy, and interstitial concentration profiles of a 1×10^{16} He^+ cm^{-2} dose overlaid on an experimental TEM images. The schematic cross-section in Fig. 19.20b illustrates the simulated concentration profiles resulting from the same dose with the photo-thermal laser assist. As illustrated, the in situ laser exposure intermittently heats the exposed region and facilitates helium and vacancy diffusion as well as interstitial-vacancy annihilation. It is worth noting that the uncoupled simulation doses not account for the interstitial-vacancy concentration represent the hypothetical maximums of each.

Figure 19.21 compares TEM cross-section microscopy images of a silicon sample exposed to variable He^+ areal doses ranging from 1×10^{16} to 1×10^{18} He^+ cm^{-2} without (a–d) and with (e–h) the simultaneous pulsed laser irradiation at a ion beam energy of 25 keV. Examination of the TEM images (a–d) demonstrate the typical damage accumulation noted in silicon, namely a clear progression from vacancy and dislocation generation (as evidenced by the slight contrast in the 1×10^{17} He^+ cm^{-2} dose image b), amorphization (observed in the 5×10^{17} He^+ cm^{-2} dose image c), and helium bubble formation (noted in the 1×10^{18} He^+ cm^{-2} dose image d) and is accompanied by surface swelling at doses of 5×10^{17} He^+ cm^{-2} and 1×10^{18} He^+ cm^{-2}. Simultaneous pulsed laser irradiation has a profound effect on the subsurface damage accumulation (Fig. 19.21e–h), and significantly attenuates the onset of Si amorphization. The averaged photon/ion flux used for this laser-assisted exposure was 1.3×10^6 photon/ion. Specifically, near surface amorphization of the Si is obvious in Fig. 19.21i when no laser assist is used. However, the Si maintains it's near surface crystallinity when a laser assisted exposure technique is used, as shown in Fig. 19.21j. Figure 19.21k shows selected area electron diffractograms (SAED) of an unexposed silicon region and a region exposed to a helium dose of 1×10^{18} He^+ cm^{-2} at a photon/ion flux ratio 5x higher (SAED regions demoted by the dashed circles in Fig. 19.21i). Comparison of the SAEDs reveals that while defects remain, as evidenced by the distorted spots, the laser heating annihilates much of the damage accumulated during ion irradiation and the single crystallinity of the silicon is maintained.

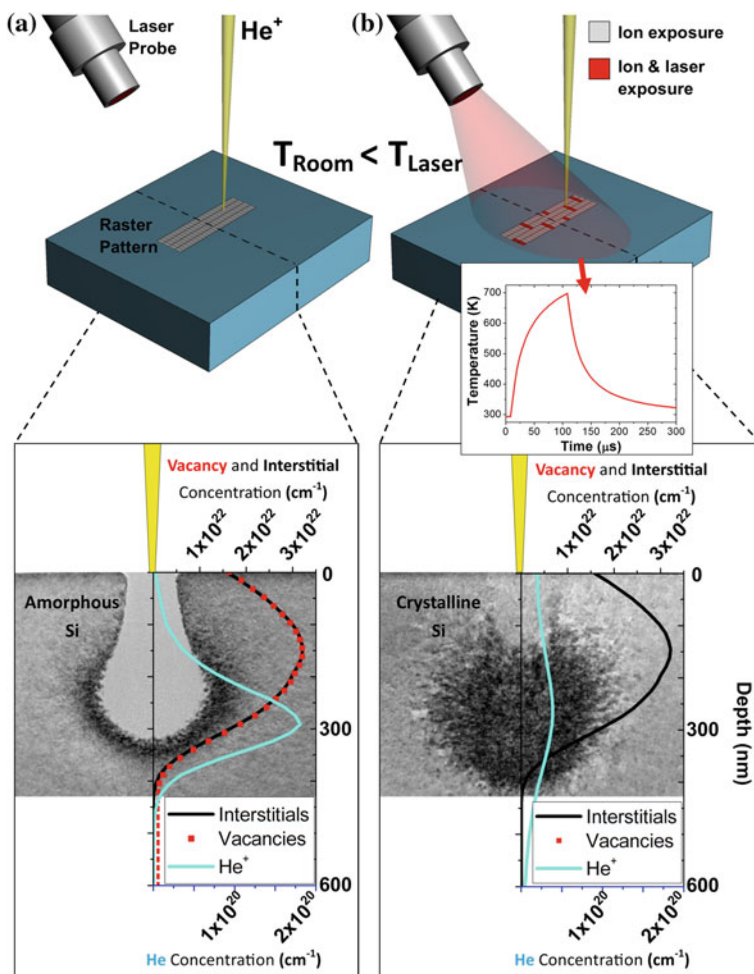

Fig. 19.20 Schematic of helium ion exposure **a** without and **b** with assist to photo-thermally enhance implanted ion diffusion and defect annihilation. *Gray* pixels in the raster pattern represent pixels irradiated solely with He^+, whereas red pixels are simultaneously irradiated with the laser and He^+ (not to scale). Cross-section TEM images illustrate **a** the amorphized silicon region and **b** damage mitigated by the in situ laser assist. Overlaid on the TEM images are calculated helium, vacancy, and interstitial concentrations, illustrating photo-thermally enhanced diffusion of He^+ and vacancies with the pulsed laser-assisted strategy of a photon/ion flux of 1.3×10^6. Inset in **b** is the simulated time-temperature profile of a single 100 μs laser pulse irradiated on Si

In situ laser annealing of neon ion beam induced damage was also studied in this paper. Due to the mass of the Ne^+ (20 amu) is 5x higher than the He^+ (4 amu), it consequently has a higher nuclear energy loss cross-section and a significantly reduced implant range, which results in the number of silicon interstitials and vacancies generated to be ~ 3.8x higher per ion as compared to He^+. The reduced

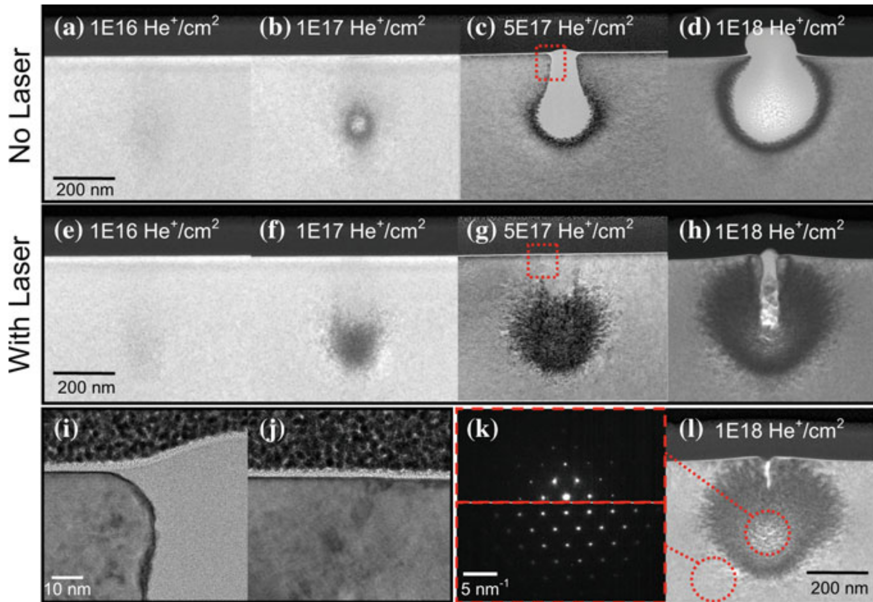

Fig. 19.21 TEM cross-section of 25 keV He^+ exposures of varying dose **a**–**d** without and **e**–**h** with a pulsed laser assisted of 1.3×10^6 photon/ion flux. High resolution TEM images showing ion beam induced damage **i** without and **j** with laser assist for a dose of 5×10^{17} He^+ cm^{-2} collected from the regions denoted by hatched boxes in **c** and **g**, respectively. **k** SAED patterns and **i** TEM cross-section of an exposure of 1×10^{18} He^+ cm^{-2} with 5x higher (6.6×10^6) photon/ion flux than **h**. Dashed circles demote where the SAED was conducted

range results in a higher peak implant concentration for neon relative to helium at an equivalent energy. At the photon/ion flux ratio of 1.3×10^6, the amorphization region introduced by a 25 keV Ne^+ can be reduced significantly, but a much higher photon/ion flux ratio is needed for the Ne^+/Si system to reach the equivalent repair level as the He^+/Si system.

Post annealing studies of helium implantation into silicon reveals that irreparable voids form at a critical dose of 1×10^{16} He^+ cm^{-2}. In order to mitigate void formation, it is important to have appropriate laser conditions in which the implanted ions diffuse and vacancies/interstitials annihilate before this critical dose is reached. For example, comparable laser exposure after ion irradiation yields much less damage mitigation compared with the in situ process. While the implanted helium can be driven out of the bubbles, voids/pores remain in the silicon.

This in situ pulsed laser assisted process is a viable technique to introduce transient thermal energy to a localized area of the sample which avoids the limitations in the heater stage approach. In addition, this in situ pulsed laser technique could be applied to improve material purity of the ion beam induced deposits and enhance etch rate of the beam induced etching processes similar to what has been demonstrated for the focused electron beam induced processes [64].

19.5 Future of GFIS Applications in Semiconductors

GFIS focused ion beams offer unique attributes that are advantageous for semiconductor imaging, metrology, and nanomachining applications. Examples discussed in this chapter include

- Helium GFIS has demonstrated sub-1 nm resolution imaging on materials and substrates prone to charging problems such as photomasks and photoresist.
- Helium IBIC has great sensitivity in identifying variations in leakage current in transistor junctions and interconnects.
- Helium and Neon has been used to demonstrate sub-5 nm nanomachining in thin film substrates and sub-15 nm in defect isolation cuts in TEM lamella.
- Neon GFIS has demonstrated sub-20 nm high aspect ratio vias and excellent material selectivity and material removal controllability.
- Early proof of concept results in using low energy neon beam for circuit edit application shows viability.
- Early results in using hydrogen GFIS for possible photomask repair applications has been published.

Although many GFIS applications have been reported in the literature, most of the novel capabilities demonstrations are limited to university, national labs, and semiconductor industry research labs. The use of GFIS FIBs for semiconductor applications is in its infancy and has yet to find a niche that will bring it into main stream application space. The current status of the GFIS is analogous to where the Ga^+ FIB was in the late 1980s; when the Ga^+ LMIS emerged as a novel micro-machining beam for the defect cross-sectional analysis and the lithography mask repair. As the Ga^+ FIB application space grew into circuit modification, TEM sample preparation, SIMS, and wafer level applications; so did the specialization of the Ga^+ FIB tools. Similarly, it is expected that the GFIS based technologies (helium, neon, and others) will continue to evolve and add value to solve complex analytical, metrology, and manufacturing problems. The future for the GFIS will be largely dependent on the maturation and the stability of the GFIS ion source technology and the ability of the SEM and alternative FIB technologies to continue to scale for meeting the challenges of sub-10 nm process node. Neon, in particular, needs to reach a point of stability where it can be routinely used for mainstream analytical, debug, and metrology labs.

Acknowledgments The authors would like to thank various external and internal collaborators and colleagues for their valuable discussions, outstanding equipment maintenance, sample preparation, cross-section, and TEM analysis support. In particular we would like to acknowledge: John Notte, Lewis Stern, Dave Ferranti, and Shawn McVey from Carl Zeiss Microscopy; Andras Vladar and Kate Klein from NIST; Philip Rack from U. of Tennessee in Knoxville; and Roy Hallstein, Darryl Shima, Paul Hack, Laxa Patel, Yuval Greenzweig, Chris Scheffler, and Waqas Ali from Intel Corporation.

References

1. J. Orloff, M.W. Utlaut, L. Swanson, *High Resolution Focused Ion Beams: FIB and Its Applications* (Springer Press, 2003)
2. L.A. Giannuzzi, F.A. Stevens, *Introduction to Focused Ion Beams: Instrumentation, Theory, Techniques and Practice* (Springer Press, 2004)
3. EDFAS, *Microelectronics Failure Analysis,* 5th edn. (ASM International, 2004)
4. http://www.intel.com
5. R. Clampitt, Nucl. Instrum. Methods Phys. Res. A **189**(1), 6 (1981)
6. L.W. Swanson, Nucl. Instrum. Methods Phys. Res. A **218**(1–3), 7 (1983)
7. B.W. Ward, J.A. Notte, N.P. Economou, J. Vac. Sci. Technol., B **24**, 2871–2874 (2006)
8. J. Notte, F. Rahman, S. McVey, S. Tan, R. Livengood, Microsc. Microanal. **16**, 28–29 (Portland, OR, 2010)
9. J.L. Hanssen, S.B. Hill, J. Orloff, J.J. McClelland, Nano Lett. **8**(9) (2008)
10. B. Knuffman, A.V. Steele, J.J. McClelland, J. Appl. Phys. **114**(4), 044303 (2013)
11. Q. Ji, X. Jiang, T.J. King, K.N. Leung, K. Standiford, S.B. Wilde, J. Vac. Sci. Technol. B **20** (6), 2717–2720 (2002)
12. L. Bischoff, Ultramicroscopy **103**(1), 59–66 (2005)
13. G. Hlawacek, V. Veligura, R.V. Gastel, B. Poelsema, J. Vac. Sci. Technol. B **32**(2), 020801 (2014)
14. D.C. Bell, Microsc. Microanal. **17**, 660–661 (Nashville, TN, 2011)
15. O. Lehtinen, J. Kotakoski, A.V. Krasheninnikov, J. Keinonen, Nanotechnology **22**(17), 175306–175315 (2011)
16. M.A.E. Jepson, B.J. Inkson, C. Rodenburg, D.C. Bell, Europhys. Lett. **85**(4), 46001–46004 (2009)
17. D.C. Bell, M.C. Lemme, L.A. Stern, J.R. Williams, C.M. Marcus, Nanotechnology **20**(45), 455301–455305 (2009)
18. V. Veligura, G. Hlawacek, R.P. Berkelaar, R. van Gastel, H.J. Zandvliet, B. Poelsema, Beilstein J. Nanotechnol. **4**, 453–460 (2013)
19. R. Livengood, S. Tan, Y. Greenzweig, J. Notte, S. McVey, J. Vac. Sci. Technol. B **27**(6), 3244–3249 (2009)
20. J.F. Ziegler, J.P. Biersack, U. Littmark, *The Stopping and Range of Ions in Solids* (Pergamon, New York, 1984)
21. S. Tan, R. Livengood, D. Shima, J. Notte, S. McVey, J. Vac. Sci. Technol. B **28**(6), C6F15–C16F21 (2010)
22. D. Pichard, in *EIPBN* (Nashville, TN, 2013)
23. J. Yang, D.C. Ferranti, L.A. Stern, C.A. Sanford, J. Huang, Z. Ren, L.C. Qin, A.R. Hall, Nanotechnology **22**(28), 285310 (2011)
24. N. Kalhor, S.A. Boden, H. Mizuta, Microelectron. Eng. **114**, 70–77 (2014)
25. M.C. Lemme, D.C. Bell, J.R. Williams, L.A. Stern, P. Jarillo-Herrero, C.M. Marcus, ACS Nano **3**(9), 2674–2676 (2009)
26. S. Nakaharai, T. Iijima, S. Ogawa, S.-L. Li, K. Tsukagoshi, S. Sato, N. Yokoyama, IEEE Trans. Nanotechnol. **13**(6), 1039–1043 (2014)
27. S.A. Cybart, E.Y. Cho, T.J. Wong, B.H. Wehlin, M.K. Ma, C. Huynh, R.C. Dynes, Nat. Nanotechnol. **10**(7), 598–602 (2015)
28. S. Tan, K. Klein, D. Shima, R. Livengood, E. Mutunga, A. Vladár, J. Vac. Sci. Technol. B **32** (6), 06FA01 (2014)
29. S. Tan, R. Livengood, Y. Greenzweig, Y. Drezner, D. Shima, J. Vac. Sci. Technol. B **30**(6), 06F606 (2012)
30. J.S. Custer, M.O. Thompson, D.C. Jacobson, J.M. Poate, S. Roorda, W.C. Sinke, F. Spaepen, Appl. Phys. Lett. **64**(4), 437–439 (1994)

31. S. Tan, R.H. Livengood, Y. Greenzweig, Y. Drezner, R. Hallstein, C. Scheffler, in *ISTFA* (Phoenix, AZ, 2012), pp. 436–439
32. K.E.D. Santamore, J. Orloff, J. Melngailis, J. Vac. Sci. Technol. B **15**(6), 2346–2349 (1997)
33. L. Scipioni, C.A. Sanford, J. Notte, B. Thompson, S. McVey, J. Vac. Sci. Technol. B **27**(6), 3250–3255 (2009)
34. G. Hlawacek, V. Veligura, S. Lorbek, T.F. Mocking, A. George, R. van Gastel, H.J. Zandvliet, B. Poelsema, Beilstein J. Nanotechnol. **3**, 507–512 (2012)
35. T.I. Shu Nakaharai, S. Ogawa, S. Suzuki, S.-L. Li, K. Tsukagoshi, S. Sato, N. Yokoyama, ACS Nano **7**(7), 5694–5700 (2013)
36. J. Berthelot, S.S. Acimovic, M.L. Juan, M.P. Kreuzer, J. Renger, R. Quidant, Nat. Nanotechnol. **9**(4), 295–299 (2014)
37. M. Melli, A. Polyakov, D. Gargas, C. Huynh, L. Scipioni, W. Bao, D.F. Ogletree, P.J. Schuck, S. Cabrini, A. Weber-Bargioni, Nano Lett. **13**(6), 2687–2691 (2013)
38. F. Aramaki, T. Ogawa, O. Matsuda, T. Kozakai, Y. Sugiyama, H. Oba, A. Yasaka, T. Amano, H. Shigemura, O. Suga, Proc. SPIE **7969**, 79691C (2011)
39. F. Aramaki, T. Kozakai, O. Matsuda, O. Takaoka, Y. Sugiyama, H. Oba, K. Aita, A. Yasaka, in *BACUS News* , vol. 29 (2013), pp. 1–8
40. C.M. Gonzalez, R. Timilsina, G. Li, G. Duscher, P.D. Rack, W. Slingenbergh, W.F. van Dorp, J.T.M. De Hosson, K.L. Klein, H.M. Wu, L.A. Stern, J. Vac. Sci. Technol. B **32**(2), 021602 (2014)
41. R.H. Livengood, M. Grumski, Y. Greenzweig, T. Liang, R. Jamison, Q. Xie, Phys. Procedia **1** (1), 143–148 (2008)
42. M.T. Postek, A.E. Vladár, Proc. SPIE **6922**, 69220B (2008)
43. E. I. C. Jr., *Microelectronics Failure Analysis, Desk Reference,* 6th edn. (2004)
44. R. Rosenkranz, J. Mater. Sci. Mater. Electron. **22**(10), 1523–1535 (2011)
45. K. Ura, S. Aoyagi, J. Electron Microsc. **49**(1), 5 (2000)
46. C.C. Ooi, K.H. Siek, K. S. Sim, in *IPFA* (2001), pp. 112–116
47. R. Reiche, R. Kaesmaier, R. Rosenkranz, U. Ritter, S. Teichert, S. Leinert, Microsc. Microanal. **121**, 11–14 (2009)
48. F. Aramaki, T. Kozakai, O. Matsuda, A. Yasaka, S. Yoshikawa, K. Kanno, H. Miyashita, N. Hayashi, Proc. SPIE **9235**, 92350F (2014)
49. R.H. Livengood, P. Winer, V.R. Rao, J. Vac. Sci. Technol. B **17**(1), 40–43 (1999)
50. S. Tan, R.H. Livengood, R. Hallstein, D. Shima, Y. Greenzweig, J. Notte, S. McVey, in *ISTFA* (San Jose, CA, 2011), pp. 40–45
51. M. Rudneva, E. van Veldhoven, S.K. Malladi, D. Maas, H.W. Zandbergen, J. Mater. Res. **28** (08), 1013–1020 (2013)
52. F.F. Rahman, J.A. Notte, R.H. Livengood, S. Tan, Ultramicroscopy **126**, 10–18 (2013)
53. S. Tan, R. Livengood, P. Hack, R. Hallstein, D. Shima, J. Notte, S. McVey, J. Vac. Sci. Technol. B **29**(6), 06F604 (2011)
54. R.H. Livengood, S. Tan, in *EIPBN* (Nashville, TN, 2013)
55. H. Wu, L. Stern, D.C. Ferranti, D. Xia, M.W. Phaneuf, in *ISTFA* (San Jose, CA, 2013), pp. 118–122
56. H. Wu, D. Ferranti, L. Stern, Microelectr. Reliab. **54**(9–10), 1779–1784 (2014)
57. S. Tan, R. Hallstein, R. Livengood, H. Prakasam, L. Patel, O. Nastasescu, C. Scheffler, in *EIPBN* (San Diego, CA, 2015)
58. S. Tan, R. Hallstein, R.H. Livengood, W. Ali, Microsc. Microanal. (Columbus, OH, 2016)
59. F.A. Stevie, C.B. Vartuli, L.A. Giannuzzi, T.L. Shofner, S.R. Brown, B. Rossie, F. Hillion, R. H. Mills, M. Antonell, R.B. Irwin, B.M. Purcell, Surf. Interface Anal. **31**(5), 345–351 (2001)
60. J. Mayer, L.A. Giannuzzi, T. Kamino, J. Michael, MRS Bull. **32**, 400–407 (2007)
61. D. Wei, C. Huynh and A. Ribbe, Microsc. Microanal. **21**(Suppl3), 1409–1410 (Portland, OR, 2015)

62. P. Jung, Nucl. Instrum. Methods Phys. Res. B **91**(1–4), 4 (1994)
63. N.A. Roberts, C.M. Gonzalez, J.D. Fowlkes, P.D. Rack, Nanotechnology **24**(41), 415301 (2015)
64. J.H. Noh, J.D. Fowlkes, R. Timilsina, M.G. Stanford, B.B. Lewis, P.D. Rack, ACS Appl. Mater. Interfaces **7**(7), 4179–4184 (2015)
65. M.G. Stanford, B.B. Lewis, V. Iberi, J.D. Fowlkes, S. Tan, R. Livengood, P.D. Rack, Small (2016)

Appendix A
The ALIS Story

Or... A Funny Thing Happened on the Way to 77 K!

Bill Ward

This is the second iteration of this foreword. The first one was full of scientific jargon and mathematics with accompanying graphs and tables. After proofing the last draft and redacting the trade secrets it just wasn't very readable. More significantly, I realized it was missing something which was very important to me, the human element and the enormous effort it took to perfect something that the scientific community had long given up on. I touched on this topic at the 2011 Applied Physical Society meeting while receiving my award where I was later questioned by several young experimenters about the practical side of the project. In the interest of encouraging the next generation of experimenters, I rewrote this forward to tell a little of the human side of the story which includes disappointments, the lucky breaks and the numerous successes that pointed us in the right direction. We had the enormous good fortune to have been funded for over 10 years, a never ending appetite for success, and a string of breakthroughs that kept us hoping that 1 day we just might solve the mysteries of the Atomic Level Ion Source (ALIS, The single atom version of the Gas Field Ion Source (GFIS).

It's important to note that the main goal of this effort was not to write scientific papers. This was my fourth high-technology startup based on the principal of developing interesting physics into useful products for the scientific community. The papers would come later but only if we were successful in delivering high performance and useful technology to the scientific community.

I was the cofounder of Ion Beam Technologies, Micrion Corporation, and ALIS Corporation, all of which developed and supplied Scanning Ion Beam instruments to the scientific community. I was also on the founding team of Varian's Electron Beam Lithography division. These scanning beam instruments had many things in common including a source of charged particles which was usually the limiting factor in the

B. Ward (✉)
Inventor and Entrepeneur, Boston, Massachusetts, USA
e-mail: billwardmail@gmail.com

© Springer International Publishing Switzerland 2016

G. Hlawacek and A. Gölzhäuser (eds.), *Helium Ion Microscopy*,
NanoScience and Technology, DOI 10.1007/978-3-319-41990-9

overall performance of these systems. I was deeply involved in these various source technologies which provided the underpinnings needed to attempt this final scientific effort of my career.

I had the great fortune of starting my profession at Extrion, a particle-accelerator company founded by Dr. Peter Rose which developed and manufactured ion-implantation equipment for the semiconductor industry. These mass-separating accelerators were a variant of the Clautron that was developed by Ernest Lawrence to isotopically purify uranium for the "Manhattan Project" during World War II. All of us at Extrion considered Dr. Rose a mentor who provided valuable practical advice for us young experimenters which would later become pivotal to the success of the ALIS source.

In 1996 Dr. Rose received the National Medal of Technology and Innovation from President Bill Clinton. Earlier, in the 1960s, Dr. Rose was the Chief Scientist at High Voltage Engineering which was founded by Dr. Robert Van de Graaff, one of the most famous physicists of the last century. Van de Graaff's company provided both high voltage systems and particle accelerators to the scientific community that were pivotal in the understanding of fundamental physics. Earlier still, in 1924, Van de Graaff enrolled in the Sorbonne University in Paris where he attended lectures by Madame Curie on radiation. Apparently, his exposure to Madame Curie, whose family accumulated 5 Nobel Prizes, set in motion a lifelong interest in charged particle accelerators. In 1893 Madame Curie worked in the industrial laboratory of Professor Gabriel Leppmann who received the 1908 Nobel Prize in Physics for color photography based on the interference phenomenon. In 1872 Leppmann was mentored by Gustav Kirchhoff who studied and later coined the term "Black Body Radiation". In 1862 he created the famous "Kirchhoff's Law". And finally, in 1847 Kirchhoff attended the lectures of Franz Ernst Neumann whose study on the specific heats of compounds included what is now known as "Neumann's Law". He is also known for the "Neumann's Principal" of crystal physics and his equations in optics closely resembled those of Agustin-Jean Fresnel.

Now I'm certainly not trying to compare our achievement with the contributions of these great scientists. I explain this amazing lineage to make a point about how practical knowledge is passed down from generation to generation in the world of physics. Most scientific knowledge is disseminated via technical papers in scientific journals. However, the actual knowhow, the practical knowledge and the all-important gut feel about physics is often transferred by word of mouth. Dr. Peter Rose often spoke of his experiences with Van de Graaff. He also repeated a few of Van's stories about Curie. Peter showed us the way around in the world of charged particles and I am deeply grateful. If it were not for this incredible lineage that provided the combined practical knowledge of 150 years we wouldn't be writing this book today!

A.1 Ion Sources

A great many ion sources were developed in the last century for applications and systems too numerous to mention here with the exception of the Scanning Ion Mi-

croscope (SIM). With the advent of the Liquid Metal Ion Source (LMIS), this microscope became practical and finally produced an image resolution on the order of a few nanometers.

The SIM produces a focused beam of ions that is raster-scanned on the surface of a sample, much like a scanning electron microscope, producing gray-scale microscope pictures. The brightness of each pixel in the picture is determined by the yield of detectable byproducts produced by the ion beam collision with the sample. These now include secondary electrons, secondary ions, Rutherford Backscattered Ions, and photons of specific wavelengths which are produced from the decaying processes of electrically excited atoms.

Due to the sputtering nature of these heavy atoms, the SIM can also be used to micro-machine structures into the surface of the sample. With the localized addition of etchant gasses, this process can be greatly enhanced. The localized adding of materials to the surface is accomplished by introducing other unique gasses near the surface that interact with the ion beam. In summary, the SIM can be used much like a 3D printer to create micro structures on the surface of a sample which is particularly useful in the design and failure analysis of semiconductors.

The LMIS has served the scientific community well for the past 40 years but there are certain downsides and limitations of this source for which there are no workarounds. The Brightness of the source is limited by the physics of its ionization processes which, in turn, limits the microscope's usable resolution to a few nanometers. Furthermore, the destructive nature of the heavy ions precludes its practical use on sensitive materials such as biological samples. Finally, heavy ions have a very short implantation range producing secondary electrons in the bulk close enough to the surface to escape and be collected by a secondary electron detector. The bulk area of collectable secondary electrons is sometimes larger than the focused ion beam dimension and often limits the resolution of the microscope image.

A brighter ion source of light ions could overcome these limitations and, by chance, there was a candidate ionization process that already existed in the Field Ion Microscope (FIM). The FIM is often operated with helium as the gas species but the Brightness was more than 100 times less than the LMIS.

The desire to solve the brightness problem quickly consumed the minds of many of us in our field and so begins the extremely difficult and often disappointing search for the "Holy Grail"... the brightest source of ions known to mankind.

A.2 The Field Ion Microscope

The Atomic Level Ion Source (ALIS) or Gas Field Ion Source (GFIS) is a variant of the Field Ion Microscope and has yet another interesting lineage.

The inventor of this microscope, Dr. Erwin Wilhelm Müller, studied under the famous Nobel Prize lauriat, Gustav Hertz. Hertz received his Ph.D. from Heinrich Rubens who conducted crucial experiments for Max Planck who later received his

Nobel Prize for his work in quantum physics. And, Planck studied under the famous physicists Hermann von Helmholtz and the aforementioned Gustav Kirchhoff.

Müller first invented the electron Field Emission Microscope in Germany in 1936 which consisted of a highly sharpened needle that was pointed at a phosphor coated plate located a few centimeters away in a vacuum chamber. Negative High Voltage was applied to the needle and electrons were field-emitted from the apex of the needle. Due to the shape of the electric fields that were defined by the sharp needle, these emitted electrons projected radially at high angles that collided with the phosphor plate producing an image of the apex. Bright to dark gray level variations on the phosphor corresponded to differences in the work function of the localized tip materials and geometries. Amazingly, that microscope produced a resolution in the order of a few nanometers but it was not a practical general purpose microscope. But it was a great apparatus that could be used to understand the principles of electron field emission processes and later enable the practical creation of the Field Emission Scanning and Transmission Electron Microscope used today.

Müller would later continue this work at Pennsylvania State University where he and Kanwar Bahadur eventually reversed the polarity of the voltage applied to the needle and added a small amount of gas into the vacuum. Ions were created at the apex atoms of the needle via the quantum tunneling process, the ions were projected to the phosphor plate producing a gray scale image that was modulated in intensity by the variations in the localized tunneling yield. These variations were primarily due to atomic size differences in the surface geometries which in turn varied the electric field. This microscope produced higher resolution but not yet at the atomic level. The gas atoms being ionized were at room temperature and their thermal vibrations confused the origin of the ion which formed an equally confusing/blurred image on the phosphor plate.

On the autumn day of October 11, 1955 Müller and Bahadur cooled the needle before turning on the instrument. Sitting in a pitch dark lab, they slowly increased the high voltage potential and within minutes saw an ordered array of dots on the screen that directly corresponded to the expected ordered array of atoms on the apex of the single crystal needle. I can only imagine what must have gone through their minds that day knowing that they were the first two humans to see atoms.

Müller and Bahadur should have received a Nobel Prize in physics for this incredible discovery as did other microscope inventors. Perhaps they will someday.

The Field Ion Microscope would later be modified to include a mass detection system and computer automation providing 3 dimensional models of compounds with atomic resolution.

A.3 The Search for the Holy Grail

As mentioned above, the Field Ion Microscope includes an exceedingly sharp needle that emits multiple ion beams from individual atoms on the surface of the apex. Due to local electric fields near the needle tip, these individual ion beams are radially

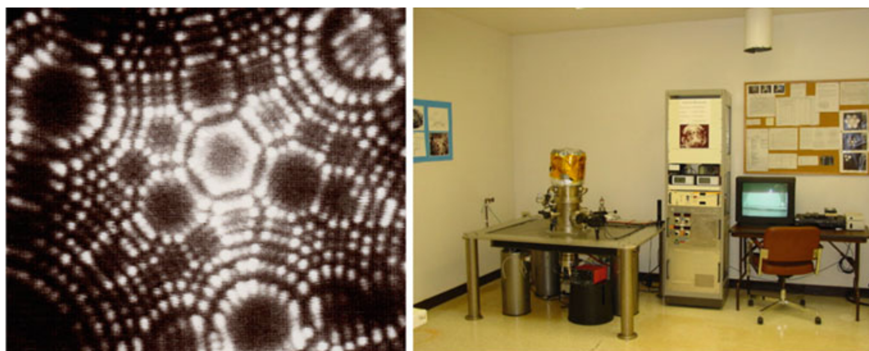

Fig. A.1 (*Left*) Typical FIM image of (111) Tungsten. (*Right*) Field Ion Microscope ALIS source test stand

separated by large angles before striking the phosphor plate for viewing. This angular magnification of over 100 million allows an instantly observable image of the atoms on the needle surface (Fig. A.1).

The sum of the current from all of the ion beams was encouraging however the ability to recombine 100 of them via an electrostatic lens into a coherent spot was thought to be physically impossible. From an optics perspective, the projected high-angle rays of each ion beam do not appear to originate from a small area, an important factor in source brightness. Furthermore, electro-optical lens aberrations in a typical optical system are severe at these high angles making it impossible to properly recombine the 100 or so individual ion beams even if they had appeared to have originated from a small area, or point source.

If one could modify the rays of all of the ion beams in such a manner that they appeared to originate from a small point the problem would be partly solved. And the only possible way to achieve this goal was by modifications to the end form of the needle which, in turn, dictates the shape of the electric fields that project the ion beams. Furthermore, these improved ion trajectories needed to be at fairly low angles to minimize the lens aberration.

A prevailing thought process was set in motion based on Müller's and other's photographs of extremely small needle tip radii. The typical FIM images found in text books at the time often included 100–200 atoms, usually of single crystal. In the 1960s Müller produced at least a few FIM images that included only a few atoms. Müller and others observed changes in the shape and apparent sharpness of a FIM tip before and after a heat process providing indisputable proof that in-situ modification to the apex end-form was possible. One photograph was comprised of a trimer which he created by heating the needle before imaging but he was unable to repeat the results. This evidence was encouraging to many of us because the angles of the beams seemed to be small, the number of beams was less and if anything was going to work, this was it. Further evidence also existed from 50 years of Cold

Electron Emitter research. It was well established that the shape of an emitter could be slightly modified by a heat or a heat+ electric field process.

The search for an ideal/magical end-form began. One that would produce a set of ion beam rays that could be focused into a small spot and a reproducible, nondestructive, in-situ process to create it.

A.4 The Gas Field Ion Source

Several attempts were made to solve the problem of combining the ion beams. One created a small hemisphere at the apex to help focus the rays better, creating a smaller virtual source.

Other processes revolved around the idea of creating a very sharp emitter with only a few atoms to be recombined.

Although randomly produced, these two techniques were now producing interesting results but neither would prevail in the end. However much was quickly learned that cast a very serious cloud over the whole idea. The source current was unstable (noisy) and the lifetime extremely limited.

Although Müller and others were not trying to perfect the GFIS source, they did see these effects in the 1960 s when they were creating and imaged extremely sharp needles. They had already explained that such an end form would never be stable for long periods of time... Let me explain.

If one uses Helium in a FIM to image the atoms of a high refractory metal, such as single crystal tungsten, a very stable real-time image is produced. 100 or so atoms in a perfect crystalline order seem to shine bright and stable on the screen. It was quickly noted that the distance between the needle and the screen determined the magnification of the image. It was also noted that changes in the tip radii would vary the magnification and also how large the image area was on the screen.

Under certain conditions the FIM image would not fill the entire screen. This is simply explained by the electric field gradient produced by a very sharp needle. The field is high enough to ionize the helium near the apex but falls off rapidly at the edges of the radius. The resulting image on the screen is bright in the center and dims rapidly towards the edges of the image. Again this change in brightness from the center to the edge is an indication of how high the field was at each surface atom near the apex. Beyond the edge of the visible image the electric field is still extremely high, just not enough to ionize helium. It eventually becomes low enough that even the vacuum background gasses will not ionize. At a low enough field, the background gas atoms can interact with the needle's surface atoms.

Müller and many others likely observed strange behaviors at the edges of this type of FIM image. The dim atoms would sometimes blink on and off in a random fashion. They would sometimes turn off forever. And new atoms seemed to appear. This was quickly explained by the random addition or subtraction of add-atoms, or contaminates, in the vacuum system. It was also the first observation of a new area of science, high electric field enhanced chemistry.

This phenomenon was little more than a nuisance to the FIM scientists because it had little effect on the majority of the image. However, it was most likely noted that it was always there regardless of the tip radius. Also likely noted was that the edge fluctuations increased in intensity as the radius of the apex decreased.

All of the GFIS experimenters were seeing the same thing that Müller saw back in the 1960s. The chemical interactions with the background gasses caused the current from the few atoms that were emitting to be unstable. Unfortunately, these few atoms would soon disappear into the vacuum via the field enhanced chemical reactions that destroyed the supporting atoms that they were attached to.

50 years of FIM microscopy combined with the GFIS efforts of the late 1900s provided the inescapable reality that a GFIS type source created from a highly sharpened needle would not work. . .ever. The random mobility of add-atoms and the field enhanced corrosion of a small radius tip created a noisy source with a very short lifetime. Not to mention the yet unsolved problem of combining the multiple ion beams.

However, the added hemispherical approach mentioned earlier was showing some promise. The Max Planck Institute had reported reasonable brightness and lifetimes but had yet to form a small enough focused beam to prove the ability to combine the ion beams.

A.5 The Micrion Effort

As a co–founder of Micrion, I was very interested in new source technologies for our focused ion beam products. The published work on the hemispherical GFIS tip was enticing. We were well connected with government funding sources and after a few meetings with the Max Planck institute we licensed this source technology and began what would become a 10 year project.

William Thompson led the research team at Micrion which soon built the most complex microscope in the world! It combined the complexities of a standard gallium ion microscope and Field Ion Microscope into one coherent package. . .. An engineering feat that later provided the test vehicle of the ALIS source (Fig. A.2).

Thompson's program was successful in so many areas. The combination microscope was a technical marvel, his team was extremely motivated, and within a couple of years we were testing the properties of the hemispherical source.

The creation of the hemispherical end-form was tedious, time consuming. . . and seldom successful. The equipment was working perfectly, his team was trained by the experts at Max Plank, but there was something missing. After years of effort we concluded two things. We were not able to stabilize the hemispherical process enough for it to be a commercial success and we were not able to recombine all of the ion beams from the hemisphere into a commercially usable probe diameter with adequate current.

Bill's group eventually abandoned the hemispherical approach and began to experiment with the sharp needle. Numerous recipes were attempted which infrequently

Fig. A.2 Prototype GFIS Ion Microscope

produced exceedingly sharp sources including at least one that had a trimer on the top shelf. However, we were still attempting to combine multiple atoms into one focused beam because the mission of the program was to produce as much current as possible. Unfortunately, we were unable to escape the early findings of Müller and others concerning the fluctuations in current due to add-atoms and the field enhanced corrosion which destroyed the tip, sometimes within minutes. We also had the same unsuccessful experiences as Müller concerning a repeatable sharpening process.

Millions of dollars, thousands of man hours and too many late nights of effort were invested to just give up! The engineering of the source test chambers was a complete success, the team perfectly executed hundreds of experiments but we just couldn't force the physics into complying with our dreams.

Something or a list of somethings was getting in our way.

A.6 A Funny Thing Happened on the Way to 77 K

This is where I came into the picture. Bill Thompson and I were friends of 30 years and I just couldn't accept that his team's great work was going to be abandoned. I relinquished a management position and went back into the labs for what would be

my last hands-on science project. I freely admit that I didn't have the slightest idea what to do, where to go or how long it was going to take... but I was going try. I owed it to Bill, his team, and the company.

Now, I'm the new guy in the lab, asking stupid questions, breaking equipment and burning up ion sources one after another. Within a few weeks I had caught up enough to understand what had been learned and soon got that sinking feeling that I wasn't going to win this time... this was a big mistake.

It is one thing to sit in a program review and think you understand a technology. It is quite another to see firsthand the enormous effort and technology needed to solve this problem. William and his team had created the perfect sets of equipment to make progress but Mother Nature was standing in the way, her arms folded, smiling daggers at us. She was not going to give us a clue as to how to get around her.

Lucky Break #1

After a couple of months of conducting experiments in the GFIS lab I was starting to go nuts with the sound of the cryo-compressors which cooled the various GFIS sources we were experimenting with. They produce a loud squishing sound about every second which is extremely unnerving after many hours of exposure.

We used cryo compressors for good reason. Everyone knew that the colder the tip was, the more current it produced... it's obvious to those skilled in the art of FIM and GFIS. It was also well known that one could work at higher temperatures and still get meaningful results. Just as important, a source could be cooled by LN2 ten times faster than a cryo compressor which allowed faster turnaround times for our experiments.

So... 1 day we turned off the brain-pounding cryo compressors and began to use liquid nitrogen. This resulted in an increase in the source operating temperature from about 10 to 77 K. The lab was quiet for the first time in years, the constantly failing experiments were a little less depressing and, unknowingly, for the first time in years we had just solved one of the major source instability problems!

We were not working on source noise at the time and wouldn't actually appreciate that this pivotal moment had even happened for many months to come. I'll come back to this later on.

Lucky Break #2

All of our efforts were centered on creating recipes to sharpen a source. At first, we didn't bother retracing much of Müller's earlier FIM efforts. We thought we knew enough about his work, it was old hat technology and who cared about watching a few hundred dots on the screen of an image intensifier. But we clearly needed to do something. Stepping back in time and repeating more of Müller's early experiments now seemed like an appropriate thing to try.

For the next few months we experimented with a number of FIM tips that were first electrochemically etched sharpened via a process well established in the FIM community. Every source needle was photographed in an SEM before installing it into the FIM to record its end-form. A FIM tip needed to have a minimum radius in order to operate properly.

The typical experiment included taking a FIM image, the execution of a sharpening procedure, and then imaging the source via FIM again to measure the change in its shape. This process required the removal and installation of high voltage cables that were directly attached to the source. Unfortunately, this cable exchange and the unusually high heat and voltages that were applied resulted in high-voltage arcs that often ripped the end of the needle off.

One day we had a source that seemed to defy high voltage arcs like no other. After later examination in the SEM we discovered that its general shape was much different than all the others we had tested. A quick study of the atomic binding forces of crystals in the presences of ultra-high electric fields provided the explanation.

This was the first step forward in the end-form design of the ALIS source... it was a significant breakthrough that is still a trade secret and the backbone of the ALIS source used today.

Lucky Break #3

The sharpening experiments of the radius portion of the end-form provided scattered knowledge that didn't allow us to formulate a clear path for experimentation. Yes we could change the shape of the radius and observe these changes via the FIM image but we really didn't seem be making orderly progress. To shorten this learning curve we needed to figure out a way to increase the number of sources that we tested per week. The actual experiments often lasted just seconds or minutes but the vacuum pump-down times usually took a couple of days.

The rate of discovery in this empirical process was directly proportional to the number of source experiments conducted. We set a goal to pump down and test one source per day.

We and all of the other FIM experimenters were totally convinced that Ultra–High Vacuum was absolutely mandatory for proper FIM operation. We all thought that these conditions provided less ad–atoms and minimized the nasty field enhanced corrosion of the tiny tip radius. Well, all of us were right... and wrong... at the same time.

To decrease our source cycle time to one source per day we decided to forget about reaching Ultra-High Vacuum level and turn on the source at pressures near 10-e-8 Torr. We had adjusted a variable in the exact opposite direction that any of us would have thought productive! We were expecting that the relatively poor vacuum might ruin our experiments.... Just the opposite occurred!

It was a eureka moment! Definitely a breath of fresh air after living in a cave for months. It was the lucky break we needed and it happened just at the right time!

As expected, the additional background gasses did have a negative effect at the periphery of the FIM image, however these gasses also dramatically effected the sharpening recipes. For the first time we were able to repeatedly modify the radius in a somewhat reproducible manner. We weren't making trimers yet but we could clearly change the end form in such a way that the current in the ion beams was considerably greater in some areas with respect to others on the apex.

It is important to point out that a Gas Field Ion Source is a gas-starved source. All of the physics involved with the creation of the conditions necessary to ionize

helium are somewhat easily achievable. Also it was known that the current from the ion beams was directly proportional to the helium gas pressure and inversely proportional to the source temperature. Sadly, if the pressure is increased too high the vacuum high voltage components will arc and destroy the source. It is absolutely impossible to increase the pressure enough to produce meaningful currents in all 300 or so atoms of a regular FIM tip. Selectively changing the end form so that only a few atoms emitted was the key! The source is gas starved but we could now control how many atoms were emitting the total current by stealing the electric field away from other atoms via end-form modification. Stealing their field meant stealing their gas!

At this point we could repeatedly create end-forms that concentrated the current from 100 atoms into about 10 or 20. We were making progress in the FIM but when we tried to pass the 20 atoms through the optical system in our Helium Ion Microscope it was a disaster. The source ion ray angles where still too high, the lens aberrations were awful, the source life was a few hours, it was still noisy, and the pictures were next to useless.

Regardless, we had made a step forward. We could control the end form to a large degree, we understood the role that background gasses played and we had stumbled onto the most profound thought process of the entire source development project!

The source end–form had to do two distant jobs that seemed to be in violent disagreement!

Let me explain. Earlier I discussed how the edges of the FIM image flickered due to add-atoms and field enhanced chemistry. However the centered portions of the FIM picture were very stable. This is easily explained when using helium as the imaging gas because helium requires a higher field to ionize than any other gas. Neon ionizes at about two thirds of this field and the rest of the chemically active gasses of concern ionize at about one half the field of helium. No gas atoms can reach the surface of the tungsten in an area where the field is high enough to ionize helium, these atoms will ionize and depart the area way before they touch the surface. This was well know and understood long ago. And again, as the electric field falls off at the edges of the radius to the point that background contaminants are able to land and create flickering as described earlier.

On one hand, we needed to sharpen the source to concentrate the area of emission into a few atoms and, at the same time, we needed a larger source radius to tailor the electric field in such a manner that add-atoms and field enhanced corrosion would occur far away from the ion-beam producing atoms.

This was an overwhelmingly awful moment for me. It seemed that the source had to be both sharp and dull at the same time.

It was time to pull the plug again. Shut down the lab and give up! But we just kept on trying anyway, hoping for a miracle.

Lucky Break #4

We continued to experiment with the 100 to 20 atom field concentration recipe for a few more weeks but had very little hope of success.

Then it happened. During the next 3 s the first crude version of the ALIS source building recipe was born!

We had to add an extra step in our experimental procedures because we were now cooling down and running the sources in a poor vacuum which was dominated by water vapor. Just before each experiment we had to apply a little filament current to the tip to evaporate the ice that had collected on the tip radii. It was only heated to the first sign of a visible red glow and then immediately turned off.

After thousands of experiments on hundreds of sources I made the mistake of not checking what the filament current was set to before pushing the on switch. It was unknowingly set to its near maximum. I flipped on the switched and bent over to look through the little vacuum window to watch the needle as I slowly turned up the filament knob. To my utter surprise the entire vacuum chamber was lit up with white light from the ion source filament which looked just like a 60 watt light bulb!

I had destroyed yet another thousand dollar ion source in seconds. The guys that change the ion source were going to be mad at me... again. It was time for a coffee break.

A half hour later I went back into the lab to vent the system but first decided to turn on the FIM and see how badly I had melted the source.

Within very few minutes I was imaging a trimer which had extremely high current! I ran and got the crew and we watched it for more than an hour. They asked the all-important question... what was the recipe?

I didn't know what temperature it had reached nor how long it was actually on but that didn't really matter. We figured it out in a few more weeks. We had a path to go down and within a month we were sending three atoms down the optical column of the helium ion microscope producing the same miserable pictures as we had for the last 5 years.

It was absolutely heart breaking.

We could now routinely build the trimer end-form like no one on the planet could do, it produced reasonable current and it was absolutely, stunningly useless! The combined ion beams from the three atoms was the best work we had ever done. It was time to quit once again... I just couldn't say the words out loud.

Lucky Break #5

I know what you're thinking, why didn't the single atom idea present itself immediately when we had just three atoms. Well, we were just a little too tired and depressed by this time, our funding was about to dry up and the goal of the project was both spot size and spot current. Throwing away 2/3 of the current didn't immediately seem like the right road to go down. Remember, until the trimer came along we were always sending 5–20 atoms down the optical system.

Then it happened! I remember that day like it was yesterday. I was sitting in the lab asking myself the same ridiculous question over and over just like we had done thousands of time before. How can we get a bunch of point sources to recombine into one coherent bundle? Then the words just came out. Let's just send one atom down the beam line and see if the focusing optics are working properly. We tilted

the already running source assembly to its extreme positions and sent only one atom down the beam line.

The next few days were glorious! Finally, we had in our hands the beginning of a practical Helium Ion Microscope!

The single atom source immediately produced startling resolution! We reached the design specification of the optical system and soon began numerous application experiments. We proved the HIM's ability to image low "Z" materials, experimented with Neon, and began to demonstrate that the surface interaction volume seemed small.

The use of a single atom's current of a field ion source produces such high brightness beams because of the very small area of the source, from which all of the flux originates. For the ALIS HIM source, the physical source is three atoms (the trimer) on the tip but only one of the atoms is projected into the beam line. As the size of the ionization disk is on the order of 1 Å, the 30 pA beam emitted corresponds to a particle flux of 1.9×10^{24} ions/(cm^2sec). No other ion source technology known can produce such a flux. If one imagines the possibility of a fantasy emitter scaled up to the centimeter size with the beam accelerated to the typical 30 kV, the power emission from the source would be 9 Gigajoules!

When we now use this beam to create a realistic focused probe, say 1 pA at 30 kV into a 0.5 nm spot, the impinged energy density is about 12 MJ/cm^2. By comparison, the sun has a paltry 6 kJ/cm^2 emission at its surface.

We had finally solved the problem of combining multiple ion beams from the GFIS into one by giving up on that crazy idea altogether.

Back to reality... It was still too noisy and the life time was only a few hours at best.

Back to Lucky Break #1

Now that we had a bright source it was time to step on the accelerator. All of our work with the single atom source was conducted at the Ln2 temperature of 77 K. Everyone knew that we would produce 10 times more current at 10 K. So we did it...and it was a total failure!

We spent a week resurrecting the brain-pounding cryo–compressor cooling system and turned on the source when it reached about 77 K. It ran just as well as before with the LN2.

Then... as it got colder the source noise got greater. It got a little colder and the source was destroyed.

We tried over and over with the source colder and colder.... It was an absolute disaster.

It didn't take long to realize that the source would never work well at these lower temperatures because we had begun to both freeze and liquefy the various background gasses in the vacuum system on the needle. These unwanted materials were attracted toward the apex of the needle which created violent processes in an environment that was already at the extreme physical limits of stable matter.

We had found yet another source noise problem that likely affected all of the early work experimenters!

We still didn't have a commercially acceptable ion source. But we found out one more reason why the source was unstable.

A.7 Micrion/FEI Merger

About this time FEI and Micrion merged into one company. The Helium Ion Microscope was considered a failure because it didn't produce enough beam current for micromachining (We all thought at the time that Nano amps were necessary in a commercial product). There was little interest in solving the final noise and lifetime problems of the ALIS source... and no one really knew how important the Helium Ion Microscope product would be to the scientific community.

After many thousands of man hours and millions of dollars over an 8 year period we were able to create a reasonable end form. We had solved the multiple beam issue via the single atom source and produced a few amazing images that demonstrated the usefulness of the Helium Ion Microscope.

All that being said, we still didn't have a commercially viable ion source. The end form was likely no different than the ones that Müller and others accidentally/randomly built so many times before.

It seemed we were now able to almost perfectly reproduce an end–form that was commercially useless.

A.8 ALIS Corporation

FEI had two choices, shut down the lab and sell the equipment to a local high–tech scrapyard company or allow me to take it all and form a new company. They chose the latter and were extremely helpful in setting up the company. We seed–funded the ALIS startup with equal funds from myself and FEI which allowed us to operate for another 2 years.

We managed to bring all of the equipment back on line within a month and began the search for venture capital investors. Surprisingly, the first phone call produced a meeting in 10 days and a scramble began to get a source running in the experimental Helium Ion Microscope.

These next few days were crucial to the success of the program. If we could get the HIM running it would mean everything! We burned up 2 sources in the first few days and finally got the third one installed the morning before the visit. However, there was one piece of the microscope that we didn't have time to install.... The helium gas filtration system.

Lucky Break #6

The helium filtration system was an assembly about 3 by 6 feet in dimension. It included four different types of high technology filters that removed unwanted con-

taminants from the already purified helium. Everyone knew that this $100k assembly was the key to the successful operation of the ion source and without it the source would likely fail in a few minutes or seconds.

We were all wrong yet again.

With less than a day before the venture capital visit I made the decision to not install the filtration system and instead connect the helium gas directly to the source assembly. We just didn't have the time to install and debug this massive and complicated unit. I figured the source might run for a minute or two and that would be enough to put on a show.

The investor arrived and the visit was going perfectly, we dazzled them with power point slides, put on a great show with the Field Ion Microscope test stand and moved over to the last part of the show… turning on the HIM and taking a few pictures. With that awful feeling of a failure about to happen, I turned up the helium pressure on the source and there it was, a perfect trimer! Within seconds we took a single picture and moved the investor over to the next part of the lab tour. We just knew the trimer wouldn't last long enough to take another.

We said our goodbyes to the investor and went back in the lab to shut down the HIM for the night but to our surprise, the trimer was still there! And, the noise was even less than before…. NOT greater!

In fact the source ran for the next 12 h! The noise was the best we had ever seen! We quickly came to a hasty scientific conclusion that the old gas filtration system must have been introducing a contaminant into the helium before it was delivered to the ion source. We quickly blamed the chemically active getter type filter which provided a perfectly good arm-waving argument! It was so believable we accepted this as a scientific fact and ran the source for the next 2 years without a filter. As mentioned earlier, we knew the source did a fair amount of filtering itself and we soon discovered a way to improve it.

Before we discuss the last breakthrough I need to come clean about the getter pump arm-waving theory. We were wrong yet again.

About a year later we needed a 3 foot length of high-vacuum line to build another source test stand. We had already cannibalized much of the unused helium gas filtration system and decided to use its output line for our experiment. We removed it and immediately tried to flush alcohol through it to remove any dust. To our great surprise, no alcohol went through!

That three foot piece of flexible vacuum pipe was the exit line in the gas filtration system which all of the super purified helium passed through before it reached the ALIS source. Calculations clearly showed us that the 99.999 % pure helium from the gas bottle should have been cleaned another two decades before it reached the sensitive ion source… and it likely was! However, there was a wooden cork inside the middle of the pipe that was left there from the day it was manufactured 10 years earlier! It was deep inside the pipe, you couldn't see it with the naked eye, and was used to keep the inside of the flexible pipe free of dust when it was shipped. It had slipped into the pipe before we received it.

Unknowingly, we had spent 8 years using dirty helium to conduct all of our HIM experiments. God only knows what chemicals/gasses were emitted from that wooden cork into the perfectly filtered helium.

That being said, if it weren't for the dirty helium we probably wouldn't have thoroughly understood what end-forms would work well in the presences of background gas contaminants.

The Last Lucky Break

Christmas was coming soon and I didn't want to come by the lab every day to fill the LN2 Dewar. Also we needed to document that the source could survive at least 12 h. It was the minimum time needed to claim it a commercially viable source.

I bought a $50 web cam that included time lapse software, pointed it at the screen to watch the trimer and a light bulb near the screen that showed when the Dewar filled to make sure it was working properly.

As expected, the trimer was gone the next morning but the web cam was still recording in the time lapse mode. I reviewed the 1 min movie that recorded 12 h of actual source operation to make sure the LN2 light came on off. Yes the LN2 light was blinking. But there was something else in that movie that literally changed everything we knew about the ALIS source.

I played the movie over and over and over. Something was happening to the end form of the source outside of normal human perception time and it was extremely important! We had seen hints of this over the last 8 years while watching the screen in real time. It just never occurred to me that the secret to solving the source lifetime problem was sitting on the computer screens for all these years. It was just happening so slow that a human couldn't perceive it!

The message in the video was extremely subtle. One needed the experience of thousands of experimental hours to even pick up on its meaning. But, after a while we realized it was the ion source equivalent of the *Rosetta Stone*. We finally understood how the source actually worked and were immediately convinced that the final lifetime and noise problems were solvable.

During the next few months I completely redesigned the end-form.

We were now adjusting the position of single atoms with ease much like a child playing with a stack of building blocks. In order to communicate with each other in the lab we give names to the atoms which identified their unique behavior. Some names already existed such as Ridge and Edge atoms but we needed a few more such as *Squatters* that described Add-Atoms that were permanently there and emitting an ion beam. *Blinkers* or *Site Swappers* which described one or two adjacent atoms that would blink on and off due to *Hidden Visitors*... Ad–Atoms nearby that were dark but still affected the electric field. A *Flower Shelf* and a *Trimer Shelf* which described the atomic arrangement of every other atomic shelf in the (111) plane of the bcc tungsten crystal. *Field Takers* and *Field Makers* described special end–form contributor atoms that, due to their position, provided special/unique functions. There were another dozen or so names as well which described the overall source behavior as a function of the end-form changes that are still a trade secret.

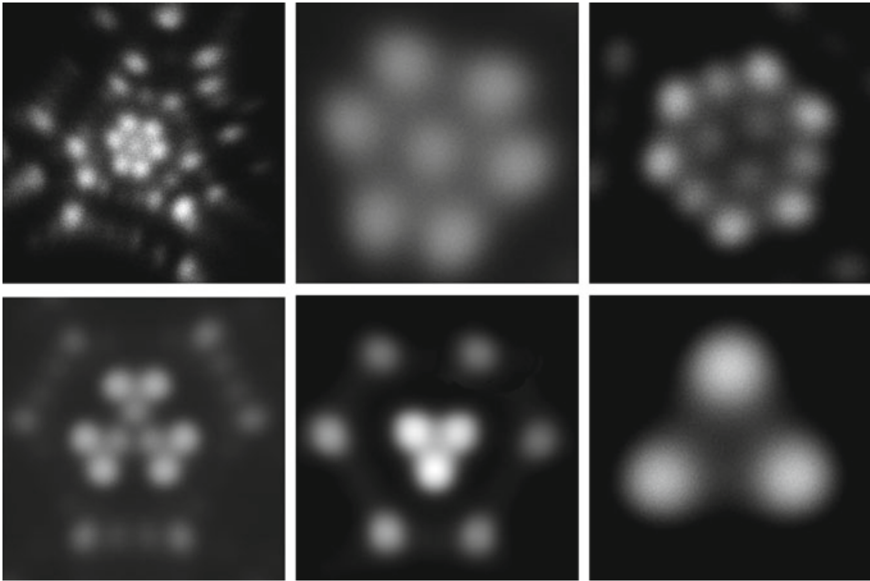

Fig. A.3 Various atomic end-forms that were considered

Needless to say, we had now developed an intimate understanding of the role that each and every atom played at the end–form. And, we had a vocabulary to communicate why and how it worked. Much more importantly, we could describe a very simple source-building recipe to a skilled technician that was not fluent in our crazy new language.

We finally knew how many end-form features were necessary, how to create each one, and how they played together in an almost magical way. We had a commercially viable source of ions and a practical Helium Ion Microscope was now possible (Fig. A.3).

During the next 18 months I conducted numerous application experiments. Due to its optical design, the HIM test microscope could only produce a few nanometers of resolution but surface interaction experiments with various materials were still possible. We soon observed the apparent transparency of thin materials and quickly modified the HIM into a crude Transmission Ion Microscope. Crystallographic contrast, elemental contrast and the lack of charging effects were noted. Rutherford Backscatter Ion images were successfully produced and unexpected ion stuttering yields were documented. Side–by–side SEM to HIM comparison were made using our high resolution SEM. We experimented with other gas species and continued to measure the robustness of the ALIS source.

After 2 years of research at ALIS we raised venture funding and soon created the first commercially viable Helium Ion Microscope. ALIS was then acquired by our friends at Carl Zeiss.

A.9 Conclusion and Final Thoughts

This multivariable problem strikes me as a perfect example of how much progress can be made via the empirical process given enough time, funding and desire for success. Although not nearly as important as the invention of the light bulb, we did get a little feeling of what it must have been like when Edison was trying to find the right material for a filament.

The reason that it took over 10 years may not be obvious from this story. Yes it's just a little needle pointing at a flat plate. However, the scientific apparatus needed to provide the environment that allows this phenomenon to occur is at the extreme practical limits of what we understand about applied physics and chemistry. The understanding of thermodynamics at the macro and micro level, quantum tunneling processes, the transportation of gases from ground to high voltage, the strange behavior of dielectrics at cryogenic temperatures, the study of extremely high electric fields at the atomic level, the inescapable flirtation with surface physics and the incredible battle against the violently destructive nature of field enhanced chemistry had to be well understood before that little needle could perform its magic trick on that little plate.

I intentionally didn't include the results of thousands of successfully executed experiments that were conducted... most of which ended in failures or dead-ends. However, it's extremely important to note that each experiment added to our experience in such a way that we could appreciate the so–called lucky breaks when they occurred. Peter Rose would often say "just do something, even though it's likely to fail, at least you will learn well one more reason why it won't work"

When we first looked at this multi-variable problem we designed experiments to take us down a best guessed path. We knew that the only possible solution to the problem was the design of a somewhat magical end-form. However, like all the other experimenters, we "went after the physics-monster with a sledge hammer rather than just asking the bastard for a dance."

I got that expression from an old physicist many years ago that was desperately trying to explain to me that the best answer from any empirical work is always the simple one, the elegant one, the natural one. He went on to say that the empirical process is all about learning and not about building. "When you learn it all the building part will be simple". And, in the end, it was.

The numerous complex shapes of the ALIS end-form is somewhat akin to a physics ballet at the atomic level. Nanometer mechanical shapes sing in perfect harmony with quantum physics in an extremely violent physical environment where matter itself can barely exist. But, Mother Nature allowed at least one end–form to survive there... and we found it.

At the end of this story... experimenters from many scientific disciplines can now see the small world through a new set of glasses. This was our dream, this is what kept us going through failure after failure for over 10 years.

At the age of 62, I still feel like a little boy every time I look into a vacuum window and see 3 tiny atoms sitting on top of that needle! To think that just one of those three

atoms is the sole reason an entirely new type of microscope is now possible still humbles me to this day.

Finally… there is really is no such thing as a lucky break in physics. Surprising and unexpected answers present themselves to those asking the challenging questions long and hard enough.

Best of luck with your experiments. I can't wait to read your story!

Bill Ward

Index

A
Abell-Tersoff formalism, 74
Aberrations, 249
Absorption, 327
Access regions, 460
Activators, 326
Adsorbates, 48, 49
Adsorbed hydrocarbons, 234
Air exposure, 47, 49, 50
Alkali halides, 327, 332, 342
Alloy liquid metal ion sources, 472
Alpha–emission, 334, 335
Alzheimer's disease, 465
Amelogenin, 340
Amorphization, 462, 474
Amorphized, 258
AMU, 474
Anaglyph, 167
Analytical potential, 73
Anderson screening, 272
Angle of incidence, 77, 80, 84
Angular current density
  averaged, 33, 34, 37
  definition, 33
Angular emission, 5
Anneal, 32, 47, 49, 50
Aperture mechanism, 16
Aperture plane, 16
Ar, 473
Areal dosage, 21
Aspect ratio, 472, 490
Astigmatism correction, 18
Atomic, 249
Atomic force microscopy (AFM), 397, 457
Atomic layer deposition (ALD), 453
Atomic mixing, 300
Atomic weight, 473
Attenuation effect, 249, 250
Au, 473
Auger neutralization, 207
Auger process, 120, 121

B
Background features, 232
Backscattered helium, 210, 326
  imaging, 215, 218
Backscattered ion (BSI), 129, 158
Backscattering, 267, 399
Backward sputtering, 476
Backward sputter yield, 477
Band gap, 246
Band structure, 326, 328, 330
Barrel distortion, 18
Base excision pathway (BER), 454
Base vacuum, 8
Be, 473
Beam acceleration energy, 474
Beam alignment, 15
Beam blanking, 19
Beam convergence angle, 138
Beam energy, 473
Beam extraction, 14
Beam induced damage, 21
Beamlets, 149
Beam profile, 472
Beam tail, 478
Best imaging
  field, 51
  voltage, 39, 41, 48, 53, 57
Bilayer, 247
Binary collision approximation, 275
Binary collision model, 66, 68, 79
Biological samples, 165
Biomarkers, 448
Biosensing, 449
Blanking plates, 285
Blister, 213
Blood clot, 168

© Springer International Publishing Switzerland 2016
G. Hlawacek and A. Gölzhäuser (eds.), *Helium Ion Microscopy*,
NanoScience and Technology, DOI 10.1007/978-3-319-41990-9

Boden, Stuart, 190
Bohr radius, 207
Bond order, 73
Born-oppenheimer approximation, 72
Boron nitride, 250
Boundary, 247
Brenner potential, 74
Brightness, 5
  average, 33
  definition, 33
  practical, 33
BSI-to-SE conversion, 133
BSI yield, 131
Bulk, 474
Butterfly wing, 167
BSHe, *see* backscattered helium

C
Cancer, 465
Can controller, 290
Carbon, 216
Carbon foil, 284
Carbon nanomembranes (CNMs), 226
Catalysts, 195
Cathodoluminescence, 327, 329, 336, 343
Center of mass system, 271
Channeling, 159, 206
  contrast, 158, 211
  critical angle, 206, 207, 210
  dip, 211
  electron, 209
  map, 218
  transparency model, 209, 211, 212
Channeltron detector, 284
Characteristic length, 345
Characterization, 245
Charge
  compensation, 229
  fraction, 275, 276
  neutralization, 165, 481
Charging, 246, 253, 254
Chemically amplified resist (CAR), 403
Chemical purifier, 10
Chemical vapor deposition, 195
Chromatic aberration, 12
Chung-Everhart model, 124
Circuit edit (CE), 471
Closest approach, 271
CNMs, 242
CNMs on solid supports, 229
Cobalt, 218
Collision cascade, 69, 80, 81, 84, 297, 335, 343
Coloration, 332
Color–center, 332, 335, 342
  alpha–center, 333
  F–center, 333, 335, 337
  H–center, 333, 335
  M–center, 339
  nitrogen–vacancy, 342
  self–trapped exciton, 334, 335, 339
  V_F–center, 334
  V_k–center, 334, 339
Column magnification, 13
Column magnification factor, 14
Comparison between HIM and SEM, 227
Composite systems, 237
Compositional/elemental contrast, 155, 158
Condenser lens, 11
Conductance population, 461
Conduction band, 126
Conservation of energy, 267
Constant fraction discriminator, 287
Contaminant, 41, 47–49, 251, 472
Contrast, 195, 247, 253
Controllability, 472
Copper, 213
Correlative, 320
Correlative microscopy, 313
Corrosion, 51
CORTEO, 288
Coulombic repulsion, 65
Coulomb potential, 271
Coulter counter, 448
Covalent bonding, 73
Cr, 473
Critical dimension (CD), 481
Critical distance, 54
Cross-linking, 226
Cryogenic Cooling, 6
Crystal, 219
  bcc, 211
  fcc, 211, 219
  twins, 214
Crystalline, 261, 476, 474
Crystallographic orientation, 159
Crystal structure, 69, 257
Cu, 474
Current density, 478
Cy3, 463

D
2D hexagonal boron nitride, 83
2D imaging, 298, 306
2D nanomagnets, 416
2D materials, 226
2D transition metal dichalcogenide, 84
3D, 167
3D elemental imaging, 306

3D imaging, 298
Damage, 163, 190, 249, 260, 331, 332, 472
Damage density, 473, 476
Damage Mitigation, 491
De Broglie wavelength, 13
Debug, 471
Dechanneling, 159, 217
  defects, 221
  surface reconstruction, 218, 221
  thin layers, 218
Defect, 217, 218, 326–329, 331, 334, 342, 344, 345
Defect classification, 78
Defect concentration, 81
Defects, 256
Deflection system, 16
Density functional theory, 72, 84
Depletion layer, 280
Depletion region, 157
Depth of field, 166
Depth of focus, 197
Depth profiles, 298, 305, 318
Depth resolution, 308
Detection limit, 308
Detector resolution, 268
Detectors, 24
Device, 253
Dielectric, 253
Dielectric breakdown, 449
Diffraction, 12
Diffusion, 464
Diffusivity, 474
Dimension, 252
Dimensions of the collision cascade, 307
Dislocation, 218, 220
Dislocations, 474
Displacement cross-section, 67
Displacements per atom (DPA), 435
Displacement threshold, 66, 67
Distribution, 476
DNA, 448
Dopant, 217, 340
Dopant contrast, 157
Doping, 257, 489
Dose, 21, 246, 261, 474
  rate, 21
  -response curve, 397
  -to-clear, 398
  -to-size, 398
Double deflection, 16
Double-focussing magnetic sector, 314
Double-focussing magnetic sector instrument, 305
Double layer graphene, 238
Double vacancy, 78
Drilling of nanopores, 242
Dual scattering, 272
Dynamic range, 297

E
Edge resolution, 164
Elastic scattering, 64
Electric field, 14
Electrodes, 251
Electron beam (EB), 484
Electron beam lithography (EBL), 395
Electron emission
  kinetic, 207, 209
  potential, 207
Electron flood gun, 165
Electron Holography, 439
Electronic collisions, 400
Electronic properties, 257
Electronic stopping, 75
Electron MFP, 120, 125
Electrostatic analyzer (ESA), 281
Electrostatic charging, 232
Elemental composition, 266
Empirical potential, 73
Energy distribution, 255
Energy filter, 281
Energy filtration, 133
Energy loss, 269, 477
Energy spread, 5, 472
Equations of motion, 70
Escape depth, 155
Everhart Thornley, 150
Exciton, 326
Exposure latitude, 398
Exposure margins (EM), 410
Extraction system, 315
Extractor, 14
Extreme-UV lithography (EUVL), 484

F
Förster resonance energy transfer (FRET), 461
Fabrication, 474
Faceting, 32, 50, 51
Failure analysis (FA), 471
Faraday cup, 285
Fast fourier transformation, 219
Fault isolation (FI), 471
Field evaporation, 32, 39, 41, 43â€“45, 48, 49, 53, 54
Field ion microscopy, 32, 37, 47, 48, 49, 53, 54, 58, 59
Fields of views (FOV), 229
Filters, 238

Final lens, 11
First lens, 11
Flood energy, 254
Flood gun, 253
Flood time, 254
Fluorescein, 340
Fluorescence, 461
Fluorophore, 161, 339, 340
Focal plane detectors, 316
Focused ion beam (FIB), 449, 471
Focused ion beam lithography, 396
Force field, 73
Forward scattering, 399
Forward sputtering, 476
Forward sputter yield, 477
Fragmentation, 297
Freestanding, 247
Free-standing foil, 226
Frenkel pair, 333, 335
Full width at half maximum (FWHM), 478
FFT, *See* Fast fourier transformation

G
Gallium (Ga), 471, 473
Gallium arsenide (GaAs), 214, 328
GaN, 328, 329
GaP, 328, 329, 331
Gas assisted etch (GAE), 38, 44, 477
  constant field, 44, 45
  forced evaporation, 44, 45
  nitrogen, 38
  oxygen, 51
Gas chemistry, 478
Gas field ion source (GFIS), 3, 31–33, 45, 53, 55, 56, 59, 471
Gaussian, 247, 478
Genetic sequencing, 465
Germanium, 218
GFIS-assisted modifications, 416
GFIS Gun performance, 4
Gold, 16, 210, 213
Gold-capped nanoparticles, 238
Graphene, 67, 68, 77, 164, 226, 242, 237, 474
Grazing angle, 140
Growth rate, 334
Gun, 149

H
Hamiltonian, 71
Heatbath, 75
He+ ion, 464
Heisenberg uncertainty principle, 56
Helium (He), 472, 473
Helium ion beam lithography (HIL), 395
Helium ion beam milling, 410
Hexamer, 39, 45, 46, 48, 49
High materials contrast, 226
High resolution, 162
High-speed video, 463
High-TC superconductors, 419
Homopolymers, 463
Hydrocarbon, 255
Hydrocarbon contamination, 163
Hydrogen silsesquioxane (HSQ), 403

I
IL intensity, 334
Image intensity, 27
Image shift, 18
Imaging, 319
Imaging gas, 32, 37, 54, 58
  helium, 38–41, 51
  neon, 40–42, 51, 52
Imaging resolution, 307, 472
Immunofluorescence, 161, 339
Impact parameter, 65, 67
Implantation, 332, 472
Implant range, 473
Impurity, 328
Inelastic scattering, 66
InGaAlP, 328
InGaN, 328
InP, 329
In situ laser annealing, 493
Insulating, 249
Insulating samples, 165
Integrated circuits, 157
Intensity, 250
Interaction volume, 151, 153, 336, 343, 344, 472
Interatomic force, 70, 71
Interatomic potential, 64, 72, 74
Invasiveness, 486
Ion beam induced damage, 474
Ion beam induced deposition (IBID), 486
Ion beam sculpting, 449
Ion channeling, 70, 81, 84
Ion channeling contrast, 155
Ion current, 31–33, 36–38, 56–58
  stability, 57–59
Ion dose, 451
Ion–electron interaction, 121, 143
Ionic resistance, 451
Ionisation, 301
Ionisation probability, 303
Ionization potential, 40–42, 54, 58
Ionoluminescence, 161, 325
Ion optical column, 11

Ion source technologies, 473
Ion species, 472
Ion stopping, 269
Ion trajectories, 273
Iron, 213
  ions, 326
Isotope ratios, 306
Isotopes, 297

J
Janus nanoparticles, 239
Josephson junctions, 417

K
Kinematic factor, 268

L
L'Ecuyer screening, 271
Lacey carbon, 235
Lamella, 490
Large area CNMs, 236
Laser chemical etching (LCE), 489
Lateral over-etch, 478
Lateral resolution, 291
Lateral resolved element analysis, 290
Lateral scattering, 436
Lattice, 249
Layers, 249
Lead
  ions, 326
Leak valve, 10
LEIS, 282
Lift out, 490
Light, 325
Light element ion, 472
Limit of structure size, 278
Linear cascade regime, 298
Line-width roughness (LWR), 397
Liquid metal ion source (LMIS), 472
Liquid nitrogen, 7
List mode, 290
Lithium, 472
Lithographic control, 451
Lithography, 395, 396
Lithography with nanomembranes, 242
Local critical dimension uniformity, 407
Local element analysis, 291
Localization, 257, 261, 463
Low energy ion scattering, 275
Low energy spread, 13
Low temperature ion source (LoTIS), 472
Luminescence, 325
  cathodo, *See* cathodoluminescence
  extrinsic, 326
  intrinsic, 326
  iono, *See* ionoluminescene
  photo, *See* photoluminescence

M
Machining mechanism, 472
Magnetic sector mass spectrometers, 305
Magnetic spectrometer, 267
Magnetic stylus, 416
Magnetism, 416
Magneto-optical ionization sources (MOTIS), 472
Magnification, 476
Magnonic devices, 433
Manganese
  ions, 326
Many-body problem, 70
Mask, 485
Mask repair, 471, 484
Mass range, 305, 313
Mass resolution, 268, 297, 304, 313
Mass spectrometer, 297, 298, 304, 305, 317
Material selectivity, 472
Matrix effect, 298
Mean free path (MFP), 121
Membrane, 472
Mesoporous silica, 164
Mica, 139
Micro channel plate (MCP), 210, 283, 284, 286
Micrographs, 474
Milling, 260
Mineral, 336
  apatite, 326
  calcite, 326
  fluorite, 338
  garnet, 338
  ruby, 337
  sapphire, 328, 336
  sodiumchloride, 332
Modification, 245, 332
Molecular dynamics, 67, 70
Molecular dynamics codes, 76
Molybdenum (Mo), 16, 132, 135
Momentum transfer, 66
Monoexponential, 458
Monovalent streptavidin (MS), 456
Monte Carlo, 151, 155
Monte-Carlo simulation, 123, 275, 276
Moore's Law, 471
Morphology, 245, 252
MoS2, 257
Multi-collection system, 315
Multiple scattering, 272, 288
Multi-scale simulations, 76

N
NaCl, 332, 343. *See also* mineral, sodiumchloride
Nano-bubbles, 476
Nanodevices, 245
Nanodiamonds, 342
Nanofabrication, 411
Nanoimprint lithography (NIL), 408
Nanomachining precision, 472, 478
Nanomagnets, 433
Nanoparticles, 340
Nanopores, 160, 229, 260, 474
Nanoribbon, 259
Nanospheres, 238
Nanostructures, 256
Nanotip, 32
Nanowire, 214, 331, 416
  coreshell, 331
Neon (Ne), 472, 473
Neutralization, 253
N–lines, 337
Nuclear scatterings, 401
Nuclear stopping range, 476
Numerical integration, 70, 75

O
Objective lens, 11
Optical axis, 15
Orientation mapping, 214
Oxygen flooding, 303

P
Parallel detection, 314
Para-sexiphenyl, 218
Particle detector, 267
Particles, 188
Passive voltage contrast (PVC), 482
Patch-clamp amplifier, 451
Patterning, 342, 344
Perforated CNMs, 238
Perforation, 240
Periodic boundary conditions, 75
pH, 454
Phase transition, 434
Photoluminescence (PL), 461
Photon, 325
Pulsed beam operation, 285
Pincushsion distortion, 18
Pixel-dose optimization, 409
Plasma cleaner, 157, 163
Plasma ion source, 472
Plasmon, 246
Plasmonic devices, 474
Platinum, 219
Plural scattering, 272
PMT, 25
Point-spread function (PSF), 346, 399
Polarizability, 40
Polycrystalline, 155, 158
Polydimethylsiloxane (PDMS), 230
Poly methyl methacrylate (PMMA), 402
Porous supports, 230
Positive magnetic patterning, 433
Potential emission, 120, 128
Potential energy, 71
Potential plasmon excitation, 121
Pre-amplifier, 287
Precision, 472
Precursor tip, 43, 44
Preferential sputtering, 258
Probe current, 11
Probe size, 252
Process node, 478
Process technology, 471
Proximity effect, 399
Pt, 135
Pulse generator, 286

Q
Quadrupole, 18
Quadrupole mass spectrometers, 304
Quantification, 303
Quantifoil, 227, 228
Quantitative evaluation of the area, 232
Quantum dots, 161
Quenching, 326, 329, 338, 342

R
Radiative centers, 462
Radiative decay, 288
Raman, 256
Rare–earth, 340
Rastering, 458
RBS cross section, 268
RBS spectrum, 270
Recoil cascade, 276
Recoils, 346
Reduced brightness, 12
Reflected ions, 138
Reflected ion yield (RIY), 140
Reflection coefficient, 141
Reflection ion microscopy, 138, 161
Reflectivity, 484
Re-ionization, 282
Relative sensitivity factors, 304
Residue, 251
Resist, 395
Resist activation map, 409

Resist contrast, 397
Resistive pulses, 447
Resolution, 13, 40, 53–55, 252, 397
RLS-tradeoff, 397
Rutherford backscattering spectrometry, 265, 267

S
Sample preparation, 471
Satellite, 41, 46, 53, 55
Saturation magnetization, 433
Scaling, 472
Scan and acquisition system (SAS), 26
Scanning Electron Microscope/Microscopy (SEM), 119, 471
Scanning transmission ion microscopy (STIM), 137, 458
Scanning transmission micrograph, 243
Scan parameters, 335
  beam current, 335
  pixel spacing, 336
Scattering, 153, 343
Scattering angle, 66, 268
Scattering integral, 65
Scattering kinematics, 267
Schrödinger equation, 71
Scintillator, 25
Screening, 65, 207, 271
  Thomas Fermi, 207
Screening effect, 271
Screening function, 271
SE3, 130, 134
Secant law, 153
Secondary electrons (SEs), 119, 150, 396
  diffusion, 208, 211
  emission, 207
  coefficient, 207
  generation, 207
  rate, 207
  yield, 212, 220, 472
Secondary ions, 297
SE contrast, 134
SE energy distribution (SEED), 120, 123
Selectivity, 484
Self-assembled monolayer (SAMs), 155, 217, 226
Semiconductor, 327, 471
Sensitivity, 247, 255, 297, 308, 397
Sensitizer, 326
SE yield, 151
Shadow cone, 208
Shank angle, 56
Shot noise, 395
SiC, 328
Signal chain, 24
Signal loss, 326
Signals, 150
Signal-to-noise ratio (SNR), 22, 456, 472
Silicon (Si), 213, 217, 471, 474
Silicon dioxide, 327
Silicon nanospheres, 238
Silicon nitride (SiN), 242, 450
Silver, 219
SIMNRA, 270
SIMS, 297
SIMS imaging, 306
SIMS instruments, 304
Simulation, 473
Single atom tip, 38, 41
Single-stranded DNA binding protein (SSB), 454
Single vacancy, 78, 83
Solid nitrogen, 7
Solid state detector (SSD), 280
Soot, 188
Source, 149
Spatial and temporal precision, 480
Spatial resolution, 307
Spectrum, 328, 329, 333, 337
Spectrum simulation, 272
Spherical aberration, 12
Spot size, 53–55
  sigma, 53–55
Sputtering, 256, 276, 278, 299, 449
  atoms, 326
  rates, 258
  yield, 67, 299, 472
SRIM, 122, 269, 276, 288, 345
SS-nanopore arrays, 448, 453
Static capacitive contrast (SCC), 157, 482
STE, *See* color–center, self–trapped exciton
Stereo
  imaging, 167
  pair, 167
Sticking coefficient, 49
Stigmator, 18
Stoichiometry, 257
Stone-Wales defect, 78
Stopping power, 123, 269
  electronic, 207, 327
Sub-nanometer, 246
Substrate, 77, 190
Subsurface
  damage, 492
  imaging, 216
Superconductivity, 416
Supertip, 32
Surface

distortions, 476
sensitivity, 154, 219, 275
terminations, 155
topography, 128
Secondary electron
emission directional, 208, 209
yield theory, 208, 209

T
Tail, 478
TDC, 288
TEM
grid, 227, 232
imaging, 474
lamella, 490
Texture, 211
Thickness, 249, 250, 255
Thinning, 456
Three dimensions, 167
Threshold, 475
Time delays in ion columns, 20
Time-of-flight (ToF), 20, 285
Time-of-flight spectrometry, 283, 304
Timing invasiveness, 488
Time-to-digital converter (TDC), 287
Tip
radius, 39, 43, 44, 52
rings, 43, 51
shape, 31, 42–46, 50, 51, 56, 59
ToF spectrum, 287
Top-down, 456
Topographic contrast, 153
Total internal reflection microscopy (TIRF), 461
Transfer, 229, 251
Transfer procedures with polymeric media, 229
Transistor, 471
Transition metal dichalcogenide, 67, 69
Transition metal oxide (TMO), 195
Translocation, 452
Transmission, 159, 304
Transmission electron microscope (TEM), 449, 471
Transmission sputtering, 457
TRBS, 288
Tri-gate, 471
TRIM, 473
Trimer, 39, 56–58
Trimer lifetime, 5
TRYDYN, 276, 288
Tungsten, 213
Two-body system, 64
Two-dimensional (2D), 225, 245

U
Ultrafine drilling, 243
Ultrathin membranes, 226
Useful yield, 308

V
Vacancy distribution, 345
Via profile, 478
Vibrational considerations, 28
Virtual source size, 5, 13, 33
Visualization, 344
Voltage contrast (VC), 482
Voltage ramps, 17

W
Wave function, 71
Weibull growth model, 334
Wide-field, 463
Wobble, 16
Work function, 120, 124, 133, 135, 209, 220, 245, 249, 250
Wrinkles, 235

X
Xe, 473
XeF2, 478

Y
Yellow emission, 328
Yield, 247

Z
ZBL, 65
ZBL univeral repulsive potential, 75
Z-factor, 397